Shiva P. Pudasaini
Kolumban Hutter

Avalanche Dynamics

DYNAMICS OF RAPID FLOWS OF DENSE GRANULAR AVALANCHES

Springer

Avalanche Dynamics

Shiva P. Pudasaini · Kolumban Hutter

Avalanche Dynamics

Dynamics of Rapid Flows of Dense Granular Avalanches

With 225 Figures and 15 Tables

Springer

Shiva P. Pudasaini

University of Bonn
Faculty of Mathematical and Natural Sciences
Department of Geodynamics and Geophysics
Nussallee 8
53115 Bonn, Germany

Kolumban Hutter

Bergstrasse 5
8044 Zürich, Switzerland

The cover pictures: Snow avalanche deposition in the Alps (Photo: Swiss Federal Institute of Snow and Avalanche Research, Davos, Switzerland) and Laboratory avalanche simulation with a mixture of sand and gravel at the Department of Mechanics, Darmstadt University of Technology, Darmstadt, Germany.

Library of Congress Control Number: 2006928957

ISBN-10 3-540-32686-3 Springer Berlin Heidelberg New York
ISBN-13 978-3-540-32686-1 Springer Berlin Heidelberg New York

Springer is a part of Springer Science+Business Media

springer.com

Cover design: Erich Kirchner, Heidelberg
Typesetting and production: LE-TEX Jelonek, Schmidt & Vöckler GbR, Leipzig

Printed on acid-free paper - 54/3100/YL - 5 4 3 2 1 0

Notation and List of Symbols

Here we give a brief account of the mathematical notation that we use. We assume that the reader is familiar with the fundamentals of vector and tensor calculus. We shall use the classical notation. Scalars are written in italics, vectors and tensors in bold small or capital Roman letters. Spatial coordinates are written as (x, y, z) or (x^1, x^2, x^3); the letters x, y, z are not reserved for Cartesian coordinates. Often they denote the three mutually perpendicular axes of a curvilinear coordinate system. The letter t is reserved for time. The operators $\partial(\cdot)/\partial x$ and $\partial(\cdot)/\partial t$ denote partial derivatives of $(\cdot)$ with respect to x and t, respectively; ∇ is the Nabla (del) operator, $\nabla\mathbf{u}$ the gradient of the vector or second rank tensor $\mathbf{u}$, in Cartesian tensor notation written as $\partial u_i/\partial x_j = (\nabla\mathbf{u})_{ij}$ or $\partial A_{ij}/\partial x_k = (\nabla\mathbf{A})_{ijk}$. The divergence, curl and dyadic tensor product operations are written as $\nabla\cdot\mathbf{u}$, $\nabla\cdot\mathbf{A}$, $\nabla\times\mathbf{u}$, $\mathbf{u}\otimes\mathbf{v}$, respectively, and possess the Cartesian components

$$\nabla\cdot\mathbf{u} = \frac{\partial u_i}{\partial x_i}, \quad \nabla\cdot\mathbf{A} \,\hat{=}\, \frac{\partial A_{ij}}{\partial x_j}, \quad \nabla\times\mathbf{u} \,\hat{=}\, \epsilon_{ijk}\frac{\partial u_k}{\partial u_j}, \quad \mathbf{u}\otimes\mathbf{v} \,\hat{=}\, u_i v_j.$$

We have used the so-called EINSTEIN summation convention according to which summation is understood over doubly repeated Latin indices and we have used $\hat{=}$ as a correspondence relation and not an equality sign. Moreover, the KRONECKER delta and the epsilon-tensor are defined as

$$\delta_{ij} = \begin{cases} 1, & \text{for } \ i = j, \\ 0, & \text{for } \ i \neq j, \end{cases}$$

$$\epsilon_{ijk} = \begin{cases} 1, & \text{if } \ i,j,k \ \text{ are even permutations of } 1,2,3, \\ -1, & \text{if } \ i,j,k \ \text{ are odd permutations of } 1,2,3, \\ 0, & \text{if } \ i,j,k \ \text{ are no permutations of } 1,2,3. \end{cases}$$

For the derivation of field equations referred to curvilinear coordinate systems, we restrict considerations to orthogonal coordinates and distinguish covariant and contravariant components of tensors by writing components as superscripts and subscripts, respectively. Ultimately, equations are referred in these cases to unit basis vectors with components being called physical. For details, see [42, 43, 222].

Latin Symbols

Symbols	Definition
a	Acceleration, characteristic speed in first-order hyperbolic PDE
a, a_1	Coefficients in avalanche equations, see (6.60)
A	Scalar coefficient in the momentum equations, see (3.58), (3.60)
$\mathcal{A}$	Area
$\mathbf{A},\ \mathbf{A}_x,\ \mathbf{A}_y$	Matrices arising in the general conservation laws
b	Variable or index defining or characterising the basal surface
B	Scalar coefficient in $\mathbf{B}$, variable defining the pitch of a helix, see (9.8)
$\mathbf{B}$	(2×2) matrix arising in the momentum equation (3.60), binormal vector
$\overline{\mathbf{B}}$	Vectorial variable defined in (3.66)
$C,\ c$	Drag coefficient
$C_1,\ C_2,\ C_3$	Coefficients in avalanche equations, see (6.64), (6.66)
d, D_P	Particle diameter
$\mathrm{d}x$	Increment of x
$\mathrm{d}s$	Increment of the arc length s
D	Scalar coefficient arising in the momentum equation (3.60)
$d^s,\ d^b$	Accumulation rate at the free surface, sedimentation rate (deposition rate) at the basal surface
e	Coefficient of restitution
$\mathbf{e}$	Unit 2 vector
E_b	Entrainment
$F,\ \mathbf{F}$	Friction force
F^b	Function defining the basal surface
F^s	Function defining the free surface
$f(t)$	Semi-width of an elliptically shaped avalanche
$\mathbf{f}$	Vector valued function in the general conservation law
$\mathbf{f}_\alpha$	General vector valued function depending on parameter α
$\mathcal{F}$	Flux function
$\mathcal{F}$	(2×2)-flux matrix arising in the momentum equation (3.60), Serret–Frénet matrix
g	Gravity constant
$\mathbf{g}$	Gravity vector, Vector valued function in the general conservation law
$\mathbf{g}_i,\ \mathbf{g}_1,\ \mathbf{g}_2,\ \mathbf{g}_3$	Basis vectors
$\mathbf{g}_i^* = \mathbf{g}_i/\lvert\mathbf{g}_i\rvert$	Unit basis vector
$g_{ij},\ g^{ij}$	Covariant, contravariant metric tensors
$g(t)$	ξ-value of margin position, avalanche semi-length
h	Thickness, depth of an avalanche
H	Typical avalanche thickness
$H_0,\ H_{\max}$	Maximum depth of an avalanche

$h_{i,j}^n$	Numerical value of h at spatial point i, j and time slice n
$\mathbf{i}$	Unit vector in the x-direction
I	Light intensity
$\mathbf{j}$	Unit vector in the y-direction
K_{act}	Active earth pressure coefficient
K_{pas}	Passive earth pressure coefficient
$K_{\text{act/pas}}$	Active or passive earth pressure coefficient
$K_x,\ K_y$	Earth pressure coefficients in the x, y-directions
$K,\ K_{\text{wall}}$	Parameter quantifying the wall dependence of the bed friction angle
L	Typical avalanche length or extent, radius of the rotating drum
$M,\ m$	Mass of a body
$N,\ \mathbf{N}$	Normal stress, unit normal vector
$\mathbf{n},\ \mathbf{n}^b,\ \mathbf{n}^s$	Unit normal vector, of the base and the free surface, respectively
O	Order symbol, origin of a coordinate system
p	Pressure
p_L	Longitudinal pressure
$\mathbf{P}$	Depth integrated pressure, coefficient in first-order ODE
$\mathbf{p},\ p_{ij},\ p_{xy}$	Pressure tensor, its ij- and xy-components
$\mathcal{P} = 2\pi B$	Pitch of a helix
PIV	Particle image velocimetry
PTV	Particle tracking velocimetry
q	Dimensionless coefficient in the VOELLMY drag
Q	Coefficient in first-order ODE, mass flux
r	Radial distance
$\mathcal{R}$	Radius of curvature
$\mathbf{r},\ \mathbf{r}^r$	Position vectors
$\mathbf{R}$	Position vector
R_{II}	Cross correlation function
$R_C,\ R_D,\ R_F$	Particular correlation functions
s	Variable, index characterising the free surface, arc length
$S,\ \mathbf{S}$	(Negative) shear force, shear traction
$s_x,\ s_y$	Driving accelerations arising in the momentum equations, see (3.37), (3.38)
$\mathbf{S},\ \mathbf{S}_V,\ \mathbf{S}_C$	Drag: Total, viscous, COULOMB
t	Time
$\mathbf{T}$	Unit vector tangential to a curve
TV	Total variation
TVD	Total variation diminishing
u	Velocity, x-component of the velocity vector
u	Depth averaged velocity
$\mathbf{u},\ \mathbf{u}_b$	Velocity vector, at the base

$\overline{\mathbf{u}}_c$	h-weighted average centre of the mass velocity vector
$\tilde{\mathbf{u}} = \mathbf{u} - \overline{\mathbf{u}}_c$	Difference velocity relative to the centre of mass
$U^n_{i,j}$	Cell average of a field variable at point ij and time slice n
$u^n_{i,j}$	Numerical value of u at the spatial point i, j, and at time slice n
v	Velocity, y-component of the velocity vector
v	Depth averaged velocity
V	Avalanche volume
w	Velocity component in the direction of the z-coordinate
$\mathbf{w}$	Vector of unknowns (conservative variables) in the general conservation law
x	Coordinate in the direction of a curve, arc length
x_0	Initial value of x
X	Cartesian coordinate in the horizontal direction
$x_f,\ x_r$	Position of the front and rear margins of an avalanche
$\mathbf{x}_c$	Centre of mass position
Y	Cartesian coordinate in the horizontal direction
z	Spatial coordinate, usually perpendicular to the avalanche base
Z	Cartesian coordinate in the vertical direction (against the direction of gravity)
z_T	Distance between the master curve of the channel and the talweg

Greek Symbols

Symbols	**Definition**
α	Parameter in a general function representation
α_s, α_B	Adjustable coefficients in avalanche equations, see Table 6.2
$\beta_x,\ \beta_y$	Earth pressure-dependent terms in the depth integrated momentum equations
β	Exponent of $\varepsilon,\ 0 < \beta < 1$
γ	Exponent of $\varepsilon, 0 < \gamma < 1$
Γ^k_{ij}	CHRISTOFFEL symbol of the second kind
$\mathbf{\Gamma}^k$	Components of Γ^k_{ij}
δ	Bed friction angle
δ_{eff}	Effective bed friction angle
$\Delta^b,\ \Delta^s$	Scale factors (3.85) at the base and free surface, respectively
$\Delta\delta$	Difference of friction coefficient in the front and in the rear
$\Delta x,\ \Delta y$	Increment in x and y, finite difference grid lengths
Δt	Increment in t, finite difference time step
ε	Aspect ratio ($= H/L \ll 1$)
ζ	Inclination angle, coefficient in coordinate representation (4.8)
ζ_s	Basal friction angle

η	Coordinate in the y-direction co-moving with the centre of mass, coefficient in coordinate representation (4.8), dimensionless coordinate in the fixed point transformation (5.6)
θ	Azimuthal angle
κ	Curvature of the reference, basal topography
λ	Interparticle distance
$\lambda = L/\mathcal{R}$	Topographic curvature parameter
$\lambda_\tau = L/\mathcal{R}_\tau$	Topographic torsion parameter
Λ	Parameter in coordinate representation, see (4.13), Parameter in rotating drum modelling, see (6.22)
μ	Friction coefficient ($= \tan\delta$), numerical viscosity, fixed-point coordinate in the η-direction (transverse coordinate)
$\mu_s = \tan\zeta$	Friction coefficient
$\overline{\mu}$	Mean friction coefficient
$\mu_F,\ \mu_R$	Value of the friction coefficient in the front and in the rear
$\Delta\mu = \mu_F - \mu_R$	Difference of friction coefficients in the front and in the rear
ν	Fixed-point coordinate in the ξ-direction, coefficient in upwind scheme
ξ	"Viscosity" coefficient in the VOELLMY drag, coordinate in the x-direction co-moving with the centre of mass
$\Xi = \varepsilon/q$	Alternative VOELLMY drag coefficient
Π	Dimensionless parameter measuring the pressure dependence of the bed friction angle
ω, Ω	Angular velocity
Ω_0	Constant angular velocity of the rotating drum
ρ	Mass density per unit volume
ρ_b	Basal density
ρ_0	Constant reference density
ρ_P	True density of particles
σ_j	Slope limiter in the TVD method
τ	Time, (geometric) torsion, shear traction
$\boldsymbol{\tau}$	Shear stress
τ_c	Collisional shear stress
τ_f	Frictional shear stress
ϕ	Internal angle of friction, flux limiter in the TVD-method
φ	Accumulation of torsion
ϕ^{LW}	LAX–WENDROFF flux limiter
ϕ^{BW}	Beam–Warming flux limiter
minmod_ϕ	Minmod flux limiter in TVD
superbee_ϕ	Superbee flux limiter in TVD
Woodward_ϕ	WOODWARD flux limiter in TVD
ϕ^{TVDLF}	TVD LAX–FRIEDRICHS flux limiter
ψ	Parameter in coordinate representation

Miscellaneous Symbols

Symbols	Definition
$\dfrac{d}{dt}$	Material (total) time derivative
$\dfrac{D}{Dt}$	Time derivative following a singular surface
$\dfrac{\partial}{\partial t}$	Partial (local) time derivative
$\dfrac{\partial}{\partial x}$	Partial derivative with respect to x
sgn (x)	$= \begin{cases} -1, & x < 0, \\ +1, & x > 0 \end{cases}$
∇	Nabla (del) operator
$\langle f \rangle = \dfrac{1}{h}\displaystyle\int_{-h}^{0} f \,\mathrm{d}y$	Depth average of f
$\hat{(\bullet)}$	Dimensionless version of $(\bullet)$
$\overline{(\bullet)}$	$= \dfrac{1}{\mathcal{A}}\displaystyle\iint_{\mathcal{A}} (\bullet)\,\mathrm{d}a$, areal average of $(\bullet)$, or
	$= \dfrac{1}{h\mathcal{A}}\displaystyle\iint_{\mathcal{A}} h(\bullet)\,\mathrm{d}a$, h-weighted areal average of $(\bullet)$, or
	$= \dfrac{1}{h}\displaystyle\int_{b}^{s} (\bullet)\,\mathrm{d}z$, depth-averaged value of $(\bullet)$
$[\![(\bullet)]\!]$	$= (\bullet)^{+} - (\bullet)^{-}$, jump of $(\bullet)$

Preface

The writing and compilation of this book was initiated by an invitation of R. Lancellotta from the Department of Structural and Geotechnical Engineering of the Polytechnical Institute in Turin, Italy, for us to hold an intensive graduate level course on the *continuum description of granular materials*. The course was held in Turin, at the Polytechnical Institute, from 8 to 12 April 2002 and a first set of notes was distributed to the approximately 35 participants of course [82]. Subsequently, it was decided to substantially revise and extend these notes and to publish them. The topic was further dealt with in a course held at the Swiss Federal Institute of Technology, Zürich, Switzerland, at the Department of Earth Sciences and it was targeted in parts in an extensive course in January 2003 for the Institute for Geotechnical and Tunnel Engineering, University of Innsbruck, Austria, for graduate and undergraduate students, as well as civil servants and engineering and science specialists from the industry in Obergurgl, Austria. In addition numerous talks were held at many universities, research laboratories and conferences to publicise the topic.

With this book we have several intentions in mind. Firstly, to publish our own work on rapid flows of cohesionless granular materials down inclined topographies. This work was developed by a relatively large number of undergraduate and PhD students, postdoctoral research fellows, as well as guest scientists and friends. Moreover, it has reached a stage at which a summary and a critical overview may be helpful for ourselves, and anybody else who is interested in this field, in order to document its important results and to elucidate the generality of the model now known in the literature as the Savage–Hutter model and its generalisation.

Secondly, even though the model equations and their extensions, which have been presented in peer reviewed, reputed international scientific journals, have received adequate attention by the specialized scientific and technological community, we feel that the model has not yet sufficiently attracted the interest of those who could use them with profit in practice, nor are its different possible extensions that fit with the interests of the people from diverse disciplines adequately known. In fact, we firmly believe that the model equations presented in this book can, if properly used, serve as a routine

tool to estimate the probability of potentially endangered zones being hit by avalanches. Moreover, with a sufficiently flexible software for the integration of the pertinent equations, this tool may further help to serve efforts to protect inhabitated regions more precisely, and perhaps it may also make the lives of inhabitants of such regions safer.

Thirdly, in the geophysical environment avalanches occur in a variety of circumstances. Mention might be made of rock and snow avalanches, landslides of catastrophic soil release, debris flows, mud flows, gravity driven motions of volcanic ash, and turbidity currents (underwater avalanches). Industrial examples are flows of cereals, pharmaceuticals, alumina, coal and concrete in storage facilities, production lines, power stations, and construction sites. Although these examples might seem of a disparate nature, they do in fact have many common features and their mathematical description can be based on very similar physical principles. This indicates that the same or nearly the same concepts have been applied to avalanching processes in different fields of science and engineering specialities with little or no knowledge of each other's work. Evidently, much profit can be gained from a broader, more general approach that highlights the common and disparate features. Thus, even though the primary intention of this book was a focus on snow avalanches, it has become much broader with time and it is now the rapid motion of cohesionless granular materials, possibly dispersed with interstitial fluids.

Fourthly, the model equations focussed on in this book are depth integrated versions of the balance laws of mass and momentum, and as such involve idealising approximations that may or may not be sufficiently satisfied. Furthermore, the equations are based on a dry granular concept and thus employ a one-constituent continuum formulation, and the derivation of the depth integrated equations is based on mathematical simplifications. All these simplified prerequisites constitute limitations that need to be quantified or delineated, if the model equations are to be used to constrain their applicability, both physically and mathematically. Such a detailed analysis will certainly enhance confidence in the model equations on the one hand, and, on the other hand, the careful presentation of the deductions will also provide hints to the alert reader to find his/her own model(s) for avalanching granular flows or debris flows for situations outside the range of validity of the equations presented in this book.

Fifthly, our past experience has told us, by both looking at the achievements of others as well as our own, that a new scientific idea or concept – no matter how small – does often not receive the attraction it deserves, if it is only published through its original paper(s). Books seem to be more effective, if they treat the topic from its entirety and if concepts are framed such that they are easily understood by a general readership. We hope to have achieved this goal.

Inevitably, the book summarises our own research; nevertheless, we have first presented a fundamental and conceptual background circumscribing avalanche dynamics and have then framed the central theoretical model by setting it within the context of the dynamics of the rapid flow of cohesionless granular materials under the action of gravity. In so doing, the scope and extent of the applicability of the model equations becomes evident not only as a model for dense flow avalanches of snow, but equally also for debris flows, landslides and sturzstroms, and for water saturated mud flows, after a relatively simple extension. Furthermore, the theoretical concepts were also motivated from a viewpoint of field events of snow avalanches and activities to control their occurrence. It is hoped that this will motivate the reader to cope with the intellectual difficulties that are unavoidable in a model of such complexity.

Conceptually, the book is written in a style that should be accessible to readers with a background in engineering and natural sciences, such as civil and mechanical engineering, geophysics and geology, but equally also applied mathematics and physics. The mathematical prerequisites that are used do not go beyond those that are generally covered in these fields. The spirit is educational as well as research oriented. A wealth of information contained in the applied avalanche and debris flow literature is touched upon and discussed in brief.

The book focuses on avalanches of snow. This is particularly motivated, because our own first and foremost involvement was with applications of the topic to snow avalanches. Therefore, a substantial part of the motivating arguments were developed with this type of catastrophic mass flow in mind. Such a view may even be historically correct, as the development of the rational scientific description, using physically and mathematically-based formulations of these catastrophic flows has first been done for these kinds of geophysical applications. We therefore also think it appropriate to give brief historical accounts of snow avalanche research in those countries worldwide that are exposed to snow avalanche catastrophes. However, the topic of dry granular avalanches equally applies to lahars, large mass rock falls, as well as to rapid flows of grains and gravel in the industrial context. We will also mention these applications, and indeed our own laboratory experiments have been exclusively performed with various sorts of grains: sugar, salt, poppy seeds, sand, gravel, glass and plastic beads, etc. This thus illustrates the great variety of applications.

Most of the first writings were done by S.P. Pudasaini. These were quickly discussed and homogenised by K. Hutter and S.P. Pudasaini, and revised by both authors with several extensions and iterations.

The work obviously profited from the works of many of K. Hutter's former students and postdoctoral assistants who, with their diploma (MSc) and PhD dissertations, and along with the joint publications contributed

immensely to the advancement of the development of the science of dry granular avalanches. We especially mention: W. Eckart, J.M.N.T. Gray, R. Greve, T. Koch, R. Lang, Y. Nohguchi, C. Plüss, Y.-C. Tai, M. Wieland, Y. Wang and T. Zwinger. The very early work also profited from the association of K. Hutter with S.B. Savage (prior to 1989), from the occasional association with the Swiss Federal Institute of Snow and Avalanche Research under the leadership of directors M. de Quervain and C. Jaccard (prior to 1992), the senior scientists B. Salm and H.-U. Gubler, and, later, the creative interaction with D. Issler, Davos/Altendorf; D. McClung, Vancouver; A. Mangeney–Castelnau, Paris; S. Noelle, Aachen; E.B. Pitman and A.K. Patra, Buffalo, New York state; R. Iverson and R. Denlinger, Vancouver; C. Ancey, Grenoble and Lausanne; S.S. Hsiau, Chung-Li and R. Katzenbach, Darmstadt on modelling, numerics and experimentation. The writing also profited indirectly from the programme "Granular and Particle-Laden Flows" which K. Hutter co-organised at the Isaac Newton Institute for Mathematical Sciences, Cambridge University, United Kingdom from 1 September until 19 December 2003, together with J.M.N.T. Gray, University of Manchester; T. Mullin, University of Manchester and J.T. Jenkins, Cornell University. Through their talks and in extensive discussions these scientists broadened our horizon and influenced our work, in later stages.

We asked individual scientists from countries in which snow avalanches play an important role to write a brief account on snow and avalanche research as it has evolved in the past approximately 100 years and received very constructive response. The help from these scientists is acknowledged in the places where their work has been used.

We also wish to mention the help that we received from N. Kirchner (University of Kaiserslautern). She took on the burden of reading the entire book, found weaknesses, clumsy formulations, drew our attention to inconsistencies in the formulation, and simply found many remaining typing errors despite our painstaking scrutiny of the text. We emphasise our appreciation and express our deep gratitude.

Similarly, three anonymous referees read a preliminary manuscript and commented in detail on particular aspects. This led in part to substantial changes and extensions. We trust that our manuscript has profited from this involvement. We would like to thank the referees for the time and efforts they devoted to our text. In writing this book we also profited immensely from the secretarial help of R. Rutscher and A. Maurer, who typed many drafts of extended and iterated versions of different chapters, especially in the final stages of writing. Our departmental librarian C. Aull painstakingly checked and united our reference list of about 470 entries. We would like to thank them very much for their contributions.

Finally, we thank all those who have supported us in this endeavour; above all the *Deutsche Forschungsgemeinschaft* (DFG) and the Darmstadt University of Technology for their continuous support since 1987, former and present PhD students and postdoctoral researchers for the fruitful collaboration that made this book possible, the authors and publishers for allowing the publication of so many figures. We also thank Springer-Verlag and especially C. Caron for publishing this book. As a matter of fact, a book has to be abandoned be finished. We have tried to make this text as perfect as possible. As always, errors remain, and for those we offer our apologies. Any suggestion from the readers pointing them out or suggesting improvements would be appreciated.

Darmstadt University of Technology
Darmstadt, 2005

Shiva P. Pudasaini · Kolumban Hutter

Table of Contents

Part IV Experimental Validation of the Theoretical Prediction with Different Measurement Techniques

Part I

Introduction, Conception and the Importance of Avalanche Research

1 Introduction

1.1 Motivation

Avalanches, debris and mudflows and also landslides are natural phenomena that occur in mountainous regions on our globe on a regular basis. They, therefore, are as such a common phenomenon for inhabitants of mountainous regions such as the Alps, the Himalayas or the Rocky Mountains, who have learned to accept their occasional occurrence and to avoid the accompanying damages. Nevertheless, accidents involving damage of life and property and devastating singular incidences have regularly occurred in the past. These are the major reasons why in such regions the study of avalanches is a topic of public concern that is of permanent significance. The *physics of the formation* of the rapid motion of a large mass of soil, gravel or snow and the *dynamics of the motion* must be understood, if the danger induced by the release of a certain mass of gravel, snow or soil is to be avoided, or the impact of a moving mass on the avalanche track or on obstructing buildings is to be estimated. One hopes that an understanding of their physical basis will enable the appropriate defensive measures to be taken.

The last few years have witnessed increased efforts devoted to the physical understanding of avalanche formation and motion in complex topography. More specifically, whilst any forecast of avalanche occurrence and estimation of size is still largely a question of experience, the motion of a given loose mass of gravel, snow or soil is more amenable to analysis. This is so because the physics of the motion of a finite mass of soil or snow may be less difficult to understand than the physics of the mass release from a soil or snow slope at rest.

This book is an attempt to provide a survey and discussions about the motion of avalanches and debris flows from initiation to run-out. To a large extent it summarises research that was conducted by the authors and many other coworkers and research fellows during the past 20 years and it brings the description to the forefront of present day research. However, we have also summarised and explicitly incorporated the research work done elsewhere by other scientists, engineers and researchers in the related topics of avalanche and debris flow dynamics. It is hoped to demonstrate that today's method

of the determination of the avalanche motion along its track promises to give to the avalanche practitioner a tool with the aid of which fairly reliable predictions of avalanche motion along its track can be made, from initiation to run-out. The model computations also allow inferences as to the distribution of the mass of gravel or snow in the deposition zone, as well as to the forces exerted on structures that are affected by the motion of the avalanche. This, in short, is the aim of this book.

To achieve this aim, the well known depth-integrated avalanche model of SAVAGE and HUTTER [375] has been generalised in different stages since the early nineties of the last century from simple to arbitrary channelised topographies, the intention being that the different extensions of the model would be able not only to describe the flow of a finite mass of snow, gravel, debris or mud, down a corrie of arbitrary curvature and twist, and arbitrary cross-sectional profile, but equally also the transportation of grains or pills in the agricultural and pharmaceutical industry, respectively. The emerging equations for the distribution of the avalanche thickness and the topography-parallel depth-averaged velocity components, to be derived in this book, are a set of hyperbolic partial differential equations. Once they are derived, new significant technical problems must be solved in order to judge their adequacy. The question arises as to how these equations are solved numerically, and how experiments are conducted to compare theoretical results with corresponding experimental findings. Both subproblems pose challenging questions, as we shall now briefly outline.

There were earlier attempts than that due to SAVAGE and HUTTER to propose forecast procedures for the dynamics of avalanches. HARBITZ [142] collects and summarises a great number of such models in the Snow Avalanche Modelling, Mapping and Warning in Europe (SAME) report of the "Fourth European Framework Programme: Environment and Climate" and discusses in a multi-author effort (*i*) statistical-empirical, (*ii*) dense snow, (*iii*) slush flow (*iv*), powder snow, (*v*) coupled dense-powder snow and (*vi*) subaquatic avalanches. In 50 pages of the SAME report a great number of avalanche models for dense avalanching flow of snow or granular materials are presented. Among these are *block models* (VOELLMY [430], PERLA et al. [315], DADE and HUPPERT [71], SALM [361, 362, 363, 364], SALM et al. [365], SALM and GUBLER [366], GUBLER [134]), *centre of mass models* (IRGENS et al. [187], NOHGUCHI [300], MAENO and NISHIMURA [261]), *quasi-two-dimensional models* (BARTELT and GRUBER [25], SARTORIS and BARTELT [368], BARTELT et al. [26]), *the biviscous modified Bingham model* (DENT [78], DENT and LANG [79]), *hydraulic-models* (EGLIT [84, 86, 87, 88, 90, 91], EGLIT and SVESHNIKOVA [85], GRIGORIYAN et al. [130], BLAGOVESHCHENSKIY and EGLIT [35], BLAGOVESHCHENSKIY et al. [36], DANILOVA and EGLIT [69, 70], KULIKOVSKIY and EGLIT [230], MIRONOVA and EGLIT [284], GRIGORIYAN [133], GRIGORIYAN and OSTROUMOV [131, 132], MIRONOVA [282, 283], OS-

TROUMOV [308], VOLODICHEVA et al. [432]), *quasi-two-dimensional viscoplastic models* (NOREM et al. [302, 303]), *quasi-two-dimensional multi-material models* (HUNGR [163]) and more. These works have in common that they are either rigid body models or founded on shallow geometry of the deforming mass. Differences may lie in the particular constitutive assumptions and in details how the shallow geometry is incorporated in the model. Many of these models are very close in structure to our model and lead to hyperbolic field equations in which advective terms play a significant role, as is the case, e.g., with the shallow water or SAINT VENANT equations of hydraulic channel flow.

Depth integrated models, obeying material constitutive laws, very similar but not identical to ours, have also been proposed in the dry debris/pyroclastic flow literature, but on the whole these papers came later and essentially used the earlier literature of the SAVAGE–HUTTER equations and some of its extensions as a basis. Research figures in this branch of granular avalanche dynamics are IVERSON, DENLINGER and LOGAN from the United States Geological Survey [74, 75, 192, 194]. Similar attempts were and are still being undertaken by an interdisciplinary group of engineers, geologists, geophysicists, mathematicians and numerical modellers at the State University of New York at Buffalo (PATRA et al. [313], PITMAN [318], PITMAN and NICHITA [319], PITMAN et al. [320, 321, 322], SHERIDAN et al. [385, 386, 387]). A further group of geophysicists and mathematicians at the University of Paris shares a similar interest in the spreading of dry granular masses from volcanic eruptions (Montserrat) and from a suddenly freed cylindrical deposit (FÉLIX and THOMAS [98], LEGROS [248], MANGENEY–CASTELNAU et al. [264, 265], LAJEUNESSE et al. [237], BOUCHUT et al. [38], BOUCHUT and WESTDICKENBERG [40]). These three latter groups, apart from the presentation of the equations, which all are based on depth averaging of the balance equations of mass and momentum and basically use frictional phenomenological laws, concentrate on the numerical integration of the deduced equations, which are generally hyperbolic and strongly convective.

Successful modelling of strongly convective hyperbolic equations is one of the most challenging problems in computational fluid mechanics, particularly when large gradients of the physical variables occur, e.g., for a moving front and boundary, or possibly arising internal shock waves in a granular avalanche. Shock formation is an essential mechanism in granular flows on an inclined surface merging into a horizontal run-out zone or encountering an obstacle when the velocity becomes subcritical from its supercritical state. This phenomenon is akin to the *sonic boom* in aerodynamics or the *hydraulic jump* in open channel flows. In the latter case, a subcritical (supercritical) flow possesses a slower (faster) velocity than the shallow water wave speed. A transition from a supercritical state – say the flow down a weir – to a subcritical state in the shallow channel below the weir must for continuity reasons be

accompanied with an increase in water depth. This transition is immediate, i.e., it takes place over a very small distance, making local surface gradients very steep. Ideally, the transition is discontinuous and manifests itself as a *jump*; realistically, i.e., in the experiment, the depth change occurs over a certain small distance, sometimes referred to as a diffusive jump or diffusive shock.

These properties of the physical system are mathematically expressed in special forms of the model equations, hyperbolic partial differential equations that require special numerical integration techniques capable of resolving the steep gradients and moving margins often observed in experiments and field events but not captured by traditional finite difference schemes. Today these are available in different versions of comparable performance and have brought the science of avalanche modelling an important step ahead.[1]

Several numerical simulations of avalanching flows from simple to complex topographies, incorporating curvature as well as torsion of the topography, demonstrate fundamental, physically interesting and practically applicable results. The original theory of SAVAGE and HUTTER [375] and their various extensions are proven to be useful in different scenarios. Moreover, the recent generalisation of the theory by PUDASAINI and HUTTER [335] for arbitrary channel topography and its numerical simulations disclose the complicated physics of flows of avalanching debris through strongly curved and twisted channels and opens an enormous spectrum of applications. In principle, the theory can be applied to any kind of topography – from a simply inclined plane to very complicated arbitrarily curved and twisted channels in industrial as well as geophysical mass flows down mountain valleys from initiation to the deposits in the run-out zones. It is at this juncture where the models of the IVERSON and PITMAN groups differ in important details from the models by PUDASAINI and HUTTER [335] and BOUCHUT and WESTDICKENBERG [40]. The ultimate aim of all models is to establish numerical solution techniques, in which direct use of geographical information systems (GIS), applied to mountainous avalanche prone regions, can be applied. This aim is materialised by using the shallowness approximation, referred to different basic coordinates. The IVERSON and PITMAN groups, and partly also the French group, refer the equations to horizontal and vertical Cartesian coordinates and define avalanche thicknesses vertically, not accounting for the differential geometric (e.g., curvature) properties of the mountain surface. This implies that slope angles must be small. PUDASAINI and HUTTER use curvilinear coordinates that allow better approximation of the basal topographic differ-

[1] Technically, these methods are known as non-oscillatory central (NOC) differencing schemes with total variation diminishing (TVD) limiters, or finite difference schemes using the method of characteristics, which often involve the so-called RIEMANN solvers, etc. The specialized literature is large and developing rapidly, see Chaps. 7 and 8.

ential geometric properties. They define the height and shallowness properties (nearly) perpendicular to the bed, at least to the extent that the curvature and twist of a master curve following the talweg of a valley or corrie affect the equations. Alternatively, equations that are constrained by the real topography were been presented recently by Bouchut and Westdickenberg [40]. Their equations closely account for the differential geometric properties of the basal topography, at least to the extent that digital elevation software allows the pointwise reproduction of the mean and Gaussian curvatures. Pudasaini et al. [341] have shown that the differences in the choice of the curvilinear coordinates and the definition of the orientation of the depth over which the three-dimensional equations are integrated to arrive at two-dimensional equations are significant in realistic avalanche scenarios. This makes future numerical modelling of avalanche dynamics more difficult than one might have initially anticipated.

Avalanche motion is difficult to observe and systematically record in nature, the reason being that the release is unpredictable unless the avalanches are artificially triggered, but equally important is that they are devastating. This is the reason why in natural avalanches only the deposit, its mass distribution and the reconstructed track are generally known. Occasionally, remote sensing techniques are used to record the moving snow, especially the front velocity as a function of position [7]. The disadvantage of such in-situ experiments is that they always contain uncontrollable components. Laboratory experiments have the advantage that almost all aspects are controllable and that errors may, therefore, be more easily estimated. Furthermore, if it can be shown that the laboratory avalanche can be up-scaled according to well-defined rules, then agreement between computed avalanche quantities and their measured counterparts in the laboratory allows inferences for the natural avalanche. This is indeed the case.

In the past, different experimental techniques, such as photogrammetry and light sheet projections were used to measure the evolution of the geometries of the flowing and deforming granular piles, e.g., of sand, gravel and quartz, on the laboratory scales, sliding down confined and unconfined, as well as straight and curved chutes, and also chutes with humps. To this end, fast speed technical measurement cameras were used. Examples of a large number of laboratory experiments and a comparison of their output with results of computations performed for the model equations will be given in Chaps. 10 and 12. Hutter and associates (Chaps. 10 and 12), Iverson and others [74, 194], McDougall and Hungr [272, 273, 274], Pouliquen [329] and Pouliquen and Forterre [330] have independently performed such experiments. Good to excellent correlations between the theory and the laboratory experiments have been generally established.

One of the dynamical aspects of an avalanche is its velocity distribution. It is very important for practitioners to have a proper knowledge of the velocity

field in order to estimate the impact pressures (on obstructions and infrastructures), stress and strain rates and so on, in the course of an avalanche sliding down a mountain topography. From a structural engineering and planning point of view, one must know the velocity field in order to design buildings, roadways and rail transportation in mountainous regions. Equally important is the fact that one is always keen to know the velocity field of flowing granular materials and fine granulates through various channels in process-engineering scenarios in order to predict the flow dynamics. In this regard, the final task is the corroboration of the physical adequacy of the model equations, the efficiency of the numerical method and their harmony with the (laboratory) experiments performed under essentially well-controllable circumstances together with an advanced measurement technique.

Recently, the particle image velocimetry (PIV measurement technique) was used by PUDASAINI and PUDASAINI et al. [334, 343] to measure the dynamics of the velocity distribution of free surface flows of avalanches down curved chutes merging into horizontal planes. To our knowledge, such experiments had not been performed before. Ultimately, it will be demonstrated that the theory, numerics and the experimental results are in excellent agreement with one another.

Remark A further specification may be necessary regarding the determination of the velocity distribution in plane view and with depth, because it is the cause of certain different views among present day specialists. Researchers focusing on the physical basis of gravity driven dense granular flows tend to distribute the transfer of the shearing through the moving avalanche layer, while modellers, with the aim of constructing a forecast model for the dynamics of avalanches in a given terrain, focus their attention on an accurate description of the velocity field parallel to the terrain and dispense with a detailed description of the velocity profile perpendicular to the terrain. This attitude is the heart of all depth-integrated models. We have shown that, except for a small number of rather extreme cases, the collapse of the shearing region to the basal surface has a very small effect on the evolution of an avalanche along its track, as well as in the deposits [183].

1.2 Goals, Methods and Structure

1.2.1 Goals

There were three main aims in writing this book. They are as follows:

– One of our basic tasks was to collect and present a systematic development of depth-integrated continuum mechanical hydraulic models of flow avalanches. Particular emphasis has been given to the development of a continuum avalanche model and the creation of a new theory that can model

flows of debris and avalanches down non-trivial and complicated mountain topographies in geophysics, as well as flows of dense powder and granulate bulk materials through general channels in process engineering scenarios (see [335, 375]).

- Of equal importance is to solve the complicated time-dependent non-linear hyperbolic model equations thus developed to describe flow avalanches from initiation to deposit in the run-out zones. Solutions of these equations should capture the underlying physics of the whole process. Therefore, the sophisticated modern numerical integration methods that are capable of capturing shock discontinuities must be applied. Such methods exist, have been and are still being developed in the mathematics and engineering communities. They have found implementations in the finite difference, finite volume and finite element techniques of solving hyperbolic partial differential equations. As one of the major challenges of debris flow is concerned with the underlying topography, we must be able to apply these numerical schemes to different topographic configurations – from simple to complex bed geometries, so that they can serve as a benchmark status for practitioners.
- Do the model equations represent the physics we are looking for? Or are they merely calculations for some artefacts? Are the numerical schemes that we are using reliable and able to cope with the physics of the model equations? The proper answers to these questions can only be established through field and/or laboratory experiments. The ultimate goal should thus be the corroboration of the theory and numerics with the experimental measurements regarding the velocity distribution and the evolution of the depth profile, as well as the impact pressures when an avalanche slides down a given topography from initiation to the deposit, describing the entire dynamics. To achieve this goal, some modern measurement techniques, such as digital-photogrammetry, particle image velocimetry and laser technology should be utilised.

1.2.2 Methodology

In order to achieve these lofty goals, various advanced methodologies must be used. For the physical-mathematical modelling of avalanches one needs advanced knowledge of the differential geometry, partial differential equations, material properties, flow rules and dynamical aspects of large as well as small-scale geophysical fluid dynamics. Due to the hyperbolicity and non-linearity of the model equations, they can only be solved properly with the help of the above-mentioned numerical schemes that damp oscillatory phenomena but are so weak in numerical diffusion that steep gradients can still be reproduced. Furthermore, in laboratory experiments the particle image velocimetry (PIV) measurement technique is used to measure the velocity distribution of the particles at the free surface and at the bottom of the

avalanching mass (see PUDASAINI and PUDASAINI et al. [334, 343]). PIV measurements can also be used to determine the evolving boundary, whereas penetrometers can be used to measure the depth profile of the deposit of the avalanche. However, for proper measurement of the three-dimensional evolution of the avalanche geometry one should use digital-photogrammetry or the laser-beam technique. Special measurement cameras (e.g., TMK 21) can be used to take a pair of stereo images of the avalanche (e.g., deposit) and through the stereoscope one can have a three-dimensional visualisation of the avalanche. Analytical stereo-evaluation devices (e.g., AC3) can be utilised to determine the free surface of the avalanche. In the field, non-invasive techniques are primarily used. Video recordings are classical. The DOPPLER radar method allows determination of the velocity (and density) profile with depth. Seismic and acoustic sensors have also been used, as have been plates installed into avalanche prone slopes prior to snow deposit, with built-in pressure and shear traction transducers. Invasive techniques also use load cells installed in dams or masts to measure impact pressure. Classical pitot tubes, light emitting diodes, capacitance probes and acoustic transducers are employed to measure pressures, arrival times of moving avalanche fronts, densities and velocities. The topic requires knowledge of advanced experimental techniques, is highly specialized and the literature is vast. For a recent in-depth review, see ISSLER and others [189, 190].

1.2.3 Structure

The entire book is divided into five parts: introduction, theory, numerics, experimental validation and avalanche protection.

Part I consists of two chapters. The first chapter presents the introduction and motivation for avalanche research, and the necessities for avalanche studies. Snow avalanche hazards, and fatalities and casualties from different kinds of avalanches are reported. Major international scientific activities in avalanche and debris flow research are discussed in brief, which provides a forum for researchers in the international community to exchange ideas on how to cope with avalanche and debris flow hazards. Chapter 2 provides a wide and general definition of avalanche dynamics as a rapid motion of large-scale geomaterials like snow and debris down the side of a complicated mountain terrain. Dynamical aspects of avalanches, such as their tracks, run-out zones and impact pressures, are discussed in brief. Some important and fundamental applications of avalanches, both in geophysics and process engineering scenarios, are presented. Other aspects contained in this chapter are the division of avalanches into flow and powder types, and intermediate states between them. A survey on some classical avalanche models is presented. The limitations and drawbacks of the classical models indicate the necessity of a new model.

Part II contains four chapters, the first two dealing with the developments of continuum mechanical theories for different topographic descriptions. A short review of a continuum mechanical theory of granular avalanches flowing down a basal topography of which the talweg lies essentially in a vertical plane aligned parallel to the steepest descent (main flow direction) is presented in Chap. 3. There, we put the avalanche model equations into a frame of a theory that is well-defined and well-structured from both a mathematical and a physical point of view. The assumptions, inputs and outputs of the theory are listed in a systematic manner. Generalisations of the theory for two- and three-dimensional basal topographies are presented. Advantages and limitations of the theory are explicitly and systematically listed, which cannot be found in the other existing literature. Chapter 4 is very important; it presents a complete and detailed derivation of a recently developed theory for the gravity-driven free surface flow of an avalanche over arbitrarily curved and twisted topography. This is a very important extension of the original Savage–Hutter model [375]. The new theory includes the simultaneous effects of curvature and torsion on flow avalanches in channels, which could not be investigated before. This makes the theory applicable to realistic avalanche motions down arbitrarily guided topographies, such as valleys and channelised corries. Digital data from geographical information systems (GIS) of mountainous avalanche-prone regions can, in principle, be applied to this model in order to use the model in realistic situations and to construct hazard maps. Special features and the importance of the new theory are presented. It is shown that these new model equations, proposed by Pudasaini and Hutter [335], can reproduce all previous extensions of the Savage–Hutter equations as special cases. The theory is developed from a completely different topographical point of view, in which not only the talweg but also the entire basal topography can be curved and twisted. The model equations are put into standard conservative form to analyse the flow behaviour. Finally, a comparison of these model equations with previous equations is presented.

Chapter 5 outlines simple analytical solutions of avalanche equations for different cases. Similarity solutions for flows down inclined surfaces are derived explicitly. Steady-state exact solutions for avalanches occurring in rotating drum configurations with and without erosion are presented. Chapter 6 presents the importance of the avalanching motion to describe the mixing phenomenon of different granular materials in a thin gap between two circular discs. It is demonstrated that such phenomena can be exactly represented in a closed mathematical form. These exact solutions, although simple and restricted in nature, may serve as fundamental tools to provide analytical insight into the full understanding of the theory. Moreover, such solutions are always very useful for checking the performance of numerical methods and computed results before they are used to solve the full system of equations. Apart from this, the example allows a non-standard comparison of compu-

tational and experimental results on particle mixing in avalanching flows. In this chapter, an alternative model describing the flow and mixing of granular material in a rorating cylinder is also presented. This model starts from information gained by nuclear magnetic resonance measurements of velocity that are in conflict with the exact solution obtained by our model. New stress closure is employed and approximations are slightly different from those of our model, but it is shown that a comparison of the new theoretical results with the corresponding results from measurements is quite convincing.

Part III is divided into three chapters. It deals with the numerical methods and simulations of the model equations (these are the hyperbolic partial differential equations mentioned earlier) presented in Chap. 4 for different topographic situations. High-resolution shock-capturing numerical methods are developed in Chap. 7. Numerical difficulties of the model equations in traditional numerical methods are discussed and appropriate modern numerical methods, such as NOC, ENOC (essentially non-oscillatory central differencing) schemes with different TVD limiters, are presented in detail for non-linear one-dimensional conservation laws. Similarly, Chap. 8 extends the one-dimensional shock-capturing numerical scheme of Chap. 7 to a two-dimensional system of conservative equations. This two-dimensional shock-capturing method is applied to the extended equations derived in Chap. 4. Chapter 9 deals with the numerical simulations of avalanches in topographies ranging from simple to complex configurations. The performances of various numerical schemes are discussed here. It is shown that the NOC scheme with the Minmod TVD limiter demonstrates the best numerical results for simulating avalanche dynamics with, among others (e.g., Woodward and Superbee), limiters and ENO cell reconstructions.[2] Firstly, numerical simulations are presented for simple and torsion-free topographies that include the basal surfaces: curved downhill but laterally flat; cylindrically curved downhill and channelised in the cross-slope direction – in both cases with constant and variable cross-slope curvatures. Simulations are presented for superimposed basal topographies with laterally flat and curved reference topographies. For all these cases, results are presented and discussed in detail. Secondly, a large number of simulations are performed for complex and non-trivial topographies. These topographies include uniformly and non-uniformly curved and twisted channels with constant and variable channel widths. It is shown via different numerical simulations that the new theory developed in Chap. 4 is able to include the simultaneous effects of curvature and torsion in the dynamics of an avalanching mass over (generally) curved and twisted (mountain) topography. This is an entirely new aspect in the field of avalanche research. These numerical simulations disclose uncovered physical features

[2] The technical terms are mentioned here for those readers having an expert knowledge of the numerical integration technique of shock capturing schemes. There are also other methods than those mentioned above that are capable of capturing shocks. Details will be given in Chaps. 7–9.

of avalanche processes and disclose some fundamental aspects of avalanches in order to judge the applicability of the new model equations in reality. Similarly, simulations are presented to investigate the sensitivity of the phenomenological parameters and the pressure dependence of the friction angles. It is shown that the dynamics of the avalanche is fairly sensitive to variations of the bed friction angle but less to the variation of the internal friction angle. Also, we have introduced a linear dependency of the bed friction angle on the overburden pressure of the granular pile. However, this destroys the scale invariance of the model equations.

Part IV deals with the experimental validation of the theoretical prediction of the model equations. There are three chapters in this part. Chapter 10 contains a wealth of information, necessary to conduct laboratory avalanche experiments. The design of the chute, selection of the material and phenomenological parameters, experimental set-up, experimental procedure and much more are presented in this chapter. It is also made clear that such laboratory experiments on avalanches are a necessity for any avalanche theory before the model is put into real practice, e.g., in land-use planning and hazard zoning it must be checked by small-scale, well-controlled laboratory experiments. A model that is not verified first by using ideal, well-controlled laboratory experiments has little chance of adequately reproducing natural phenomena, where input and boundary data are much less reliable. We explain in detail avalanche experiments on simple to bumpy chutes with or without sidewise confinements. The hard test of an avalanche model is its performance for avalanches across irregular three-dimensional terrain. This test is also performed in this chapter on two different levels. Laboratory tests of an avalanche on a realistic topography are compared with results from computations. These experiments were conducted in the US Geological Survey by Denlinger and Iverson and Iverson et al. [74, 194], at the University of British Columbia by McDougall and Hungr [273], and at the State University of New York at Buffalo by Patra et al. [313]. Comparisons of computational results with data collected from real events are also given. We shall reproduce descriptions by McDougall and Hungr [273, 274]. The coincidence is very encouraging. Chapter 11 gives a brief review of the theory of the PIV measurement technique that is primarily designed for velocity measurements in transparent fluids. Next, we introduce a "granular-PIV" in order to measure the velocity distribution of the particles at the surface and bottom of the free surface motion of an avalanche (see Eckart et al., Pudasaini and Pudasaini et al. [83, 334, 343]). Technical details, such as the set-up of the "granular-PIV" and particular and general problems arising in the "granular-PIV" are pointed out in brief. Chapter 12 presents experimental results and brings all items together (i.e., theory, numerics and experiments). It is unquestioned both from a conceptual as well as practical point of view that one should have proper knowledge of the velocity field. It provides information on the orders of magnitude of the specific momentum and kinetic

energy and thus gives hints as to the orders of magnitudes that the stagnation pressure may assume. The PIV measurement technique is used to measure the dynamics of the velocity distribution of an avalanching flow down a curved chute that merges continuously into the horizontal run-out zone. Similarly, the evolution of the avalanche boundary and the depth profile of the deposit are measured. Experimental details are explained and the problems are outlined. Excellent agreements between the theoretical predictions and experimental measurements are established.

Part V, which is divided into two chapters, focuses on avalanche protection and interaction between avalanching masses and defence structures such as catching dams, deflecting dams, avalanche splitters, avalanche mounds and galleries and fences. Chapter 13 presents a collective review of the most important avalanche defence and protection measures used to date in different countries in Europe and America. Before the construction of avalanche protection structures one must know the dynamic behaviour of the potential avalanche and debris flow hazards. How large can the avalanche be in some particular mountain sub-region, how fast can it move and how big an area may it occupy for settlement? These fundamental questions must be understood and solved before starting the construction of the protection structures, i.e., during the structural design of the houses, sheds and galleries in the avalanche and debris-flow prone regions. The basic theme of this chapter is practical structural design, and our presentation can only be a brief introduction that is not in-depth. Specialized literature is generally difficult to find because it is contained in internal reports of snow and avalanche research institutions and civil offices, and perhaps lecture notes of courses in earth science departments of some universities. Of interest may be Ancey's book on Dynamique des Avalanches [8], lecture notes by Salm et al. [367], and the reference listed in Sect. 1.4.2 on snow and avalanche research in various countries. Finally, Chap. 14 contains a detailed summary of the book and provides an outlook for future research.

1.3 Necessities for Avalanche Studies

Snow avalanches, landslides, rock falls and debris flows are extremely destructive and dangerous natural calamities. The frequency of occurrence and amplitudes of these disastrous events appear to have increased in recent years, possibly due to increase in development activities, anticipated warming of the Earth's atmosphere, the associated increase of extreme storms, poor forestry practices and land misuse in mountainous areas. This implies an increase in damage and consequently leads to large casualties. Mountainous regions are always gravely affected by such phenomena because they endanger public life and properties and infra-structures. Reliable methods for the prevention and/or reduction of the effects of such disasters are, therefore, of great need.

Evidently, civil engineers, forestry engineers and concerned authorities who are responsible for the planning and development in these regions have considerable interest in such methods.

1.3.1 Snow Avalanche Hazards and Fatalities

Avalanche conditions are usually caused by a combination of heavy snowfall, wind and changing temperatures. The number of avalanches falling annually in the United States is of the order of 10^5 and the number of avalanches falling annually worldwide is on the order of 10×10^5. Millions of snow and ice avalanches occur each year worldwide causing numerous casualties (American Avalanche Association). According to the US statistics (around 1986) about one percent of the total avalanches causes serious problems: injury, death and destruction of property. Based on this report, about 140 people are caught annually in avalanches, 60–70 are partly or wholly buried, 12 sustain injury, and 17 are killed. Average annual property damage is approximately $ 400,000. Austria and Switzerland each report 25–40 persons killed by avalanches per year, France 31, Italy 20–30, Japan 30, Norway 10–15, Germany 10 and Canada 7 [13]. Furthermore, the capital that is invested for direct and indirect *prevention* of damage and casualties due to snow avalanches is much more than the average amount spent on insurance claims, more than 50 million Swiss francs per year in Switzerland alone [180].

Snow and debris avalanches are natural hazards that occur in many parts of the world. They are responsible for casualties of injured and dead people, as well as the destruction of railways, bridges and houses. Avalanches are typically associated with steep mountainous areas. Early avalanche victims were travellers and soldiers. By the Middle Ages, the mountain valleys of the Alps were inhabited but a dramatic population increase occurred in the 20th century. The earliest reference to avalanche deaths is from the year 1118 in Iceland [33, 34]. Flury Sprecher von Bernegg (who was responsible for recording all kinds of unusual events occurring in the Davos environs) was the first to record avalanche related deaths in Davos, Switzerland. In 1449, he described an avalanche that destroyed 4 buildings and killed 11 people. Four people were buried for 24 hours but were rescued alive. This was the first entry in the Swiss avalanche history. The next entry was made on 16 January 1602 to describe a similar type of avalanche hazard in which 13 people were found dead under the snow; a fourteen year old girl was found alive after having been buried in the snow for 36 hours. Schneebeli et al. [382] compile the history of avalanche events in Switzerland from 1440 until 1999. According to this source, the most devastating years must have been 1689, 1749 and 1951, when 120, 129 and 98 people died, respectively. The source also indicates that there has been a continuous occurrence of avalanches throughout the years, often with between 10 and 30 deaths.

For France, Ancey [5] collects data in table form compiled by himself and Mougin [289]. It covers the entire history of the principal avalanche catastrophes in France and Andorra from 1408 until 1999, with many single incidences causing between 10 and 30 deaths and extensive property damage per annum. According to this source, the most tragic events occurred in 1601 in the villages Chèze and Saint Martin in the Pyrenees with 107 people dying. Another, very severe avalanche event, occurring in 1806 in the village Talau of the East Pyrenees resulted in 64 deaths. Consistent with the Swiss records, there has been a steady non-interrupted sequence over more than 500 years of avalanche history that documents a regular repetitive accident toll with property damage and deaths, on average more than 10 each year.

Two of the worst years in the avalanche history of Norway were 1679, when between 400–600 people were killed, and 1755, when about 200 people died, as records show [13]. Avalanche history in North America is just over a century old but full of devastating property damage and loss of human life. McClung [268] reports about the avalanche deaths in the Himalaya. From 1895 to 1979 some 200 mountaineers and porters died in avalanches, making this the greatest killer of a number of expeditions to the worlds highest mountains. Mt. Everest tops the list with 34 killed, followed by Nanga Parbat (20), Dhaulagiri (17), Manaslu (17) and Annapurna (12). As for the US in 1898, during the month of April alone, 72 gold seekers died in an avalanche, while another 49 were buried or caught in Alaska. "The worst disastrous avalanche in the history of the United States occurred on 1 March 1910 near the town of Wellington in Washington. The final death toll was 96, with 22 survivors among 118 victims. Beneath the snow lay two trains, three steam locomotives, four electric locomotives, a rotary snowplow, several boxcars, an engine shed, a water tower, and telegraph poles and wires!" [13]. Also a surprising fact is that during World War II, soldiers fought battles in the mountains of alpine regions and avalanches were used as weapons of destruction. Fraser [101, 102] estimates that some 40,000–80,000 soldiers were lost in the avalanche warfare. From the winters 1940/41 to 1978/88 more than 7,000 snow avalanches were recorded in Switzerland with damaged property leading to a total of 1,269 deaths. In Europe, a suddenly released debris flow in North Italy in August 1998 buried five German tourists on the superhighway "Brennerautobahn". The deadliest avalanches in recent years struck Southeast Turkey in 1992. Heavy snowfall resulted in about 10 m of snow. The thick layer of snow on the steep mountain side triggered numerous devastating avalanches over several days. Whole villages were buried and hundreds of people were killed. Included in that total are as many as 104 paramilitary police officers [469, 470].

The Alpine region of Europe is said to suffer more avalanches than any other region in the world. In two months (January and February 1999), more than 70 people were killed in avalanches throughout resort towns in France, Italy

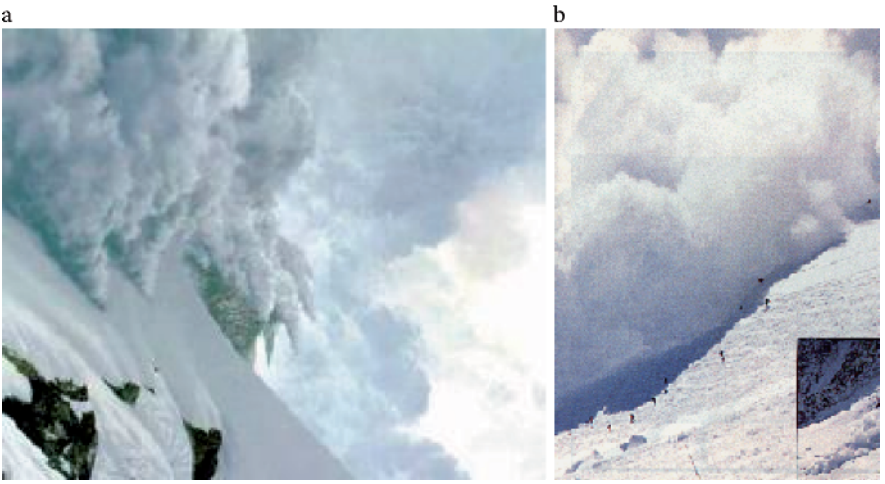

Fig. 1.1. Snow avalanches killed more than 30 people in the tiny town of Galtür, Austria in 1999 [451, 452].

and Switzerland, and the rest of Europe [454]. A four-week period, beginning in late January 1999, provided a tragic reminder that ski resorts are an environment prone to natural disaster, in Galtür, Austria and elsewhere in Europe (Fig. 1.1a,b). It was the worst alpine natural disaster in more than 40 years. On 25 February 1999, heavy snow in the central Alps provoked avalanches that killed more than 30 people. A snowslide hit the village of Galtür at more than 160 $\mathrm{kmh}^{-1} \cong 44\ \mathrm{ms}^{-1}$, while an avalanche as tall as a house plunged down the Chamonix valley in France. The heavy death-toll is the result of avalanches penetrating inhabited areas; as a rule, the victims are climbers, skiers and snowboarders on the slopes. However, what provokes the snowslide is often a skier or snowboarder: most victims die in an avalanche of their own making. For skiers going off-piste in unfamiliar terrain when there is an avalanche risk, an essential precaution is to be accompanied by a qualified mountain guide.

1.3.2 Debris and Mud Flows, Pyroclastic Flows and Lahars

Avalanches also occur in the form of the motion of soil or rock down mountain sides, usually mixed with uprooted bushes, trees and often containing water. When water does not play any significant role in the motion of these granular masses, geologists also talk of *avalanches* or *rockfalls* (if the material has broken off from a rock formation). If water is likely to be the triggering element of the soil motion, then the terminology is *debris flow*, even if eventually, i.e., during the catastrophic motion of the granular mass, the water can be ignored as a dynamic element. *Mud flows* are flows of soil and added

debris that is substantially mixed with interstitial fluid, and this fluid substantially contributes to the dynamics of the solid-fluid mixture. Mud flows are formed during heavy rains and storms when stagnant soil is soaked with water much like a sponge and then breaks loose. They can also arise in water swollen rivers in which the bed breaks loose and develops into a catastrophic sediment transport. Since these speeds are large and occur often suddenly, geologists also denote them as "*sturzstroms*", a terminology that has crept into English and, perhaps, can be translated as "*fallstreams*".

Volcanic eruptions also generate avalanching motions of debris. What is meant here are not the lava streams but the dense to dilute flows of volcanic ash down the mountain side. These flows are formed by the debris spat out by the volcano that is too heavy to stay completely airborne. It then forms a dense boundary layer flow of hot ash that may carry on it a more dilute, airborne component, moving down steep mountain flanks. This material is generally hot. Its debris flow is referred to as *pyroclastic* because of its considerable heat and burning temperature. Another denotation is *lahar*, but then it is understood that the flowing material is not only hot but also muddy and mixed with a large proportion of very fine components. Debris-flow hazards, including mud flows and pyroclastic lahars, are often caused by exceptional meteorological and geological events and are always only one part of a natural disaster. When initiating on steep slopes they can travel unexpectedly large distances before they come to rest. Their occurrence is largely unpredictable and in mountainous regions, like the Alps and the Himalaya, they continue to be a threat both to human life and property. Research in avalanche and debris flow prevention and the study of their dynamics are, therefore, important responsibilities of most mountainous nations.

Volcanic activity can ruin vast areas of productive land, destroy structures and injure or kill the population of entire cities. World-wide, volcanoes erupt regularly, about 50 each year. The emerging mass flows of surficial material include rock falls, debris flows or avalanches, often accompanied by large quantities of water. A debris flow associated with the eruption of Nevado del Ruiz in Columbia in 1985 resulted in the death of some 26,000 people and the destruction of 5,000 homes. Similarly, Ruapehu, a large complex volcano with a summit crater lake on the North Island of New Zealand has erupted four times in the past half century. This produced ash falls on the snow cap and caused the crater lake to overspill, producing more than 60 large mudflows. The debris flow resulting from the 1953 eruption destroyed the Tangiwai railroad bridge, killing 151 passengers on a passing train. The above-mentioned research groups in the US and France are working on such problems, see Sect. 1.1.

Figure 1.2 shows a view of the Gondo spitting mudflow of 14 October 2000, and the destruction of the village of Gondo (Switzerland) and roadways [457]. The rain that had been falling incessantly in the area around the village

Fig. 1.2. Destruction by mudflow and landslide. On 14 October 2000, the rain that had been falling incessantly in the area around the village of Gondo, Switzerland, for 48 hours triggered off a 10,000 m^3 spitting mud flow. The flow composed of mud and blocks caused 14 deaths and destroyed a dozen buildings, including the 400 year old Stockalper tower [457].

of Gondo for 48 hours triggered off a 10,000 m^3 spitting mud flow. The flow, composed of mud and blocks, caused 14 deaths and destroyed a dozen buildings.

Being a mountainous country, Nepal is frequently and badly affected by hundreds of landslides each year during the rainy season. The biggest and most massive landslides triggered by heavy monsoon rains in the year 2002 buried alive at least 44 persons and displaced nearly 228 families of two villages in the eastern hilly district of Khotang, 200 km southeast of the Nepalese capital Kathmandu. 42 persons were buried in their sleep in Sanmal village,

including seven members of a family and 13 travellers lodged for the night in one house. Another landslide buried two others in Dipsey village. The heavy rains triggered the landslides at 2 am, 15 July 2002. The landslides fell about two kilometres above the villages. Sixteen victims were rescued and airlifted to Kathmandu and nearby hospitals for treatment. Around 300 livestock were also killed by the landslides. Most of the people killed in the landslides were children and elderly people who could not escape from the areas in the night hours. A week later, in a period of five days, 94 persons were killed in Makwanpur district in floods and landslides triggered by rains, while 26 died in Kathmandu Valley. Similarly, in the last week of August 2001, in Khotang and Okhaldhunga districts, a landslide buried 15 houses. In the year 2000, floods and landslides triggered by heavy rains claimed at least 160 lives across the country [465].[3] Table 1.1 presents an overview of selected landslides worldwide of the last century [396].

The eruption of Mount Saint Helens in Washington State, 1980, which was the most destructive in the history of the United States, resulted in scores of injuries and the loss of 60 lives. The lateral blast, debris avalanche, mudflows, and flooding caused extensive damage. All buildings and related man-made structures in the vicinity of Spirit Lake were damaged or buried. Two hundred houses were destroyed and many more were damaged in Skamania and Cowlitz Counties, leaving many people homeless. The total cost of the destruction and damage caused by this eruption was about $1 billion.

Figure 1.3 shows the destruction of settlement and roads caused by debris flow in the Aosta-Valley in Italy. Similarly, Fig. 1.4 depicts the devastating debris slide in January 2001 in Las Colinas, El Salvador. This landslide was induced by an earthquake and may have buried as many as 500 homes. Figure 1.5a shows another debris deposition in a forest area of Taiwan with a huge amount of boulders on the surface of the deposition. Figure 1.5b represents quite a different situation. The picture demonstrates a moraine debris in Kyrgyzstan that might have been formed during the last Ice Age(s) by a glacier in Tuyk Valley, Alaarcha basin North Tien Shan. The moraine to the left has been displaced by a debris flow. Geologists conjecture that this debris could probably have been induced by a strong seismic wave.

The 1998 mudflow at Casito Volcano in Nicaragua caused thousands of deaths [323]. Massive mudslides are often generated by intense rainfall on

[3] Observations (since approximately 1980) indicate that debris and mud flow events in Nepal may increase dramatically in future. The likely reason has been identified as the retreat of glaciers due to climate warming. This process may lead to the formation of ice dammed lakes and lakes in the forefield of the glaciers that may frequently break out. These outburst events may generate tremendous flood waves moving down the valleys as catastrophic debris and mud flows. The increase in such devastating events has alerted international organisations to call for fundamental research and protective measures.

Table 1.1. Overview of the natural hazard induced by landslides in different parts of the world. * includes earthquakes, ** includes floods, data source [396].

Selected Landslides of the 20th Century		
Year	Location	Approximate Death Toll
1916	Italy/Austria	10,000
1920	China*	200,000
1945	Japan**	1,200
1949	Former USSR*	12,000–20,000
1954	Austria	200
1962	Peru	4,000–5,000
1963	Italy	2,000
1970	Peru*	70,000

Fig. 1.3. Deposit of devastating debris: showing the destruction caused by debris flow in the Aosta-Valley in Italy.

Fig. 1.4. Initiation, channelling, spreading and deposit of a devastating debris slide in Las Colinas (on the outskirts of San Salvador), El Salvador, January 2001. This landslide was induced by an earthquake and may have buried as many as 500 homes [460].

hillsides that are devoid of vegetation, often due to irresponsible deformation. Frequently, mudslides are triggered during other environmental catastrophes. A recent example is the devastating action of the Hurricanes Ivan and Jeanne that struck Haiti in September 2004 and caused approximately 3000 deaths. A large portion of casualties was due to the debris flow and mudslides that were triggered by the heavy rain falls that accompanied the hurricane while it struck the Caribbean area, and many of the casualties and much property damage is due to this secondary effect.

Another dramatic mudflow event was triggered by a huge glacier mass breaking off from Kolka glacier, triggering the mud-ice flow in the Genaldon Valley, North Ossetia on 20 September 2002. The estimated mass of ice set in motion was 115×10^6 m^3. It generated a huge flow of ice, water and debris that came to a halt 2 km from the village Gizel. 18 people died, 108 people remained missing, and a large number of buildings, electrical lines and gas pipe lines were destroyed (see HAEBERLI et al. and POPOVNIN et al. [136, 326]).

Remarks on Common Properties of Natural and Industrial Avalanches There are many common properties of natural and industrial avalanches. Usually, granular avalanches occur when a large layer of granular material becomes unstable. Rockfalls, landslides, debris flows and snowslab avalanches are examples of granular avalanches in geophysical contexts. Sim-

Fig. 1.5. a) Debris deposition in Taiwan (from [397], courtesy of Sino-Geotechnics, Sino-Geotechnics Research and Development Foundation, Taipei, Taiwan). **b**) Debris flow in Kyrgyzstan – Glacier moraines in Tuyk Valley, Alaarcha basin North Tien Shan. The moraine to the left has been displaced by a (probably seismically induced) debris flow. (Courtesy of V. Aizen, University of California at Santa Barbara.)

ilarly, flows in silos, hoppers, rotating drums and slag heaps are examples of granular avalanches in industrial applications (see Fig. 1.6). Another application of avalanching flow in industry is the coating of thin-films by generating avalanches made of powdery grains of the *micrometre* scale down an inclined surface that is to be coated by the powder. These flows are gravity driven with thicknesses of *milimetre* size, and the coated layers have *micrometre* thickness. Surprisingly, as long as cohesive forces between the particles are not effective, these tiny avalanche flows behave very similarly to gigantic geophysical mass flows. The physical principles seem to be much the same. So, although there is an enormous difference in the length-scale between geophysical and industrial avalanche flows, the dominant and principal physical mechanisms that drive the flows are similar. Dense flow avalanches of rock, ice and snow are gravity-driven flows that are observed in the natural environment on a very wide range of length scales. Gray et al. [123] mention that in geophysical contexts, rockfalls, landslides and snow-slab avalanches

Fig. 1.6. Piling of a mixed bed of granular materials in a cement factory; an example of granular flow and avalanche in process engineering. Different grey scales of the heap correspond to different ingredients of the mixture of the cement. The material is continuously deposited from a quasi-static point source. The material flows rapidly down the faces of the heap in shallow layers. During the downward flux of the fine mixture of granular material, particle segregation according to size, density or resilience takes place. (Courtesy of MVT Materials Handling GmbH, Dillingen.)

may set in motion up to 10^{10} m^3 of material, whereas in industrial flows in silos, hoppers, rotating drums and slag heaps the volume of the material is of the order of several cubic centimetres to several hundreds of cubic metres. Three key prehistoric events in rockslides are presented in Table. 1.2. These are huge events in the history of rockslides. In fact, it is believed that size effects enter into account only for very large avalanches [374].[4]

1.3.3 International Scientific Activities

The large number of calamities expressed in huge economic losses, as well as insured and dead people, are the reasons why the general assembly of the United Nations passed a resolution on 11 December 1987, designating the 1990s as the *International Decade for Natural Disaster Reduction*. This resolution was aiming at the promotion of international awareness and scientific research activities on natural and man-made disasters (for more details, see [396]). In Germany, the *Deutsches Komitee für Katastrophenvorsorge e.V.* is an active committee for disaster reduction within the *International Strategy for Disaster Reduction* (ISDR). Special, regularly held international conferences are devoted to these topics, e.g., CALAR (Concerted Action on Forecasting, Prevention, and Reduction on Landslide and Avalanche Risks)-*Conference on Avalanches, Landslides, Rock Falls and Debris Flows*, Vienna, January 2000. This conference was held under the auspices of the United

[4] This statement assumes that avalanches are dry or the effects of the interstitial fluid can be ignored. Pore pressure generates a size effect [339].

Table 1.2. Three key (huge) rockslides in the prehistoric period. *Frictionite* was observed in the case of Köfels. The table also demonstrates the long run-out of large events in terms of the total overall slope corresponding to the total overall distance travelled by the moving mass in the longitudinal flow direction. The data are taken from [94].

Prehistoric Huge Rockslides			
Event	Volume	Material	Overall slope
Flims (Switzerland)	10^{12} m^3	Limestone	0.07
Köfels (Austria)	10^{10} m^3	Augengneiss	0.18
Langtang (Nepal)	10^{10} m^3	Migmatite/gneiss	$--$

Nations International Decade for National Disaster Reduction/International Strategy for Disaster Reduction (IDNDR/ISDR), the International Association for the Study of Insurance Economics (the Geneva Association) and the International Society for Soil Mechanics and Geotechnical Engineering (ISSMGE). Similarly, INTERPRAEVENT annual conferences on the *protection of inhabited areas from flooding, debris flows, avalanches and slope movements* are being held every year with the following objectives: prevention and protection from natural hazards, promotion of research in the field of protection against flooding, debris flows, avalanches and slope movements, exchange of interdisciplinary experience at an international level in the field of science, techniques, ecology and economics. Furthermore, the first, second and third *International Conferences on Debris Flow Hazards Mitigation*, respectively, were held in San Francisco, California, USA; Taipei, Taiwan and Davos, Switzerland, in order to provide fora for debris-flow researchers in the international community to exchange ideas on how to cope with debris-flow hazards using the most advanced, state-of-the-art methodology both in mechanics and hazard prediction and risk assessment. This has drawn attention to the importance of reliable recognition of natural avalanche paths and predicting deposition zones.

Within the avalanche research community regular conferences, workshops and symposia are held that are exclusively devoted to snow behaviour in its cover and to avalanching motion of snow. The International Glaciological Society has held two conferences, in 1992 and 2000, that were exclusively devoted to snow, and additional conferences in 1996 and 1998, in which the dynamics and thermodynamics of snow and ice were central topics of interest. The society also held the International Symposium on Snow and Avalanches on 2–6 June 2003, in Davos, Switzerland. The conference proceedings, *Annals*

of Glaciology,[5] are a continuing source flow of the most recent research both from a fundamental and an applied point of view.

Apart from these international activities, there are numerous national and regional events organised and conducted by local universities, institutes, civil servant offices and societies.

1.4 A History of Avalanche Research

Avalanches occurred in the mountainous regions throughout the Holocene (and earlier), and people in the Alps have been continuously exposed to the devastating events and forced to live with them. Documentation of catastrophic events is reported in local annals and community periodicals, and for Switzerland and France excerpts of those are given by Schneebeli et al. [382], Mougin [289] and Ancey [5]. Such reports have also been collected for Iceland by Jónsson et al. [208] and include landslides from volcanic eruptions. These writings from the Middle Ages show that common people who lived in the mountains and travellers or postal officers who were frequently exposed to avalanche danger had a good understanding of its nature. It is also known that scientific geologists in Europe in the Middle Ages ridiculously debated about the nature of rocks, and the different contenders were called volcanists and neptunists, but many people living near volcanoes in Iceland (and presumably also elsewhere) know the nature of igneous rocks quite well. It appears that during this early scientific phase lay persons were ahead of scientists.[6]

Within the scientific community, the field of snow and avalanche research is relatively new and young. Until the 20th century scientists had not attempted any systematic studies of the physical aspects of the mountain snowpack, mechanical forces causing avalanches or avalanche dynamics. Winter mountaineering and skiing seems to have become fashionable only at the beginning of the last century. Interest in avalanche research developed gradually due to mountaineering and skiing. First avalanche studies took place in the European Alps around the beginning of the 20th century and half a century later in the United States. Serious research in this field was started in 1936 when the Swiss founded their own Snow and Avalanche Research Institute in Davos [349]. Subsequently, similar centres were established in France, Canada, USA, USSR/Russia and other countries as well. These institutes are now leading centres for fundamental and applied avalanche research.

---

[5] The particular volume numbers are 23, 27, 30, 32 and 38.

[6] T. Johannesson, from the Icelandic Meteorological Office, personal communication.

1.4.1 Early History

There exists a great number of historical reports on snow avalanches. ARMSTRONG and WILLIAMS [13] and HUTTER [180] have given reports on the early history. The first historic record of an avalanche encounter may have been in the third century B.C. when the Carthagian general HANNIBAL led his army on an epic crossing of the Alps during the Second Punic War. There have since been some 24 centuries of battle between man and avalanche, at least, as the people of the Alps have fought to be successful while living in the shadow of the mountains. During the Middle Ages mountain inhabitants, mainly of Europe, viewed avalanches as an "act of God or evil forces from above". They took it as an unavoidable happening. The first ever and systematic publication on avalanches, "Description of the National History of Switzerland", was made by JOHANN SCHEUCHZER, see [19]. The book was published in Zürich in 1706 and contains many insightful observations on means of protection from avalanches. As an example, we quote the following paragraph: *"... practically never erect buildings at the foot of a steep mountain unless there is a hill or a wood appropriately located on the slope which could divert the rolling avalanche to the sides or force it temporarily to loose its power upon arrival in the valley."* Triangular shaped "patches of pine woods" above villages were protected by law. *"... triangular walls were found at the foot of the mountains, their apexes pointed in the direction of the most dangerous walls [direction], so as to break up the avalanches and keep them from doing damage to buildings."* [13].

SCHEUCHZER described an avalanche as a *huge snow ball* and assumed its size to be that of a house or even a mountain. Although it seems to be an inaccurate definition, he mentioned a lot of other correct features of avalanches similar to what we consider today. However, the concept of the huge snow ball prevailed for centuries; see Figs. 1.7 and 1.8, which indeed show snow balls in a wooden engraving and a painting.

Even in the 19th century paintings of avalanches still showed huge snow balls rolling down a mountain side. This is probably be due to the fact that in the Middle Ages mountainous regions were not sufficiently populated or visited by intellectuals, scientists and artists. Consequently, pictures of avalanches turned out to be the result of imagination rather than observation.

1.4.2 Modern History

Mountain climbers and early skiers were the first avalanche researchers who gained knowledge of it from years of observation and experience. The first scientific publication on avalanches, "Avalanches of the Swiss Alps", was made by a Swiss forester, JOHANN COAZ in 1881, see [13]. The main intention of this work was to study avalanche forces so that avalanche defence structures could

Fig. 1.7. Wood engraving Nr. 34 of H.T. Burgkmair in the *Theuerdank* depicting an imagined avalanche in the Middle Ages as a huge snow ball. Wood engraving in Emperor Maximilian's *Theuerdank*. (Photo reproduced with permission from [421]).

be designed and one could learn where and how often avalanches occurred, so that a long-turn record would exist for planning purposes, for locating protection structures and re-forestation projects. In a book called "The Ski-Runner", Richardson in 1909 classified avalanches according to their prime causes – wind, snowfall, rain, etc. [13]. Up to 1930, many other researchers from central Europe contributed their works on avalanches through publications mainly for climbers and skiers. Flaig wrote two books, *Der Lawinen-Franzjosef*, in 1941 and *Lawinen*, in 1955, with a wealth of information about snow and avalanches [99, 100].

Remarks on the Voellmy Model Avalanche research as a field of physical science attempting to derive the equations of motion of a moving snow mass down an inclined chute started in 1955 with Voellmy's four short papers "Über die Zerstörungskraft von Lawinen" in the "Schweizerische Bauzeitung", i.e., "About the destructive forces of avalanches" in the "Swiss

Fig. 1.8. *Die Lawinenkugel [The avalanching snow ball].* Until the 19th century people of Alpine regions thought that a snow avalanche as a huge snow ball rolling and sliding on a mountain side. (Photo reproduced with permission from Hasli-Museum Meiringen, Switzerland).

Civil Engineering Magazine" [430]. These papers entered the scenario of snow research in mountainous regions as a big bang and kept researchers busy for many decades and are still keeping them busy today. For many years, they remained unchallenged. Attempts for improvement were made in 1966 by SALM [361] and in 1980 by PERLA et al. [315]. In the mid 80s of the last century a whole surge of models emerged. A summary of a large number of models, including very recent ones is compiled in the SAME report [142], mentioned earlier. Interesting about the avalanche research by VOELLMY is that he was not working at the Swiss Federal Institute for Snow and Avalanche Research, but was an engineer at the Swiss Federal Institute of Materials Testing, and prior to his landmark papers the properties of steel, aluminium and wood were probably much more familiar to him than snow.

In the following paragraphs we present histories and contributions to avalanche research in the most avalanche prone countries. The reader wanting to skip these in a first reading may directly pass to Chap. 2.

The Swiss Contribution to Avalanche Research[7] The Swiss are the pioneers in avalanche awareness, research and application. First scientific statements related to the behaviour of snow and avalanches can be traced back to the beginning of the 18th century with work by JOHANN JACOB SCHEUCHZER, 1706. Early serious attempts aiming at a closer understanding of the physical behaviour of snow in its cover and in motion were undertaken by the head of the Swiss Forest Inspectorate, JOHANN COAZ, who from 1876 until the early years of the twentieth century played an influential role in establishing a public awareness of the danger of snow avalanches in Switzerland and abroad. In 1931, the Snow and Avalanche Commission of Switzerland was formed. It soon recognised that fundamental research was required. ROBERT HAEFELI, a geotechnical engineer and HENRI BADER,[8] a young crystallographer, started the first snow mechanical measurements in the winter of 1934/35 and continued these in the early winter of 1936 together with EDWIN BUCHER, a civil engineer, and a few helpers at the Weissfluhjoch, 2670 m above sea level. This was the birth of the Swiss Federal Institute of Snow and Avalanche Research,[9] which was stationed at the Weissfluhjoch from 1936 until 1996, when it moved to its new headquarters in Davos-Dorf. BADER, HAEFELI and BUCHER published their first report "Snow and its metamorphism" [19] in 1939, which to date still remains worthwhile reading for any snow scientist. In the last approximately 70 years of its existence, the institute was headed by four directors, E. BUCHER (1936–1949), M. DE QUERVAIN (1950–1979), C. JACCARD (1980–1991) and W. AMMANN (1992–today). Through the years, more than 250 scientists have been employed, and more than a 1'000 scientific memoirs and several thousand technical reports have been published. The institute slowly grew from the small beginnings of a handful people to a considerable size of approximately 40 employees in the sixties and seventies to more than 100 full-time and temporary employees at the turn of the millennium.

Researchwise, EISLF has concentrated its activities on four different divisions:

- weather, snow cover, and avalanches,
- snow cover and avalanche protection,
- snow cover and vegetation,
- basic research on snow and ice.

---

[7] The authors thank W. AMMANN for making the brochure "Eidgenössisches Institut für Schnee- und Lawinenforschung, Davos, 1996" available to them, from which a large part of this information is drawn.

[8] BADER later left Switzerland and assumed a leading position as a snow and ice researcher in the army of the United States in the Snow, Ice and Permafrost Research Establishment (SIPRE), Wilmett and the US Army Cold Regions Research and Engineering Laboratory (CRREL) in Hanover, USA.

[9] Eidgenössisches Institut für Schnee- und Lawinenforschung (EISLF).

In most of these special fields, lasting contributions were made. For instance, Bruno Salm, Hans-Ueli Gubler and Dieter Issler essentially contributed to the theoretical description of the mechanics of the snow cover and of dense flow and dilute powder snow avalanches, as well as to the development of experimental techniques, and this activity is continued today by many PhD students and post-doctoral assistants under the leadership of Perry Bartelt.

Samuel Steinemann contributed in the 1950s with his far-reaching dissertation on the creep behaviour of monocrystalline and polycrystalline ice, published in 1958 [404]. Much of this work was done concurrently with the work performed on the same subject by John Glen at Cambridge University, which would justify renaming the flow law of ice as the Glen–Steinemann flow law. Furthermore, Ronald List and Bruno Federer pushed ahead the study of the formation of hale. Interestingly, the four brief, but very influential papers by A. Voellmy, published in 1955 [430] in the "Schweizerische Bauzeitung", are not contributions of the EISLF, as Voellmy was an engineer at the Swiss Institute of Materials Testing in Dübendorf, Switzerland. These may well be called the most influential papers on snow mechanics and motion of the twentieth century. Similarly, early papers on flow avalanches were written by Savage–Hutter at ETH, Zürich, and laboratory experiments by T. Scheiwiller and K. Hutter [380], T. Scheiwiller [380], F. Herrmann [150] and S. Keller [212] were initiated by K. Hutter at the Laboratory of Hydraulics, Hydrology and Glaciology at ETH, Zürich and B. Salm at EISLF; most early work was performed in Zürich but with close cooperation of scientists from EISLF.

The French Contribution to Avalanche Research[10] CEMAGREF[11] is a French public research institute working on agriculture and environmental problems. It was created in 1981 and employs approximately 1000 persons. One of its laboratories, nowadays referred to as *Torrential Erosion, Snow and Avalanches* (TESA), focuses on snow avalanches, blowing snow, debris flows, and bed load transport. Although CEMAGREF is quite a recent institute, TESA takes its roots in a long standing tradition of avalanche engineering, which dates back to the middle of the 19th century.

In 1860, after a series of catastrophic floods in the 1850s, the French government created a new department inside the powerful Forest and Water Administration (*Eaux et Forêts*): the *Restauration des terrains en montagne* (RTM or restoration of mountain terrains), whose objective was primarily to

[10] This historical overview of the CEMAGREF was kindly written and provided by Christophe Ancey from Ecole Polytechnique Fédérale de Lausanne, Laboratoire d'Hydraulique Environnementale, Switzerland.

[11] CEMAGREF (Centre National d'Etudes du Machinisme Agricole, du Génie Rural, et des Eaux et Forêts) is a French research institute focused on environmental science for sustainable management of land and water.

deal with erosion and floods by covering erodible terrains with forests and drying up torrents. At the end of the 19th century, the RTM service also started trying to fight against avalanches.

In 1899, a young forest engineer, Paul Mougin, went to Switzerland, met J. Coaz, who was the head of the Swiss forest service at that time, and went back to France full of ideas. He organised a system of field observation, including meteorological measurements (notably snowfall) and monitoring the avalanche activity in some avalanche paths. After becoming the head of the RTM service, he continued the scientific study of snow and avalanches. In 1922, he published his results on the physical characteristics of snow and proposed a simple model to compute avalanche velocity and impact pressure: an avalanche was considered to be a sliding block experiencing a Coulomb force.[12] The model was used in a few engineering applications, e.g., the cableway at the Aiguille du Midi in the Chamonix Valley.

After Mougin, research into snow and avalanches was dormant in France till 1970; the *Eaux et Forêts* administration had its own research centre, shared with the meteorological services and *Electricité de France*, but only limited work was done. In February 1970, an avalanche killed 39 people in a chalet in Val d'Isère. This catastrophe caused deep commotion in the population, and the French government took a series of measures to avoid the occurrence of such catastrophic events. This led to the creation of the Avalanche Science laboratory of CTGREF (an applied research centre of the *Eaux et Forêts* administration, which became CEMAGREF in 1981).

One of the first engineers employed at CEMAGREF was Claude Charlier. As a forest engineer, he was mainly interested in the naturalist's knowledge of avalanches and in rational ways of studying avalanche paths. At the end of 1980s and the beginning of the 1990s, he worked with Laurent Buisson on how to translate expert rules into formal (mathematical or logical) rules that could be incorporated into a programme. Despite its interests and promising results, this research route was abandoned when Laurent Buisson left CEMAGREF in 1995.

In 1978, two engineers, Brugnot and Pochat, suggested using the analogy between snow avalanches and floods; they adapted the shallow flow (Saint Venant) equations to model avalanches. They faced severe mathematical issues when trying to numerically solve the depth-averaged equations of motion. One of the first theses launched in this laboratory was that by Jean-Paul Vila [429] (now mathematics professor in Toulouse), who implemented Godunov and van Leer schemes[13] to solve the shallow flow equations numerically.

[12] This proves that the Voellmy model had a French precursor 33 years earlier.
[13] These are shock capturing schemes.

At the same time, another PhD student, PIERRE BEGHIN [31], started conducting small-scale experiments to investigate the properties of powder snow avalanches in the laboratory. In 1981, he provided evidence that the simplified model, proposed by the two Soviet researchers KULIKOVSKIY and SVESHNIKOVA [231], was able to provide the key characteristics of buoyancy-driven particle clouds. In the 1980s, he continued his experimental research and explored the effect of various parameters on dust-cloud dynamics. PIERRE BEGHIN was also a great alpinist who successfully reached the summits of several Himalaya peaks above 8000 m. He tragically disappeared in 1992 when he descended the south face of the Annapurna (one of the central Himalaya peaks in Nepal), during a storm.[14]

Avalanche Research in Canada[15] The research on snow and avalanches in Canada originated when ROBERT F. LEGGET visited the Federal Institute of Snow and Avalanche Research in Switzerland in 1946. Being impressed by the work of the institute, LEGGET decided that this was what Canada needed as well because Canada has more snow than Switzerland.

In 1948, when LEGGET had become the Director of Building Research of the National Research Council of Canada, he arranged for MARCEL DE QUERVAIN of the Swiss Avalanche Research Institute to spend a year in Canada with the task of recommending activities about snow, ice and avalanche research. After touring Western Canada, DE QUERVAIN recommended that avalanche research be carried out. In 1950, LEGGET created the Snow and Ice Section within the Division of Building Research. LORNE W. GOLD became the section head. In 1956, the Department of Public Works of Canada requested the National Research Council to assist with the design of the avalanche control at the highway at Rogers Pass in British Columbia. The Snow and Ice Section, which previously had carried out only studies on snow and ice, made weather instruments and snow observation equipment available and in 1957 added PETER SCHAERER to its staff for the avalanche studies.

Besides designing the avalanche control for the Trans Canada Highway at Rogers Pass, SCHAERER analysed the weather and snow conditions that produce avalanches. Avalanche research was dormant after the completion of the Rogers Pass highway in 1962. SCHAERER was engaged in highway engineering and research on the control of snow and ice on roads.

In 1966, ROBERT LEGGET, recognising a future demand for information on avalanches, decided that PETER SCHAERER resume the avalanche studies.

[14] The French work in this active period is summarised in two reviews by HOPFINGER [155] and HUTTER [180]. It may also be of interest that most of this work concentrated upon airborne density currents, appropriate for powder snow avalanches rather than dense flow avalanches.

[15] This historical overview was kindly written and provided to us by PETER SCHAERER, Vancouver, Canada.

Consequently, in September 1966, SCHAERER began a new avalanche research program. The research objective was to develop information with application to locating and designing engineered avalanche control. The studies included:

- observations of the speed of avalanches,
- observations of the mass of avalanches and determination of the volume of a design avalanche,
- observations of avalanche impact pressures on load cells in avalanche paths,
- correlation of avalanche frequencies with features of the terrain,
- variation with elevation of the maximum amount of snow on the ground.

Rogers Pass in the Selkirk Mountains became the outdoor laboratory of avalanche research. The avalanche research staff of the National Research Council was initially comprised of a research officer, a full-time technician and two temporary technicians during the winter. LORNE GOLD at the headquarters in Ottawa was the supervisor. The administration of Glacier National Park, where Rogers Pass is located, made accommodation, office space and technical support available.

In 1975, the geophysicist TONY SALWAY joined the staff as a temporary research associate. His principal duty was to develop the equipment for measuring avalanche impact pressures and to analyse the observations. When the term of SALWAY's employment expired in 1979, DAVID MCCLUNG, also a geophysicist, obtained the position. He was later appointed to a regular research officer.

The avalanche research program of the National Research Council ended in March 1991, when the Canadian government reduced funds and the Research Council reassigned its priorities. The avalanche research officers and technicians were laid off. PETER SCHAERER retired and DAVID MCCLUNG obtained a teaching and research position in the Geography Department of the University of British Columbia at Vancouver.

In 1998, MCCLUNG secured a chair for avalanche research at the university with the support of the Government of British Columbia and CMH Heli Skiing. His research includes fracture mechanics of the start of avalanches, dynamics of avalanches, and the prevention of avalanche damage in forests.

In 1989, COLIN JOHNSTON at the Department of Civil Engineering of the University of Calgary began an avalanche research project in collaboration with Mike Wiegele Helicopter Skiing at Blue River in British Columbia. The National Sciences and Engineering Research Council gave financial support. BRUCE JAMIESON was in charge of the field work and the analysis of data. The research concentrated on the stability of snowpacks including studies of the strength of weak layers, the development of stability tests, fracture propagation and the spatial distribution of snowpack weakness. COLIN JOHNSTON

has since retired and the project now runs under the designation Applied Snow and Avalanche Research of the University of Calgary under Bruce Jamieson, with financial support of the skiing industry and governments. Field observations take place at Blue River and at Rogers Pass.

In summary, the National Research Council of Canada carried out avalanche research from 1948 until 1991. The University of British Columbia (David McClung) and the University of Calgary (Bruce Jamieson) continue the research. In addition, the following agencies are engaged in avalanche observations, public warnings and education:

- Canadian Avalanche Center, with headquarters at Revelstoke,
- National Parks of Canada,
- Ministry of Transportation of British Columbia,
- Canadian Avalanche Foundation (a funding agency).

The Norwegian Contribution to Avalanche Research[16] Avalanches may occur at any altitude in Norway, right down to sea level along the fjords with their high, steep slopes. In many areas, especially along the west coast, safe ground for settlements is very scarce, and avalanches have claimed 20 lives per year on average over three centuries. This was brought to public attention by Arthur Klabo's book *Farlige fjell* (*Dangerous Mountains*) in 1942. After World War II, Gunnar Ramsli was commissioned by the state as a consultant to counties, communes and the road authorities to help plan mitigative measures; in 1951, he also issued a popular booklet *Snø og snøskred* (*Snow and Snow Avalanches*). Somewhat later, the hydrologist Knut Wold began to systematically collect data on snow depth and snow water equivalents on behalf of the National Water and Electricity Board.

Several tragic avalanche accidents between 1968 and 1972, where locals, workers, ski tourists and rescuers lost their lives, aroused the emotions of the public. The parliament passed a resolution to initiate snow and snow avalanche research in Norway. The Norwegian Geotechnical Institute (NGI), a nonprofit foundation in Oslo active in geotechnical research and consulting, was chosen as the host institution in January 1973. The newly formed group, headed by Karstein Lied, soon set-up a snow research field at Fonnbu near Stryn, western Norway. Besides the by then classical types of measurement, loads on poles and snow bridges due to snow creep and gliding were systematically investigated. As one of the first activities, data on extreme avalanches in all of Norway were collected. Analysis of these data led Lied, Bakkehøi and others to the still widely used α-β model. This is a statistical correlation between the run-out angle α (measured from the fracture crown to the toe

[16] This text was written by D. Issler from NADESCOR, Altendorf, Switzerland with help of K. Lied and S. Bakkehøi. The authors gratefully acknowledge this input.

of the deposit) and the mean inclination angle β of the avalanche track from the crown to the beginning of the run-out zone. It captures the observation that, for a given fall height, fast avalanches with steep tracks generally have a shorter run-out than slower avalanches on more gentle slopes.

In the early 1980s, the full-scale avalanche test site Ryggfonn was established in Grasdalen near Fonnbu. Dynamic loads were measured at a high steel pylon (with internal strain gauges), a concrete wedge (instrumented with load plates) and on cables across the width of the path. The 16 m high and 100 m wide dam is a unique feature of this test site. The equipment has changed over time, partly in response to destructive avalanche events, and was extended in 2004 by a Doppler and a profiling radar system for measuring internal velocity spectra, flow depths, velocity profiles and erosion rates. From the data, various formulas for dimensioning structures have been derived. The measurements has also led to the formulation of two avalanche dynamics models based on different approaches to the granular nature of snow avalanches. The PLK model by the American Perla, Lied and Kristensen [316] simulates the avalanche as a collection of mini-avalanches (each of them described by the PCM (Perla–Cheng–McClung) [315] model, which is similar to the Voellmy–Salm model) with stochastic interaction among each other. It is presently the most often used model for consulting in America. Harald Norem, Fridtjov Irgens and Bonsak Schieldrop [302, 303] specialized the rheology of a Criminale–Ericksen–Filbey fluid to snow avalanches that may exhibit both granular and viscoplastic behaviour and implemented it in the NIS (Norem–Irgens–Schieldrop) model, routinely used for consulting by NGI.

The 1990s have seen continued full-scale measurements, refinements of the existing models, studies of the interaction of avalanches with deflecting dams, improved hazard mapping and risk analysis techniques, and many studies of slush avalanches. Since 2000, research on avalanches and other gravitational mass movements both on land and in the water has been coordinated and intensified in intense collaboration with other European institutes. In particular, more detailed measurements at Ryggfonn and extensions and an improved implementation of the NIS model are at the centre of the activities up to 2005.

The Austrian Contribution to Avalanche Research First attempts of avalanche research in Austria[17] began with the construction and erection of protective shelters at the western ramp of the Arlberg railway track in 1880–1884 by Vincenz Pollak. He may justly be regarded as the founder of avalanche research in Austria. However, an official bureau was only es-

[17] This contribution is based on material and advice obtained from M. Kuhn and B. Lackinger from the University of Innsbruck. Part of the text is based on an unpublished text in the German language by H. Schaffhauser.

tablished after World War II by the Innsbruck branch of the Torrent and Avalanche Control Office in the Wattener Lizum. Its duties were research on the prevention of avalanches.

In the aftermath of the avalanche catastrophes of 1951 and 1954, with a total of 271 deaths, it was realized that roughly two-thirds of all avalanches are released below the timber line. The research office was moved to Obergurgl in the Ötz-Valley at 2000 m above sea level. Research then concentrated on methods of afforestation at high altitudes, which should have replaced the expensive protective measures of structural engineering. In 1963, this research office was incorporated as an external station for subalpine forest research into the Federal Forest Institute (Forstliche Bundes Versuchsanstalt, FBVA) in Vienna, and later, in 1966, it became part of the Forest Engineering Service in Torrent and Avalanche Control.[18] Increasing urbanisation in the alpine valleys and the accompanying demand for the necessary infrastructure led in the 70s of the last century to extraordinary protective measures. Financial restraints demanded a close cooperation with the Swiss Federal Institute of Snow and Avalanche Research at the Weissfluhjoch, Davos with emphasis on structural-geotechnical problems. In 1975, Fritsche, Aulitzky and Rabofsky critically analysed the state-of-the-art of avalanche research in Austria and drew attention to its unsatisfactory conditions [17, 236, 350, 351, 378], thus vehemently requesting the foundation of an institute exclusively devoted to avalanche research.

However, the time was not yet ripe; research was still being done by individuals. Hoinkes and Ambach at the University in Innsbruck, Fritsche at the Technical University in Graz and Aulitzky at the Institute of Torrent and Avalanche Control at the "University of Natural Resources and Applied Life Sciences"[19] in Vienna all contributed to avalanche related problems. Moreover, Lackinger at the University of Innsbruck contributed to glide avalanches and foundation problems and Slupetzky at the University of Salzburg contributed successfully for over two decades to the analysis of avalanche casualties.

The avalanche catastrophes in 1974 and 1981, finally, led to the foundation in 1985 of the Avalanche Institute at the Federal Forest Institute in Innsbruck. It was merged in 1995 with the Institute for Torrent Studies and then renamed Institute for Avalanche and Torrent Studies.

Since 1985 avalanche research at the Innsbruck office of the Federal Forest Institute comprises national and international projects related to avalanche dynamics, avalanche forecast, avalanche formation within forests, forest ecology and afforestation in the sub-alpine regime, risk analysis of landslides,

[18] Institute für Wildbach- und Lawinenverbauung.
[19] Universität für Bodenkultur, Wien.

rockfalls, debris flows, mud flows, floods and avalanches. Of particular interest is the initiation in 1992 and subsequent development of a mathematical–numerical model for the hindcast and forecast of the dynamics of mixed avalanches, comprising of a bottom layer for a dense granular flow overlaid by a particle laden turbulent flow of air, the powder avalanche atop of the dense particle flow (see ZWINGER and ZWINGER et al. [449, 450]). The software of this coupled SAVAGE–HUTTER and powder avalanche model called SAMOS (snow avalanche modelling and simulation) allows the determination of avalanche geometry and velocities along the concomitantly determined track.

The Japanese Contribution to Avalanche Research[20] Scientific snow avalanche research in Japan was started by MIKIO SHODA from the Railway Technical Research Institute [388]. He released avalanches artificially on a test slope in Niigata and measured front velocities and impact forces on structures from 1959 to 1962. After his pioneering work, avalanche studies were executed mainly under the leadership of the Institute of Low Temperature Science (ILTS), Hokkaido University, which was founded in 1941.

EIZI AKITAYA conducted a series of experiments on depth hoar in a cold laboratory in 1975 and quantitatively revealed the growth conditions of skeleton type and solid type snow [2]. The quick growth of depth hoar crystals near the snow surface was investigated by TAKUYA FUKUZAWA and EIZI AKITAYA in 1993 [105]. They found that depth hoar was formed under clear skies after a thin deposition of new snow on denser snow, and obtained the relationship between the growth rate and the temperature gradient both in the laboratory and the field. In 2001, AKIHIRO HACHIKUBO and EIZI AKITAYA measured vapour sublimation rates and meteorological conditions in the fields, and discussed the effect of wind on the growth of surface hoar [135].

Avalanche observation was made in the Kurobe Canyon by a joint group from Toyama University and ILTS from 1972 to 1978. The test site is in the North Japanese Alps and is known as a district of frequent large-scale powder snow avalanches, named "hou" in the local dialect. Observations were made in the Shiai-dani area to discover the overall features and dynamics of this avalanche type (see SHIMIZU and HUZIOKA [390]).

In January 1985, an avalanche broke out at Gongen-dake, Maseguchi, Niigata; it was so large that it killed 13 people and destroyed more than 10 houses. After the disaster, Japanese avalanche researchers organised a systematic project of snow avalanche observations in the Shiai-dani area in 1987. Velocities in the snow cloud were measured with an ultra sonic anemometer.

[20] This text was kindly provided by KOUICHI NISHIMURA, Nagaoka Institute of Snow and Ice Studies, Snow and Ice Research Group, National Research Institute for Earth Science and Disaster Prevention, Nagaoka, Japan.

Velocities of the lower flowing layer were calculated by differencing measurement of the impact pressure (see NISHIMURA et al. [298, 299]).

Physical properties of fluidised snow were investigated by NORIKAZU MAENO and KOUICHI NISHIMURA from ILTS with experiments of a fluidised bed of snow and the chute system set in a cold laboratory, from 1978 to 1996. They revealed that shear stresses are linearly proportional to the shear rate in a lower shear rate region, and shear stresses depend on the square of the shear rate in the higher shear rate region. A strong increase of the viscosity coefficients with the density was also observed. In 1987, TSUTOMU NAKAMURA from the National Research Center for Disaster Prevention in Shinjo constructed a 20 m outdoor chute and measured the impact forces by snow blocks with speeds of about 12 ms^{-1} [292].

Based on the above observations and experiments, several avalanche models were proposed. In 1989, YASUAKI NOHGUCHI from the Nagaoka Institute of Snow and Ice Studies derived a three-dimensional model for the motion of the centre of mass of an avalanche on a surface of arbitrary configuration [300]. NORIKAZU MAENO and KOUICHI NISHIMURA (1989) considered the snow entrainment and viscous resistance in the prediction of the motion of this centre-of-mass model [296]. FUKUSHIMA described the suspension layer of a powder snow avalanche with his quasi-two-dimensional block model in 1990 [104].

In 1995, KOUICHI NISHIMURA and YASUAKI NOHGUCHI started ping-pong ball avalanche experiments at the Miyanomori ski jump in Sapporo to study three-dimensional granular flows. Up to 550,000 balls were released near the top of the landing slope [213, 297]. Ping-pong balls are particularly suitable, since they reach the terminal velocity in only a few metres, so fully developed flows occur even on relatively short slopes. The aim of these experiments was to elucidate the dynamics of two-phase granular flows rather than to directly extrapolate the results to dense snow avalanches. The experiments provided detailed data and insights on the physically significant dynamical processes controlling avalanches. This work was carried out with the help of STEFAN KELLER from ETH, Zürich and JAMES MCELWAINE from Cambridge University [275].

Avalanche Research in Iceland[21] Snow avalanches and landslides have caused many catastrophic accidents and severe economical damage in Iceland since the country was settled in the ninth century. Avalanche problems are relevant to most populated areas of the country, although they are by far most serious in the northwestern, northern and eastern coastal regions [34]. The pioneering work of ÓLAFUR JÓNSSON in 1957, which was updated in

[21] Written by TÓMAS JÓHANNESSON from the Icelandic Meteorological Office. We appreciate this input very much.

1992 [208], lists avalanches reported in annals and other sources since the twelfth century. Avalanches and landslides have killed 194 people in Iceland since 1901 and the direct economic damage due to avalanches and landslides in the period between 1974 and 2000 has been estimated at about 40 million USD [206].

Apart from the work of Ólafur Jónsson, snow avalanches were not seriously considered as a natural hazard in Iceland until a catastrophic avalanche occured in Neskaupstaður in eastern Iceland that killed 12 people in 1974. During the next several years following this accident, a few studies of the avalanche hazard situation in Iceland were conducted, including a short report [348] from a visit by Marcel R. de Quervain in 1975, head of the SLF in Davos at the time, and preliminary suggestions for protection measures for Neskaupstaður written in 1976 by Karstein Lied and Steinar Bakkehøi at NGI in Oslo. Somewhat later, Erik Hestnes, also at NGI, made a short report about the snow avalanche hazard situation in several villages in western and northwestern Iceland, [153]. Furthermore, civil defence authorities in Neskaupstaður and at the national level conducted some studies of snow avalanche hazard after the Neskaupstaður accident. These studies did not lead to significant action, neither in terms of improved safety measures nor much scientific research on snow avalanches in Iceland. This situation did not change until 1995, when two catastrophic avalanches in the villages Súðavík and Flateyri in northwestern Iceland killed 34 people and caused extensive economic damage. These two accidents totally changed the view of the public and the political system regarding avalanche safety in Iceland.

Following the accidents in 1995, the law regarding snow avalanche and landslide hazard was changed and the Icelandic Meteorological Office was given the responsibility of issuing avalanche warnings to settlements and ordering evacuations together with local civil defence authorities. The office was also made responsible for hazard zoning for areas at risk, it advises the government regarding the build-up of protection measures, and conducts scientific research on avalanches (see [262]). Most avalanche research in Iceland since 1995 has been directly connected with the aftermath of the accidents at Súðavík and Flateyri.

Avalanche hazard zoning methods based on individual risk were developed at the University of Iceland and at the Icelandic Meteorological Office [209], utilising among other things dynamical and statistical studies of the run-out of avalanches [392]. Studies of the run-out of Icelandic avalanches included a calibration of the Norwegian α-β-model [252] using a data set of avalanches with the longest run-out in the respective paths [203]. New regulations about hazard zoning of settlements based on individual risk were formalised by The Ministry for the Environment [419]. Since then, hazard maps have been made for 14 villages [14]. The regulations specify acceptable risk in terms of individual annual probability of being killed in an avalanche accident.

In the year following the accidents in 1995, an overview study was made of the avalanche situation and the need for avalanche protection measures in Iceland [202]. Based on this study, the Icelandic government drew up a ten-year plan to construct avalanche protection measures for hazard areas and/or to purchase endangered property in order to reduce the death toll and the economic damage caused by avalanches. Laboratory experiments with avalanches of granular materials in scale models were carried out in order to study the dynamics of snow avalanches that hit obstacles, such as breaking mounds, catching dams and deflecting dams [139, 140]. These experiments led to the realisation that discontinuities or shocks in the flow depth and velocity are an important, but often ignored, aspect of the interaction of snow avalanches with obstacles such as protection dams. An evaluation of the effectiveness of such protection measures cannot be obtained except by properly considering this aspect of the dynamics.

Avalanches that hit the dams constructed in Iceland since 1995 are closely monitored in order to obtain much needed field data about the effectiveness of these structures. Since 1999 a total of 11 avalanches have hit six deflecting dams and deflecting wedges in northwestern and northern Iceland. The avalanches have in all cases been successfully diverted away from the settlements. It should, however, be noted that none of these avalanches have come close to the dams in terms of size, so a full-scale test of the effectiveness of the dams has yet to be made. In some of these cases, observations indicate that the impact with the dam channelled a part of the width of the avalanche into a stream along the dam where the thickness of the flow seems to have increased with respect to the undisturbed flow farther away from the dam side (see [205, 207]), in a similar way as seen in the above-mentioned laboratory experiments. In many or most cases, detailed observations of avalanches that hit dams are difficult because the avalanches fall during snow storms and much of the evidence about run-up on the dam sides and even the outlines of the avalanches are partly obscured by snowfall after the avalanche and by snow drift. A CW-Doppler was recently installed on the deflecting dam at Flateyri by the Icelandic Meteorological Office in collaboration with avalanche research institutes in other European countries in order to study the flow of the avalanches hitting the dam more closely, [394].

In summary, a large effort has been made in Iceland during the last ten years to build up avalanche research, establish an avalanche warning service, to construct protection measures and implement other safety requirements such as relocating settlements at risk. Much work remains to be done, however, before a satisfactory safety situation can be achieved, as was evidenced by two relatively serious avalanche cycles in northwestern and northern Iceland in 2004 and 2005, which led to the loss of one life and caused significant property damage.

The Soviet/Russian Contribution to Avalanche Research[22] First serious studies of snow avalanches in Russian territory started in the 19th century and were initiated for, and related to, the transportation on road and by rail through the Caucasus Ridge. Avalanche danger and meteorological conditions along the "Military-Georgian Road" were estimated and were first published in "The Caucasian Calendar" in 1852. The avalanche map along this road – the first of its kind in Russia – was prepared by B.N. Statkovskii, who also participated in building the first Russian snow protection constructions. The investigations were finalised at the beginning of the 20th century by the appearance of the railroad around the Caucasus Ridge along the Black Sea coast.

This provisional end was actually only an intermission; indeed, avalanche research was relaunched and rehabilitated in the thirties of the 20th century due to the revitalisation of the idea of the construction of a railroad through the Caucasus Ridge. G.G. Saatchan [360], A.G. Goff and G.F. Otten [117] applied equipment and experimental methods from soil mechanics to the study of the mechanical properties of snow. For the first time, the pressure exerted by a moving snow avalanche on an obstacle was measured by mechanical sensors. They also developed methods of determination of some mechanical properties of snow. The results of the studies led to schemes of estimations of avalanche velocities and avalanche pressures on obstacles, published in the first Soviet Handbook on Snow and Avalanche Research [117]. Almost simultaneously, another centre of snow and avalanche research was founded in the Khibiny mountains (Kirovsk) by the Apatite mining industry. (The Apatite mining company's snow avalanche department has been active in avalanche research until today.) Here, I.K. Zelenoi organised the Snow Meteorological Service and the first Snow Avalanche Station in the Soviet Union. The scientific research efforts resulted in the construction of a forecast method of the time of avalanche danger, the first of its kind in the history of snow and avalanche research. With their experiments A.G. Goff and G.F. Otten [11] obtained records of the temporal evolution of the pressure on an obstacle that was subjected to an avalanche. Some of the protective constructions that they designed were unique worldwide. Artificial snow avalanches, released by detonations from artillery shells, were also used; they led to a detailed account of the basis of avalanche release phenomena published in [10, 11].

The growing industrial development in mountainous regions after World War II increased avalanche research activities in various regions of the Soviet Union. Results on investigations of snow avalanche research by G.K. Tushinskii at the mountain passes of the Caucasus, published in 1949 [427],

[22] This text was written by Sergey Sokratov from the Geography Department of the Moscow State University. The authors would like to thank him very much for this contribution.

belong to these, as do the numerous investigations on thermodynamic and mechanical properties of snow and avalanche dynamics in the Elbrus region by SULAKVELIDSE [408].

In the late fifties of the 20th century, the institutions dealing with the observation and physical description of snow avalanches in the territory of the Soviet Union were subordinated to the State Committee of Hydrometeorology and Environmental Control. The Meteorological Centre of Snow Avalanche Observations and Forecast was concentrated in the Central Asian V.A. Bugaev-Hydro-Meteorological Research Institute (SANIGMI) in Tashkent; it subsequently collected information on avalanche events from all snow avalanche stations in the Soviet Union. SANIGMI was responsible for the development of a theoretical basis and of applied methods of snow avalanche forecast [210]. The Laboratory of Snow Avalanches and Mudflows (LSAM) at the Faculty of Geography, Moscow State University, became the centre of developing methods of grading and mapping avalanche danger, and studying mechanical and thermodynamical properties of snow and their spatial and temporal variability. K.F. VOITKOVSKII, E.S. TROSHKINA and V.N. GOLUBEV are today's representatives of this research.

The sixties to eighties of the 20th century were characterised in the Soviet Union by a focus of snow and avalanche research on experimental studies and mathematical modelling of snow stability on slopes, dynamics of dense, powdery and slush avalanches and their interaction with the underlying slopes and obstacles. Principal investigators are S.S. GRIGORIYAN, M.E. EGLIT, A.N. BOZHINSKII and K.S. LOSEV, [44, 84, 85, 86, 87, 88, 89, 130, 131, 132, 133].

The peak of snow avalanche research in the Soviet Union had been reached at the end of the eighties in the 20th century. From 1984 until 1991, twenty volumes on snow avalanches of the USSR were published. About 40 institutions of the State Hydro-Meteorological Service maintained snow avalanche departments in various regions of the country. Such intensive concentration resulted in several monographs entirely related to avalanche research [12, 44, 384, 434].

Since the foundation of the Russian Federation, recent activities on snow avalanche research are primarily concentrated at the Moscow State University and in the Snow Avalanche Department of the Apatite mining company. Nevertheless, some of the institutions that were actively involved in avalanche studies during the Soviet times are still active now as institutions of their own countries. These include SANIGMI in Uzbekistan, the Institute of Geography of the Kazakh Academy of Sciences, and others.

The History of Avalanche Research in the USA[23] The history of avalanche research in the United States is the story of the Frontier West and the practical need for defense against avalanches. Hence it is also the story of a community of dedicated, practical avalanche professionals working closely and cooperatively with a cadre of avalanche scientists and research engineers.

Avalanches and the need to reduce their hazards to life and property began in the west of the US with the mining boom of the 1800s. As a consequence, by the late 1800s, miners in the San Juan mountains of Colorado were already protecting their surface facilities with avalanche barriers and splitters.

Year-round mountain communities and attendant transportation needs flourished in the post-World War II era, as isolated mining and ranching communities began to grow, and winter recreation, especially ski resort development, began in earnest. During this time, systematic avalanche research began to address the growing need for understanding avalanches and reducing their hazards.

Avalanche research activities took root during this time at Alta, Utah, where Monty Atwater was hired as a snow ranger by the US Forest Service. As a 10th Mountain Division veteran of the European war, he quickly put his skills and experience to work on the avalanche problems at Alta, instituting a rigorous avalanche forecasting program, and utilising explosives and artillery for avalanche mitigation work [16]. With Alta as the model, other Forest Service snow rangers began to address their own local problems in a systematic way in places like Berthoud Pass, Colorado, and the passes of Washington's Cascade range.

In 1949, the Forest Service brought Swiss avalanche expert Andre Roch to the US to tour the most avalanche prone areas and to provide advice and expertise. In addition, the Forest Service started the Alta Avalanche School, which grew into what is today: the National Avalanche School. These early schools became a focal point for the exchange of information between practitioners and scientists of the time. In the 1950s, Ed LaChapelle [233] joined Atwater in Alta, and with the later addition of Ron Perla, a formidable research team assembled in Alta to investigate a wide range of avalanche problems.

[23] This history on avalanche research in the United States was written jointly by Rand Decker, Department of Civil and Environmental Engineering, College of Engineering and Natural Sciences, Northern Arizona University, and Avalanche Scientist Karl Birkeland, USDA Forest Service National Avalanche Center, Bozeman, Montana. The authors gratefully acknowledge their contribution.

At this same time, avalanche research was also taking hold in other locations around the country. The US Army's Snow, Ice and Permafrost Research Establishment (SIPRE), which was to become the US Army Cold Regions Research and Engineering Lab (CRREL) in Hanover, New Hampshire had a mission to provide support for the US military and civilian needs. They imported European avalanche researchers and engineers, mainly from the Swiss Federal Institute for Snow and Avalanche Research, and translated their knowledge and experience into monograms for both military and public consumption (see [19, 278]).

Avalanche research also took hold at Montana State University (MSU) in Bozeman. The research of Charles Bradley and John Montagne, both 10th Mountain Division veterans like Atwater, grew out of practical needs; Bradley had some close calls with avalanches, and Montagne was the ski patrol leader for Bridger Bowl, which was expanding up the mountain and into significant avalanche terrain. Bradley's work focused on depth hoar and snowpack structure. He developed the *resistograph* to investigate these problems, an instrument that has seen many improvements and continues to be refined today. Montagne's work focused on studying and mitigating the dangerous cornices overhanging Bridger Bowl [243]. In time, they enlisted the help of the MSU Civil Engineering Department in their work, launching the notable contributions of Ted Lang and Bob Brown, and later their students Ed Adams, Rand Decker and Jimmy Dent, among others. Lang and Brown's pioneering work on snow microstructure and metamorphism has been integrated into the latest snowpack evolution models.

By the late 1960s, realignment in the Forest Service resulted in the transfer of the duties of the Alta Avalanche Study Center to the Forest Service's Rocky Mountain Research Station in Fort Collins, Colorado. Perla left for work in Canada, while LaChapelle began a successful academic career at the University of Washington, where he mentored students like Dave McClung, Sam Colbeck, Sue Ferguson and Mark Moore. A new Forest Service research team emerged in Colorado, led by Pete Martinelli. It included Art Judson, Dick Sommerfeld and R.A. Schmidt [314]. They expanded the facilities at Berthoud Pass, and began investigating a variety of avalanche and snow problems. They also saw the need to address the growing demand for public awareness, and avalanche information and forecasts; and in the early 1970s they founded the Colorado Avalanche Warning Center under the direction of Knox Williams.

Also in the early 1970s, the San Juan research project was launched on Red Mountain Pass in Colorado in a cooperative effort between Jack Ives at the University of Colorado and LaChapelle at the University of Washington. Led by Richard Armstrong, the project aimed at improving understanding and forecasting of avalanches along this hazardous mountain highway. The research team investigated snow metamorphism, the role of snow struc-

ture in avalanche release, and statistical techniques of avalanche forecasting, amongst other important and practical issues.

In the 1980s, the Forest Service began to scale back its support for avalanche research, cutting the program at the Rocky Mountain Research Station in Colorado. In addition, they had already begun transferring much of the snow ranger program and responsibility for avalanche mitigation to individual ski areas and departments of transportation. At the same time, an increasing demand for avalanche information for a growing back-country recreational population led to increasing numbers of regional avalanche centers, providing awareness, education and *real-time* avalanche forecasts to the public. These centres were mostly staffed by the Forest Service, with the exception of the Colorado Center, which became an activity supported by Colorado's state government.

Today's Forest Service National Avalanche Center, led by Doug Abromeit and Karl Birkeland, supports a number of separate regional avalanche forecast centres across the country and in Alaska, with coordination and modest amounts of research, funded by competitive grants from the National Science Foundation (NSF). The research work is primarily in the practical field of snowpack spatial variability. The National Avalanche Center also continues to coordinate the on-going use of surplus military weapons by ski areas and highway departments in their efforts to control avalanches.

Today, avalanche research in the US has become more decentralised, with research taking place at a number of different institutions and universities, including those in Arizona, California, Colorado, Montana, New Hampshire, Oregon, Utah, Washington and Wyoming. Despite this dispersed nature of avalanche research in the US, practitioners and scientists still gather with their colleagues from Canada and around the world at the biennial meetings of the International Snow Science Workshops (ISSW). The ISSW's are valuable gatherings that provide for information exchange and catalyse avalanche research activities in North America. As in the past, ISSW is founded on and serves to connect today's avalanche researchers with the on-going, practical needs of the avalanche hazard reduction community working in the field.

2 Granular Avalanches: Definition, Related Concepts and a Review of Classical Models

2.1 The Complexity of Granular Materials

A granular material is a collection of a large number of discrete solid particles with interstices filled with a fluid or gas. Granular materials show a distinctive behaviour that manifests itself either as that of solids or liquids or gases. For instance, powders pack like solids and flow like liquids. All these effects originate in the ability of granular materials to form a hybrid state between fluid and solid. In fields such as process engineering and production technology, feeding and discharging particulate materials into and from storage systems of any kind (e.g., silos and hoppers) are typical operations of bulk solids handling that give rise to granular flows. Snow, rock or powder avalanches, debris or pyroclastic flows, or the formation of dunes are typical examples of granular flows in the geophysical context. Many interesting properties of granular materials can be observed through granular flows. Among these are species segregation, avalanches, dilatancy, reverse grading, formation of shear bands, the Brazil nut effect and fluidisation, all important phenomena arising in cohesionless particle systems of geophysical or industrial applications. Such a rich and diverse appearance of granular materials is the result of its complex disparate response to dynamic external agitation. Processes can be continuous or intermittent, even if external driving mechanisms are continuous. Such a complex and apparently unpredictable reaction contributes considerably to the fact that granular systems may oscillate in their response between chaos and order.

In this chapter we collect a number of observations on moving granular materials and offer an interpretation. The description is somewhat distant at first from a direct application to snow avalanches and landslides, but it demonstrates the common behaviour of a wealth of phenomena, and thus lays the basic physical foundation at an early stage of the development. The subject is treated in physics, geophysics, powder technology and other literature, and is presently being very extensively researched, with a great number of books and conference proceedings being published. Restricted overviews can, for instance, be obtained from Campbell [57], Hutter and Rajagopal [178], Herrmann and Luding [152], Ristow [356] and many others. Proceedings

of Powder and Grains and Traffic and Granular Flow conferences may equally provide extensive complementary information, see [107, 148, 220].

2.2 Applications of Granular Flows

There are numerous applications of flows of granular materials both in nature, technology and engineering applications. Here, we will explain some of these applications that are often encountered in process engineering and geophysical flow systems of particulate materials.

2.2.1 Chemical Process Engineering

Particles are important products of chemical process industries, agricultural products, pharmaceuticals, paints, dyestuffs and pigments, cement, ceramics, and electronic materials. Solids handling and processing technologies are thus essential to the operation and competitiveness of these industries. In chemical engineering, mention might be made of fluidised beds, spouted beds and manufacturing of pharmaceuticals. All these arise in one form or another when bulk matter has to be moved. Methods of xerography (called electrophotography, a method of dry photocopying in which the image is transferred by using the attractive forces of electric charges; ionised plastic particles, called toner that sticks to the charged areas is introduced, the powder is then fused to the paper with heat), powder material forming (the development of new materials by means of powder consolidation), powder metallurgy processes (material forming processes based on powders that are used in various industries such as automobile industries to produce motors, gears and brake pads; in abrasives for polishing and grinding wheels; in manufacturing for cutting and drilling, etc.) and ultra-structural processing of ceramics and novel coating techniques (advanced coating technology for granular and other materials) are just a few examples requiring knowledge of granular flows.

Fluidised Bed A *fluidised* bed is a bed of solid particles with a stream of air or gas passing upward through the particles at a rate great enough to set them in motion, see, e.g., [64, 441]. Thus the primary factor influencing a fluidised bed process is airflow. Significant amounts of solid materials are processed using fluid-bed technology. Fluidisation technology is employed not only in chemical production, it is also applied in coal gasification and combustion for power generation, mineral processing, food processing, soil washing and other related waste treatment, environmental remediation, and resource recovery processes.

Spouted Bed A *spouted bed* is a combination of a jet-like, upward-moving, dilute, fluidised phase, which is surrounded by a slow, downward-moving bed

through which gas percolates upward, see, e.g., [65]. The spouted bed principle is successfully implemented for coating of granular materials. Whether or not a particle bed can be made to spout depends on the gas flow, bed depth, inlet-nozzle diameter and particle diameter. In this process, the particles or tablets to be coated are fluidised, as explained earlier, in an upward-moving air stream. A high-velocity air stream is introduced into the fluidised bed, causing a spout. A draft-tube partition is placed around the spout to prevent the particles in the spout from colliding with the particles descending in the fluidised bed. A cyclical flow of particles is thus created.

2.2.2 Geophysical Flows

In natural sciences, one can find examples of granular flows in geophysical applications such as landscape formation by landslides, rock, ice and snow avalanches, debris and pyroclastic flows. Although these examples might seem to be of a very disparate nature, they in fact have many similarities. This is why during the past few decades research into the fundamental mechanisms of granular and geophysical flows have increased both in space and scope. Despite their everyday familiarity, granular systems have become paradigmatic systems of complexity. Because of their practical importance, granular flows and avalanches have been studied by many researchers from different disciplines who have presented their own models. Collective reviews can be found, e.g., in Voight [433], Hopfinger [155], Hutter [180], Simpson [395], Erismann and Abele [94] and others.

2.3 Distinctive Properties of Granular Materials

Granular materials have attracted scientists in engineering, mathematics, geology and physics. Because they are of immense practical significance in technological and industrial applications, they are extremely complex in their physical behaviour and thus demanding in the theoretical description of the mathematical models. Granular materials exhibit a number of distinctive features that are not sheared by other "ordinary" solids, fluids or gases. In fact, they behave somewhat like solids or fluids or gases depending on the externally applied forces and actions. There is an abundance of literature available where mathematical models are developed in which the granular material behaves as a solid, fluid or gas, respectively, but it is equally evident that the mathematical description of processes encompassing solid, fluid and gaseous dynamical behaviour, including the transition regimes, must be very difficult. In what follows, we shall present a short account of the most significant distinctive features of granular materials.

This richness of behaviour has been experienced by us as children, when playing in the sand box. The quality of the solid behaviour depends on the humidity of the sand. With dry sand, we were never able to build a stable tunnel or castle. To this end, the sand needed to be slightly humid; this moisture content makes it sufficiently cohesive for vertical walls or holes to be built. Alternatively, we all know too well that rain will destroy all the beautiful buildings, fortresses, streets and tunnels made of sand. The sand-water mixture flows away and ends up in a ugly muddy pulp. By adding water, the sand becomes liquefied and under these conditions it reacts much more like a fluid than a solid. Moreover, when one shakes flour or sand in a sieve to separate fine from coarse grains, the layer of powder or sand experiences "fluidisation" at its bottom through the impact of the particles with themselves and with the sieve. Here the particles behave much like molecules in a gas and, indeed, the behaviour is gaseous, at least as long as energy is provided to the system.

2.3.1 Single-phase and Multi-phase Flows

Granular media under natural conditions on Earth are always mixtures of a loose solid phase, a liquid and/or a gas. If the interstitial fluid plays an insignificant role in the transportation of momentum, flows of such materials can be considered as dispersed single-phase flows. Rockfalls, landslides and flow avalanches of snow, but also pipe flows of grains and pills in the food and pharmaceutical industries are examples of this. On the other hand, when the mass of the interstitial fluid is comparable to that of the solids, the interaction between the fluid and solid phases is significant. The motion of the fluid can then provide the driving force for the flow of the solid phase. Such flows are frequently initiated on soil slopes during or after heavy rainfall and yield catastrophic avalanches, landslides or mudflows, leaving behind a devastating destruction of the slope. However, in many realistic situations, the interstitial fluid does not play a significant role, and thus we may ignore its effects in modelling such phenomena as flow avalanches of dry snow or rockfalls on a mountainside. The dynamics of dense flow avalanches and debris flows is in many situations sufficiently accurately described by a single-phase continuum. Water saturated debris flows and mud flows must be described by a two-phase model of solids and water, and the dilute, particle laden motion of a powder snow avalanche or a subaquatic turbidity current is equally describable by a two-phase model of turbulent flow of air and water with suspended solid particles.

The theory of single constituent dense gravity flow is the main subject of this book. The problem of two-phase flows has, however, also been attacked by constructing theories from "easy to more complex" situations. Early attempts to describe the flow of powder snow avalanches, turbidity currents,

sand storms, etc., were based on density current concepts, see, e.g., EGLIT and VEL'TISHECHEV [89], HUTTER [180], SIMPSON [395] in which mass balance is treated for the individual constituents, whilst momentum balance is that of the mixture as a whole. The two-phase descriptions, treating the solid and air/fluid phases alike, formulate mass and momentum balances for both constituents and possibly also incorporate turbulent closure conditions. In the powder snow literature, these activities were initiated by SCHEIWILLER and HUTTER [380], TESCHE [418], HERRMANN and HUTTER [151], in the dense avalanche, debris flow and mud flow research by IVERSON et al. [74, 75, 192, 194], PITMAN and others [320, 321, 322, 323], SHERIDAN et al. [385, 386, 387] and MANGENEY et al. [264, 265], LAJEUNESSE et al. [237], MABSSOUT and PASTOR [259], PASTOR et al. [310, 311, 312], QUECEDO et al. [345, 346, 347] and others. Of relatively recent attention is the fact that such gravity driven shear flows often comprise a combination of a lower layer dense granular flow overlain by a turbulent two-phase flow of a dusty cloud. This combination, treating the dense layer essentially by the SAVAGE–HUTTER model and the turbulent powder part as a density or two-phase current is fairly recent and due to ZWINGER [449] and ZWINGER et al. [450]. Often varied turbulent closure models are suggested and analyses restricted to steady state behaviour and subtle entrainment mechanisms (ELLISON and TURNER [92], FUKUSHIMA et al. [103], PARKER et al. [309] and CHU et al. [62]). An up-to-date summary is given by ISSLER [188, 189, 190].

2.3.2 Dilatancy

Deformations in a granular body are always accompanied by corresponding volume changes. Experimental evidence shows that there exists a mechanical and geometrical relationship between the applied stress and the voidage filled with a fluid or a gas in any neighbourhood of a granular material in motion or at rest. One of the most interesting and basic observations of such a relationship was first presented by REYNOLDS in 1885 [354]. He called this phenomenon *dilatancy*. If an array of identical spherical grains at closest packing is subject to a load so as to cause a shear deformation, then from pure geometrical considerations those particles must ride one over another and it follows that an increase in volume of the bulk material will occur (see Fig. 2.1). Dilatancy in this case is a consequence of kinematic restrictions. The presence of internal pressure forces is responsible for the tendency of granular material to *expand* under shearing deformations. This is the reason why granular materials are often called *dilatant materials*.

REYNOLDS used this concept of dilatancy to explain the phenomenon observed when walking along a seashore near the water edge, namely that upon stepping on saturated sand. The sand around the foot appears to be whiter, indicating that it has dried momentarily, as shown in Fig. 2.2a. Then upon

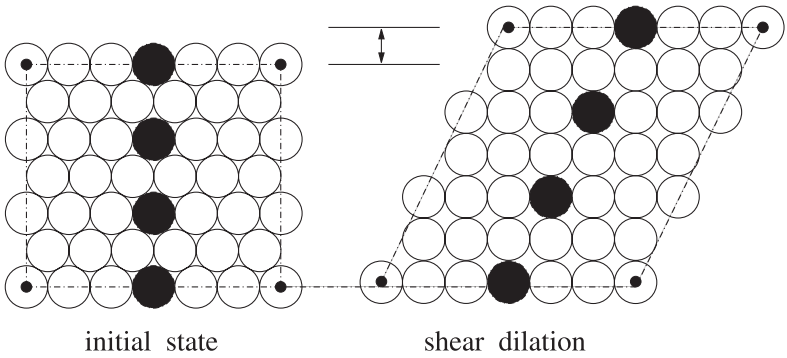

Fig. 2.1. Shearing of a close packing of spheres introduces a volume expansion (dilatation).

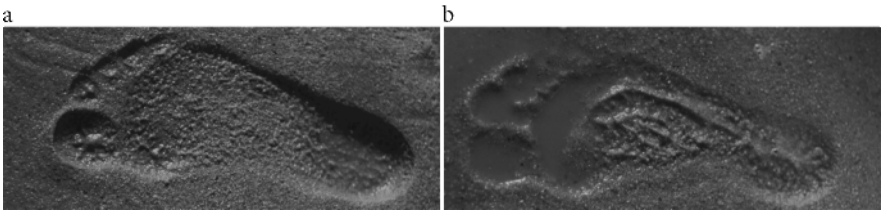

Fig. 2.2. Dilatancy effect in the sand mixed with water. *a*) Walking on a seashore near the water edge, upon stepping on the sand, the sand around the foot becomes whiter, indicating the fact that it has dried momentarily. *b*) Upon removing the foot one observes that a puddle of water has formed in the imprint in the sand.

removing the foot, one observes that a puddle of water has formed in the imprint in the sand (see Fig. 2.2b). The reasoning of REYNOLDS was that the sand on the seashore is in a densely packed state due to the washing of the water, and that upon subsequent deformation, because of the external stress supplied by the foot, the sand around the foot must experience an overall increase in volume. This increase in volume allows the surface water around the foot to drain downward, leaving the surface granules dry. Conversely, when the foot is lifted from the sand, the reduction of stress by releasing the surface traction causes the void volume to decrease. This ultimately results in the expulsion of water from the voids and hence the puddle in the footprint. This is why REYNOLDS concluded that it is the concept of dilatancy that characterises granular materials and it may be regarded as distinguishing these materials from the other two large classes of materials generally known as solids and fluids.

This dilatancy property implies that granular materials exhibit what rheologists and continuum mechanicians call the "normal stress effect". This means that the (nearly) simple shearing deformation as sketched in Fig. 2.1 must

induce a normal stress perpendicular to the direction of shearing. When postulating explicit forms of the constitutive relations for the stress tensor, only those candidates have a chance to model the dilatancy phenomenon correctly that generate normal stresses under simple shear. A NEWTONian (NAVIER–STOKES) fluid, or its nonlinear extension of a power law fluid have *no chance* to model this correctly, because these stress-strain-rate relations do not produce these normal stresses.

2.3.3 Cohesion

It is today's understanding that in granular deposits the contact forces between particles can be normal and tangential. If the normal forces are restricted to pressures, the granular material is said to be cohesionless. If also some tension can be applied, then the contact is *cohesive*. Such tensile forces can be induced in many ways, e.g., by electrostatic forces or humidity, or both.

Loose sand under static loadings may behave as a solid material; for a given sand it can form heaps with slopes of fixed angle. However, when excavations are made, soil walls of one or more metres depth may stay without a sheet-piling wall, at least for some time. The slope stability under an *effective angle of repose* (considerably) larger than the *critical angle of repose* at which the dry sand becomes unstable is possible, because the soil is humid. At low water content below saturation the water within the soil accumulates along the surfaces of the particles but is not sufficient to form a water-saturated soil. So, the pore space is mostly filled with air and the liquid film between the particles forms menisci. The surface tension then leads to adhesion, so that the resulting contact forces between the particles may also be tensile (see Fig. 2.3). A similar phenomenon is also active in snow close to the melting point, even though there the bonding forces are also of electrostatic nature.

Cohesion is a physical mechanism that is likely to be more significant for snow, soil and rock masses at rest than in motion as granular flows. Indeed, cohesion may have the effect that a snow cover, soil slope or rock mass may delay its break-off or not start to move catastrophically simply because cohesion is effective. In such circumstances, cohesion may be active within the endangered mass at its basal surface, as well as at its lateral and proximal surfaces. A simple and obvious question related to cohesion could be as follows: Does the *strength of the material* suffice to resist the load exerted by the mass as a consequence of gravity and possibly other forces? The answer requires parameterisation of cohesion inside the mass of material breaking off, as well as along the bounding surfaces. To quantify the cohesion (i.e., the strength of the material) is by no means an easy task, at least for the prediction of initiation of debris and rockslides, because for an adequate response of such

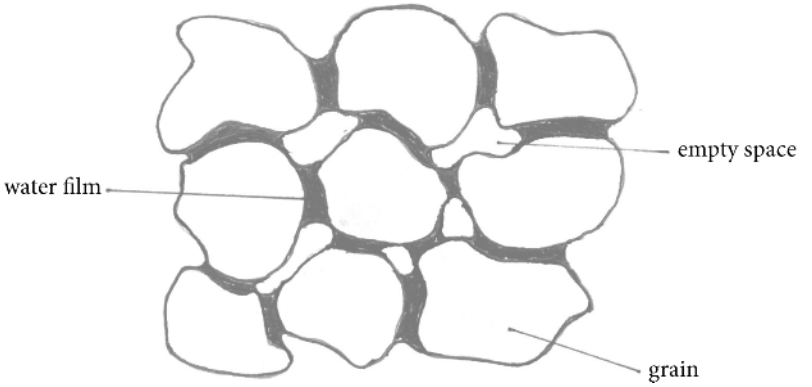

Fig. 2.3. In slightly humid soil the water accumulates in liquid films with menisci. The surface tension is then responsible for cohesion.

materials one should take into account several parameters such as weathering, intact strength and parameters concerning joints: spacing, orientation, width, continuity of the material constituents, infill, outflow of the interstitial gas or fluid (like water), and so on, see [383]. Because of this complexity, cohesion is mostly ignored in avalanche dynamics.

2.3.4 Lubrication

There are several distinct mechanisms to reduce friction in granular materials in motion. One of them is *lubrication*, a technical term, which is related to the reduction of frictional resistance by introducing a further medium, "the lubricant", between the surfaces of two bodies displaced with respect to each other. This definition of lubrication implies the very mechanism of economising the frictional energy. Lubrication, for example, in *technical bearings* may refer to a liquid of low or high viscosity (e.g., water or oil), a gas (e.g., air), a near-to-liquid or otherwise particular solid (grease, graphite), and it may be kept in place either by its own coherence (oil, grease) or by means of other agents such as hydraulic pressure.

Water or air, snow or ice, mud or clay, dust or powder, fire or heat, and many other material entities, can act as hypothetical and theoretical lubricating agents in connection with rockslides, debris flows and snow avalanches in motion. In the literature, hypothetical lubricating materials are divided into *four principal groups* according to their mechanisms: *water, air, fire, earth*, correspondingly for liquid, gas, heat and solid. These are also called the *four classic elements* of lubricants [94].

Whenever granular materials move under gravity, lubrication is particularly important because of possible long run-out to low slope angles. However,

from a technical point of view, there are conflicting requirements concerning viscosity in problems of optimising frictional resistance. Viscosity is required to be low to minimise the resistance in the relative displacement between the involved materials (bodies), whilst it should be high to reduce its rate of escape from the gap between the bodies to locations of lower hydraulic pressure.

In flow avalanches of snow, lubrication in the form of a liquid water film between the surface of the sliding snow and the ground can occur. It probably often occurs, since the frictional energy may produce so much heat that some snow particles melt and produce their own lubricating liquid. The phenomenon is hardly discussed in the literature.

In very large rock avalanches, the frictional heat at the sliding surface can be demonstrated to cause a local temperature rise of more that 1000 K, so that the rock gravels melt, and the molten rock liquid lubricates the sliding surface. Erismann and Abele [94] detail this analysis and for the historic avalanche event at Köfels (Austria) show that rock material must have melted and subsequently solidified. Such "volcanic rock" was indeed found in the area. These rock pieces have received their own name by geologists: "*frictionites*". Such melting processes are a certainty where lahars from volcanic eruptions with hot ash form a debris flow over a glacier surface and bring the glacier ice to melt. This is likely to have occurred in the Sherman landslide in Alaska in 1964 [389] and also the devastating debris flow in the 20 September 2002 glacial catastrophe in the Karmadon gorge in North Ossetia (North Caucasus of Russia) where more that 100 people were burried, see Popovnin et al. [326].

2.3.5 Fluidisation

Fluidisation refers to those gas-solid and liquid-solid systems in which the solid phase behaves more or less like a fluid by the upwelling current of gas or liquid stream moving through the bed of solid particles. Fluidisation starts at a point when the bed pressure drop exactly balances the net downward forces (gravity minus buoyancy forces) on the bed packing. When fluidising sand with water, the particles move further apart and their motion becomes more vigorous as the velocity is increased, but the bed density at a given velocity is the same in all sections of the bed. This is called particulate fluidisation and is characterised by a large but uniform expansion of the bed at high velocities.

Water need not be added to a granular material, such as sand or soil, to make it behave like a fluid. The sand may become fluidised simply if it is set in motion, e.g., by vibrations from outside or by external forces that make individual grains on a granular surface move. An individual rock falling

down a soil slope may by its impact with other boulders generate the release of a large soil mass. The multitude of collisions of the solid particles will then induce an internal pressure that may generate an increase of the mean free distance between the particles and thence reduce the frictional resistance between them. This is one of the reasons why granular avalanches (of snow or debris or rock) move much larger distances than one would expect according to their natural *angle of repose*, the maximum critical angle that the heap of a granular material can make with the horizontal plane. On the basis that the loss of potential energy from the recorded initiation to the run-out zones is balanced by the work done by basal sliding, it can be shown that the basal friction angle between the particles and the sliding surface must be smaller than the given internal angle of friction ϕ. Therefore, such sturzstroms often spread out into very thin layers and flow on surfaces that are much less inclined than the angle of repose of the granular material under consideration.

For over 120 years, since HEIM [146, 147] observed and described the Elm rockfall in Switzerland, attempts have been made to explain the apparent fluid-like behaviour and high mobility of these slides. There are many diverse conjectures and controversial explanations for the reduced sliding resistance such as upward current of air, hovercraft action at the base, melting of rock, fluidisation aided by the presence of the fine dust, acoustic fluidisation, etc., see [375]. Nevertheless, the most acceptable explanation is that in a very thin layer immediately above the sliding surface strong shearing gives rise to enhanced collisions of the particles, leading to an increase of the mean particle distance. This reduces the effective friction angle. One way to handle this situation is to ignore the thickness of the boundary layer and to introduce a MOHR–COULOMB-type friction law with a bed friction angle δ, which is smaller than the internal friction angle ϕ; this will be explained in more detail in Chaps. 3 and 4. This fact is also a reason why the nose of a landslide or avalanche moves surprisingly long distances. It indicates that the fluidisation of the granular material takes place at the boundary layer (see Fig. 2.20, Sect. 2.7.1). Such fluidisation or liquefaction phenomena also act when the soil or gravel in a mountain slope suddenly becomes unstable, for any reason, e.g. seismic wave or a sudden change in temperature, and catastrophically moves downhill (see Fig. 1.5b, Sect. 1.3.2).

Vibrations are used in industries to fluidise a granular mass that must move through pipes. Grains in the food industries and pills in the pharmaceutical industries are often transported by reducing the internal friction with induced vibrations. If air is blown through the granular material, the mean free path between the individual particles may become so large and the number of particle collisions so frequent that the medium in this situation now behaves as a gas.

At a glance, lubrication and fluidisation seem to be similar, but actually they need not be. ERISMANN and ABELE [94] differentiate between them as follows: "The fundamental difference between lubrication and fluidisation lies in the location of the mechanism achieving a reduction of frictional resistance. In case of lubrication this mechanism, irrespective of its physical nature, is considered as concentrated in the immediate vicinity of the boundary between moving mass and ground; in fluidisation, on the other hand, the mechanism is active at least in a considerable portion, normally even in the entire thickness of the mass. In this context, roughly speaking, lubrication might be considered as a *quasi-bidimensional* phenomenon, while fluidisation is *fundamentally three-dimensional*. Therefore, in motion, a fluidised mass, like a liquid, normally generates relative displacements within its entire volume. Lubricated motion, on the other hand, entails moderate relative displacements between the particles of disintegrated mass, thus keeping it "in shape" and preserving to a large extent the sequential order of constituent parts".[1] Whilst this differentiation seems to be meaningful it does not correspond to today's common practice, which often uses the two terms synonymously.

2.3.6 Unlubricated Sliding

As mentioned above, there are numerous practical difficulties related to lubrication and fluidisation of a material in motion, particularly in geophysical flows such as snow avalanches, debris flows and rockslides. Therefore, in many engineering practices, unlubricated (or non-fluidised) friction between coherent sliding bodies is normally treated according to the classical COULOMB law. In this rule, it is postulated that *the resistance opposed to a sliding motion of a granular body be proportional to the compressive force acting at right angles to the contact basal surface*. The factor of proportionality is called the *coefficient of friction* and is assumed to be a constant throughout the entire motion. This means that it depends only on the characteristics of the contact surfaces (e.g., material), but it is independent of load, relative velocity and time. It is therefore important to notice that as long as no further mechanisms have to be considered, COULOMB's rule gives a *reliable basis* for a quantitative treatment of unlubricated sliding.

When using the simple COULOMB rule, the basic differential equation of displacements yields the velocities in a first and the distance in a second integration. So, for the motion of a mass point (see Fig. 2.4) along an inclined plane the equation of motion can be written in its simple form

$$a = g\,(\sin\zeta - \mu\cos\zeta)\,, \tag{2.1}$$

[1] ERISMANN and ABELE obviously use the term "fluidisation" to characterise "gliding or shearing" and "lubrication" to denote "sliding".

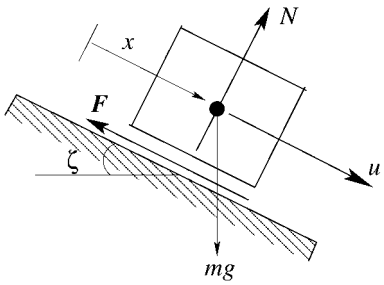

Fig. 2.4. Motion of a rigid body down an inclined plane. The frictional force **F** may only be of COULOMB type, $|\mathbf{F}| = \mu N$, or also contain a velocity-dependent contribution $|\mathbf{F}| = \mu N + Cu^2$.

where a is the acceleration of the mass in its flow direction, g the gravitational acceleration, ζ the slope angle to the horizontal of the surface on which the flow takes place, and μ the coefficient of friction of the material with the basal surface.

The second term on the right-hand side of (2.1) accounts for dry friction, generally not dependent on the velocity. Such a "viscous" drag, if it is present, is likely to depend on the square of the velocity with a drag coefficient C. In this case, COULOMB's rule should be modified and (2.1) written as follows:

$$a = g\,(\sin\zeta - \mu\cos\zeta) - Cu^2\,. \tag{2.2}$$

In practical applications, (2.2) has to be solved only for a finite (short) time. As the coefficient C is (very) small, the third term on the right-hand side of (2.2), therefore, is smaller than the first two. ERISMANN and ABELE argue that in such a case the second term may be substituted by an increased value of the coefficient of friction, μ, approximately accounting for its presumed average. Expressed in terms of velocity and distance, the resulting errors will very often be tolerable [94]. Therefore, the practical suitability of the COULOMB rule is backed up by more than the frequently negligible contribution of velocity-bound resistance during the flow.

The above two simple formulas, however also point at a basic difference exhibited by COULOMB and viscous type sliding laws. If we let

$$a = \frac{du}{dt} = \frac{d^2x}{dt^2}\,, \tag{2.3}$$

where u is the velocity and x the distance travelled by the particle, integration for an inclined plane yields for (2.1)

$$u = g\,(\sin\zeta - \mu\cos\zeta)\,t + u_0\,,$$
$$x = \frac{g}{2}\,(\sin\zeta - \mu\cos\zeta)\,t^2 + u_0 t + x_0\,. \tag{2.4}$$

For positive $g\,(\sin\zeta - \mu\cos\zeta)$ the velocity u and distance x grow indefinitely. It follows that *an avalanching mass subject to* COULOMB *type resistance with constant* μ *on an inclined plane cannot reach a steady state.* Alternatively, integration of (2.2) with (2.3) yields for $g\,(\sin\zeta - \mu\cos\zeta) > 0$

$$u = \sqrt{\frac{g\,(\sin\zeta - \mu\cos\zeta)}{C}}\,\tanh\left\{\sqrt{Cg\,(\sin\zeta - \mu\cos\zeta)}\,(t - t_0)\right\}\,,$$
$$x = \ln\cos\left\{\sqrt{\frac{g\,(\sin\zeta - \mu\cos\zeta)}{C}}\,(t - t_0)\right\} + x_0\,. \tag{2.5}$$

As $t \to \infty$, these two formulas imply that

$$u \to \sqrt{\frac{g\,(\sin\zeta - \mu\cos\zeta)}{C}}\,, \qquad x \to x_0 + \sqrt{\frac{g\,(\sin\zeta - \mu\cos\zeta)}{C}}\,t\,. \tag{2.6}$$

Thus *for velocity-dependent sliding an avalanching mass reaches a steady asymptotic flow state* given by (2.6). As $t \to \infty$, from $(2.6)_1$ it follows that $\sqrt{a/C}$ is the constant steady velocity. Similarly, from $(2.6)_2$, it follows that the distance for the steady motion is given by $x_0 + (\sqrt{a/C})t$, where x_0 is the initial position of the mass at time $t = 0$. The question whether the viscous or velocity-dependent effect should be incorporated or not is still not completely settled, and it may, perhaps, never need to be settled, because *travel distances in field events that allow identification of steady conditions are too short for clear identification.* Laboratory experiments may provide better information and, indeed, we shall discuss this in more detail later.

The above result may occasionally have led to misinterpretations by stating that COULOMB sliding alone may not lead to steady state solutions. However, *one* such solution exists on an inclined plane. Indeed, according to $(2.4)_1$, $u = u_0$ is constant, and this requires that $\tan\zeta = \mu$. So, if a sliding mass has an initial velocity u_0, and it slides along a plane with inclination $\tan\zeta = \mu$, it will continue this motion forever. However, there exist also other solutions that allow steady motion of a particle down a curved surface. SAVAGE and NOHGUCHI [373], NOHGUCHI et al. [301] and HUTTER and NOHGUCHI [173] have determined such solutions for the SAVAGE–HUTTER equations. An in-depth analysis will be given in Chap. 5. As a precursor to that analysis we mention that ANCEY and MEUNIER [7] in a back analysis of 173 avalanches in the French Alps conclude that velocity-dependent sliding cannot convincingly be inferred and that COULOMB sliding may be sufficiently detailed to adequately reproduce the motion of dense flow avalanches. Moreover, in Chap. 12

results of the flow of sand down inclined planes are reported that indicate that with steep slope angles above 35° steady velocities are not reached even in very long flows, whilst such final velocities may be reached for slope angles smaller than or equal to 35°. This agrees qualitatively with laboratory results of Pouliquen [329] and Pouliquen and Forterre [330].

2.3.7 Segregation, Inverse Grading and the Brazil Nut Effect

The dynamics of loose granular materials also shows behaviour that is responsible for further complexity, but is simultaneously annoying for many engineers in applications: the segregation of particles with different properties, mostly size. It is a common experience for everyone who wishes to mix different types of granular particles that it is very difficult to achieve homogeneous mixing of several sorts of grains, whereas it is, in general, fairly easy to achieve homogeneous mixing with miscible fluids. A system containing particles of different properties usually tends to show segregation. Particles with the same properties collect together. The nature of segregation depends on many factors, such as the geometry and surface properties of the particles, velocity gradients and the boundary conditions, etc. The extent of segregation mainly depends on the size ratio and relative number of large and small particles in the mixture [152, 333]. Shaking a new box of muesli before use brings many of the large nuts to the surface, much to the benefit of the first user and the disadvantage of the later ones. Transport of a mixture of granules of different size by fluidisation, conveyer belt or by any other means, will demix the grains of different sizes, often against the intention of the process engineer. This segregation mechanism operates optimally in certain ranges of the external driving mechanisms and may then lead to an ordering of some sort. For example, in a binary mixture of particles of two sizes, the larger and smaller particles may separate and occupy different regions, or they may continuously demix, such that concentrations of the larger particles in the small particles change smoothly. Alternatively, such ordering may again be completely destroyed, if the external driving mechanism is changed. Even though many particular aspects can be explained, this transition from order to chaos and vice versa is still an enigma today.

Many rather astonishing phenomena are known to occur when granular materials such as sand and powders move. When the mixture of grains of the same material (equal density) but different size is shaken in a container, the larger particles rise to the top. This phenomenon, called the *Brazil nut effect* [152], has much importance in numerous industrial and geological processes. When a granular material consisting of grains differing in size, shape, density, etc. is agitated or deformed in the presence of a gravitational field, *segregation* or *grading of particles* can occur, and particles having the same or similar properties tend to collect together in one part of the system. In gravity driven

shear flows with a free surface, it is observed that the fine particles collect at the lower parts of the layer, whereas the largest particles move towards the free surface. In the geological literature, this phenomenon is called *reverse* or *inverse grading* [178].

Such particle size separations are often observed in avalanches, debris flows and pyroclastic flow deposits. In dynamical systems of such flows, one generally observes that the large particles move to the front and to the top surface, whilst small particles accumulate at the bottom and in the rear part of the avalanche. In deposits of pyroclastic flows due to volcanic eruptions or in marine sediments of turbidity currents the following phenomena are observed: Deposition profiles show a repetitive occurrence of "flow units" with the dust particles at the bottom and particle size increasing as one moves higher up until a level is reached where a new flow unit commences, as shown in Fig. 2.5a, a sketch of the eruption of Mount St. Helens, 1980. Each flow unit corresponds to the passage of an avalanche. It is obviously characterised by inverse grading.

Similar structures of inverse grading can also be seen in debris or mud flow deposits. Figure 2.5b depicts the particle size segregation after the deposition of a devastating debris flow that occurred in Taiwan in 1996. The lower part of the deposition consists of the fine material, whilst the free surface is covered by large boulders. It is thus evident from Fig. 2.5b that often a thin "mantle" of large particles covers the top, whereas the main part of the body is composed of smaller size particle components.

At this point, we shall describe a table-top experiment that demonstrates segregation and inverse grading phenomena by particle size in the rapid flow of an avalanche. Let us consider a chute having a parabolic profile inclined at a given angle, say 45° (with the horizontal) and merges smoothly into a horizontal plane as shown in Fig. 2.6a. The talweg[2] of the chute follows the steepest descent. An almost uniform mixture of two different granular materials (one small and dark, the other large and pale) is released from the upper end out of a position at rest by suddenly removing a gate that fits exactly with the chute. The photographs of deposits from above and below are shown in Figs. 2.6b and 2.6c, respectively. It is evident, as explained above, that the large particles are primarily at the top and in the front, whilst the small ones are at the bottom and at the rear of the settled body of the granular avalanche. This phenomenon of inverse grading can be relatively easily understood. In a segregation process particles fall through holes between other particles. Now, it is obvious that the small particles have a larger probability of falling through existing holes than the bigger ones. This explains the phe-

[2] The set of all points with minimum altitude in each cross-section perpendicular to the channel topography.

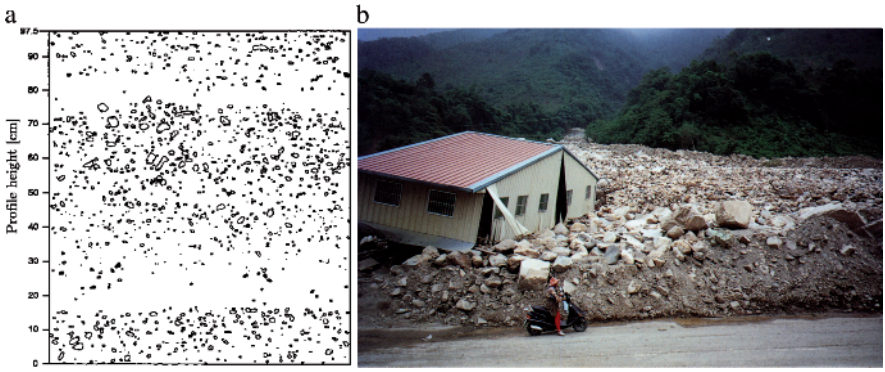

Fig. 2.5. **a**) Sketch of a profile from a deposit of a pyroclastic flow due to the volcanic eruption of Mount St. Helens, 1980. The profile is taken from a position about 6.7 km north of the crater and 1 km southwest of Spirit Lake. One complete "flow unit" is shown that is underlaid and overlaid by other flow units. The profile depicts a clear reverse grading in which larger grains are at the upper portion of the flow unit, while smaller grains are in its lower parts. Each flow unit corresponds to the passage of a pyroclastic flow. (From [406], courtesy of S. Straub.) **b**) Debris flow deposit from a disastrous flow event on 31 July–01 August 1996 in Taiwan. The front side of the road has been cleared. The picture also demonstrates particle size separation. The free surface of the deposit is covered by large boulders, whilst the lower part consists of the fine material. (From [397].)

nomenon when gravity forces are present. More details on this will be given below.

We conclude this brief description on segregation by stating that not all dynamical processes lead to inverse grading under the action of gravity. There are situations that lead to "normal" grading. They are described by, among others, Breu [45] and Krülle [223].

2.4 Granular Avalanches

2.4.1 Definition

By the term *avalanche* we mean a rather large mass of snow, ice, sand, soil or rock that slides rapidly down the side of a mountain. Avalanches are often huge and sweep down the mountainside with tremendous impact force and roar like thunder. Everything in their path is swept away – railways, highways, automobiles, buildings, trees, people and animals. Nevertheless, often they may be small, simply block a path, do no damage at all and stop after a movement of a very short distance. An avalanche will continue down a mountain until the elevation of the mountain starts to decrease and flatten

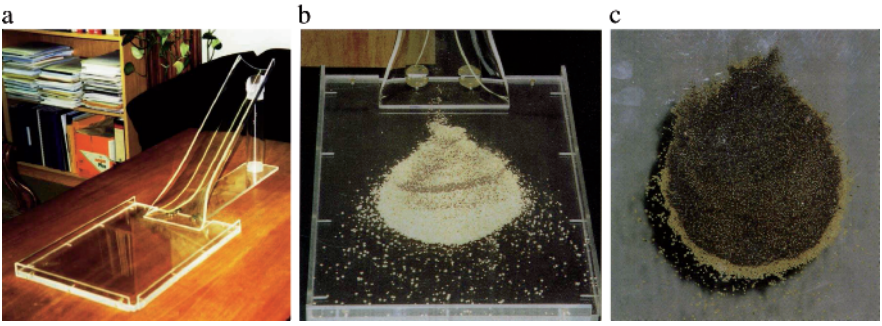

Fig. 2.6. Experiment demonstrating inverse grading in avalanche deposition of a bidisperse granular mixture. The particles were, initially almost uniformly, mixed and segregated during their motion due to gravity. a) Small scale laboratory model with a parabolic chute inclined at 45° and continuously emerging into a horizontal plane. **b**) Photograph, from above, of the deposited binary mixture small (dark) and large (pale) particles. The large particles are primarily at the top and in the front. c) Photograph, from below, of the same deposited mixture. A frontal ring of pale, large particles is clearly seen and the remainder of the basal deposit are basically small particles.

out where the avalanche will then pile up. It can also lose speed down the mountain, depending on how large the slope is and how much material forms the total mass. The more snow, the longer an avalanche will travel.

The word avalanche directly derives from the old French *avalanste*, meaning to "let down", "lower", or "go downstream". Similarly, the Latin derivative of "lavina" gives rise to the German word for avalanche, which is *Lawine*, meaning "to slip" or "glide down". There are different types of avalanches: *rock avalanches* that can bring down millions of tons of granite or other mountain-forming materials, which may change the land for geological times; *soil avalanches* and *mudslides* that are caused when water-saturated soils break loose and flow down a mountain side, also *ice avalanches*, which always contain some snow but are primarily made up of fragmented ice from junks of glaciers. More generally and broadly speaking, a granular avalanche represents the gravity-driven free surface flow of a continuum granulate medium down a steep slope, often initiated by the instability of a granular layer. For a better understanding, see Figs. 2.7a,b, which show (panel a)) a deposit of (wet) snow from a flow avalanche and (panel b)) a snapshot of a laboratory avalanche, for which a mixture of sand and gravel (40 kg) is released from a spherical plexiglass cap and moves down the gully. Both pictures indicate similarities at least in the run-out zones, which may be a good motivation to model avalanches from a physical-mathematical point of view and validate the model from a well-controlled laboratory test.

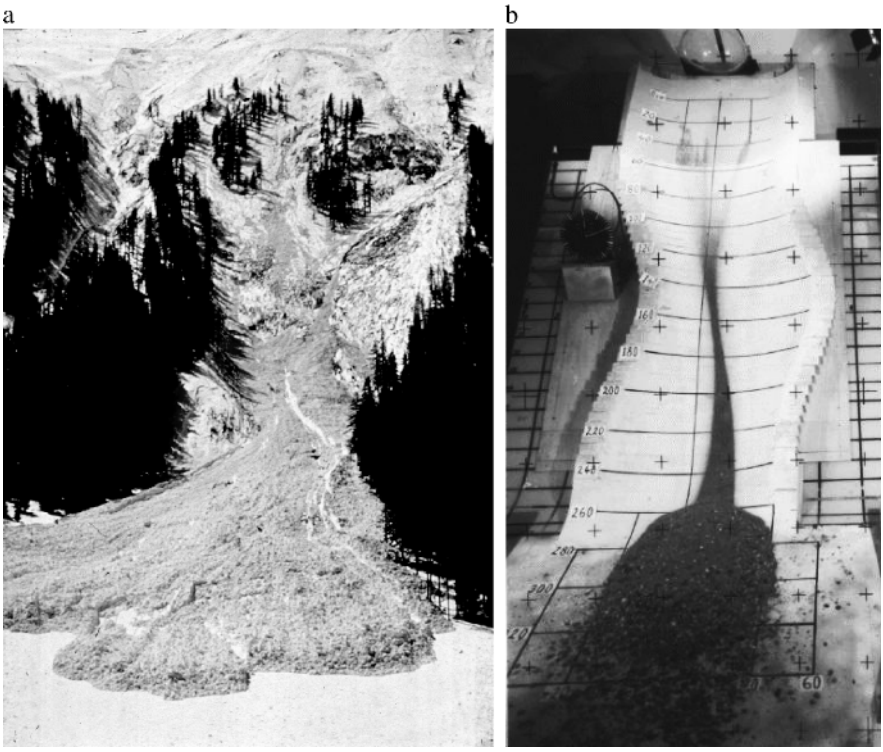

Fig. 2.7. Deposits of avalanches in two different situations. **a**) A real snow avalanche in the Alps, a geophysical application of granular flows. (Courtesy of the Swiss Federal Institute of Snow and Avalanche Research, SLF, Davos.) **b**) Laboratory avalanche simulation with a mixture of sand and gravel. (From [121].)

The most characteristic feature of rockfall, rockslide, landslide and mud flow avalanche events consists in the dominance of a rapid descent over a steep mountain slope. If the displacements take place on a very steep slope, they are also called *fallings*. While descending, a large amount of the total weight acts as a motor and only limited weight is able, by generating friction, to produce a breaking effect. The result is not only a high rate of acceleration but also an almost equal velocity of all moving elements as long as the atmospheric drag is not a substantial limiting factor.[3] An interesting fact in the case of a rockslide is that sometimes the event can be triggered neither by a particularly heavy earthquake nor by abnormal precipitation but entirely by the long-term degradation of the material strength of rock.

[3] The atmospheric drag can be estimated by $\tau = c\rho_s u^2/2$, where c is the drag coefficient, ρ_s the density of snow and u the avalanche velocity. Typical values for these parameters are $c = 0.002$, $\rho_s = 300$ kgm^{-3}, $u = 20$ ms^{-1}. With these values $\tau = 120$ Pa, which is a very small quantity.

These phenomena, collectively referred to as avalanches, can be physically characterised as multi-phase gravity flows, which consist of randomly dispersed, interacting phases, the properties of which change with respect to both time and space. An avalanche can be described as the transient, three-dimensional motion of a variable mass system made up of a non-uniform assemblage of non-rigid, non-rotund granular (snow) fragments flowing down a non-uniform slope of varying surface resistance [240]. In this complexity, an exact analysis of the motion of an avalanche is perhaps an unattainable goal. However, strictly identical particles yield a narrow, while polydispersed sized grains are expected to give a broad avalanche distribution [428]. Thus, we may define the avalanche as follows [335]:

Definition *An avalanche can be described as a transient, three-dimensional gravity-driven free surface motion of a mass system made up of an assemblage of granular fragments initiated by an instability of a granular layer and flowing down to the run-out zone on an arbitrarily steep topography with varied surface resistance.*

2.4.2 Pattern Formation by Granular Avalanches

In this section, we will give a brief account on small-scale avalanches in a thin gap between two vertical plates, rectangular or circular. The development of patterns and mixing, demixing and segregation of particles in silos, hoppers, heap formations and in transportation of mixtures of fine grains are related to the nature of avalanches. This justifies the fact that the study of avalanches is important not only in nature but also in process engineering scenarios.

A successive deposit of granular avalanches may exhibit a strong pattern formation. Continuous deposition, erosion or rotation gives rise to intermittent avalanche release at low flow rates. Once in motion, kinetic sieving of a bidisperse granular mixture creates two-layer shear bands in which the larger particles overlie the smaller particles. When this motion is suddenly brought into rest by the upstream propagation of a shock wave, a pair of stripes is generated in the deposition. Successive releases of the granular materials create a large-scale pattern, leaving a strong imprint of the flow [120]. In the following paragraphs, we describe three mechanisms for avalanche initiation and particle size segregation together with shock waves that bring the avalanche quickly to rest. These phenomena lead to pattern formation within the deposited material. All the experiments take place between parallel plates with a spacing of 3 mm, which prevents lateral spreading of the avalanche and exerts an additional wall friction that slows the avalanche speed. A binary mixture of cohesionless (white) sugar crystals and (dark) spherical iron powder with mean grain diameters of 0.5 mm and 0.34 mm, respectively, is used with mixing ratio 1:1 by volume. The mixture is fed from a point source from

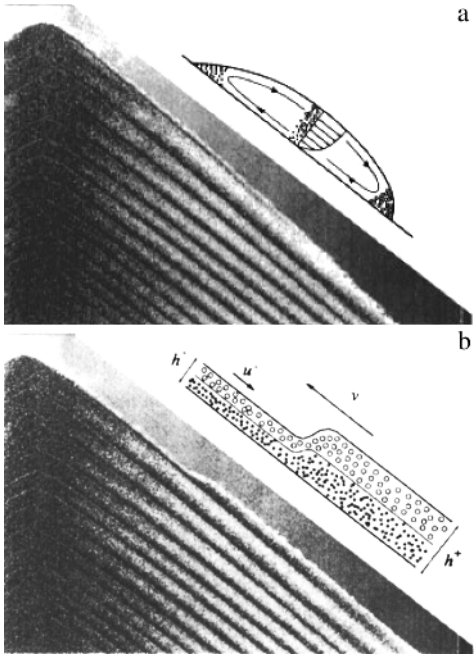

Fig. 2.8. Pile formation by pouring a mixture of large (*white*) and small (*dark*) particles between the slit of two parallel plexiglass plates. **a**) Photograph and schematic diagram of a granular avalanche in a typical roll wave configuration. An inverse graded particle size distribution rapidly develops in which the large particles overlie the small particles forming a stripe. Shearing of the velocity through the avalanche thickness transports the larger particles to the front of the deposit. **b**) Photograph and schematic diagram of the upward propagating dispersed shock wave. The material below the shock is at (or nearly at) rest, whilst the grains above it are flowing rapidly downslope. (From [120].)

above with a continuous flux, thus forming the triangular heap of which half is shown in Fig. 2.8a,b.

Particle Size Segregation and Shock Waves One of the most fundamental characteristics of an avalanche is that it has the ability to act as a kinetic sieve; this, in turn, sorts the granular material by grain size. Consider a typical roll wave configuration on an inclined slope as shown in Fig. 2.8a. As the grains are sheared gaps between the particles are continuously created and destroyed. Under the action of gravity the smaller particles are more likely to fall into the space available in the granular heap. An *inverse grading* of the particles rapidly develops in which the larger particles overlie the smaller particles. The white particles overlie the dark (smaller) particles, thus forming two-layered shear bands (i.e., stripes). The larger grains are transported to the front, whilst the smaller grains concentrate at the rear of the

avalanche. This phenomenon, as shown in Fig. 2.8b, is due to the fact that the surface of the avalanche moves faster than the base. Dispersed shock waves in granular avalanches, which bring the granular material rapidly to rest, are important agents for pattern formation. These shock waves are initiated when the avalanche front reaches the base of the slope or a solid wall, and propagate rapidly upslope, thereby freezing the particle size distribution into the deposited granular material, thus preserving the pattern formed during the avalanche motion.

Avalanches in Thin Vertical Piles of a Binary Mixture of Fine Granules In a first experiment, consider two vertical plexiglass plates forming a narrow gap. Together with a basal plate and two side walls, they form a plane two-dimensional "silo". The mixture is poured into this silo that is 70 cm high by 34 cm wide in dimension from a point source at the top-centre. Although the material is continuously deposited at the top of the pile, it does not flow immediately down the faces because of the difference between the static and dynamic internal friction angles.[4] Once the static friction angle is exceeded, the avalanche flows down the face of the pile and forms a *roll-wave*,

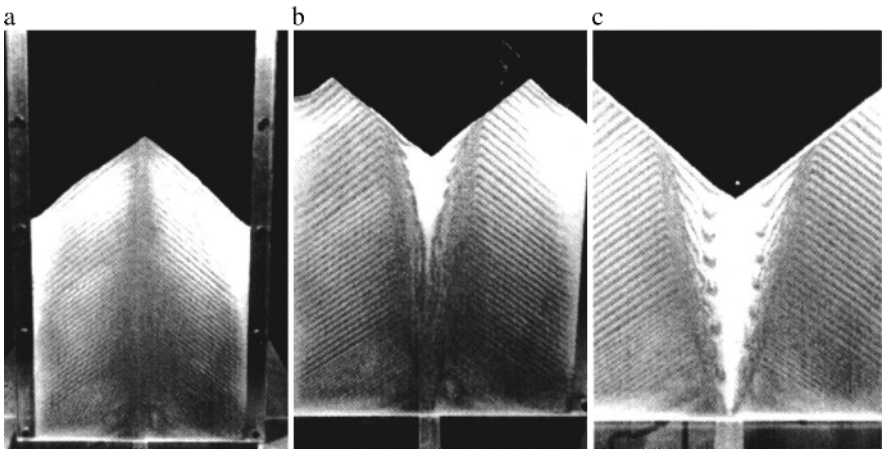

Fig. 2.9. Pattern formation and destruction by avalanches in a pile of a bidisperse granular heap. **a**) A pine tree effect is built up through successive stripe formation and burial. **b**) When a small hole is opened at the base, a core flow develops with the large (*white*) particle at the centre and the small (*dark*) at the side. **c**) At low flow rates, intermittent granular avalanches penetrate into the central core, leaving a straight stripe on the free surface that acts as a tracer particle in the flow. (From [120].)

[4] The tangent of the static angle of friction ϕ_s is the ratio of the shear and normal tractions between two surfaces at vanishing relative motion, the dynamic angle of friction ϕ_d is the corresponding angle when the surfaces slide over one another. Generally, $\phi_d < \phi_s$.

in which kinetic sieving takes place (see Fig. 2.8a). Successive and alternating avalanche releases on both faces of the triangular pile build up a sequence of layers giving rise to a *pine tree* pattern, as shown in Fig. 2.9a. It is worth mentioning that there is a tendency for the upslope propagating shock wave to destabilise the granular material on the opposite face of the pile, so that avalanches tend to form first on one side and then on the other [120].

Once this pile has been formed, a small hole of 5 mm width opens at the centre of the silo base. The granular material then develops into an internal core flow, and a *vee-shaped rat-hole* is quickly formed, as shown in Fig. 2.9b. The granular material on either side of the core is at rest and the pine tree pattern is preserved there. Material is fed to the core by a sequence of intermittent avalanches that flow down the faces of the rat-hole and are initiated by erosion at the base of the avalanche slope. As before, kinetic sieving takes place within the avalanche and the larger particles concentrate in the centre of the core, whilst the smaller particles are drawn into a dark shear band on either side of the central white core of the silo. If the flow rate is low, avalanches can penetrate into the centre of the core and come to rest when they hit the opposite side of the rat-hole. A series of initially straight stripes have been sheared and deformed into regular eddy like structures due to the discharge of material from the bottom hole of the silo, as shown in Fig. 2.9c, [120, 121].

The Catherine Wheel Effect Consider a thin closed circular disk with a diameter of 25 cm, filled with the same granular mixture as before with a free surface that lies above the centre, as shown in Fig. 2.10. In order to emphasise the pattern formation due to small avalanches, the disk is first laid horizontally and then gently shaken so that all the small dark particles fall to the bottom. Once gently turned to the vertical position, one side of the disk is completely dark, whilst the other is completely white. When the disk is rotated in its vertical position at a constant rate of 100 s per revolution intermittent avalanches form at the free surface. The intermittency again stems from the difference between static and dynamic internal friction angles. The central circular core of the material remains completely undisturbed due to the slow rotation of the disk. Each avalanche release sorts the granular material, forming a stripe, which is frozen into the deposit by the shock wave and subsequently buried and rotated in the undisturbed material below the free surface. Subsequent releases create a sequence of stripes tangent to the central core (see Fig 2.10a). This process ultimately creates a *Catherine wheel effect* after a complete revolution, as shown in Fig 2.10b, [120].

At faster rotation rates (here < 20 s per revolution), the intermittency of the avalanche release, shock waves and stripes disappear and a steady-state flow regime dominates (see Fig. 2.10c). The material is continuously released on the upper side and continuously deposited on the lower side of the concave free surface, and is transported between the two positions by a quasi-steady

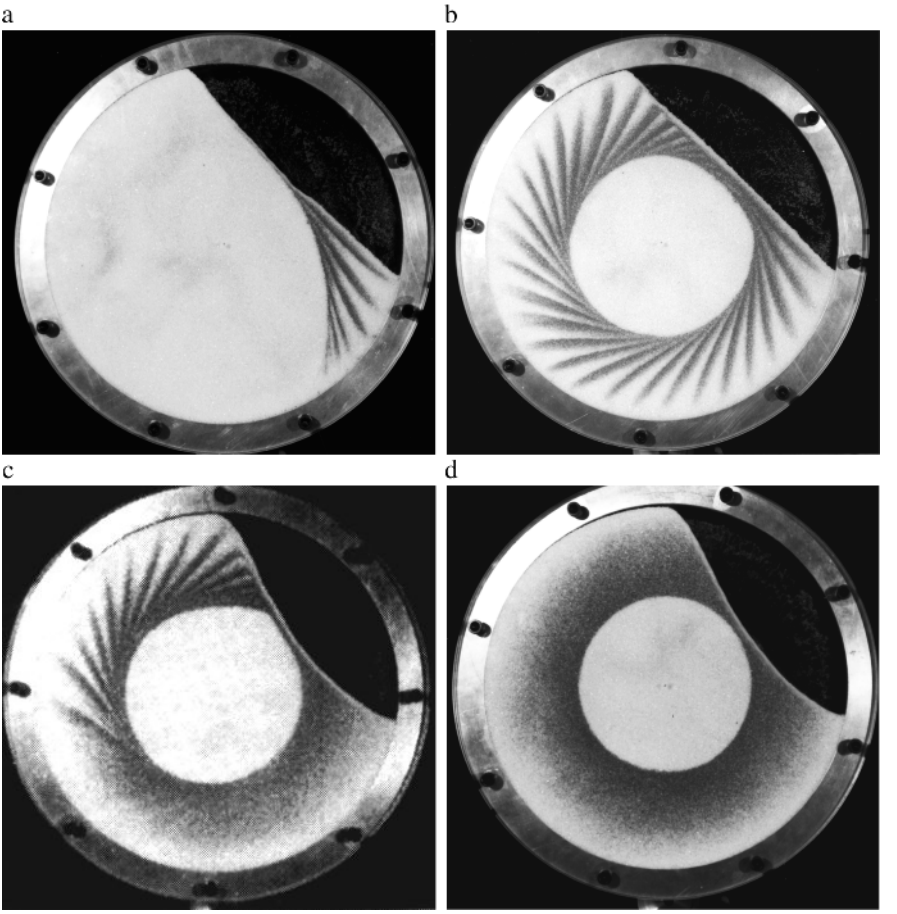

Fig. 2.10. Demonstration of the formation and collapse of the Catherine wheel effect. **a**) At low rotation rates intermittent avalanche release in a thin rotating disk filled with the granular mixture leads to the formation of stripes tangent to the free surface. **b**) The disk is rotated to a full revolution to form a Catherine wheel effect. **c**) At faster rotation speed a quasi-steady flow develops. **d**) In such a situation, the free surface is fixed in space and there is a continuous distribution of particle sizes outside the centre core. (From [120].)

avalanche in which kinetic sieving takes place. The smaller particles are the first to get deposited on the lower half of the free surface because they are concentrated at the bottom of the avalanche and a new pattern develops in which the central core is undisturbed. There is a continuous distribution of grain sizes outside the central core. The distribution starts with a high concentration of small particles near the core and ends with a high concentration of large particles near the outer wall (see Fig 2.10d).

The pine tree structure exhibited by the bidisperse depositions in the heaps of Figs. 2.8 and 2.9 and in the Catherine wheel effect, and their transition into completely differently ordered arrangements by an outflow through a bottom hole (Fig. 2.9b,c), or an increase of the rotation speed, shows how critically the mixing processes react to the exerted forces or outside motions and forces. In the rotating disk experiment, two different orderings have been established by only changing the rotation speed of the wheel. Loss of intermittency was the reason for the configurational change. An analogous change in the particle patterns has similarly occurred in the granular pile structure. The eddies of Fig. 2.9c are the result of the strong shearing and not of intermittency. It is not difficult to imagine situations in which the pattern would mimic total chaos. This can be reached in the rotating disk problem by increasing the rotation rate such that the centrifugal forces acting on the particles make them fly away from the free surface. The violent motion results in an unstructured deposition of the large and small particles.

The above text reports on experiments of particle size segregation in small gaps of vertical rotating cylinders. Many additional experiments have been performed on these, including theoretical analyses. Later, in Chap. 6 we shall explicitly demonstrate that the theoretical model due to Gray [124] allows a surprisingly adequate reproduction of the particle mixing induced by the avalanching motion of the grains in a rotating gap. Further analyses on such rotating particle mixing have also been conducted by Khakhar et al. [218, 219] and Orpe and Khakhar [307]. Although it is true that these rotational granular flows may be distant from real avalanche processes in nature, they are, however, ideal laboratory scenarios by which the theoretical model can be tested. From this point of view they justify the treatment in this book.

Finally, it is worth mentioning that a long cylinder, rotating about its horizontal axis and partly filled with a bidispersed mixture of dry particles develops on long time scales a different segregation patterns by size. Here, the large and small particles separate in layers perpendicular to the rotation axis and the number of stripes depends on the geometry of the rotating cylinder, the filling ratio and the particle properties. Breu [45] and Krülle [223] have conducted work on this. When water is added, the situation is different again; Breu conducts a literature review of earlier work on experiments on this. In the sequel we shall not be concerned with these kinds of three-dimensional rotating granular experiments, except for mentioning that particles now diffuse also sidewise. Segregation of large particles to the sides along a wide, but channelised topography have occasionally also been seen in snow and debris avalanches. A detailed description of these, also known as "levées" is given by Félix and Thomas [98]. Figure 2.11 provides a demonstration of this segregation phenomena.

Fig. 2.11. Lobe-shaped deposits produced by the 1993 pyroclastic flows of the Lascar volcano (Chile): (*top*) levées enriched in large pumices (flow moving ahead), and (*bottom*) global view of lobes observed on the southeast flank of the volcano. The cube (*upperpicture*) gives a three-dimensional scale: the edges are 78 cm long. (From [98].)

2.5 Snow Avalanche Regions, Formation and Dynamics

Avalanches arise only in certain regions and are triggered to a larger or lesser extent according to the topographic and meteorological conditions to which they are exposed. Their speeds and consequently their dynamics, however, also depend upon the surface roughness and the shape of the mountain side on which they are formed. We will briefly address these points.

2.5.1 The Home of Natural Snow Avalanches

Here we present some facts on snow avalanches. About 20% of the continental land mass is covered by mountains. These mountain ranges are situated at sufficiently cold latitudes or reach high enough elevations to favour a deep mantle of (winter) snow. They are the habitat of (snow) avalanches. In simple terms, an avalanche requires only two ingredients: a snow cover and some mechanisms for it to slide down. Nature is always ready to provide both. Snow and wind are the architects to design and create avalanches in these steep mountains.

The world's largest mountains produce the largest avalanches. The Himalayas of Asia, with about 10 peaks above 8,000 m (nine of them, including Mt. Everest (8,848 m), the highest peak of the world, in Nepal, and the second highest peak, Mt. K2-Godwin-Austen, in China-Pakistan), produce wonderful and awesome, but equally dangerous and deadly avalanches (see Fig 2.15).

No part of the world, however, has seen a longer and harder struggle against avalanches than the Alps of Austria, France, Italy and Switzerland. To a lesser extent, avalanches fall in the other great mountain range of Europe, the Caucasus of southern Russia and the Republic of Georgia. Similarly, the Scandinavian countries must also deal with avalanches, mainly in the mountainous and glacier-carved fjords of Norway. Occasionally, people in Scotland and more often in Iceland also face avalanche danger. Still other mountainous countries of the world fight against avalanche fatalities. The main island Honshu of Japan, the southern mountains of New Zealand, the mountains of southeast Australia and the Andes of South America also produce avalanche hazards on a vast scale. To close this list, we must mention the Rocky Mountains of North America, one of the greatest mountain systems on Earth covering the states of California, Colorado, Nevada, Utah, Montana, Washington, Alaska and the Provinces, British Columbia and Alberta. In these regions, avalanches also arise in abundance and they are equally devastating but of lesser impact than, e.g., in Europe because these areas are much more sparsely populated.

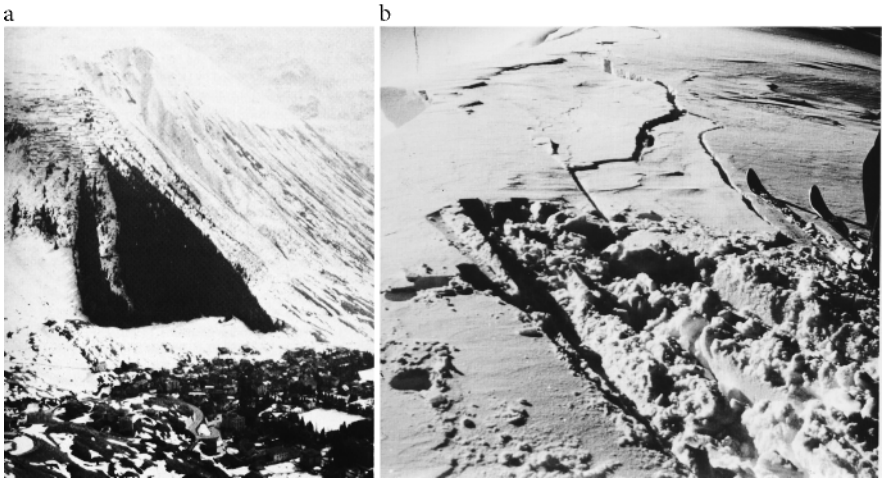

Fig. 2.12. **a**) The Swiss village Andermatt and the wedge of trees that protects it from avalanches. The remainder of the steep slope is bare, thus providing a perfect track for the run of a snow avalanche. (From [4], courtesy of Birkhäuser Verlag, and Swiss Federal Institute of Snow and Avalanche Research, SLF, Davos). **b**) A flow avalanche on Wasatch Mountain, Utah initiated from a crack of a snow pack. (From [235].)

2.5.2 Topographic Conditions

In the ensuing paragraphs, a number of qualifications, properties and conditions are stated that influence the avalanching motions.

Steepness Experience reveals that slopes of 30–45° or more are most favourable for the initiation of an avalanche. The reason is that at these steepnesses the balance between strength (the bonding of the snow trying to hold it in place) and stress (the force of gravity trying to pull it loose) are most critical.[5]

Elevation Mountains that rise above the *timberline* are more likely to produce avalanches. This is because above the timberline avalanches are free to start, and once they are set in motion, they can easily sweep away the trees below, so as to provide favourable tracks by themselves (see Fig. 2.12a).

[5] This is an indication that small slopes below approximately 30° inclination give rise to an avalanche behaviour that is different from that above it. This is indeed so: There seem to exist two regimes, boldly characterised by steep and shallow slopes. On shallow slopes, shearing within the avalanche body plays the more dominant role relative to sliding than on steep slopes, see Hutter et al. [183].

Orientation More avalanches fall on slopes facing north, northeast and east than those facing south through west. The effect of slope orientation is due to its interaction with solar radiation and wind.

Shape of the Terrain Avalanche paths may form in all shapes and sizes, some on open slopes, others in narrow and twisted gullies. Some are straight and maintain a nearly constant slope from initiation to stopping. There are paths of which the vertical profile has convex curvature in the upper portion of the path when viewed from the side, whilst others have concave shaped paths. Still other paths are of composite type, having a convex portion followed by a concave one with smooth transition to the straight run-out zone. However, there are two main path configurations that are particularly prone to producing devastating avalanches. First is the large bowl-shaped starting zone in which a section of snow breaks away and thus removes support from the adjacent sections in which the stress increases until these sections can neither support themselves and also break loose. Second is the path that consists of several gullies (probably twisted) that feed into a common track lower down. One gully might turn loose its load of snow before the other has quite reached that point of readiness, but they remain prone to dumping their loads at approximately the same time.

Roughness of the Ground Usually, the surface conditions of a starting zone control and determine the size and type of a released avalanche. For example, the rough ground surface of mixed boulder fields do not allow an avalanche to be produced early in the winter, for it takes considerable snow fall to cover the ground anchors. What is likely to occur is that, if the avalanche is not formed during the entire winter, it will run to ground in spring, once melt water percolates through the snow and lubricates the ground surface. Vegetation, on the other hand, has a mixed effect on avalanche release. Generally, bushes provide anchoring support until they become totally covered by snow. A dense stand of trees can easily provide enough anchors to prevent avalanches from releasing and make them less rapid and destructive even if they have already been released (Fig. 2.12a). Since isolated trees provide concentrated weak points on the slopes, they are more harmful than good. This is why reforestation of bare slopes is always an effective means of controlling avalanches.

2.5.3 Snowpack and Weather Conditions

There are three main factors of snow avalanche release.[6] They are terrain, snowpack and weather. The terrain factors, which we have just dealt with

[6] We only give a brief list of characterisations. A detailed account may be obtained from Ancey [8].

above, are more or less fixed and do not need to be re-evaluated for a long time once these factors have been identified. However, the state of snowpack and weather changes on a regular basis, often daily or hourly, and these changes are particularly pronounced in winter. Below, we give an account of such temporal agents of avalanche potential.

Snowfall More than 80% of all avalanches fall during or just after a surge of snowfall. This indicates that snowfall is the most important of all events that lead to avalanches. The question is, why does it happen? Because the fresh snow provides extra weight on the existing snow cover, and if the snow cover neither absorbs the extra weight nor bonds it in place to the snow in deposit, avalanche release is inevitable. There is also a very rough relationship between the size of an avalanche and new snowfall. As a rule, snowfalls greater than 1 m are able to produce major avalanches, whereas snowfalls of less than 15 cm seldom produce avalanches [13].

Snowfall Intensity Snow in the snow cover behaves much like an elasto visco-plastic material. So, under a slow load, snow can absorb the load by changing its shape with a slow deformation or compression. Recovery is never complete. However, under a rapid load, there is less time for the snow to absorb the weight by changing its shape. Here the response is elastic with fracturing if the dynamic stress reaches a certain threshold. Thus, the snow is much more likely to break under the applied stress. It follows that the rate at which snowfall accumulates on top of an old snow cover is almost as important as the amount of snow itself. A snowfall of 1 m in one day is far more hazardous than 1 m in three days.

Rainfall Light rain, falling on a cold snowpack, always freezes into an ice crust adding strength to the snow cover. At a later time, though, this smooth crust may become a favourable sliding layer beneath the newly fallen snow. Heavy rain, however, greatly weakens the snow cover in two ways. Firstly, it adds weight. 1 cm of rain is equivalent in weight to about 10 cm of snow. Secondly, it adds no internal strength of its own, as new snow would, while at the same time it dissolves bonds between snow grains as it percolates through the top snow layer, resulting in a reduction of strength.

Temperature Although there is no direct correlation of an avalanche onset with temperature, a rapid temperature change is often more important than its absolute value.

There are also some other factors causing avalanche formation. They are wind speed and direction, new snow density and crystal type, the depth of the snow cover, the nature of the snow surface, formation of depth hoar, etc., but we do not go into details here, see, e.g., [4, 13, 235].

2.5.4 Size and Speed of Snow Avalanches

There are various kinds of snow avalanches: thin, thick or deep, broad and narrow, and short and long. Thin avalanches slide down as a thin film and remove the top thin layers of snow just a few centimetres thick; deep ones may take away the snow cover of an entire winter and transport it down the valley. Short avalanches generally travel a small distance, often only a few metres, whilst long ones can descend several kilometres. With respect to speed, small avalanches are also slow with speeds as low as 5 $\text{kmh}^{-1} \cong 1.4\ \text{ms}^{-1}$, whilst ultra-speedy demons can exceptionally travel with a speed as high as 500 $\text{kmh}^{-1} \cong 140\ \text{ms}^{-1}$.

Sluffs, very small avalanches, are mostly harmless and are common in the mountains. After a fresh snowfall, the small shallow mantle of dry snow travels some metres down. Artificial means, such as detonations or outside triggers, e.g., a skier, are very effective in releasing small to medium size avalanches, mostly in shallow snowpacks. The other end of the avalanche spectrum is covered by huge moving snow masses. They are mainly released by their own weight, a natural cause.

A typical large avalanche might set in motion $(1-10)\times 10^5\ \text{m}^3$ snow. To have an idea about its size, imagine a mountain side of snow having a depth of 3 m and an area of 20 football fields; next let this amount of snow break loose and fall 1,200 m in elevation (the equivalent of a slope distance of 2,000 m to 3, 200 m). Two huge avalanches fell near the remote community of Gothic, Colorado, during a storm in March 1978. The first broke loose in a snow layer only 1 m deep, but this layer was about 900 m wide and 900 m long. The second avalanche was 1–2 m deep and 3,000 m wide. Both fell about 800 m in elevation. One especially large avalanche fell down the slope of Mount Sanford (N. America) on 12 April 1981. This contained an estimated 7.7×10^5 m^3 of ice and snow and fell about 3,000 m in elevation and travelled almost 13 km before coming to a stop [13]. An interesting fact was that the avalanche threw up a powder cloud many thousands of metres that was visible for more than 160 km.

An average avalanche of snow is about one metre deep at the fracture line, 30 to 60 m wide and falls 100 to 150 m in elevation. For dry snow, the average speed of such an avalanche is roughly 65 to 100 $\text{kmh}^{-1} \cong$ (18 to 28 ms^{-1}). However, for wet snow (due to rain or thaw), the speed will be less, probably in the range of 25 to 50 $\text{kmh}^{-1} \cong$ (7 to 14 ms^{-1}). On the other hand, larger avalanches attain higher speeds. Japanese scientists have measured velocities in an ultra-speedy avalanche as being in the range of 370 $\text{kmh}^{-1} \cong$ 103 ms^{-1} [13].

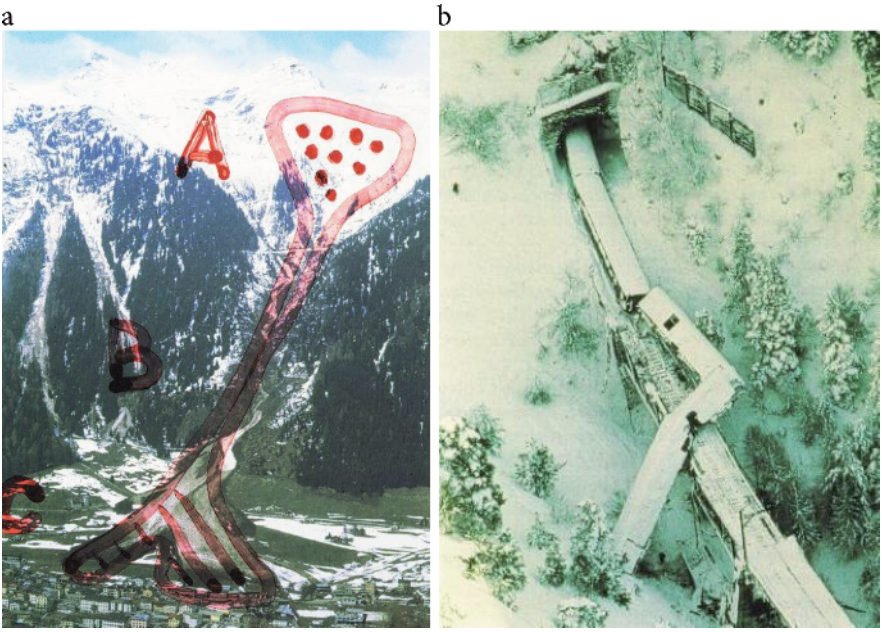

Fig. 2.13. a) The avalanche path and its deposition. A: the starting zone, B: the track and C: the deposition area of an avalanche in the Swiss Alps. **b**) Manifestion of the destructive power of an avalanche that derailed a train from its track. (From [4], courtesy of Birkhäuser Verlag, and Swiss Federal Institute of Snow and Avalanche Research, SLF, Davos, only a.)

2.5.5 Avalanche Dynamics

How does an avalanche move, how fast, how far and with how much destructive power? The answers to these, and similar, questions are contained in the topic *avalanche dynamics*. The science of avalanche dynamics was not well-advanced until the middle of the 20th century. A reason could be a lack of measured data for avalanche *velocity*, *dynamic and impact pressures* and *geometric deformation* and the complicated topographic features on which the flow takes place. Methods to predict avalanche velocity, run-out zones and associated impact forces were first developed in Switzerland in the 1950s due to the availability of historical and initial experimental data of their own [4, 13]. Here, we address some important aspects of avalanche dynamics.

Avalanche Paths They are generally divided into three parts that are distinguished according to the dynamics (Fig 2.13a). The *starting zone* is usually the steepest part of the entire path. Here the avalanche breaks away, accelerates down the slope and picks up additional material (snow) as it moves. No reliable model exists to date that would allow the prediction of the mass

that is breaking loose and its geometry. These must be estimated. For this reason, the unstable mass, its geometry and velocity are treated as an initial condition for the subsequent motion. The additional gravel (snow) mass, entrained from the ground along the track is described phenomenologically in the equations of motion that follow, if it is accounted for. From the starting zone, the avalanche moves into the *track*, where the velocity generally remains more or less constant and little or no additional snow is added to the moving avalanche, and the average slope angle has become less steep. This is where small avalanches stop, because they do not have enough inertia to flow any further. After travelling down the track, the avalanche reaches the *run-out zone* where its motion ends, either abruptly when it crashes into the bottom of a gorge or slowly when it enters a flat plane region (see Fig 2.13a), or as it decelerates across a gradual slope. As a general rule, the slope angle of starting zones is in the range of 30° to 45° or more, that of the track is 20° to 30°, and the run-out zones are less steep than 20°. In most cases, the avalanche simply flows along a path down the steepest route on the slope while being guided or channelled by terrain features, such as the side walls of a gully, which normally direct the flow of the avalanche to the bed. This holds for so-called dense flow avalanches but not for airborne powder snow avalanches.

Run-Out Zones Large masses move more "efficiently" and thus reach farther distances than smaller ones. This effect was first investigated by Heim [147]. The observations indicate that avalanche run-outs exhibit a size effect, i.e., on geometrically similar tracks large avalanches move farther distances than small ones. The existence of *long-run-out* events is a significant obstacle for a reliable mathematical modelling of such flows of very large masses.[7]

One of the most complicated and practically relevant aspects of avalanche dynamics is the effort to predict how far an avalanche will continue to flow or travel after it has reached the run-out zone. An equally important question for avalanche practitioners is to determine the area of impact in the deposition zone and how the deposited mass is distributed. These areas are important from an infrastructure point of view because they may potentially be used for habitation (see Fig 2.13a).

Dynamic and Impact Pressures Besides the reach of an avalanche, or a rockslide, also the *velocity* at any point of its travel is of outstanding importance. The destructive power of an avalanche may be estimated by its velocity v and density ρ, since $\rho v^2/2$ has the dimension of a pressure. This is called the *dynamic pressure* and when multiplied by 2, the *impact pressure* by

[7] Compilations of run-out distances of dry avalanches of various sizes indicate that there seems to be a threshold value for the avalanche size, below which the run-out distance is independent of size, whilst above it there is such a dependence. This threshold seems to be of the order of 10^6 m^3, see [372].

avalanche dynamicists and *stagnation pressure* by fluid mechanicians, shows that the speed is a decisive variable in determining the forces exerted on the structures by the moving snow. Small and medium sized events may have impact pressures of 10^4 Pa (0.1 bar), but in very large avalanches they may reach as much as 10^6 Pa (10 bar) and are then able to uproot a large part of a forest and destroy solid buildings. Sometimes they can even derail an entire train in transport (see Fig 2.13b).

2.6 Types of Granular Avalanches

There are two limiting cases of avalanche, landslide and rockfall dynamics depending upon the form of motion rather than the quality of the material. Between the two limiting cases discussed below, a wide variety of avalanches can be found that are sometimes referred to as *mixed-type avalanches*.

2.6.1 Flow Avalanches

The so-called *flow avalanche* (see Figs. 2.7a,b and 2.14a,b) can be understood as a dense gravity driven "laminar type flow" avalanche.[8] In this case, the role of the solid particles dominates, while that of the interstitial fluid is minor or even negligible. Such flows are typical for many debris- and mudflows, rockfalls, landslides and snow avalanches. On average, the density is fairly high, for snow avalanches it ranges from 150 kgm^{-3} to 500 kgm^{-3}. The typical mean velocity ranges from 18 kmh^{-1} to 90 kmh^{-1} $\cong$ (5 ms^{-1} to 25 ms^{-1}). These flows usually follow the local topographic features and run along channels and/or corries. It follows that the basal friction must be significant. Most snow and ice avalanches, when they are formed from a fractured snowpack, develop as flow avalanches (see Figs. 2.12b and 2.14). The size of their particles depends upon the thermodynamic state of the snowpack. Fresh dry snow tends to form small granules of perhaps, 2–3 mm diameter, wet snow develops into hard snow balls (from several tens of mm to dm diameter), and old snow in the spring that has undergone several metamorphoses (so-called "greasy snow") consists of ice grains of 5–10 mm diameter. While their behaviour under flow must be different from other flow avalanches simply because of their different appearance in the deposit, they have similarities with dense granular flows. Avalanches may grow in mass along their tracks by entrainment of snow from the snow layer that is overrun or they may loose mass by sedimenting snow, but these entrainment processes are relatively poorly known, although they are very important and sometimes play a decisive role in the overall dynamics.

[8] We set "laminar" in quotation marks, because it is debatable whether this flow is really laminar, but the term is popular in avalanche dynamics.

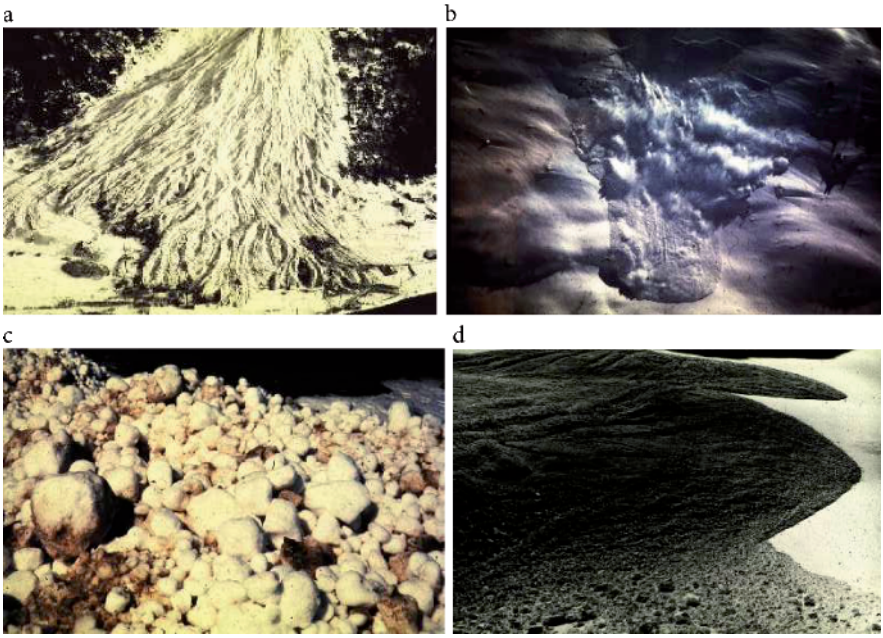

Fig. 2.14. **a**) Deposition of a flow avalanche. **b**) Avalanche "Marianne" at Bernina, blasting: Artificially released flow avalanche. **c**) Deposit of a wet flow avalanche. (Courtesy of E. Wengi, Swiss Federal Institute of Snow and Avalanche Research, SLF, Davos, Switzerland.) **d**) Snow deposit of a dry flow avalanche. (Courtesy of E. Wengi, Swiss Federal Institute of Snow and Avalanche Research, SLF, Davos, Switzerland.)

In debris and rockfalls and in certain fast landslides, such as pyroclastic flows, these "flow avalanches" indeed correspond to "dense granular flows" with a solid volume fraction of the order of 0.4 to 0.7. Particle diameters in these flows range from the sizes of clay to grabbos (about fist size), or boulders.

2.6.2 Powder Avalanches

Powder (snow) avalanches occur in very cold, dry climates. The light powdery snow grains do not stick together well. Sometimes, when strong winds cause this snow to move down a mountain side, it swirls and spins like a huge white cloud. These avalanches can be so forceful as to uproot large trees and carry them along like match-sticks. A powder avalanche is accompanied with induced and added wind, and much damage is caused by the wind alone. These avalanches are much less dense than flow avalanches and may be called "turbulent-type flows" of airborne particles. They are very rapid flows and the role of the fluid and particles is of similar significance. These flows are called particle-laden flows; they are often treated as *turbulent two-*

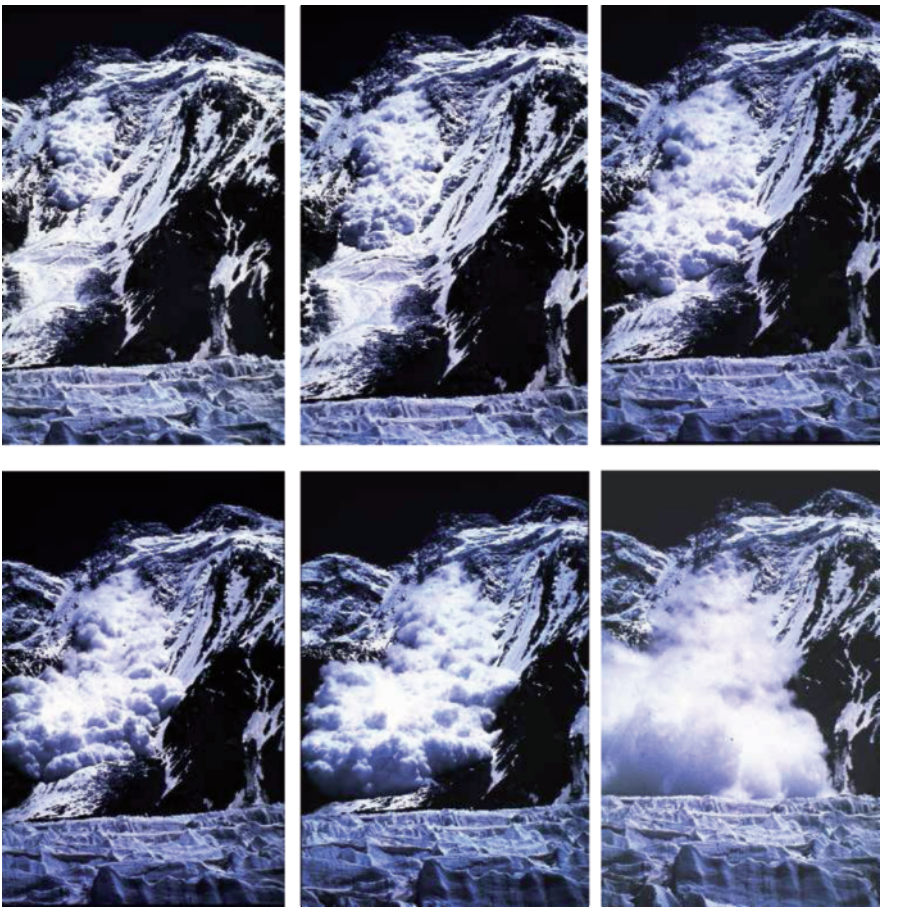

Fig. 2.15. A sequence of snapshots of a powder snow avalanche in the Himalaya. (Photo F. Tschirky, courtesy of Swiss Federal Institute of Snow and Avalanche Research, SLF, Davos, Switzerland.)

phase flows or, at solid particle concentrations larger than 10^{-3} in volume, as turbulent binary mixtures, and they are typical for density and turbidity currents, e.g., dust clouds occurring in the desert, in pyroclastic volcanic eruptions, in subaquatic turbidity currents and in snow and ice avalanches (see Figs. 2.15, 2.16 and 2.17). However, such avalanches are less frequent than flow avalanches. Typically, the mean-flow depth, velocity and density are of the order of 10–100 m, 50–100 ms^{-1} and 5–50 kgm^{-3}, respectively, see [6]. A further distinction is also that powder snow avalanches follow the direction of the steepest descent of a considerably averaged topography and not the particular small-scale troughs and deepenings that are relevant for dense flow avalanches. This implies that details of basal friction cannot be significant for

Fig. 2.16. Photographs of a powder avalanche taken from a helicopter. The avalanche moves uphill after passing through a valley, bottom picture. (Courtesy of Swiss Federal Institute of Snow and Avalanche Research, SLF, Davos, Switzerland.)

the description of their gross motion. A summary of the different typical scales is given in Table 2.1.

The above-mentioned two situations actually present idealised, limiting cases. Neither of the two types of avalanches is less dangerous. Once either has been triggered off, there is usually little or no chance for walkers, skiers, or climbers to escape its path. By far the avalanche occurring most often is of mixed type, e.g., a flow avalanche overlaid by some snow dust, or a powder snow avalanche underlaid at its bottom by a boundary layer of a flow avalanche. A closer look at the physical behaviour of such mixed avalanches shows that there exists a number of layers in which the dominant dynamical processes are characterised by a distinct physical behaviour, compare Table 2.2. The lowest layer is the ground, which either consists of soil, rock or a snow cover of at most a few metres thickness, typically less than 10 m. The dense avalanche

Fig. 2.17. Pyroclastic flow of the volcanic eruption in Goma, Congo, 17 January 2002, that destroyed 40% of the largest city in the region. This eruption was the largest in the volcano's history, according to geological evidence.

Table 2.1. Typical scales of flow and powder snow avalanches.

	Flow avalanches	Powder avalanches
Flow type	Laminar	Turbulent
Velocities	$\sim$ 5–30 ms^{-1}	$\sim$ 40–100 ms^{-1}
Flow height	$\sim$ 1–10 m	$\sim$ 100 m
Density	100–300 kgm^{-3}	$\sim$ 5 kgm^{-3}
Stagnation pressure	0.5–5 bar	0.25–0.6 bar
Topography	Often bound to local topography	Topographic details are insignificant
Friction	Basal friction is everywhere significant	Basal friction mainly significant in the run-out

comprises the next layer and may be fed from the ground layer by entrained snow, or snow may be deposited on the ground by deposition of snow from the dense flow avalanche. This snow settlement, of course, only arises in the run-out zone.

The dense flow avalanche constitutes the source of mass for the dusty, very thick layer of the powder snow avalanche, but this mass transfer takes place in a very thin saltation layer of a few centimetres thickness. There are also observations indicating that this layer may reach several decimetres (Schaerer

Table 2.2. Structure of a mixed avalanche. The avalanche may be divided into four interacting layers: The visible layer on top is the largest and forms a turbulent boundary flow in air. Below it the very thin saltation layer transmits the snow particles torn from the dense flow avalanche to the suspension layer. The latter interacts with the ground through entrainment and deposition of snow.

Avalanche type	Layer description	Thickness	Flow characterisation
Powder snow avalanches	Fully turbulent powder flow layer, *suspension layer*	~ 100 m	Turbulent particle laden flow at small concentration, diffusive solid-fluid *mixture* or *two-phase flow*
	⇕		
Saltation layer	Two-phase viscous wall layer	Few cm to at most 1 m	Turbulent two-phase flow with particles in saltating motion, colliding with each other and with flow avalanche layers
	⇕		
Dense flow avalanche	Flow avalanche layer	1–10 m	Laminar flow with granular structure entraining mass into the saltation layer with snow entrainment/deposition from/into the ground
	⇕		
Ground	Stagnant snow layer or base ground	< 10 m	Snow at rest

and Salway [377]). At the lower boundary of this thin layer the snow or ice particles are torn from the flow avalanche surface. The particles then go into ballistic motion and bounce back to the flow avalanche surface, where they may trigger additional particles to bounce to the surface, or they collide with each other. A number of particles receive enough vertical momentum to leave the saltation layer and become the airborne particles in the suspension layer. All these particles then form the particle laden flow in the suspension layer that is characterised by strong aerodynamic turbulence. Particle collisions are likely to be much less frequent than in the saltation layer, interaction is rather through collisions between particle laden eddies. This uppermost suspension layer is bounded above by the still atmosphere or a geostrophic flow at the upper edge of the suspension layer. This makes it plausible that the flow within the saltation layer is that of a true solid-fluid two-phase continuum, whilst the suspension layer can be simpler, and a diffusive mixture suffices. The saltation layer in a mixed avalanche has not been observed and it may for obvious reasons never be observed, but it is akin to the saltation layer in snow or sand drift. Gauer [108, 109] has drawn attention to this saltation layer in snow drift and Fig. 2.18 shows photographs taken by Kobayashi [224]. This figure shows the grain motion within the saltation layer. In this case, the mean length of the saltation paths of snow particles falls in the intervals (0.05, 0.14) m and (0.11, 0.3) m for the wind speed of 5.0 ms^{-1} and 10.0 ms^{-1}, respectively.

A separate study of the dense flow and dilute powder snow avalanche is helpful because the relevant physics can be more easily described, which makes it easier to understand the corresponding physical processes.

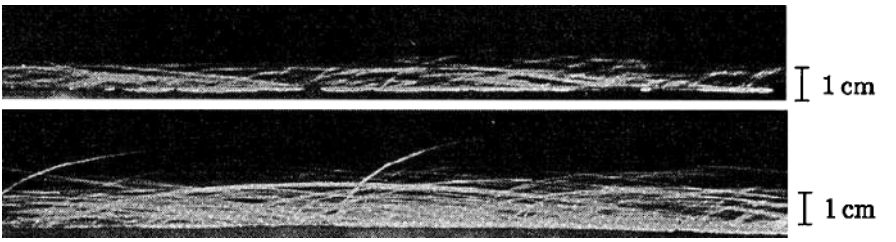

Fig. 2.18. *Top*: Saltation at very low speed (3.8 ms^{-1}) during light snowfall. *Bottom*: Saltation of typical shallow drift in the absence of snowfall (wind speed 5.0 ms^{-1}). (From [224].)

2.6.3 Landslides and Avalanches on other Planets

Like on Earth, scientists have also observed avalanches, debris flows and landslides on other planets of our solar system, such as Mars and Venus. The

Fig. 2.19. Avalanches on Mars. **a**) Valles Marineris – a close-up view of a landslide on the south wall of Valles Marineris, which partially removed the rim of the crater that is on the plateau adjacent to Valles Marineris. Several distinct layers can be seen in the walls of the trough. (Picture source [461]). **b**) Canyon landslide – debris of a canyon landslide in a very steep crater similar to that of Valles Marineris. (Picture source [462].)

reason is that these planets also consist of large ranges of mountains covered by ice, rocks and soil.

Mars has (perhaps) the largest avalanches of the planets in our solar system. It has many large avalanches but underlying processes are still concealed. The landslides on this planet are very wide, typically about 100 km. The volume of the landslide debris of Ophir Chasma, a large west-northwest-trending trough, is more than 1000 times greater than that of the debris avalanche of Mount St. Helens on 18 May 1980, see Sect. 2.3.7. Figure 2.19a shows a close-up view of a landslide on the south wall of Valles Marineris (on Mars). This landslide partially removed the rim of the crater bordering the plateau adjacent to Valles Marineris. Several distinct layers can be seen in the walls of the trough. These layers may be regions of distinct chemical composition or mechanical properties in the Martian crust. Similarly, Fig. 2.19b shows debris of canyon landslide.[9]

Mass movements on Venus, seen in radar images acquired by the Magellan spacecraft during its first mapping cycle, are easily interpreted within the scheme commonly used to classify terrestrial landslides. Rock slumps, rock and/or block slides, rock avalanches, debris avalanches, and possibly debris flows are seen in areas of high relief and steep slope gradients, and are most abundant in the tectonic troughs that criss-cross much of the equatorial region of Venus. Venusian landslides, like those found within the Valles Marineris on Mars, tend to come from escarpments typically higher than those on Earth. Faulting and seismically-induced accelerations are probably responsible for the majority of these non-volcanic mass movements. The atmosphere may participate in promoting the movement of some of the landslide debris, but environmental factors (e.g., rainfall, temperature cycling) do not appear to play as dominant a role as they do on Earth. Venus shows clear and unambiguous evidence of mass movements at a variety of scales. Measurements and observations show that Venus is covered by, at most, a very thin mantle of debris. Similar avalanches are also found on the Moon.

[9] For many more pictures and a detailed description, see [255].

a

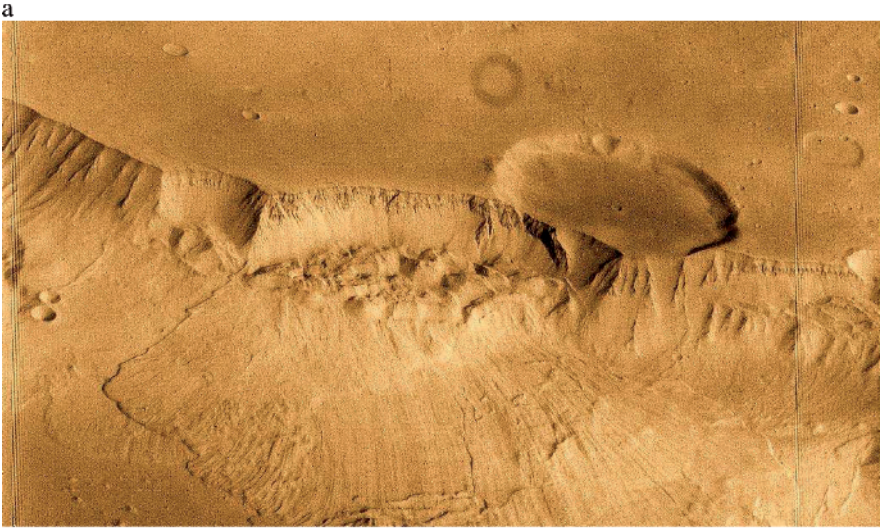

b

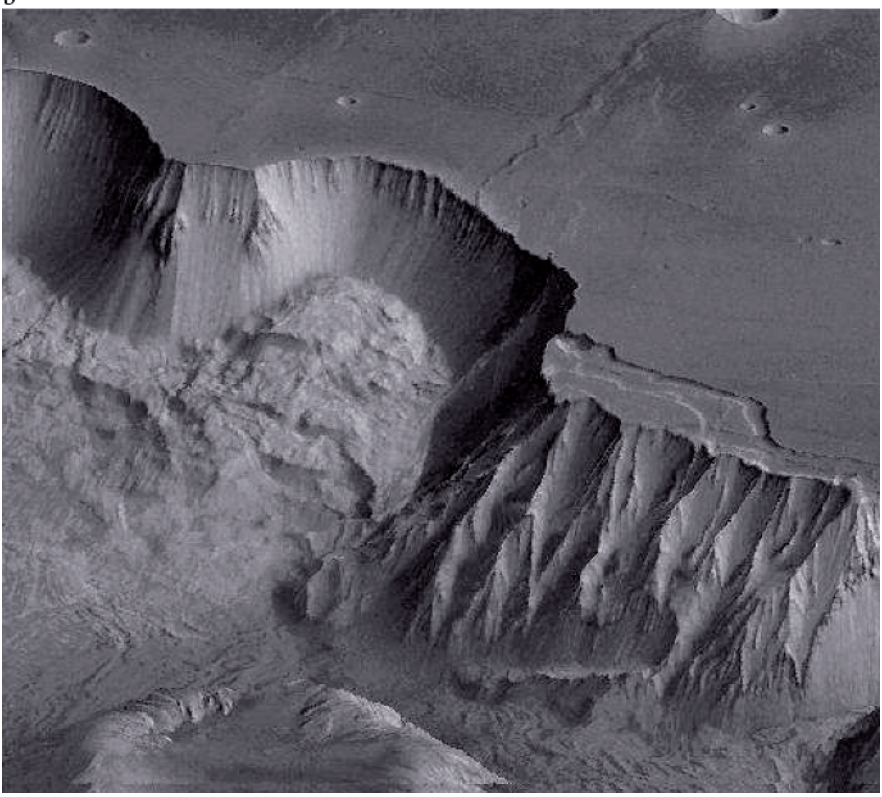

2.7 Fundamentals of Granular Avalanches

2.7.1 Some Characteristics of Flow Avalanches

Simple analysis of a gravity driven shear flow of a material with shear resistance shows that the longitudinal velocity profile consists of two contributions: a component due to *sliding* of the material along the basal surface and a second component due to *shearing* within the moving pile (see Fig. 2.20). Observations in laboratory granular chute flows indicate that strong shear is usually restricted to a thin basal layer, whilst its contribution to the total velocity throughout most of the moving pile is small. Scrutiny of the structure of this shear layer also indicates that the particle concentration and thus apparent densities are smaller than in the thick layer above it. This behaviour motivated SAVAGE and HUTTER to replace, as an approximation, the shearing altogether and to add it to the sliding mechanism [375]. This will be mathematically implemented in the models presented later. At this stage, two questions remain to be answered: (*i*) are there observational evidences from flow avalanches which support this and (*ii*) what is the physical mechanism for the velocity reduction in the thin shear layer?

As to the first question, limited evidence is provided by GUBLER [134] and DENT et al. [80]. By using radar DOPPLER technology, GUBLER successfully studied the dynamics of artificially released snow flow avalanches. He concluded that the rear bottom boundary layer is not negligibly thin in comparison to the entire thickness of the moving flow mass. He also found density variations throughout the depth, but measurements were not sufficiently conclusive in this regard. DENT et al., on the other hand, observed a mov-

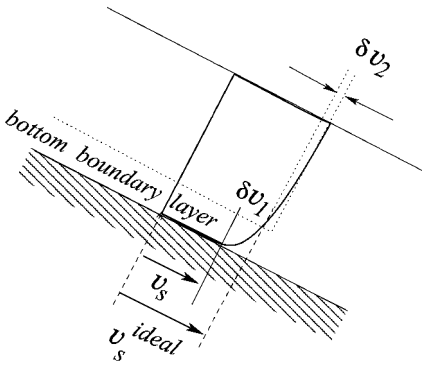

Fig. 2.20. Velocity profile in a gravity driven shear flow. The velocity at a certain depth is composed of a sliding contribution v_S, a contribution of strong shearing in a bottom boundary layer δv_1, and a very small shearing contribution δv_2 in the larger top layer. In general, the velocity of the flowing material can be idealised by taking an approximate sliding velocity at the base.

ing flow avalanche from a window of a cage, built behind a rock but within the avalanche track in Montana and concluded from cinefilms taken during an event that the observed velocity profile indeed suggested negligible shearing throughout almost the entire depth and substantial shearing possibly in a thin basal boundary layer and strong sliding at the ground as shown in Fig. 2.21.

Measurements in the field of velocity profiles in debris or mud flows are not known to us. So, in this granular flow realisation of avalanching flows, inferences on the velocity distribution can only be drawn from laboratory experiments. These are performed under idealised situations and show that, on surfaces with bed friction angles in the range of 30–50°, the concentration of all shearing at the base in a sliding surface is adequate. Only when basal surfaces are very bumpy, may this extreme concentration of shearing in the bottom layer have to be revised. More details on this analysis can be found in [183].

The reduction of the particle concentration in the thin boundary layer is due to the dilatation that is necessarily accompanied with the remaining deformation of a granular material (see Fig. 2.20). The effect of dilatancy is also a significant mechanism in a granular material that is responsible for it to behave as a *non*-NEWTONian fluid exhibiting, in particular, *normal stress effects*. By this it is meant that *a shearing deformation with constrained volume changes must necessarily be accompanied with normal stress.*

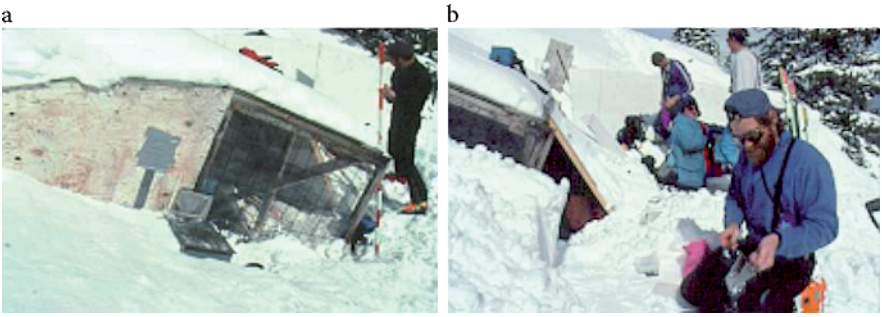

Fig. 2.21. **a**) Revolving door instrumentation shed. **b**) Revolving door data collection. The instrumentation, of a large-scale dry snow avalanche, includes: optical sensors to measure velocity and density profiles, a capacitance probe to also measure density profiles, a mechanical gauge to measure flow depth, and a strain gauged plate mounted on the avalanche running surface to measure shear and normal stress. These properties were measured for avalanches of up to 1.5 m in depth and moving at speeds greater than 10 ms^{-1}. The information collected is being used to help construct and validate models of avalanche movement. (From [453].)

A striking observation in landslides and snow avalanches is that they often spread out in very thin layers and flow on surfaces that are much less inclined than the angle of repose of the material. From the field observations of Gubler and Norem et al. [134, 302, 303] it is found that distances travelled by landslides or avalanches are very large and deposition lengths long and avalanche depths correspondingly small. Furthermore, for very large rockfalls or landslides with volumes exceeding 10^6 m^3, the run-out distance is volume-dependent [374]. For a given profile, the larger the avalanche volume, the larger its relative run-out distance [179].

A collection of these observations from landslides on the Earth, Moon, Mars and Venus disclosed this scale dependence, but it has not been explained theoretically and still remains an enigma. An account of this will be given in Sect. 2.7.5. The large distance travelled, however, can be explained. For landslides, gravel and rock avalanches it is due to the *fluidisation* of the material, i.e., the bouncing of the individual grains against each other, in which the above-mentioned dilatation is active. This fluctuating motion generates a *dispersive pressure* that accompanies the shearing and reduces the effective shear resistance within this boundary layer and, therefore, also increases the sliding.[10] This is by far the most plausible cause of the large distances travelled by avalanches and their considerable spreading in the deposition. In snow avalanches and extremely large rock avalanches, the frictional heat may also melt basal snow or rock, and so add the molten material as a further lubricant.[11]

2.7.2 Stress Generating Mechanisms

Following common rules of physics, one distinguishes three different mechanisms that operate in generating stresses due to deformations of cohesionless granular bulk material. In relative motion, particles can slide and rub against each other, bounce and loose energy in collisions and perform ballistic motions between encounters. In general, all these mechanisms are effective in a high to a moderate density regime. The first of the following mechanisms is applicable for dense avalanche flows, it reflects solid and fluid-like behaviour. The other two are mainly applicable for granular gases.

Dry Coulomb Rubbing Friction Such a frictional behaviour is typical when particles are in contact and ride one over the other without losing

[10] This description means that the internal angle of friction or the bed friction angle will decrease as soon as the interstitial pressure is sufficiently large.

[11] In geology, rocks formed from solidification of molten materials in landslides are called *frictionites*. This term is defined as "*... any at least partially melted products generated by friction near the surface and allowing to be put down exogenous processes exclusively depending on terrestrial gravitation ...*" [94].

contact. In this state, the associated internal forces develop through contact mechanisms. During quasi-static processes, or when collisional activity is small, these frictional processes are dominant. The so-called *natural densities* are normally huge here, and the behaviour is plastic and of COULOMB-type.

Collisional Interactions These take place when particles bounce against each other. When the particle contact is of short duration so that COULOMB rubbing friction cannot effectively develop, the momentum transport is caused by collisional interactions and the behaviour is *rate-dependent* (viscous).

Translational Transport The third mechanism to generate stresses is due to the transport of momentum by particle translation. In this case, the COULOMB-type rubbing friction is practically insignificant, collisions are infrequent, the mean free paths are long, and particle concentrations are correspondingly small.

These three limiting states essentially characterise solids, fluids and gases. In gravity driven shear flows, all three act simultaneously, but often one of them is dominant, whilst the others can be ignored. In dense snow avalanches or reasonably wet snow bouncing is seldom observed, so collisional interactions and translational transport may be ignored. Alternatively, in dry snow or sand avalanches on very steep slopes, the particles may be agitated throughout the entire granular layer, so that rubbing friction may be ignored. Depending on which limit is considered, different concepts apply.

2.7.3 Density Variations

When a finite mass of granular material starts to move from rest, the major part of volume expansion takes place immediately at the start, such that the subsequent motion may be nearly *isochoric* [180]. The incompressibility assumption is based on descriptive field observations (see MELOSH [279]) and on deductions from the study of confined laboratory chute flows of a finite mass of gravel [172]; it makes implicit use of the fact that the basal zone be the active zone in which nearly all shearing takes place [241].

While the true mass density of the material making up the individual grains is constant or nearly so, noticeable variation in bulk density may exist as a result of variations in void spaces between grains. Here, we would like to give an outlook on why we can treat the bulk density of the flow avalanche as a constant. An understanding of how such bulk density variations might develop in a practical problem can be inferred from earlier studies of constitutive behaviour of rapidly sheared granular materials derived from considerations of individual particle interactions [195]. Immediately after the pile accelerates from rest down the bed, a particle layer of sheared material will develop due to

the friction between the moving mass and the rough basal surface. Dispersive pressures normal to the bed develop as a result of the collisions between the randomly fluctuating particles. This causes the accelerating sheared layer to expand. If the bed is steep and the flow accelerates rapidly for a long enough time, the reduction in bulk density can be significant. However, if the bed slope is close to the angle of repose of the granular material, the granular mass will accelerate slowly. In such a case, the thickness of the rapidly sheared basal layer can be a small portion of the total depth of the flowing granular body, so that the vertical dilatation of this layer will be relatively small. As will be seen in the sequel, a crucial step in the development of the continuum mechanical theory is the process of depth-averaging of the field equations. The variations of bulk density that might be present are of less consequence and may be assumed to have a small effect on the convective terms in the resulting equations of motion.

Two-dimensional laboratory experiments on gravel and plastic beads flowing down curved beds are presented in [172, 175, 179, 324]. There it is reported that the observations of these laboratory avalanches through the glass side walls of the confining channel show variations in overall average bulk density from the initiation of the motion until the material comes to rest that are typically less than a few percent [376]. The largest density changes are right at the start and immediately prior to settlement. In a moving mass, the density variations are generally small.

2.7.4 Constitutive Relations

When considering snow avalanches as continuous deforming masses, an essential step in their description is the postulation of the stress closure. In particular, due to the strong stress–strain–history dependence and the nonlinear behaviour of snow, constitutive relations seem to be quite complicated. Quoting Salm [364], Lang [242] writes *"There exists no universal constitutive equation for snow and other granular materials, only equations reflecting the behaviour under certain conditions"*. For various specific problems of snow, both microstructural theories [244, 245] and continuum theories [47, 48, 49, 50, 51] have been proposed and applied successfully. Unfortunately, all these models require detailed information on the particular type of snow in question [242].

Modern theoretical models of engineering nivology make use of the substantial achievements of modern thermodynamics of solids and fluids [1, 28, 47], fracture mechanics [30, 269] and techniques of homogenisation. Modern tools of elasto-viscoplasticity, structural porous, granular and heterogeneous media are used [1] and subjected to experimental scrutiny. The two main fields, (*i*) the description of snow in its cover and subject to creeping deformations and (*ii*) its behaviour in catastrophic motion are so *disjoint* that to date no

proposed stress-deformation relation that would reproduce both regimes exists, including the breaking of the snow cover into a catastrophically moving avalanche. The two regimes of behaviour are theoretically disjoint and are largely still thus treated. Snow at rest and snow in motion seems to be two separate scientific fields. In the debris and dense pyroclastic flow science the situation is similar.

In 1954, for the first time, BAGNOLD conducted laboratory experiments with annular shear cells to determine the dependence of the shear and normal stresses upon rapid shear rates and particle concentration [20, 21]. A number of other experiments were also performed following this pioneering work, see, e.g., SAVAGE and SAYED [372], BUGGISCH and STADLER [55], STADLER AND BUGGISCH [402, 403] and CAMPBELL [57]. The results of such tests depend upon whether shear tests are performed at constant volume or at a constant normal stress, respectively. *In both cases*, it is found that the shear and normal stresses are related by a MOHR–COULOMB-type criterion with an internal angle of friction that is nearly constant. At high shear rates, when shear cell tests (see Fig. 2.22) are conducted so as to maintain a *constant volume*, it is found that *stresses vary with the square of the shear rate*. When the layer of particles is allowed to expand freely, and shear cell tests are performed with a *constant normal load*, then it is found that the *shear stress is nearly independent of the shear rate* [141, 369, 371]. It is in fact this distinguished behaviour of granular materials that motivated and prompted the authors to apply it in developing the theory on avalanching motion of a finite mass of

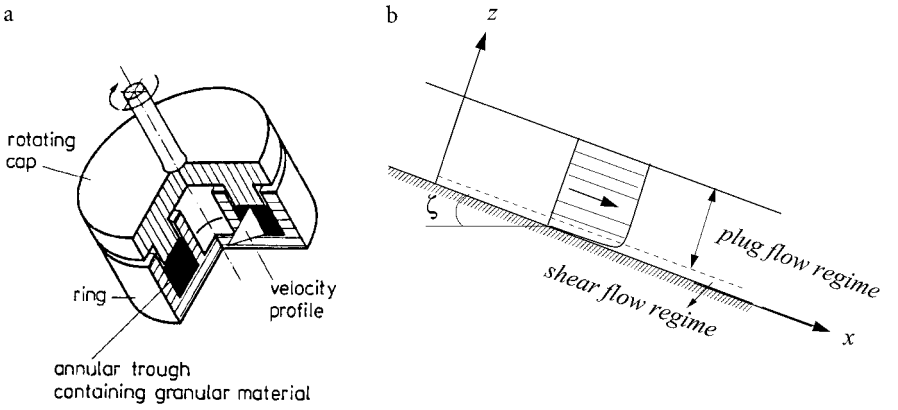

Fig. 2.22. **a**) Sketch of an annular shear cell; the granular material is contained in the annular trough in the lower half of the shear cell and capped by an annular ring attached to the upper half of the shear cell. The cap is rotated with constant angular velocity, thus inducing a shear flow in the granular material. (From [375].) **b**) Gravity-driven granular motion with large plug flow regime lying on top of a thin shear flow regime on the basal surface. The shear layer is magnified.

granular materials. HUTTER and co-workers [175, 375, 376] exclusively discussed its relevance for the flow of granular materials down an inclined chute. Afterwards, they successfully applied this idea in more general situations with respect to an underlying topography [123, 334, 335, 337, 341, 342, 445]. Indeed, the use of the MOHR–COULOMB yield criterion with constant internal angle of friction, ϕ is justified, which we will see explicitly in the following considerations when the continuum mechanical theory is discussed in detail. For the collisional and translational transport of momentum, statistical theories have also been developed along the lines of the kinetic theory of a dense gas, e.g., by JENKINS and others [195, 196, 197, 198], for a review see HUTTER and RAJAGOPAL [178].

In many laboratory experiments of dense granular avalanches [123, 128, 175, 179, 227, 241, 334, 343, 445] and probably in real situations too, it is observed that in the *flow avalanche regime* most of the moving granular mass rides more or less passively on a fluidised bed. This means that only a very thin basal boundary layer tends to be fluidised, while the major upper part of the moving and deforming mass is in the regime where a COULOMB-type rubbing friction is effective. In fact, despite the dynamic nature of the flow, instead of treating the fluidised layer as a granular material in COULOMB-dry rubbing friction and collisional interaction regions, one practically *collapses* the thin boundary layer to a boundary condition (see Fig. 2.22b), namely the COULOMB-type sliding law with bed friction angle δ at the basal surface. For this reason, in their original paper [375] SAVAGE and HUTTER proposed a simplified constitutive model to treat the granular materials as being of rate-independent COULOMB-type, both in the interior and at the bed, with constant internal and bed friction angles ϕ and δ, respectively. Later, other avalanche dynamicists, see for instance [198], used this type of simple yield criterion to model the frictional behaviour of debris flows and avalanches with a rough sliding surface. Similar ideas were also put forth in debris flows research (DENLINGER and IVERSON [74, 75], IVERSON et al. [192, 194], PITMAN et al., [320, 321, 322] and PATRA et al. [313]).

2.7.5 The Size Effect

Whenever reading about size effects in avalanche dynamics we were puzzled by not exactly understanding what the authors might mean. So, let us state how *we* understand it. To this end, consider an avalanche track and a mass of granular materials with its initial locations of release and end deposition as, e.g., shown in Fig. 2.23. Imagine a second, analogous situation, similar to this by geometry but much bigger. When scaling this larger avalanche down to the size of the smaller one, two situations can arise: the two pictures, one of which is scaled down, are either congruent or they are not. If they are, then there is no size effect, if they are not, then there is such a size effect.

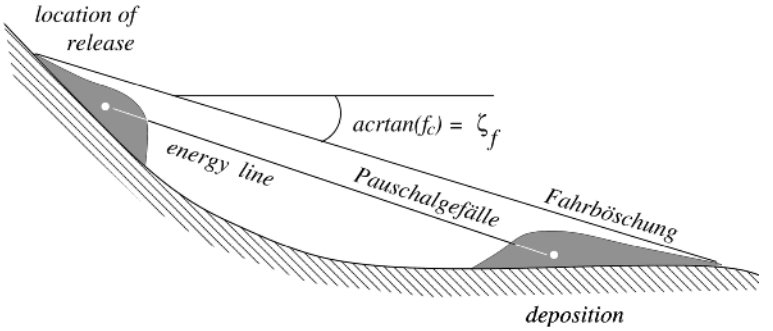

Fig. 2.23. A sketch of the *overall-angle*, "Fahrböschung", and its counterpart *overall-height-drop*, "Pauschalgefälle", of an avalanche. The line corresponding to "Pauschalgefälle" is also called the energy line since it counts the drop of potential energy of the mass falling downslope due to the driving force of gravity. The white points are the centres of mass of the granular piles.

It follows that size effects manifest themselves in changes of the slope of the "Fahrböschung" and "Pauschalgefälle" (see Fig. 2.23).[12]

HEIM and other avalanche and rockslide scientists observed that large masses generally travel farther than smaller ones [94, 146, 147]. He considered the *size effect* as an important tool for investigating the travel distance of a flowing mass. There are two special terms used in the literature concerning the travel distance of the mass. One of them is the "Fahrböschung" (*overall slope*), which is defined to be the tangent of the angle between the horizontal and the line connecting the crown of the head scrap with the most distal debris along the midstream path of the mass [94] (see Fig. 2.23). The other term, "Pauschalgefälle", is defined as *the angle between a line connecting the centres of mass in the initial and end positions and the horizontal*, as illustrated in Figs. 2.23 and 2.24b. The line connecting the centres of mass, in this definition is also called the *energy line*. These terms may be useful parameters distinguished by two important advantages. Firstly, they can often be determined even if most of the debris of the event has been carried away by erosion. So they are useful for *post-eventum analysis*. Secondly, they may facilitate *prediction*. In many cases, the presumptive location of a head scrap of the avalanche or a rockslide can somehow be marked by a large crack. Thus, one of the two required points of the dynamics is known. If the value of the

[12] The denotation of these two different slopes in English by these two German technical words seems to be common in the geological literature. "Pauschalgefälle" agrees with the energy line. The height travelled by the displaced mass determines the loss in gravitational potential energy, which equals the total energy loss in the catastrophic motion. The "Fahrböschung" has no physical, but perhaps a morphological significance. It provides information on the terrain that is affected by the avalanche and it is relatively easy to determine.

overall slope can be determined by past experiences, the material properties and the topographic features of the ground, and then, the longitudinal reach of the debris can be estimated.

The size effect of the total masses on the dynamics of rockslides, debris- and mudflows, and avalanches is at first of secondary importance in the study, but it manifests itself in the distance travelled. It exerts a direct influence upon the resistance and an indirect one on the track. Most of these effects are positive, which means that larger masses reach farther. However, there are examples where size effects have a negative influence, for instance, avalanches and rockslides that are lubricated by air [94]. However, because of the great variety of effects, the theoretical deduction of a generally acceptable dependence between size and resistance is probably extremely complex. As a *rule of thumb*, large masses move faster than smaller ones. This fact further increases the complexity induced by the size effect. Due to this complexity, the size effect is considered by some rockfall and rockslide dynamicists as a *black box* [15].

Scheidegger presented a model equation depending on the total volume as a tool for the prediction of the *run-out* distance of rockslide events [379]. He correlates the slope of the "Fahrböschung" f_c via

$$f_c = 10^{C_1 + C_2 \mathrm{Log} V}, \tag{2.7}$$

with the total volume V of the moving mass, where C_1 and C_2 are constants determined by a large number of data points. The function $f_c = f_c(V)$ is a continuous function obtained by a regression (interpolation) fit of a large number of $f_i(V_i)$ data, where i is the index running through the number of events and $f_i = \tan \zeta_f(V_i)$ is the tangent of the "Fahrböschung" (*overall slope*, ζ_f) of the event with volume V_i (see Fig. 2.23).

This is a purely empirical method and is based on a large number of data points obtained from field evidence. As pointed out by Erismann and Abele, since the resulting function f_c depends on the individual data of the events employed for its calculation, there is always a risk of a non-representative choice and other sources of errors [94].

In principle, both the analysis and prediction of the one-dimensional avalanche travel distance determined on the basis of the positions assumed by the centre of gravity would be preferable. However, in many realistic situations these positions are either not known or very difficult to estimate.

2.8 Survey on Avalanche Modelling

Of course, in the past numerous avalanche models were proposed, most of them being direct adoptions or extensions of the Voellmy model, but also

new, innovative models. In this section, we present an account of some of them, ranging from stochastic models to continuum mechanical models to discrete multi-particle models. A detailed review of such models was compiled by HARBITZ [142] in the SAME report; we have already reported on it in Chap. 1. It is hoped that the selection below gives an objective cross-section of the attempts that were made.

2.8.1 A View on Some Classical Avalanche Models

Statistical Models[13] In mountainous regions, *mapping models* are used to determine *avalanche zoning* for land use and planning. This normally demands either an accurate knowledge of past avalanche spreads or methods for computing boundaries of the avalanches. To this end, several statistical models have been proposed. Two widely used stochastic models are due to LIED and BAKKEHØI and MCCLUNG and LIED [252, 267]; they establish

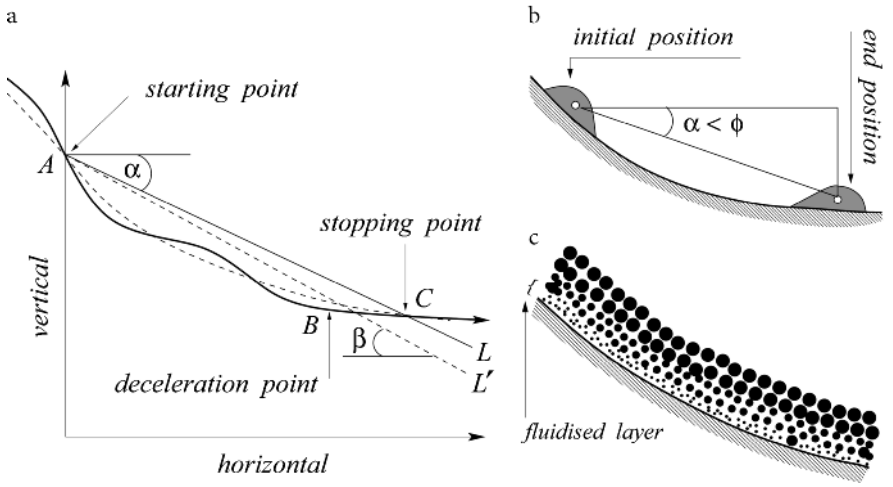

Fig. 2.24. **a**) Parameter fit in the statistical model. The *dark thick line* is the real one-dimensionally curved topography that is approximated by the *dashed parabola*. The *solid straight line* L determines the stopping point of the avalanche that is described by the angle α to the horizontal axis. Similarly, the *broken straight line* L' is the representative of the average inclination angle, characterised by the angle β, of the real topography, starting from point A and ending at point B. **b**) Pauschalgefälle ($\tan\alpha$): Since during motion a thin fluidised boundary layer is formed just above the bed, this angle is smaller than the internal angle of friction ϕ. **c**) A portion of the avalanche in motion: "{" indicates a thin boundary layer lying on the bed. Also seen is the effect of inverse grading due to kinetic sieving.

[13] These are not models based on statistical mechanics, but rather regression models correlating pairs of variables thought to possess such correlation.

correlations between the run-out distances and the underlying topographic parameters of an avalanche track. These parameters include the location of the initiation point (A), an intermediate point (B) somewhere in the transition zone (to the run-out) and the position of the stopping point (C) (see Fig. 2.24a). A simple continuous curve (e.g., parabola) is used to fit the natural path of the avalanche in the downhill direction by assuming that the longitudinal profile of the avalanche path governs its dynamics. The *average inclination angle*, β, to the horizontal of the avalanche path is determined by a straight line, L', joining the initial point and the intermediate point, the point at which the deceleration of the avalanche starts. The position of the stopping point of the avalanche motion is described by using a *stopping angle*, α, that is, the angle of a straight line, L, joining the starting and stopping point to the horizontal. This angle is the *Pauschalgefälle* as shown in Fig. 2.24b. Using regression methods, this angle can be expressed as a function of the average inclination angle, thus providing the one-dimensional extent and consequential boundaries of the avalanches. The model equation can be explicitly written as $\alpha = \lambda\beta + \gamma$, where the regression coefficient λ and the constant γ are to be determined by real field data [252, 253]. These models are explained in somewhat greater detail in [142]. They have also been extended in the recent past and subjected to scrutiny by application to realistic avalanche events, see Keylock [216], Keylock et al. [217] and Jóhannesson [203]. Further complexity has also been added by employing multi-variate statistics. Buser et al. [56], Bakkehøi and Norem [22, 23] have put these methods to scrutiny with field observations.

The upshot of these models consists in variations of the parameters and a fit of the model with a particular topography. Although statistical models have been extensively used in practice and give fairly reliable and objective results *for fixed sites*, many shortcomings are attached to these approaches. This method needs a long return period, typically 100 years, of avalanches for a given avalanche track. The dynamics of avalanches is governed not only by topographic features of their paths, but also depends on many other rheological and mechanical properties of the material, such as basal and internal angles of friction of the base and the material, respectively. The statistical model is limited to one-dimensional path profiles and thus cannot predict the areal spread of the avalanche, which, among others, is one of the most important features of avalanche mapping.

Mass Point Models Until late 80s of the last century, the most widely used and applied avalanche models utilised a centre of mass approach. They were based on the ideas suggested by Voellmy [430], who related the shear traction at the base of the flow to the square of the velocity and postulated an additional Coulomb friction contribution to it. On the one hand, Voellmy assumed uniform and steady conditions, whilst on the other hand, in this model a number of subjective parameters must be predetermined in

order to obtain results that match observational data. The simplicity of the model constitutes its power, because, depending upon the parameter choice, it may be applicable to flow as well as powder snow avalanches, but this flexibility also makes it difficult to handle. Many attempts have been undertaken to improve VOELLMY's model, e.g., by SALM, GUBLER, PERLA, CHENG, MCCLUNG, MELLOR and BARTELT et al. [27, 134, 278, 315, 361]. Unfortunately, none of these extensions could be advanced beyond the centre of mass approach. They are not able to provide information as to the spatial and temporal properties of an avalanche, such as the velocity distribution and the evolution of the avalanche height and spread. These are certainly not constant, neither in space nor in time [76, 77]. The height of the flow may merely be included as a parameter value, but is not calculated as a function of space and time. One mass point model due to VOELLMY is so popular and has been so influential that we give a separate outline of it in Sect. 2.8.2.

Hydraulic Models[14] Some other, hydraulic, models attempt to idealise these complicated materials as linear NEWTONian fluids and are discussed by BRUGNOT, DENT and LANG [52, 76]. They lead to the NAVIER–STOKES equations, which may be solved numerically. Although it is perhaps not feasible to assume that this type of constitutive relation adequately describes the media, some success has been achieved in modelling certain aspects, such as the geometric properties of the motion of the avalanche, with this approach. Several hypotheses have been proposed to explain the mechanisms for fluidisation that occurs in a thin layer close to the basal surface [93, 134, 156, 214, 389]. For fluidised granular materials, apparent viscosities may be measured [391], but the range of conditions that sustain fluidisation varies greatly among solid-fluid gravity current systems [242].

Hydraulic models are generally developed in the context of gravity driven flows down inclined planes and are mostly restricted to steady flow within vertical planes. Such a model was developed in the 1980s of the last century by the Norwegians on the basis of a nonlinear rheological behaviour and it was an attempt to resolve a velocity profile that was not quadratic in the variable perpendicular to the basal plane, but showed a form with large shearing close to the basal pane and near plug-like behaviour in an upper

[14] Hydraulic models are channel flow models in which the flow depth and the downflow velocities are the principal field variables. They are often motivated from river hydrodynamics. The depth integrated models for plane channel flow, derived for an incompressible ideal fluid, in which the hydrostatic pressure assumption is employed, are among the most famous equations of hydraulic engineering. They were first derived and used by SAINT VENANT. This is the reason why depth integrated equations for shallow flows are sometimes called SAINT VENANT equations, even if other than ideal fluid behaviour is in focus. MANGENEY et al. [264, 265], for example, refer to granular flow equations as SAINT VENANT equations.

layer. NOREM et al. [303] employ the constitutive behaviour of an ERICKSEN–FILBEY fluid and combine this with a COULOMB plastic behaviour that is based on rate-independent stretching behaviour. This model is able to resolve the shearing-plug flow combination. Its generalisation to an unsteady and three-dimensional situation was constructed by IRGENS et al. [187]. Similar attempts at a determination of the velocity profile of plane flow were also undertaken by TAKAHASHI [416] in the debris flow context. TAKAHASHI starts from a rheological model with a quadratic dependence of the shear stress on shearing, but this model was not easy to extend to three dimensions. That was done by HUTTER et al. [181], however the three-dimensional extension has so far not been applied to general avalanching conditions of debris flows.

Kinetic Models Methods of statistical mechanics can be used to derive the fundamental governing equations, including rheological closure conditions, if it is assumed that the particles are in high agitative motion and this motion is maintained by successive collisions. The result is a mathematical description of a dense granular gas (see, e.g., HAFF, JENKINS and SAVAGE, JENKINS and RICHMAN, LUN et al., HWANG and HUTTER and many others [137, 185, 195, 196, 258]). However, these theories are difficult to apply to avalanche flows as shown by GUBLER, HUTTER et al., SALM and GUBLER [134, 170, 171, 366]. Such kinetic theories involve as field equations the balance laws for mass, momemtum and fluctuation energy, corresponding to the field variables: density, velocity and granular temperature. The latter is a measure of the fluctuating kinetic energy due to the particle collisions. Construction of solutions entails the use of rather complex boundary conditions for the granular temperature, velocities and stresses. For ideal situations of identical spheres and regular bumpy boundaries, JENKINS and RICHMAN [197] derive explicit forms of boundary conditions, but for less ideal situations their motivation is still ad hoc. In any case it has been demonstrated by HUTTER et al. [170] that the construction of solutions to the related problem, even for steady chute flows, is very complicated.

JENKINS outlined a hydraulic theory applied to a debris of a dry granular mass in which the greater part of the depth is assumed to behave as a frictional plastic material [198]. This frictional plastic material is supported at its base by a thin shear layer in which collisional transfers of momentum and energy dominate. Assuming the heap to be deformed by frictional shearing while supported at its base by a relatively thin region of intense shear in which grains interact through collision, he described the frictional shearing by using the MOHR–COULOMB yield criterion. Together with balance laws and boundary conditions of the kinetic theory for dense granular flows to describe the region of colliding grains at the base, he determined the relation between the shear stress, normal stress and relative velocity of the boundaries in this shear layer using an analysis of a steady shear flow between identical bumpy boundaries.

The Discrete Element Method (DEM) This is a direct numerical simulation method in which the motion of individual particles is followed by interpreting the particles as solid bodies and accounting for the particle–particle interaction. For particular aspects of grain interaction the model is also known as *molecular dynamics* or *event driven dynamics*. The calculations are typically carried out for a fixed number of spherical particles (or in two dimensions, circular disks) that are usually bounded on the four sides by stationary or periodic boundaries. Initially, the particles have assigned random velocities. The numerical method involves explicit integration of NEWTON's second law of motion. Whereas the collisions between molecules can be treated elastically, this is generally not so for collisions between particles. They are inelastic and require to account for a *coefficient of restitution* that is smaller than unity. Slip is also allowed during contact with frictional resistance. For grains with arbitrary shape, the full EULER equations of translational and rotational motion must be solved for the motion between encounters; this integration is substantially simplified for spherical particles since it is not necessary to determine all the EULER angles.[15]

Intellectually the method is easy. NEWTON's second law of motion and possibly EULER's balance of moment of momentum must be formulated for each grain in free flight and subject to the forces exerted by the contacting particles under collision. Since all forces, except the external forces such as gravity, only act during particle contacts, one must keep track of all the collisions during numerical simulations. A naive implementation would check at each time step for all N particles whether they are in contact with any of the other $N-1$ particles. This is very inefficient and hardly feasible for system sizes of more that a few thousand particles. In order to achieve as effective numerical simulations as possible, different numerical methods have been suggested, see [3, 53, 277, 356]. Numerical results obtained by the molecular dynamic simulations generally exhibit good agreement with observations. For example, in a simulation of plane Couette flow by THOMPSON and GREST [422], a HOOKE-type elastic force model with 750 soft particles with equal radii was employed. A plug-like motion of the core and a thickness of the boundary shear layers of 6 to 12 particle diameters was found, which shows good agreement with experimental results [141]. Surprisingly, the shear stress did not show a quadratic dependence on the mean shear rate as expected [20], but became constant for large shear rates; this is explained by the dilatancy in

[15] For a non-spherical body the angular momentum equation is derived in a frame fixed with the body and yields the so-called EULER equations. The generalised coordinates are the so-called EULER angles; they describe at each instance the orientation of the body relative to a fixed coordinate system. The rotational degree of freedom per particle is three. Since a sphere is symmetric relative to any plane through its centre, only one equation is needed to describe its rotational motion. This leads to a substantial reduction of the complexity of the numerical integrations of many particle systems.

the steady-state regime. Moreover, *segregation by size or density* can also be modelled by the use of molecular dynamics [138, 306, 357].

Such direct simulations can hardly handle real practical problems involving hundreds of thousands, in fact millions of particles, in which the interactions between any particle and its neighbours are far from simple. Nonetheless, they do provide useful insight into the formulation of theories, much the same as experimental results. This is demonstrated in various simulations that have been developed and are in use (see the reviews of Campbell and Savage [57, 370]).

Above all, most molecular dynamic simulations have been performed for dry granular materials. The stickiness due to the humidity of the surrounding air may make it necessary to account for *cohesion*. In such cases and when the viscous nature of the surrounding fluid is large, the interstitial fluid is significant. Then the Navier–Stokes equations can be used to model the fluid phase. What remains is to adequately incorporate the interactions between the grains and the fluid.

2.8.2 Voellmy's Pioneering Work

It is unquestioned that A. Voellmy from the Swiss Institute of Materials Testing (Eidgenössische Materialprüfungsanstalt, EMPA) in 1955 presented the first theoretical analysis of avalanche dynamics that was internationally recognised. [See also Sect. 1.4.2, the text on "The French Contribution to Avalanche Research"]. Voellmy's pioneering work appeared in a paper "About the destructive power of avalanches" (über die Zerstörungskraft von Lawinen [430]), published as a series of four consecutive articles in the Swiss Civil Engineering Magazine (Schweizerische Bauzeitung). The work was initiated by a consultancy to EMPA commissioned by the private company "VOBAG AG" to record and evaluate the damage done on properties in the Vorarlberg, Austria by the catastrophic avalanche event in January 1954. Voellmy's paper is 20 printed pages long, and covers the subject of analysis of the destructive power of avalanches in its entirety.

Part 1 is devoted to an estimation of the forms that avalanches exhibit on obstructing objects and their effects. A back analysis is performed on the buildings and train composition that were destroyed, broken, displaced or overturned. This analysis led to an estimation of the kind and order of magnitude of the pressures that can be exerted by avalanches.

Part 2 stretches over five pages and has the simple title "About the dynamics of avalanches". Only about half a page is devoted to deriving the model equations. After explaining that the flow in an avalanche must be turbulent because of the fractionation of the snow slab, and after motivating that such

turbulent flow must be accompanied with a flow resistivity $\tau_s \sim \rho v^2/\xi$ in which ρ, v and ξ are the density, the flow velocity and the drag coefficient, he continues to say:[16]

"A snow layer, with vertically measured height h, sliding down an incline of constant slope ζ, generates at the base a frictional resistance that is proportional to the slide area (sliding coefficient ξ), and in turbulent motion proportional to the mean velocity v and the density ρ. In addition, a frictional resistance acts that is proportional to the slide area and to the normal pressure acting on it. Little is known about the frictional coefficient μ. The friction angle at rest is usually 30° to 40°; most avalanches arise in this range of slope inclinations.

If the buoyancy of the air with density $\rho_L = 0.127\ \mathrm{kgm}^{-3}$ is accounted for, the equation of motion of a portion of a sliding snow layer whose horizontal projection equals the unit area, is

$$\text{force} = \text{mass} \times \text{acceleration},$$

$$g\,(\rho - \rho_L)\,h \sin\zeta - g\,(\rho - \rho_L)\,h \cos\zeta\mu - \frac{\rho g}{\xi} v^2 = \rho h \frac{dv}{dt} \tag{2.8}$$

or

$$\frac{dv}{dt} = \frac{g}{\rho h}\left[h\,(\rho - \rho_L)\,(\sin\zeta - \mu\cos\zeta) - \frac{\rho v^2}{\xi}\right], \tag{2.9}$$

where h is the constant flow height of the moving layer. With $k = \xi h/g$ the solution of this differential equation is

$$v = v_{\max} \tanh\left(\frac{v_{\max}}{k} t\right), \tag{2.10}$$

in which the maximum velocity is given by

$$v_{\max} = \sqrt{\xi h \left(1 - \frac{\rho_L}{\rho}\right)(\sin\zeta - \mu\cos\zeta)}\,. \tag{2.11}$$

In most cases, ρ_L/ρ and μ can be ignored; one may then set

$$v_{\max}^2 \cong \xi h \sin\zeta\,. \tag{2.12}$$

If initially ($s = 0$), the snow layer of the investigated travel distance s already possesses a velocity v_0, and then one must, with the aid of (2.10), determine

[16] We use a notation in conformity with this book. For example, inclination angles are denoted by ζ and instead of specific weights γ, popular at VOELLMY's time, we use mass densities ρ.

the corresponding time t_0, and for the further considerations use the time $t_0 + t$ instead of t in (2.10).

The travel distance s is obtained as the integral of (2.10)

$$s = k \ln \cosh \left(\frac{v_{\max}}{k} t \right) . \tag{2.13}$$

For the starting time t^* until 80% of the limit velocity $v_{\max}$ is reached, one has

$$\tanh \left(\frac{v_{\max}}{k} t^* \right) = 0.8 , \tag{2.14}$$

and by substituting the value t^* obtained from this into (2.13), one obtains

$$s^* \cong 0.5k , \tag{2.15}$$

that is, for $\xi = 500$ ms^{-2}, one obtains $s^* = 25h'$. Already after a very short starting distance, almost the maximum velocity is reached ..."

These are the few central lines of VOELLMY's text in our translation into English. VOELLMY continues to discuss the applicability of the model to flow avalanches comprising of only part of the total snow layer or the full layer, and shows that it also reproduces the dynamics of powder snow avalanches correctly. The latter point is particularly rewarding as a number of measured velocities for flow as well as powder snow avalanches can be shown to conform in magnitude with those predicted by the model.

Part 3 of VOELLMY's paper addresses questions of pressure. The basis is the BERNOULLI equation for a compressible fluid. Energy considerations are then used to find the run-out distance of the avalanche and to estimate stagnation pressures.

Part 4, finally summarises the formulas and demonstrates their applicability to real situations.

VOELLMY's paper is a landmark not only because of the derivation of the model equation and its integration, but it is even more worth reading because of many side issues that are touched and that demonstrate a superb physical understanding of the dynamic problem concerning fundamental as well as applied aspects.

2.8.3 Experimental Data

Field Experiments and Their Complexities A major problem in avalanche dynamics has been the availability of experimental data on various

aspects of the avalanche motion. Field measurements are limited and difficult to obtain and similitude is difficult to achieve when attempting to scale-down and model such flows in the laboratory [172]. Direct field observations and experiments of the dynamics of catastrophic rockfalls or avalanches are extremely difficult to make as they occur in nature, and they are probably only possible by remote sensing techniques. As already has previously been mentioned, by using radar DOPPLER technology, GUBLER [134] successfully studied the dynamics of artificially released snow flow avalanches in central Switzerland; depth, velocity and density profiles were determined. The modern trend in snow avalanche research is the installation of stable test sites. The Swiss Federal Institute of Snow and Avalanche Research is now continuously operating such a site in the Vallée de la Sionne and each winter releases enough snow artificial avalanches, equips the site heavily with instrumentation and exploits the measurements in internal reports; for an account of this, see ISSLER [190]. This site is particularly apt for powder snow avalanches. Flow avalanches are studied in a field test site at Ryggfonn in Norway. NOREM et al. [302] measured avalanche frontal speeds and forces from a measuring pillar built into the track of a proposed avalanche when real avalanches were treated during three consecutive winters in Norway. A summary is given by NOREM [304].

In Japan, avalanche dynamicists performed interesting experiments and numerical simulations of *ping-pong ball avalanches* to study three-dimensional granular flows [275] (see Fig. 2.25a). Natural snow weighing 300 kg at maximum was released in winter, whereas up to 550,000 ping-pong balls where used in summer to simulate three-dimensional granular flows along the inclined chute. Experiments were performed at the Miyanomori ski jump in Sapporo, where the balls were released near the top of the leading slope of gently varying concave and convex curvature followed by a horizontal run-out zone. The slope was 160 m long and 60 m high, and covered with an artificial surface. Since the effect of the air drag acting on a ping-pong ball is fairly large, the flow arrived at a steady state within a short distance. The attained terminal velocities showed a remarkable growth as the number of ping-pong balls increased. This is indicative of a mass or size effect. MCELWAINE and NISHIMURA and NISHIMURA et al. [275, 466] observed many similarities between natural snow and ping-pong ball avalanches. Similarity analysis shows that the experiment at the ski jump corresponds to a natural powder snow avalanche running for several kilometres. The mentioned authors are involved in computer simulations of three-dimensional, inhomogeneous two-phase flows that use DEM for the particles and the REYNOLDS-averaged NAVIER–STOKES equations for the fluid. They conclude that the unique nature of the ping-pong ball experiment provides a wonderful opportunity for testing a theory and simulation of strongly coupled two-phase flows.

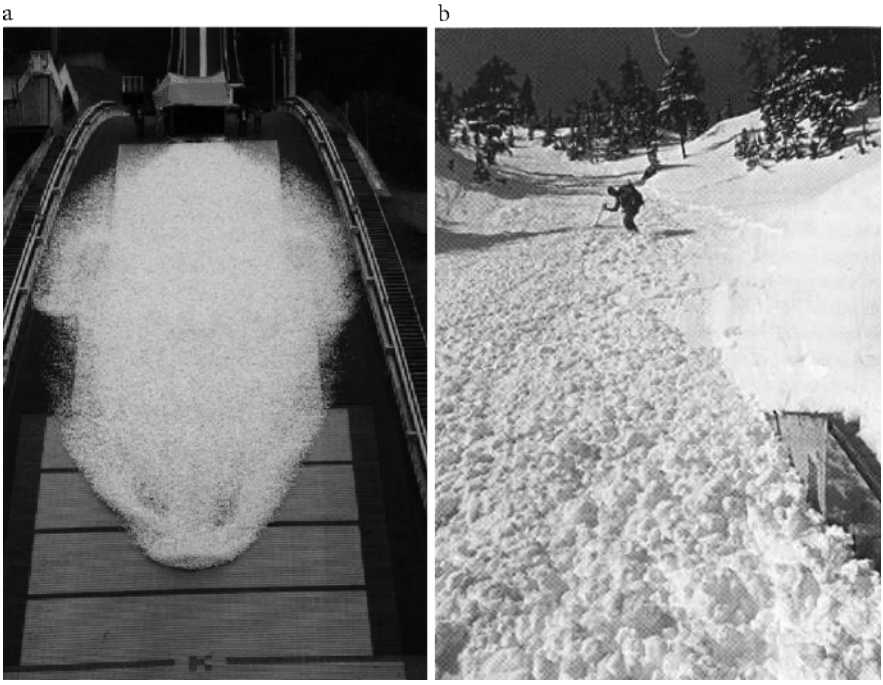

Fig. 2.25. a) Front view of a 550,000 ping-pong ball avalanche at the Miyanomori ski jump in Sapporo, Japan. The motion of this avalanche looks like a powder avalanche and less like a dense granular flow. (From [275].) **b**) The revolving door avalanche path of a large-scale dry snow avalanche looking upslope from the instrumented shed. (From [80].)

Large-scale dry snow avalanche experiments have been conducted by DENT et al. [80] (see Fig. 2.25b). They instrumented a small avalanche path near the Bridger Bowl ski area in southwest Montana to measure density, velocity, pressure, height, normal and shear stresses and dynamic friction in a flowing avalanche (see Fig. 2.21). The path was 100 m long on a nearly uniform 35° east-facing zone. A bowl-shaped starting zone provided snow for avalanches of up to 1.5 m depth and 1,000 m^3 in volume. *Both experiments imply that the tangential velocity components parallel to the bed are nearly independent of the depth of the avalanche.*

The Role of Laboratory Experiments Most observations in the field are indirect and generally provide only after-the-fact information. As a result, most theoretical models contain certain hypothetical facts. There are only a limited number of observations that would permit a partial verification of the theoretical models. In addition, comparison of models with results from field events is often aggravated because these events can be extremely complex in terms of the kind and size of materials that are present, as well

as the bed and avalanche geometries that might be involved. In view of these complexities and the lack of detailed field data against which the theoretical model can be tested, laboratory experiments are very important; they permit a control of both material properties and bed geometries. They thus facilitate a comparison of theory with experiment.

Most avalanche studies deal with the mathematical formulation of model equations, their integration and, when possible, verification by means of field observations. Such attempts are limited even though estimation of the run-out distance is very important prognostic information. By and large models are limited to one spatial dimension. Illustrative examples are given by Ancey and Meunier [6, 7, 8], Gubler [134] and many others. Because of their spatial one-dimensionality (and a number of ad hoc assumptions) such model calculations give global "order of magnitude" information of the flow implications and may also require adjustment of the model parameters of the site. It is, however, practically important to try to obtain a fundamental understanding of the physics involved in avalanche flow and from this to test the governing equations and closure relationships that describe them. Laboratory simulation of avalanches is, therefore, an extremely important means of developing basic theoretical concepts. Probably for the first time, systematic laboratory experiments involving the motion of a finite mass of dry gravel flow down an inclined plane were conducted by Huber [160] to predict the surface water waves (tsunamis) in lakes due to rockfalls plunging into the water. Advances in this area have been made by many avalanche experts, such as Lang and Dent, Nakamura et al. and Plüss and Hutter et al. [172, 239, 292, 324]. At the time, these experiments were probably the only ones against which a theoretical model could be tested [375].[17]

In the hope of isolating the simplicities inherent in the response behaviour of rapidly flowing granular materials, Gray et al., Greve and Hutter, Hutter and Koch, Hutter et al., Koch et al., Lang et al., Wieland et al., Pudasaini, Pudasaini et al. [123, 128, 175, 179, 227, 241, 334, 343, 445] performed well-defined laboratory experiments and compared their results with the findings from computations of the extended Savage–Hutter-theory. They showed fairly good to excellent agreement between the theoretical predictions and experimental data. A satisfactory fit of such a theory with laboratory data still does not imply that the theory is adequate to describe large-scale natural processes. Apart from the idealisations of the laboratory

[17] In the meantime other debris flow and granular scientists have followed the initiative of Hutter and coworkers and have conducted their own laboratory, or as they say, table-top experiments. Among these are Denlinger and Iverson [74] and Iverson et al. [194], who also performed large-scale outdoor experiments. Similarly, Patra et al. [313] and McDougall and Hungr [273, 274] also performed experiments on granular flows. In debris- and mudflow science, extensive outdoor experiments are described by Takahashi [416].

experiment, scale effects might falsify the conclusions in natural hazards. However, the above authors are confident that the formulation of theory (that in fact is scale invariant) and laboratory experiments is superior to the previous simpler treatments. It examines the problem in a more detailed way than other formulations have done in the past and is a very important step in the direction of treating the full problem [175].

Artificial laboratory avalanches show some typical features. They are initiated by releasing a finite mass of granular material, held within a cap or behind a shutter (see Figs. 2.26a,b and 2.27). The freed mass then moves downslope, expands and contracts as it moves into the deposition area, where it comes (very) quickly to rest. The following facts have been observed in experiments on an unconfined shallow and curved chute flow (see Fig. 2.28): The initial motion is typical for an unconstrained flow due to gravity; the mass of the suddenly released granules collapses and flows outward and downward in such a manner that the potential energy of the pile due to static or overburden pressure and gravity is converted to the kinetic energy of its motion. After this initial yield, the material, having previously been in a state of consolidation, dilates (see Fig. 2.26a). If the angle of inclination, ζ, of the inclination zone is greater than the bed friction angle, δ, for a particular material and surface roughness, the mass continues to flow downward and outward due

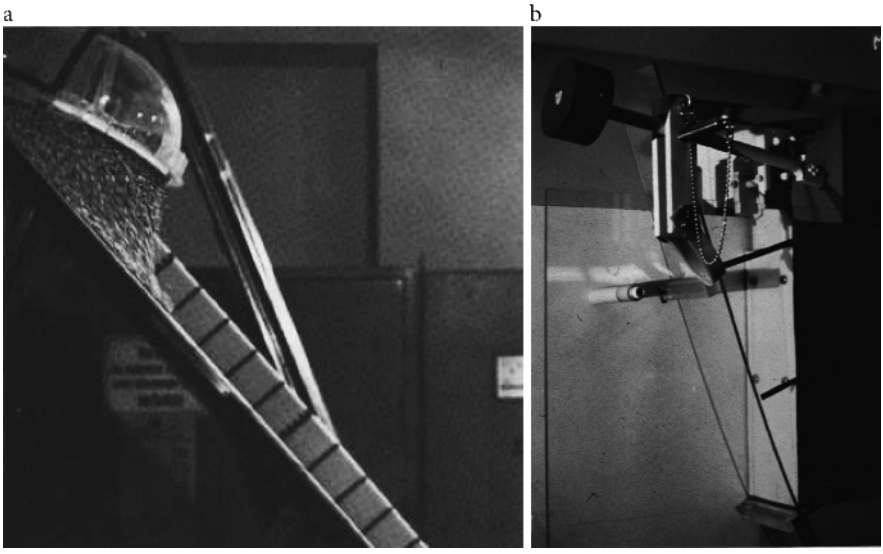

Fig. 2.26. a) Side view demonstrating initial yield and dilatant effect after release of granular material. (From [241].) **b**) The vertical plate designed to confine the granular material. By pulling the bolt, the plate rotates about the horizontal axle in the counter-clockwise direction, thereby immediately releasing the material. (From [175].)

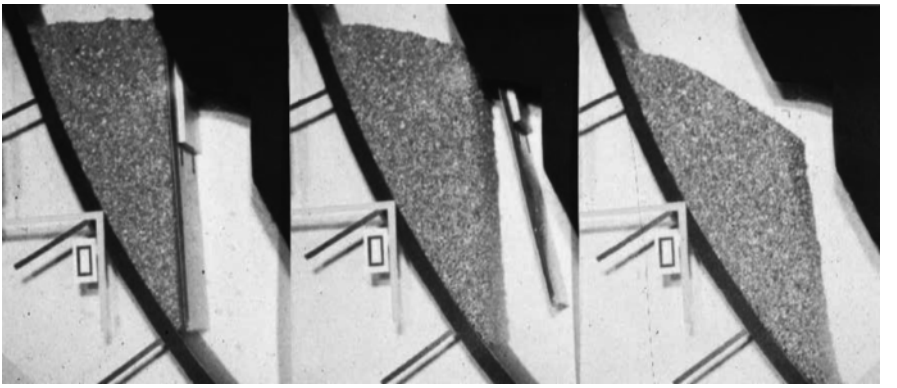

Fig. 2.27. Consecutive snapshots of the release of a granular material in a curved chute. (From [175].)

both to shear failure at the surface material interface and to loss of internal resistance. The rate of shear increases rapidly in the initial phase of the motion and generates large impulsive contact pressures; the particles become randomly separated, and the mass appears to continue to dilate [241]. Also, an interesting fact is that, at the initiation of the motion, the leading edge accelerates quite rapidly, whilst the tail remains static for a while or initially even moves upward. The internal friction and the bed friction exert retarding forces on those parts of the mass that are trying to move at higher relative speeds. However, as the leading edge moves out, the shear rate increases; this in turn enlarges the impulsive contact pressure so that both the front and the surface of the flow continues to dilate, reducing the internal resistance of the flow. The granules attain their maximum travel distance as the leading edge reaches the transition region to the run-out zone. The movement of the lower layers is then retarded by the resistance of the basal surface and this has a considerable effect on the form of the leading edge of the flowing mass. The lower layers are decelerated at the front of the mass, but the tail continues to accelerate. The avalanche thickness in the curved part of the bed is governed by this breaking action and also under the influence of the "centrifugal" force generated by the curvature of the basal surface. When the lower layers come to rest, the leading edge is still fluidised. The final shape in the run-out zone appears to indicate that the tail of the flow has sufficient momentum to continue moving in the vicinity of the deposited pile. *The final deposit of the pile is found to be in the shape of a compact hump* (see Fig. 2.28).

As is clear from the above discussion, laboratory experiments are a very important means to validate model equations of avalanching motions of a granular body, an extensive study of experimental results and their comparisons with model equations will be carried out in Chaps. 10–13.

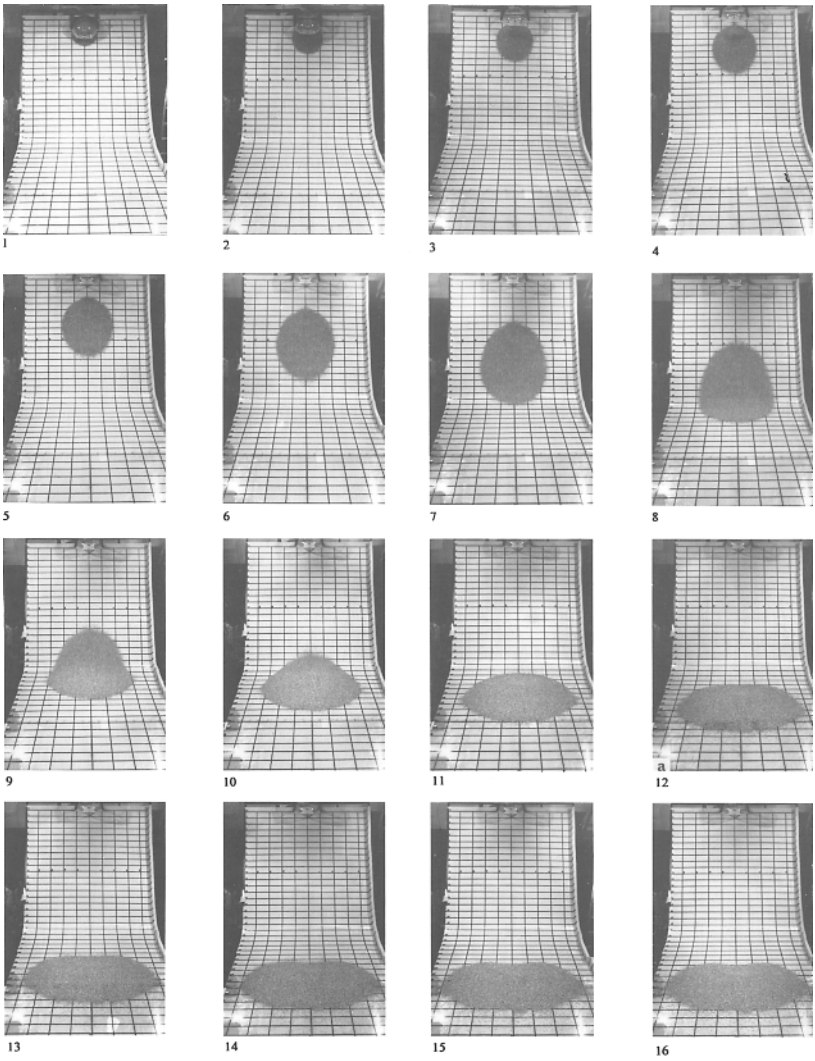

Fig. 2.28. A series of laboratory avalanches on an unconfined shallow chute of which the initiation zone angle is 45°. 20.5 kg of 5 mm quartz particles is used. The time interval between two consecutive snapshots is 0.1 s. (From [241].)

2.8.4 Necessity for a New Model

The simple two-parameter mass point models, e.g., of Voellmy [430], Salm [361] and Perla et al. [315] have only been tested against field data as far as run-out distances are concerned, and this comparison shows considerable scatter. This means that the field data against which theoretical models could

be tested were too scarce to calibrate the existing models of that time with sufficient certainty: the classical theoretical formulations of VOELLMY and SALM are known to be oversimplified. Obviously, because of the mass point assumption, the temporal evolution of the geometry of the moving avalanche cannot be calculated in these models. The reasons why the run-out distances and deposition areas cannot be predicted by these models with significant accuracy can be attributed to the difficulties of the parameter identification, but more likely to an inadequate description of (*i*) the physical (rheological) properties, (*ii*) the sliding conditions and (*iii*) the geometries of the moving avalanches, see [177]. Furthermore, *these models do not allow the determination of the spreading of the avalanching mass and thus cannot give information on the mass distribution in the run-out zone*, see [179]. There are other models describing the avalanches as linear NEWTONian fluids [52, 76] leading to NAVIER–STOKES equations. These are, in principle, able to somehow describe the geometrical properties of the motion. However, *real avalanches are governed by nonlinear constitutive relations*, so that the above ansatz can only serve as a very rough approximation. Alternatively, statistical models are limited to one-dimensional situations and depend on both the topographic features and long-run period. They cannot incorporate the rheological and mechanical behaviour of the material. Moreover, kinetic theory and molecular dynamics models are very complicated to handle even for simple geometries [134, 170, 171, 366].

It is very difficult to postulate a constitutive relation for the *stress tensor* in terms of a *deformation measure* that correctly describes avalanche behaviour under *rapid motion* and possible *large shearing* for which the phenomenological parameters can be identified. Fortunately, observations suggest that the major part of the shearing in many avalanches takes place in a very thin *boundary layer* near the bottom, and it is therefore possible to circumvent the detailed determination of the constitutive response by depth averaging the field equations. Instead of prescribing a detailed constitutive relation (stress-stretching relation), a COULOMB dry friction law for the basal friction and a MOHR–COULOMB yield criterion for the interior behaviour are used. The information obtained in this way is sufficient to essentially reduce information about the stresses to the traction conditions at the free and basal surfaces and thus involves only a closure relation for the basal shear traction (depth-averaged equations). Based on these prerequisites, dynamic equations are derived that describe the temporal-spatio evolution of the height and the depth-averaged streamwise velocity of the moving avalanche pile [129].

Since the late 1970s and early 1980s, new mathematical descriptions for the motion of rockfalls, ice and snow avalanches have been presented for an obvious reason, namely the need for a better prediction of the run-out distances and deposition zones. Earlier attempts of such geophysical flows either dealt with hydraulic-type models that treat the problem as a gradually varying

open channel flow of *infinite mass* or the *mass point* model of VOELLMY. As explained above, the avalanche models existing before the late 1980s were generally too restrictive. The trend at that time, and till now in the research of flowing snow and other granular materials was directed at determining the predominant mechanisms governing the motion of flow avalanches. Despite the significant role of avalanches in mountainous regions like the Alps and the Himalaya, where accurate predictions of forces exerted by, and the travel distances arising in, the other existing avalanche forecast models seemed to be weak and fraught with uncertainties.

The model proposed by SAVAGE–HUTTER [375] and their various extensions and generalisations for real as well as complicated topographies incorporate a great number of the above discussed important features of granular avalanches [123, 335, 337, 340, 341, 342, 343, 376, 445]. It is a *more complete* theory in the sense that it provides a clear formulation of the problem in physical-mathematical terms and leads to well-defined initial boundary value problems to questions of practical relevance. Thus, advanced numerical techniques are being developed and successfully implemented. Consequently, theoretical predictions can be and have been validated by many different laboratory experiments. Thus, in many situations it may provide a complete knowledge of the avalanche motion on steep slopes from initiation to run-out.

Part II

A Continuum Mechanical Theory for Dense Avalanches Sliding Down Non-Trivial Topographies

3 A Continuum Mechanical Theory for Granular Avalanches

3.1 General Introduction

It is probably fair to state that in 1989 SAVAGE and HUTTER [375] developed the first *continuum mechanical theory*, abbreviated in this book as "SH-theory" or "SH-model", capable of describing the evolving *geometry* of a finite mass of a granular material and the associated *velocity* distribution as it slides down an inclined surface. This model provides a more *complete analysis* of such flows than previous models, and its extension as well as a comparison with laboratory experiments demonstrate it to be *largely successful*. This depth-averaged hydraulic model is rather sophisticated, accepted by researchers but is only on the verge of being used by today's practitioners. The reason for this is that the model is simple to understand and very economical to implement, even for extremely huge natural phenomena such as avalanches of snow and rock, and debris flows, e.g., from volcanic eruptions. Another *very important feature* of the model is that it is based on *physical reasoning* and *rigorous mathematical foundations*. Equally important is the fact that the model in its simplest form is *scale invariant* and can predict the dynamics of the flow of granular material quite well in chemical and process engineering, as well as geophysical circumstances. Several simplifying, but nevertheless realistic, assumptions were made that streamlined the mathematical formulation. They are as follows:

- The moving mass was assumed to be *volume preserving*. This assumption is based on observations in the laboratory that possible volume expansions and compactions arise at the initiation and still stand, whilst during its motion the moving mass nearly preserves its volume. Since the dynamics define the motion, assuming volume preserving is an adequate approximation.
- The moving and deforming *dry* granular mass is *cohesionless* and obeys a MOHR–COULOMB *yield criterion* both inside the deforming mass, as well as at the sliding basal surface, but with different internal, ϕ, and bed, δ, friction angles. This assumption is based on the experimental fact that on any plane, at which shear and normal tractions may act, their ratio is constant and equal to the tangents of ϕ or δ, respectively. This

classical criterion is quite appropriate for materials with rate-independent constitutive properties.
- The shear stresses lateral to the main flow direction can be neglected.
- The body is supposed to be in an *isothermal* state or, if not, thermal effects can be ignored.
- The *geometries* of the avalanching masses are *shallow* in the sense that typical avalanche thicknesses are small in comparison to the extent parallel to the sliding surface. This assumption allows the introduction of a shallowness parameter and simplification of formulas in terms of it.
- The avalanching motion consists of shearing within the deforming mass and sliding along the basal surface. However, on the basis of observations, the shearing deformation commonly takes place within a very small basal boundary layer, so that it is justified to collapse this boundary layer to zero thickness and to combine the sliding and shearing velocity to a single sliding law with a somewhat larger modelled *sliding velocity*. This then effectively means that variations of the material velocities across the thickness may be ignored and thickness-averaged equations may be employed. This method was introduced by VON KÁRMÁN [435] and later refined by POHLHAUSEN [325], where the equations are averaged over depth and the velocity profile is assumed.
- In order to obtain a spatially reduced theory for the flow down a slope of constant inclination angle, the leading order two-dimensional equations are *integrated through the avalanche depth*.
- *Scaling analysis* identifies the physically significant terms in the governing equations and isolates those terms that can be neglected.

The assumptions of the theory are formally stated in Sect. 3.4.3. We also wish to mention at this early stage that the equations have been criticised. Detailed answers to such criticisms are given in [183]. Here we are content to presenting a simple deduction of the model, quasi as an introduction in its simplest form. An account on its limitations will be given later.

This simple spatially one-dimensional model, applicable along a straight sliding surface, has been generalised in various different ways. In fact, one of the strengths of the procedure is that the model can be generalised to higher dimensions, to more complex geometries and for multi-phase flows such as debris and pyroclastic flows, see [75, 123, 124, 128, 129, 177, 191, 192, 194, 313, 321, 334, 335, 336, 337, 338, 339, 340, 341, 342, 343, 375, 376]. A generalisation to flows along a simple curved basal topography was performed in 1991 [376] in order to obtain a complete knowledge of the avalanche motion from initiation on a steep slope to run-out on a shallow slope. The coordinates were generated by a basal curve following the direction of steepest decent and assuming no topographic variations perpendicular to it. This led to an orthogonal metric and a description of the motion that predominantly singles out the talweg direction. This allowed the local inclination angle to vary as a

function of the downslope coordinate. This idea was equally used in yet more complex situations of channelised flows. The ultimate goal, of course, is the reference of the metric to the real topography. A first step towards this end is taken in [40].

3.2 The SH-Model, Reduced to its Essentials

Let us commence with a derivation of the SH-equations, reduced to their essentials. We follow a simple "strength of materials approach" that will disclose the most significant properties of the model and so highlight its essentials. Therefore, consider the plane flow of a granular mass down an inclined plane. Let the x-coordinate point in the downflow direction and the z-coordinate be perpendicular to it. Isolate a column of length dx and formulate the mass balance and x-momentum balance for the element (see Fig. 3.1). Assume, to this end, that the downslope velocity is constant over depth, so that $u = u(x,t)$, and that the density ρ of the granular material is constant. Equating the growth rate of mass within the column by a change of height to the inflow of mass from above and outflow below, yields

$$\begin{aligned}\frac{\partial}{\partial t}\left(\rho h(x,t)\right)dx &= \rho h(x,t)u(x,t) - \rho h(x+dx,t)u(x+dx,t)\\ &= -\frac{\partial}{\partial x}\left(\rho h(x,t)u(x,t)\right)dx + O\left((dx)^2\right), \qquad (3.1)\end{aligned}$$

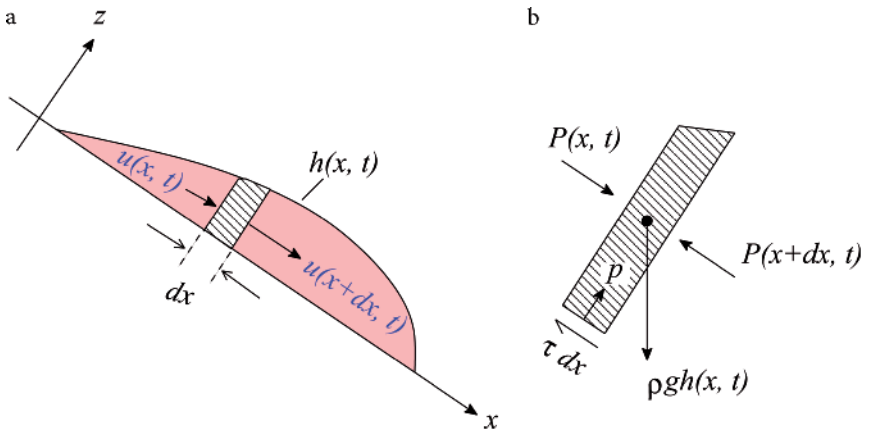

Fig. 3.1. Plane flow of a finite mass of granular material down an inclined plane. **a**) Sketch of the geometry, coordinate system and an infinitesimal column for which mass and momentum balances are formulated. **b**) Free body diagram of the column with acting forces, where $P(x,t) = \int_0^{h(x,t)} p_L(x,z,t)dz$ and $P(x+dx,t) = \int_0^{h(x+dx,t)} p_L(x+dx,z,t)dz$.

where, on the right-hand side TAYLOR-series expansion has been used. Here, the $O\left((dx)^2\right)$ symbol means that the next term would be of the order $(dx)^2$. Since ρ is a constant, (3.1) reduces to

$$\frac{\partial h}{\partial t} + \frac{\partial (hu)}{\partial x} = 0, \tag{3.2}$$

in which the arguments (x, t) and the terms of higher order in (dx) have been dropped.

Balance of momentum states that the time rate of change of the x-momentum of the column equals the convected flux of momentum into and out of the column plus the sum of the forces acting on the isolated column. Since $\rho hu\, dx$ is the x-momentum of the column, one easily may write

- Time rate of change of $\rho hu\, dx$:

$$\frac{\partial}{\partial t}\left(\rho h(x,t)u(x,t)\right) dx. \tag{3.3}$$

- Flux of x-momentum through the column walls:

$$\begin{aligned} &\rho h(x,t)u^2(x,t) - \rho h(x+dx,t)u^2(x+dx,t) \\ &= -\frac{\partial}{\partial x}\left(\rho h(x,t)u^2(x,t)\right) dx + O\left((dx)^2\right). \end{aligned} \tag{3.4}$$

- Forces: these consist of three contributions

$$\begin{aligned} (i) &= \rho g h \sin\zeta\, dx && \text{(driving component of gravity)} \\ (ii) &= -\tau dx && \text{(basal friction)} \\ (iii) &= \int_0^{h(x,t)} p_L(x,z,t)dz && \text{(longitudinal pressure)} \\ &\quad - \int_0^{h(x+dx,t)} p_L(x+dx,z,t)dz, \end{aligned}$$

  in which the index L indicates that the *longitudinal pressure* may be different from the overburden pressure. To specify item (iii), a force balance in the z-direction yields a hydrostatic pressure distribution

$$p(x,z,t) = \rho g\left(h(x,t) - z\right)\cos\zeta.$$

  This may be called the *overburden pressure* perpendicular to the bed.

Following common practice in soil mechanics, we now postulate

$$p_L(x,z,t) = K_{\text{act/pas}}\, p(x,z,t), \tag{3.5}$$

where $K_{\text{act/pas}}$ is the (dimensionless) *earth pressure coefficient*, and we assume that

$$K_{\text{act/pas}} = \begin{cases} K_{\text{act}}, & \text{if} \quad \partial u/\partial x > 0, \\ \\ K_{\text{pas}}, & \text{if} \quad \partial u/\partial x < 0, \end{cases}$$

where K_{act} and K_{pas} correspond to the extensive and compressive modes of deformation. With this, one easily deduces from (iii) above that

$$(iii) = -\rho g \frac{1}{2} \frac{\partial}{\partial x} \left(K_{\text{act/pas}} h^2(x,t) \right) \cos\zeta dx + O\left((dx)^2 \right).$$

Applying a COULOMB-type friction law for the basal shear traction with bed friction angle δ and $\tau = (\tan\delta)p$, we obtain

$$(ii) = -\text{sgn}(u) \, (\tan\delta) \, \rho g h(x,t) \cos\zeta dx.$$

Now, adding $(i), (ii)$ and (iii) together, we have

$$\begin{aligned} x-\text{force} = \Big\{ & \rho g h(x,t) \left(\sin\zeta - \text{sgn}(u) \tan\delta \cos\zeta \right) \\ & - \frac{\rho g}{2} \frac{\partial}{\partial x} \left(K_{\text{act/pas}} h^2(x,t) \right) \cos\zeta \Big\} dx + O\left((dx)^2 \right). \end{aligned} \tag{3.6}$$

If we now collect (3.3) + (3.4) = (3.6) and drop the common factor ρdx in the emerging equation, we have

$$\begin{aligned} & \frac{\partial}{\partial t} (hu) + \frac{\partial}{\partial x} \left(hu^2 \right) \\ & = g \left\{ \left(\sin\zeta - \text{sgn}(u) \tan\delta \cos\zeta \right) h - \frac{1}{2} \frac{\partial}{\partial x} \left(K_{\text{act/pas}} h^2(x,t) \right) \cos\zeta \right\}. \end{aligned} \tag{3.7}$$

Equations (3.2) and (3.7) constitute a system of two partial differential equations for the avalanche thickness $h(x,t)$ and the longitudinal velocity $u(x,t)$. These equations are correct to $O\left((dx)^2\right)$. The *driving force* is the downslope component of the *gravity force* (first term on the right-hand side). This force is counteracted by the *frictional force* (second term on the right-hand side), which here is modelled by a COULOMB*-type dry friction law*. There is a third contribution on the right-hand side of (3.7) that, by its derivation, is due to the *longitudinal pressure variation* and is expressed only in *changes of geometry*; it may have either sign and its role will be explained below.

Equations (3.2) and (3.7) together are the SAVAGE–HUTTER equations for the flow of a finite mass of granular material down an inclined plane with inclination angle ζ. However, in their original paper, the model was not derived in this way. In the above, they appear in a so-called "conservative" form.[1] If

[1] The terms "conservative", "conserved quantity" and "conservation law" are used in the literature of continuum mechanics and applied mathematics in two dif-

product differentiations on the left-hand side of (3.7) and in the third term on the right-hand side are performed, then (3.7), after dividing it by h and using the mass balance (3.2), becomes

$$\rho\left(\frac{\partial u}{\partial t}+u\frac{\partial u}{\partial x}\right)$$
$$=\rho g\left(\sin\zeta-\operatorname{sgn}(u)\tan\delta\cos\zeta\right)-\rho g K_{\mathrm{act/pas}}\frac{\partial h}{\partial x}\cos\zeta, \tag{3.10}$$

in which the constant density has been re-substituted to make NEWTON's second law more explicit. In this form, the last term on the right-hand side becomes more transparent. It corresponds to a "pull" where $\partial h/\partial x$ is negative and a "friction" where $\partial h/\partial x$ is positive. So, looking at Fig 3.1, the last term on the right-hand side of (3.10) accelerates the mass in the frontal part and decelerates it in the rear part of the pile. Evidently, the term $-\rho g\partial h/\partial x$ is responsible for the change of the geometry of the moving mass. Omitting this term from (3.10) reduces the equation to the momentum balance of a rigid mass model that cannot account for the geometric changes of the moving mass, e.g., VOELLMY model [430].

The above analysis outlines the essential elements of the derivation of the one-dimensional depth-averaged equations. From a physical point of view, the essential elements are (i) the implementation of the hydrostatic pressure assumption, i.e., the pressure p at the elements below a column of moving snow or gravel is the weight of the material above that column corrected by the cosine of its inclination angle, plus (ii) the account of the longitudinal

ferent forms. Both are based on the balance law

$$\frac{\partial}{\partial t}(\rho f)+\nabla\cdot\left(\rho f\mathbf{u}+\mathbf{\Phi}^f\right)=\rho s^f+\rho\Pi^f \tag{3.8}$$

for a specific quantity f, its flux $\mathbf{\Phi}^f$, supply s^f and production Π^f densities, which in view of the mass balance $\partial\rho/\partial t+\nabla\cdot(\rho\mathbf{u})=0$ may, upon differentiation, also be written as

$$\rho\frac{df}{dt}=-\nabla\cdot\Pi^f+\rho s^f+\rho\Pi^f. \tag{3.9}$$

In continuum mechanics, the statements (3.8) and (3.9) are conservation laws, or f is called conservative, if $\Pi^f\equiv 0$. In mathematics today, an equation of the form of (3.8) is called a conservation law, whilst (3.9) is said not to be in conservative form. This has historically not been so. Indeed, originally in mathematics, (3.8) was only denoted to be in conservative form if $\rho\left(s^f+\Pi^f\right)=0$. Today, $\rho\left(s^f+\Pi^f\right)$ may be different from zero and (3.8) is then still called a conservation law by mathematicians, sometimes made more precise by saying "conservative equation with source term". We admit that all this is unsystematic and confusing. Which version of conservatism is addressed must be understood from the context. However, in this book, we consider a conservative law in the form of (3.8).

pressure, p_L. When $p = p_L$, the pressure distribution is that of a liquid (and $K_{\text{act/pas}} = 1$). In this form, the equations correspond to the usual hydraulic models and are often called SAINT VENANT or BOUSSINESQ equations, and have so been used in avalanche models in Russia (the former USSR) (see GRIGORIYAN and others [130, 131, 132, 133], EGLIT and others [84, 85, 86, 87, 88, 89, 90, 91]). When $p \neq p_L$, then $K_{\text{act/pas}} \neq 1$ and non-isotropic pressure distribution prevails; in the soil mechanics literature two different values of $K_{\text{act/pas}}$ are suggested according to whether the flow is extending or compressing, respectively.

What remains, therefore, in the above analysis is the determination of the active and passive earth pressure coefficients $K_{\text{act/pas}}$. To this end, we consider the granulate as behaving as a cohesionless COULOMB material with internal angle of friction, $\phi > \delta$, the bed friction angle. For a plane material element at the base (see Fig. 3.2a), the state of stress $(p, -\tau)$ in the stress space must lie on the straight line through the origin and inclined at the angle $-\delta$ (see Fig. 3.2b). All other elements that are rotated relative to the element shown in Fig. 3.2a must lie on those circles through the point $(p, -\tau)$ that are also tangential to the lines through the origin with inclination $\pm\phi$. There are two such circles, a bigger, passive and a smaller, active one. The stress state (p_L, τ) on the perpendicular elements lie on opposite sides of these MOHR circles as indicated in Fig. 3.2b. The centre of the bigger MOHR circle lies at $\frac{1}{2}(p + p_L)$ and its radius is given by $r = (\tau^2 + \frac{1}{4}(p_L - p)^2)^{1/2}$. Furthermore, pure trigonometric relations yield

$$\frac{\tau}{p} = \tan\delta, \qquad \sin^2\phi = \frac{\tau^2 + \frac{1}{4}(p_L - p)^2}{\frac{1}{4}(p + p_L)^2}.$$

Substituting the first into the second equation yields a quadratic equation for $p_L/p = K_{\text{act/pas}}$ for which the solution is given by

$$K_{\text{act/pas}} = 2\sec^2\phi\left\{1 \mp \left(1 - \cos^2\phi\sec^2\delta\right)^{1/2}\right\} - 1, \tag{3.11}$$

in which the upper (lower) signs apply for K_{act} (K_{pas}) and $\sec\phi = 1/\cos\phi$. This shows that two phenomenological constants, the internal, ϕ, and bed, δ, friction angles describe the material response of the granular material. These can in practical circumstances be determined or estimated relatively easily.

The above derivation is somewhat restrictive and sketchy, not suitable for generalisation. However, it contains the two essential features of the avalanche flow, (*i*) the important geometric term in the x-momentum equation (third term on the right-hand side of (3.7) or (3.10)) and, (*ii*) dilating and compacting flows are differently treated via the earth pressure coefficient. This coefficient only arises in the geometric term.

The above equations have all been written in dimensional form. Later, they will be written in non-dimensional form, which for reasons of comparison will

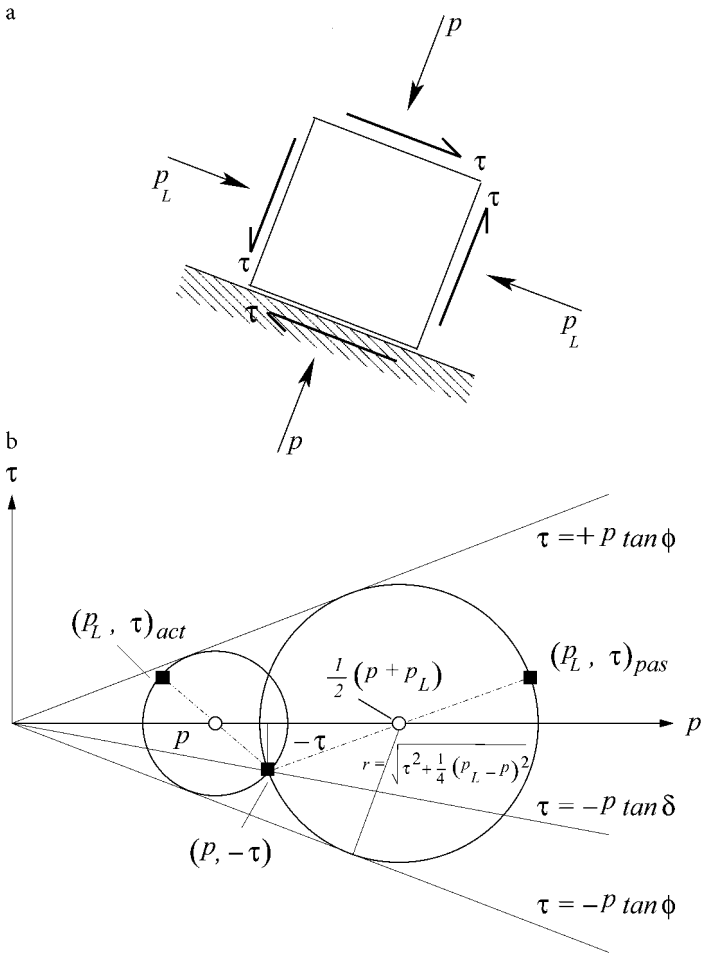

Fig. 3.2. **a**) Material plane element at the basal plane with the stresses (p, τ) and (p_L, τ), acting at the faces as indicated. **b**) MOHR circles, representing active and passive stress states: the element touching the base, the side element, $p_L/p = K_{\mathrm{act/pas}}$ follows from trigonometric relations.

also be done here. In this process we shall recognise the equations also to be *scale-invariant*. Thus, let

$$\{x, z, h, u, t\} = \left\{L\hat{x}, H\hat{z}, H\hat{h}, \sqrt{gL}\hat{u}, \sqrt{L/g}\hat{t}\right\}, \tag{3.12}$$

in which L and H are length and depth scales, $\sqrt{L/g}$ is a time scale, reminiscent of free fall, $\sqrt{gL}$ a free fall velocity and the overbarred quantities are dimensionless. These scales are *not* those of shallow water equations. If the scales (3.12) are substituted into (3.2), (3.7) or (3.2) and (3.10) and overbars

are dropped, the following dimensionless forms of the governing equations are obtained.

– In conservative form

$$\begin{aligned}&\frac{\partial h}{\partial t}+\frac{\partial}{\partial x}\left(hu\right)=0,\\&\frac{\partial}{\partial t}(hu)+\frac{\partial}{\partial x}\left(hu^2\right)=\left(\sin\zeta-\operatorname{sgn}(u)\tan\delta\cos\zeta\right)h-\frac{\partial}{\partial x}\Big(\frac{\varepsilon}{2}K_{\mathrm{act/pas}}h^2\cos\zeta\Big);\end{aligned}\tag{3.13}$$

– in non-conservative form

$$\begin{aligned}&\frac{\partial h}{\partial t}+\frac{\partial}{\partial x}\left(hu\right)=0,\\&\frac{\partial u}{\partial t}+u\frac{\partial u}{\partial x}=\left(\sin\zeta-\operatorname{sgn}(u)\tan\delta\cos\zeta\right)-\varepsilon\cos\zeta K_{\mathrm{act/pas}}\frac{\partial h}{\partial x},\end{aligned}\tag{3.14}$$

in which ε is the aspect ratio, defined by

$$\varepsilon=\frac{H}{L}\ll 1,\tag{3.15}$$

which, usually, is very small.

Equations (3.13) or (3.14) disclose an additional property of the avalanche model equations. They do not contain a typical physical quantity such as, e.g., the FROUDE number. In particular, for ϕ = constant and δ = constant, there is no dimensionless physical parameter (e.g., FROUDE or REYNOLDS numbers, etc.) upon which the equations would depend. The *equations are scale-independent* and, therefore, cannot reproduce a possible mass dependence of the run-out distance.

We shall see that, as long as ϕ and δ are constants, all these derived properties are shared by all generalisations of the model equations.

3.3 Generalisations of the Original Theory

There are two main streams of generalisation of the theory, one depending on the coordinate system, the other on the topography. In the following discussion, we will consider both of them separately.

3.3.1 Generalisation with Respect to the Coordinate System

The original paper of SAVAGE and HUTTER was based on a formulation using Cartesian coordinates [375]. This initial investigation considered the idealised

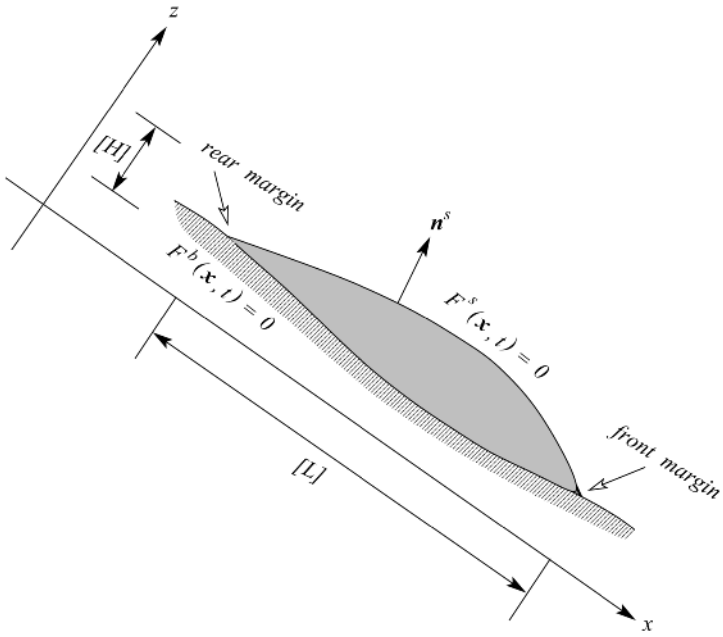

Fig. 3.3. Sketch of the geometry of a finite mass of granular material moving along a curved rigid bed showing the definition of the free surface given by $F^s(\mathbf{x},t)=0$ and the equation of the bed $F^b(\mathbf{x},t)=0$. Also indicated are the scales $[L]$ and $[H]$ for the spread and the maximum height of the avalanche, and the free surface unit normal $\mathbf{n}^s$ pointing outward from the body.

problem of a finite mass of granular material released from rest on a rough inclined plane. Consider now the free surface flow of a granular material along a slowly varying bottom topography, as shown in Fig. 3.3. When the underlying topography varies moderately along the longitudinal direction but has no variation in the transverse direction, a treatment using Cartesian coordinates is likely to be a first good approximation of the problem. However, in many situations the downslope variation of the topography may deviate strongly from a straight line. In such cases, it is quite natural and convenient to adopt a coordinate system that can better describe the topography of the base of the flowing material. In 1991, SAVAGE and HUTTER [376] extended their model [375] to describe the flow of an initially stationary mass of cohesionless dry granular material down rough curved beds (see Fig. 3.4). By depth integration of the incompressible conservation of mass and linear momentum equations that were written in terms of a curvilinear coordinate system aligned with the curved bed, evolution equations for the depth h and the depth-averaged velocity u were obtained. In this way, the bed curvature effects in the longitudinal direction were incorporated in the theory. Such a curvilinear coordinate system, for instance, can adequately describe a chute

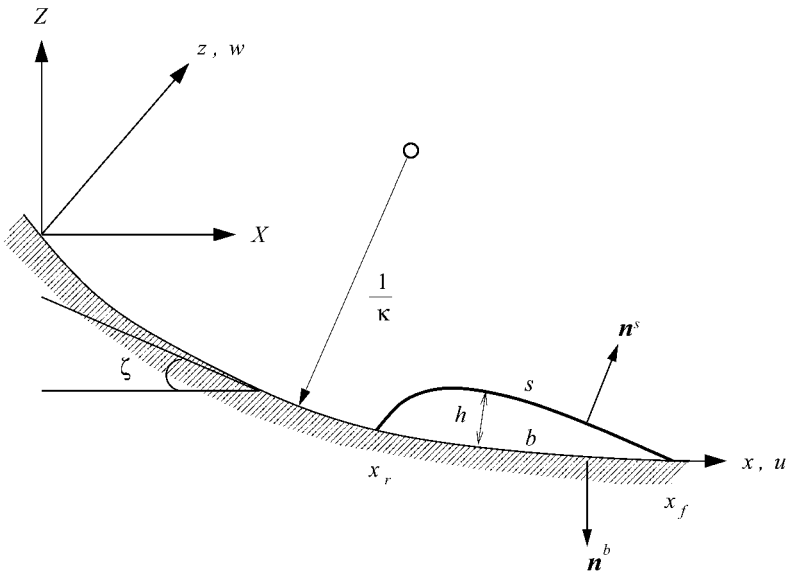

Fig. 3.4. Definition sketch of the coordinate system and geometry of a finite mass of granular material moving down a rough curved rigid bed. Here, x, z are curvilinear coordinates in the direction of the flow and normal to the bed, whereas X, Z are their Cartesian counterparts. u and w are the velocity components along the x and z coordinates. x_f and x_r indicate the front and rear margins, whilst s, b and h are the free and basal surfaces and the height of the moving and deforming avalanche on a rough bed whose local inclination angle with the horizontal is ζ and the local radius of curvature is κ. Also shown are the free surface and basal unit normals $\mathbf{n}^s$ and $\mathbf{n}^b$, respectively, pointing outwards from the avalanching body.

having a bed made up of a straight inclined portion followed by a curved part and a horizontal part. In all subsequent developments and extensions of the theory for confined and unconfined chutes, two-dimensional and three-dimensional flows, the basal topographies were modelled by using curvilinear coordinate systems in a natural way, and all equations of motion were written in such an appropriate coordinate form.

3.3.2 Generalisation with Respect to the Basal Topography

a) One-Dimensional Generalisation

The major part of the extensions of the original model [375] is concerned with the basal topography on which the flow of cohesionless incompressible granular avalanches takes place. As described earlier, the first model was developed for flow along a rough *inclined plane* or a situation in which the main flow direction is nearly parallel to such a plane, as shown in Fig. 3.3.

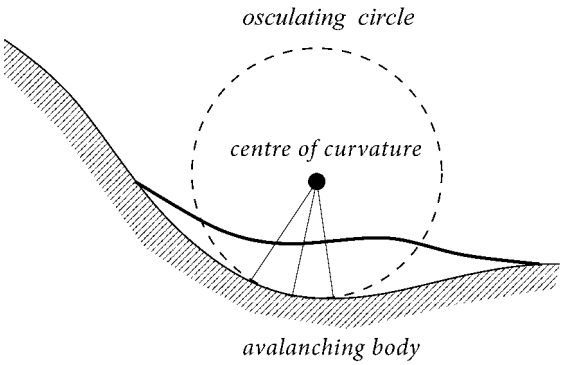

Fig. 3.5. The avalanching body does not pass through the centre of curvature of the basal surface. The centre of curvature is the point of singularity of the coordinate system under consideration.

The model was immediately extended to a two-dimensional *curved bed* [376], which could better predict the flow of an avalanche on a slightly curved topography. The bed is assumed to have a steep slope at the initial position of the pile and is curved so as to approach a horizontal flat area in the downstream direction. It is convenient to introduce curvilinear coordinates x and z as shown in Fig. 3.4. The x-coordinate, i.e., the coordinate line $z = 0$, follows the basal profile and the coordinate lines $x =$ constant are straight rays perpendicular to the basal profile. There are some restrictions of application of this coordinate system. It possesses a singularity at all centres of the curvature where z equals the radius of curvature. Physically, these points correspond to the positions at which consecutive z-axes (which vary locally) intersect with one another. Therefore, in applications we require that the avalanche does not pass through one of these points during the course of its motion (see Fig. 3.5).

Hutter and Koch [175] successfully implemented the theory for curved channels to the motion of granular avalanches in an exponentially curved and two-dimensionally confined chute. Greve and Hutter [128] subsequently extended the implementation of such a theory to a motion of an avalanche in a convex and concave chute (see Fig. 3.6). Because of the bump and depending upon the granulate-bed combination, an initial single pile of the granular body evolved as a single pile throughout its motion and be deposited above or below the bump of the bed; or it separated in the course of the motion into two piles that were separately deposited above and below the bump.

b) Two-Dimensional Generalisation

Hutter et al. [177] added one more dimension to the theory, namely the *cross-slope direction*, which is concerned with the motion of an unconfined finite mass of granular material released from rest on an inclined plane. They

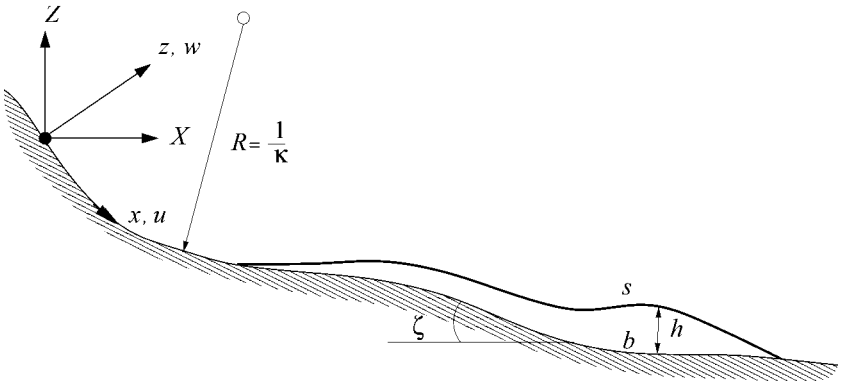

Fig. 3.6. Same as Fig. 3.4 but for a convex and concave chute.

considered a *free surface flow* of granular material down a slowly varying topography and identified the mean plane surface of this topography with a plane that is parallel to the (x, y)-plane of the three-dimensional Cartesian coordinate system. To explain the model, let the x-coordinate follow the direction of steepest descent, the y-coordinate be parallel to the horizontal lines and the z-coordinate perpendicular to these (see Fig. 3.7). Thus, the z-axis is inclined with respect to the vertical by the angle ζ. The bottom and the free surfaces of the moving mass will be defined by $z = b\,(x, y, t)$ and $z = s\,(x, y, t)$, respectively. The depth-averaged equations are deduced from the three-dimensional dynamical equations by scaling the equations and im-

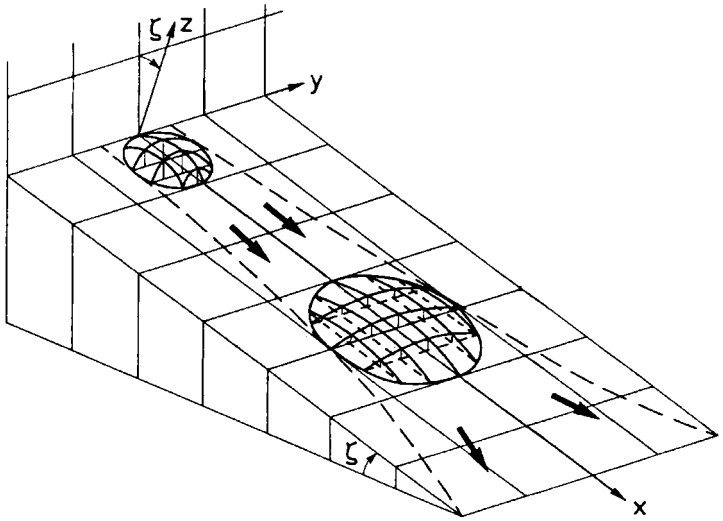

Fig. 3.7. Definition of the coordinate system and configuration.

posing the shallowness assumption that the moving piles are long and wide but not deep. The assumption of confined plane flow conditions is adequate to describe many *flow avalanches*, particularly if they are wide and move on evenly sloped mountain sides. However, avalanches often experience unconfined conditions or are suddenly subject to a relief from a sidewise confinement, as will occur when the avalanche moves out of a gorge. In this first analysis of an avalanche with variation of the width of the moving mass, an additional transversal averaging was performed [177]. This process was performed by assuming a parabolic depth distribution across the width, and longitudinal and transverse velocities, which, respectively, have uniform and linear distribution across the width of the pile. A system of spatially one-dimensional partial differential equations in x (the longitudinal variable) and t (time) then yields differential equations for the evolution of the centerline depth of the pile, the combined depth-averaged and width-averaged longitudinal velocity components, the distribution of the width of the avalanche and its time rate of change. This model was developed by LANG [242] but has never been closely followed or explored in any detail. It may be of limited use in narrow corrie flow or free channel flow in industrial applications.

c) Three-Dimensional Generalisation

GREVE et al. [129] presented in detail a three-dimensional extension of the two-dimensional theory that deals with gravity driven free surface flows of piles of granular materials along bottom profiles that are weakly curved downwards and plane laterally (see Fig. 3.8). The motion is essentially in the direction of steepest descent with small sidewise dispersion. In the laboratory arrangement, a pile of granular material held within a hemispherical cap is suddenly released from its rest position and moves down the bed until it comes to rest in the *run-out zone*. In this situation, a convenient curvilinear coordinate system x, y, z is introduced as follows: x is the downward coordinate fitting the curve profile of the bed that follows the direction of steepest descent; y is the lateral coordinate (in this direction the bed is assumed to be flat); and z is the coordinate perpendicular to the local *tangent plane* of the curved bed as shown in Fig. 3.8.

A further extension of the theory was proposed by GRAY et al. [123]. They presented a two-dimensional depth-integrated theory for the gravity-driven free surface flow of cohesionless granular avalanches, with cross-flow variation of the topography as shown in Fig. 3.9. The *talweg* in this case is still a curve in a vertical plane and has no twist. The situation nevertheless points at an important extension of the one-dimensional model equations. In it a simple curvilinear coordinate system is adopted, which is fitted to the mean downslope chute topography. This defines a quasi-two-dimensional reference on top of which a shallow three-dimensional basal topography is superposed. We will deal in detail with this extension in the sequel. The reason is that *we can reproduce all of the previous theories as special cases of this model.*

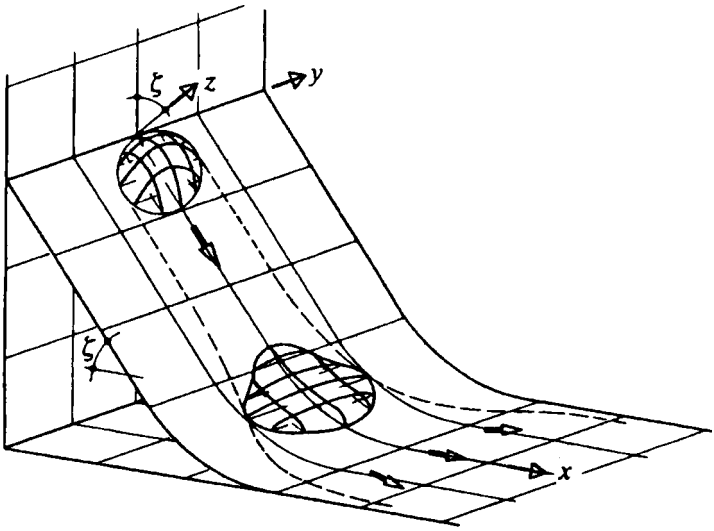

Fig. 3.8. Definition sketch of the curvilinear coordinate system fitting the experimental curved surface and geometry of a moving pile of granular material.

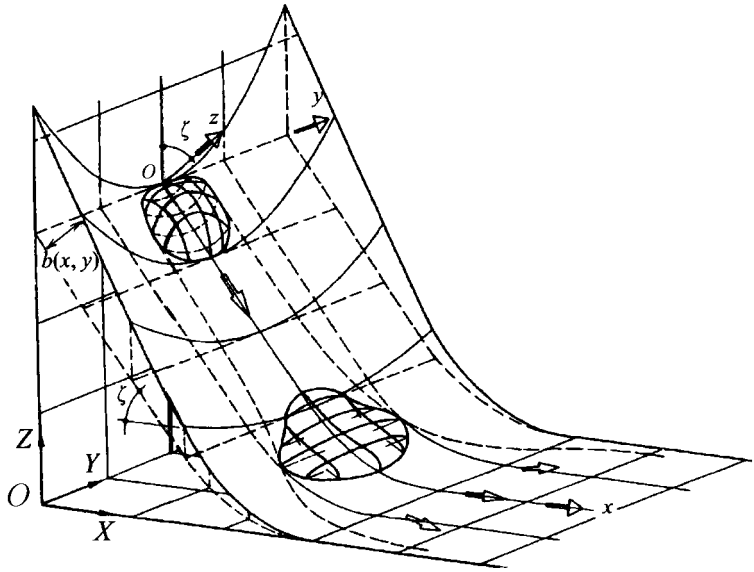

Fig. 3.9. The rectangular Cartesian coordinate system $OXYZ$ aligned so that the Z-axis is parallel but opposite in direction to the gravity acceleration vector, and the Y-axis is parallel to the cross-slope reference surface coordinate y. The basal topography (*solid lines*), on which the avalanche slides, $F^b(\mathbf{x}, t) = 0$, is defined by its height above the curvilinear reference surface $F^b = b(x, y, t) - z$ (*dashed lines*). The shallow complex three-dimensional geometry is therefore superposed on the two-dimensional curved reference surface.

The propagation of *dense flow avalanches*, as well as their transition into flows of turbulent particle suspensions in air, i.e., *powder snow avalanches*, has been studied by ZWINGER [449] who modified the COULOMB law for dry friction to complement it with a velocity-dependent basal friction law while using the SH-theory for the dense flow part of the avalanche. A comparison between numerical results of the coupled computational model and field data shows generally good agreement [450].

Recently, some further advancements of the theory have been achieved. PUDASAINI et al. [337] extended the theory to cases in which curvature and torsion effects of the basal topography are included. In this sense, this is an important extension of the original theory. All previous extensions were done in a traditional manner, as they did not incorporate the *effect of the torsion* of the basal topography through the underlying metric. Natural corries in steep mountainous regions "meander" in the landscape, which implies that their *talwegs are three-dimensional curves* in three-dimensional space, and these are locally characterised by curvature and torsion (twist). The most conceivably simple situation is a *helical chute*. For such situations it is feasible to base the curvilinear coordinate system on such a three-dimensional curve (here helix). PUDASAINI et al. [337] extended the theory to rapid *shear flows* of dry granular masses in such a rather strongly curved channel having both *curvature* and *torsion*.

Quite recently, PUDASAINI and HUTTER [335] extended the theory to a basal topography generated by an *arbitrary space curve having slowly varying curvature and torsion*. This extension has many important features as well as far-reaching applications in real flow situations. In contrast to other previous extensions, this local coordinate system is based on a generating line with curvature and torsion. Its derivation was necessary because *real avalanches are often guided by rather curved and twisted corries*. In this way, the equations provide fundamental insight into the effects of *non-uniform curvature and torsion*, using an orthogonal coordinate system that rotates with torsion, and find an analytic description for flow avalanches. This theory is explained in detail in Chap. 4. The major parts of this book rely on this theory, which *can reproduce all previous extensions of the* SAVAGE–HUTTER*-theory*. In this sense, this theory is very important both from a theoretical as well as an applicational point of view.

3.4 A Three-Dimensional Granular Avalanche Model

Two variants of extensions of the SH-theory will be considered and presented in detail, which are applicable to unconfined, confined and curved and twisted avalanche paths with increasing complexity. We present both, because it turns out that they are mathematically very similarly structured and give rise to

unified analytical and numerical solution procedures. This recognition is of much help later when explicit solutions are constructed. The ultimate goal is to present a critical comparison and to outline the physical meanings and applicabilities of the equation sets in different configurations. The remainder of this chapter deals with a three-dimensional avalanche model that is associated with an orthogonal curvilinear coordinate system. This model will be referred to as the *orthogonal complex system*, complex in the sense that a three-dimensional basal topography that varies both in the longitudinal and lateral directions is superposed on top of a *quasi-two-dimensional* basal reference surface. The other extension and generalisations of the theory for an *arbitrary reference surface*, generated by an orthogonal general coordinate system will be presented in Chap. 4.

In the ensuing presentation we shall not derive the model equations as generalised by GRAY et al. [123], but simply state and explain them, and establish the connection with the equations derived boldly in Sect. 3.2. This derivation will carefully be done for the most general case in Chap. 4. The earlier equations will then fall out from the general ones as special cases.

3.4.1 Field Equations

The avalanche is assumed to consist of an incompressible, dry and cohesionless material with constant density ρ throughout the entire body. Then the *mass and momentum conservation laws* reduce to

$$\nabla \cdot \mathbf{u} = 0, \tag{3.16}$$

$$\rho \left\{ \frac{\partial \mathbf{u}}{\partial t} + \nabla \cdot (\mathbf{u} \otimes \mathbf{u}) \right\} = -\nabla \cdot \mathbf{p} + \rho \mathbf{g}, \tag{3.17}$$

where ∇ is the gradient operator, $\mathbf{u}$ is the velocity, $\partial/\partial t$ indicates differentiation with respect to time, $\otimes$ is the tensor product, $\mathbf{p}$ is the pressure tensor (the negative CAUCHY stress tensor) and $\mathbf{g}$ is the gravitational acceleration.

Phenomenologically, the granular mass is assumed to satisfy a MOHR–COULOMB *yield criterion* in which the internal shear stress $\mathbf{S}$ and the normal pressure N on any plane element (see Fig. 3.10) are related by

$$|\mathbf{S}| = N \tan \phi, \tag{3.18}$$

where the sign is given by the direction of the sliding velocity and ϕ is the *internal angle of friction*. At the base ϕ will be replaced by δ, the bed friction angle.

The conservation laws (3.16) and (3.17) are complemented by *kinematic boundary conditions* at the free surface, $F^s(\mathbf{x}, t) = 0$, and at the base, $F^b(\mathbf{x}, t) = 0$, of the avalanche, namely

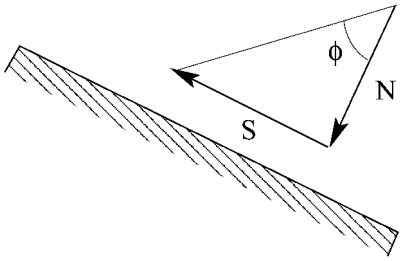

Fig. 3.10. Sketch showing the internal shear stress $\mathbf{S}$ and the normal pressure N on a plane element in the granular body. ϕ is the internal angle of friction. The orientation of the plane is arbitrary except at the base, where it is parallel to the bed.

$$F^s(\mathbf{x},t)=0, \quad \frac{\partial F^s}{\partial t}+\mathbf{u}^s\cdot\nabla F^s=0, \tag{3.19}$$

$$F^b(\mathbf{x},t)=0, \quad \frac{\partial F^b}{\partial t}+\mathbf{u}^b\cdot\nabla F^b=0, \tag{3.20}$$

where the superscripts "s" and "b" indicate that a variable is evaluated at the surface and the base, respectively.

There are also *dynamical boundary conditions* that must be satisfied. The *free surface* of the avalanche is *traction free*, while the base satisfies a COULOMB *dry-friction sliding law*:

$$F^s(\mathbf{x},t)=0, \quad \mathbf{p}^s\mathbf{n}^s=\mathbf{0}, \tag{3.21}$$

$$F^b(\mathbf{x},t)=0, \quad \mathbf{p}^b\mathbf{n}^b-\mathbf{n}^b\left(\mathbf{n}^b\cdot\mathbf{p}^b\mathbf{n}^b\right)=\left(\mathbf{u}^b/|\mathbf{u}^b|\right)\left(\mathbf{n}^b\cdot\mathbf{p}^b\mathbf{n}^b\right)\tan\delta, \tag{3.22}$$

where the surface and basal unit normals are

$$\mathbf{n}^s=\frac{\nabla F^s}{|\nabla F^s|}, \quad \mathbf{n}^b=\frac{\nabla F^b}{|\nabla F^b|}. \tag{3.23}$$

Remarks

- Notice that $\mathbf{pn}$ is the negative traction vector, $N=\mathbf{n}\cdot\mathbf{pn}$ is the normal pressure and $\mathbf{S}=\mathbf{pn}-\mathbf{n}\left(\mathbf{n}\cdot\mathbf{pn}\right)$ is the negative shear traction. It follows that the COULOMB dry-friction law (3.22) expresses the fact that the magnitude of the basal shear stress equals the normal basal pressure multiplied by a coefficient of friction, $\tan\delta$. The parameter δ is termed the basal angle of friction.
- Also notice that the shear traction is assumed to point in the opposite direction to the basal velocity $\mathbf{u}^b$ in (3.22). This implicitly assumes that $\mathbf{u}^b\cdot\mathbf{n}^b=0$ by (3.20). It also implies that the basal velocity $\mathbf{u}^b$ is tangential to the basal surface. This then explicitly indicates the condition that the basal surface is independent of time, i.e., $\partial F^b/\partial t=0$. However, for notational

convenience we will retain the term $\partial F^b/\partial t$ in the field equations wherever it appears.

– Defining the direction of the shear stress in this way introduces a singularity into the equations at $\mathbf{u}^b = \mathbf{0}$. In practical modelling of landslides, rockfalls, debris flows and snow and ice avalanches this restriction only requires attention at the onset and near the end of the avalanche motion, when it seeks to come to rest. This singularity may be avoided by replacing $\mathbf{u}^b/|\mathbf{u}^b|$ by the vector valued function

$$\mathbf{f}_\alpha = (f_u, f_v, f_w)\,, \tag{3.24}$$

where

$$f_u = \tanh(\alpha u)\,, \qquad f_v = \tanh(\alpha v)\,, \qquad f_w = \tanh(\alpha w)\,, \tag{3.25}$$

and $\alpha > 1$ is a real number. This parameterisation is continuous and removes the singularity at $\mathbf{u}^b = \mathbf{0}$; moreover, as $\alpha \to \infty$, $\mathbf{f}_\alpha$ approaches the function $\mathbf{u}^b/|\mathbf{u}^b|$.

■

3.4.2 Curvilinear Coordinate System in a Vertical Plane[2]

As explained in the previous sections, Gray et al. [123] extended the SH-theory to model the flow of avalanches over a shallow parabolic three-dimensional topography. This led to the first description of the flow of a finite mass of granular material down a valley or corrie. A reference surface that follows the mean downslope bed topography is used to define an orthogonal curvilinear coordinate system, $oxyz$ (see Fig. 3.9). The z-axis is normal to the reference surface and the x- and y- coordinates are tangential to it, with the x-axis oriented in the downslope direction. The downslope inclination angle, ζ, is used to define the reference surface as a function of the downslope coordinate, x. *The reference surface does not vary as a function of the cross-slope coordinate, y.* The chute geometry is superposed by defining its height, $z = b(x, y, t)$ above the reference surface, $z = 0$, through the kinematic boundary conditions, as illustrated in Fig. 3.9, and the depth integration. Even though the local downslope direction of the basal topography may not coincide with the direction of the x-coordinate, for notational simplicity, the components in the x-direction are referred to as downslope components and those in the y-direction as cross-slope components.

[2] In this section and henceforth, knowledge of the basic elements of tensor calculus is assumed. There is a great number of books on this, e.g., Bowen and Wang, Sokolnikoff, Klingbeil, Brillouin [42, 43, 46, 222, 398] and many others.

Here, we will present a brief derivation of the model equations of the theory. For the precise explanation, a rectangular Cartesian coordinate system $OXYZ$ is defined with unit basis vectors $\mathbf{i}, \mathbf{j}, \mathbf{k}$ aligned so that the vector $\mathbf{k}$ is parallel, but in the opposite sense, to the gravity acceleration vector, $\mathbf{i}$ lies in the vertical plane in which the reference surface varies, and $\mathbf{j}$ is perpendicular to both. A simple curvilinear coordinate system $oxyz$ is introduced. In this coordinate system, the position vector $\mathbf{r}$ is given by

$$\mathbf{r} = \mathbf{r}^r(x, y) + z\mathbf{n}^r, \tag{3.26}$$

where $\mathbf{r}^r$ is the position vector of the reference surface and $\mathbf{n}^r$ is the normal vector to this surface. In Cartesian coordinates, the normal to the reference surface is

$$\mathbf{n}^r = \sin\zeta\mathbf{i} + \cos\zeta\mathbf{k}, \tag{3.27}$$

where ζ is the inclination angle of the normal of the reference surface relative to the Z-axis. For ease of notation, the identification $(x, y, z) = \left(x^1, x^2, x^3\right)$ is made. These are the contravariant components in the curvilinear coordinate system (see, e.g., Bowen and Wang and Klingbeil [42, 43, 222]), and the associated covariant basis vectors, $\mathbf{g}_i$, are given by

$$\mathbf{g}_i = \frac{\partial \mathbf{r}}{\partial x^i}. \tag{3.28}$$

The gradients $\partial\mathbf{r}/\partial x^1$ and $\partial\mathbf{r}/\partial x^2$ are simply the tangent vectors to the reference surface in the x^1- and x^2-directions, respectively. Thus, choosing the mutually orthogonal tangent vectors with the x-axis in the OXZ plane, it follows that $\partial\mathbf{r}^r/\partial x^1 = \cos\zeta\mathbf{i} - \sin\zeta\mathbf{k}$ and $\partial\mathbf{r}^r/\partial x^2 = \mathbf{j}$, so that

$$\begin{aligned} \mathbf{g}_1 &= \left(1 - \kappa x^3\right)(\cos\zeta\mathbf{i} - \sin\zeta\mathbf{k}), \\ \mathbf{g}_2 &= \mathbf{j}, \\ \mathbf{g}_3 &= \sin\zeta\mathbf{i} + \cos\zeta\mathbf{k}, \end{aligned} \tag{3.29}$$

where the curvature κ is given by

$$\kappa = -\frac{\partial\zeta}{\partial x^1}. \tag{3.30}$$

The covariant metric coefficients are defined as $g_{ij} = \mathbf{g}_i \cdot \mathbf{g}_j$. Thus, it follows from (3.29) that

$$(g_{ij}) = \begin{pmatrix} \left(1 - \kappa x^3\right)^2 & 0 & 0 \\ 0 & 1 & 0 \\ 0 & 0 & 1 \end{pmatrix}. \tag{3.31}$$

Since the off-diagonal elements of this metric tensor are all zero, this simple curvilinear coordinate system is called *orthogonal*. The region above the reference surface $z = 0$ can be described by the coordinates xyz that are based on the metric with the square arc length

$$ds^2 = (1 - \kappa z)^2\, dx^2 + dy^2 + \ dz^2. \tag{3.32}$$

The metric is uniquely defined as long as the z-coordinate is locally smaller[3] than $1/\kappa$. In the theory this is assumed to be satisfied automatically. It is clear that (3.32) defines an orthogonal metric because there is no products term in it.

3.4.3 The Model Equations

Conservative Form The coordinate invariant governing equations of Sect. 3.4.1 are expressed in a first step in the curvilinear coordinate system of Sect. 3.4.2 as shown in Fig. 3.9. Equations are then non-dimensionalised via a scaling that introduces an aspect ratio $\varepsilon = \textit{typical height/typical extent}$ and is used to simplify the equations. In a second step, the mass and momentum balance equations are integrated through the avalanche depth along the normal of the reference geometry. In this process terms of order higher than $O(\varepsilon)$ are neglected. For an incompressible cohesionless material the continuity equation yields, together with the kinematic boundary conditions at the free surface and the base of the avalanche,

$$\frac{\partial h}{\partial t} + \frac{\partial}{\partial x}(hu) + \frac{\partial}{\partial y}(hv) = 0, \tag{3.33}$$

where h represents the evolving geometry of the avalanche and $\mathbf{u} = (u, v)$ is the depth-averaged surface-parallel velocity with components u and v in the downslope and cross-slope directions, respectively. Similarly, the momentum balance equations in the downslope and cross-slope directions reduce to

$$\frac{\partial}{\partial t}(hu) + \frac{\partial}{\partial x}\left(hu^2\right) + \frac{\partial}{\partial y}(huv) = hs_x - \frac{\partial}{\partial x}\left(\frac{\beta_x h^2}{2}\right), \tag{3.34}$$

$$\frac{\partial}{\partial t}(hv) + \frac{\partial}{\partial x}(huv) + \frac{\partial}{\partial y}\left(hv^2\right) = hs_y - \frac{\partial}{\partial y}\left(\frac{\beta_y h^2}{2}\right). \tag{3.35}$$

Equations (3.33)–(3.35), which are in *conservative form*, will henceforth be referred to as an *orthogonal complex system*. The factors β_x and β_y are defined as

$$\beta_x = \varepsilon \cos\zeta K_x \quad \text{and} \quad \beta_y = \varepsilon \cos\zeta K_y, \tag{3.36}$$

respectively. The terms s_x and s_y represent the *net driving accelerations* in the downslope and cross-slope directions, respectively, given by

[3] Physically, these points correspond to the positions at which consecutive z-axes, which vary locally, intersect with one another. Therefore, the superimposed topography b should also be shallow. Provided that the avalanche does not pass through one of these points during the course of its motion, the curvilinear coordinates (3.31) represent a valid coordinate system.

$$s_x = \sin\zeta - \frac{u}{|\mathbf{u}|}\tan\delta\left(\cos\zeta + \lambda\kappa u^2\right) - \varepsilon\cos\zeta\frac{\partial b}{\partial x}, \tag{3.37}$$

$$s_y = \quad -\frac{v}{|\mathbf{u}|}\tan\delta\left(\cos\zeta + \lambda\kappa u^2\right) - \varepsilon\cos\zeta\frac{\partial b}{\partial y}, \tag{3.38}$$

in which

$$\varepsilon = \frac{\text{typical height}}{\text{typical extent}} = \frac{H}{L},$$

$$\lambda = \frac{\text{typical extent}}{\text{typical topographic radius of curvature}} = \frac{L}{\mathcal{R}},$$

and δ is the *bed friction angle* of the granular material with the basal topography, namely $b = b(x, y, t)$. K_x and K_y are called the *earth pressure coefficients*, which are equal to the ratio of the in-plane to vertical pressure in the downslope and cross-slope directions, respectively (that is, $K_x = p_{xx}/p_{zz}$ and $K_y = p_{yy}/p_{zz}$). Elementary geometrical arguments may be used to determine these values as functions of the internal, ϕ, and basal, δ, angles of friction, see [177]; they are given by

$$K_{x_{\text{act/pas}}} = 2\sec^2\phi\left\{1 \pm \left(1 - \cos^2\phi\sec^2\delta\right)^{1/2}\right\} - 1, \qquad \frac{\partial u}{\partial x} \gtrless 0, \tag{3.39}$$

$$K_{y_{\text{act/pas}}} = \frac{1}{2}\left\{K_x + 1 \mp \left(\left(K_x - 1\right)^2 + 4\tan^2\delta\right)^{1/2}\right\}, \quad \frac{\partial v}{\partial y} \gtrless 0, \tag{3.40}$$

where K_x and K_y are *active* during dilatational motion (upper sign) and *passive* during compressional motion (lower sign). The detailed presentation of these statements and computations will be given in Chap. 4, Sect. 4.7. For (3.39), however, see, also (3.11).

The conservation laws (3.33)–(3.35) are written in *non-dimensional curvilinear form*. The non-dimensional variables, $(x, y, h, b, u, v, t, \kappa)$ can be mapped back to their physical counterparts $\left(\hat{x}, \hat{y}, \hat{h}, \hat{b}, \hat{u}, \hat{v}, \hat{t}, \hat{\kappa}\right)$ by applying the scalings

$$\begin{aligned} &(\hat{x}, \hat{y}) = L\,(x, y)\,, \qquad (\hat{h}, \hat{b}) = H\,(h, b)\,, \\ &(\hat{u}, \hat{v}) = \sqrt{gL}\,(u, v)\,, \quad \hat{t} = \sqrt{L/g}\,t, \quad \hat{\kappa} = \kappa/\mathcal{R}, \end{aligned} \tag{3.41}$$

where g is the gravitational acceleration. It is, moreover, assumed that both the aspect ratio $\varepsilon = H/L$ and the characteristic curvature of the chute $\lambda = L/\mathcal{R}$, arising in (3.36)–(3.38), are small.

Let us pause and compare (3.33)–(3.41) with (3.2)–(3.12) in Sect. 3.2. Equation (3.33) is the depth-integrated balance of mass. Other than (3.2), as variables it now contains h and two topography-parallel depth-averaged velocity

components (u, v). Note that x and y are now curvilinear coordinates, but the equation appears as if it were written in Cartesian coordinates. As we shall see in Chap. 4, this is the result of ignoring terms of order higher than $O(\varepsilon)$. This is important to recognise: *In general, the conservative form is not obtained when curvilinear coordinates are used; the shallowness assumption and ordering or re-definition of variables (see* BOUCHUT *and* WESTDICKENBERG *[40]) puts the equations back to conservative form.*[4]

Equations (3.34), (3.35) with the definitions (3.36)–(3.40) are the dimensionless forms of the downslope and cross-slope momentum equations. Equation (3.34) is analogous to $(3.13)_2$ with the addition of the third term on the left-hand side, the transverse flux of the downslope momentum flow, and the topographic gradient effect, the third term on the right-hand side of (3.37). Equation (3.35) is new, but its structure is analogous to (3.34). The last two terms on the right-hand sides of (3.34) and (3.35) with β_x and β_y as given in (3.36), are the analoga to the corresponding term in (3.7). These terms account for the variation of the vertically integrated pressures p_{xx} and p_{yy} of an infinitesimal column of cross-section $dxdy$ (see Fig. 3.1b, in which p_{xx} or p_{yy} correspond to p_L). Moreover, as before, they are responsible for the changes of the geometry of the granular pile and the basal topography. Only these terms contain the earth pressure coefficients and thus account for the distinction between dilatational and compressional flow states.

The source terms s_x and s_y in (3.37) and (3.38) are also slightly different from the corresponding terms in (3.7). In (3.37) $\sin\zeta$ is the dimensionless component of the gravity force in the downslope direction. The second term is the component of the basal friction in the downslope direction, but here *the basal pressure is enlarged by* $\lambda\kappa u^2$, the "centrifugal" contribution due to the downslope curvature of the bed. The last term, finally, is the influence of the basal topography; it accounts for an additional resistive force due to the fact that the basal surface does not agree with the reference surface. As for an interpretation of s_y, it is obvious that in this coordinate system the y-coordinates are always horizontal, so gravity has no component in this direction. The contribution of the second term is analogous to that in s_x, and so is the third, geometric term. Note that the prefactors of the frictional forces are such that the resultant frictional traction has the magnitude

$$\tau = -\tan\delta\left(\cos\zeta + \lambda\kappa u^2\right).$$

[4] To understand this properly, recall that in the footnote on pages 119/120 various terminologies of "conservatism" of balance laws were introduced. Here the strongest version is meant, namely a balance law without a production term, and a source term that is truly a source, i.e., determined by outside "agents", such as, e.g., gravity. In this strong definition s_x and s_y in (3.37) and (3.38) contain a term that depends on u, v. It is extremely important for mathematical reasons that the unknown variables appear as far as possible in the flux terms rather than the "source terms".

Finally, we mention that the conservative form (3.34) and (3.35) is again only obtained, since, owing to the shallowness assumption, terms higher than order $O(\varepsilon)$ have been ignored. There are also further delicate ad hoc assumptions that will be made clear in Chap. 4.

Non-Conservative Form For *smooth solutions*, the mass balance (3.33) can be used to simplify the convective terms in the momentum equations (3.34) and (3.35). With the operator

$$\frac{d}{dt} = \frac{\partial}{\partial t} + u\frac{\partial}{\partial x} + v\frac{\partial}{\partial y}, \tag{3.42}$$

the conservative equations of momentum balance change into the following non-conservative form

$$\frac{du}{dt} = \sin\zeta - \frac{u}{|\mathbf{u}|}\tan\delta\left(\cos\zeta + \lambda\kappa u^2\right) - \varepsilon\cos\zeta\left(K_x\frac{\partial h}{\partial x} + \frac{\partial b}{\partial x}\right), \tag{3.43}$$

$$\frac{dv}{dt} = \quad - \frac{v}{|\mathbf{u}|}\tan\delta\left(\cos\zeta + \lambda\kappa u^2\right) - \varepsilon\cos\zeta\left(K_y\frac{\partial h}{\partial y} + \frac{\partial b}{\partial y}\right), \tag{3.44}$$

provided that $h \neq 0$. The system of equations (3.33), (3.43) and (3.44) constitutes a *non-conservative system of equations*, derived originally by Gray et al. [123] to generalise the one-dimensional SH-theory [375, 376]. As we shall see later on, the non-conservative form is useful in implementing the Lagrangean numerical scheme, for more details see [123, 412, 445].

Given the reference surface (slope) $\zeta(x)$, a basal topography $b(x, y, t)$ and the material slip parameters δ and ϕ, both of these systems of equations allow three independent variables h, u and v to be computed once the initial conditions and boundary conditions are prescribed.

We summarise the above findings formally in a compact and precise mathematical form quasi as a "theorem". The theory is based on a *hydraulic* framework and generalises the *mass point model* of Voellmy [430].

Extended Savage–Hutter Avalanche Model[5] We consider the following assumptions:

(i) **Topography** A reference surface can be described by an orthogonal curvilinear coordinate system $Oxyz$ in which the z-axis is normal to the surface and the x-axis and y-axis are tangential to it, with the x-axis oriented downslope. The function $\zeta = \zeta(x)$ represents the downslope inclination angle to the horizontal and $\kappa = -\partial\zeta/\partial x$ is its curvature. Suppose $z = b(x, y, t)$ is the chute geometry above this surface and $z = s(x, y, t)$ the free surface so that $h(x, y, t) = s(x, y, t) - b(x, y, t)$ represents the avalanche height along the z-axis.

[5] For further extension and generalisation of this model, we refer to Sect. 4.9.1.

It will be assumed that a typical value of $h(x, y, t)$, say H, is small in comparison to a typical extent, L; hence $H/L \ll 1$. This is the shallowness assumption.

(*ii*) **Material** The avalanche is assumed to consist of an incompressible, non-cohesive, isothermal, dry and dense granular continuum material.

(*iii*) **Closure** Assume that the material satisfies the COULOMB dry friction law at the bottom and the MOHR–COULOMB plastic yield criterion in the interior, and the dominant deformation takes place in the downslope direction. Assume, moreover, that the shear stresses lateral to the main flow direction can be neglected and suppose that the downslope and cross-slope pressures vary linearly with the normal pressure through the depth of the avalanche, and that shearing takes place in a very small basal layer so that the velocity distribution is almost uniform over the depth.

(*iv*) **Pressure Coefficients and Parameters** Let δ and ϕ be the bed and internal friction angles, respectively, of the granular material and let the pressure coefficients $K_{x,y} = K_{x,y}(\delta, \phi)$ be functions, constructed by using the MOHR circle, of the form

$$K_x = 2\sec^2\phi\left\{1 \mp \left(1 - \cos^2\phi\sec^2\delta\right)^{1/2}\right\} - 1, \qquad \frac{\partial u}{\partial x} \gtrless 0, \quad (3.45)$$

$$K_y = \frac{1}{2}\left\{K_x + 1 \mp \left(\left(K_x - 1\right)^2 + 4\tan^2\delta\right)^{1/2}\right\}, \quad \frac{\partial v}{\partial y} \gtrless 0, \quad (3.46)$$

for extension and contraction of the material body. Moreover, let H, L and $\mathcal{R} = 1/\kappa$ be a typical avalanche thickness, length and radius of the curvature. Define, $\varepsilon = H/L$, $\lambda = L/\mathcal{R}$, and

$$\beta_x = \varepsilon\cos\zeta K_x, \qquad \beta_y = \varepsilon\cos\zeta K_y, \quad (3.47)$$

$$s_x = \sin\zeta - \frac{u}{|\mathbf{u}|}\tan\delta\left(\cos\zeta + \lambda\kappa u^2\right) - \varepsilon\cos\zeta\frac{\partial b}{\partial x}, \quad (3.48)$$

$$s_y = \quad - \frac{v}{|\mathbf{u}|}\tan\delta\left(\cos\zeta + \lambda\kappa u^2\right) - \varepsilon\cos\zeta\frac{\partial b}{\partial y}, \quad (3.49)$$

where $\mathbf{u} = (u, v)$ is the depth-averaged surface-parallel velocity with components u and v along the x- and y-coordinates, respectively.

(*v*) **Smoothness** Suppose that all field variables are sufficiently smooth so that the order of integration and differentiation can be interchanged.

Then, under a realistic non-dimensionalisation, the dynamics of a granular avalanche can be described by the set of partial differential equations

$$\frac{\partial h}{\partial t} + \frac{\partial}{\partial x}(hu) + \frac{\partial}{\partial y}(hv) = 0, \tag{3.50}$$

$$\frac{\partial}{\partial t}(hu) + \frac{\partial}{\partial x}\left(hu^2\right) + \frac{\partial}{\partial y}(huv) = hs_x - \frac{\partial}{\partial x}\left(\frac{\beta_x h^2}{2}\right), \tag{3.51}$$

$$\frac{\partial}{\partial t}(hv) + \frac{\partial}{\partial x}(huv) + \frac{\partial}{\partial y}\left(hv^2\right) = hs_y - \frac{\partial}{\partial y}\left(\frac{\beta_y h^2}{2}\right), \tag{3.52}$$

accurate to order $\varepsilon^{1+\gamma},\ 0 < \gamma < 1$.

Note The physical variables are recovered by realistic non-dimensionalisations as pointed out by (3.41).

■

3.4.4 Differences Between Geophysical Mass Flows and Shallow Water Equations

The avalanche equations (3.50)–(3.52) presented above look structurally similar to the classical shallow water equations. However, there are fundamental differences between these two classes of equations. These differences are mainly reflected by the scalings, on which the equations are based, the constitutive behaviour and the physical conditions at the boundaries to which these flows are subjected.

(*i*) ***Constitutive Behaviour*** The fundamental assumption in the above equations is frictional resistance according to MOHR–COULOMB plasticity; by contrast, the shallow water theory applies to ideal or NAVIER–STOKES fluids. The implementation of the former into a depth-integrated model is far more complicated than the implementation of the latter. In particular, the concept of active and passive states of stresses is introduced. This implies, firstly, that the "pressures" in the three space directions are not the same and thus deviate markedly from hydrostaticity and, secondly, coefficients (i.e., β_x and β_y in (3.51) and (3.52) or (3.47)) may be discontinuous whenever the flow goes from a dilatational state of deformation to a compacting one.

(*ii*) ***Scalings*** Avalanches fall, water layers do not, but motions in both are due to the presence of gravity. Thus, besides g, the acceleration due to gravity, a characteristic length to characterise speeds and time are a typical avalanche extent, L, and the water depth, H, respectively, leading to the characterisation in Table 3.1. This means that a typical speed for avalanches is the free fall velocity and for water the shallow water velocity. This avalanche scaling has been used in (3.41).

(*iii*) ***Mathematical Differences*** We have just remarked that β_x and β_y may be discontinuous, since the earth pressure coefficients K_{act} and K_{pas} may

Table 3.1. Characteristics of the avalanche and shallow water equations. Typical scales to non-dimensionalise the avalanche and shallow water equations.

Characteristic quantity	Avalanche	Shallow water
Length	L	H
Time	$\sqrt{L/g}$	$\sqrt{H/g}$
Velocity	$\sqrt{gL}$	$\sqrt{gH}$

suffer jump discontinuities. This makes the governing equations a system of hyperbolic partial differential equations with discontinuous coefficients. Mathematically, this is a major step into complexities, because a theory of existence proofs is still not known in this case. One idea is, therefore, to make K_x and K_y continuous functions of $\partial u/\partial x$ and $\partial v/\partial y$, see (3.39) and (3.40), but then the system of equations may lose the hyperbolicity property and shocks may now be smoothed.[6] All these peculiarities are not encountered in the shallow water theory.

(*iv*) ***Erosion and Deposition*** Erosion and deposition at the sliding bed and accumulation at the free surface (usually not significant) may well be dominating processes in avalanches and debris flows; if incorporated, they will add production terms to the mass and momentum balance equations, and they will also change the basal boundary conditions. We know that these processes are not significant in water. The erosion process in avalanches and debris flows is sometimes so significant that the deposited mass in the run out zone is much larger than the initial mass in the starting zone. Or erosion of a river bed in a mud flow may enlarge the cross-section of the river by as much as ten times and more, see also Chap. 10.

3.4.5 Features and Limitations of the Extended Model

There are many distinguished advantageous features of the extended model. Needless to say, there are also some limitations. We point them out systematically as follows:

Advantages:

- *A Complete Theory* The extended model equations provide a complete dynamic description of the avalanche, debris flow or small-scale industrial flows in channels, hoppers, silos or heap formations from initiation along

[6] Such a regularisation has been proposed in [410].

their paths to the run-out or standstill and deposition. The dynamics of any avalanche is associated with the evolution of the avalanche geometry and the velocity distribution over the entire body. Consequently, one can predict the dynamic pressure on obstructions along the path of the avalanche or the debris. The main intention of the model is to provide these properties of the flowing geo- and industrial granular masses.[7]

- *Three-Dimensional Mapping* With the exception of the Russian models there is no other simple avalanche model[8] that can provide a three-dimensional avalanche mapping along its path to the run-out. There are mass-point and statistical models (as explained earlier in Sect. 2.8), but they can only provide one-dimensional mapping. The extended SH-model provides the required three-dimensional mappings sought by the avalanche practitioners to separate a mountain valley into "red, yellow and green" regions implying high danger, moderate danger and relative safety, in order to protect the lives and properties of valley inhabitants.
- *Scale Invariance* The model equations are scale-invariant if friction is restricted to be of COULOMB-type. Since the model equations are non-dimensionalised, they can be used for very small (several cubic centimetres) laboratory motions up to very huge (several million cubic metres) natural events.
- *Slope Fitted Model Equations* The equations are derived in slope fitted coordinates that are compatible with the real bed over which the avalanche moves at least for simple topographies where downslope curvature is included. Consequently, this model can capture the effects of topographic curvature. None of the other existing models possesses this property.
- *Handy and Economical* The model is very simple to implement in the sense that one needs to know only two physical parameters: the internal angle of friction and the bed friction angle and the flow topography. In many cases, the material or the phenomenological parameters can be determined in the laboratory or they are known from experience in the field and the basal surface can be constructed from remote digital altimeter data. What is most needed is the initial geometry at the time of the trigger and the initial velocity (usually zero). In the laboratory this is not problematic. In the field, estimation of the initially breaking mass is more difficult and can, in re-analyses or hindcasts of events be determined from the deposits. Fortunately, the final deposit does not seem to critically depend on the

[7] Russians scientists [35, 36, 84, 85, 86, 87, 88, 89, 90, 91, 130, 131, 132, 133, 282, 283, 284, 308, 432] were very much ahead in their developments of avalanche models, but whereas they accounted for all geometric ingredients, they used fluid constitutive behaviour analogous to the SAINT VENANT equations with VOELLMY type basal friction. It is known that this makes non-planar free surfaces of depositions impossible, see [40].

[8] Exceptions are NAVIER–STOKES-models, but they are physically inadequate, and there are a number of more complex models that, perhaps, aim at the same goals, see, e.g., [74, 75, 191, 192, 194, 313, 321].

initial conditions – except its total volume. Computationally, the economy of the programs is optimal: Usual CPU times for a single run on complex geometry are minutes and not hours or days, so that computations can easily be performed for random sets of initial data.

- *Mathematically Well-Structured* The model equations can be brought into the standard form of two-dimensional non-linear hyperbolic partial differential equations with source terms. Robust numerical solution schemes have been and are still being developed to solve these equations successfully, from the classical finite difference methods to modern finite element schemes. Moreover, shock capturing and front tracking total variation diminishing numerical schemes are being implemented for these equations in order to capture possible shocks. We will develop and implement such numerical schemes in Chaps. 7, 8, 9 and 12.
- *Possibility of Validation by Laboratory Experiments* The model equations can easily be validated by well-controlled laboratory experiments of confined and non-confined avalanche motions of different granular materials. Previous experiences have demonstrated good to excellent correlations between the theoretical predictions and the laboratory simulations via numerical computations.
- *Reduction to Shallow Water Equations* As a special case, the model equations reduce to the classical shallow water equations. For this, one needs only to set the earth pressure coefficients to unity, because fluids, like water, do not extend or contract as they pass through a topography with variable curvature. Moreover, these model equations can be used to model actual river dynamics as they include the real topography of the river bed. The equations are then identical to those due to Saint Venant; consequently the SH-type equations are also referred to as Saint Venant-type equations, see Mangeney–Castelnau et al. [264, 265] and Bouchut et al. [38, 40].
- *Extension to Complicated Mountain Topography* One of the most important features of the model is that it can be extended to describe the real flow of an avalanche and debris in natural and complicated mountain terrain. We will make this fact clear in Chap. 4 by developing a new theory that can predict such flows.

Limitations

- *Parameters* The theory holds true only if the internal friction angle is greater than or equal to the bed friction angle. In most engineering and geophysical flows this restriction is not a problem. However, otherwise the theory fails, because the earth pressure coefficients become complex-valued.
- *Geometry* The theory gives good to excellent results if the topography varies gently. One may not expect good results if there are abrupt changes in the topography in a large sub-region of the flow path. For instance, the motion over a cliff may cause the avalanche to go into a ballistic motion

without any contact with the basal surface. Under these circumstances the model equations fail. Moreover, the avalanching body should not exceed, in its height, the radius of curvature and not pass through the centre of the curvature of the basal topography.

- *Frictional Resistance* There are two opinions about the dry COULOMB friction law implemented in the SH-theory. ANCEY and MEUNIER [7] recently implemented field data of different avalanches in order to infer the bulk frictional forces on the basis of the knowledge of the velocity variation and the depth profiles of the events. They concluded that the COULOMB friction model is adequate to describe variations in velocity and frictional forces during the course of an avalanche. On the other hand, some people argue that it would be better to include a viscous or velocity-dependent contribution to the basal drag [329, 330, 449, 450]. To some extent this is correct. However, its incorporation is conceptually trivial, and it is most likely not necessary for many flows of cohesionless granular materials. The incorporation of this velocity-dependent drag has not been convincingly demonstrated for such restricted applications.[9] For snow avalanches some authors claim it will be necessary and when real computations are performed, this viscous drag can be incorporated [449, 450], others come to the opposite conclusion [7].
- *Velocity Profile* In the model, it is assumed that the velocity profile varies uniformly through the depth of the avalanche. Actually, a closure would be needed to include other possibilities that would produce additional parameters for all averaged product quantities. However, it is very difficult to identify them. Nevertheless, we have estimated the influence of shearing and found it is almost never necessary to include it, see [183].
- *Lateral Pressure* In the derivation of the model equations, it is assumed that the lateral confinement pressure is close to a principal stress. Expressed in the introduced coordinates x, y, z, this is tantamount to ignoring τ_{xy}, which is an ad hoc criterion. Incidentally, this assumption is justified whenever lateral velocities and their variations are small as compared to "downhill" velocities.
- *Incompressibility* The model equations are designed to describe the overall dynamics of an avalanche. However, locally, in the starting region, while approaching the deposition zone and in the vicinity of obstructions of the avalanche path, the prediction of the model may not be as good as in other parts of the topography. This is due to the large (relative) dilatation of the body in these critical zones.
- *Combination of the First- and Leading-Orders* The final governing equations involve terms of $O(1)$ and $O(\varepsilon)$, which is standard in the SH-theory.

[9] In our own experiments of flow of a sheet of granular materials down inclined planes we were not able to conclusively demonstrate that a steady motion is be reached. This is an argument in favour of COULOMB friction rather than viscous behaviour, see [83, 183].

No other techniques, such as a different scaling or a formal perturbation expansion, have been found so far that yield only $O(1)$ terms in the final equations.

In Chap. 4, we will generalise this theory so as to study the dynamics of avalanches, debris-flows, mud flows, landslides and rockslides over a non-trivial mountain topography that might be arbitrarily curved and twisted.

3.5 Avalanches with Coulomb-Type and Viscous-Type Frictional Resistance

Up to now the granular mass is treated as a dry Coulomb continuum both within the interior of the material and on the sliding surface. In this section, we will generalise this concept. The basal frictional force will now be assumed to be composed of a Coulomb-type component with a bed friction angle and a viscous Voellmy-type *resistive stress* that is proportional to the squared velocity. Such consideration adds further understanding of the dynamics of flow avalanches, which have a negligible airborne powder snow contribution. It also aims at an improved description of the classical Voellmy, Salm, and Perla et al. models [315, 362, 430]. It is at this point where the model provides the necessary flexibility sought by the avalanche dynamicist.

3.5.1 Model Equations Including Voellmy Drag

We extend the bed friction law (3.18) by adding to the Coulomb drag a *viscous drag* as follows:

$$\mathbf{S} = \mathbf{S}_C + \mathbf{S}_V. \tag{3.53}$$

The first is given by $|\mathbf{S}_C| = N \tan\delta$. The second is a *viscous drag*, very much like the classical Voellmy drag in the early avalanche models and has the form

$$\mathbf{S}_V = \rho q |\mathbf{u}| \mathbf{u}, \tag{3.54}$$

where $q = q(|\mathbf{u}|, N)$ is the dimensionless drag coefficient that may depend on the modulus of the velocity vector and the stress normal to the basal surface. If q is independent of $\mathbf{u}$, then $\mathbf{S}_V$ has a quadratic dependence on the velocity, but any other dependence (e.g., on normal stress) is also possible. The important point here is the following. The avalanche dynamicists used to dealing with the Voellmy model usually define the viscous drag $\mathbf{S}_V$ as follows:

$$\mathbf{S}_V = \frac{\rho g}{\xi} |\mathbf{u}| \mathbf{u}, \tag{3.55}$$

where $\xi = g/q$ is called "viscosity" but has the dimension of an acceleration.

If (3.55) is incorporated in the model equations, the governing equations (3.33)–(3.40) remain the same except for the driving terms, which now read[10]

$$s_x = s_{x_{(3.37)}} - \frac{1}{\Xi}|\mathbf{u}|u, \quad s_y = s_{y_{(3.38)}} - \frac{1}{\Xi}|\mathbf{u}|v, \tag{3.56}$$

where (from (3.55))

$$\Xi := \frac{\varepsilon}{q} = \frac{\varepsilon\xi}{g} \tag{3.57}$$

may be called VOELLMY drag coefficient. Thus, with (3.56) the model equations (3.33)–(3.35) or (3.33) and (3.43), (3.44) are also valid for a frictional model that incorporates both COULOMB-type and viscous-type friction. This extended model still exhibits the properties of similitude, if the phenomenological parameters δ, ϕ and Ξ are kept constant with the change of the scale.[11]

Finally, let us prepare the equations to a form that is particularly convenient for analytical studies. At the same time, a better physical understanding will thereby be obtained. To this end, let

$$A = \sin\zeta, \quad B = \varepsilon\cos\zeta K_x, \quad C = \cos\zeta\tan\delta, \quad D = \varepsilon\cos\zeta K_y \tag{3.58}$$

be constants and

$$\mathcal{F} = \begin{pmatrix} hu^2 & huv \\ huv & hv^2 \end{pmatrix}, \quad \mathbf{B} = \begin{pmatrix} B & 0 \\ 0 & D \end{pmatrix}, \quad \mathbf{u} = (u, v), \quad \mathbf{e} = \begin{pmatrix} 1 \\ 0 \end{pmatrix}. \tag{3.59}$$

Here, all quantities are self-explanatory and $\mathbf{e}$ is the unit vector in the downslope (curvilinear) direction. With these definitions it is easy to show that (3.33)–(3.35), with s_x and s_y defined in (3.56), take the forms

$$\begin{aligned} &\frac{\partial h}{\partial t} + \operatorname{div}(h\mathbf{u}) = 0, \\ &\frac{\partial (h\mathbf{u})}{\partial t} + \operatorname{div}\mathcal{F} = Ah\mathbf{e} - \mathbf{B}\operatorname{grad}(h^2/2) - Ch\frac{\mathbf{u}}{|\mathbf{u}|} - \frac{1}{\Xi}|\mathbf{u}|\mathbf{u}. \end{aligned} \tag{3.60}$$

This form of the model equations allows a particularly convenient separation of the avalanche motion into the motion of the centre of mass plus the deformation. This will now be done.

[10] Note that (3.56) contain velocity-dependent source terms, which are unknown. This fact has its bearings in the handling of the governing equations with respect to their conservative characteristics, see the footnote on page 119/120.

[11] Actually, Ξ exhibits scale-dependence through the appearance of g, but as long as the gravity constant does not change, it is ineffective. However, if, instead of a quadratic viscous drag, a linear drag had been postulated, the scale dependence would become very explicit.

3.5.2 Equations for the Motion of the Centre of Mass

In Chap. 5 we will construct solutions that preserve the shape and structure of the velocity field. For this purpose, we need to decompose the motion into that of the centre of mass and the deformation relative to it [176]. This decomposition is possible provided that the variation of the Voellmy drag on the deformation is ignored; instead, it is assumed to be *symmetrically distributed* throughout the motion and finally replaced by a "suitable average value". With it, the depth and velocities relative to those of the centre of mass of the moving pile can be determined analytically.

Equations (3.60) will now be separated into two sets of equations, one governing the motion of the centre of mass, the other describing the deformation or the deviation from the rigid-body motion. To this end, let $\mathcal{A} = \mathcal{A}(t)$ be the domain in the (x, y) space at time t covered by the avalanching mass. Furthermore, let $\partial\mathcal{A}$ be its boundary margin. Integrating the mass balance equation $(3.60)_1$ over $\mathcal{A}$ yields

$$\iint_{\mathcal{A}} \left(\frac{\partial h}{\partial t} + \operatorname{div}(h\mathbf{u}) \right) da = 0, \tag{3.61}$$

where da is the element of the areal integral. By using Reynolds' *transport theorem* in the first term and Gauss' or divergence *theorem* in the second,

$$\begin{aligned} \iint_{\mathcal{A}} \frac{\partial h}{\partial t}\, da &= \frac{d}{dt} \iint_{\mathcal{A}} h\, da - \oint_{\partial\mathcal{A}} h\, (\mathbf{u} \cdot \mathbf{n})\, ds, \\ \iint_{\mathcal{A}} \operatorname{div}(h\mathbf{u})\, da &= \oint_{\partial\mathcal{A}} h\, (\mathbf{u} \cdot \mathbf{n})\, ds, \end{aligned} \tag{3.62}$$

where $\mathbf{n}$ is the outward unit vector normal to $\partial\mathcal{A}$ and ds is the element of the line-integral. Equation (3.61) now takes the simple form

$$\frac{d}{dt} \iint_{\mathcal{A}} h\, da = 0. \tag{3.63}$$

This equation says that *the total volume of the avalanche is conserved throughout the motion*. Obviously, entrainment of snow is ignored. In much the same way, the momentum equation $(3.60)_2$ may be transformed in a straightforward manner to the form

$$\frac{d}{dt} \iint_{\mathcal{A}} h\, \mathbf{u}\, da = \iint_{\mathcal{A}} \left(A\, h\, \mathbf{e} + (\operatorname{div}\mathbf{B})\, \frac{h^2}{2} - Ch \frac{\mathbf{u}}{|\mathbf{u}|} - \frac{\mathbf{u}|\mathbf{u}|}{\Xi} \right) da. \tag{3.64}$$

Note that in order to achieve the *global momentum balance* (3.64), the *divergence theorem* has been employed in various places, and the boundary condition that h vanishes along the boundary $\partial\mathcal{A}$ has been implemented.

Furthermore, REYNOLDS' *transport theorem* has also been employed in this process.

In order to deduce the simplified equation describing the motion of the centre of the avalanching mass, we define *averaged field quantities* as follows:

$$\begin{aligned}
\overline{h} &= \frac{1}{\mathcal{A}} \iint_{\mathcal{A}} h \, da, & \frac{1}{2}\overline{\mathbf{B}}\,\overline{h} &= \frac{1}{\overline{h}\mathcal{A}} \iint_{\mathcal{A}} (\mathrm{div}\mathbf{B}) \frac{h^2}{2} \, da, \\
\overline{\mathbf{u}}_c &= \frac{1}{\overline{h}\mathcal{A}} \iint_{\mathcal{A}} h\mathbf{u} \, da, & \overline{\left(C\frac{\mathbf{u}}{|\mathbf{u}|}\right)} &= \frac{1}{\overline{h}\mathcal{A}} \iint_{\mathcal{A}} Ch\frac{\mathbf{u}}{|\mathbf{u}|} \, da, \\
\overline{A} &= \frac{1}{\overline{h}\mathcal{A}} \iint_{\mathcal{A}} Ah \, da, & \overline{\left(\frac{\mathbf{u}|\mathbf{u}|}{\Xi h}\right)} &= \frac{1}{\overline{h}\mathcal{A}} \iint_{\mathcal{A}} h\frac{\mathbf{u}|\mathbf{u}|}{\Xi h} \, da.
\end{aligned} \tag{3.65}$$

Here $\overline{h}\mathcal{A}$ is the averaged *pile volume* and $\overline{\mathbf{u}}_c = (\overline{u}_c, \overline{v}_c)$ the averaged velocity of the centre of mass. Other averaged quantities are only formal. This will become clear in the sequel. Also notice that with the definition $(3.59)_2$, $\overline{\mathbf{B}}$ is a vector with the components

$$\overline{\mathbf{B}} = \frac{2}{\overline{h}^2\mathcal{A}} \left\{ \iint_{\mathcal{A}} \frac{\partial B}{\partial x}\frac{h^2}{2} \, da, \iint_{\mathcal{A}} \frac{\partial D}{\partial y}\frac{h^2}{2} \, da \right\}^T, \tag{3.66}$$

where $\{\}^T$ denotes the transpose of the vector quantity $\{\}$. With the definitions (3.65), the *global momentum balance*, (3.64) takes the following *differential form*:

$$\frac{d\,\overline{\mathbf{u}}_c}{dt} = \overline{A}\mathbf{e} + \frac{1}{2}\overline{\mathbf{B}}\,\overline{h} - \overline{\left(C\frac{\mathbf{u}}{|\mathbf{u}|}\right)} - \overline{\left(\frac{\mathbf{u}|\mathbf{u}|}{\Xi h}\right)}. \tag{3.67}$$

This equation is *not independent of the deformation of the moving pile*, because all overbarred quantities generally depend upon the evolution of the pile. It follows that *a centre of mass model alone cannot in general adequately describe the motion of the centre of a deforming mass*. This is only so provided special conditions are satisfied. For instance, if A, B, C, D are all constant, which means that the avalanche moves down an inclined plane and δ and ϕ are constant, then $\overline{A} = \sin\zeta, \overline{\mathbf{B}} = 0$ and $\overline{C(u/|\mathbf{u}|)} = C(\overline{u}/|\overline{\mathbf{u}}|)$; however, even with Ξ = constant, the viscous sliding term cannot be expressed in terms of u_c alone. Thus, under the above-stated simplifications

$$\frac{d\,\overline{\mathbf{u}}_c}{dt} = \sin\zeta\mathbf{e} - \cos\zeta\tan\delta\frac{\overline{\mathbf{u}}_c}{|\overline{\mathbf{u}}_c|} \tag{3.68}$$

is an exact equation and independent of the deformation of the moving granular mass, but

$$\frac{d\,\overline{\mathbf{u}}_c}{dt} = \sin\zeta\mathbf{e} - \cos\zeta\tan\delta\frac{\overline{\mathbf{u}}_c}{|\overline{\mathbf{u}}_c|} - \frac{\overline{\mathbf{u}}_c|\overline{\mathbf{u}}_c|}{\overline{\Xi}\,\overline{h}} \tag{3.69}$$

is approximate and the VOELLMY drag coefficient $\overline{\Xi}$ is a new (and not consistent) parameterisation, which decouples (3.69) from the deformational motion of the pile. In general, such ad hoc assumptions, however, need be made for all terms on the right-hand side of (3.68) and (3.69). Next, assume *dynamic and geometric symmetry* of the avalanche with respect to the x-axis, i.e., in the direction of steepest descent, as shown in Fig. 3.7. Then,

$$\begin{aligned} u(x,y,t) &= u(x,-y,t), \\ v(x,y,t) &= -v(x,-y,t), \\ h(x,y,t) &= h(x,-y,t). \end{aligned} \tag{3.70}$$

This means that u and h are even functions of y, but v is odd in y. Then $(3.65)_2$ implies that v_c is identically equal to zero at all times. Similarly, the second component of the vectorial equation (3.67) is identically satisfied, if for instance,

$$\begin{aligned} C(x,y) &= C(x,-y), \\ \Xi(x,y) &= \Xi(x,-y), \\ \overline{B}_y &= 0. \end{aligned} \tag{3.71}$$

In view of (3.66), $(3.71)_3$ is satisfied only if D is symmetric, i.e.,

$$D(x,y) = D(x,-y). \tag{3.72}$$

The requirements (3.71) and (3.72) are fulfilled only if the friction angles δ, ϕ and the VOELLMY drag coefficient Ξ are *symmetrically distributed* throughout the motion.

Centre of Mass Velocity The centre of mass velocity $\overline{\mathbf{u}}_c$ of $(3.65)_2$ can be determined by integrating the equation of motion

$$\frac{d\,\overline{\mathbf{x}}_c}{dt} = \overline{\mathbf{u}}_c, \tag{3.73}$$

where $\overline{\mathbf{x}}_c = (\overline{x}_c, \overline{y}_c)$ is the position of the centre of mass given by

$$\overline{\mathbf{x}}_c = \frac{1}{\overline{h}\,\mathcal{A}} \iint_{\mathcal{A}} h\,\mathbf{x}\,da, \tag{3.74}$$

with $\mathbf{x} = (x, y)$. Due to the symmetry assumptions (3.71)–(3.72), only the downslope component of (3.73) is non-trivial, namely

$$\frac{d\,\overline{x}_c}{dt} = \overline{u}_c, \tag{3.75}$$

whilst $d\,\overline{y}_c/dt = 0$, because $\overline{v}_c \equiv 0$.

3.5.3 Equations for the Deformation and Motion of Mass

With (3.73)–(3.75) for the centre of mass motion at hand, we now proceed to the derivation of the deformation equations. To this end, we define the new independent variables

$$\xi = x - \overline{x}_c, \quad \eta = y - \overline{y}_c, \quad \tau = t. \tag{3.76}$$

From these equations, we obtain the following relationships between the differential operators of the new and old variables

$$\frac{\partial}{\partial x} = \frac{\partial}{\partial \xi}, \quad \frac{\partial}{\partial y} = \frac{\partial}{\partial \eta}, \quad \frac{\partial}{\partial t} = \frac{\partial}{\partial \tau} - \overline{u}_c \frac{\partial}{\partial \xi} - \overline{v}_c \frac{\partial}{\partial \eta}. \tag{3.77}$$

Introducing the difference velocity relative to the centre of mass velocity

$$(\tilde{u}, \tilde{v}) = \tilde{\mathbf{u}} = \mathbf{u} - \overline{\mathbf{u}}_c = (u - \overline{u}_c, v - \overline{v}_c) \tag{3.78}$$

and the transformation rules (3.76)–(3.77) into the governing equations (3.60), we may, on account of (3.67), derive the following *deformation equations*:

$$\begin{aligned}
&\frac{\partial h}{\partial \tau} + \operatorname{div}_{\xi,\eta}(h\,\tilde{\mathbf{u}}) = 0,\\
&\frac{\partial \tilde{\mathbf{u}}}{\partial \tau} + \left(\operatorname{grad}_{\xi,\eta}\tilde{\mathbf{u}}\right)\tilde{\mathbf{u}} = \left(A - \overline{A}\right)\mathbf{e} - \mathbf{B}\left(\operatorname{grad}_{\xi,\eta} h\right) - \frac{1}{2}\overline{\mathbf{B}}\,\overline{h}\\
&\quad - \left\{ C\frac{\mathbf{u}}{|\mathbf{u}|} - \overline{\left(C\frac{\mathbf{u}}{|\mathbf{u}|}\right)} \right\} - \left\{ \frac{\mathbf{u}|\mathbf{u}|}{\Xi h} + \overline{\left(\frac{\mathbf{u}|\mathbf{u}|}{\Xi h}\right)} \right\},
\end{aligned} \tag{3.79}$$

where the suffix notations ξ, η indicate differentiations with respect to these variables. The derivation of (3.79) is somewhat long but straightforward. For a motion along an inclined plane configuration with constant internal and bed friction angles, the coefficients A, B, C and D are constant, implying $A - \overline{A} = 0, \overline{\mathbf{B}} = \mathbf{0}$. Moreover, if the difference velocities $\tilde{u}, \tilde{v}$ are small in comparison to $\overline{u}_c$, then the quadratic and higher-order terms can be ignored and yield the following approximations:

$$\begin{aligned}
&C\frac{\mathbf{u}}{|\mathbf{u}|} \approxeq C\left\{ \frac{\overline{\mathbf{u}}_c}{|\overline{u}_c|} + \frac{\tilde{\mathbf{u}}}{|\overline{u}_c|} - \frac{\overline{\mathbf{u}}_c \tilde{u}}{|\overline{u}_c|^2} \right\},\\
&\overline{\left(C\frac{\mathbf{u}}{|\mathbf{u}|}\right)} \approxeq C\frac{\overline{\mathbf{u}}_c}{|\overline{u}_c|},\\
&\frac{\mathbf{u}|\mathbf{u}|}{\Xi\, h} \approxeq \frac{|u_c|\left(\overline{\mathbf{u}}_c + \tilde{\mathbf{u}} - (\tilde{u}/\overline{u}_c)\,\overline{\mathbf{u}}_c\right)}{\overline{\Xi}\,\overline{h}},\\
&\overline{\left(\frac{\mathbf{u}|\mathbf{u}|}{\Xi\, h}\right)} \approxeq \frac{|\overline{u}_c|\overline{\mathbf{u}}_c}{\overline{\Xi}\,\overline{h}}.
\end{aligned} \tag{3.80}$$

In order to avoid formation of a singularity at the margin, h is replaced by the mean depth $\overline{h}$ in $(3.80)_{3,4}$, while in compensation the VOELLMY drag coefficient Ξ has been replaced by $\overline{\Xi}$, a "suitable average" over the avalanche that has not explicitly been defined before [176].

Note On the one hand, the above relations (3.80) correspond to additional ad hoc assumptions and are needed if the separation of field equations into two sets, one describing the centre of mass motion and the other describing the deformation of the entire body is concerned. On the other hand, these expressions are also physically reasonable, because with the exception of the onset of the motion, the *dispersive velocity* is small in comparison to the *centre of mass velocity*. Furthermore, singularities at the margins of the VOELLMY resistive force are physically very unlikely and variations of the drag coefficients Ξ within the avalanche are very difficult to determine.

With the help of the expressions (3.80), (3.67), (3.75) and (3.79) reduce to the form

$$
\begin{aligned}
&\frac{d\,\overline{x}_c}{dt} = \overline{u}_c,\\
&\frac{d\,\overline{y}_c}{dt} = \overline{v}_c,\\
&\frac{d\,\overline{u}_c}{dt} = \sin\zeta - C\frac{\overline{u}_c}{\sqrt{\overline{u}_c^2+\overline{v}_c^2}} - \frac{1}{\overline{\Xi}\,\overline{h}}\sqrt{\overline{u}_c^2+\overline{v}_c^2}\;\overline{u}_c,\\
&\frac{d\,\overline{v}_c}{dt} = \quad - C\frac{\overline{v}_c}{\sqrt{\overline{u}_c^2+\overline{v}_c^2}} - \frac{1}{\overline{\Xi}\,\overline{h}}\sqrt{\overline{u}_c^2+\overline{v}_c^2}\;\overline{v}_c,\\
&\frac{\partial h}{\partial \tau} + \frac{\partial\,(h\tilde{u})}{\partial \xi} + \frac{\partial\,(h\tilde{v})}{\partial \eta} = 0,\\
&\frac{\partial \tilde{u}}{\partial \tau} + \tilde{u}\frac{\partial \tilde{u}}{\partial \xi} + \tilde{v}\frac{\partial \tilde{u}}{\partial \eta} = \quad - B\frac{\partial h}{\partial \xi} - 2\frac{|\overline{u}_c|\tilde{u}}{\overline{\Xi}\,\overline{h}},\\
&\frac{\partial \tilde{v}}{\partial \tau} + \tilde{u}\frac{\partial \tilde{v}}{\partial \xi} + \tilde{v}\frac{\partial \tilde{v}}{\partial \eta} = -C\frac{\tilde{v}}{|\overline{u}_c|} - D\frac{\partial h}{\partial \eta} - \frac{|\overline{u}_c|\tilde{v}}{\overline{\Xi}\,\overline{h}}.
\end{aligned}
\tag{3.81}
$$

The first four equations are equivalent to (3.69) and (3.73), and correspond to the classical VOELLMY model, but they are here more general than in the VOELLMY model, because they are written for the motion down a two-dimensional surface and are comprised of a motion in the downslope and cross-slope directions. On the other hand VOELLMY, SALM and others, and PERLA et al. [315, 361, 362, 365, 366, 315, 430] dealt only with a one-dimensional motion of the centre of mass. The resistive force is composed of a dry COULOMB drag and a viscous drag that are proportional to the

squared velocity. The remaining three equations of (3.81) go beyond the classical VOELLMY model as they describe the deformation of the avalanche as well. The equations are in general coupled, but in the approximation, which is based on (3.80), the equations of the motion of the centre of mass can be integrated first and those for the deformation afterwards.

Note There are several mechanisms that influence the spreading of the avalanche in motion. In the downhill direction the term $B\,(\partial h/\partial \xi)$ contributes to a dilatation as $\partial h/\partial \xi > 0\,(< 0)$ in front of (behind) the centre of gravity. On the other hand, only the velocity-dependent drag force resists dilatation. However, the sidewise spreading, which is incorporated by the term $D\,(\partial h/\partial \eta)$, is reduced by both the COULOMB-type and viscous-type friction forces. ■

In Chap. 5 we will present semi-exact similarity solutions of $(3.81)_{3-5}$ to investigate some basic physical properties of a two-dimensionally deforming avalanche.

3.6 Avalanches with Erosion and Deposition

In this section we will present an extension of the SH-theory that includes granular avalanches flowing on a moving and deforming bed in which erosion and deposition of granular material can occur. Such an extension was first developed by GRAY [124]. Physically, it is important, because a snow avalanche will often accumulate snow mass from the snow layer it overrides if its kinetic energy is sufficiently large, and it will deposit snow on the way or in the run-out zone. In an actual event these processes may well dominate its dynamics, but practically it is still unclear how they could be incorporated in a natural event.

For simplicity, we deal only with the two-dimensional plane flow of a granular mass that outlines the basic issues. To this end, we rewrite the COULOMB *dry-friction sliding law*, i.e., (3.22), as

$$F^b\,(\mathbf{x},t) = 0, \quad \mathbf{p}^b\mathbf{n}^b - \mathbf{n}^b\left(\mathbf{n}^b\cdot\mathbf{p}^b\mathbf{n}^b\right) = \left(\mathbf{u}^r/|\mathbf{u}^r|\right)\left(\mathbf{n}^b\cdot\mathbf{p}^b\mathbf{n}^b\right)\tan\delta, \quad (3.82)$$

where the factor $(\mathbf{u}^r/|\mathbf{u}^r|)$ ensures that the COULOMB *friction law* opposes the avalanche motion. The relative velocity vector $\mathbf{u}^r = \mathbf{u}^{b+} - \mathbf{u}^{b-}$ is the velocity difference between the base of the avalanche, $\mathbf{u}^{b+}$, and the basal topography, $\mathbf{u}^{b-}$. This definition differs from the original SH-equations [375] in the sense that the basal topography can have a non-vanishing velocity component parallel to the interface of the avalanche.[12] For simplicity, additional

[12] This is peculiar to the laboratory experiment considered by GRAY in which the base itself is moving [124].

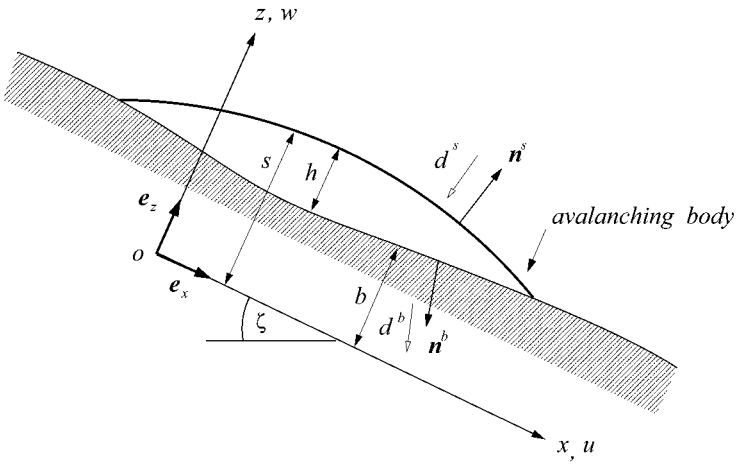

Fig. 3.11. A definition sketch of a fixed Cartesian coordinate system in which the x-axis is inclined at an angle ζ to the horizontal and points in the downslope direction. The basal topography lies at $z = b(x,t)$ and the avalanche free surface at $z = s(x,t)$. The avalanche depth is measured along the z-axis, which is parallel and in the direction of the upward pointing normal. The normal accumulation rate d^s is the equivalent volume of the granular material deposited on the avalanche free surface per unit area per unit time. Similarly, d^b is the normal deposition rate, which is equivalent to the volume of granular material deposited at the base per unit area per unit time. u and w are the velocity components along the downslope and normal directions. Also shown are the unit basal and free surface normals, $\mathbf{n}^s$ and $\mathbf{n}^b$, respectively, and $\mathbf{e}_x$ and $\mathbf{e}_z$ are the unit vectors along the coordinate axes.

effects, such as air drag, rate-dependent basal drags and momentum thrust terms due to mass interaction are neglected.

3.6.1 Coordinate System

A fixed Cartesian coordinate system oxz is defined as illustrated in Fig. 3.11, with origin o so that the x-axis lies approximately parallel to the basal interface and points in the down-hill direction with an inclination angle ζ to the horizontal. The z-axis is chosen along the upward pointing normal. The free surface is mathematically described by the equation $F^s = z - s\,(x,t)$ and the interface between moving avalanche and differently moving base is given by $F^b = b\,(x,t) - z$. Both are movable and, in general, non-material,[13] if accumulation, erosion and deposition can arise.

[13] A surface is non-material if matter can flow through it. For instance, the free surface of a snow cover is non-material *during snow fall*, because snow flakes are continuously added to it.

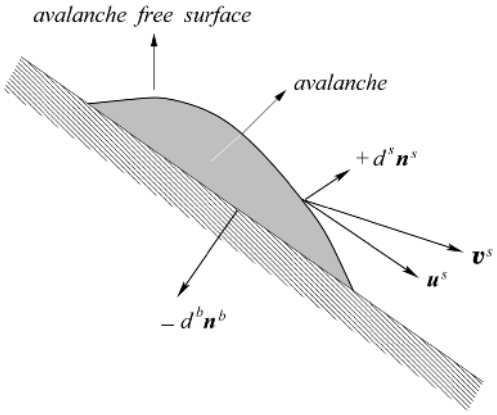

Fig. 3.12. A sketch of the avalanche and avalanche-free surface. d^s and d^b are the normal accumulation rates at the free surface and the bed, respectively. $\mathbf{n}^s$ and $\mathbf{n}^b$ are the unit normals of the free surface and the bed pointing outward from the avalanching body. $\mathbf{u}^s$ is the velocity field of the free surface without accumulation and $\mathbf{v}^s = \mathbf{u}^s + d^s\mathbf{n}^s$ is the velocity of the free surface with accumulation.

3.6.2 Accumulation and Deposition

Surface accumulation and basal deposition can occur in many industrial and geophysical situations: sediment transport in rivers, moving sand dunes in the desert, erosion of soil in debris flows, erosion of the snow cover in an avalanche and heap formation of granular materials are typical examples. The granular material that is poured onto the top of the pile provides a source of continuous surface accumulation to the avalanche and as the granular material comes to rest at the far end of the slant side it is deposited and buried into the solid body region of the granular material beneath it. This deposition mechanism can be viewed as a moving phase boundary between the solid and fluidised regions.

The free surface and basal interfaces are modified by accumulation and deposition. Let d^s be the *normal accumulation rate*, which is defined to be the equivalent volume of granular mass deposited on the *avalanche free surface* per unit area per unit time (see Fig. 3.12). Similarly, let the *normal deposition rate*, d^b, be the equivalent volume of deposited granular material at the avalanche base per unit area per unit time. Then, the velocities of the free and basal interfaces, respectively, are $\mathbf{v}^s = \mathbf{u}^s + d^s\mathbf{n}^s$ and $\mathbf{v}^b = \mathbf{u}^b - d^b\mathbf{n}^b$. It follows that the basal and surface kinematic conditions are

$$z = b(x,t), \quad \frac{\partial b}{\partial t} + u^b\frac{\partial b}{\partial x} - w^b = \Delta^b d^b, \tag{3.83}$$

$$z = s(x,t), \quad \frac{\partial s}{\partial t} + u^s\frac{\partial s}{\partial x} - w^s = \Delta^s d^s, \tag{3.84}$$

where

$$\Delta^b = \left\{1 + \varepsilon^2 \left(\partial b/\partial x\right)^2\right\}^{1/2}, \quad \Delta^s = \left\{1 + \varepsilon^2 \left(\partial s/\partial x\right)^2\right\}^{1/2} \tag{3.85}$$

are the non-dimensional normalisation factors of the basal and free surface unit normals, $\mathbf{n}^b$, $\mathbf{n}^s$, respectively, pointing outward from the avalanching material. Let us derive the second of these relations and leave the first as an exercise to the reader. To this end, we first note that $F^s \equiv z - s(x,t) = 0$ is the equation of the free surface, which as mentioned above, moves with the velocity $\mathbf{v}^s$. Then, the time derivative of $F^s = 0$ following the surface must equally vanish for all time. This argument implies

$$\frac{DF^s}{Dt} = \frac{\partial F^s}{\partial t} + \left(\operatorname{grad} F^s\right) \frac{D\mathbf{x}}{Dt}, \tag{3.86}$$

in which $D\mathbf{x}/Dt = \mathbf{v}^s$ is the velocity of the surface (and not necessarily of the particles instantaneously sitting upon it). The next step consists in writing $\mathbf{v}^s = \mathbf{v}^s - \mathbf{u}^s + \mathbf{u}^s$, so that the kinematic equation becomes

$$\frac{\partial F^s}{\partial t} + \left(\operatorname{grad} F^s\right) \cdot \mathbf{u}^s = \left(\mathbf{u}^s - \mathbf{v}^s\right) \cdot \frac{\operatorname{grad} F^s}{|\operatorname{grad} F^s|} |\operatorname{grad} F^s|. \tag{3.87}$$

Recognising that $\operatorname{grad} F^s$ is a vector perpendicular to the free surface, $F^s = 0$, we may write

$$\frac{\operatorname{grad} F^s}{|\operatorname{grad} F^s|} = \mathbf{n}^s$$

and thus obtain

$$\frac{\partial F^s}{\partial t} + \left(\operatorname{grad} F^s\right) \cdot \mathbf{u}^s = |\operatorname{grad} F^s| \underbrace{\left(\mathbf{u}^s - \mathbf{v}^s\right) \cdot \mathbf{n}^s}_{-d^s}. \tag{3.88}$$

There remains the interpretation of the term $-d^s$. It is the flow per unit surface area per unit time perpendicular to the surface into the direction of the exterior unit vector $\mathbf{n}^s$. Thus, d^s physically represents the accumulation rate of volume per unit surface area. Straightforward computation with $F^s(x,z,t) = z - s(x,t)$ now shows that (3.88) agrees with (3.84). Note that the factors ε^2 in (3.85) appear from the non-dimensionalisation process.

In the above, as a first approximation, the effects of accumulation and deposition are taken into account only for the kinematic boundary conditions, and it is assumed that they have no effect on the dynamical boundary conditions at the free and basal surfaces of the avalanche. In general, more complex boundary conditions apply, which also account for the corresponding alterations in

the dynamic jump conditions.[14] What is meant here are the convective contributions to the surface jump conditions when such surfaces are non-material. Since in this book we have not derived such jump conditions, this is difficult to explain here, see [182]. It is, however, clear that, if mass is added at the top, this mass must also be accelerated to reach the motion of the particles at the top. This no longer makes the traction vanish at the surface.

3.6.3 The Model Equations

To derive the governing equations we start with the continuity equation, $\mathrm{div}\mathbf{v} = 0$, and integrate it in z from $z = b$ to $z = s$

$$0 = \int_b^s \left(\frac{\partial u}{\partial x} + \frac{\partial w}{\partial z}\right) dz = \frac{\partial}{\partial x}\int_b^s u dz - \left[u^s \frac{\partial s}{\partial x} - w^s\right] + \left[u^b \frac{\partial b}{\partial x} - w^b\right],$$

in which LEIBNIZ' rule has been used in interchanging the integration and x-differentiation. The terms in brackets can be replaced by (3.83) and (3.84), i.e.,

$$\left[u^s \frac{\partial s}{\partial x} - w^s\right] = -\frac{\partial s}{\partial t} + \Delta^s d^s, \quad \left[u^b \frac{\partial b}{\partial x} - w^b\right] = -\frac{\partial b}{\partial t} + \Delta^b d^b.$$

With these replacements and the definition of $h\overline{u} = \int_b^s u dz$, $h = s - b$, the conservation equation of mass is obtained in the form

$$\frac{\partial h}{\partial t} + \frac{\partial}{\partial x}(h\overline{u}) = \Delta^s d^s - \Delta^b d^b. \tag{3.89}$$

An analogous procedure is also applied for the balance of momentum. Here, one starts with the x-momentum equation in dimensionless form,

$$\frac{\partial u}{\partial t} + \frac{\partial}{\partial x}\left(u^2\right) + \frac{\partial}{\partial z}(uw) = -\varepsilon\frac{\partial}{\partial x}(p_{xx}) - \mu\frac{\partial}{\partial z}(p_{xz}) + \sin\zeta \tag{3.90}$$

and again performs an integration in z from $z = b$ to $z = s$. In this process, integrations and differentiations are interchanged and LEIBNIZ' rule is observed. This yields

$$\underbrace{\frac{\partial}{\partial t}\int_b^s u dz}_{h\overline{u}} + \underbrace{\frac{\partial}{\partial x}\int_b^s u^2 dz}_{h\overline{u^2}} - u^s \underbrace{\left[\frac{\partial s}{\partial t} + u^s\frac{\partial s}{\partial x} - w^s\right]}_{\Delta^s d^s} + u^b \underbrace{\left[\frac{\partial b}{\partial t} + u^b\frac{\partial b}{\partial x} - w^b\right]}_{\Delta^b d^b}$$
$$= (\sin\zeta)\, h - \frac{\partial}{\partial x}\underbrace{\int_b^s \varepsilon p_{xx} dz}_{\varepsilon\overline{p_{xx}}h} - \underbrace{\left[\mu p_{xz}^s - \varepsilon p_{xx}^s\frac{\partial s}{\partial x}\right]}_{0} + \left[\mu p_{xz}^b - \varepsilon p_{xx}^b\frac{\partial b}{\partial x}\right],$$

[14] Here we mean that the free and basal surfaces are now no longer material surfaces; therefore, $[\![\mathbf{pn}]\!]$ is no longer continuous but given by the jump in normal mass flux $\rho[\![\mathbf{v}]\!]$. This latter term can often be ignored, but must then be justified.

in which the terms identified by parentheses either define the overbarred quantities or are given by (3.83), (3.84) and the shear traction condition at the free surface. If it is also observed that $p^b_{xz} = -\Delta(u_r/|u_r|)p^b_{xx}$ and that $p^b_{xx} = \mathbf{n}^b \cdot \mathbf{p}^b \mathbf{n}^b$, the above equation reduces to

$$\begin{aligned}&\frac{\partial}{\partial t}\left(h\overline{u}\right) + \frac{\partial}{\partial x}\left(h\overline{u^2}\right) - \left(u^s \Delta^s d^s - u^b \Delta^b d^b\right)\\ &= h\sin\zeta - \left(\Delta^b \left(u^r/|u^r|\right)\tan\delta + \varepsilon\frac{\partial b}{\partial x}\right)\left(\mathbf{n}^b \cdot \mathbf{p}^b \mathbf{n}^b\right) - \varepsilon\frac{\partial}{\partial x}\left(h\overline{p_{xx}}\right). \quad (3.91)\end{aligned}$$

The final form of the (approximate) x-momentum equation is obtained if we set

$$\overline{u^2} = \overline{u}^2, \quad \varepsilon\overline{p_{xx}}h = \beta_x\frac{h^2}{2}, \quad \Delta^s = \Delta^b \approx 1, \quad p^b_{xx} = h\cos\zeta.$$

Equations (3.89) and (3.91) then take the forms

$$\frac{\partial h}{\partial t} + \frac{\partial}{\partial x}\left(hu\right) = d^s - d^b, \quad (3.92)$$

$$\frac{\partial}{\partial t}\left(hu\right) + \frac{\partial}{\partial x}\left(hu^2\right) + \frac{\partial}{\partial x}\left(\beta_x h^2/2\right) = hs_x + u\left(d^s - d^b\right), \quad (3.93)$$

where $\beta_x = \varepsilon\cos\zeta K_x$, and for simplicity, the averaging bar is now dropped on the downslope velocity component. Notice that $u^s = \overline{u} + O\left(\varepsilon^{1+\gamma}\right)$ and $u^b = \overline{u} + O\left(\varepsilon^{1+\gamma}\right)$ are also employed in (3.93). The net driving acceleration s_x is given by

$$s_x = \sin\zeta - \left(u^r/|u^r|\right)\cos\zeta\tan\delta - \varepsilon\cos\zeta\frac{\partial b}{\partial x}. \quad (3.94)$$

Given a slope inclination angle ζ, basal friction angle δ, internal friction angle ϕ, the basal topography b, the surface accumulation rate d^s and the basal deposition or erosion rate d^b, (3.92) and (3.93) form a closed system for spatio-temporal evolution of the avalanche depth h and the depth-averaged streamwise downslope velocity u. In a typical flow avalanche of snow and in debris flow avalanches the surface accumulation rate usually vanishes, $d^s = 0$, whilst the deposition or erosion rate, d^b, must functionally be described. It is the determination of this functional relation that we regard as the *grand unsolved problem* of avalanche dynamics.

Note The MOHR–COULOMB yield criterion may not always be an appropriate assumption for a rapidly flowing granular material. Moreover, it is a rather strong condition when the material is *far beyond the point of yield* [124]. The inviscid fluid model proposed by EGLIT [87] with an isotropic pressure distribution

$$p_{xx} = p_{zz}, \quad (3.95)$$

may also be considered as an alternative method of closure. In this case, $K_x = 1$ and there is no jump in the longitudinal stress component, because $p_{xx} = K_x p_{zz} + O\left(\varepsilon^{1+\gamma}\right)$ and p_{zz} is a smooth quantity. For diverging and extending flow it may be difficult to differentiate between these two closure models, as $K_{x_{\mathrm{act/pas}}}$ is close to unity for typical values of the internal and basal friction angles ϕ and δ, respectively, see Chap. 4. However, as $\partial u/\partial x$ passes through the zero value, in other words, when flow changes its state from extending to contractive (mainly) in the run-out zone, or around an obstacle, the inviscid fluid model is not appropriate [123, 445]. This same proviso also applies to the theory of GRAY et al. [126].[15]

3.7 Granular Flows in Rotating Drums

Partly filled rotating drums are often used in industry to transport and mix granular matter. In these applications the cylinders are very long. Here we are concerned with a small gap between two co-rotating circular plates. In such situations, the motion is characterised by a (large) solid-like region of slowly rotating mass about the horizontal axis of rotation, on top of which there is a very thin rapidly moving fluid-like avalanche of grains close to the free surface. On the other hand, rotating drum experiments, in which a cylinder that is partially filled with a granular material is rotated, are an ideal laboratory set-up to observe the disparate features that a granular moving system can have; and – under certain restrictions – it is ideal to experimentally test whether the extended SH-equations withstand experimental proof. It is quite clear that the dynamics of granular materials in partly filled rotating *long* cylinders is more complicated, but for extremely *short* cylinders, forming only a small gap between two disks the motion is plane. This is the restriction we shall look at here. The experiments described below were conducted by GRAY [124] who clearly elucidated the suitability of the avalanche theory.

3.7.1 Solid-Like and Fluid-Like Regions

One of the biggest problems with granular materials is that they undergo strong phase transitions between solid, liquid and gaseous states. Solving particular problems, therefore, often involves not only determining the flow in each of the three regions, but also the evolution of an unknown interface between two different states. However, the phase transitions are much more complicated and are still poorly understood.

[15] It is interesting to observe that the paper [126] shows the motion of the avalanche only in the rapid flow region and not close to the deposit. The inadequacy of the model would have become visible there.

Here we consider only the steady flow in a partially filled slowly rotating drum in order to investigate the *coupling* between a *solid rotating region* and a *fluid-like avalanche* close to the free surface. In the theoretical treatment the fluid-like avalanche and the solid-like rotating region are *treated as separate bodies* with a *non-material singular surface* between them, at which the field variables are discontinuous. This is a mathematical idealisation, and in practice there is a thin layer between the two regions, where there are large gradients of the density and velocity. GRAY [124], however, has proven it to be a very good approximation for at least a *differently coloured monodispersed granular mixture*. It is very important to point out the fact that the dominant physical processes are the mass transfer between the solid region and the avalanche above it and the dynamics of the avalanche itself.

3.7.2 Coordinate System

In the following, we will make use of the avalanche model developed in Sect. 3.6 for the avalanche motion inside a rotating drum. It is therefore convenient to use two different Cartesian coordinate systems OXZ and oxz to reflect different geometries in the solid body and avalanching region (see Fig. 3.13). The avalanche coordinate system is already defined in Fig. 3.11 and the angle of inclination ζ may now be chosen so that the downslope x-axis lies approximately parallel to the free surface of the avalanche (this consideration is also applicable to the basal surface). As defined in the same figure, the z-axis is normal to it and points upward. The solid body coordinate system OXZ is similarly defined so that its axes are parallel to those in oxz, but the origin O is shifted so that it lies on the axis of revolution. The two coordinate systems are thus related by

$$Z = l + z, \quad X = x, \tag{3.96}$$

where the constant l defines the *fill level* of the drum [124], as illustrated in Fig. 3.13. It follows from (3.96) that the free surface height $S = S(X,t)$ and non-material singular surface height $B = B(X,t)$ in the solid body coordinate system OXZ are related to their avalanching counterparts, $s = s(x,t)$ and $b = b(x,t)$ in the oxz system by

$$S = l + s, \quad B = l + b. \tag{3.97}$$

If the rotating drum is taken to have a radius L, the typical length scales in the solid region will be of order L, in both X and Z directions. Due to $(3.96)_2$, the avalanche is also of a length of the order L in the x-direction. Nevertheless, it is shallow, its thickness is only of the order H such that $\varepsilon = H/L \ll 1$.

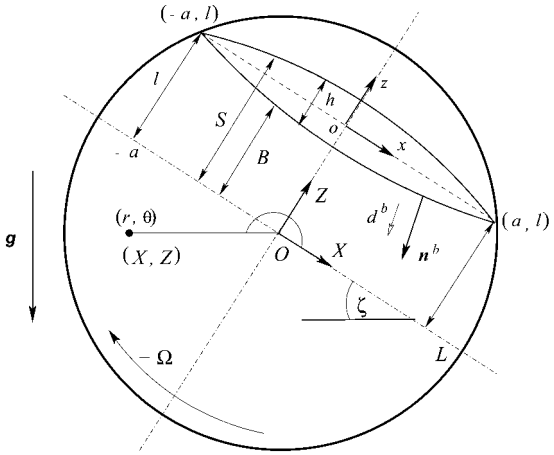

Fig. 3.13. Definition sketch of the coordinate systems in a slowly rotating drum of radius L, partly filled with granular material. oxz and OXZ, respectively, represent the avalanching and solid body coordinate systems. This configuration is for clockwise rotation and the angular velocity of the drum is denoted by $-\Omega$ because Ω is the angular velocity for positive rotation in the counterclockwise direction. Both coordinate systems are parallel to each other with a shift of origin. The downhill coordinates of both systems are inclined at an angle ζ with the horizontal. Also shown in the picture is the vector $\mathbf{g}$ of the gravitational acceleration, the fill level l, the polar coordinate (r, θ), the downhill (uphill) coordinate a $(-a)$ of the intersection of the avalanche with the drum wall. (Redrawn from [124] with changes).

Therefore, the *shallowness assumption* holds also for flow of granular materials in the rotating drum and thus the avalanche equations can be directly used for the fluidised regions of the whole system of mass in the drum. The motion of the avalanche can, therefore, be computed by solving the system of (3.92) and (3.93), together with the corresponding earth pressure coefficient (3.39).

3.7.3 Governing Equations in a Solid Rotating Body

Governing equations in a solid rotating body may be determined once the angular velocity and the position of particles (in the granular bulk material) from the centre of revolution of the drum are known. Since there is a coupling of the solid body rotation and the avalanching motion on top of it, a new kinematic boundary condition must be introduced at the non-material singular surface.

In what follows, the field quantities, i.e., velocity and density, "within the solid granular material" will be denoted with the superscript "$^-$". It is, therefore, assumed that the solid granular material is a rigid body with constant uniform

density ρ^- and rotates with angular velocity $\Omega(t)$ about the horizontal axis of revolution O of the drum. Let r be the distance from the axis of revolution O and $\hat{\theta}$ the unit vector in the azimuthal direction; then the linear velocity field is simply defined by

$$\mathbf{u}^- = \Omega r\hat{\theta}, \tag{3.98}$$

provided that the slip at the boundary between the granular material and the drum is ignored (this will be considered later). It follows that the downslope and normal velocity components in the solid region are given by

$$u^- = -\Omega Z, \quad w^- = \Omega X. \tag{3.99}$$

At the non-material singular interface, F^b, with the avalanching granular material the solid body is subject to a kinematic boundary condition

$$F^b(\mathbf{x}, t) = 0 : \quad \frac{\partial F^b}{\partial t} + v_n^{b-}\mathbf{n}^b \cdot \nabla F^b = 0, \tag{3.100}$$

where v_n^{b-} is the normal speed of the interface in the direction of the normal $\mathbf{n}^b$, which points outwards from the avalanche.

3.7.4 Interfacial Conditions and Scalings

For notational brevity, in the following, the superscript notations "$b-$" and "$b+$" is introduced to differentiate between variables evaluated on the solid body (lower) side and avalanching (upper) side of the singular interface, F^b, respectively.

These are discontinuities in the density and velocity at the interface between the rotating material and the avalanche. At such a surface, the mass jump condition is

$$[\![\rho\left(\mathbf{u}\cdot\mathbf{n}^b - v_n^b\right)]\!] = 0, \tag{3.101}$$

where the jump bracket $[\![(\cdot)]\!] = (\cdot)^{b+} - (\cdot)^{b-}$ is the difference between the values of the corresponding expressions on the upper and lower sides of the singular interfacial surface. Equation (3.101) simply implies that the *mass jump* through the interface is zero, *but this provides a means of coupling between the velocities, as well as densities in the avalanche and solid.*

We need to use new scalings for all quantities arising from the introduction of the coupling of the solid body with the avalanche. For this region, let Ω^* be the typical angular velocity magnitude of the rotating granular bulk material. Then the linear velocities in the solid body are of the order of magnitude $\Omega^* L$. Since density changes are relatively small, a balance between the normal velocity components (3.101) implies that

$$v_n^b = \mathbf{n}^b \cdot \mathbf{u}, \quad \text{i.e.} \quad \Omega^* L = \varepsilon\sqrt{gL}, \tag{3.102}$$

because, $\mathbf{n}^b \cdot \mathbf{u}$ is associated with w and w is multiplied by ε in the scalings, see Chap. 4, which also holds for the avalanche in the rotating drum. However, new scalings must be introduced for the fill height, the free surface and singular surface variables and other variables in the solid rotating body. These are as follows:

$$\begin{aligned}
&(X, Z, B, S, l) = L\left(\hat{X}, \hat{Z}, \hat{B}, \hat{S}, \hat{l}\right), \\
&\left(u^-, w^-, v_n^{b-}\right) = \varepsilon\sqrt{gL}\left(\hat{u}^-, \hat{w}^-, \hat{v}_n^{b-}\right), \\
&\Omega = \varepsilon\sqrt{g/L}\hat{\Omega},
\end{aligned} \tag{3.103}$$

where the hats, as before, represent the non-dimensional variables.[16] The variables are differently scaled in the avalanching and the solid body motion, see Chap. 4. In the avalanche, the downslope and normal characteristic lengths are scaled differently to reflect the thinness of the geometry, whilst in the solid body the coordinates are scaled using the same lengths. Equations (3.96) and (3.103) imply that the non-dimensional coordinates are related by

$$Z = l + \varepsilon z, \quad X = x, \tag{3.104}$$

where for simplicity the hats are dropped. Henceforth, hats are dropped and all variables are non-dimensional unless stated otherwise. Then, it follows that the free surface-heights and interface-heights are

$$S = l + \varepsilon s, \quad B = l + \varepsilon b. \tag{3.105}$$

The solid body velocity components are

$$u^- = -\Omega Z, \quad w^- = \Omega X. \tag{3.106}$$

From (3.104), $(3.105)_2$ and (3.106), in particular, the velocity components at the lower side of the singular surface are

$$u^{b-} = -\Omega\left(l + \varepsilon b\right), \quad w^{b-} = \Omega x \tag{3.107}$$

in the avalanche coordinate system.

Let d^{b+} and d^{b-} be the equivalent volumes of the avalanching and solid granular material deposited from the avalanche to the solid per unit area per unit time, respectively. It follows that the normal speed v_n^b in the direction of the basal normal $\mathbf{n}^b$ is equal to

$$v_n^{b+} = \mathbf{u}^{b+} \cdot \mathbf{n}^b - d^{b+}, \quad v_n^{b-} = \mathbf{u}^{b-} \cdot \mathbf{n}^b - d^{b-}, \tag{3.108}$$

where $\mathbf{n}^b = \mathbf{n}^{b+} = \mathbf{n}^{b-}$ is required to conserve mass and prevent void space opening up between the solid and avalanching layers. Assuming that the

[16] Here ε enters all velocities because the rigid body motion is slow everywhere.

avalanching density on the upper side of the singular surface is ρ^+, the mass jump condition (3.101), together with (3.108), implies that

$$d^{b+} = \left(\rho^-/\rho^+\right) d^{b-}. \tag{3.109}$$

Moreover, in realistic situations, the ratio of densities from the lower and upper sides of the singular surface is close to unity [124]. The velocities on the solid body (lower side) of the singular surface are prescribed by the nature of the rigid rotation (3.107). Since $\mathbf{u}^{b-} = (-\Omega(l+\varepsilon b), \Omega x)$ (from (3.107)) and $\mathbf{n}^b = (\varepsilon \partial b/\partial x, -1)/\Delta^b$, it follows from (3.108) that the deposition rate on the lower side of the singular surface is

$$\begin{aligned} d^{b-} &= \mathbf{u}^{b-} \cdot \mathbf{n}^b - v_n^{b-} \\ &= (-\Omega(l+\varepsilon b), \Omega x) \cdot (\varepsilon \partial b/\partial x, -1)/\Delta^b - v_n^b \\ &= -\varepsilon \left(\Omega/\Delta^b\right)(l+\varepsilon b)\frac{\partial b}{\partial x} - \left(\Omega/\Delta^b\right) x - v_n^b. \end{aligned} \tag{3.110}$$

From (3.100) the normal speed is equal to $v_n^b = -(\partial b/\partial t)/\Delta^b$. Since $\Delta^b = 1 + O\left(\varepsilon^{1+\gamma}\right)$, (3.110) implies

$$d^{b-} = -\varepsilon \Omega l \frac{\partial b}{\partial x} - \Omega x + \frac{\partial b}{\partial t} + O\left(\varepsilon^{1+\gamma}\right). \tag{3.111}$$

An approximate deposition rate d^{b+} on the upper side of the singular interfacial surface can now be obtained from (3.109) and (3.111) to order $O\left(\varepsilon^{1+\gamma}\right)$.

3.7.5 Governing Equations in the Avalanche Region

Intermittent Flows At slow rotation rates there are essentially two flow regimes: *intermittent flow* and *continuous flow*. Intermittent flow occurs typically at rotation periods above 100 seconds per revolution [124]. In intermittent flow, the rotation of the drum increases the inclination of the free surface until the whole or part of it reaches the maximum angle of repose of the granular material [161, 162]. Failure then occurs along an internal slip surface and an avalanche is created, which flows rapidly downslope. When the avalanche head reaches the front wall of the drum, a shock wave is generated that propagates upslope bringing the avalanche to rest [120], see also Chap. 2, Sect. 2.4. The free surface inclination angle now lies below the critical angle of repose of the material and must wait until the rotation of the drum brings it up to the maximum angle of repose, which is the necessary criterion for the re-occurrence of the failure. The intermittent flow regime is therefore characterised by discrete avalanche events and upstream shock wave propagation.

Continuous Flows Continuous flow typically occurs in the range between 10–100 seconds per evolution of the drum [124]. In this situation, the avalanche flows continuously downslope and both the basal interface and the free surface are spatially fixed. This implies that there is a continuous steady erosion and deposition across the avalanche and the solid body interface. It follows that material is fed to the top half ($x < 0$) of the avalanche by the relatively fast rotation of the solid body region. The avalanche then transports this material rapidly downslope, where it is re-absorbed into the solid body region ($x > 0$) and transported to the top again by the solid body rotation. All processes take place smoothly with a stable configuration in a wide range of rotation rates.

Figure 2.10 of Chap. 2 shows the pattern formed in a thin circular drum filled with a binary mixture of sugar crystal and spherical iron powder and rotated. The intermittent flow regime is clearly visible in Fig. 2.10b. Within the avalanche the particles are segregated by their size, so that the larger ones (white) lie on top of the smaller ones (dark). However, the dynamics of the bulk motion is essentially the same as when a single grain size is present. On the other hand, Fig. 2.10d shows the steady flow regime generated by a continuous erosion and deposition of the basal interface.

Model Equations The fluid-like region in the rotating drum can be modelled as a granular avalanche with erosion and deposition at its basal interface. The theory presented in Sect. 3.6 is, therefore, appropriate and the coordinate system oxz and all the variables, scalings and results are adopted here. In addition, the avalanche is assumed to have constant density $\rho^+ = \rho_0$, and since there is no surface accumulation in a (slowly) rotating drum, the surface accumulation, d^s, defined in Sect. 3.6.2 is taken equal to zero. The conservation laws (3.92)–(3.93), therefore, reduce to

$$\frac{\partial h}{\partial t} + \frac{\partial}{\partial x}(hu) = -d^{b+}, \tag{3.112}$$

$$\frac{\partial}{\partial t}(hu) + \frac{\partial}{\partial x}(hu^2) + \frac{\partial}{\partial x}\left(\beta_x h^2/2\right) = hs_x - ud^{b+}, \tag{3.113}$$

to order $O\left(\varepsilon^{1+\gamma}\right)$, where $\beta_x = \varepsilon K_x \cos\zeta$, the deposition rate d^{b+} is given by (3.109) and (3.111), and the earth pressure coefficient K_x is defined by (3.39). Note that, for an inviscid fluid, the value of K_x may simply be taken to be unity. However, great care should also be given to the geometric and curvature effects of the basal topography. In the rotating drum experiments there is a downslope (slip) velocity in the solid region. The scalings (3.41) and (3.103) imply that the relative slip velocity $u^r = u - \varepsilon\Omega l + O\left(\varepsilon^{1+\gamma}\right)$. This is incorporated into the source term (3.94) to give the resultant driving acceleration

$$s_x = \sin\zeta - \operatorname{sgn}(u - \varepsilon\Omega l)\cos\zeta\tan\delta - \varepsilon\cos\zeta\frac{\partial b}{\partial x}. \tag{3.114}$$

Steady-state solutions of the model equations (3.112)–(3.113) are presented in Chap. 6 in detail in order to investigate mixing of a granular material in a slowly rotating horizontal cylindrical drum that is partially filled.

3.8 Summary

The main purpose of this chapter was to provide an introduction to the equations that govern the motion of cohesionless granular avalanches. In so doing, the intention was to give a fundamental physical understanding of the methods how these dynamical equations are derived. Section 3.2 offered a simple introduction to the derivation of the dynamical equations as they hold for plane two-dimensional flows of a finite mass of granular material down an inclined plane. The goal was to isolate the physical foundation and to keep the mathematics as simple as possible to generate equations for this reduced case that disclose already essential ingredients typical for all avalanche formulations later in this book. Conservative and non-conservative systems of equations were deduced, COULOMB-type friction for the plastic yield behaviour of the material and a similar sliding law were introduced, as were the active and passive stress states under dilatational and compacting flow states.

Section 3.3 gave a descriptive summary of several configurations for which the avalanche equations, commonly called the SH-type equations, were derived. These comprise channel flows in chutes that allow the interpretation of the flow as two-dimensional, so that considerations can be restricted to processes arising in vertical planes bounded by topographic lines. Furthermore, sidewise spreading was then looked at, for unconfined and confined flows along topographies where the talweg was curved but not twisted and thus lying in a vertical plane.

Section 3.4 then outlined the set of avalanche model equations, formulated with respect to an orthogonal curvilinear coordinate system, of which the major coordinate axis, following the talweg of a channelised topography, lies in a vertical plane. These equations, while being more complex in their appearance than the previous ones, exhibit the same physical properties as those of the simple example in Sect. 3.2. This section also contains an explanation as to in what respect the extended avalanche-equations differ from the shallow water equations and lists the advantages and limitations that they may exhibit.

Having presented these model equations for relatively complex geometries, it is interesting to see how the most popular mass point model fits into this context. Thus, Sect. 3.5 extends the basal drag to include both COULOMB and velocity-dependent, viscous-type basal friction and then transforms the governing equations to a composition of a set of equations governing the

motion of the centre of mass and a second set for the deformation of the moving granular pile. It is shown that for a deforming mass there is, in general, no centre-of-mass model that can be integrated without also simultaneously solving the equations describing the deformation of the pile. A decoupling is only possible for the motion of an avalanche down an inclined bed with constant bed, δ, and internal, ϕ, angles of friction, and when the velocity-dependent drag is ignored. Because the latter is an essential ingredient of the VOELLMY model, one is compelled to conclude that *the* VOELLMY *model can never be an exact reduction to a mass point model of a deforming granular mass.*

Section 3.6 presented an introduction to the phenomena of erosion and deposition. For simple two-dimensional flow accumulation of mass from above and entrainment to and deposition of mass from the avalanche are introduced into the governing equations.

These additional concepts introduced into the description of granular flows in rotating drums were given in Sect. 3.7. For these flows, the governing equations of steady avalanche motion were described, but solutions were deferred to later Chap. 6.

4 Rapid Flows of Dry Granular Masses in Arbitrarily Curved and Twisted Channels

4.1 Motivation

In Chap. 3 a set of dynamic equations for the motion of a finite mass of granular material down a certain guiding topography was presented. The equations were motivated by deriving their reduced form for the conceivably most simple version of plane flow down an inclined plane. The intention was to give the reader the underlying ideas of the physics in constructing the various models. The derivation of the equations for the more complex basal geometries outlined in Chap. 3 was discussed and equations were only presented but not derived. Since in this chapter the flow along a general channelised topography will be considered, depth integrated equations that are a fairly general version of the SH-type equations will be described. Moreover, since all previous versions are deducible as special cases from this case, it was decided to present the explicit analysis only once. The reader interested in the derivations of the simplified versions may consult the pertinent literature. Readers wishing to focus first on the implications may directly pass to Sect. 4.9.

The model equations presented, e.g., in [123, 375, 376] were derived with the intention of describing the motion of a finite mass of granular material down a mountain side into a deposition area. The underlined curvilinear coordinate system was based on a so-called *ruled surface*[1] of which the generating base curve was in a vertical plane, and the ruled straight lines were kept parallel to one another, whilst the third coordinate were perpendicular to these (see Fig. 4.1). The topographies permissible for this special coordinate system were small deviations from the reference surface $z = 0$. Whereas this

[1] A ruled surface is one that can be swept out by a moving straight line in space and therefore has a parameterisation (with parameters u and v) of the form

$$\mathbf{R}(u, v) = \mathbf{b}(u) + v\mathbf{d}(u),$$

where $\mathbf{b}$ is called the *base curve* (also called the *directrix*) and $\mathbf{d}$ is the *director curve*. The straight lines themselves are called *rulings*. The rulings of a ruled surface are *asymptotic curves*.

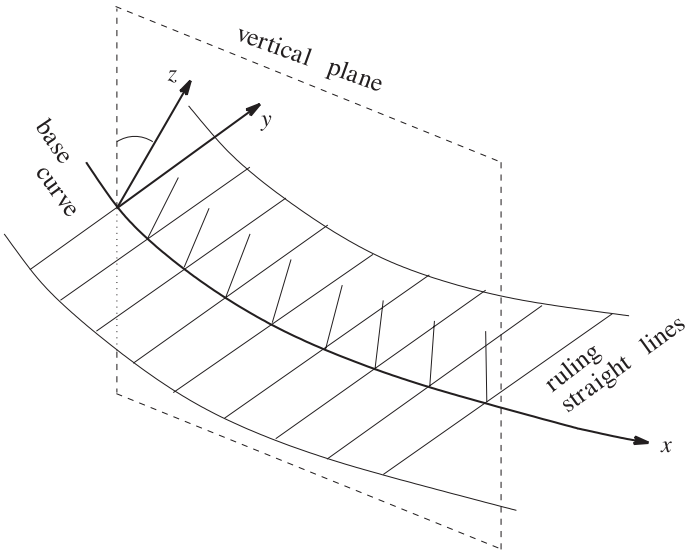

Fig. 4.1. Ruled surface, constructed from a generating base curve in a vertical plane and parallel ruling straight lines. The three families of curves define the curvilinear coordinate system x, y, z.

allows a large variety of topographies to be studied, see Chap. 3, *the geometries are* nevertheless *restricted*. For instance, the motion in a rather strongly curved channel having both curvature and torsion cannot be analysed with mentioned curvilinear coordinate system. Such cases do, however, realistically occur. In the transportation of solid materials, a finite mass of a dry granular material may have to be transported through a curved and twisted channel (e.g., with a helicoidal surface). Similarly, the flow of snow or debris avalanches down a mountain corrie may be treated as a flow through a channel, of which the talweg is any prescribed three-dimensional curve with curvature and torsion in the physical space (see Figs. 4.2 and 4.3). Both situations give rise to alternative formulations in settings with their own coordinate systems.

In this chapter, we present a review of the recent two-dimensional depth-integrated theory developed by Pudasaini and Hutter [335] for the gravity-driven free surface flow of a granular avalanche over an arbitrarily curved and twisted topography, which is a very important extension of the class of SH-equations. In contrast to other previous extensions, this local coordinate system is *based on a generating line with the curvature and torsion*. The theory is based on an orthogonal metric, associated with the curvature and torsion of a basal topography that is generated by an arbitrary three-dimensional curve in physical space. It allows relatively easy access to comparison with laboratory experiments as well as field events. The aim of the theory is to

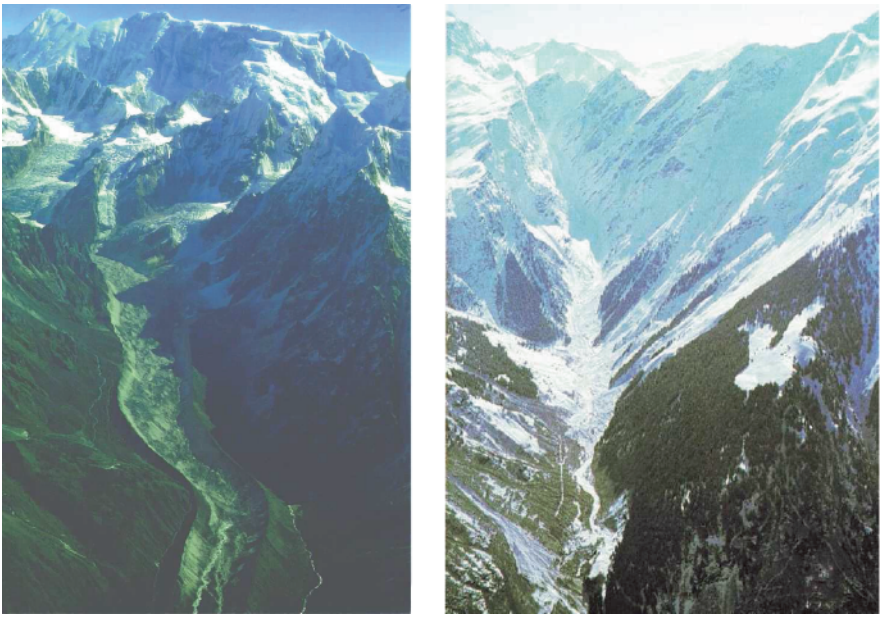

Fig. 4.2. Examples of curved and twisted natural corries in geophysical scenarios. In both pictures, the talweg of the valley can easily be identified as a smooth three-dimensional space curve. (Right picture from [4], courtesy of Birkhäuser Verlag, and the Swiss Federal Institute of Snow and Avalanche Research, SLF, Davos).

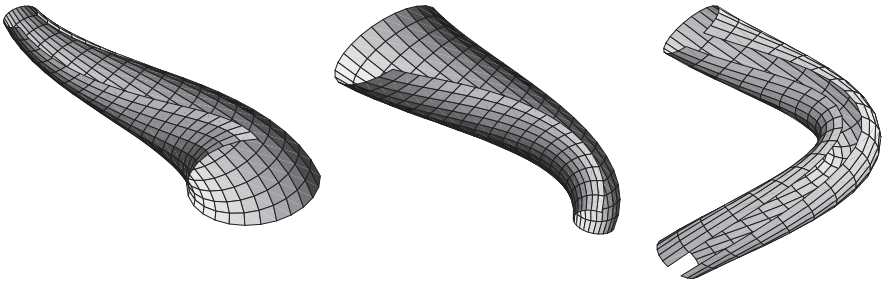

Fig. 4.3. Diverging, converging and uniform curved and twisted channels that can be used in the transportation of the granular materials. (From [342].)

gain fundamental insight into the *effects of non-uniform curvature and torsion*, using an orthogonal coordinate system that rotates with the curvature and torsion, and to find an analytic description of flow avalanches. As before [335], we assume a shallow avalanche of a dry cohesionless granular material, which is incompressible, i.e., with constant density ρ throughout the motion from initiation to the run-out zone. The motion (approximately) follows the talweg of a curved and twisted channel. Balance laws of mass and

momentum, kinematic boundary conditions on the basal and free surface, the COULOMB-dry friction law at the base and the tractionless free surface condition constitute the underlying *moving boundary value problem*. Depth averaging the field equations leads to a set of non-linear partial differential equations for the space and time evolution of the granular pile height and the depth-averaged streamwise velocity distribution of a finite mass of granules. COULOMB-like constitutive behaviour both for the bed and interior of the granular body is employed. An enormous and significant simplification is achieved by the depth averaging process.

The emerging equations constitute a generalised avalanche theory and are capable of predicting the flow of dense granular materials over curved and twisted channels of general type. The derivation of this new theory starts from quite a different geometrical and analytical setting, but, surprisingly enough, the present model can exactly reproduce all previous model equations of the class of SH-theory. The equations are tested and validated by numerical simulations, as well as controlled laboratory avalanches of dry and cohesionless finite mass of different granules that have similar properties to those of natural avalanches and debris. This will be dealt with in detail in Chaps. 7–12.

4.2 The Essence of the New Theory

As has been mentioned, PUDASAINI and HUTTER [335] presented a theory for rapid flows of dry granular masses in a *non-uniformly curved and twisted channel* having both *curvature and torsion*. In the study of the flow of an avalanche in a channel of which the *axial line*, henceforth called the "master curve" or the "reference curve", is a *generic spatial line*, it is important to choose an appropriate system of coordinates. In this theory, one may assume that the curvature κ and torsion τ of the master curve are known as functions of the arc length s, $\kappa = \kappa(s), \tau = \tau(s)$. Alternatively, they can be determined, e.g., from the digital elevation model (DEM). Then, an orthogonal coordinate system along the generic master curve can be introduced and the equations for a non-steady, incompressible, dry and cohessionless granular avalanche explicitly derived in this frame of reference. Thus in [335] we studied the simultaneous effects of curvature and torsion on the flow of avalanches in channels, something that could not be investigated before.

This theory aims at providing evidence that the model equations work well also for topographies having curvature and torsion. This makes the present model *amenable to realistic avalanche motions down arbitrarily guided topographies*, such as valleys and channelised corries. In fact, *geographic information systems* (GIS) applied to mountainous avalanche prone regions can, in principle, be applied to this model. GIS provides the analytical and ge-

ometrical basis for an application close to realistic situations and tuned to practical use. This chapter lays the theoretical foundation towards this end. Different from in the original theory [375, 376], we choose an arbitrary space curve and use it to define an orthogonal-curvilinear coordinate system. As in the SH-model, we formulate the balance laws of mass and momentum, as well as the boundary conditions in terms of these coordinates, non-dimensionalise the equations and average them over the depth of the avalanche. There is, however, a subtle difference in non-dimensionalising the equations and in the ordering analysis as compared to the original theory. The final governing balance laws of mass and momentum appear to be much less complicated with the averaging operation performed due to the use of an orthogonal basis constructed in a special way.

In what follows, we will present this theory in detail. The derivation of the field equations in their coordinate free form can be taken from Sect. 3.4.1. Here we will just refer to those equations whenever they are explicitly needed. Therefore, we will start the analysis of the flow by presenting the underlying curvilinear coordinate system.

4.3 General Orthogonal Coordinate System

Consider an avalanche prone landscape and a subregion of it where the topography allows the identification of an avalanche track (see Fig. 4.2). A curve following the landscape topography (e.g., the talweg of a valley) is singled out as a master curve C from which the track topography will be modelled. Let this three-dimensional curve be smooth; in the global coordinate system it may be given by $\mathbf{R}(x, y, z)$, where x, y and z are the Cartesian coordinates. A moving coordinate system is constructed (see, e.g., KLINGBEIL, BOWEN and WANG, GERMANO, ZABIELSKI and MESTEL [42, 43, 112, 113, 222, 447, 448]) by considering this spatial curve described by the position vector $\mathbf{R}(s)$, where s is the parameter that measures the arc length from some convenient reference point.[2] At any point of the curve we may erect the orthonormal triad $\{\mathbf{T}, \mathbf{N}, \mathbf{B}\}$ that, comprises the tangent, principal normal and binormal unit vectors, respectively, also expressible as functions of s. The vector pair $\{\mathbf{N}, \mathbf{B}\}$ spans a plane perpendicular to C. Any vector $\mathbf{X}$ in three-dimensional space can be expressed as

[2] We assume here that the arc length is either known or can be computed. If t is another parameterisation of the reference curve, then

$$s = \int_{t_0}^{t} |\dot{\mathbf{R}}(t')| dt',$$

where t_0 is the parameter value for which $s = 0$.

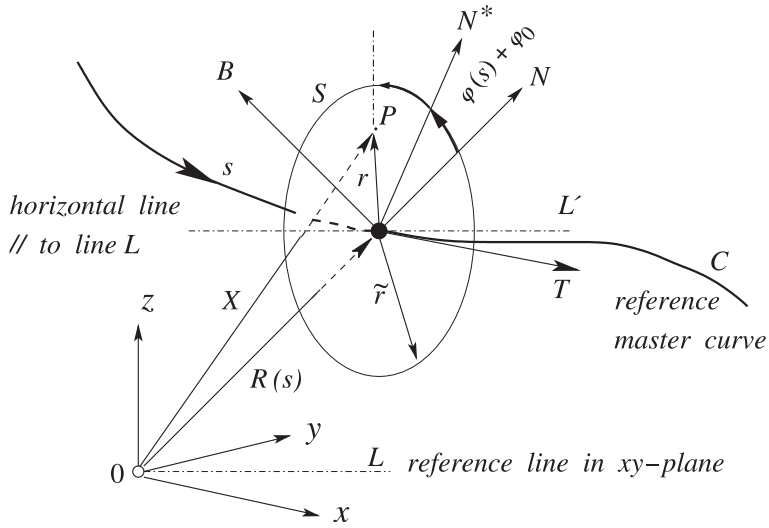

Fig. 4.4. Sketch and description of a moving coordinate system and generation of a mountain corrie: $\mathbf{R}(s)$ describes the reference (master) curve C embedded in $\mathbb{R}^3$, s is the arc length, $\{\mathbf{T}, \mathbf{N}, \mathbf{B}\}$ is the moving orthonormal unit triad following the curve. (r, θ) are polar coordinates spanning the plane of circle S with radius $\tilde{r}$ normal to the axis of C. The origin of the azimuthal angle, θ, in this plane is arbitrary, but measured from the unit vector $\mathbf{N}^*$, which is rotated from $\mathbf{N}$ by a phase $(\varphi(s) + \varphi_0)$ for an $s \in [s_0, \infty)$, $s_0 \in [0, \infty)$ and $\theta \in (0,\, 2\pi)$. φ_0 is an arbitrary constant and P is any point in space. (From [335].)

$$\begin{aligned}\mathbf{X} :=& \mathbf{X}(s, r, \theta)\\ =& \mathbf{R}(s) + r\cos(\theta + \varphi(s) + \varphi_0)\,\mathbf{N}(s) + r\sin(\theta + \varphi(s) + \varphi_0)\,\mathbf{B}(s). \quad (4.1)\end{aligned}$$

Here, (r, θ) are polar coordinates spanning the plane normal to the axis of the master curve C in Fig. 4.4. The origin of the azimuthal angle, θ, in this plane is arbitrary but measured from the unit vector $\mathbf{N}^*$, which is rotated from $\mathbf{N}$ by *a phase* $(\varphi(s) + \varphi_0)$. Moreover, φ_0 is an arbitrary constant (in applications often conveniently taken as 0 or $\pm\pi/2$) and

$$\varphi(s) = -\int_{s_0}^{s} \tau(s')ds' \quad (4.2)$$

is the *accumulation of the torsion* of the curve as it proceeds from the initial point s_0. Hence the torsion, $\tau(s)$, enters into the equations through the auxiliary function $\varphi = \varphi(s)$[3]. From differential geometry (see, Bowen and Wang and Klingbeil [42, 43, 222]) we recall the following results:

[3] This system of coordinates is well-known to researchers involved in studies on hydromagnetic equilibria. It was first introduced by Mercier [280] and was extensively used by Solove'v and Shafranov [399] in their computations of plasma confinement in closed magnetic systems. Germano [112] wrote the

$$\mathbf{T}(s) = \frac{d\mathbf{R}(s)}{ds}, \quad \mathbf{N}(s) = \frac{1}{\kappa(s)} \frac{d\mathbf{T}(s)}{ds}, \quad \mathbf{B}(s) = \mathbf{T}(s) \times \mathbf{N}(s), \tag{4.3}$$

where $\kappa(s)$ is the curvature of the master (reference) curve C and "$\times$" stands for the "cross product" of two vectors in $\mathbb{R}^3$. Curvature and torsion can be computed from the function $\mathbf{R} = \mathbf{R}(x, y, z)$ and are intrinsically expressible as functions of the arc length s: $\kappa = \kappa(s)$ and $\tau = \tau(s)$. The SERRET–FRÉNET formulas provide a connection between the curvature and torsion and the changes of $\mathbf{T}, \mathbf{N}, \mathbf{B}$ along s as follows:

$$\frac{d\mathbf{T}}{ds} = \kappa\mathbf{N}, \quad \frac{d\mathbf{N}}{ds} = \tau\mathbf{B} - \kappa\mathbf{T}, \quad \frac{d\mathbf{B}}{ds} = -\tau\mathbf{N}, \tag{4.4}$$

or in matrix notation

$$\frac{d}{ds}\begin{pmatrix}\mathbf{T}\\ \mathbf{N}\\ \mathbf{B}\end{pmatrix} = \begin{pmatrix}0 & \kappa & 0\\ -\kappa & 0 & \tau\\ 0 & -\tau & 0\end{pmatrix}\begin{pmatrix}\mathbf{T}\\ \mathbf{N}\\ \mathbf{B}\end{pmatrix} = F(s)\begin{pmatrix}\mathbf{T}\\ \mathbf{N}\\ \mathbf{B}\end{pmatrix}, \tag{4.5}$$

with the skewsymmetric matrix F.

Because GIS refer the topography to the global Cartesian system $\{x, y, z\}$, this must in a particular application first be transformed to the orthogonal moving coordinate system. This can be done, e.g., by using NURBS (non-uniform rational B-spline), see PIEGL and TILLER [317]. In this chapter it will not be of any concern because our focus will be on the derivation of the model equations for an arbitrary topography. The most advantageous fact of this moving coordinate system along a curved and twisted line is that one is free to choose the *master curve*. Hence it may have applications in investigations of the flow behaviour of fluids as well as moving granular materials in a curved and twisted channel.

For ease of notation the identifications

$$(x^1, x^2, x^3) := (s, \theta, r) \tag{4.6}$$

will be made.

The tangent vectors to the coordinate lines, i.e., the associated covariant basis vectors, $\mathbf{g}_i = \partial\mathbf{X}/\partial x^i$ (see Fig. 4.5), are given by[4]

NAVIER–STOKES equations for an incompressible viscous fluid in these coordinates and GERMANO [113] extended the DEAN equations [72, 73] to the case of a helical pipe flow in this orthogonal system of coordinates. Recently, GAMMACK and HYDON [106] studied steady and unsteady flows in pipes with small, slowly varying curvature and torsion using GERMANO's extension of the DEAN equations.

[4] Note that in the derivation of these basis vectors (4.2)–(4.4) are implemented.

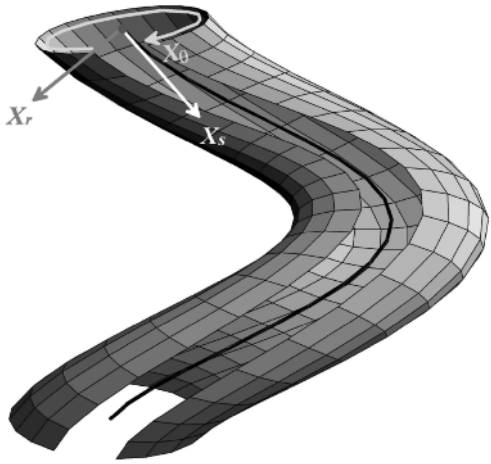

Fig. 4.5. Representation of a curved and twisted channel, a reference curve and the tangent vectors along the coordinate lines. The *dark line* along the channel is the axis of the channel. (From [342]).

$$\begin{aligned}\mathbf{g}_1 &= (1-\kappa r\eta)\,\mathbf{T}(s),\\ \mathbf{g}_2 &= -r\zeta\mathbf{N}(s) + r\eta\mathbf{B}(s),\\ \mathbf{g}_3 &= \eta\mathbf{N}(s) + \zeta\mathbf{B}(s),\end{aligned} \tag{4.7}$$

where

$$\eta = \cos\left(\theta + \varphi(s) + \varphi_0\right), \qquad \zeta = \sin\left(\theta + \varphi(s) + \varphi_0\right). \tag{4.8}$$

The covariant metric, defined as $(g_{ij}) = (\mathbf{g}_i \,.\, \mathbf{g}_j)$ and the associated contravariant metric $\left(g^{ij}\right)$, determined by $\left(g^{ij}\right)(g_{jk}) = \delta^i_k$, turn out to be

$$(g_{ij}) = \begin{pmatrix} (1-\kappa r\eta)^2 & 0 & 0\\ 0 & r^2 & 0\\ 0 & 0 & 1\end{pmatrix}, \quad \left(g^{ij}\right) = \begin{pmatrix} 1/(1-\kappa r\eta)^2 & 0 & 0\\ 0 & 1/r^2 & 0\\ 0 & 0 & 1\end{pmatrix}. \tag{4.9}$$

It is clear that in contrast to the standard Cartesian unit vectors $\mathbf{i}, \mathbf{j}, \mathbf{k}$, the covariant vectors $\mathbf{g}_i$ vary as functions of position. One can easily show that the metric for the chosen coordinate system is given by

$$\begin{aligned} ds^2 &= d\mathbf{X}\cdot d\mathbf{X} = g_{ij}\,dx^i\,dx^j\\ &= \left[1-\kappa(s) r\cos\left(\theta+\varphi(s)+\varphi_0\right)\right]^2 (ds)^2 + (dr)^2 + (rd\theta)^2\,. \end{aligned} \tag{4.10}$$

This corroborates the orthogonality of the system (4.1) and (4.3). It is also easy to see that when $\tau = 0$, this system of coordinates reduces to the simple toroidal system, while it reduces to the cylindrical coordinate system when $\kappa = \tau = 0$.

The CHRISTOFFEL symbols of the second kind[5] are needed to express the differential operators grad and div in order to transfer the equations of motion from the coordinate free form to the curvilinear coordinates. This is a standard method when tackling geophysical flow processes with complicated boundary and topographic conditions. In an orthogonal coordinate system, they are defined as (see, e.g., BOWEN and WANG and KLINGBEIL [42, 43, 222])

$$\Gamma^k_{lm} = \tfrac{1}{2} g^{(kk)} \left(g_{mk,l} + g_{kl,m} - g_{lm,k}\right). \tag{4.11}$$

For the curvilinear coordinates (4.9) the components of the CHRISTOFFEL symbols are

$$\mathbf{\Gamma}^1 = -\psi \begin{pmatrix} \Lambda r & -\kappa r\zeta & \kappa\eta \\ -\kappa r\zeta & 0 & 0 \\ \kappa\eta & 0 & 0 \end{pmatrix}, \; \mathbf{\Gamma}^2 = \frac{1}{r} \begin{pmatrix} -\kappa\zeta/\psi & 0 & 0 \\ 0 & 0 & 1 \\ 0 & 1 & 0 \end{pmatrix}, \; \mathbf{\Gamma}^3 = \begin{pmatrix} \kappa\eta/\psi & 0 & 0 \\ 0 & -r & 0 \\ 0 & 0 & 0 \end{pmatrix}, \tag{4.12}$$

where

$$\Lambda = \kappa'\eta + \kappa\tau\zeta, \quad \psi = 1/(1-\kappa r\eta) \;\text{ and }\; \kappa' = \partial\kappa/\partial s. \tag{4.13}$$

The (covariant) unit vectors are defined[6] as $\mathbf{g}^*_i = \mathbf{g}_i/\sqrt{g_{(ii)}}$. Further, the vector differential operator ∇ is defined as

$$\nabla = \mathbf{g}^k \frac{\partial}{\partial x^k}, \tag{4.14}$$

with components given in terms of the contravariant basis $\mathbf{g}^k$ and the gradient of a given scalar field F is $\nabla F = F_{,k}\, \mathbf{g}^k$. For the curvilinear coordinate system defined in (4.9), in terms of the covariant unit basis, this can be expressed as

$$\nabla F = \psi \frac{\partial F}{\partial s}\mathbf{g}^*_1 + \frac{1}{r}\frac{\partial F}{\partial \theta}\mathbf{g}^*_2 + \frac{\partial F}{\partial r}\mathbf{g}^*_3, \tag{4.15}$$

in which $\mathbf{g}^*_j = \mathbf{g}_j/\sqrt{g_{(jj)}}$. The prefactors of $\mathbf{g}^*_j$ are called the *physical components* of the gradient of F.

The physical components of the vector $\mathbf{u}$ are defined[7] by $u^{i*} = u^i\sqrt{g_{(ii)}}$. Similarly, the physical components p^{ij*} of a second-order tensor $\mathbf{p}$ are related to the contravariant components by $p^{ij*} = p^{ij}\left(\sqrt{g_{(ii)}}\sqrt{g_{(jj)}}\right)$. The divergence

[5] The CHRISTOFFEL symbols of the second kind are defined as $\Gamma^k_{ij} = \left(\partial\mathbf{g}_i/\partial x^j\right)\cdot\mathbf{g}^k$, where $\mathbf{g}^k$ are the contravariant basis vectors.

[6] We employ the summation convention over doubly repeated indices. However, the summation is not carried out when such indices are put in parentheses.

[7] This can be obtained as follows: $\mathbf{u} = u^i\mathbf{g}_i = u^i\sqrt{g_{(ii)}}(\mathbf{g}_i/\sqrt{g_{(ii)}}) = u^i\sqrt{g_{(ii)}}\mathbf{g}^*_i = u^{i*}\mathbf{g}^*_i$. This implies that $u^{i*} = u^i\sqrt{g_{(ii)}}$, which by definition are the physical components of $\mathbf{u}$.

of a vector field $\mathbf{u} = u^i \mathbf{g}_i$ and a symmetric second-order pressure tensor $\mathbf{p} = p^{ij} \mathbf{g}_i \otimes \mathbf{g}_j$, respectively, are expressible as

$$\nabla \cdot \mathbf{u} = \left(\mathbf{g}^k \frac{\partial}{\partial x^k} \right) \cdot \left(u^i \mathbf{g}_i \right) = u^i_{,\,i} + u^i \Gamma^k_{ik}, \quad \Gamma^k_{ik} = \mathbf{g}^k \cdot \mathbf{g}_{i,k}, \tag{4.16}$$

$$\nabla \cdot \mathbf{p} = \left(\mathbf{g}^k \frac{\partial}{\partial x^k} \right) \cdot \left(p^{ij} \mathbf{g}_i \otimes \mathbf{g}_j \right) = \{ p^{ki}{}_{,\,k} + p^{ji} \Gamma^k_{jk} + p^{kj} \Gamma^i_{jk} \} \sqrt{g_{(ii)}} \mathbf{g}^*_i . \tag{4.17}$$

For notational brevity and to make the present theory compatible with previous model equations of the extended SH-theory, we define the following new variables:

$$(x, y, z) := (s, r\theta, r). \tag{4.18}$$

From now on all derivations are done with respect to these new variables: Firstly we take the differentials with respect to these variables and then again shift the z coordinate by an amount z_T, i.e., we replace z by $z + z_T$, where z_T is the distance between the master curve and the talweg (see Fig. 4.6), where $0\tilde{0} = z_T$.

Therefore, from now on (x, y, z) are *not* Cartesian coordinates, but rather the coordinates of the curved and twisted channel, and the origin of this new coordinate system lies in the talweg. Furthermore, the manifold $z =$ constant forms a curved and twisted reference surface and the new variable z is the coordinate in the direction normal to it. We refer to the x, y, and z-coordinates as downslope, cross-slope and normal directions, respectively. For notational brevity, in the following computations we write

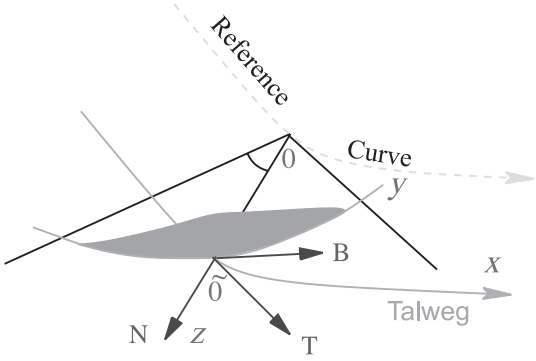

Fig. 4.6. For a given value of the arc length, the avalanche domain in the lateral direction occupies a region in a circular section of a plane perpendicular to the talweg of the valley and θ is the azimuthal angle in this plane. $O\tilde{O} = z_T$ is the radial distance between the master (reference) curve and the talweg. The lateral coordinate, y, is determined by the transformation $y = \theta z_T$. $\{\mathbf{T}, \mathbf{N}, \mathbf{B}\}$ is the moving orthonormal unit triad following the talweg (equivalently the master curve). (From [341].)

$$\mathcal{Z} = z + z_T. \tag{4.19}$$

With the CHRISTOFFEL symbols and physical components of $\mathbf{u}$ and $\mathbf{p}$ expressions (4.16) and (4.17), in curvilinear coordinates, respectively, read

$$\begin{aligned}\nabla \cdot \mathbf{u} = {} & \frac{\partial}{\partial x}\left(\psi u^{1*}\right) + \frac{\partial u^{2*}}{\partial y} + \frac{\partial u^{3*}}{\partial z} \\ & - \psi^2 \Lambda \mathcal{Z} u^{1*} + \psi\kappa\zeta u^{2*} - \left(\psi\kappa\eta - \frac{1}{\mathcal{Z}}\right) u^{3*},\end{aligned} \tag{4.20}$$

$$\begin{aligned}\nabla \cdot \mathbf{p} = {} & \left[\frac{\partial}{\partial x}\left(\psi p^{11*}\right) + \frac{\partial p^{12*}}{\partial y} + \frac{\partial p^{13*}}{\partial z}\right. \\ & \left. - \psi^2 \Lambda \mathcal{Z} p^{11*} + 2\psi\kappa\zeta p^{12*} - 2\psi\kappa\eta p^{13*} + \frac{1}{\mathcal{Z}} p^{13*}\right] \mathbf{g}_1^* \\ & + \left[\frac{\partial}{\partial x}\left(\psi p^{12*}\right) + \frac{\partial p^{22*}}{\partial y} + \frac{\partial p^{23*}}{\partial z}\right. \\ & \left. - \psi\kappa\zeta p^{11*} - \psi^2 \Lambda \mathcal{Z} p^{12*} + \psi\kappa\zeta p^{22*} - \left(\psi\kappa\eta - \frac{2}{\mathcal{Z}}\right) p^{23*}\right] \mathbf{g}_2^* \\ & + \left[\frac{\partial}{\partial x}\left(\psi p^{13*}\right) + \frac{\partial p^{23*}}{\partial y} + \frac{\partial p^{33*}}{\partial z}\right. \\ & \left. + \psi\kappa\eta p^{11*} - \frac{1}{\mathcal{Z}} p^{22*} - \psi^2 \Lambda \mathcal{Z} p^{13*} + \psi\kappa\zeta p^{23*} - \left(\psi\kappa\eta - \frac{1}{\mathcal{Z}}\right) p^{33*}\right] \mathbf{g}_3^*.\end{aligned} \tag{4.21}$$

The derivation of these expressions is not difficult, but it is somewhat lengthy and requires careful attention to details. Notice, moreover, that (4.20) and (4.21) are so structured that their components have the form

$$\left[\frac{\partial}{\partial x}(\bullet) + \frac{\partial}{\partial y}(\diamond) + \frac{\partial}{\partial z}(\star) \;+\; \text{additional terms}\right]. \tag{4.22}$$

When the "additional non-divergent terms" are absent, one says that (4.20) and (4.21) have conservative forms. The non-conservative form is due to the contributions of the CHRISTOFFEL symbols.

4.4 Non-Dimensional Equations

For the ensuing developments it is assumed that the avalanche motion is sufficiently distant from the master curve C. More explicitly, for the fixed value s = constant, the avalanche domain occupies a region in the plane $S \perp C$, so that the avalanche is distant from the centre of the channel (see Figs. 4.4 and 4.7). This then justifies identifying the radial direction with the "thickness" direction and postulating that the typical

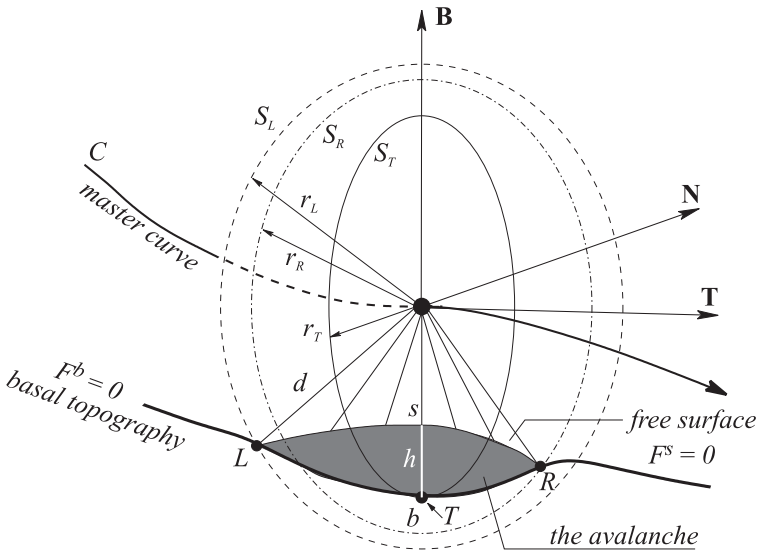

Fig. 4.7. For a given value of $s = x$, the avalanche domain in the lateral direction occupies a region in the plane of the circle $S_T \perp C$, so that the avalanche is distant from the centre of the moving triad $\{\mathbf{T}, \mathbf{N}, \mathbf{B}\}$. The concentric and coplanar circles S_T, S_L, and S_R (with the centres at the master curve and radii r_T, r_L, and r_R), respectively, pass through the talweg (T) and the left (L) and right (R) marginal points of the avalanche with its basal topography in the lateral direction. In this plane section the basal topography $F^b = 0$ and the free surface $F^s = 0$ of the avalanche are shown. The depth of the avalanche in this section is represented by a height function $h(x, y, t)$ and is measured in the radial direction. Also shown, for instance, is the distance d of the avalanche from the centerline to the circle S_L [335].

"radial thickness" is small relative to a typical length (or width) of the avalanche.

In this section, the coordinate independent equations of Sect. 3.4.1 are expressed in terms of the curvilinear coordinate system introduced in Sect. 4.3. The physical components of the velocity field $\mathbf{u}$ are defined as u, v and w. Similarly, the physical components of the symmetric pressure tensor $\mathbf{p}$ are $p_{xx}, p_{yy}, p_{zz}, p_{xy}, p_{xz}, p_{yz}$ where the convention that superscripts define contravariant quantities is now dropped, i.e., p_{xx}, etc. are now and henceforth physical components. Also, for notational brevity, from now on, we will simply write $\mathbf{e}_i$ for covariant unit base vectors $\mathbf{g}_i^*$, so that $\mathbf{u} = u\mathbf{e}_x + v\mathbf{e}_y + w\mathbf{e}_z$ defines the physical components u, v, w and $(\mathbf{e}_x, \mathbf{e}_y, \mathbf{e}_z) = (\mathbf{e}_1, \mathbf{e}_2, \mathbf{e}_3)$. The physical variables are non-dimensionalised by using the scalings

$$
\begin{aligned}
\left(x, y, z, F^s, F^b, t\right) &= \left(L\hat{x}, L\hat{y}, H\hat{z}, H\hat{F^s}, H\hat{F^b}, (L/g)^{1/2}\,\hat{t}\right), \\
(u, v, w) &= (gL)^{1/2}\,(\hat{u}, \hat{v}, \varepsilon\hat{w}), \\
(p_{xx}, p_{yy}, p_{zz}) &= \rho g H\,(\hat{p}_{xx}, \hat{p}_{yy}, \hat{p}_{zz}), \\
(p_{xy}, p_{xz}, p_{yz}) &= \rho g H \mu\,(\hat{p}_{xy}, \hat{p}_{xz}, \hat{p}_{yz}), \\
(g_x, g_y, g_z) &= g\,(\hat{g}_x, \hat{g}_y, \hat{g}_z), \\
(\kappa, \tau) &= (\hat{\kappa}/\mathcal{R}, \hat{\tau}/\mathcal{R}_\tau),
\end{aligned}
\tag{4.23}
$$

where the hats represent non-dimensional variables. The scalings (4.23) assume that the avalanche has a typical length, L, tangential to the reference surface and a typical thickness, H, normal to it. Furthermore, $\mathcal{R}$ and $\mathcal{R}_\tau$ are, respectively, the typical radius of curvature and torsion of the reference geometry. Assuming a granular static balance, the typical normal pressures at the base of the avalanche are of the order[8] $\rho g H$, and the COULOMB dry friction law (3.18) suggests that the basal shear stresses are of the order $\rho g H \tan\delta$, where δ is a typical basal angle of friction. Also, notice that g_x, g_y and g_z in these equations are dimensional physical components of the gravitational acceleration along the x-, y- and z-coordinates, respectively, and g is the magnitude of the gravitational acceleration. Finally, the curvature κ and torsion τ are assumed to be of order $1/\mathcal{R}$ and $1/\mathcal{R}_\tau$, respectively. These scalings introduce the following *non-dimensional parameters*:

$$
\varepsilon = H/L, \quad \lambda = L/\mathcal{R}, \quad \lambda_\tau = L/\mathcal{R}_\tau, \quad \mu = \tan\delta, \tag{4.24}
$$

where ε is the *aspect ratio* of the avalanche, λ and λ_τ are *measures of the curvature and torsion* of the reference geometry with respect to the length of the avalanche and μ is the *coefficient of friction* of the granular material, related here to a typical bed friction angle.

4.4.1 Components of the Gravitational Acceleration

The non-dimensional physical components of the gravitational acceleration along the x-, y- and z-coordinates, respectively, can be determined as known functions of curvature and torsion referred to the moving triad of the given master curve. Their derivation is as follows:

Consider the orthonormal unit basis vectors along the coordinate lines (see (4.7)),

[8] This scaling for the normal pressure tacitly assumes a "hydrostatic nature" of the pressure in a granular heap. This is in fact untypical for granular systems for which the pressure is not the overburden weight as it "saturates" after a certain depth.

$$\begin{aligned}\mathbf{e}_x &= \mathbf{T}(x),\\ \mathbf{e}_y &= -\zeta\mathbf{N}(x) + \eta\mathbf{B}(x),\\ \mathbf{e}_z &= \eta\mathbf{N}(x) + \zeta\mathbf{B}(x).\end{aligned} \tag{4.25}$$

The gravity vector $\mathbf{g}$ can be written in the form

$$\mathbf{g} = (0, 0, -g) = 0\mathbf{i} + 0\mathbf{j} - g\mathbf{k}, \tag{4.26}$$

where $\{\mathbf{i}, \mathbf{j}, \mathbf{k}\}$ forms the standard Cartesian basis and g is the magnitude of the gravitational acceleration. We need to express $\mathbf{g}$ in terms of the unit basis, $\{\mathbf{e}_i\}$, as follows:

$$\begin{aligned}\mathbf{g} &= g_x\mathbf{e}_x + g_y\mathbf{e}_y + g_z\mathbf{e}_z\\ &= g_x\mathbf{T} + g_y\left(-\zeta\mathbf{N} + \eta\mathbf{B}\right) + g_z\left(\eta\mathbf{N} + \zeta\mathbf{B}\right)\\ &= g_x\mathbf{T} - \left(\zeta g_y - \eta g_z\right)\mathbf{N} + \left(\eta g_y + \zeta g_z\right)\mathbf{B}\\ &= g\left[\hat{g}_x\mathbf{T} - \left(\zeta\hat{g}_y - \eta\hat{g}_z\right)\mathbf{N} + \left(\eta\hat{g}_y + \zeta\hat{g}_z\right)\mathbf{B}\right],\end{aligned} \tag{4.27}$$

where $\{g_x, g_y, g_z\} = g\{\hat{g}_x, \hat{g}_y, \hat{g}_z\}$ are the physical components of $\mathbf{g}$ with respect to the basis $\{\mathbf{e}_i\}$. Let t_i, n_i and b_i, $i = 1, 2, 3$, be, respectively, the components of the tangent, normal and binormal unit vectors of a given space curve with respect to the standard Cartesian basis $\{\mathbf{i}, \mathbf{j}, \mathbf{k}\}$. We must express the right-hand side of (4.27) in terms of this basis as follows:

$$\begin{aligned}\mathbf{g} = g\Big[&\hat{g}_x\left(t_1\mathbf{i} + t_2\mathbf{j} + t_3\mathbf{k}\right)\\ &- \left(\zeta\hat{g}_y - \eta\hat{g}_z\right)\left(n_1\mathbf{i} + n_2\mathbf{j} + n_3\mathbf{k}\right)\\ &+ \left(\eta\hat{g}_y + \zeta\hat{g}_z\right)\left(b_1\mathbf{i} + b_2\mathbf{j} + b_3\mathbf{k}\right)\Big]\\ = g\Big[&t_1\hat{g}_x - n_1\left(\zeta\hat{g}_y - \eta\hat{g}_z\right) + b_1\left(\eta\hat{g}_y + \zeta\hat{g}_z\right)\Big]\mathbf{i}\\ + g\Big[&t_2\hat{g}_x - n_2\left(\zeta\hat{g}_y - \eta\hat{g}_z\right) + b_2\left(\eta\hat{g}_y + \zeta\hat{g}_z\right)\Big]\mathbf{j}\\ + g\Big[&t_3\hat{g}_x - n_3\left(\zeta g_y - \eta g_z\right) + b_3\left(\eta\hat{g}_y + \zeta\hat{g}_z\right)\Big]\mathbf{k}.\end{aligned} \tag{4.28}$$

Comparing the similar terms of this equation with (4.26), we obtain the following set of linear equations in $\hat{g}_x, \hat{g}_y, \hat{g}_z$:

$$\begin{aligned}t_1\hat{g}_x + \left(b_1\eta - n_1\zeta\right)\hat{g}_y + \left(n_1\eta + b_1\zeta\right)\hat{g}_z &= 0,\\ t_2\hat{g}_x + \left(b_2\eta - n_2\zeta\right)\hat{g}_y + \left(n_2\eta + b_2\zeta\right)\hat{g}_z &= 0,\\ t_3\hat{g}_x + \left(b_3\eta - n_3\zeta\right)\hat{g}_y + \left(n_3\eta + b_3\zeta\right)\hat{g}_z &= -1.\end{aligned} \tag{4.29}$$

This system can be solved to obtain values for $(\hat{g}_x, \hat{g}_y, \hat{g}_z)$ in terms of t_i, b_i and n_i. The solution is

$$\begin{aligned}
\hat{g}_x &= [b_1 n_2 - b_2 n_1] / \Delta \\
\hat{g}_y &= [t_2 (n_1 \eta + b_1 \zeta) - t_1 (n_2 \eta + b_2 \zeta)] / \Delta \\
\hat{g}_z &= [t_1 (b_2 \eta - n_2 \zeta) - t_2 (b_1 \eta - n_1 \zeta)] / \Delta \\
\Delta &= t_1 (n_2 b_3 - b_2 n_3) + t_2 (b_1 n_3 - n_1 b_3) + t_3 (n_1 b_2 - b_1 n_2) \\
&= \mathbf{T} \cdot (\mathbf{N} \times \mathbf{B}),
\end{aligned} \tag{4.30}$$

which is the scalar triple product of $\mathbf{T}, \mathbf{N}$ and $\mathbf{B}$. Therefore, the possible values of Δ are ± 1.

4.4.2 Balance Equations

Applying the scalings (4.23) and (4.24) to the condition $\nabla \cdot \mathbf{u} = 0$, it follows that the non-dimensional curvilinear form of the mass balance equation (4.20) is

$$\begin{aligned}
&\frac{\partial}{\partial x}(\psi u) + \frac{\partial v}{\partial y} + \frac{\partial w}{\partial z} \\
&\qquad - \varepsilon \lambda \psi^2 \Lambda \mathcal{Z} u + \lambda \psi \kappa \zeta v - \left(\varepsilon \lambda \psi \kappa \eta - \frac{1}{\mathcal{Z}} \right) w = 0,
\end{aligned} \tag{4.31}$$

where the hats, identifying non-dimensional quantities, are now and henceforth dropped, and

$$\psi = 1/(1 - \varepsilon \lambda \kappa \eta \mathcal{Z}), \quad \Lambda = (\kappa' \eta + \lambda_\tau \kappa \tau \zeta). \tag{4.32}$$

The prime now expresses differentiation with respect to the dimensionless arc length. The momentum balance equation (3.17) can be written in curvilinear coordinates by using relation (4.21) to transform the tensor $\mathbf{u} \otimes \mathbf{u}$ and the pressure tensor $\mathbf{p}$. After a somewhat lengthy calculation it follows that the non-dimensional components of the momentum balance in the downslope and cross-slope directions and the direction normal to the reference surface are, respectively,

downslope:

$$\begin{aligned}
&\frac{\partial u}{\partial t}+\frac{\partial}{\partial x}\left(\psi u^2\right)+\frac{\partial}{\partial y}\left(uv\right)+\frac{\partial}{\partial z}\left(uw\right)\\
&-\varepsilon\lambda\psi^2\Lambda\mathcal{Z}u^2+2\lambda\psi\kappa\zeta uv-2\varepsilon\lambda\psi\kappa\eta uw+\frac{1}{\mathcal{Z}}uw\\
&=-\Bigg\{\varepsilon\frac{\partial}{\partial x}\left(\psi p_{xx}\right)+\varepsilon\mu\frac{\partial}{\partial y}\left(p_{xy}\right)+\mu\frac{\partial}{\partial z}\left(p_{xz}\right)\\
&-\varepsilon^2\lambda\psi^2\Lambda\mathcal{Z}p_{xx}+2\varepsilon\lambda\mu\psi\kappa\left(\zeta p_{xy}-\eta p_{xz}\right)+\frac{\mu}{\mathcal{Z}}p_{xz}\Bigg\}+g_x,
\end{aligned}\tag{4.33}$$

cross-slope:

$$\begin{aligned}
&\frac{\partial v}{\partial t}+\frac{\partial}{\partial x}\left(\psi uv\right)+\frac{\partial}{\partial y}\left(v^2\right)+\frac{\partial}{\partial z}\left(vw\right)\\
&-\lambda\psi\kappa\zeta\left(u^2-v^2\right)-\varepsilon\lambda\psi^2\Lambda\mathcal{Z}uv-\left(\varepsilon\lambda\psi\kappa\eta-\frac{2}{\mathcal{Z}}\right)vw\\
&=-\Bigg\{\varepsilon\mu\frac{\partial}{\partial x}\left(\psi p_{xy}\right)+\varepsilon\frac{\partial}{\partial y}\left(p_{yy}\right)+\mu\frac{\partial}{\partial z}\left(p_{yz}\right)\\
&-\varepsilon\lambda\psi\kappa\zeta P_y^x-\varepsilon^2\lambda\mu\psi^2\Lambda\mathcal{Z}p_{xy}-\mu\left(\varepsilon\lambda\psi\kappa\eta-\frac{2}{\mathcal{Z}}\right)p_{yz}\Bigg\}+g_y,
\end{aligned}\tag{4.34}$$

normal:

$$\begin{aligned}
&\varepsilon\left\{\frac{\partial w}{\partial t}+\frac{\partial\left(\psi uw\right)}{\partial x}+\frac{\partial\left(vw\right)}{\partial y}+\frac{\partial w^2}{\partial z}\right\}\\
&+\lambda\psi\kappa\eta u^2-\frac{v^2}{\varepsilon\mathcal{Z}}-\varepsilon\lambda\left(\varepsilon\psi^2\Lambda\mathcal{Z}u-\psi\kappa\zeta v\right)w-\left(\varepsilon^2\lambda\psi\kappa\eta-\frac{\varepsilon}{\mathcal{Z}}\right)w^2\\
=&-\Bigg\{\varepsilon\mu\frac{\partial}{\partial x}\left(\psi p_{xz}\right)+\varepsilon\mu\frac{\partial}{\partial y}\left(p_{yz}\right)+\frac{\partial}{\partial z}\left(p_{zz}\right)\\
&+\varepsilon\lambda\psi\kappa\eta P_z^x-\frac{1}{\mathcal{Z}}P_z^y-\varepsilon^2\lambda\mu\psi^2\Lambda\mathcal{Z}p_{xz}+\varepsilon\lambda\mu\psi\kappa\zeta p_{yz}\Bigg\}+g_z,
\end{aligned}\tag{4.35}$$

where

$$P_y^x=\left(p_{xx}-p_{yy}\right),\ P_z^x=\left(p_{xx}-p_{zz}\right),\ P_z^y=\left(p_{yy}-p_{zz}\right).\tag{4.36}$$

Further simplification of these equations is possible, but they are left in the given form as this proves to be particularly useful when the free surface and basal boundary conditions are included once the depth-integration process in Sect. 4.5 is performed.

4.4.3 Kinematic Surface Conditions

The free surface of the avalanche, $F^s(\mathbf{x},t) = 0$, and the basal topography over which the avalanche is assumed to slide, $F^b(\mathbf{x},t) = 0$, are defined by their respective heights above the curvilinear reference (see Fig. 4.7),

$$F^s \equiv z - s(x,y,t) = 0, \quad F^b \equiv -z + b(x,y,t) = 0. \tag{4.37}$$

The functions are so chosen that gradient vectors computed from them point into the exterior of the avalanche body. The functions $F^s(\mathbf{x},t)$ and $s(x,y,t)$ are, in general, time dependent, but for a stagnant non-moving mass they are time-independent; on the other hand, $F^b(\mathbf{x},t)$ and $b(x,y,t)$ are only time-dependent provided that snow is entrained from the bottom or is deposited along the avalanche track. The kinematic surface equations in dimensional form are[9]

$$\frac{\partial F^b}{\partial t} + \mathbf{u}^b \cdot \nabla F^b = 0, \quad \frac{\partial F^s}{\partial t} + \mathbf{u}^s \cdot \nabla F^s = 0. \tag{4.38}$$

We deduce from (4.14), (4.23), (4.24), (4.32), (4.37) and (4.38) the following *non-dimensional* curvilinear kinematic conditions for the basal and free surfaces[10]

$$z = b(x,y,t): \quad \frac{\partial b}{\partial t} + \psi^b u^b \frac{\partial b}{\partial x} + v^b \frac{\partial b}{\partial y} - w^b = 0, \tag{4.39}$$

$$z = s(x,y,t): \quad \frac{\partial s}{\partial t} + \psi^s u^s \frac{\partial s}{\partial x} + v^s \frac{\partial s}{\partial y} - w^s = 0. \tag{4.40}$$

4.4.4 Traction-Free Condition at the Free Surface

From the definition (4.14) of the gradient of a scalar field, the traction-free condition (3.21) reads

$$\frac{p^{ij}}{\sqrt{g_{(jj)}}} \frac{\partial F^s}{\partial x^j} \mathbf{g}_i = 0 \tag{4.41}$$

and has downslope, cross-slope and normal physical components as follows:

---

[9] It is emphasised that here $\mathbf{u}^b$ is the material velocity of particles at the base; when processes of bed erosion or sedimentation are included, $\mathbf{u}^b$ in (4.38) has to be replaced by say, $\mathbf{w}$, the non-material velocity with which the base moves when erosion from, and deposition of material to, the base are accounted for, see also Sect. 3.6. This is not the case here.

[10] For notational convenience, we write $z = b(x,y,t)$ instead of $z = b(x,y)$.

$$
\begin{aligned}
-\varepsilon\psi^s p^s_{xx}\frac{\partial s}{\partial x} - \varepsilon\mu p^s_{xy}\frac{\partial s}{\partial y} + \mu p^s_{xz} &= 0,\\
-\varepsilon\mu\psi^s p^s_{yx}\frac{\partial s}{\partial x} - \varepsilon p^s_{yy}\frac{\partial s}{\partial y} + \mu p^s_{yz} &= 0,\\
-\varepsilon\mu\psi^s p^s_{zx}\frac{\partial s}{\partial x} - \varepsilon\mu p^s_{zy}\frac{\partial s}{\partial y} + p^s_{zz} &= 0,
\end{aligned}
\tag{4.42}
$$

written here again in *dimensionless* form.

4.4.5 The Coulomb Sliding Law at the Base

From (4.15), (4.23), (4.24) and (4.32), we obtain the *non-dimensional form* of the gradient of the basal surface as follows:

$$
\nabla F^b = \varepsilon\psi^b\frac{\partial b}{\partial x}\mathbf{g}_x + \varepsilon\frac{\partial b}{\partial y}\mathbf{g}_y - \mathbf{g}_z. \tag{4.43}
$$

The Coulomb basal sliding law (3.22) states that the basal shear traction is proportional to the pressure perpendicular to the surface, the factor of proportionality being the bed friction coefficient $\tan\delta$. This implies the relation

$$
\underbrace{\mathbf{p}^b\mathbf{n}^b - \left(\mathbf{n}^b\cdot\mathbf{p}^b\mathbf{n}^b\right)\mathbf{n}^b}_{\text{negative shear traction}} = \left(\frac{\mathbf{u}^b}{|\mathbf{u}^b|}\right)\underbrace{\left(\mathbf{n}^b\cdot\mathbf{p}^b\mathbf{n}^b\right)}_{\substack{\text{pressure}\\ \text{normal to}\\ \text{surface}}}\underbrace{\tan\delta}_{\substack{\text{friction}\\ \text{coeff.}}}, \tag{4.44}
$$

or

$$
\mathbf{p}^b\mathbf{n}^b = \left(\mathbf{n}^b\cdot\mathbf{p}^b\mathbf{n}^b\right)\left\{\left(\mathbf{u}^b/|\mathbf{u}^b|\right)\tan\delta + \mathbf{n}^b\right\}. \tag{4.45}
$$

It follows from this and (4.42) and (4.43) that the *dimensionless* downslope, cross-slope and normal components of the basal sliding law (traction vector) read, respectively,

$$
\begin{aligned}
\varepsilon\psi^b p^b_{xx}\frac{\partial b}{\partial x} + \varepsilon\mu p^b_{xy}\frac{\partial b}{\partial y} - \mu p^b_{xz} &= \left(\mathbf{n}^b\cdot\mathbf{p}^b\mathbf{n}^b\right)\left(\Delta_b\frac{u^b}{|\mathbf{u}^b|}\tan\delta + \varepsilon\psi^b\frac{\partial b}{\partial x}\right),\\
\varepsilon\mu\psi^b p^b_{yx}\frac{\partial b}{\partial x} + \varepsilon p^b_{yy}\frac{\partial b}{\partial y} - \mu p^b_{yz} &= \left(\mathbf{n}^b\cdot\mathbf{p}^b\mathbf{n}^b\right)\left(\Delta_b\frac{v^b}{|\mathbf{u}^b|}\tan\delta + \varepsilon\frac{\partial b}{\partial y}\right),\\
\varepsilon\mu\psi^b p^b_{zx}\frac{\partial b}{\partial x} + \varepsilon\mu p^b_{zy}\frac{\partial b}{\partial y} - p^b_{zz} &= \left(\mathbf{n}^b\cdot\mathbf{p}^b\mathbf{n}^b\right)\left(\Delta_b\frac{\varepsilon w^b}{|\mathbf{u}^b|}\tan\delta - 1\right),
\end{aligned}
\tag{4.46}
$$

where $|\mathbf{u}^b| = \left((u^b)^2 + (v^b)^2 + \varepsilon^2(w^b)^2\right)^{1/2}$, the basal unit normal vector $\mathbf{n}^b$ is given by $\Delta_b\mathbf{n}^b = \nabla F^b$, $\Delta_b := \nabla F^b|$ and the associated normalisation factor is

$$\Delta_b = \left\{ 1 + \varepsilon^2 \left(\psi^b\right)^2 \left(\frac{\partial b}{\partial x}\right)^2 + \varepsilon^2 \left(\frac{\partial b}{\partial y}\right)^2 \right\}^{1/2} . \tag{4.47}$$

Note The dry friction law (4.46) may be extended to incorporate a velocity-dependent contribution, but given the fact that a large number of laboratory experiments and observations of field events did not call for an alteration of the sliding law, this will not be done here. For related topics, see also [7, 329, 330, 449, 450].

This completes the transformation of the governing equations from the coordinate independent form of Sect. 3.4.1 to the curvilinear coordinates of Sect. 4.3 using the non-dimensional variables defined in (4.23) and (4.24).

4.5 Depth Integration

The distance between the free surface, $s(x, y, t)$ and the basal topography, $b(x, y, t)$, defines the *thickness*, or *depth*, of the avalanche

$$h(x, y, t) = s(x, y, t) - b(x, y, t), \tag{4.48}$$

measured in the normal (radial) direction within the plane perpendicular to the reference curve (see Fig. 4.7). A *crucial step* in deriving the equations of motion for the evolution of the shallow geometry of the granular material is the process of integration of the mass and the momentum balance equations through this thickness. In order to perform this step, it is useful to define the mean value of a function $f = f(x, y, z, t)$ over the avalanche thickness

$$\bar{f}(x, y, t) = \frac{1}{h(x, y, t)} \int_{b(x,y,t)}^{s(x,y,t)} f(x, y, z, t) dz, \tag{4.49}$$

where the overbar is a shorthand notation for the *mean* of the depth-integrated value.

In the process of depth-integration, we need Leibniz' rule to interchange the order of integration and differentiation. According to this rule, if $G(x, t)$ and $\partial G(x, t)/\partial t$ are continuous functions with respect to x and t, and if the functions $a(t)$ and $b(t)$ are differentiable with respect to t, then the following holds:

$$\frac{d}{dt} \int_{a(t)}^{b(t)} G(x, t) dx = \int_{a(t)}^{b(t)} \frac{\partial}{\partial t} \left(G(x, t)\right) dx + \left[G(x, t) \frac{dx}{dt} \right]_{a(t)}^{b(t)}, \tag{4.50}$$

where the square bracket defines the difference of the enclosed function at the two limiting points of integration, $[f]_a^b = f^b - f^a$.

Using LEIBNIZ' rule (4.50), the mass balance (4.31) is integrated through the avalanche depth. This yields

$$\begin{aligned}
&\int_b^s \left\{ \frac{\partial}{\partial x}(\psi u) + \frac{\partial v}{\partial y} + \frac{\partial w}{\partial z} - \varepsilon\lambda\psi^2 \Lambda \mathcal{Z} u + \lambda\psi\kappa\zeta v - \left(\varepsilon\lambda\psi\kappa\eta - \frac{1}{\mathcal{Z}}\right) w \right\} dz \\
&= \frac{\partial}{\partial x}\left(h\overline{\psi u}\right) + \frac{\partial}{\partial y}(h\overline{v}) - \left[\psi u \frac{\partial z}{\partial x} + v\frac{\partial z}{\partial y} - w\right]_b^s \\
&\quad -\varepsilon\lambda h\overline{\psi^2 \Lambda \mathcal{Z} u} + \lambda h\overline{\psi\kappa\zeta v} - h\overline{\left(\varepsilon\lambda\psi\kappa\eta - \frac{1}{\mathcal{Z}}\right) w}.
\end{aligned} \tag{4.51}$$

The function contained in square brackets in (4.51) has a number of terms in common with the equations expressing the kinematic boundary conditions (4.39) and (4.40). Thus, from (4.39), (4.40) and (4.48), we obtain

$$0 = \frac{\partial h}{\partial t} + \left[\psi u \frac{\partial z}{\partial x} + v\frac{\partial z}{\partial y} - w\right]_b^s. \tag{4.52}$$

Equations (4.51) and (4.52) therefore imply that the depth-integrated form of the mass balance (4.31) takes the form

$$\begin{aligned}
&\frac{\partial h}{\partial t} + \frac{\partial}{\partial x}\left(h\overline{\psi u}\right) + \frac{\partial}{\partial y}(h\overline{v}) \\
&-\varepsilon\lambda h\overline{\psi^2 \Lambda \mathcal{Z} u} + \lambda h\overline{\psi\kappa\zeta v} - h\overline{\left(\varepsilon\lambda\psi\kappa\eta - \frac{1}{\mathcal{Z}}\right) w} = 0,
\end{aligned} \tag{4.53}$$

which is valid for a density preserving material. Notice, it does *not* possess "usual" conservation law structure. Only if the terms on the left-hand side in the second line are interpreted as source terms, is a conservation law form obtained.

The process of depth integration of the momentum balance equations (4.33)–(4.35) is performed in a number of steps. Integrating the first four terms of the left-hand side of (4.33) (the downslope acceleration) and then using the kinematic conditions (4.39) and (4.40), we have

$$\begin{aligned}
&\int_b^s \left\{ \frac{\partial u}{\partial t} + \frac{\partial}{\partial x}\left(\psi u^2\right) + \frac{\partial}{\partial y}(uv) + \frac{\partial}{\partial z}(uw) \right\} dz \\
&= \frac{\partial}{\partial t}(h\overline{u}) + \frac{\partial}{\partial x}\left(h\overline{\psi u^2}\right) + \frac{\partial}{\partial y}(h\overline{uv}) - \left[u\left(\frac{\partial z}{\partial t} + \psi u\frac{\partial z}{\partial x} + v\frac{\partial z}{\partial y} - w\right)\right]_b^s \\
&= \frac{\partial}{\partial t}(h\overline{u}) + \frac{\partial}{\partial x}\left(h\overline{\psi u^2}\right) + \frac{\partial}{\partial y}(h\overline{uv}).
\end{aligned} \tag{4.54}$$

Similarly, the first three terms in the right-hand side of (4.33), after integrating and employing $(4.42)_1$ and $(4.46)_1$, reduce to

$$\int_b^s \left\{ \varepsilon \frac{\partial}{\partial x}\left(\psi p_{xx}\right) + \varepsilon\mu \frac{\partial}{\partial y}\left(p_{xy}\right) + \mu \frac{\partial}{\partial z}\left(p_{xz}\right) \right\} dz$$
$$= \left[\varepsilon \frac{\partial}{\partial x}\left(h\overline{\psi p_{xx}}\right) + \varepsilon\mu \frac{\partial}{\partial y}\left(h\overline{p_{xy}}\right) \right] - \left[\varepsilon\psi p_{xx}\frac{\partial z}{\partial x} + \varepsilon\mu p_{xy}\frac{\partial z}{\partial y} - \mu p_{xz} \right]_b^s$$
$$= \varepsilon \frac{\partial}{\partial x}\left(h\overline{\psi p_{xx}}\right) + \varepsilon\mu \frac{\partial}{\partial y}\left(h\overline{p_{xy}}\right) + \left(\mathbf{n}^b \cdot \mathbf{p}^b \mathbf{n}^b\right)\left(\Delta_b \frac{u^b}{|\mathbf{u}^b|} \tan\delta + \varepsilon\psi^b \frac{\partial b}{\partial x} \right), \quad (4.55)$$

where the COULOMB dry-friction law and the downslope component of the basal normal pressure enter through the boundary conditions. In a similar fashion we can derive corresponding expressions for the depth-integrated cross-slope and normal components of the momentum balances. It then follows that the depth-integrated downslope, cross-slope and normal components of the momentum balances, respectively, are

$$\frac{\partial}{\partial t}\left(h\overline{u}\right) + \frac{\partial}{\partial x}\left(h\overline{\psi u^2}\right) + \frac{\partial}{\partial y}\left(h\overline{uv}\right)$$
$$- \varepsilon\lambda h\overline{\psi^2 \Lambda \mathcal{Z} u^2} + 2\lambda\kappa h\overline{\psi\zeta uv} - 2\varepsilon\lambda\kappa h\overline{\psi\eta uw} + h\overline{\left(\frac{uw}{\mathcal{Z}}\right)}$$
$$= -\left(\Delta_b \frac{u^b}{|\mathbf{u}^b|} \tan\delta + \varepsilon\psi^b \frac{\partial b}{\partial x} \right)\left(\mathbf{n}^b \cdot \mathbf{p}^b \mathbf{n}^b\right) - \varepsilon \frac{\partial}{\partial x}\left(h\overline{\psi p_{xx}}\right) - \varepsilon\mu \frac{\partial}{\partial y}\left(h\overline{p_{xy}}\right)$$
$$+ \varepsilon^2\lambda h\overline{\psi^2 \Lambda \mathcal{Z} p_{xx}} - 2\varepsilon\lambda\mu\kappa h\overline{\psi\left(\zeta p_{xy} - \eta p_{xz}\right)} - \mu h\overline{\left(\frac{p_{xz}}{\mathcal{Z}}\right)} + h g_x, \quad (4.56)$$

$$\frac{\partial}{\partial t}\left(h\overline{v}\right) + \frac{\partial}{\partial x}\left(h\overline{\psi uv}\right) + \frac{\partial}{\partial y}\left(h\overline{v^2}\right)$$
$$- \lambda\kappa h\overline{\psi\zeta\left(u^2 - v^2\right)} - \varepsilon\lambda h\left(\overline{\psi^2 \Lambda \mathcal{Z} uv} - \kappa\overline{\psi\eta vw}\right) + 2h\overline{\left(\frac{vw}{\mathcal{Z}}\right)}$$
$$= -\left(\Delta_b \frac{v^b}{|\mathbf{u}^b|} \tan\delta + \varepsilon \frac{\partial b}{\partial y} \right)\left(\mathbf{n}^b \cdot \mathbf{p}^b \mathbf{n}^b\right) - \varepsilon\mu \frac{\partial}{\partial x}\left(h\overline{\psi p_{xy}}\right) - \varepsilon \frac{\partial}{\partial y}\left(h\overline{p_{yy}}\right)$$
$$+ \varepsilon\lambda\kappa h\overline{\psi\zeta P_y^x} + \varepsilon^2\lambda\mu h\overline{\psi^2 \Lambda \mathcal{Z} p_{xy}} + \varepsilon\lambda\mu\kappa h\overline{\psi\eta p_{yz}} + 2\mu h\overline{\left(\frac{p_{yz}}{\mathcal{Z}}\right)} + h g_y, \quad (4.57)$$

$$\varepsilon\left\{ \frac{\partial}{\partial t}\left(h\overline{w}\right) + \frac{\partial}{\partial x}\left(h\overline{\psi uw}\right) + \frac{\partial}{\partial y}\left(h\overline{vw}\right) \right\}$$
$$+ \lambda\kappa h\overline{\psi\eta u^2} - \frac{h}{\varepsilon}\overline{\left(\frac{v^2}{\mathcal{Z}}\right)} - \varepsilon^2\lambda h\overline{\psi^2 \Lambda \mathcal{Z} uw}$$
$$+ \varepsilon\lambda\kappa h\overline{\psi\zeta vw} - \varepsilon^2\lambda\kappa h\overline{\psi\eta w^2} + \varepsilon h\overline{\left(\frac{w^2}{\mathcal{Z}}\right)}$$
$$= -\left(\Delta_b \frac{\varepsilon w^b}{|\mathbf{u}^b|} \tan\delta - 1 \right)\left(\mathbf{n}^b \cdot \mathbf{p}^b \mathbf{n}^b\right) - \varepsilon\mu \frac{\partial}{\partial x}\left(h\overline{\psi p_{xz}}\right) - \varepsilon\mu \frac{\partial}{\partial y}\left(h\overline{p_{yz}}\right)$$
$$- \varepsilon\lambda\kappa h\overline{\psi\left(\eta P_z^x + \mu\zeta p_{yz}\right)} + h\overline{\left(\frac{p_{yy}}{\mathcal{Z}}\right)} + \varepsilon^2\lambda\mu h\overline{\psi^2 \Lambda \mathcal{Z} p_{xz}} - h\overline{\left(\frac{p_{zz}}{\mathcal{Z}}\right)} + h g_z. \quad (4.58)$$

The formal depth-integration process is now complete. We emphasise that no approximations have been made so far. The depth-integrated mass balance (4.53) and the downslope and cross-slope momentum balances (4.56) and (4.57), form *the basis of the shallow granular motion*. The depth integrated normal component of the momentum equation (4.58) will thereby serve as an *auxiliary equation defining the pressure*. This will now be made clear.

4.6 Ordering

Equations (4.53) and (4.56)–(4.58) constitute four scalar field equations for h, u, v and w as unknowns. However, they contain more than just these unknowns because many "correction terms" arise, which are thickness averages of product quantities of h, u, v and w, as well as stress components. The number of these unknown variables can be reduced by introducing a further *approximation* based on the ordering of the various terms arising in the stated equations. Such orders of magnitudes are now assumed for the *parameters* λ, λ_τ and μ. Realistic avalanche lengths are generally larger than typical radii of curvatures and torsions of the topography. Of course, this is not unanimously so, but $0 < (\lambda, \lambda_\tau) < 1$ is correct almost everywhere. Similarly, δ being a typical friction angle is smaller than 45° (usually between 20° and 30°, both in field and in the laboratory). Thus, also $0 < \mu < 1$ must hold. Since the aspect ratio is generally much smaller than unity, from (4.24) it follows that such corrections are fulfilled for

$$\varepsilon \ll 1, \quad \lambda = O\left(\varepsilon^{\alpha}\right), \quad \lambda_\tau = O\left(\varepsilon^{\alpha_\tau}\right), \quad \mu = O\left(\varepsilon^{\beta}\right), \tag{4.59}$$

where $0 < (\alpha, \alpha_\tau, \beta) < 1$ are realistic for the typical reference surface curvature, torsion and coefficients of basal friction. As typical values of these parameters we can take[11] $\alpha = 1/2$, $\alpha_\tau = 1/2$, $\beta = 1/2$, $\varepsilon = 1/100$ and $\mu = 1/10$. Therefore, the functions ψ and Δ_b in (4.32) and (4.47), respectively, can be estimated by

$$\psi = 1 + O\left(\varepsilon^{1+\alpha}\right), \quad \Delta_b = 1 + O\left(\varepsilon^{2}\right). \tag{4.60}$$

With these orderings, the depth-integrated mass balance equation (4.53) reduces to

$$\frac{\partial h}{\partial t} + \frac{\partial}{\partial x}\left(h\overline{u}\right) + \frac{\partial}{\partial y}\left(h\overline{v}\right) + \lambda h\overline{\kappa\zeta v} - h\overline{\left(\frac{w}{\mathcal{Z}}\right)} + O\left(\varepsilon^{1+\alpha}\right) = 0, \tag{4.61}$$

with an error of the order of $\left(\varepsilon^{1+\alpha}\right)$.

[11] As long as no formal perturbation expansion involving higher-order terms is pursued the exponents α, α_τ and β need not further be specified except $\alpha \neq 1$, $\alpha_\tau \neq 1$, $\beta \neq 1$.

The downslope and cross-slope components of the depth-integrated momentum balances (4.56) and (4.57) must be approximated to leading order, ε^0, and first-order, ε^1, in the small parameter ε, so as to obtain *a realizable theory that includes some constitutive properties of granular material*. These equations contain a common term that is multiplied by the factor $\mathbf{n}^b \cdot \mathbf{p}^b \mathbf{n}^b$. From the normal component of the momentum balance (4.58), it follows that, to *leading-order*,

$$\mathbf{n}^b \cdot \mathbf{p}^b \mathbf{n}^b = \lambda \kappa h \overline{\psi \eta u^2} + hC - hg_z + O(\varepsilon) = hC - hg_z + O(\varepsilon^\gamma), \quad (4.62)$$

where

$$C = \overline{\left(\frac{p_{zz}}{\mathcal{Z}}\right)} - \overline{\left(\frac{p_{yy}}{\mathcal{Z}}\right)} - \overline{\left(\frac{v^2}{\varepsilon \mathcal{Z}}\right)}, \quad (4.63)$$

and $\gamma = \min(\alpha, \alpha_\tau, \beta)$. The component of the *local momentum balance* (4.35) in the normal, i.e., z-direction, also reduces to

$$\frac{\partial}{\partial z}(p_{zz}) = \frac{p_{yy}}{\mathcal{Z}} - \frac{p_{zz}}{\mathcal{Z}} + \frac{v^2}{\varepsilon \mathcal{Z}} + g_z + O(\varepsilon^\gamma). \quad (4.64)$$

Integrating this from $\tilde{z} = z$ to $\tilde{z} = s$ and employing the boundary condition $p_{zz}(\tilde{z} = s) = 0$, we obtain (with $\tilde{\mathcal{Z}} = \tilde{z} + z_T$)

$$p_{zz} = -\int_z^s \left\{ \frac{p_{yy}}{\tilde{\mathcal{Z}}} - \frac{p_{zz}}{\tilde{\mathcal{Z}}} + \frac{v^2}{\varepsilon \tilde{\mathcal{Z}}} + g_z \right\} d\tilde{z} + O(\varepsilon^\gamma), \quad (4.65)$$

from which, owing to (4.63), it follows that

$$p^b_{zz} = hC - hg_z + O(\varepsilon^\gamma). \quad (4.66)$$

This, together with $(4.46)_3$ and (4.62), eventually proves the *consistency* of our computations, namely that

$$\left(\mathbf{n}^b \cdot \mathbf{p}^b \mathbf{n}^b\right) = p^b_{zz}. \quad (4.67)$$

In the SH-theory, a linear variability of the pressure with depth is assumed. This is fulfilled if

$$\int_z^s \left\{ \frac{p_{yy}}{\tilde{\mathcal{Z}}} - \frac{p_{zz}}{\tilde{\mathcal{Z}}} + \frac{v^2}{\varepsilon \tilde{\mathcal{Z}}} \right\} d\tilde{z} = O(\varepsilon^\gamma), \quad (4.68)$$

so that it follows from (4.65) that

$$p_{zz} = -(s - z) g_z + O(\varepsilon^\gamma), \quad p^b_{zz} = -hg_z + O(\varepsilon^\gamma). \quad (4.69)$$

This assumption is not as dramatic as it might seem, because in applications z_T is of the order $O\left(\varepsilon^{-1}\right)$.

Since we are deriving depth-averaged model equations, we must be able to eliminate the effects of the normal component w of the velocity field and the

normal coordinate z from the balance equations. In typical avalanche flows, the dominant deformation takes place mainly in the downhill direction. It is, therefore, legitimate to assume that $|p_{xz}/z_T| = O(\varepsilon)$. Usually, in applications we have $z/z_T \ll 1$ and $p_{xz}/z_T \ll 1$. With this rational, we have the following approximation:

$$\begin{aligned}\overline{\left(\frac{p_{xz}}{\mathcal{Z}}\right)} &= \frac{1}{h}\int_b^s \frac{p_{xz}}{\mathcal{Z}}dz = \frac{1}{h}p_{xz}\int_b^s \frac{1}{z+z_T}dz + O(\varepsilon)\\ &= \frac{p_{xz}}{hz_T}\int_b^s \frac{1}{(1+z/z_T)}dz + O(\varepsilon) = \frac{p_{xz}}{hz_T}\int_b^s 1\,dz + O(\varepsilon)\\ &= \frac{p_{xz}}{hz_T}h + O(\varepsilon) = \frac{p_{xz}}{z_T} + O(\varepsilon) = O(\varepsilon). \end{aligned} \tag{4.70}$$

An analogous approximation holds for $\overline{(p_{yz}/\mathcal{Z})}$. Hence, we have the following results:

$$\overline{(p_{xz}/\mathcal{Z})} = O(\varepsilon), \quad \overline{(p_{yz}/\mathcal{Z})} = O(\varepsilon). \tag{4.71}$$

Finally, we need to approximate three terms, namely, $\overline{(uw/\mathcal{Z})}, \overline{(vw/\mathcal{Z})}, \overline{(w/\mathcal{Z})}$. For this, we assume that the velocity components u, v and w vary only negligibly with depth and that $w/z_T \ll 1$, i.e., z_T is relatively large and w is small. With these assumptions we have the following approximation:

$$\begin{aligned}\overline{\left(\frac{uw}{\mathcal{Z}}\right)} &= \frac{1}{h}\int_b^s \frac{uw}{\mathcal{Z}}dz = \frac{1}{hz_T}\int_b^s \frac{uw}{(1+z/z_T)}dz\\ &= \frac{uw}{hz_T}\int_b^s \frac{1}{(1+z/z_T)}dz + O\left(\varepsilon^{1+\gamma}\right) = \frac{uw}{hz_T}\int_b^s 1\,dz + O\left(\varepsilon^{1+\gamma}\right)\\ &= \frac{uw}{z_T} + O\left(\varepsilon^{1+\gamma}\right) = O\left(\varepsilon^{1+\gamma}\right). \end{aligned} \tag{4.72}$$

So, we may also assume that $\overline{(uw/\mathcal{Z})}, \overline{(vw/\mathcal{Z})}, \overline{(w/\mathcal{Z})}$ are $O\left(\varepsilon^{1+\gamma}\right)$ and therefore negligible. Moreover, since we consider the shallow geometry of the basal topography, for small curvature and torsion, we may also consider $\lambda\kappa\zeta$ to be of order $O\left(\varepsilon^{\alpha+\alpha_\tau}\right) \sim O\left(\varepsilon^{1+\gamma}\right)$ and, therefore, negligible.

Summarising the above analysis and restricting considerations to $O\left(\varepsilon^1\right)$ terms, we deduce from (4.59), (4.60), (4.62), (4.67), (4.69), (4.71) and (4.72) that the mass balance (4.61) and the downslope and cross-slope momentum components (4.56) and (4.57) reduce to

$$\frac{\partial h}{\partial t} + \frac{\partial}{\partial x}\left(h\overline{u}\right) + \frac{\partial}{\partial y}\left(h\overline{v}\right) = 0, \tag{4.73}$$

$$\begin{aligned}&\frac{\partial}{\partial t}\left(h\overline{u}\right) + \frac{\partial}{\partial x}\left(h\overline{u^2}\right) + \frac{\partial}{\partial y}\left(h\overline{uv}\right)\\ &= hg_x - h\frac{u^b}{|\mathbf{u}^b|}\tan\delta\left[-g_z + \lambda\kappa\eta\overline{u^2}\right] + \varepsilon hg_z\frac{\partial b}{\partial x} - \varepsilon\frac{\partial}{\partial x}\left(h\overline{p_{xx}}\right),\end{aligned} \tag{4.74}$$

$$\begin{aligned}&\frac{\partial}{\partial t}\left(h\overline{v}\right) + \frac{\partial}{\partial x}\left(h\overline{uv}\right) + \frac{\partial}{\partial y}\left(h\overline{v^2}\right)\\ &= hg_y - h\frac{v^b}{|\mathbf{u}^b|}\tan\delta\left[-g_z + \lambda\kappa\eta\overline{u^2}\right] + \varepsilon hg_z\frac{\partial b}{\partial y} - \varepsilon\frac{\partial}{\partial y}\left(h\overline{p_{yy}}\right),\end{aligned} \tag{4.75}$$

correct to $O\left(\varepsilon^{1+\gamma}\right)$. Before continuing, let us pause and see what all these assumptions have brought us. *The left-hand sides of* (4.73)–(4.75) *are reduced to conservation form as if* x *and* y *were Cartesian coordinates*, which they are not. The right-hand sides of (4.74)–(4.75) only contain "forces" as was already the case for the simpler formulation in Chap. 3.

Note There are publications in dynamics of avalanches and debris flows, that use the Cartesian coordinates $Oxyz$, with Oxy defining the horizontal plane and Oz the vertical direction. When this is the case, the true approximations are hidden, because the non-divergent terms in (4.20) and (4.21) and subsequent equations are then missing. However, this does not only mean that those formulations are more restricted in their application than the model equations (4.73)–(4.75). Rather, they are also likely to be less accurate because they do not employ topography following coordinates. We acknowledge, however, that our equations are not strict either, because the general orthogonal coordinate system in Sect. 4.3 does not strictly follow the exact mountain topography, but only approximately.

4.7 Closure

Further reduction of equations (4.74) and (4.75) requires "constitutive information" about the pressure tensor $\mathbf{p}$ and the depth-integrated tangential velocity $\mathbf{u}$. Note that the pressure p_{zz} need only be approximated to order ε^{γ}, since it is used to simplify the depth-integrated downslope and cross-slope pressure terms $\overline{p_{xx}}$ and $\overline{p_{yy}}$, which are already order ε terms in (4.74) and (4.75).

We assume that a very simple state of stress prevails within the avalanche. Following common practice in soil mechanics, we assume that the pressures p_{xx} and p_{yy} can be expressed in terms of the overburden pressure p_{zz} with the aid of the MOHR circle. This holds at the base and at the stress free surface.

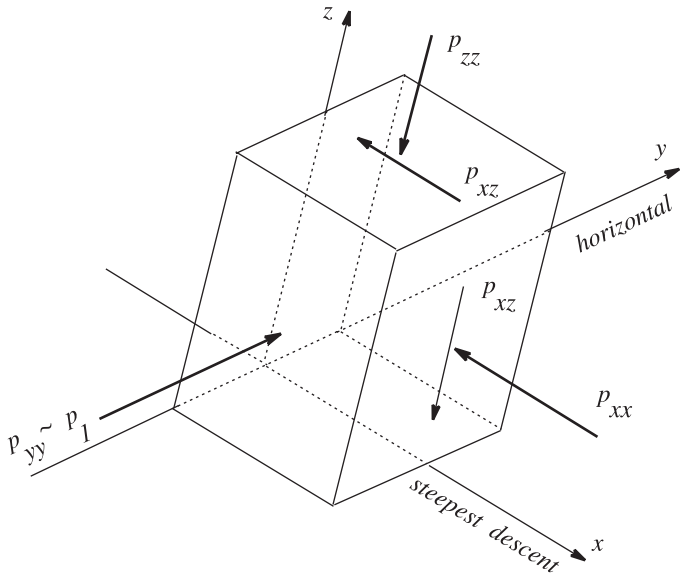

Fig. 4.8. Infinitesimal cubic element cut out of the avalanche with surfaces perpendicular to the coordinates. The motion is predominantly in the direction of steepest descent and the dominant shearing is parallel to the xz-plane. This gives rise to the dominant shear stresses p_{xz} and normal pressures p_{xx}, p_{yy}, p_{zz}. Shear stresses p_{yz} and p_{xy} also arise but are much smaller than p_{xz}. Thus, p_{yy} is approximately equal to p_1, one of the principal stresses. (When p_{yz} and p_{xy} vanish exactly, then p_{yy} is exactly p_1). The other two principal stresses, p_2 and p_3, act on surface elements of which the surface normals lie in the (xz)-plane.

Thus, its validity through depth is justified by the continuity requirement. Because the predominant shearing takes place in vertical surfaces parallel to the direction of tangential velocity, it may as a rough approximation be justified to assume that the lateral confinement pressure p_{yy} is close to a principal stress, say p_1 (see Fig. 4.8). Furthermore, it shall be assumed that one of the other principal stresses acting on the (x, z) surface, p_2 and p_3, equals p_1. This is an ad hoc assumption that is not guaranteed by any physical argument,[12] but it reduces the three MOHR circles that describe all possible combinations of normal stresses and shear stresses to only one MOHR circle as for the case in two dimensions. Thus, to a given stress state $\left(p^b_{xx}, -p^b_{xz}\right)$ at the base, two MOHR stress circles can be constructed to satisfy both the basal sliding law and the internal yield criterion simultaneously. Their construction is shown in Fig. 4.9.

[12] This assumption is equivalent to the statement that, of the three MOHR circles in a three-dimensional stress state, one circle collapses to a point.

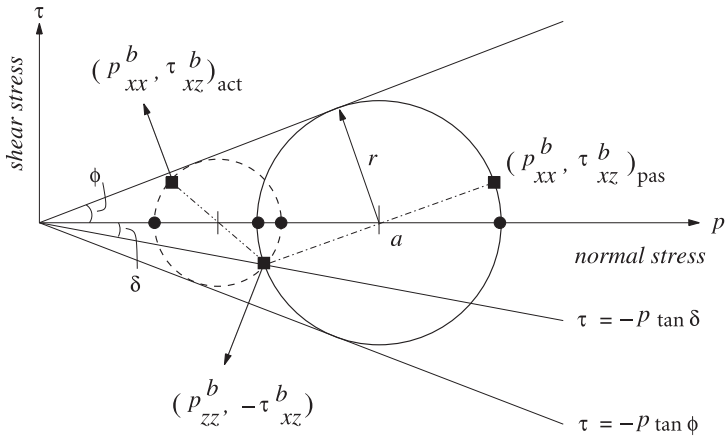

Fig. 4.9. MOHR circle diagram representing the stress state within the avalanche. The yield criterion corresponds to the two straight lines at angles $\pm\phi$ to the horizontal. Similarly, the COULOMB basal dry friction is indicated by the line at an angle $-\delta$ to the horizontal. The *passive* basal stress state is indicated by the *solid circle* of radius r and the centre at $p = a$. The circle is both tangent to the yield curves and passes through the point $(p_{zz}, -p_{zz}\tan\delta)$. The *broken line circle* represents a second *active* stress state that also satisfies these conditions. ■ indicate the possible stress states in the xz-plane, ● show possible stress states for p_{yy}.

The principal stresses p_2 and p_3 in the xz-plane are given by

$$(p_2, p_3) = \frac{1}{2}(p_{xx} + p_{zz}) \pm \frac{1}{2}\sqrt{(p_{xx} - p_{zz})^2 + 4\mu^2 p_{xz}^2}, \tag{4.76}$$

and the cross-slope principal stress is $p_{yy} = p_2$ or p_3 depending on the nature of the deformation.[13] We assume that the basal normal pressure equals p_{zz}^b and the shear stress equals $-p_{xz}^b$ [375, 376]. The basal downslope pressure p_{xx}^b can, therefore, assume two values, one on the smaller circle, $p_{xx}^b \le p_{zz}^b$, and one on the larger circle $p_{xx}^b > p_{zz}^b$, that are related to *active* and *passive* stress states, respectively. Since there are four possible values for the principal stresses, p_x^b and p_z^b, there are four values for the basal cross-slope pressure p_{yy}^b. The earth pressure coefficients K_x^b and K_y^b are defined as follows:

$$K_x^b = \frac{p_{xx}^b}{p_{zz}^b}, \quad K_y^b = \frac{p_{yy}^b}{p_{zz}^b}. \tag{4.77}$$

To determine the values of these pressure coefficients, we used (see [127, 129,

[13] The selection is made according to whether $\partial v/\partial y < 0$ or $\partial v/\partial y > 0$. If $\partial v/\partial y < 0$, then the state of stress is compressive in the y-direction and the larger of the peripheral principal stresses at the abscissa on one of the two circles must be chosen.

177]) elementary geometrical arguments and the MOHR circle representation (4.76) (see also Fig. 4.9) as a function of the internal and basal angles of friction to derive

$$K^b_{x_{\mathrm{act/pas}}} = 2\sec^2\phi\left\{1 \mp \left(1 - \cos^2\phi\sec^2\delta\right)^{1/2}\right\} - 1, \tag{4.78}$$

$$\left(K^x_{y_{\mathrm{act/pas}}}\right)^b = \frac{1}{2}\left\{\left(K^b_x + 1\right) \mp \left(\left(K^b_x - 1\right)^2 + 4\tan^2\delta\right)^{1/2}\right\}, \tag{4.79}$$

which are real for $\delta \leq \phi$. Active and passive earth pressure coefficients in downslope and cross-slope directions are plotted in Fig. 4.10 as functions of the internal friction angle for the constant bed friction angle $\delta = 20°$. Similarly, Fig. 4.11 shows active and passive earth pressure coefficients in both directions, but now as functions of the bed friction angle for the constant internal friction angle $\phi = 30°$.

Indeed, with reference to Fig. 4.9, one may write

$$\begin{aligned}
\tan^2\delta &= \left(\frac{p^2_{xz}}{p^2_{zz}}\right)_b, \\
\sin^2\phi &= \left.\frac{r^2}{\frac{1}{4}\left(p_{xx} + p_{zz}\right)^2}\right|_b = \left.\frac{\left(p_{xx} - p_{zz}\right)^2 + 4p^2_{xz}}{\left(p_{xx} + p_{zz}\right)^2}\right|_b \\
&= \frac{\left(K^b_x - 1\right)^2 + 4\tan^2\delta}{\left(1 + K^b_x\right)^2},
\end{aligned}$$

which is a quadratic equation for K_x. On the other hand, again with reference to Fig. 4.9, one has

$$p^b_{yy} = \frac{1}{2}\left(p^b_{xx} + p^b_{zz}\right) \mp \sqrt{\frac{1}{4}\left(p^b_{xx} - p^b_{zz}\right)^2 + \left(p^b_{xz}\right)^2},$$

from which, on using (4.77), (4.79) follows immediately.

Remark Obviously, for $\delta > \phi$ the earth pressure coefficients are complex-valued and the theory fails. In this case, there may be a strong shearing and the depth averaging is no longer adequate. A likely chain of transformations in this case is as follows: At the onset of the motion, strong shearing is established, which leads to violent collisional activity of the particles. This will obviously increase the mean particle distance, homogenise the velocity profile and reduce the bed friction angle to $\delta \leq \phi$.

■

To uniquely determine the value of the earth pressure coefficient associated with a particular deformation, the earth pressure coefficient K_x is defined to be *active* (upper sign) or *passive* (lower sign) according to whether the

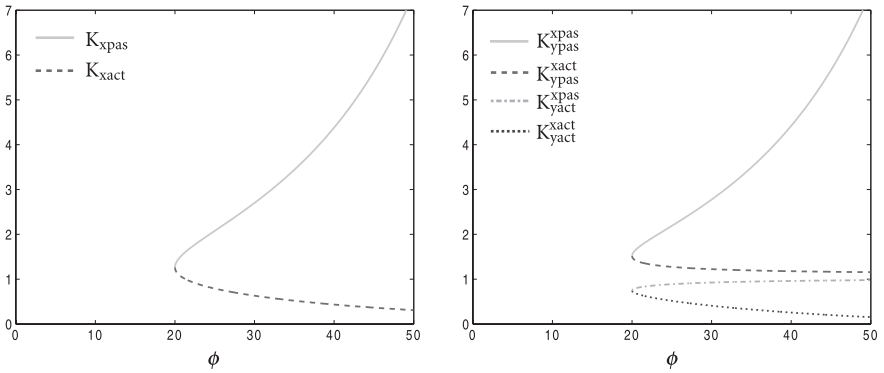

Fig. 4.10. Earth pressure coefficients: The *left panel* shows the downslope and the *right panel* the cross-slope earth pressure coefficients as functions of the internal friction angle ϕ with constant bed friction angle $\delta = 20°$.

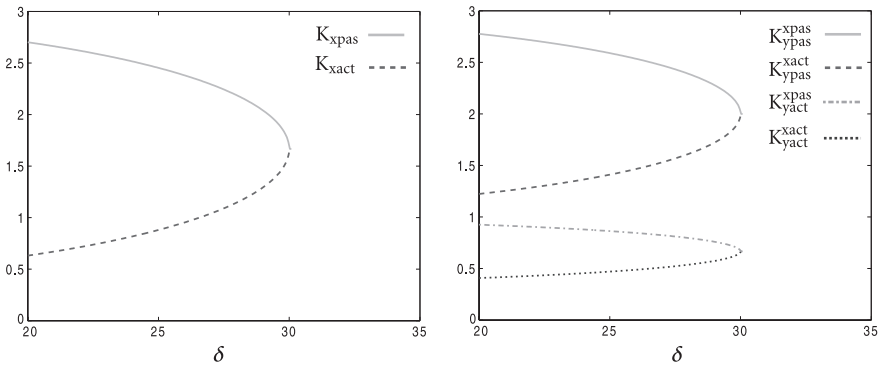

Fig. 4.11. Earth pressure coefficients: The *left panel* shows the downslope, and the *right panel* the cross-slope earth pressure coefficients as functions of the bed friction angle δ with constant internal friction angle $\phi = 30°$.

downslope motion is *dilatational* or *compressional* as given by the following equation:

$$K_x^b = \begin{cases} K_{x_{\text{act}}}, & \partial u/\partial x > 0, \\ \\ K_{x_{\text{pas}}}, & \partial u/\partial x < 0. \end{cases} \tag{4.80}$$

Analogously, the earth pressure coefficients in the lateral direction are computed by considering whether the downslope and cross-slope deformations are dilatational or compressional:

$$K_y^b = \begin{cases} K_{y_{\text{act}}}^{x_{\text{act}}}, & \partial u/\partial x > 0, \quad \partial v/\partial y > 0, \\ K_{y_{\text{pas}}}^{x_{\text{act}}}, & \partial u/\partial x > 0, \quad \partial v/\partial y < 0, \\ K_{y_{\text{act}}}^{x_{\text{pas}}}, & \partial u/\partial x < 0, \quad \partial v/\partial y > 0, \\ K_{y_{\text{pas}}}^{x_{\text{pas}}}, & \partial u/\partial x < 0, \quad \partial v/\partial y < 0. \end{cases} \tag{4.81}$$

At the traction-free surface of the avalanche $(4.42)_3$ implies $p_{zz}^s = 0$, to $O(\varepsilon)$, and so to order ε^γ the MOHR–COULOMB yield criterion collapses to a single point, and the downslope and cross-slope normal surface pressures are

$$p_{xx}^s = 0 + O(\varepsilon^\gamma), \quad p_{yy}^s = 0 + O(\varepsilon^\gamma). \tag{4.82}$$

With the values of p_{xx} and p_{zz} at the base and the free surface, intermediate values are now interpolated accordingly. We assume that the downslope and cross-slope pressures vary linearly with normal pressure through the avalanche depth. This is achieved to leading order by the following expressions:

$$p_{xx} = K_x^b p_{zz} + O(\varepsilon^\gamma), \quad p_{yy} = K_y^b p_{zz} + O(\varepsilon^\gamma). \tag{4.83}$$

Substituting for the normal pressure p_{zz} from (4.69) and integrating through the avalanche depth the depth-integrated pressures in the downslope and cross-slope directions, respectively, are given by

$$h\overline{p_{xx}} = K_x^b g_z \int_b^s (z-s)\,dz = K_x^b g_z \left[\frac{z^2}{2} - sz\right]_b^s = -\frac{1}{2} K_x^b h^2 g_z + O(\varepsilon^\gamma), \tag{4.84}$$

$$h\overline{p_{yy}} = K_y^b g_z \int_b^s (z-s)\,dz = K_y^b g_z \left[\frac{z^2}{2} - sz\right]_b^s = -\frac{1}{2} K_y^b h^2 g_z + O(\varepsilon^\gamma). \tag{4.85}$$

Remark The linearity of the pressure distributions with depth causes p_{xx}, p_{yy} and p_{zz} to depend on g_z. Thus, "hydrostatic" conditions are the basis to obtain this. The lack of mass dependence of the SH-equations may lie in this assumption.

■

4.8 Flow Profile

In a *depth-integrated hydraulic model* there is no possibility of evaluating the depth variation of the velocity. It must rather be postulated and here it is assumed that the velocity profiles are approximately uniform through the avalanche depth, so that *mostly sliding and little differential shearing* takes place. Figure 4.12 explains how the velocity of the flowing material can be idealised by considering an approximate sliding velocity at the base. In the

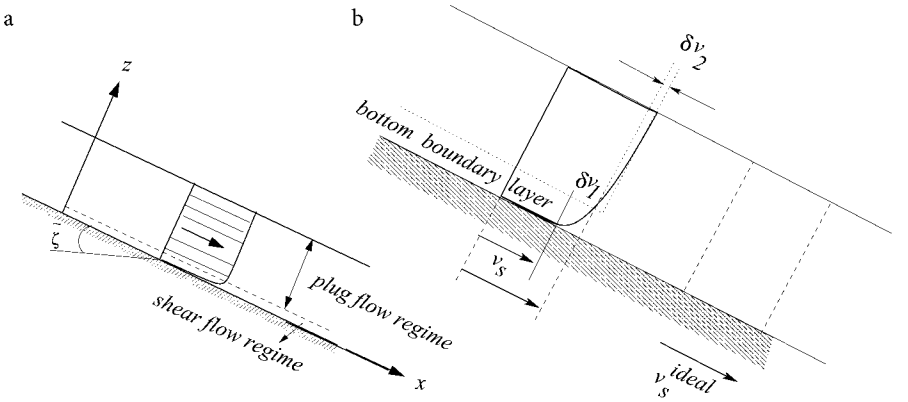

Fig. 4.12. a) Gravity-driven granular motion with a large plug flow regime lying on top of a thin shear flow regime on the basal surface. The shear layer is magnified. **b**) Velocity profile in a gravity-driven shear flow. The velocity at a certain depth is composed of a sliding contribution, v_s, strong shearing contribution for consistency in a bottom boundary layer, δv_1, and a very small shearing contribution, δv_2, in the larger top layer. In general, the velocity of flowing material can be idealised by taking an approximate sliding velocity at the base, v_s.

literature, such an assumption was first introduced by Boussinesq [41] and is mathematically written in the form

$$\overline{u} = u^b + O\left(\varepsilon^{1+\gamma}\right), \quad \overline{v} = v^b + O\left(\varepsilon^{1+\gamma}\right). \tag{4.86}$$

This means that the characteristic mean velocities in the longitudinal and lateral directions can be approximated by their basal counterparts to order $\varepsilon^{1+\gamma}$. The velocity product may then be factorised as

$$\overline{uv} = u^b v^b + O\left(\varepsilon^{1+\gamma}\right) = \overline{u}\,\overline{v} + O\left(\varepsilon^{1+\gamma}\right). \tag{4.87}$$

These assumptions are supported by measurements in different avalanches and debris flows in nature, large-scale, dry snow and artificial ping-pong ball avalanches, see, e.g., Ancey and Meunier, Dent et al., McElwaine and Nishimura [7, 80, 213, 275], as well as by small-scale laboratory granular avalanches, see Eckart et al. and Pudasaini et al. [83, 334, 343]. A detailed investigation on this will be given in Chap. 12.

Remark Consider the depth-averaged u-component of the velocity having the form

$$\overline{u^2} = \frac{1}{h}\int_b^s u^2 dz = \alpha_1 \overline{u}^2, \tag{4.88}$$

where α_1 is a constant emerging from the integration operation. Values of α_1 in this equation, which deviate from unity, give information about the deviation of the velocity profile from uniformity. For example, for a parabolic

velocity profile with vanishing basal velocity (corresponding to no sliding and all differential shear) $\alpha_1 = 6/5$, whereas for a uniform profile (all sliding and no differential shear) $\alpha_1 = 1$. Since it is likely that sliding is present, the active shear zone is confined to a thin basal layer and the velocity profile is blunt [279]. Thus, without introducing a large error one may choose $\alpha_1 \approx 1$. This justifies the presence of the $O\left(\varepsilon^{1+\gamma}\right)$-term in (4.86) and (4.87). A detailed study on this was done in [183]. This study has shown that deviation from $\alpha_1 = 1$ only influences the spreading of an avalanche in exceptional situations.

■

4.9 The Model Equations in Conservative Form

In this section, we present the final form of the model equations, proposed by PUDASAINI and HUTTER model [335], in conservative form that can be used to describe the avalanche and debris motion down arbitrarily curved and twisted channels. We will also make it clear how the new model equations can exactly be reduced to previous model equations of the SH-type. Moreover, we will outline some important features of the new model equations. Finally, we will compute the characteristic speeds and critical flows by introducing the standard conservative form of the model equations.

4.9.1 Avalanche Motions Down Curved and Twisted Channels

With (4.86) the mass balance equation (4.73) reduces to

$$\frac{\partial h}{\partial t} + \frac{\partial}{\partial x}(hu) + \frac{\partial}{\partial y}(hv) = 0, \tag{4.89}$$

which is correct to $O\left(\varepsilon^{1+\gamma}\right)$. Moreover, with the results (4.84)–(4.87), the depth-integrated downslope and cross-slope momentum balances (4.74)–(4.75) yield

$$\frac{\partial}{\partial t}(hu) + \frac{\partial}{\partial x}\left(hu^2\right) + \frac{\partial}{\partial y}(huv) = hs_x - \frac{\partial}{\partial x}\left(\frac{\beta_x h^2}{2}\right), \tag{4.90}$$

$$\frac{\partial}{\partial t}(hv) + \frac{\partial}{\partial x}(huv) + \frac{\partial}{\partial y}\left(hv^2\right) = hs_y - \frac{\partial}{\partial y}\left(\frac{\beta_y h^2}{2}\right), \tag{4.91}$$

again correct to $O\left(\varepsilon^{1+\gamma}\right)$. The factors β_x and β_y are defined as

$$\beta_x = -\varepsilon g_z K_x \quad \text{and} \quad \beta_y = -\varepsilon g_z K_y, \tag{4.92}$$

respectively. The terms s_x and s_y represent the *net driving accelerations* in the downslope and cross-slope directions, respectively, and are given by

$$s_x = g_x - \frac{u}{|\mathbf{u}|}\tan\delta\left(-g_z + \lambda\kappa\eta u^2\right) + \varepsilon g_z \frac{\partial b}{\partial x}, \tag{4.93}$$

$$s_y = g_y - \frac{v}{|\mathbf{u}|}\tan\delta\left(-g_z + \lambda\kappa\eta u^2\right) + \varepsilon g_z \frac{\partial b}{\partial y}, \tag{4.94}$$

where $|\mathbf{u}| = \left(u^2 + v^2\right)^{1/2}$ is the magnitude of the velocity field tangential to the reference (basal) topography, $\eta = \cos\left(\theta + \varphi(x) + \varphi_0\right)$, $\zeta = \sin\left(\theta + \varphi(x) + \varphi_0\right)$, $\theta = y/(\varepsilon z_T)$ and the superscript "b" has been dropped.

The first terms on the right-hand sides of (4.93) and (4.94) are due to the gravitational acceleration. The second terms represent the dry COULOMB friction in which the normal tractions comprise the overburden pressure $(-g_z)$ plus a contribution due to the curvature and torsion of the master curve $\left(\lambda\kappa\eta u^2\right)$. Finally, the third terms are the projections of the topographic variations along the normal direction. For a more extensive discussion, see PUDASAINI et al. [342]

Given the reference surface or the basal topography b, the material parameters δ and ϕ, (4.89)–(4.91), written in non-dimensional form, constitute a *two-dimensional conservative system of equations*. Equations (4.89)–(4.91) will henceforth be referred to as an *orthogonal general system* or the PUDASAINI–HUTTER model or the extended SH-model. They allow determination of three independent variables, h, the avalanche geometry, and u and v, the depth-averaged bed-parallel velocity components in the longitudinal and lateral directions, respectively, as functions of time and space, once appropriate initial and boundary conditions have been prescribed.

4.9.2 The Importance of the New Theory

(I) Reduction to the Previous Models The present theory can directly be reduced to the class of previous models of the SAVAGE–HUTTER theory. Note that in applications and numerical computations, it is convenient to take the sign of g_z to be negative.[14] With this convention, the model equations (4.89)–(4.94) can exactly reproduce the previous equations of GRAY et al. [123] as a special case. We shall prove this in the following paragraphs.

For this purpose, we consider a basal topography that is torsion-free and curved only in the downslope direction as described by the following mathematical representation:

[14] This means that the direction of z is reversed. In (4.89)–(4.94) it only affects (4.92), (4.93) and (4.94), in which g_z is replaced by $-g_z$.

$$\tilde{\zeta}(x) = \begin{cases} \tilde{\zeta}_0, & 0 \le x \le x_l, \\ \tilde{\zeta}_0 \left(\dfrac{x_r - x}{x_r - x_l} \right), & x_l \le x \le x_r, \\ 0, & x \ge x_r, \end{cases} \tag{4.95}$$

where $\tilde{\zeta}_0$ is the inclination angle[15] of the straight upper part of the reference surface, which merges continuously into a horizontal run-out plane as shown in Fig. 4.13a. $\tilde{\zeta}$ is the slope angle of the talweg with the horizontal. In this figure and the corresponding equation, x_l and x_r are the left and right end points of the continuous transition connecting the two straight parts, an upper inclined part and another horizontal part, respectively. If the topography is laterally flat, we consider the azimuthal angle θ to be very small and the distance between the reference curve and the talweg, $0\tilde{0} = z_T$, relatively large (see Fig. 4.13b). Then the components of the gravitational acceleration in the downslope, cross-slope and normal directions of the basal topography, respectively, are given by

$$g_x = \sin\tilde{\zeta}, \quad g_y = 0, \quad g_z = -\cos\tilde{\zeta}. \tag{4.96}$$

Furthermore, when the topography is flat in the lateral direction it is torsion-free, so that $\varphi(x) = 0$. We take the value of φ_0 (which in the derivation of the theory is an arbitrary constant) to be zero. Thus, we have the following additional conditions corresponding to the restricted topography considered previously by GRAY et al., WIELAND et al. [123, 445] and many others:

$$\theta = 0, \quad \varphi(x) = 0, \quad \varphi_0 = 0, \quad \eta = 1, \quad \zeta = 0. \tag{4.97}$$

With conditions (4.96) and (4.97), the model equations presented in Sect. 4.9.1 can exactly reproduce all previous model equations of the SAVAGE–HUTTER-type theory as mentioned in Chap. 3, Sect. 3.4.3. Therefore, the theory presented in this chapter, which can be applied to arbitrarily curved and twisted mountain topography and channels in industrial flow configurations, is very important both from a theoretical and application point of view.

(II) Special Features of the New Theory Previously, the SH-theory was *only directly generalised* from the one-dimensional configuration to the quasi-two-dimensional flow situations in which the talweg of the topography varies only in the vertical plane. In [335] we started the derivation of the new theory from a *completely different geometrical point of view* where not only the talweg but also the entire basal topography can be *curved and twisted*. Although this new theory was started from quite a different topographical and analytical setting, the model equations can directly be reproduced to achieve all previous relatively simple and restricted model equations.

If we consider the model equations derived by GRAY et al. [123], we immediately see that there is no mechanism that would produce and represent the

[15] Note here that $\tilde{\zeta}$ corresponds to ζ in Chap. 3.

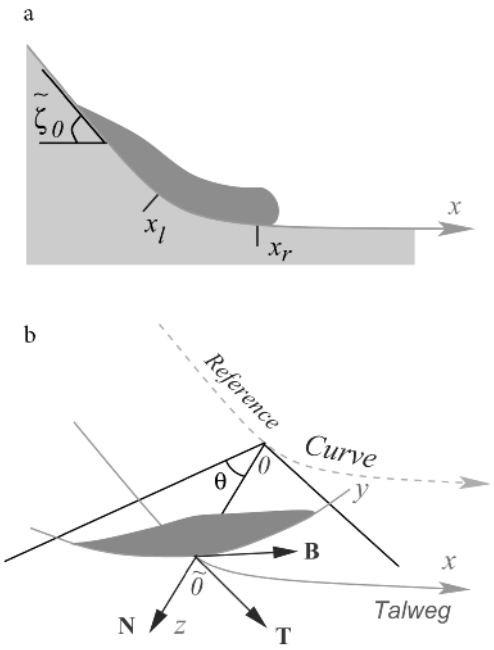

Fig. 4.13. **a**) Avalanche passing through the transition into the run-out zone in a vertical plane containing the talweg of the valley. In this picture, x_l and x_r are the left and right end points of the continuous transition between the straight inclined upper part with inclination angle $\tilde{\zeta}_0$ and horizontal run-out in the valley. **b**) For a given value of the arc length, the avalanche domain in the lateral direction occupies a region in a circular section of a plane perpendicular to the talweg of the valley and θ is the azimuthal angle in this plane. The depth of the avalanche in this section is represented by a height function (of the avalanche) that at different positions is not parallel but radial. $O\tilde{O}(= z_T)$ is the radial distance between the master (reference) curve and the talweg. The lateral coordinate, y, is determined by the transformation $y = \theta z_T$. $\{\mathbf{T}, \mathbf{N}, \mathbf{B}\}$ is the moving orthonormal unit triad following the talweg (equivalently the master curve). (From [341].)

sidewise component of the gravitational acceleration for a channelised flow. This means that these model equations can, in general, not be applied to a channelised flow, for which the talweg is a plane curve in a vertical plane. To model the channelised flow GRAY et al. superimposed a basal topography that enters into the model equations through the kinematic boundary conditions and the depth integration procedure. However, there is no term in the final governing equations that can replace the lateral component of the gravity force in a fundamental way. If the sidewise bent of the channel is strong, the lateral component of the gravity is an important factor to force the mass to concentrate along a small longitudinal vicinity of the talweg. This drawback is eliminated in the new model equations by PUDASAINI and HUTTER [335]

and is reproduced here. The physics of the sidewise motion of the avalanche is modelled by inclusion of the component of the gravitational acceleration in the lateral direction, e.g., g_y, in the first term on the right-hand side of the net driving acceleration, (4.94), in the cross-slope direction. Due to the topographic restriction, this lateral component of the gravity force always remains zero, $g_y = 0$, in the model equations derived by GRAY et al. and all previous model equations.

Of course, the non-vanishing of g_y is the result of the choice of the coordinate system. Neither that of GRAY et al. nor this one yields an y-component of the gravity force that locally corresponds to the driving force tangential to the bed, unless the bed agrees locally with the particular choice. We consider ours to be more ideally-suited to channel flows than that of GRAY et al.

4.9.3 The Standard Form of the Differential Equations

Definition A system of partial differential equations is said be of "conservative form" or of "conservative form with source" $\mathbf{s}$ if it can be written as

$$\frac{\partial \mathbf{w}}{\partial t} + \frac{\partial \mathbf{f}(\mathbf{w})}{\partial x} + \frac{\partial \mathbf{g}(\mathbf{w})}{\partial y} = \mathbf{s}(\mathbf{w}), \tag{4.98}$$

where $\mathbf{w}$, $\mathbf{f}$, $\mathbf{g}$ and $\mathbf{s}$ are vector-valued quantities. Otherwise it is said to be of non-conservative form.[16]

Now, we will write the *two-dimensional conservative system of equations* (4.89)–(4.91), with the specifications (4.92)–(4.94), in the general and "compact" vector form (4.98), where $\mathbf{w}$ denotes the vector of the *conservative veriables* and $\mathbf{f}$, $\mathbf{g}$ represent the *transport fluxes* in the x- and y-directions, respectively. Similarly, $\mathbf{s}$, on the right-hand side of the equation represents the vector of the source terms. Let us define the conservative variables as h, $m_x = hu$ and $m_y = hv$. Then, the model equations (4.89)–(4.91) can be written in the form (4.98), where $\mathbf{w}$, $\mathbf{f}$, $\mathbf{g}$ and $\mathbf{s}$ are given by

$$\mathbf{w} = \begin{pmatrix} h \\ m_x \\ m_y \end{pmatrix}, \qquad \mathbf{f} = \begin{pmatrix} m_x \\ m_x^2/h + \beta_x h^2/2 \\ m_x m_y/h \end{pmatrix},$$
$$\mathbf{g} = \begin{pmatrix} m_y \\ m_x m_y/h \\ m_y^2/h + \beta_y h^2/2 \end{pmatrix}, \qquad \mathbf{s} = \begin{pmatrix} 0 \\ h s_x \\ h s_y \end{pmatrix}. \tag{4.99}$$

The values of the terms β_x, β_y, s_x and s_y must be carried over from (4.92)–(4.94).

[16] In a strict definition of a conservative equation, $\mathbf{s}$ does not depend on $\mathbf{w}$. This ought to be so, because any first-order PDE takes the form (4.98).

4.9.4 Characteristic Speeds and Critical Flow

In order to compute the characteristic speeds of the system of (4.98) and (4.99), we rewrite it as

$$\frac{\partial \mathbf{w}}{\partial t} + \mathbf{A} \begin{pmatrix} \dfrac{\partial \mathbf{w}}{\partial x} \\ \dfrac{\partial \mathbf{w}}{\partial y} \end{pmatrix} = \mathbf{s}, \quad \mathbf{A} = (\mathbf{A}_x, \ \mathbf{A}_y), \tag{4.100}$$

where

$$\mathbf{A}_x := \frac{\partial \mathbf{f}}{\partial \mathbf{w}} = \begin{pmatrix} 0 & 1 & 0 \\ -m_x^2/h^2 + \beta_x h & 2m_x/h & 0 \\ -m_x m_y/h^2 & m_y/h & m_x/h \end{pmatrix},$$
$$\mathbf{A}_y := \frac{\partial \mathbf{g}}{\partial \mathbf{w}} = \begin{pmatrix} 0 & 0 & 1 \\ -m_x m_y/h^2 & m_y/h & m_x/h \\ -m_y^2/h^2 + \beta_y h & 0 & 2m_y/h \end{pmatrix}. \tag{4.101}$$

We now define the characteristic speeds in a spatially one-dimensional situation. To achieve this at a fixed position $\mathbf{x} = (x, y)$ in the avalanche, a rotation of the coordinate system must be performed such that in the rotated coordinate system (identified by the asterisks) (4.100) reduces to

$$\frac{\partial \mathbf{w}^*}{\partial t} + \mathbf{A}^* \begin{pmatrix} \dfrac{\partial \mathbf{w}^*}{\partial x^*} \\ \mathbf{0} \end{pmatrix} = \mathbf{0}, \quad \mathbf{A}^* = \left(\mathbf{A}_x^*, \ \mathbf{A}_y^*\right), \tag{4.102}$$

implying that the characteristic equation is now given by

$$\det\left(\mathbf{A}_x^* - \lambda \mathbf{I}_3\right) = 0. \tag{4.103}$$

Note that condition $\partial \mathbf{w}^*/\partial y^* = \mathbf{0}$ defines the rotation matrix $\mathbf{O}$ of the coordinate system,[17] see PUDASAINI et al. [337].

We restrict ourselves in this discussion to the situation where this rotation does not have to be performed, namely those lines where either $\partial \mathbf{w}/\partial y = \mathbf{0}$ or else $\partial \mathbf{w}/\partial x = \mathbf{0}$. Equation (4.103) then reads

[17] The condition $\partial \mathbf{w}^*/\partial y^* = \mathbf{0}$ in general may not even have a solution. However, when locally plane flow conditions prevail, such solutions do exist.

$$\det\left(\mathbf{A}_x - \lambda \mathbf{I}_3\right) = 0, \quad \text{and} \quad \det\left(\mathbf{A}_y - \lambda \mathbf{I}_3\right) = 0, \tag{4.104}$$

with the solutions

$$\begin{aligned} \lambda_1 &= u, \qquad \lambda_{2,3} = \frac{m_x}{h} \pm \sqrt{\beta_x h}, \\ \lambda_4 &= v, \qquad \lambda_{5,6} = \frac{m_y}{h} \pm \sqrt{\beta_y h}. \end{aligned} \tag{4.105}$$

$\lambda_{1,4}$ give as characteristic speeds the particle velocity in the x- and y-directions, respectively; alternatively, the other solutions in each case give a subcritical and a supercritical speed in the x- and y-directions, respectively.

When a finite avalanching mass of granular material moves down a steep slope and approaches the run-out zone with a supercritical speed, a considerable deceleration will suddenly occur and lead to a transition from a supercritical to a subcritical flow. Any such transition from a *supercritical* to a *subcritical* flow state produces a shock as shown in Fig. 2.8 and described in its caption, which is accompanied with changes from small heights and larger speeds to larger heights and smaller speeds. In this book, we will develop and implement shock capturing numerical schemes for this system. An explicit analysis is given in Chaps. 7–9.

4.10 Erosion and Deposition for the Full Set of Equations

In Sect. 3.6 we presented model equations with erosion and deposition for plane flow situations. Here we extend this idea for the full set of equations in the general orthogonal coordinates of this chapter. The main task is to introduce some empirical functional relation to define erosion (and deposition).

4.10.1 Inclusion of Erosion and Deposition

To take into account the erosion or deposition at the bed and accumulation (or melting) at the free surface of the avalanche, we perform the following four steps:

- Formally, define the bed profile to be time-dependent:

$$b = b(x, y, t). \tag{4.106}$$

- As in (3.82), define the Coulomb sliding law (or the dynamic boundary condition) at the bed according to

$$\mathbf{p}^b \mathbf{n}^b - \mathbf{n}^b \left(\mathbf{n}^b \cdot \mathbf{p}^b \mathbf{n}^b\right) = \left(\mathbf{u}^r / |\mathbf{u}^r|\right) \left(\mathbf{n}^b \cdot \mathbf{p}^b \mathbf{n}^b\right) \tan\delta, \tag{4.107}$$

where $\mathbf{u}^r = \mathbf{u}^{b+} - \mathbf{u}^{b-}$ is the velocity difference between the upper side of the basal interface, u^{b+}, and the basal topography, u^{b-}, on the lower side of the interface. Until now we had $u^{b-} = 0$, so there was no time-dependent basal topography.

- Add the accumulation rate d^s and the deposition (erosion) rate d^b in the kinematic boundary condition:[18]

$$s = s(x, y, t): \quad \frac{\partial s}{\partial t} + u^s \frac{\partial s}{\partial x} + v^s \frac{\partial s}{\partial y} - w^s = d^s, \tag{4.108}$$

$$b = b(x, y, t): \quad \frac{\partial b}{\partial t} + u^b \frac{\partial b}{\partial x} + v^b \frac{\partial b}{\partial y} - w^b = d^b. \tag{4.109}$$

Here, the left-hand side of (4.109) is the normal speed of the interface. Usually, the accumulation rate d^s is not important.

- Now, through depth integration these new effects enter the balance equations of mass and momentum as follows:

$$\frac{\partial h}{\partial t} + \frac{\partial}{\partial x}(hu) + \frac{\partial}{\partial y}(hv) = d^s - d^b, \tag{4.110}$$

$$\frac{\partial}{\partial t}(hu) + \frac{\partial}{\partial x}\left(hu^2\right) + \frac{\partial}{\partial y}(huv) = hs_x - \frac{\partial}{\partial x}\left(\frac{\beta_x h^2}{2}\right) - u\left(d^s - d^b\right), \tag{4.111}$$

$$\frac{\partial}{\partial t}(hv) + \frac{\partial}{\partial x}(huv) + \frac{\partial}{\partial y}\left(hv^2\right) = hs_y - \frac{\partial}{\partial y}\left(\frac{\beta_y h^2}{2}\right) - v\left(d^s - d^b\right). \tag{4.112}$$

The main new contributions are:

- The rate of change of mass (or mass production): $d^s - d^b$.
- Momentum productions along the downslope and cross-slope directions $u^s d^s - u^b d^b = u\left(d^s - d^b\right)$ and $v^s d^s - v^b d^b = v\left(d^s - d^b\right)$ in which use has been made of the fact that the velocity profile is uniform.

4.10.2 Functional Relation for Erosion and Deposition

Ordinarily, the accumulation rate at the surface, d^s, is zero. Only if accidently an avalanche were to fall onto the avalanche under consideration would a non-vanishing additional mass have to be considered from above. We shall not

[18] Note that $d^b > 0$ implies deposition. Note also that in (4.108) and (4.109) the shallowness assumption is incorporated. Indeed, an exact form of the kinematic boundary conditions (4.108) and (4.109) would be

$$\frac{\partial s}{\partial t} + u^s \frac{\partial s}{\partial x} + v^s \frac{\partial s}{\partial y} - w^s = N^s d^s, \quad N^s = \left\{1 + (\partial s/\partial x)^2 + (\partial s/\partial y)^2\right\}^{1/2},$$

$$\frac{\partial b}{\partial t} + u^b \frac{\partial b}{\partial x} + v^b \frac{\partial b}{\partial y} - w^b = N^b d^b, \quad N^b = \left\{1 + (\partial b/\partial x)^2 + (\partial b/\partial y)^2\right\}^{1/2}.$$

deal with this case. Usually, it is very difficult to find the functional relation or the expressions for both d^s and d^b. This law must involve the mechanical properties of the flowing materials, the geomorphology of the bed topography, the meteorological conditions, the geometric features of the mountain terrain and so on. However, there have been some preliminary attempts to define this quantity for real applications.

Erosion Rate Depending upon the Stress Threshold As a basic step towards a full understanding of the erosion process along the avalanche track PITMAN and others [321] defined the erosion rate as an empirical factor:

$$d^b = \begin{cases} \alpha|\mathbf{u}|; & \text{if} \quad T^\sigma \geq T^0, \\ 0; & \text{if} \quad T^\sigma < T^0, \end{cases} \tag{4.113}$$

where $|\mathbf{u}| = \left(u^2 + v^2\right)^{1/2}$ is the magnitude of the velocity parallel to the bed, T^σ is the total shear traction at a given point, T^0 is a threshold stress and α a proportionality constant to be fitted by a specific experiment or to be calibrated from the data of a field event. PITMAN and others took $d^s = 0$, because for the rapid motion of huge geomaterials, surface accumulation (such as snowfall or snowdrift during the motion) is not important.

Typical values for the two new parameters α and T^σ, taken by PITMAN and others from table-top experiments on sliding sand of about 400 g in mass over an inclined chute are $\alpha = 0.1$ (erosion rate, a non-dimensional constant) and $T^0 = 0.1$ (threshold value, dimension of stress). This means that in the erosion simulation, the threshold for the initiation of the erosion is 10% of the maximum initial pressure. Also, simulation results match experimental findings qualitatively for the case of a sliding sand pile on an inclined plane, which at a distance of 0.8 m from the top abruptly meets a horizontal plane. The total length of the experimental flat chute is about 1 m and the width is 0.5 m. A coarse sandpaper was glued on the top of the chute. To perform experiments with erosion, the plane surface was covered with a layer of sand about 1 cm thick. Since the friction angle between the sandpaper and the sand is large, this layer remains stable for the required range of inclination angles for the experiments. This erosion model was then implemented into the numerical reproduction of the 1963 rockfall avalanche at the Little Tahoma Peak [321]. That avalanche consisted of 10^7 m^3 of rock material. For the back calculations of this event, the $\alpha = 0.1$ value was fixed as in the table-top experiment, but erosion was activated whenever the shear stress was greater than 1% of the initial gravitational pressure. The final deposit with erosion was about twice as large as that without erosion. During the simulation the sliding pile swept out an area that was in good agreement with the field reconstruction of the deposit of this event.

Nevertheless, in this erosion model, PITMAN and others disregard the changes in elevation of the basal surface due to erosion, and they solve the equations of motion with a frozen bed surface. This means that changes in the basal surface slopes and curvatures induced by erosion are neglected. They also do not change the digital elevation map that defines the terrain. Therefore, the net effect of erosion consists only in changing the net mass and momentum of the avalanche. They argue that for large-scale flows this assumption is justified, but for small-scale table-top experiments the assumption may not be accurate. A similar erosion model was also introduced by MCDOUGALL and HUNGR [274] and applied in a re-analysis of the Nomash River landslide, see Chap. 10, Sect. 10.5.

Remark The erosion rate parameterisation (4.113) is certainly preliminary, but in form it resembles the entrainment rate proposed by MORTON et al. [288] in turbulent plumes. The turbulent literature is full of different entrainment parameterisations, which may serve as suggestions for analogous postulates in avalanche flows. Among others, the work of PARKER, FUKUSHIMA and PANTIN covers entrainment processes in powder snow avalanches [104, 309].

4.11 Discussion

4.11.1 Summary and Embedding of Earlier Models

Equations (4.89)–(4.91) with the precisions (4.92)–(4.94), or the equivalent system (4.98)–(4.99), comprise a hyperbolic system of partial differential equations for three unknown field quantities, h, u and v; these are representative of an avalanche thickness and downslope and cross-slope thickness averaged velocity components. The equations are formally analogous, almost identical, to those of previous derivations under (much) simpler situations, see [123, 375, 376, 445]. For $\eta = 1$ and $\zeta = 0$, which corresponds to a large distance between the master curve and the talweg and a small azimuthal angle in the cross-sectional plane, these equations reduce to those of GRAY et al. and WIELAND et al. [123, 445].

By varying the azimuthal angle and the distance between the talweg and the master curve, it is now possible to analyse the motion of avalanches in channels with different cross-sections. Another major advantage of these new model equations is that they include the effect of torsion in the avalanching motion, which was not be achieved by other previous models. Therefore, the applicability of the present model equations is by far broader than in the previous cases. This has been achieved by use of a different and appropriate coordinate system.

Obviously, for different azimuthal angles the radial directions are not parallel; at this point the present model deviates from previous ones. It implies that the earlier equations of the SH-type model with torsion-free master curves are exactly reproduced when these master curves are moved far away. Practically, the master curve does not need to be moved infinitely far away from the talweg; it suffices if $z = b(x, y, t) = O\left(\varepsilon^{-1-\eta}\right)$, $\eta > 0$ to obtain numerical coincidence.

The *careful derivation* of the model was important because it delineates its applicability by explicitly stating the underlying simplifications. These are explicitly stated in the Introduction and primarily pertain to *shallowness*, but also involve a significant *principal stress assumption* on the basis of which downslope shearing in planes parallel to the basal surface is dominant. With this assumption, the rotational invariance of the original equations is not maintained by the model equations, but this is no significant restriction, since avalanches primarily move downhill with small transverse spreading. A further important underlying assumption of the model is the *uniformity with depth of the downslope and cross-slope velocity components*. There is limited observational evidence under simpler conditions both in the field (Dent et al., Keller et al., McElwaine and Nishimura [80, 213, 275]) and the laboratory (Eckart et al. and Pudasaini et al. [83, 334, 343]) in support of this assumption. This will also be discussed in Chap. 12. Incidentally, the assumption is popular in fluid mechanics and corresponds to the neglect of the correlation integrals of velocity differences from uniformity akin to the omission of the Reynolds stresses in turbulence theory. This analogy, however, is merely formal with no physical bearing to turbulence. Assuming power law distributions of the velocity with depth will show that $\overline{u^2} = \alpha\left(\overline{u}\right)^2$ with $1 \leq \alpha \leq 1.2$, where the upper value applies for a parabolic distribution. Measured velocity profiles are much closer to uniformity than parabolas (see [83, 183, 334, 343]) and so α is very close to unity.

The underlying assumptions described above are important ingredients of the model to reduce the governing partial differential equations to conservation form. They eliminate all Christoffel symbols that would "destroy" the conservation property of the emerging equations. This is mathematically and numerically pleasing, since established methods exist for conservation equations to prove existence of solutions and convergence of numerical integration schemes including those of *front-tracking* and *shock-capturing*. In spite of this, (4.98)–(4.99) are still a challenge both to mathematical and numerical analysts. The equations involve coefficients (e.g., the earth pressure coefficient) that may be discontinuous when the flow changes from diverging to converging conditions. To our knowledge, mathematicians are still trying to prove the existence of solutions under such general prerequisites.

Nevertheless, for strictly diverging flow conditions, the equations allow the construction of restricted similarity solutions analogous to those already constructed by SAVAGE and HUTTER [375]. Such parabolic cap and M-wave solutions are explicitly presented by PUDASAINI et al. in [337, 338]. We believe them to be important despite their simplicity, because they demonstrate well-posedness under at least restricted conditions and may, furthermore, be used to partly verify a code for their numerical integration [412]. For more details, see Chap. 5.

At this point, it is worthwhile to have a systematic comparison of the model equations of this chapter with the previously developed model presented in the last chapter.

4.11.2 The Orthogonal Complex vs. the Orthogonal General System

In situations when the talweg is a curve in a vertical plane, it has already been proven (for instance, see [123, 445]) that this system, called the *orthogonal complex system* can reproduce laboratory experiments to a very good approximation. The equations derived in these papers were also used to reproduce the flow of a granular avalanche down a channel with a rather *slowly* meandering talweg with fair to good agreement of experimental and computational findings [121]. All this is demonstrated in Chap. 10. The major problem in extending this model was to introduce non-uniform curvature *and* torsion in the metric that describes the whole flow behaviour. It is made possible by using the *orthogonal general system* of equations derived in this chapter. In many cases, the orthogonal complex system seems to be very useful. Nevertheless, in general, the orthogonal general system may serve as a good theoretical foundation in order to investigate the flow of granular masses in more complicated topographies. Here, we discuss the connection and differences between these two theories.

- **Broad Applicability** The general equations (4.89)–(4.91) with the specifications (4.92)–(4.94) are analogous to the equations obtained in the previous derivations (3.33)–(3.35), see also [123, 175, 445]. However, this general system of equations can be applied over a large variety of topographies. It is made possible by the choice of an arbitrarily varying orthogonal coordinate system along the talweg of the valley. For this reason, these new model equations can be used in realistic flow situations both in nature and in industrial applications.
- **Introduction of Non-Uniform Curvature and Torsion** The key idea was the use of an orthogonal curvilinear moving coordinate system that is based on a master line in three dimensions that exhibits *non-uniform curvature and torsion*. The talweg of a valley (possibly shifted a cer-

tain distance in the normal or vertical direction) or the axis of a three-dimensionally curved and twisted channel or pipe may be the basis for the construction of this master curve. Planes perpendicular to this master curve give rise to the introduction of a polar coordinate system within these planes, of which the origin is the intersection point with the master curve. The topographic profile of the avalanche within these planes can be described in terms of these polar coordinates; the normal (radial) direction determines the direction of the height, the cross-slope (azimuthal) direction embraces its width. A shift in the normal coordinate makes it possible to bring the origin of the coordinate system down in the valley to a point in the talweg.

- **Flexible and More Realistic** The advantage of the formulation of a model of depth-integrated avalanche equations of this chapter lies in its flexibility of application. The flow down an inclined plane or within a channel whose the axis lies in a vertical plane but may be curved and the flow of a granular avalanche in a helicoidal channel of arbitrary cross-section can be described as can the flow down mountain valleys with arbitrarily curved and twisted talwegs. It is this last application that motivated us to derive this model, because it is ideally-suited to application in realistic situations in connection with the use of *geographical information and visualisation systems* (GIVS).

4.12 Concluding Remarks and Future Outlook

The above discussion should have made it convincingly clear that the proposed model equations (4.89)–(4.91) are suitable for the prediction of avalanche flows of granular materials down arbitrarily curved and twisted tracks. Since the equations reduce to earlier models for which the extended SAVAGE–HUTTER-theory has been demonstrated to reproduce results from laboratory experiments well, there is no question about the validity and the applicability of the new theory. The theory presented in this chapter is to date probably *one of the most sophisticated and most advanced theories* in the field of dry granular avalanche research. The model equations have numerous applications in geophysical and industrial avalanches.

The next and immediate goal for researchers may be to perform numerical simulations with the intention of providing a general purpose software for practitioners involved with the prediction of avalanche run-out in mountainous regions. The intention should be the use of *geographical information systems* (GIS) from which digitised realistic topographies in mountainous regions are available. With these GIS particular avalanche prone subregions can be selected and for individual sites the master curve and the cross-sectional topography constructed. From a preselected release of a finite mass of gravel, sand or snow at a breaking zone it is then intended to determine the flow

from initiation to run-out. This step requires numerical integration via an avalanche purpose software using total-variation-diminishing non-oscillating or shock-capturing schemes. Its output can, in a final step, be used in visualisation software to identify endangered zones. A multitude of applications will then be at the disposal of practitioners to investigate with the software. Needless to say that a comparison with photographic observational data in the field taken from helicopters and airplanes, or digital video cameras positioned at a fixed station, or the satellite data, then will become possible and more reliable.

5 Exact and Semi-Exact Solutions of the Model Equations

5.1 Solutions of the Model Equations

There are basically two fundamental approaches by which knowledge and understanding in any field of research in science and technology is acquired. The first is to understand the physics and nature of the physical phenomena and to put them into proper form, usually as a mathematically expressible system of equations. The system of equations must exhibit certain obvious properties, e.g., it must be well-posed and possess a solution; if it does, it is commonly called a *model*. With the model equations at hand, the next important step is to solve them and to interpret them either by comparing them with observations or by comparing such solutions with experience known already prior to the development of the model. Both steps are equally significant from a physical point of view for applications in real-life problems. There are three main ways of solving a set of model equations, which we shall now briefly outline.

5.1.1 A Complete Analytical Solution

First, one should try to solve the full set of model equations analytically with all principal parameters and boundary and initial values left as general as possible. Such a solution, if one is able to compute it analytically and explicitly, is superior to all other possible solutions, because analytical solutions provide qualitative insight and usually enhance the general understanding. Unfortunately, construction of a general analytical solution is almost impossible, at least in complicated cases such as geophysical flows. This is the actual case in the formulation of the original SH-theory, all of its further extensions[1] and also other models, see, e.g., [38, 40, 74, 75, 163, 191, 194, 273, 274, 321, 323]. This is clearly due to the complexity of the non-linear partial differential equations and the moving boundary conditions, which together describe the

[1] For the development of and detailed studies on such models we refer the reader to [123, 128, 129, 173, 175, 176, 177, 179, 227, 301, 335, 336, 337, 338, 375, 376, 445].

dynamic behaviour of flow avalanches from simple to complicated topographies. One must find a way to avoid this complication.

5.1.2 Particular Solutions

This special way, in fact, must be sought in almost all situations, since exact analytical solutions can usually only be obtained for some special cases. If these solutions turn out to be problem-significant, they will provide crucial insight into the full system. Such special exact analytical solutions are important, because (*i*) they can in many cases predict phenomena that are observable in nature, (*ii*) they may help in comparing results with corresponding results obtained from other existing models, and (*iii*) they are crucial to test the efficiency and applicability of numerical solutions. Here we will construct some analytical and semi-analytical[2] solutions.

In this second step, one simplifies the complicated equations by, e.g., substituting typical values for the parameters, by considering the problem for some particular situations like steady-state and homogeneous flows, by decreasing the dimension of the problem or specifying the conditions of the environment (boundary and initial conditions). In such situations, one may then find exact analytical solutions of some particular type. Although such solutions cannot describe the behaviour of the posed problem in a full form, they are still important to provide some qualitative insight into its behaviour. Furthermore, such solutions may also be useful to analyse numerical schemes. Below we will address this possibility.

5.1.3 Numerical Solutions

Thirdly, and this is today probably most the popular and convenient way, one seeks to solve the complicated system of equations by numerical techniques. With the growing development of hardware and software, and with the rapid increase of numerical and scientific computing techniques, this method has become a dominant approach in analysing systems *expressible in standard mathematical form*. This is no different for the SH-theory. Its original equations [375] and all of its further developments have successfully been solved by applying different numerical techniques, and the results have been tested against reliable indoor and outdoor laboratory experiments, as well as natural events such as avalanches and debris flows and rockslides; good to excellent agreement has been found between theoretical and experimental results. These procedures are so important in the development of the theory that

[2] A solution is called semi-analytical, if either some steps are performed computationally or ad hoc assumptions are introduced in the process of solution.

we will discuss the numerical techniques and the experiments in detail in Chap. 7.

Let us begin with the presentation of the simplest possible form of (analytical) solutions that still reflect the motion of avalanches, the *similarity solutions*. There are several forms of these in one and two spatial dimensions, exhibiting sidewise confined or unconfined flows. As we shall see, these solutions provide a surprisingly large amount of qualitative information that enhances the understanding of the underlying physics, information that could otherwise be obtained only by relatively cumbersome output of numerical computations. Apart from this basic information, the solutions presented in this chapter also provide a first understanding of the dynamics of avalanching flows.

5.2 One-Dimensional Similarity Solutions

Imagine the situation that a finite mass of granular material in a narrow chute initially has a parabolic longitudinal shape and is then released to evolve. The question is, does this mass upon release, perhaps, preserve its shape, thus remain a parabola and only change its aspect ratio? It has been shown that such similarity solutions do indeed exist. The forms of the preserving geometries are in this case indeed parabolas and the evolution of their length is described by a system of non-linear ordinary differential equations in time. The main conclusions that are deducible from these computations are that these results demonstrate useful quantitative physical behaviour but do not indicate whether similarity solutions can be in any way suitable for prognostic purposes [174].

Savage and Hutter [375] constructed some similarity solutions of permanent shape for the depth-integrated spatially one-dimensional equations of motion. They found two such solutions and called them *parabolic cap* and *M-wave* similarity solutions. They were constructed for a chute of constant inclination using a Cartesian coordinate system and for a constant bed friction angle. These solutions were later extended to more general cases [63, 97]. Here we will follow this spirit.

In this section, we consider the system of equations of motion (3.33), (3.43) and (3.44) developed for complex basal topography by Gray et al. [123].

5.2.1 One-Dimensional Flow Down Inclined Planes

In the following computations, we will consider the flow of granular materials down an inclined plane. The flow is one-dimensional and lies in a vertical plane. For diverging motions the avalanche always extends. Thus, no shocks

will form. This explicitly means that the downslope velocity is always positive, $u > 0$, and $\mathrm{sgn}(u) = 1$. Also, in real situations the variations of the downslope earth pressure coefficient with respect to the downslope coordinate are small. With these assumptions the model Eqs. (3.33), (3.43) and (3.44) reduce to the following standard non-conservative form:

$$\frac{\partial h}{\partial t} + \frac{\partial}{\partial x}(hu) = 0, \quad \frac{\partial u}{\partial t} + u\frac{\partial u}{\partial x} + \beta\frac{\partial h}{\partial x} = s_x, \tag{5.1}$$

where $\beta = \varepsilon \cos\zeta K_x, s_x = \cos\zeta(\tan\zeta - \tan\delta)$. A detailed derivation can also be found in [125, 337, 338, 375]. Ancey, Chugunov et al. and Farwig equally constructed similarity solutions that go beyond those presented here [8, 63, 97].

Consider a point within the moving avalanche for which $\partial h/\partial x = 0$, identify it with the location of the *avalanche centre of mass* and employ the index m as its identifier. For this point $(5.1)_2$ reduces to

$$\frac{du_m}{dt} = s_x, \quad \frac{d}{dt} = \frac{\partial}{\partial t} + u_m\frac{\partial}{\partial x}.$$

Thus, the velocity of the centre of the avalanche is

$$u_m(t) = u_{m_0} + \int_0^t s_x dt', \tag{5.2}$$

and it translates the distance

$$x_m(t) = x_{m_0} + \int_0^t u_m(t')\,dt', \tag{5.3}$$

in time t. Next define, a new *moving coordinate system* (ξ, t) that translates with the *centre of mass velocity*, and the *relative velocity* $\tilde{u}$ in this coordinate system,

$$\xi = x - x_m(t), \quad \tilde{u} = u - u_m(t). \tag{5.4}$$

We are looking for solutions of (5.1) having a *symmetric avalanche thickness distribution* and a *skew symmetric relative velocity distribution* about $\xi = 0$, i.e.,

$$h(\xi, t) = h(-\xi, t), \quad \tilde{u}(\xi, t) = -\tilde{u}(-\xi, t). \tag{5.5}$$

With these restrictions the *front* and *rear* of the avalanche always lie at $\xi_F = g(t)$ and $\xi_R = -g(t)$, respectively, see Fig. 5.1.

To find particular solutions to this *moving boundary value problem* we apply a *fixed domain mapping* by which the span interval is mapped onto a fixed interval with variable η. η has values in the fixed domain $[-1, 1]$, with $\eta = \pm 1$ for the front and rear margins and $\eta = 0$ for the (moving) centre of the avalanche. In this way, we define new coordinates (see Fig. 5.1), namely

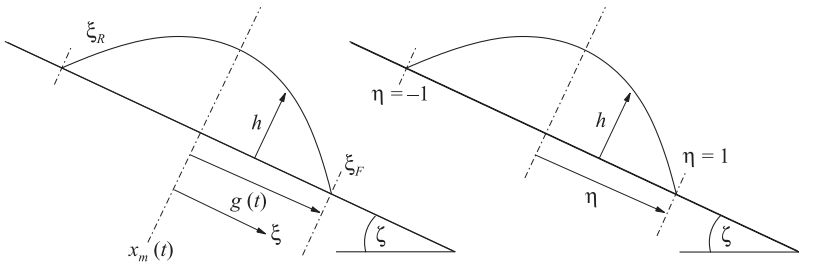

Fig. 5.1. Mapping from the moving coordinate ξ, *left*, to the fixed domain η, *right*.

$$\eta := \frac{\xi}{g\,(t)} = \frac{[x - x_m\,(t)]}{g\,(t)}, \qquad \tau := t, \tag{5.6}$$

where g is the spreading factor (i.e., half the length) of the support of the avalanche. With this change of variables, the differential operators reduce to

$$\begin{aligned}
\frac{\partial}{\partial t} &= \frac{\partial}{\partial \tau}\frac{\partial \tau}{\partial t} + \frac{\partial}{\partial \eta}\frac{\partial \eta}{\partial t} = (1)\frac{\partial}{\partial \tau} + \frac{\partial}{\partial t}\left(\frac{x - x_m(t)}{g(t)}\right)\frac{\partial}{\partial \eta} \\
&= \frac{\partial}{\partial \tau} + \left\{\frac{-x_m'(t)g(t) - (x - x_m(t))\,g'(t)}{g^2(t)}\right\}\frac{\partial}{\partial \eta} \\
&= \frac{\partial}{\partial \tau} - \left\{\frac{u_m}{g} + \eta\frac{g'}{g}\right\}\frac{\partial}{\partial \eta}, \\
\frac{\partial}{\partial x} &= \frac{\partial}{\partial \eta}\frac{\partial \eta}{\partial x} + \frac{\partial}{\partial \tau}\frac{\partial \tau}{\partial x} = \frac{\partial}{\partial \eta}\frac{\partial \eta}{\partial x} + (0)\frac{\partial}{\partial \tau} \\
&= \frac{\partial}{\partial x}\left(\frac{x - x_m(t)}{g(t)}\right)\frac{\partial}{\partial \eta} = \frac{1}{g}\frac{\partial}{\partial \eta}.
\end{aligned}$$

i.e.,

$$\frac{\partial}{\partial t} = \frac{\partial}{\partial \tau} - \left(\eta\frac{g'}{g} + \frac{u_m}{g}\right)\frac{\partial}{\partial \eta}, \qquad \frac{\partial}{\partial x} = \frac{1}{g}\frac{\partial}{\partial \eta}, \tag{5.7}$$

with $g' = dg/d\tau$. With these operators, the left-hand side of $(5.1)_1$ can be rewritten as

$$\begin{aligned}
&\frac{\partial h}{\partial t} + \frac{\partial}{\partial x}(hu) \\
&= \left(\frac{\partial}{\partial \tau} - \left(\eta\frac{g'}{g} + \frac{u - \tilde{u}}{g}\right)\frac{\partial}{\partial \eta}\right)(h) + \frac{1}{g}\frac{\partial}{\partial \eta}(hu) \\
&= \frac{\partial h}{\partial \tau} - \left(\eta\frac{g'}{g} + \frac{u - \tilde{u}}{g}\right)\frac{\partial h}{\partial \eta} + \frac{h}{g}\frac{\partial u}{\partial \eta} + \frac{u}{g}\frac{\partial h}{\partial \eta} \\
&= \frac{\partial h}{\partial \tau} + \frac{1}{g}\left(\tilde{u} - \eta g'\right)\frac{\partial h}{\partial \eta} + \frac{h}{g}\frac{\partial u}{\partial \eta}.
\end{aligned}$$

A similar transformation can be made with the left-hand side of $(5.1)_2$

$$\begin{aligned}
&\frac{\partial u}{\partial t}+u\frac{\partial u}{\partial x}+\beta\frac{\partial h}{\partial x}=\left(\frac{\partial}{\partial\tau}-\left(\eta\frac{g'}{g}+\frac{u_m}{g}\right)\frac{\partial}{\partial\eta}\right)(u)+u\frac{1}{g}\frac{\partial u}{\partial\eta}+\beta\frac{1}{g}\frac{\partial h}{\partial\eta}\\
&=\left(\frac{\partial}{\partial\tau}-\left(\eta\frac{g'}{g}+(u-\tilde{u})\frac{1}{g}\right)\frac{\partial}{\partial\eta}\right)(u)+u\frac{1}{g}\frac{\partial u}{\partial\eta}+\beta\frac{1}{g}\frac{\partial h}{\partial\eta}\\
&=\left(\frac{\partial}{\partial\tau}+\frac{1}{g}(\tilde{u}-\eta g')\frac{\partial}{\partial\eta}\right)u+\frac{\beta}{g}\frac{\partial h}{\partial\eta}\\
&=\left(\frac{\partial}{\partial\tau}+\frac{1}{g}(\tilde{u}-\eta g')\frac{\partial}{\partial\eta}\right)(\tilde{u}+u_m)+\frac{\beta}{g}\frac{\partial h}{\partial\eta}\\
&=\frac{\partial\tilde{u}}{\partial\tau}+\frac{1}{g}(\tilde{u}-\eta g')\frac{\partial\tilde{u}}{\partial\eta}+\frac{\beta}{g}\frac{\partial h}{\partial\eta}+\frac{\partial u_m}{\partial\tau}+\frac{1}{g}(\tilde{u}-\eta g')\frac{\partial u_m}{\partial\eta}\\
&=\frac{\partial\tilde{u}}{\partial\tau}+\frac{1}{g}(\tilde{u}-\eta g')\frac{\partial\tilde{u}}{\partial\eta}+\frac{\beta}{g}\frac{\partial h}{\partial\eta}+s_x+0,
\end{aligned}$$

in which $\partial u_m/\partial\tau = s_x$ from $(5.1)_2$, since $(\partial h/\partial x)\big|_{x=x_m} = 0$, and $\partial u_m/\partial\eta = 0$, since u_m does not depend on η. Hence, the non-conservative system (5.1) may, alternatively, be written as

$$\begin{aligned}
&\frac{\partial h}{\partial\tau}+\frac{1}{g}(\tilde{u}-\eta g')\frac{\partial h}{\partial\eta}+\frac{h}{g}\frac{\partial\tilde{u}}{\partial\eta}=0,\\
&\frac{\partial\tilde{u}}{\partial\tau}+\frac{1}{g}(\tilde{u}-\eta g')\frac{\partial\tilde{u}}{\partial\eta}+\frac{\beta}{g}\frac{\partial h}{\partial\eta}=0,
\end{aligned}\tag{5.8}$$

and shows that explicit knowledge of the net driving force is not necessary.

The Parabolic Cap Solution The above (5.8) serve as the basis for the construction of the similarity solution of the reduced system of equations (5.1). "Technically", similarity solutions are obtained if one succeeds in transforming the partial differential equations (5.8) to ordinary differential equations. The transformed system (5.8) can be simplified considerably by assuming that the velocity profile has a solution of the form

$$\tilde{u}=\eta g'.\tag{5.9}$$

This states that the *difference velocity relative to the velocity of the centre of mass varies linearly with the distance from the centre.* The sign of g' will define whether the flow is diverging or compacting. Using (5.9), the momentum balance equation $(5.8)_2$ reduces to

$$\frac{\partial h}{\partial\eta}=-\frac{gg''}{\beta}\eta.\tag{5.10}$$

Integration subject to the boundary conditions that $h(\eta = \pm 1) = 0$ implies that the avalanche thickness has a *parabolic* profile,

$$h = \frac{gg''}{2\beta}(1 - \eta^2), \tag{5.11}$$

with vanishing thickness at the margins and maximum thickness at the centre. Substituting the assumed velocity profile (5.9) and the computed thickness profile (5.11) into the mass balance $(5.8)_1$ yields an ordinary differential equation for the *spreading*, g, of the avalanche,

$$\left(\frac{1-\eta^2}{2\beta}\right)\frac{\partial}{\partial\tau}\left(gg''\right) + \left(\frac{1-\eta^2}{2\beta}\right)g''\frac{\partial}{\partial\eta}\left(\eta g'\right) = 0.$$

This implies

$$\left(gg''\right)' + g'g'' = 0, \tag{5.12}$$

and thus

$$\frac{g'''}{g''} = -2\frac{g'}{g}. \tag{5.13}$$

Integrating this yields

$$g^2 g'' = A, \tag{5.14}$$

where A is a constant. As the pile is assumed to be of finite size and there is no mass transfer, the total volume, V, must be conserved,

$$V = \int_{\xi_R}^{\xi_F} h\left(\xi, t\right) d\xi = \int_{-1}^{+1} h\left(\eta, \tau\right) g(\tau) d\eta. \tag{5.15}$$

Substituting for the thickness expression (5.11) and integrating determines the unknown constant A in (5.14),

$$V = \int_{-1}^{+1} \frac{gg''}{2\beta}\left(1 - \eta^2\right) g d\eta = \frac{g^2 g''}{2\beta}\left[\eta - \frac{\eta^3}{3}\right]_{-1}^{+1} = \frac{2g^2 g''}{3\beta},$$

implying

$$g^2 g'' = \frac{3}{2}\beta V = A, \tag{5.16}$$

relating the constant of integration, A, to volume V and to β. Initially the front and the rear of the avalanche are assumed to lie at $\xi = \pm 1$, and the difference velocity relative to the velocity of the centre of mass is zero throughout the pile. This is equivalent to the conditions

$$g(0) = 1, \quad g(0)' = 0. \tag{5.17}$$

We next integrate (5.14). Changing the independent variable from τ to g and making the substitution $p = g'$, (5.16) becomes

$$p\frac{dp}{dg} = \frac{A}{g^2}. \tag{5.18}$$

This can be integrated subject to (5.17) to give

$$p^2 = 2A\left(1 - \frac{1}{g}\right), \tag{5.19}$$

and since $p = dg/d\tau$, this is equivalent to the separable equation

$$\frac{\sqrt{g}}{\sqrt{g-1}}\frac{dg}{d\tau} = \sqrt{2A}. \tag{5.20}$$

Substituting $g = \omega^2$ transforms the term on the left-hand side into standard integrable form with the solution

$$\sqrt{g(g-1)} + \ln\left|\sqrt{g} + \sqrt{g-1}\right| = \sqrt{2A}\tau = \sqrt{3\beta V}\tau, \tag{5.21}$$

defining τ as a function of g, see, e.g., [81, 119]. Figure 5.2 displays the function $g(\tau)$ for various values of β, see PUDASAINI et al. [337]. For $g \to \infty$, the left-hand side of (5.21) is equivalent to g. This implies

$$g \sim \sqrt{2A}\tau, \quad \text{as} \quad g \to \infty. \tag{5.22}$$

Thus, the spread grows rapidly at first and becomes linear in time as time increases. To summarise, with the help of (5.16) and (5.20), the thickness and velocity solutions can be written in parametric form as follows:

$$\begin{aligned} \tilde{u} &= g'\eta = \eta\sqrt{2A\,(1-1/g)} = \eta\sqrt{3\beta V(1-1/g)}, \\ h &= \frac{gg''}{2\beta}\left(1-\eta^2\right) = \frac{A}{2\beta g}\left(1-\eta^2\right) = \frac{3}{4}\frac{V}{g(\tau)}\left(1-\eta^2\right). \end{aligned} \tag{5.23}$$

Figure 5.3 displays the temporal evolution of $h\,(\eta, \tau)$ [337]. The results, expressed by (5.22) and (5.23), state that for large time the avalanche spread increases linearly with time, $g \sim \tau$, its height decreases as $g^{-1} \sim \tau^{-1}$ and its difference velocity (for fixed η) remains constant. In other words, on an infinitely long inclined chute, a finite granular mass having a parabolic cap profile accelerates indefinitely, and simultaneously spreads asymptotically linearly in time, thereby equally thinning to preserve the volume. Still otherwise stated: *there is no steady state motion of a finite mass developing into a parabolic cap.* This is a property of COULOMB friction on a plane surface.

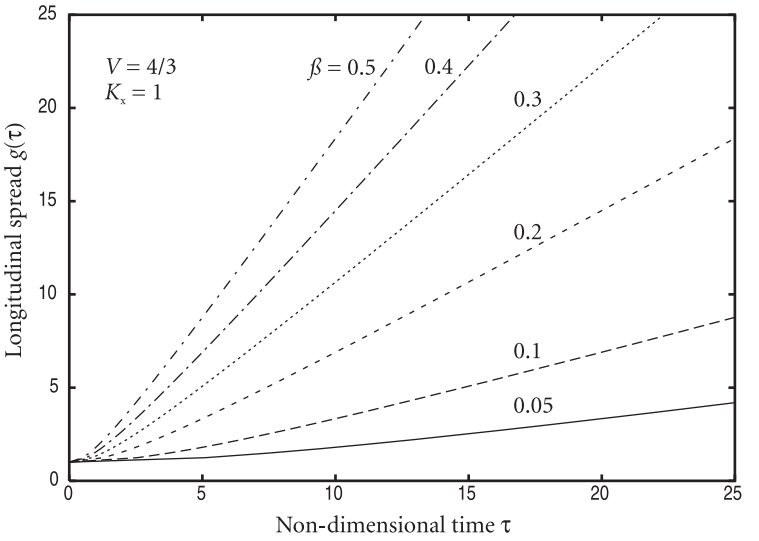

Fig. 5.2. The spreading factor g for different parameter values of $\beta = \varepsilon K_x \cos\zeta$ and $V = 4/3, K_x = 1$. (From [337].)

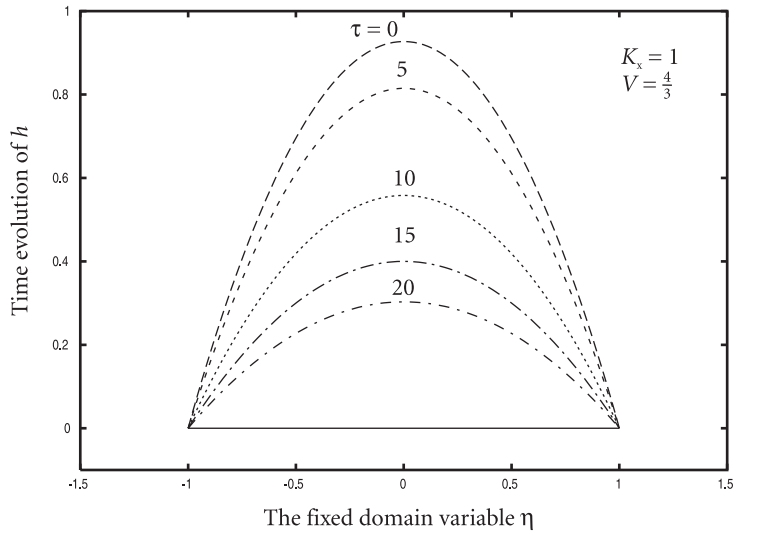

Fig. 5.3. The time and space evolution of the parabolic cap similarity solution. (From [337].)

The M-Wave Solution The transformed system (5.8) can also be solved by seeking a separable variable solution of the form

$$h = l(\tau)H(\eta), \qquad \tilde{u} = k(\tau)F(\eta). \tag{5.24}$$

Substituting these relations into (5.8) yields the following two ordinary differential equations for the new functions H and F:

$$\begin{aligned} H - \eta\frac{g'l}{gl'}H' + \frac{kl}{gl'}(HF)' = 0, \\ F - \eta\frac{g'k}{gk'}F' + \frac{k^2}{gk'}FF' + \frac{\beta l}{gk'}H' = 0, \end{aligned} \tag{5.25}$$

where $(\cdot)' = d(\cdot)/d\eta$ for H and F, but $(\cdot)' = d(\cdot)/d\tau$ for g, l and k. Assuming all quotients

$$\frac{g'l}{gl'}, \quad \frac{kl}{gl'}, \quad \frac{g'k}{gk'}, \quad \frac{k^2}{gk'}, \quad \frac{l}{gk'}, \tag{5.26}$$

to be constants and seeking power solutions of the form

$$g = \tau^{\alpha}, \quad l = \tau^{\gamma}, \quad k = \tau^{\varsigma}, \tag{5.27}$$

the coefficients in (5.26) are all indeed time-independent and (5.25), therefore, indeed ordinary differential equations provided that

$$\gamma = 2\varsigma, \quad \varsigma = \alpha - 1. \tag{5.28}$$

A third relationship follows from the conservation of the total volume

$$\int_{-1}^{+1} h(\eta,\tau)g(\tau)d\eta = \tau^{\alpha+\gamma}\int_{-1}^{+1} H(\eta)d\eta, \tag{5.29}$$

which is also time-independent provided that

$$\alpha + \gamma = 0. \tag{5.30}$$

The three linear equations (5.28) and (5.30) are easily solved to give

$$\alpha = \frac{2}{3}, \quad \gamma = -\frac{2}{3}, \quad \varsigma = -\frac{1}{3}. \tag{5.31}$$

Using (5.31) and substituting the power solutions (5.27) into the governing equations (5.25), two ordinary differential equations for H and F are obtained, namely

$$\left(F - \frac{2}{3}\eta\right)' H + \left(F - \frac{2}{3}\eta\right) H' = 0, \tag{5.32}$$

$$\left(F - \frac{2}{3}\eta\right) F' + \beta H' = \frac{1}{3}F. \tag{5.33}$$

The first may be integrated directly to give

$$\left(F - \frac{2}{3}\eta\right) H = C, \tag{5.34}$$

where C is a constant of integration. Substituting (5.34) into (5.33), a single ordinary differential equation is obtained for the thickness profile,

$$H' = \frac{H^2}{9}\left(\frac{2\eta H - 3C}{\beta H^3 - C^2}\right). \tag{5.35}$$

The symmetry requirement in the fixed domain mapping (5.5) dictates that $H(\eta) = H(-\eta)$ and $H'(\eta) = -H'(-\eta)$. Applying these conditions to (5.35) implies that

$$C = 0, \tag{5.36}$$

and the solution is simply

$$F = \frac{2}{3}\eta, \qquad H = \frac{1}{9\beta}\left(h_m + \eta^2\right), \tag{5.37}$$

where h_m is assumed to be greater than zero as it is the thickness at the centre of the avalanche. It follows that the thickness and the velocity profiles are

$$h = \frac{1}{9\beta}\tau^{-2/3}\left(h_m + \eta^2\right), \qquad \tilde{u} = \frac{2}{3}\tau^{-1/3}\eta, \tag{5.38}$$

where h_m must be positive because the pile will not develop into two separate piles. It can be connected to the (constant) avalanche volume V by stating that $\int_{-1}^{1} h(\eta)d\eta = V$, the result being

$$V = \frac{2}{9\beta}\left(d_m - 1 + \frac{1}{3}\right) = \frac{2}{9\beta}\left(h_m + \frac{1}{3}\right), \tag{5.39}$$

where $d_m = h_m + 1$ is the normalised depth of the avalanche margin and thus automatically greater than zero. The results (5.38) show that the depth distribution is parabolic but with increasing depth as one moves away from the centre and maximum thicknesses arising at the margins. Furthermore, the difference velocity varies linearly with distance from the centre. This latter result is analogous to the corresponding behaviour of the parabolic cap. However, the thickness distribution is different, not like a cap but more like an M, which is the reason for calling the solution (5.38) an *M-wave*.

It is, furthermore, worth noticing that the temporal evolutions of the parabolic cap and the M-wave are different. In particular, the above results suggest that

- *For the Parabolic Cap*[3]

$$g \sim \tau, \qquad h \sim \tau^{-1}\left(\frac{3}{4}V\left(1 - \eta^2\right)\right), \qquad \tilde{u} \sim \sqrt{3\beta V}(\eta) \quad \text{as} \quad \tau \to \infty.$$

[3] Here $\sim$ indicates that the two expressions are asymptotically equal.

• *For the M-Wave*

$$g = \tau^{2/3}, \quad h = \tau^{-2/3}\left(\frac{1}{9\beta}\left(h_m + \eta^2\right)\right), \quad \tilde{u} = \tau^{-1/3}\left(\frac{2}{3}\eta\right) \quad \text{for} \quad \tau \in [0, \infty).$$

Note that these are *asymptotic* results for the parabolic cap, but *exact* statements at all times for the M-wave solution. The results obviously confirm the non-existence of a steady-state at large times, but they also draw attention to the question of whether both similarity solutions may indeed exist in reality. In an attempt to gain clarity in this regard, Savage and Hutter [375] performed a restricted linear perturbation analysis of these two similarity solutions to see whether they would prove to be stable (it was hoped that the M-wave would turn out to be unstable, because by mere intuition it "looked" to be unrealistic). However, both solutions turned out to be stable against the investigated perturbations. This does not rule out instabilities against nonlinear perturbations; in any case the result makes both the parabolic cap and M-wave solutions likely candidates for realistic motions to look for in experiments.

This was done by using very rough experiments in [375]. In fact they used photographs from Huber's experiment [160] for gravel motions along an inclined plane to see whether the asymptotic evolution of the semi-spread would asymptotically grow as τ or $\tau^{2/3}$. The M-wave could not definitely be excluded, but the experiments showed a better coincidence for large times with a linear τ rather than with a $\tau^{2/3}$ dependence. Thus, it appears that physics selects the parabolic cap rather than the M-wave solution to which piles along inclined planes converge.

Figures 5.3 and 5.4 show the time evolutions of the parabolic cap and M-wave similarity solutions for the height of the granular avalanches, see Pudasaini et al. [337]. The reader should keep in mind that these figures were drawn in terms of the fixed domain variables, so that one can not directly notice the preservation of the volume. It is seen, however, that the profiles for h are *shape preserving* and that the avalanche spread and the amplitude of the pile vary with time. The parabolic cap solution is of special importance particularly in checking the efficiency of numerical codes, as done by Tai and Koschdon and Schäfer [228, 412].

5.2.2 Flow Over an Arbitrarily Curved and Twisted Channel

It is also possible to construct exact solutions of the system (4.89)–(4.91) of Chap. 4 for the orthogonal general coordinates that correspond exactly to the parabolic cap and M-wave solutions. For this purpose, let us assume that the avalanching mass is moving along the talweg of a narrow valley. It is then legitimate to assume that the transversal velocity component is

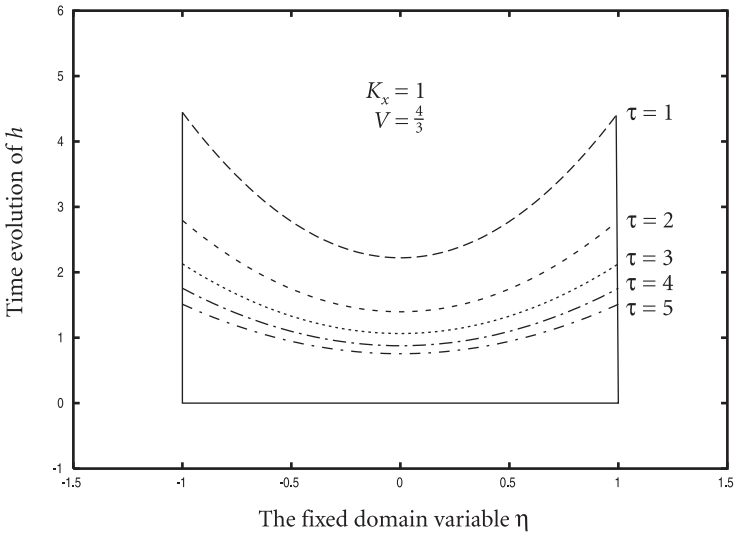

Fig. 5.4. The time and space evolution of the M-wave similarity solution. (From [337].)

almost zero, i.e., $v \approx 0$ and that the net driving force in the transversal direction is almost negligible. It is further assumed that $\partial K_x/\partial x = O(\varepsilon^\gamma)$, which means that the downhill earth pressure coefficient does not vary with respect to the downslope coordinate. Finally, we assume that there is no variation of basal topography in the downhill direction and that $\partial g_z/\partial x = O(\varepsilon^\gamma)$ or equivalently, that the master curve is almost a plane curve. With these assumptions the system of equations (4.89)–(4.91) (after using the mass balance in the downslope momentum balance) reduces to the following simple one-dimensional system:

$$\begin{aligned} &\frac{\partial h}{\partial t} + \frac{\partial}{\partial x}(hu) = 0, \\ &\frac{\partial u}{\partial t} + u\frac{\partial u}{\partial x} + \beta_x \frac{\partial h}{\partial x} = s_x, \end{aligned} \tag{5.40}$$

where $s_x = (g_x + g_z \tan\delta)$ is the net driving acceleration.[4]

These equations have the same form as (5.1), but now x is the downslope arc length coordinate of a curved and twisted channel and s_x may vary with position through such a dependence in g_x and g_z. If these are constant, then (5.40)

[4] For plane flow configuration $g_x = \sin\zeta$ and $g_z = -\cos\zeta$, where ζ is the inclination angle of the channel with the horizontal. However, in general, we do not explicitly need to know these components exactly in order to construct the similarity solutions, see (5.8) for how s_x disappears.

has parabolic cap and M-wave solutions as derived above. For instance, in a helical channel with constant cross-section and constant pitch, such solutions do indeed exist and have been constructed [337]. These solutions are, however, only approximate, because the transverse velocity v was assumed to be negligible, which must be enforced in a real experiment by side walls of the twisted (e.g., helical) channel. The solution may also be an adequate model for the flow down a bob run of constant inclination and small curvature and torsion.

5.2.3 Moderately Curved Beds

Let us now construct similarity solutions of the parabolic cap type for the plane motion of a granular avalanche down a curved bed. For this case, (5.40) remain valid, but the inclination angle ζ now varies with the downslope position, and it is no longer justified to ignore this variation. Savage and Nohguchi [373] constructed similarity solutions for this case.

As before, we let x be the curvilinear coordinate (arc length) and t the time. Consider (5.40) with

$$s_x = \sin\zeta - \mu\cos\zeta, \quad \beta = \varepsilon K_{\mathrm{act/pas}}\cos\zeta \tag{5.41}$$

with constant bed friction angle, $\mu = \tan\delta = \text{constant}$, but variable $\zeta(x)$. Let us define

$$\overline{u}(t) = \int_0^t (\sin\zeta - \tan\delta\cos\zeta)\, dt \tag{5.42}$$

which corresponds to the velocity of a mass point released from rest on a roughcurved bed. Define a new streamwise coordinate relative to the position of this point mass as

$$\xi = x - \int_0^t \overline{u}(t')dt'. \tag{5.43}$$

In addition, we can think of this translation as shifting the origin of the frame (ξ, t) moving with the velocity $\overline{u}(t)$ to the location where $\partial h/\partial x = 0$. It is also convenient to introduce the difference velocity

$$\tilde{u} = u - \overline{u}(t). \tag{5.44}$$

It is further supposed that the depth profile is symmetric and the difference velocity is skew-symmetric with respect to $\xi = 0$, i.e.,

$$h(\xi, t) = h(-\xi, t), \quad \tilde{u}(\xi, t) = -\tilde{u}(-\xi, t), \tag{5.45}$$

hence the leading edge (front margin) and trailing edge (rear margin) of the pile are, respectively, given by

$$\xi_F = g(t), \quad \xi_R = -g(t). \tag{5.46}$$

As in Sect. 5.2.1, we can transform the equations from the (x,t) plane to the (ξ,τ) plane using

$$\frac{\partial}{\partial t}=\frac{\partial}{\partial \tau}-\overline{u}(\tau)\frac{\partial}{\partial \xi},\qquad \frac{\partial}{\partial x}=\frac{\partial}{\partial \xi}.$$

In the following we write t for τ.

Now, expanding $\sin\zeta$ and $\cos\zeta$ in a TAYLOR series using $\zeta(x)=\zeta(\xi,t)$ about the position $\xi=0$ we find, for example,

$$\sin\zeta(x,t)=\sin\zeta(0,t)+\cos\zeta(0,t)\frac{\partial\zeta}{\partial\xi}\Big|_{\xi=0}\xi+\cdots. \tag{5.47}$$

Note that

$$\frac{\partial\zeta(0,t)}{\partial\xi}=\frac{\partial\zeta(0,t)}{\partial x}=-\lambda\kappa(0,t), \tag{5.48}$$

where we will take λ to be of order ε. Using these results with (5.42) and neglecting terms of order higher than ε in the sin and cos expansions, we find that the balance laws of mass and linear momentum can be expressed in the forms

$$\frac{\partial h}{\partial t}+\frac{\partial\left(h\tilde{u}\right)}{\partial\xi}=0, \tag{5.49}$$

$$\frac{\partial\tilde{u}}{\partial t}+\tilde{u}\frac{\partial\tilde{u}}{\partial\xi}=-\lambda\kappa(0,t)\cos\zeta(0,t)\,\xi-\varepsilon K_{\mathrm{act/pas}}\cos\zeta(0,t)\frac{\partial h}{\partial\xi}. \tag{5.50}$$

We anticipate a solution in which the shapes of the depth and difference velocity distributions are preserved, and the profiles are merely stretched or compressed in the streamwise direction. With this in mind, we choose a new similarity variable normalised by the half-length of the pile

$$\eta=\frac{\xi}{g(t)}=\frac{1}{g(t)}\left\{x-\int_0^t\overline{u}(t')dt'\right\}, \tag{5.51}$$

where $g(t)$ represents the half-spread of the pile (assuming symmetry about $\xi=0$). Thus, the leading and trailing edges of the pile correspond, respectively, to $\eta=1$ and $\eta=-1$. Now we transform from the (ξ,t) plane to the (η,t) plane by using[5]

$$\frac{\partial}{\partial t}:=\frac{\partial}{\partial t}-\eta\frac{g'}{g}\frac{\partial}{\partial\eta},\qquad \frac{\partial}{\partial\xi}=\frac{1}{g}\frac{\partial}{\partial\eta}. \tag{5.52}$$

[5] Note that we formally write t for τ, so $(5.52)_1$ should read

$$\frac{\partial}{\partial t}=\frac{\partial}{\partial\tau}-\eta\frac{g'}{g}\frac{\partial}{\partial\eta}.$$

This is why we use the assignment symbol := and not equality in $(5.52)_1$.

With (5.52), (5.49) and (5.50) can then be expressed in the forms

$$\frac{\partial h}{\partial t} - \eta \frac{g'}{g} \frac{\partial h}{\partial \eta} + \frac{1}{g} \frac{\partial}{\partial \eta} (h\tilde{u}) = 0, \tag{5.53}$$

$$\frac{\partial \tilde{u}}{\partial t} - \eta \frac{g'}{g} \frac{\partial \tilde{u}}{\partial \eta} + \frac{\tilde{u}}{g} \frac{\partial \tilde{u}}{\partial \eta} = -\lambda \kappa(0,t) \cos\zeta(0,t) g\eta - \beta_0 \frac{1}{g} \frac{\partial h}{\partial \eta}, \tag{5.54}$$

where $\beta_0 = \varepsilon \cos\zeta(0,t) K_{\text{act/pas}}$ and primes denote differentiation with respect to time t. We attempt a solution of the form

$$\tilde{u}(\eta, t) = \eta g'(t), \tag{5.55}$$

which is consistent with the assumption (5.45) of skew-symmetry. With (5.55), (5.54) reduces to

$$\frac{\partial h}{\partial \eta} = -\frac{g}{\beta_0} \left(\lambda \kappa(0,t) \cos\zeta(0,t) g + g''\right) \eta.$$

Integrating this and taking the thickness to be zero at the front and rear margins, we obtain the depth profile

$$h = \frac{g}{2\beta_0} \left(\lambda \kappa(0,t) \cos\zeta(0,t) g + g''\right) \left(1 - \eta^2\right). \tag{5.56}$$

In this solution, material elements can expand or contract in the direction parallel to the bed (i.e., g' can be positive or negative), so the stress state can correspond to either the active or the passive case. The choice of K_{act} or K_{pas} for $K_{\text{act/pas}}$ is thus linked to the solution for $g(t)$.

We can obtain the differential equation for the evolution of g from the overall mass conservation equation, i.e.,

$$\int_{\xi_R}^{\xi_F} h(\xi, t)\, d\xi = V = \text{constant}. \tag{5.57}$$

At time $t = 0$, we take $h = (1 - \xi^2)$, which amounts to putting $g(0) = 1$, hence

$$V = \int_{-1}^{1} \left(1 - \xi^2\right)\, d\xi = \frac{4}{3}. \tag{5.58}$$

Furthermore, in general, since $d\xi = g d\eta$

$$\int_{-1}^{1} h\,(\eta, t)\, g(t) d\eta = V = \frac{4}{3} \left(\frac{g^2}{2\beta_0}\right) \left(\lambda \kappa(0,t) \cos\zeta(0,t) g + g''\right). \tag{5.59}$$

Hence, the evolution equation for $g(t)$ is

$$g'' g^2 + \lambda \kappa(0,t) \cos\zeta(0,t) g^3 = 2\beta_0. \tag{5.60}$$

We shall solve (5.60) subject to the initial conditions

$$g(0) = 1, \quad g'(0) = 0, \tag{5.61}$$

corresponding to a pile of physical length $2L$, at rest at $t = 0$.

It is not possible to find analytical solutions to the above equations, but numerical solutions have been constructed for a number of basal geometries. To this end, it is advantageous to first collect the governing equations in one place.

Numerical Computations We can express the bed shape in terms of horizontal and vertical (downward) coordinates X, Y of which the origin corresponds to the initial centre of mass at time $t = 0$. Thus, $dX/dx = \cos\zeta$ and $dY/dx = \sin\zeta$. If we express these in terms of the derivatives with respect to time and complement them with the equations of motion for the centre of mass (5.42) and those for the semi-spread (5.60), the following system of ordinary differential equations is obtained:

$$\begin{aligned}
&\frac{dX}{dt} = \overline{u}\cos\zeta(\overline{x}), && \frac{dY}{dt} = \overline{u}\sin\zeta(\overline{x}),\\
&\frac{d\overline{x}}{dt} = \overline{u}, && \frac{d\overline{u}}{dt} = \sin\zeta(\overline{x}) - \tan\delta\cos\zeta(\overline{x}),\\
&\frac{dg}{dt} = f, && \frac{df}{dt} = \varepsilon\left(\frac{2}{g^2}\right)K_{\mathrm{act/pas}}\cos\zeta(\overline{x}) + \frac{\partial\zeta}{\partial x}\Big|_{\overline{x}}\, g\cos\zeta(\overline{x}),
\end{aligned} \tag{5.62}$$

where (5.47) has been used and $\overline{x}$ and $\overline{u}$ are the position and velocity of the mass point, respectively. These equations are coupled insofar as the centre of mass motion influences the semi-spread, but not vice versa. The equations were integrated by Savage and Nohguchi [373] by using a fourth-order Runge–Kutta technique. Two particular profiles were examined, one in which the bed slope corresponds to the shape of a circular arc, i.e.,

$$\zeta = \zeta_0\,(1 - ax)\,, \tag{5.63}$$

and one in which the bed slope decays exponentially with the downstream distance,

$$\zeta = \zeta_0 \exp(-ax)\,, \tag{5.64}$$

where a is a constant bed shape parameter and the initial slope is given by

$$\zeta_0 = \zeta(x = 0) = \zeta(\xi = 0, t = 0).$$

By varying the parameters ζ_0 and a, we can generate a number of plausible realistic bed shapes.

Figures 5.5a,b show typical results of the computations for the circular bed and Figs. 5.5c,d display the analogous results for the exponential bed. They display the half-spread $g(x,t)$ as a function of x and t. Details of the parameter choices are given as insets. In all considered cases, the pile starts out from rest, the centre of mass accelerates and reaches a maximum velocity, then decelerates and finally comes to rest. The end points of the curves of $g(t)$ versus time correspond to the position where $\overline{u} = 0$.

It is important to recall that it was assumed in the specification of the bed friction in the present similarity analysis that $\overline{u} > 0$ everywhere. This implies that $|\tilde{u}| < \overline{u}$, or in other words $g' < \overline{u}$. This condition needs to be satisfied, and indeed it is satisfied for all curves of Fig. 5.5. As can be seen from the curves, the semi-spread may monotonously increase from the start to the settlement of the granular pile; or it may first increase, reach a maximum and then decrease, or it may first decrease, go through a minimum and then increase. Some piles move initially as rigid or nearly rigid bodies, others first deform and reach a steady state at a later time (in Fig. 5.5 the regions of steady states are hatched). Clearly, which behaviour will evolve depends on the relative balance of the two terms on the right-hand side of $(5.62)_6$. Since the first term is positive, contracting flow can only form, if $(\partial\zeta/\partial x)\big|_{\overline{x}}$ is negative. SAVAGE and NOHGUCHI [373] discuss conditions for extensional, rigid and compacting flows.

In short, whereas the flow of a (plane) parabolic cap of a granular material with constant friction angles ϕ and δ down an inclined plane is persistently extending, the corresponding flow down a slightly curved bed may go through phases of extending, compacting and rigid body motions. The order in which these phases follow one another depends on the geometry of the bed and the initial conditions from which the avalanche evolves.

5.2.4 Variable Bed Friction

The above results were derived for a flat plane bed and a constant friction coefficient, or weakly curved beds and constant frictional resistance. For curved beds it was found that the centre of mass of the granular pile could accelerate or decelerate depending on the shape of the bed and the initial conditions. In this section, we investigate the case of flat beds again, but allow the friction angle to depend on position, velocity, or both. We shall see that the spreading rate and the motion of the centre of mass of the pile can be influenced by varying the bed friction angle.

The governing equations for plane flow down an inclined plane again take the form (5.1) but, since the friction angle may now vary and extending or compressing flow may arise, we write them as

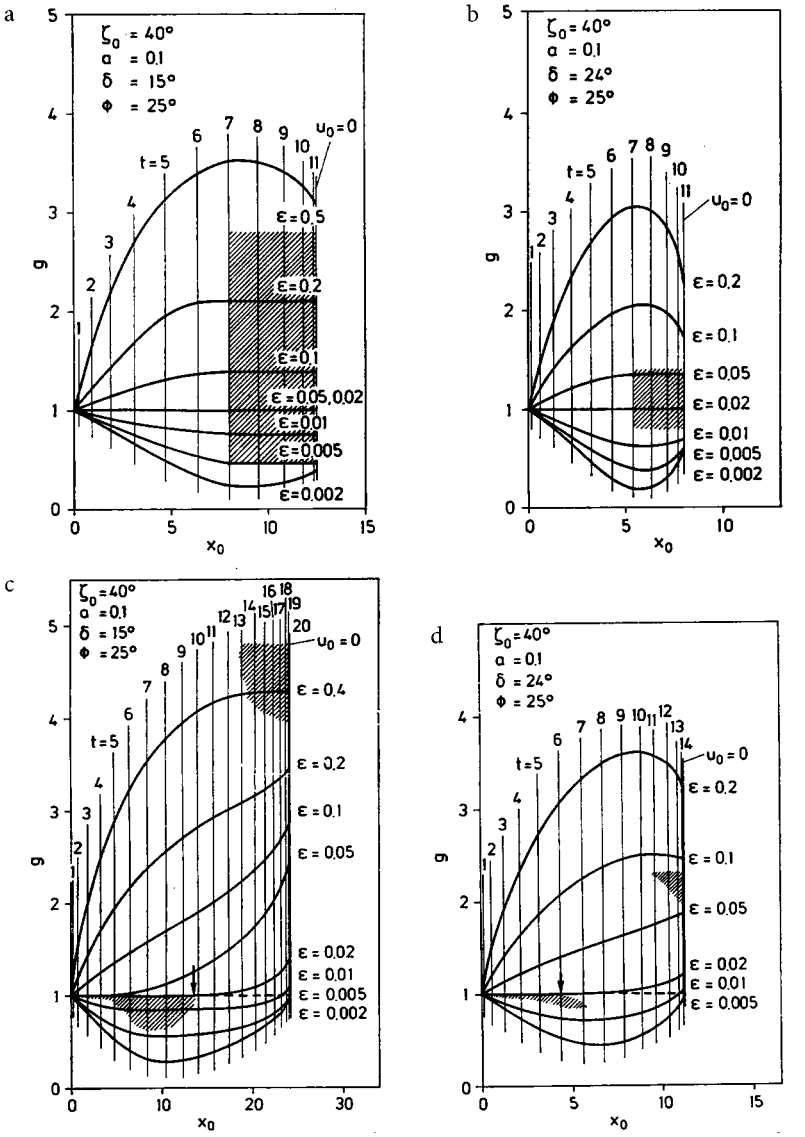

Fig. 5.5. Evolution behaviour of $g(t)$ for the circular arc (**a,b**) and exponential (**c,d**) bed profiles for the parameters as given in the *insets*. Rigid regions are hatched. The *vertical arrow* on the x-axis indicates the maximum extent of the rigid zone for cases in which $g(t)$ is initially constant. The curves terminate when $\overline{u} = 0$. (From [373].)

$$\begin{aligned}
&\frac{\partial h}{\partial t}+\frac{\partial (hu)}{\partial x}=0,\\
&\frac{\partial (hu)}{\partial t}+\frac{\partial (hu^2)}{\partial x}=h\sin\zeta-h\mu\cos\zeta-\beta h\frac{\partial h}{\partial x},
\end{aligned}\tag{5.65}$$

in which

$$\mu=\operatorname{sgn}(u)\tan\delta\quad\text{and}\quad\beta=\varepsilon K_{\text{act/pas}}\cos\zeta.\tag{5.66}$$

x is measured along the bed in the downward direction. Equation $(5.65)_1$ is the mass balance averaged over the height of the pile, while $(5.65)_2$ is the longitudinal momentum balance. Equations (5.65) will be solved subject to the boundary conditions

$$h_F=h\left(x_F(t)\right)=0,\quad h_R=h\left(x_R(t)\right)=0,\tag{5.67}$$

where $x=x_F(t)$ and $x=x_R(t)$ are the positions of the front and rear margins, respectively.

Equations for the Centre of Mass Motion and the Deformation By integrating $(5.65)_2$ from $x=x_R(t)$ to $x=x_F(t)$, we may show by use of the Reynolds' transport theorem in the first term and the Gauss' divergence theorem in the second term that

$$\begin{aligned}
&\int_{x_R(t)}^{x_F(t)}\left[\frac{\partial}{\partial t}(hu)+\frac{\partial}{\partial x}(hu^2)\right]dx=\frac{d}{dt}\int_{x_R(t)}^{x_F(t)}hu\,dx,\\
&\int_{x_R(t)}^{x_F(t)}h\left(\sin\zeta-\mu\cos\zeta\right)dx=\sin\zeta\int_{x_R(t)}^{x_F(t)}h\,dx-\cos\zeta\int_{x_R(t)}^{x_F(t)}\mu h\,dx,\\
&\int_{x_R(t)}^{x_F(t)}\beta h\frac{\partial h}{\partial x}dx=-\frac{1}{2}\int_{x_R(t)}^{x_F(t)}h^2\frac{\partial\beta}{\partial x}dx\cong 0,\quad\text{since}\quad\frac{\partial\beta}{\partial x}\ll 1.
\end{aligned}\tag{5.68}$$

The last approximation is justified, since β varies via the earth pressure coefficient through the variation of μ, which cannot be large. It follows that

$$\frac{d}{dt}\int_{x_R(t)}^{x_F(t)}hu\,dx=\sin\zeta\int_{x_R(t)}^{x_F(t)}h\,dx-\cos\zeta\int_{x_R(t)}^{x_F(t)}\mu h\,dx.\tag{5.69}$$

A similar procedure, applied to the mass balance $(5.65)_1$, yields

$$\frac{dV}{dt}=\frac{d}{dt}\int_{x_R(t)}^{x_F(t)}h\,dx=0,\quad\Longrightarrow\quad V=\int_{x_R(t)}^{x_F(t)}h\,dx=\text{constant}.\tag{5.70}$$

The last two equations suggest the definitions

$$\overline{x}=\frac{1}{V}\int_{x_R}^{x_F}hx\,dx,\quad\overline{u}=\frac{1}{V}\int_{x_R}^{x_F}hu\,dx,\quad\overline{\mu}=\frac{1}{V}\int_{x_R}^{x_F}h\mu\,dx,\tag{5.71}$$

which define the centre of mass position, the mean velocity and the mean basal friction coefficient. With these and (5.70), (5.69) implies

$$\frac{d\overline{x}}{dt} = \overline{u}, \qquad \frac{d\overline{u}}{dt} = \sin\zeta - \overline{\mu}\cos\zeta. \tag{5.72}$$

These are the equations of motion of the granular pile as a whole.

Having defined the centre of mass motion through (5.71), we now proceed to the derivation of the deformation equations. To this end, it is convenient to define, as before,

$$\tau = t, \quad \xi = x - \overline{x}(t), \tag{5.73}$$

from which one obtains (after setting $\tau = t$)

$$\frac{\partial}{\partial x} = \frac{\partial}{\partial \xi}, \quad \frac{\partial}{\partial t} := \frac{\partial}{\partial t} - \overline{u}\frac{\partial}{\partial \xi}. \tag{5.74}$$

Introducing the difference velocity

$$\tilde{u} = u - \overline{u}(t) \tag{5.75}$$

into the evolution equation (5.65) and transferring from the (x,t) coordinates to the (ξ,τ) coordinates, we obtain, on using (5.72), the deformation equations

$$\begin{aligned} &\frac{\partial h}{\partial t} + \frac{\partial}{\partial \xi}(h\tilde{u}) = 0, \\ &\frac{\partial \tilde{u}}{\partial t} + \tilde{u}\frac{\partial \tilde{u}}{\partial \xi} = -(\mu - \overline{\mu})\cos\zeta - \beta\frac{\partial h}{\partial \xi}. \end{aligned} \tag{5.76}$$

Generally, equations of motion (5.72) and (5.76) are mutually dependent and decouple only in special situations. This coupling may arise because $\overline{\mu}$ may depend on $\overline{u}$ so that the deformation equations (5.76) depend on the centre of mass motion, or $\overline{\mu}$ in (5.76) may vary such that it depends on variables characterised by the deformation of the pile, thus affecting the centre of mass motion. The degree of this coupling will be studied in the remainder of this Section via the introduction of various different basal sliding laws.

Variable Friction Models It is not possible to measure the bed friction angle in a moving granular mass, but it is likely that the bed friction angle may vary as a function of position and be smaller in the rear part than in the front part region of an avalanche. It may, e.g., occur that some finer material is deposited in the larger troughs of the basal topography, implying a decrease of the frictional resistance from the front to the rear margin. Another possible mechanism may be particle size segregation with large particles in the front

and smaller ones in the rear. In any case, it is instructive to see how such variations affect the qualitative evolution of the motion of an avalanche.

We now wish to solve the above equations with the bed friction coefficients μ, which vary with position (models type I), velocity (models type II) or both (models type III). In Table 5.1 the friction models studied are numbered from 1 to 8 and separated in columns according to their type. We analyse these different cases because we will see in the results that subtle differences in the frictional assumptions that may seem natural to an engineer may imply great qualitative mathematical differences of the emerging dynamical system.

- In model I the basal friction angle varies linearly between the front and rear margins such that the front and rear friction coefficients μ_F and μ_R, are held constant. It is also assumed that $\mu_F \geq \mu_R$. When $\mu_R = \mu_F$ holds, no variation of μ arises in this model and the results are those derived in Sect. 5.2.1. When $\mu_F > \mu_R$, the model can be physically interpreted in two different ways. We may think of the model to account for certain *plowing effects*, which is a realistic assumption for snow avalanches. Or we may interpret the reduction of the bed friction angle from the front to the rear margin as a *smoothing mechanism* due to say, the deposition of some fine material. This may also occur in snow avalanches, but is certainly effective in debris flows.
- Model 2 is very similar. It has a fixed frontal resistance, μ_F, and a linear decrease as one moves backwards, but here the gradient is fixed and not the value μ_R.
- In model 3, μ depends linearly on the local velocity. Because the velocity of the front is expected to be larger than further back, we expect the model to have similar features to models 1 and 2.
- Models $4, 5, 6$ differ from model 3 in the fact that μ now does not depend on the local velocity but on that of the centre of mass. Quantitative but no qualitative differences in the behaviour of the model are expected.
- Finally, models 7 and 8 are combinations of the models type I and II. In model 7, μ is formed as the product of functions of models 1 and 4 (or 5 and 6) and in model 8 this product is formed with the functions from models 2 and 4 (or 5 and 6).

It is sufficient to motivate these models by a "microscopic" physical argument; they are here proposed to scrutinise the influence of the suggested variations. It will be shown that small differences may have large qualitative influences.

Similarity Solutions of the Deformation Equations for Different Models We will now establish the governing equations for the spreading rate for each model. In other words, we will derive similarity solutions for a granular pile with parabolic shape. Strictly speaking, such similarity solutions do not exist for the above models $1, 2, 3, 7$ and 8. For their exis-

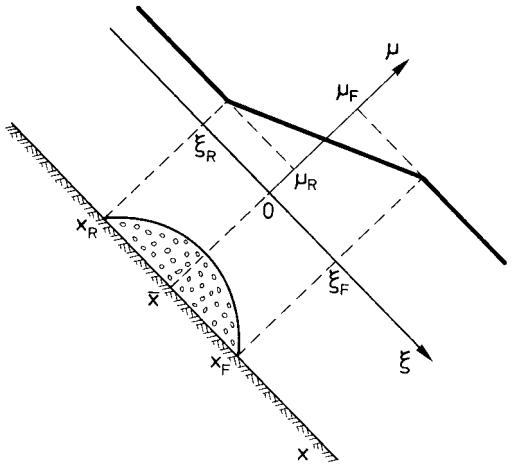

Fig. 5.6. Parabolic granular pile with centre of mass position $\overline{x}(\xi = 0)$ and margin positions $x_F(\xi_F)$ at the front and $x_R(\xi_R)$ at the rear end. Plotted is also the tangent of the bed friction angle for model 1. (From [301].)

tence a further assumption has to be invoked. The earth pressure coefficient $K_{\mathrm{act/pas}}$ must be independent of the variables ξ or $\tilde{u}$ and can only depend on a bed friction angle that may be expressed as a functional of a reference value of ξ, say the semi-spread, g and/or a reference velocity, say the centre of mass velocity $\overline{u}$: $K = K(\mu_{\mathrm{Ref}}(\overline{u}, g))$. Such conditions are automatically fulfilled for models 4 to 6. Eventually we shall, however, also limit attention to constant μ_{Ref}-values in these cases. This limits considerations to small variations of μ. This is consistent with the earlier assumption in $(5.68)_3$. We shall also suppose that the depth profile is symmetric and the difference velocity is skew-symmetric with respect to $\xi = 0$, i.e.,

$$h(\xi, t) = h(-\xi, t), \quad \tilde{u}(\xi, t) = -\tilde{u}(-\xi, t), \tag{5.77}$$

hence the leading and trailing edges of the pile are given, respectively, by

$$\xi_F = -\xi_R = g(t). \tag{5.78}$$

With these preliminaries we are now in a position to derive the evolution equation for $g(t)$ for each of the models.

• **Model 1** Let

$$\overline{\mu} = \mu_c = \frac{\mu_F + \mu_R}{2}, \quad \Delta\mu = \mu_F - \mu_R. \tag{5.79}$$

Then, using Table 5.1, it follows that $\mu - \overline{\mu} = \Delta\mu\xi/2g$. When substituting this, as well as the ansatz

$$\tilde{u} = \eta g' = \frac{\xi}{g} g' = \frac{g'}{g} \xi \tag{5.80}$$

into the deformation equations (5.76), we obtain[6]

$$\frac{\partial h}{\partial \xi} = -\frac{1}{\varepsilon K \cos\zeta} \left(\frac{g''}{g} + \frac{\cancel{4}}{2g} \cos\zeta \right) \xi, \tag{5.81}$$

in which we will now approximately set

$$K \approx \frac{2\left(1 \mp \sqrt{1 - (1+\mu_c^2)\cos^2\phi}\right)}{\cos^2\phi} - 1, \quad \begin{cases} g' > 0, \\ g' < 0. \end{cases} \tag{5.82}$$

A prime denotes differentiation with respect to time. With the approximation (5.82), (5.81) is separable and can be integrated. By taking the depths at the front and rear margins to be zero, the integration yields

$$h = \frac{1}{2\varepsilon K \cos\zeta} \frac{1}{g} \left(g'' + \frac{\cancel{4}}{2} \cos\zeta \right) \left(g^2 - \xi^2 \right). \tag{5.83}$$

If we finally impose the overall conservation equation $\int_{-g}^{g} h d\xi = V = \text{constant}$, we are led to the evolution equation of the semi-spread of model 1

$$g'' = \frac{3}{2} \varepsilon K \cos\zeta \, V \frac{1}{g^2} - \frac{\cancel{4}}{2} \cos\zeta. \tag{5.84}$$

Equation (5.83) proves that the profile for h is parabolic in ξ. The factor in front is a function of t alone and still not determined, but the differential equation for the semi-spread g is given in (5.84). It is seen that the profile h is shape preserving; however, the avalanche spread and the amplitude of the parabola vary in time. Below, we shall solve equations like (5.84) numerically and shall thus determine the temporal evolution of g.

• **Model 2** Here we let

$$\overline{\mu} = \mu_F - ag \tag{5.85}$$

and thus have $\mu - \overline{\mu} = a\xi$, implying a variable bed friction angle, where $a = d\mu/d\xi$, from Table 5.1, is a constant. When substituting (5.85) together with (5.80) into $(5.76)_2$ we again obtain an equation similar to (5.81). This equation is separable only provided that K is constant or merely a function of g. Under such simplifying assumptions the evolution equation for g reads

$$g'' = \frac{3}{2} \varepsilon K \cos\zeta \, V \frac{1}{g^2} - a \cos\zeta \, g, \tag{5.86}$$

Table 5.1. Description of the basal friction coefficients for three model types. For type I models the friction coefficient μ depends on the spatial variable, for type II models μ is velocity-dependent, whilst for type III models the friction coefficient is both position-dependent and velocity-dependent.

Type I models	Type II models	Type I $\cup$ II models
1) $\mu = \begin{cases} \mu_F, & \xi_F < \xi, \\ \frac{\mu_F - \mu_R}{\xi_F - \xi_R}\xi + \frac{\mu_R \xi_F - \mu_F \xi_R}{\xi_F - \xi_R}, & \xi_R \le \xi \le \xi_F, \\ \mu_R, & \xi < \xi_R, \end{cases}$ where μ_F and μ_R are constants independent of ξ 2) $\mu = a\,(\xi - \xi_F) + \mu_F, \qquad \xi_R \le \xi \le \xi_F,$ $a = \dfrac{d\mu}{d\xi} = \dfrac{\mu_F - \mu_R}{\xi_F - \xi_R},$ where μ_F and a are constants independent of ξ	3) $\mu = \mu_0(1 + cu),$ where μ_0 and c are constants independent of ξ and u $\mu = \mu(u) = f(u)\mu_0,$ where $f(0) = 1$; in particular, 4) $f\,(\overline{u}) = 1 + c\,\overline{u},$ 5) $f\,(\overline{u}) = 1 + c\,\overline{u}^2,$ 6) $f\,(\overline{u}) = 1 - \dfrac{\mu_\infty}{\mu_0} e^{-\lvert\overline{u}\rvert} + \dfrac{\mu_\infty}{\mu_0},$ where c, μ_0, μ_∞ are constants independent of $\overline{u}$ and ξ	7) $\mu = f\,(\overline{u}) \begin{cases} \mu_F^0, & \xi_F < \xi, \\ \frac{\mu_F^0 - \mu_R^0}{\xi_F - \xi_R}\xi + \frac{\mu_F^0 + \mu_R^0}{2}, & \xi_R \le \xi \le \xi_F, \\ \mu_R^0, & \xi < \xi_R, \end{cases}$ where $f\,(\overline{u})$ is given by models 4), 5), or 6) 8) $\mu = f\,(\overline{u})\big[a_0\big(\xi - \xi_F^0\big) + \mu_F^0\big], \quad \xi_R \le \xi \le \xi_F,$ where $f\,(\overline{u})$ is given by models 4), 5), or 6)

where

$$K \approx \frac{2\left(1 \mp \sqrt{1-(1+\mu_{\mathrm{Ref}}^2)\cos^2\phi}\right)}{\cos^2\phi} - 1, \quad \begin{cases} g' > 0, \\ g' < 0. \end{cases} \tag{5.87}$$

As is evident from (5.85), appropriate values for μ_{Ref} are μ_F and $\overline{\mu}$, respectively. The former is constant, the latter is a linear function of g. We shall choose here $\mu_{\mathrm{Ref}} = \mu_F$ only.

• **Model 3** As is evident from Table 5.1, we here have

$$\overline{\mu} = \mu_0 \left(1 + c\,\overline{u}\right), \tag{5.88}$$

so that $\mu - \overline{\mu} = \mu_0 c\tilde{u}$, where $\tilde{u} = u - \bar{u}$. Separable solutions of an equation similar to (5.81) exist provided that K is approximated by $K \approx K\left(\mu_{\mathrm{Ref}}\right)$ in which μ_{Ref} is constant, or only depends on $\overline{u}$. As is seen from (5.88), two choices are natural, $\mu_{\mathrm{Ref}} = \mu_0$ and $\mu_{\mathrm{Ref}} = \mu_0(1 + c\,\overline{u})$; a dependence on g does not arise. For either case, proceeding as before we will obtain

$$g'' = \frac{3}{2}\varepsilon K \cos\zeta\, V \frac{1}{g^2} - c\mu_0 \cos\zeta\, g, \tag{5.89}$$

and we shall focus attention on the case $\mu_{\mathrm{Ref}} = \mu_0$.

• **Models 4–6** When μ is dependent on the velocity of the centre of mass, then

$$\overline{\mu} = \mu = \mu_0 f\left(\overline{u}\right). \tag{5.90}$$

This makes the deformation equations (5.76) particularly simple, because $\mu - \overline{\mu} = 0$ and leads to the evolution equation for $g(t)$ in the form

$$g'' = \frac{3}{2}\varepsilon K \cos\zeta\, V \frac{1}{g^2}, \tag{5.91}$$

in which no approximation on K needs to be introduced, since μ only depends on $\overline{u}$. However, in the spirit of the previous approximations, we shall set

$$K\left(\mu_{\mathrm{Ref}}\right) = K\left(\mu_0\right), \tag{5.92}$$

where K is given in (5.87).

• **Models 7 and 8** The remaining models are now a combination of the models of type I and type II. For model 7, one has

$$\overline{\mu} = f\left(\overline{u}\right)\mu_c^0, \quad \mu - \overline{\mu} = \frac{f\left(\overline{u}\right)\mathcal{A}\mu_0}{2g}\xi, \tag{5.93}$$

[6] This formula makes it particularly clear that $K_{\mathrm{act/pas}}$ may be treated as a constant since $\varepsilon\partial K/\partial\xi$ would be $O\left(\varepsilon^{\gamma}\right), \gamma > 1$.

with

$$\overline{\mu}_c^0 = \frac{\mu_F^0 + \mu_R^0}{2}, \quad \Delta\mu_0 = \mu_F^0 - \mu_R^0. \tag{5.94}$$

Application of the same integration procedure as before now yields

$$g'' = \frac{3}{2}\varepsilon K \cos\zeta \, V \frac{1}{g^2} - \frac{f(\overline{u})\,\Delta\mu_0}{2}\cos\zeta, \tag{5.95}$$

in which $K = K(\mu_{\mathrm{Ref}})$. This is only meaningful as long as μ_{Ref} is either a constant or a function of $\overline{u}$. We shall choose $\mu_{\mathrm{Ref}} = \mu_c^0$.

Finally, for model 8 we have

$$\overline{\mu} = f(\overline{u})\left(\mu_F^0 - a_0 g\right) \tag{5.96}$$

and $\mu - \overline{\mu} = f(\overline{u})\, a_0 \xi$. In this case, we may deduce

$$g'' = \frac{3}{2}\varepsilon K \cos\zeta \, V \frac{1}{g^2} - a_0 f(\overline{u}) \cos\zeta \, g, \tag{5.97}$$

where again $K = K(\mu_{\mathrm{Ref}})$ and $\mu_{\mathrm{Ref}} = \overline{\mu}$ or $\mu_{\mathrm{Ref}} = \mu_F^0$. We shall only deal with this latter case.

Summary of the Models We can summarise the above derivations with the following two equations that govern the spread and the motion of the centre of mass:

$$\begin{aligned} g'' &= \frac{3}{2}\varepsilon K\left(\mu_{\mathrm{Ref}}(\overline{u}, g)\right)\cos\zeta \frac{V}{g^2} - F(\overline{u}, g, g')\cos\zeta, \\ \overline{u}' &= \sin\zeta - \overline{\mu}(\overline{u}, g)\cos\zeta. \end{aligned} \tag{5.98}$$

Herein, the functions $F(\overline{u}, g, g')$, $\mu_{\mathrm{Ref}}(\overline{u}, g)$ and $\overline{\mu}(\overline{u}, g)$ are coupling coefficients. If F and μ_{Ref} are independent of $\overline{u}$, then the evolution of the avalanche spread is independent of that of $\overline{u}$, but the centre of mass motion may still be affected by the evolution of the spread through a dependence of $\overline{\mu}$ on g. Alternatively, if $\overline{\mu}$ does not depend on g, the centre of mass motion is unaffected by the evolution of the spread. Table 5.2 lists all functions for the eight models. In all but models 4 to 6 the similarity solutions are approximate, because no exact value for the earth pressure coefficient could be used. In fact, in most models, two possible values for μ_{Ref} are suggested. In actual computations, only the choices with $\mu_{\mathrm{Ref}} =$ constant were selected. For these cases, we infer the following from Table 5.2:

1. In models 1 and 3–6 the centre of mass motion and the spreading are decoupled.
2. In model 2 the centre of mass motion is influenced by the evolution of the spreading rate, while in model 7 the spreading rate is affected by the centre of mass motion and not vice versa. A full two-sided coupling only exists for model 8.

Table 5.2. Description of the functional dependence of $F, \overline{\mu}$ and μ_{Ref} as defined in (5.98) for the various models. The function $f(\overline{u})$ for each model is defined in Table 5.1. In all but models 4–6 the earth pressure coefficient is evaluated approximately.

Model	$F\,(\overline{u}, g, g')$	$\overline{\mu}(\overline{u}, g)$	$\mu_{\mathrm{Ref}}(\overline{u}, g)$
1	$\frac{A_R}{2} = \frac{\mu_F - \mu_R}{2}$	$\frac{\mu_F + \mu_R}{2}$	$\frac{\mu_F + \mu_R}{2}$
2	ag	$\mu_F - ag$	$\begin{cases} \mu_F - ag \\ \mu_R \end{cases}$
3	$c\mu_0 \frac{dg}{dt}$	$\mu_0 f(\overline{u})$	$\begin{cases} \mu_0\,(1 + c\,\overline{u}) \\ \mu_0 \end{cases}$
4–6	0	$\mu_0 f(\overline{u})$	$\begin{cases} \mu_0 f(\overline{u}) \\ \mu_0 \end{cases}$
7	$\frac{A_R\ 0}{2} f(\overline{u})$	$\mu_c^0 f(\overline{u})$	$\begin{cases} \mu_c^0 f(\overline{u}) \\ \mu_c^0 \end{cases}$
8	$a_0 f(\overline{u}) g$	$\left(\mu_F^0 - a_0 g\right) f(\overline{u})$	$\begin{cases} \left(\mu_F^0 - a_0 g\right) f(\overline{u}) \\ \mu_F^0 \end{cases}$

3. As can be seen from the first of (5.98), a rigid body motion can only exist for $F(\overline{u}, g, g') \neq 0$. All but models 4–6 possess the flexibility for this rigid body motion.
4. A limiting steady speed for the centre of mass motion only exists provided that the right-hand side of $(5.98)_2$ can vanish. Thus,

$$\overline{\mu}\,(\overline{u}, g) = \tan\zeta, \quad \text{with} \quad g' = 0 \tag{5.99}$$

describes these steady states. For a constant $\overline{\mu}$ or $\overline{\mu}(g)$, this equation does not define a velocity; a final velocity simply does not exist (models 1 and 2).[7] For models 3 to 5, the above condition leads formally to

$$\overline{u} = \left\{ \frac{1}{c} \left(\frac{\tan\zeta}{\mu_0} - 1 \right) \right\}^{1/p}, \quad p = 1, 2, \tag{5.100}$$

if $f(\overline{u}) = 1 + c\,\overline{u}^p$ (models 3 to 5). Alternatively,

$$\overline{u} = \ln \frac{\mu_\infty}{\mu_0 + \mu_\infty - \tan\zeta} \tag{5.101}$$

[7] If $\overline{\mu} = \overline{\mu}(g)$, then (5.99) defines $g = g_{\mathrm{steady}}$, but this value is, in general, in conflict with $(5.98)_1$.

for model 6. If μ depends on both $\overline{u}$ and g as in model 8, a steady centre of mass velocity only exists together with a rigid body motion of the pile. A solution of this equilibrium state is obtained by setting the right-hand sides of (5.98) simultaneously to zero and imposing the condition $g' = 0$.

In short, *a* COULOMB*-type model allows a steady state rigid body motion of a parabolic cap down an inclined bed in the stated approximation only if the bed friction angle varies both with position and velocity.*[8]

Computational Results To construct numerical solutions of the governing equations, we write (5.98) in standard form as

$$\begin{aligned} \frac{dg'}{dt} &= \frac{3}{2}\varepsilon K\left(\mu_{\mathrm{Ref}}\left(\overline{u}, g\right)\right)\cos\zeta\frac{V}{g^2} - F\left(\overline{u}, g, g'\right)\cos\zeta, \quad \frac{dg}{dt} = g', \\ \frac{d\overline{u}}{dt} &= \sin\zeta - \overline{\mu}\left(\overline{u}, g\right)\cos\zeta, \quad \frac{d\overline{x}}{dt} = \overline{u}, \end{aligned} \tag{5.102}$$

and solved by a fourth-order RUNGE–KUTTA scheme subject to the initial conditions

$$\overline{x}(0) = 0, \quad \overline{u}(0) = u_0, \quad g(0) = g_0, \quad g'(0) = g'_0. \tag{5.103}$$

In all but model 8 this initial value problem decouples such that the equations of the centre of mass motion can be solved first and those for the spreading afterwards or vice versa. The initial conditions have been chosen so general in order to obtain a full coverage of the *phase plane* (g, g') under a broad range of practically possible situations. When putting the equations into dimensionless form it was understood that the length scale L would be identified with the semi-spread at rest, implying $g_0 = 1$. Snow avalanches often start as moving rigid slabs and only break after having reached a finite speed. At this moment their initial shape may be close to a parabola; obviously then, one may have $g_0 > 1, g'_0 \neq 0$ and $u_0 \neq 0$. The solution of the equations of motion for a range of initial conditions (5.103) permits exploration of the particular models for a variety of practically relevant conditions.

• *Model 1 (Bed friction angle position-dependent):* Table 5.2 indicates that the motion of the centre of mass and the deformation are independent of each other. Depending upon whether $\Delta\mu \neq 0$ or $\Delta\mu = 0$ (this is the difference between the bed friction coefficient at the front and rear margins), the two models exhibit different qualitative behaviour. Figure 5.7 displays phase space orbits, g versus g', for $\Delta\mu = 0$ and conditions otherwise stated in the figure caption. To interpret this figure, consider an avalanche starting from

[8] In soil mechanics it is sometimes claimed that the internal angle of friction and the bed friction angle are pressure-dependent. This assumption can be translated here to a dependence of μ on ξ. It immediately follows that with this parameterisation no steady rigid motion can be generated.

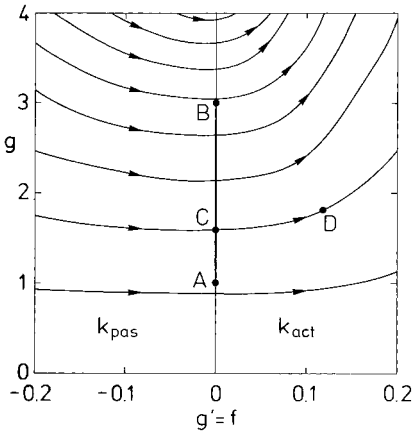

Fig. 5.7. Phase space orbits g versus g' for a parabolic cap avalanche sliding down an inclined plane when the bed friction angle is constant, i.e., $\mu_{\mathrm{Ref}} = \mu$. The *arrows* indicate the direction in which the trajectories are traversed when the avalanche moves down the slidepath. C represents a point when the pile neither extends nor contracts. D is a point when the avalanche is in a state of extension. (From [301].)

$g = g_0$ and $g' = g'_0$. As the avalanche moves down the slidepath, the corresponding point in phase space moves along an orbital trajectory to the right as indicated by the arrows. If the initial condition is $g_0 > 0, g'_0 < 0$, one would start in the left half plane, and g would initially decrease as the trajectory is traversed, the granular pile would compress and passive stresses would be established. In the right half plane when $g' > 0$, g will monotonically increase; here the flow is extending and an active state of stress is established. Usual initial conditions start from a state $g'_0 = 0$, i.e., point C in the graph. Thus, irrespective of the location of the starting point along the axis $g' = 0$, the granular avalanche will extend without limits as t tends to infinity. When $\not{A} \neq 0$, the qualitative behaviour is quite different. Figures 5.8a,b show phase space trajectories for various different initial conditions and the same configuration and physical conditions as in Fig. 5.7, but two different internal friction angles ($\phi = 15°$ in panel a and $\phi = 25°$ in panel b). The granular avalanche may start to disperse from any point C on the axis $g' = 0$. Trajectories now "wind" themselves around the ordinate axis and all end within the interval $[A, B]$, which corresponds to a rigid body motion of the parabolic pile. Indeed, from $(5.102)_{1,2}$ and Table 5.2 we may deduce a non-deforming motion when $g'' = g' = 0$, or equivalently when

$$g'' = \frac{3}{2}\varepsilon K \cos\zeta \frac{V}{g^2} - \frac{\not{A}}{2}\cos\zeta = 0, \tag{5.104}$$

from which we obtain

$$g_{\mathrm{act}} = \sqrt{\frac{3\varepsilon K_{\mathrm{act}} V}{\not{A}}} < g_{\mathrm{rigid}} < \sqrt{\frac{3\varepsilon K_{\mathrm{pas}} V}{\not{A}}} = g_{\mathrm{pas}}, \tag{5.105}$$

and g_{act} defines point A, and g_{pas} point B.

If the starting point C of the avalanche lies below A, then the avalanche is extending in time until its orbit in phase space again crosses the g-axis at $g' = 0$. If this intersection lies above the interval $[A, B]$, the avalanche will subsequently contract and follow the trajectory in the left half plane of (g, g') until it again intersects the g-axis at $g' = 0$. This process continues until a point within the interval $[A, B]$ is reached. In this process the avalanche goes through several expanding and contracting phases. When a point within $[A, B]$ is reached, it can easily be shown with the aid of $(5.102)_{1,2}$ that neither extending nor contracting flow is possible. Indeed, for a point between A and B the right-hand side of (5.104) is positive (negative) when $K = K_{\mathrm{pas}}$ (K_{act}) so that $g'' > 0\,(g'' < 0)$, which leads to extensional (contracting) flow, a contradiction to the choice $K = K_{\mathrm{pas}}(K_{\mathrm{act}})$! Thus, the parabolic pile can only move as a rigid body.

The existence of the rigid body motion is a new and essential feature of this model and is due to (i) the variability of the basal friction coefficient and (ii) the fact that $K_{\mathrm{act}} \neq K_{\mathrm{pas}}$. When $K_{\mathrm{act}} = K_{\mathrm{pas}}$, we see from (5.105) that the points A and B coalesce; consequently no rigid body motion exists in this case except when $g = g_{\mathrm{act}} = g_{\mathrm{pas}}$. This happens when $\delta = \phi$. The differences between Figs. 5.8a and 5.8b reflect the fact that $\phi - \delta$ is smaller in Fig. 5.8a

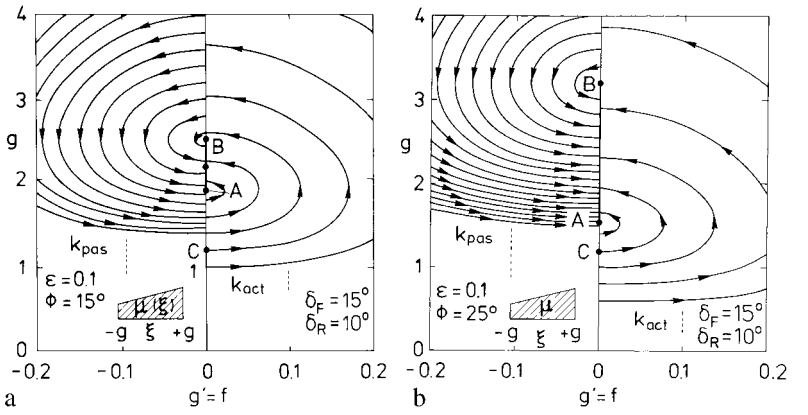

Fig. 5.8. Phase space orbits g versus g' as in Fig. 5.7 but for a bed friction angle that varies with position ($\not{A}$ is a constant, μ varies linearly and $\mu_{\mathrm{Ref}} = \mu(\xi = 0)$). The interval $[A, B]$ represents states $(g, g' = 0)$ corresponding to rigid body motions of the parabolic pile. *Panel a* holds for an internal angle of friction of $\phi = 15°$ and *panel b* for $\phi = 25°$. When $\not{A} = 0$, the interval $[A, B]$ moves to infinity. (From [301].)

than it is in Fig. 5.8b. On the other hand, we can also look at the limit $\mu_F \to \mu_R$ of uniform and constant basal friction. In this limit $\Delta \to 0$, and both points A and B will move to infinity along the g-axis. In this case, the situation of Fig. 5.7 is recovered.

When the volume V is prescribed and the parabolic shape is given, the height for the rigid body motion at the location of the centre of mass can be obtained from (5.105) to lie within the interval

$$\frac{1}{4}\sqrt{\frac{3\Delta V}{\varepsilon K_{\text{pas}}}} \leq h_{\text{rigid}} \leq \frac{1}{4}\sqrt{\frac{3\Delta V}{\varepsilon K_{\text{act}}}}. \tag{5.106}$$

By combining (5.105) and (5.106), the ratio of this height to the spread $2g$ must satisfy the inequality

$$\frac{\Delta}{8\varepsilon K_{\text{pas}}} \leq \left(\frac{h}{2g}\right)_{\text{rigid}} \leq \frac{\Delta}{8\varepsilon K_{\text{act}}}. \tag{5.107}$$

This interval of the aspect ratio of the rigid body granular pile is proportional to Δ and independent of the total volume V.

Formulas (5.106) and (5.107) are helpful for rough estimates. To be useful, however, the value of the avalanche semi-length g in the rigid body motion must be known. This value depends on the initial values of g_{initial} and $g'(=0)$. NOHGUCHI et al. [301] compute g_{rigid} as a function of g_{initial} ($g'_{\text{initial}} = 0$) and show that *for an avalanche to reach a rigid steady motion, it may have to go through several extensional and contracting motion phases.* They also demonstrate via an extensive parameter study that an avalanche of *model type* 1 may – realistically – hardly ever reach this rigid body motion, since travel times and lengths are too long. Figure 5.9 displays the temporal evolution of g for a number of initial states, how this rigid body state is reached. As can be seen, on its motion the avalanche may go through several increasing and decreasing "cycles" before proceeding as a rigid body. In the figure we have hatched the time interval that may realistically cover real avalanches.

• *Model 2:* The results of this model are similar to those of *model 1*; so our discussion will be brief. The evolution equations (5.102) in this case become

$$\frac{dg'}{dt} = \frac{3}{2}\varepsilon K \cos\zeta \frac{V}{g^2} - a\cos\zeta g, \qquad \frac{dg}{dt} = g',$$

$$\frac{d\overline{u}}{dt} = \sin\zeta - (\mu_F - ag)\cos\zeta, \qquad \frac{d\overline{x}}{dt} = \overline{u}, \tag{5.108}$$

and explicitly show that the centre of mass motion depends on the spread g, whereas the spread is independent of the centre of mass motion. Phase space trajectories are qualitatively the same as those shown in Fig. 5.8 and will

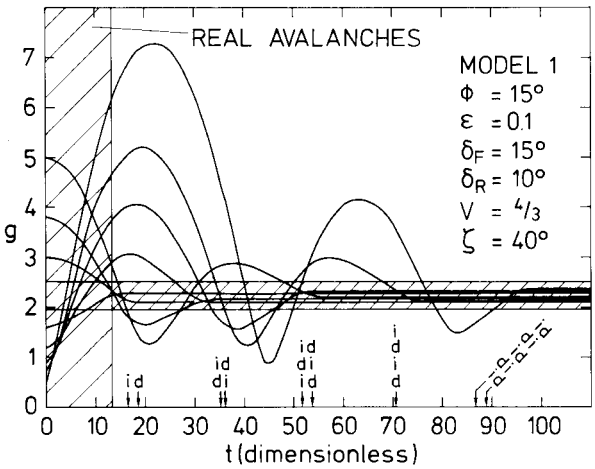

Fig. 5.9. Temporal evolution of the semi-spread g of an avalanche for various initial values g_{initial}, for $\phi = 15°$ and conditions as indicated in the *inset*. The time interval in which typical real avalanches occur is shown hatched. i indicates increasing and d decreasing spreading of the body. (From [301].)

therefore not be repeated here. Rigid body motions are characterised by the equilibrium points of $(5.108)_{1,2}$. This yields

$$g_{\text{act}} = \left(\frac{3}{2}\frac{\varepsilon K_{\text{act}} V}{a}\right)^{1/2} \leq g_{\text{rigid}} \leq \left(\frac{3}{2}\frac{\varepsilon K_{\text{pas}} V}{a}\right)^{1/2} = g_{\text{pas}}. \tag{5.109}$$

Furthermore, with the volume V given, the height for the rigid body motion at the location of the centre of mass lies within the interval

$$\left(\frac{9}{32}\frac{aV^2}{\varepsilon K_{\text{pas}}}\right)^{1/3} \leq h \leq \left(\frac{9}{32}\frac{aV^2}{\varepsilon K_{\text{act}}}\right)^{1/3}. \tag{5.110}$$

From (5.109) and (5.110) we may deduce that the aspect ratio of the pile in the rigid body state lies in the interval

$$\frac{1}{4}\left(\frac{3}{2}\frac{a^2 V}{\varepsilon^2 K_{\text{pas}}^2}\right)^{1/3} \leq \left(\frac{h}{2g}\right)_{\text{rigid}} \leq \frac{1}{4}\left(\frac{3}{2}\frac{a^2 V}{\varepsilon^2 K_{\text{act}}^2}\right)^{1/3}. \tag{5.111}$$

Contrary to the result (5.107), the boundaries of this interval depend on the volume of the avalanche and on the value of a.

- *Model 3:* The evolution equations for g and $\overline{x}$ for this model are

$$\begin{aligned} \frac{dg'}{dt} &= \frac{3}{2}\varepsilon K \cos\zeta \frac{V}{g^2} - c\mu_0 g' \cos\zeta, & \frac{dg}{dt} &= g', \\ \frac{d\overline{u}}{dt} &= \sin\zeta - \mu_0 (1 + c\,\overline{u}) \cos\zeta, & \frac{d\overline{x}}{dt} &= \overline{u}, \end{aligned} \tag{5.112}$$

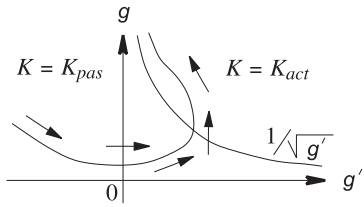

Fig. 5.10. Phase plane $g(g')$ or (g', g) and typical behaviour of a phase plane orbit $g(g')$ for model 3. *Arrows* indicate the directions in which the trajectories are traversed.

in which $K = K_{\rm act}$ and $K = K_{\rm pas}$, depending on whether $g' > 0$ or $g' < 0$. They show that the centre of mass motion and the spreading are independent of each other. The second term on the right-hand side of $(5.112)_1$ plays the role of a resistance against the spreading of the pile. In spite of this, no rigid body motion can exist. This can be understood as follows (see Fig. 5.10). The hyperbola in this figure represents those values of g and g' for which the right-hand side of $(5.112)_1$ vanishes. Along this curve $dg/dg' = \infty$, since $0 = dg'/dt = (dg'/dg)(dg/dt)$ and $dg/dt \neq 0$; consequently all phase orbits $g(g')$ cross this line with a vertical tangent as indicated by the arrow. Moreover, at $g' = 0$ we have

$$0 = g' = \frac{dg}{dt} = \frac{dg}{dg'}\frac{dg'}{dt} \Longrightarrow \frac{dg}{dg'} = 0, \tag{5.113}$$

because for $g' = 0$ we have $dg'/dt \neq 0$, according to $(5.112)_1$; phase space trajectories $g(g')$ intersect the axis $g' = 0$ with a horizontal tangent, also indicated by a thick arrow. In the remaining regions, the general direction is as indicated by the arrows. So, for $g' < 0$ the granular pile is contracting, whereas it is extending for $g' > 0$. Even though the phase orbit bends towards the g-axis after crossing the hyperbola, the axis $g' = 0$ is only approached asymptotically as g tends to infinity. Indeed, it was shown above that all phase space trajectories must cross the hyperbola with a vertical tangent. Obviously, such a second crossing is only possible at $g \to \infty$. This proves the non-existence of a rigid body state.

• *Models 4–6:* The spreading of the granular pile in these models is qualitatively the same as for *model 1* with $\mathcal{A} = 0$ and as illustrated in Fig. 5.7. The centre of mass motion depends on the form of the functional relation $\mu(\overline{u})$. These models are capable of attaining a terminal velocity (see (5.100) and (5.101) for their representations), but no simultaneous steady spread exists. This makes these models unrealistic candidates for practical use.

• *Models 7 and 8:* Even though in *model 8* the centre of mass motion and the deformation of the parabolic pile depend on each other, whereas in *model 7* the centre of mass motion is independent of the deformation, the qualitative

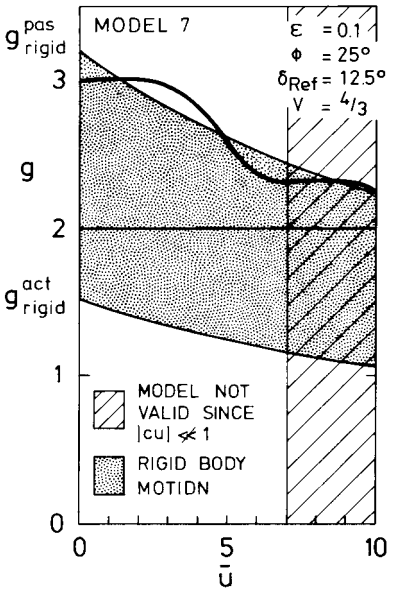

Fig. 5.11. Domain of the semi-spread g_{rigid}, where a rigid body motion of the granular parabolic pile prevails for *model 7*, indicated by the *shaded area*. Regions of the centre of mass motion, where the application of the model is doubtful are also indicated (hatched). The *thick solid curve* shows the evolution of the spreading when $g_0 = 3$. A rigid body state is followed by a contraction and subsequently another rigid body state. (From [301].)

behaviour of the two models is similar. For *model 7* the equation for the spreading rate is

$$\frac{dg'}{dt} = \frac{3}{2}\varepsilon K \cos\zeta \frac{V}{g^2} - \frac{f(\overline{u})\tan\phi_0}{2}\cos\zeta, \quad \frac{dg}{dt} = g', \tag{5.114}$$

with a rigid body motion being possible in the interval

$$g_{\text{rigid}}^{\text{act}} = \sqrt{\frac{3\varepsilon K_{\text{act}} V}{f(\overline{u})\tan\phi_0}} < g_{\text{rigid}} < \sqrt{\frac{3\varepsilon K_{\text{pas}} V}{f(\overline{u})\tan\phi_0}} = g_{\text{rigid}}^{\text{pas}} \tag{5.115}$$

(the right-hand side of (5.114) vanishes). This condition of rigid body motion includes the velocity of the centre of mass through $f(\overline{u})$. Figure 5.11 displays this dependence when $f(\overline{u}) = 1 + c\overline{u}$ (shaded variable band). When $c = 0.1$ and $\overline{u} > 7$, $|cu|$ is not very much smaller than 1, and the prerequisites of the model are no longer fulfilled. This right most region is hatched in Fig. 5.11. The temporal evolution of the semi-spread g and of the velocity of the centre of mass u for several choices of the initial spread g_0 is shown in Fig. 5.12. For $g_0 = 1$, the granular pile first extends and then reaches a rigid body state with a value of g_{rigid} close to 2. When $g_0 = 4$, the initial phase of the motion

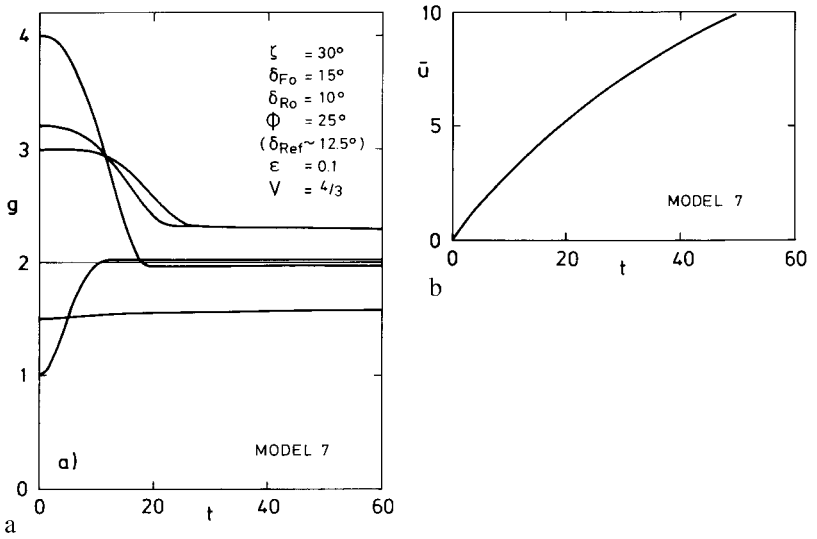

Fig. 5.12. **a**) Spreading g plotted against time for various different initial values g_0. **b**) Evolution in time of the velocity of the centre of mass when started from rest for *model 7*. (From [301].)

of the pile is a contraction, followed by a rigid body motion. On the other hand, when $g_0 = 3$ (compare also Figs. 5.11 and 5.12), the pile starts with a rigid body motion, then contracts, and goes through another rigid body state. The motion of the centre of mass is not influenced by these properties. This is the reason why in Fig. 5.12b only one curve, which is valid for all cases is drawn. This is a rather dubious behaviour and eliminates *model 7* as a candidate for a realistic avalanche model. This is not so in *model 8*.

Closing Remarks We made use of the depth-averaged SH-equations of motion and obtained one-dimensional approximate similarity solutions for the motion of a finite mass of an incompressible cohesionless granular material moving down a rough inclined plane. Basal resistance was introduced as a MOHR–COULOMB-type friction law with a friction coefficient that could depend on position, velocity or both. On the basis of very mild to relatively strong simplifying assumptions regarding the dependence of the earth pressure coefficient on the basal friction angle, the depth profiles of the moving and deforming piles were found to have a parabolic cap shape and the difference velocity (depth-averaged velocity minus the centre of mass velocity) was found to vary linearly with the distance from the centre of mass of the moving pile. For all investigated basal friction laws the dynamical equations could be reduced to a set of ordinary differential equations describing the motion of the centre of mass and the extension or contraction of the pile.

The behaviour of eight different friction models was studied. The analysis showed that the dependence of the bed friction angle in the COULOMB-type basal sliding law on local field variables is crucial. *For a constant bed friction angle* it was shown that *the centre of mass motion of a granular mass persistently accelerates, and its deformation is monotonically extending.* A proper dependence of the bed friction angle on other (local) field variables allows these qualitative features to be changed. Qualitatively, *when bed resistance is large in the front of the avalanche and smaller in its back, the deformation is no longer monotonically extending, and the avalanche may go through phases in its motion in which extending, contracting and rigid-body states are possible.* The exact performance is model-dependent, but the possibility of an evolution with a bounded length can be achieved by either making the tangent of the bed friction angle position or velocity-dependent, or both. Furthermore, the centre of mass motion need no longer have to accelerate indefinitely along the infinitely long inclined plane. In cases *when the bed friction angle depends on the depth-averaged velocity, a finite terminal velocity of the centre of mass might exist.* Such steady state conditions, however, do not exist for all investigated models. Of course, an experimental corroboration of the existence of such steady state conditions would be rewarding, but it is hardly possible. Nevertheless, the construction of the solutions is useful because the qualitative behaviour shows how sensitively the dynamical system "avalanche" reacts to subtle changes in the friction law.

The analysis also showed that *the dependence of the bed friction angle on velocity and/or spread is crucial for the existence of steady state conditions.* A model in which the centre of mass motion is capable of reaching a steady state but the stretch can not, or vice versa, is likely to be physically unrealistic. Finally, the analysis has been approximate insofar as the split of the total motion into that of the centre of mass and the deformation with a parabolic shape of the moving mass only led to a coupled set of ordinary differential equations for the centre of mass displacement and the semi-spread by invoking ad hoc assumptions. Of course, a mathematical proof or disproof of the outlined properties from the original equations would be a worthwhile endeavour.

5.2.5 Variable Bed Friction, Curved Bed and VOELLMY Drag

In an attempt to investigate whether inclusion of the VOELLMY drag would qualitatively yield alterations of the results derived so far, HUTTER and NOHGUCHI [173] looked at the plane flow of a granular material down a curved bed of which the basal friction law consisted of a COULOMB term $\mathbf{S}_C$ and a velocity-dependent term $\mathbf{S}_V$ such that $\mathbf{S} = \mathbf{S}_C + \mathbf{S}_V$ with a quadratic dependence of $\mathbf{S}_V$ on the downslope velocity $\mathbf{u}$ (see also Sect. 3.5.1):

$$\mathbf{S}_V = \rho\, q\,(|\mathbf{u}|, |\mathbf{N}|)\, |\mathbf{u}|\mathbf{u}, \tag{5.116}$$

where $\mathbf{u}$ is the basal velocity, $\mathbf{N}$ is the traction normal to the bed, ρ is the density and q a dimensionless phenomenological coefficient that may also depend on $\mathbf{u}$ and $\mathbf{N}$. VOELLMY writes

$$\mathbf{S}_V = \frac{\rho\, g}{\xi}|\mathbf{u}|\mathbf{u}, \tag{5.117}$$

where ξ is called "viscosity", even though it has the dimension of an acceleration. Obviously,

$$q = \frac{g}{\xi}. \tag{5.118}$$

If x is the downslope coordinate and t the time, then the dimensionless depth-integrated conservation laws of mass and linear momentum take the forms

$$\begin{aligned} &\frac{\partial h}{\partial t} + \frac{\partial}{\partial x}\,(hu) = 0, \\ &\frac{\partial u}{\partial t} + u\frac{\partial u}{\partial x} = \sin\zeta(x) - \left(\mu\cos\zeta(x) + \frac{qu^2}{\varepsilon h}\right) - \varepsilon K_{\text{act/pas}}\cos\zeta(x)\frac{\partial h}{\partial x} \end{aligned} \tag{5.119}$$

and must be solved subject to the boundary conditions

$$h\,(x_F(t)) = 0, \quad h\,(x_R(t)) = 0,$$

where $x = x_F(t)$ and $x = x_R(t)$ are the positions of the front and rear margins, respectively.

Defining averaged field quantities as before by

$$\overline{f} = \frac{1}{V}\int_{x_{R(t)}}^{x_{F(t)}} hf\,dx, \qquad V = \int_{x_{R(t)}}^{x_{F(t)}} h(x)\,dx, \tag{5.120}$$

the equations of motion for the centre of mass take the forms (see (5.72)),

$$\frac{d\,\overline{u}}{dt} = \sin\zeta(\overline{x}) - \overline{\mu}\cos\zeta(\overline{x}) - \frac{1}{\varepsilon}\overline{\left(\frac{qu^2}{h}\right)}, \qquad \frac{d\,\overline{x}}{dt} = \overline{u}, \tag{5.121}$$

provided that $\overline{u} > 0$ for all $t > 0$. To deduce the governing equations for the deformation, we let

$$\tilde{u} = u - \overline{u}(t), \quad \xi = x - \overline{x}(t), \quad \tau = t, \tag{5.122}$$

and then may derive in a manner similar to before

$$\begin{aligned} &\frac{\partial h}{\partial t} + \frac{\partial}{\partial \xi}\,(h\tilde{u}) = 0, \\ &\frac{\partial \tilde{u}}{\partial t} + \tilde{u}\frac{\partial \tilde{u}}{\partial \xi} = \cos\zeta(\overline{x})\left.\frac{d\zeta}{dx}\right|_{x=\overline{x}} - (\mu - \overline{\mu})\cos\zeta(\overline{x}) \\ &\qquad\qquad -\frac{1}{\varepsilon}\left\{\frac{qu^2}{h} - \overline{\left(\frac{qu^2}{h}\right)}\right\} - \varepsilon K_{\text{act/pas}}\cos\zeta(\overline{x})\frac{\partial h}{\partial \xi}, \end{aligned} \tag{5.123}$$

describing the deformation of the pile. In (5.123), $\zeta(x)$ has been expanded to first-order about the centre $\overline{x}$ to account for the curvature effects of the bed, $(d\zeta/dx)\,\big|_{x=\overline{x}}$. This implies that (5.121) and (5.123) are exact only for flows down inclined panes.

The sets of evolution equations (5.121) and (5.123) are not in a form that is integrable for the unknowns $\overline{x}, \overline{u}, h$ and $\tilde{u}$. To this end, the VOELLMY term needs further simplification. For this, the following condition must be imposed:

$$\begin{aligned} \overline{\left(\frac{qu^2}{h}\right)} &= \frac{\overline{q}\,\overline{u}^2}{\overline{h}} + O\left(\varepsilon^{\alpha}\right), \quad \alpha > 1, \\ \frac{qu^2}{h} - \overline{\left(\frac{qu^2}{h}\right)} &= O\left(\varepsilon^{\beta}\right), \quad \beta > 1. \end{aligned} \tag{5.124}$$

These assumptions require the velocity profiles to be nearly uniform and extending and contracting rates to be negligible in the VOELLMY term. This assumption leads to significant quantitative inferences. The final system of equations then becomes

$$\begin{aligned} &\frac{d\,\overline{u}}{dt} = \sin\zeta(\overline{x}) - \overline{\mu}\cos\zeta(\overline{x}) - \frac{\overline{q}\,\overline{u}^2}{\varepsilon\overline{h}}, \qquad \frac{d\,\overline{x}}{dt} = \overline{u}, \\ &\frac{\partial h}{\partial t} + \frac{\partial}{\partial \xi}\left(h\overline{u}\right) = 0, \\ &\frac{\partial \tilde{u}}{\partial t} + \tilde{u}\frac{\partial \tilde{u}}{\partial \xi} = \cos\zeta(\overline{x})\frac{d\zeta}{dx}\bigg|_{x=\overline{x}} - (\mu - \overline{\mu})\cos\zeta(\overline{x}) - \varepsilon K_{\text{act/pas}}\cos\zeta(\overline{x})\frac{\partial h}{\partial \xi}. \end{aligned} \tag{5.125}$$

Evidently, the VOELLMY drag coefficient directly affects only the centre of mass motion.

With the experience gained in the previous sections it is now straightforward to construct similarity solutions of the parabolic cap type. To this end, let us choose $q =$ constant and

$$\begin{aligned} \mu &= \frac{\mu_F - \mu_R}{2g}\xi + \frac{\mu_F + \mu_R}{2} = \frac{\Delta\mu}{2g}\xi + \mu_c, \\ g &= \xi_F = -\xi_R, \quad \tilde{u} = \eta g' = \frac{\xi}{g}g' = \frac{g'}{g}\xi = \frac{1}{g}\frac{dg}{dt}\xi, \end{aligned} \tag{5.126}$$

where g is the semi-spread, μ_c the mean of the tangent of the bed friction angle and $\Delta\mu$ its linear variation from the front to the rear margin. Moreover, $\tilde{u}$ has been assumed to be linearly distributed over the pile length. With equations (5.126), (5.125) become

$$
\begin{aligned}
\frac{dX}{dt} &= \overline{u}(t)\cos\zeta(\overline{x}),\\
\frac{dY}{dt} &= \overline{u}(t)\sin\zeta(\overline{x}),\\
\frac{d\,\overline{u}}{dt} &= \sin\zeta(\overline{x}) - \mu_c\cos\zeta(\overline{x}) - \frac{2q}{\varepsilon}\frac{\overline{u}^2}{V}g,\\
\frac{d\,\overline{x}}{dt} &= \overline{u},\\
\frac{dg'}{dt} &= \frac{3}{2}\varepsilon\overline{K}_{\mathrm{act/pas}}\cos\zeta(\overline{x})\frac{V}{g^2} - \frac{4\mu}{2}\cos\zeta(\overline{x}) + \left.\frac{d\zeta}{dx}\right|_{x=\overline{x}}\cos\zeta(\overline{x})\,g,\\
\frac{dg}{dt} &= g',
\end{aligned}
\tag{5.127}
$$

where $\overline{K}_{\mathrm{act/pas}} = K_{\mathrm{act/pas}}(\overline{x}_{\mathrm{Ref}})$ and the first two equations have been added to directly determine the horizontal (X) and vertical (downward, Y) components of the centre of mass position.

The ordinary differential equations (5.127) exhibit a two-sided coupling: the centre of mass motion is affected by the deformation. On the other hand, the centre of mass motion also affects the deformation via the VOELLMY term. However, as is evident from the right-hand sides of $(5.127)_{3,5}$, rigid body motions are possible, as are extensional and compressional motion phases. In fact, the qualitative behaviour of the solutions is easily seen to be as follows:

(*i*) When the right-hand side of $(5.127)_5$ is negative for both K_{act} and K_{pas}, $dg'/dt < 0$, so g' will decrease and phase space trajectories will be traversed from right to left, as indicated in the left graph of Fig. 5.13. Such a behaviour cannot correspond to a rigid body motion and the pile will contract.

(*ii*) When $(dg'/dt)\,\big|_{K=K_{\mathrm{act}}} < 0 < (dg'/dt)\,\big|_{K=K_{\mathrm{pas}}}$, one has $dg'/dt < 0$ for $g' > 0$, and $dg'/dt > 0$ for $g' < 0$. Phase space trajectories are traversed such that they move towards the ordinate both from the left and from the right. Hence a constant length g is approached, corresponding to a rigid body motion, as illustrated in the middle graph of Fig. 5.13.

(*iii*) When the right-hand side of $(5.125)_5$ is positive, $dg'/dt > 0$, so g' will increase and phase space trajectories are traversed from left to right, as shown in the right graph of Fig. 5.13. The pile is extending.

Phase plane orbits look qualitatively the same as those in Fig. 5.8. The graphs in Fig. 5.13 correspond to the neighbourhoods of the coordinate axis below point A, within the interval $[A, B]$ and above point B, respectively.

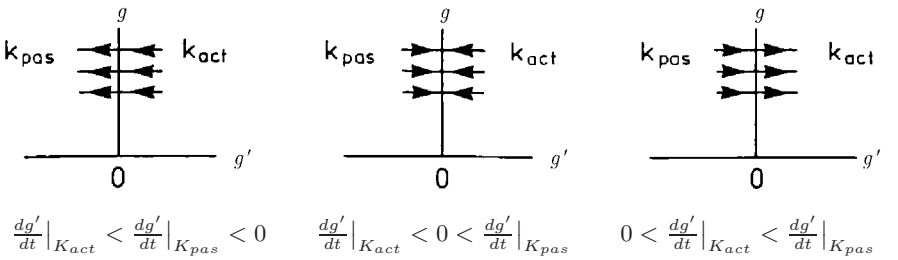

Fig. 5.13. Directions of traverses of phase space orbits (indicated by *arrows*) in the neighbourhood of $g' = 0$ for contracting (*left*), rigid body (*middle*) and extending (*right*) flow. (From [173].)

5.3 Two-Dimensional Similarity Solutions

Two-dimensional similarity solutions have been derived by HUTTER and GREVE [176] for the avalanching motion of a finite mass of granules *with* COULOMB*-dependent and velocity-dependent frictional resistance* for a granular pile with elliptical shape in plane view and parabolic distributions of the height both in the downflow and crossflow directions. The motion is decomposed into that of the centre of mass and the deformation relative to it. This decomposition is possible provided that the effect of the VOELLMY drag on the deformation is ignored. With it, the depth and velocities relative to those of the centre of the mass of the moving pile can be determined analytically. For this purpose, we consider (3.79) of Sect. 3.5.3 describing the deformation and motion of a granular mass down an inclined plane. From (3.79) similarity solutions cannot be derived; additional assumptions are needed. These are stated immediately below (3.79) and include the additional approximations (3.80). With all these assumptions, the existence of similarity solutions can be demonstrated. These similarity solutions were constructed when the COULOMB friction angles ϕ and δ were kept constant [176, 177]. Here we slightly generalise these equations. The basis is (3.81), which are now specialized for the case that the centre of mass lies in a vertical plane defining the downhill direction. For a motion from rest along an inclined plane this is necessarily so. In (3.81), we then have $\overline{v}_c = 0$ and $\overline{y}_c = 0$ so that $(3.81)_{1\text{-}4}$ reduce to two equations for $\overline{u}_c$ and $\overline{x}_c$, whilst $(3.81)_{5\text{-}7}$ can be used without any changes.

As in the one-dimensional case of Sects. 5.2.1 and 5.2.2, we anticipate a solution in which the shape and difference velocity distributions are preserved, and the profiles are merely stretched or compressed in the streamwise and lateral directions. In view of this, we choose new similarity variables that are normalised by the half extent of the pile in the two principal flow directions,

$$\nu = \frac{\xi}{g(\tau)}, \quad \mu = \frac{\eta}{f(\tau)}, \quad t = \tau. \tag{5.128}$$

From (5.128), we deduce the following relation of the differential operators between the new and old variables

$$\begin{aligned} \frac{\partial}{\partial \xi} &= \frac{1}{g}\frac{\partial}{\partial \nu}, \quad \frac{\partial}{\partial \eta} = \frac{1}{f}\frac{\partial}{\partial \mu}, \\ \frac{\partial}{\partial \tau} &= \frac{\partial}{\partial t} - \frac{g'}{g}\nu\frac{\partial}{\partial \nu} - \frac{f'}{f}\mu\frac{\partial}{\partial \mu}, \end{aligned} \tag{5.129}$$

where primes denote univariate differentiation. Substituting relations (5.128) and (5.129) into $(3.81)_{5\text{-}7}$ and seeking solutions for the difference velocity in the form

$$\tilde{u} = g'\nu, \quad \tilde{v} = f'\mu, \tag{5.130}$$

yields the following set of deformation equations:

$$\begin{aligned} &\frac{\partial h}{\partial t} + \frac{h}{g}\frac{\partial \tilde{u}}{\partial \nu} + \frac{h}{f}\frac{\partial \tilde{v}}{\partial \mu} = 0, \\ &\frac{\partial \tilde{u}}{\partial t} = -\frac{B}{g}\frac{\partial h}{\partial \nu} - 2\frac{|\overline{u}_c|}{\overline{\Xi}\,\overline{h}}g'\nu, \\ &\frac{\partial \tilde{v}}{\partial t} = -\frac{D}{f}\frac{\partial h}{\partial \mu} - \frac{|\overline{u}_c|}{\overline{\Xi}\,\overline{h}}f'\mu - C\frac{f'}{|\overline{u}_c|}\mu, \end{aligned} \tag{5.131}$$

in which τ has been replaced by t. Again replacing $\tilde{u}$ and $\tilde{v}$ by (5.130), the momentum balance equations $(5.131)_{2,3}$ reduce to

$$\begin{aligned} \frac{\partial h}{\partial \nu} &= -\frac{\nu}{B}g\left\{g'' + 2\frac{|\overline{u}_c|}{\overline{\Xi}\,\overline{h}}g'\right\}, \\ \frac{\partial h}{\partial \mu} &= -\frac{\mu}{D}f\left\{f'' + \left(\frac{C}{|\overline{u}_c|} + \frac{|\overline{u}_c|}{\overline{\Xi}\,\overline{h}}\right)f'\right\}, \end{aligned} \tag{5.132}$$

where B, C and D, as defined in (3.58), are

$$B = \varepsilon\cos\zeta K_x, \quad C = \cos\zeta\tan\delta, \quad D = \varepsilon\cos\zeta K_y, \tag{5.133}$$

and Ξ is the Voellmy drag coefficient, see (3.57). Both equations appear in separable form. The right-hand sides of each equation are a product of ν (and μ, respectively) and a function of time. In order to solve these equations, we assume that the granular mass initially has a circular paraboloidal shape that in the course of motion deforms into an elliptic pile height. Such geometries of the pile are, however, not exactly observed in laboratory experiments (see

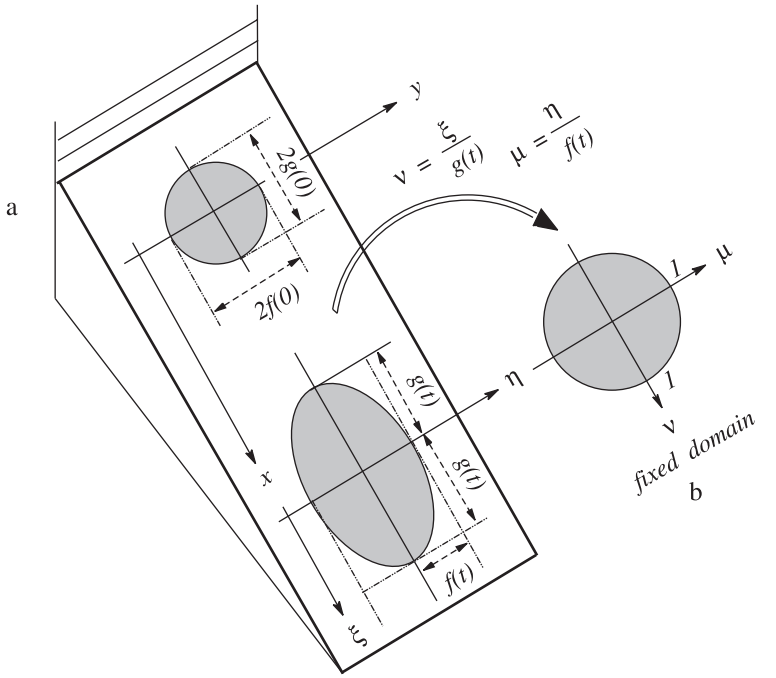

Fig. 5.14. Different coordinate systems, plane view of the granular piles and explanation of similarity solution: **a**) Initial circular projection of the granular pile and general position in elliptic form. **b**) Fixed domain transformation, again into a circular form.

Figs. 5.17 and 5.18).[9] In the present considerations, the semi-spread functions g and f are interpreted as principal semi-axes of the ellipse. Therefore, the transformation of the ellipsoidal hump into the (ν, μ)-plane by the rule (5.128) maps the elliptical domain into the interior of a fixed circle with unit radius, as shown in Fig. 5.14.

We, therefore, assume the avalanche geometry to have the form

$$h(\nu, \mu, t) = H_0(t)\left(1 - \nu^2 - \mu^2\right), \tag{5.134}$$

where $H_0(t)$ is the avalanche depth at the centre of the ellipse. Substituting (5.134) into (5.132) yields

[9] Elliptical pile shapes were never observed in our laboratory experiments. This may be an indication that the assumptions leading from (3.79) to (3.81) and then to (5.131) are too severe. The similarity solutions of the simplified equations, however, still give insight into the qualitative behaviour of two-dimensional idealised motions, as will be demonstrated later.

$$H_0(t) = \frac{g}{2B}\left\{g'' + 2\frac{|\overline{u}_c|}{\overline{\Xi}\,\overline{h}}g'\right\},$$
$$H_0(t) = \frac{f}{2D}\left\{f'' + \left(\frac{C}{|\overline{u}_c|} + \frac{|\overline{u}_c|}{\overline{\Xi}\,\overline{h}}\right)f'\right\}. \tag{5.135}$$

These equations form two second-order ordinary differential equations for the *avalanche expansion coefficients* $g(t)$ and $f(t)$, respectively, *provided* that $H_0(t)$ is a known function of time. A connection between these coefficients and $H_0(t)$ can be established from the conservation law of the volume of the avalanching mass. We thus evaluate the total volume V

$$\begin{aligned} V &= \iint_{\mathcal{A}} h\,d\xi d\eta = H_0(t)\iint_{\mathcal{A}_0}\left(1-\nu^2-\mu^2\right)g(t)f(t)\,d\nu d\mu \\ &= H_0 gf\iint_{\mathcal{A}_0}\left(1-\nu^2-\mu^2\right)d\nu d\mu = H_0 gf\int_0^1\int_0^{2\pi}\left(1-r^2\right)r d\theta dr \\ &= 2\pi H_0 gf\int_0^1 r\left(1-r^2\right)dr = \frac{\pi H_0}{2}gf, \end{aligned} \tag{5.136}$$

where $\mathcal{A}_0$ is the unit circle, i.e., since the initial volume is preserved,

$$H_0 = \frac{2V}{\pi gf}. \tag{5.137}$$

We thus have,

$$h = \frac{2V}{\pi gf}\left(1-\nu^2-\mu^2\right), \tag{5.138}$$

and the mean height is given by

$$\begin{aligned} \overline{h} &= \iint_{\mathcal{A}} h\,d\nu d\mu = \iint_{\mathcal{A}}\frac{2V}{\pi gf}\left(1-\nu^2-\mu^2\right)d\nu d\mu \\ &= \frac{2V}{\pi gf}\int_0^1\int_0^{2\pi}\left(1-r^2\right)r d\theta dr = \frac{2V}{\pi gf}2\pi\int_0^1 r\left(1-r^2\right)dr \\ &= \frac{4\pi V}{4\pi gf} = \frac{V}{gf}. \end{aligned} \tag{5.139}$$

Equation (5.138) indicates that the temporal evolution of the height profile is known once g and f are determined. Substituting the value of H_0 and $\overline{h}$ from (5.137) and (5.139), respectively, into (5.135) we obtain two second-order ordinary differential equations for g and f as follows:

$$g'' + \left(2\frac{|\overline{u}_c|\pi gf}{\overline{\Xi}V}\right)g' = \frac{4BV}{\pi g^2 f},$$
$$f'' + \left(\frac{C}{|\overline{u}_c|} + \frac{|\overline{u}_c|\pi gf}{\overline{\Xi}V}\right)f' = \frac{4DV}{\pi gf^2}. \tag{5.140}$$

What remains is to corroborate the mass balance $(5.131)_1$ with the definition of the difference velocity (5.130). This is not difficult to show. Indeed, from (5.130) and (5.138) one concludes that

$$\begin{aligned}
&\frac{\partial h}{\partial t}+\frac{h}{g}\frac{\partial \tilde{u}}{\partial \nu}+\frac{h}{f}\frac{\partial \tilde{v}}{\partial \mu}\\
&=\frac{\partial}{\partial t}\left\{\frac{2V}{\pi g f}\left(1-\nu^2-\mu^2\right)\right\}+\frac{2V}{\pi g f}\left(1-\nu^2-\mu^2\right)\left\{\frac{1}{g}\frac{\partial\left(g'\nu\right)}{\partial \nu}+\frac{1}{f}\frac{\partial\left(f'\mu\right)}{\partial \mu}\right\}\\
&=\frac{2V}{\pi}\left(1-\nu^2-\mu^2\right)\left\{\left(-\frac{f'}{gf^2}-\frac{g'}{g^2 f}\right)+\frac{1}{gf}\left(\frac{g'}{g}+\frac{f'}{f}\right)\right\}\\
&=\frac{2V}{\pi}\left(1-\nu^2-\mu^2\right)\frac{1}{g^2f^2}\left(-gf'-g'f+g'f+gf'\right)=0.
\end{aligned}$$

This means that we are consistent in our calculations.

Numerical Integration To determine the motion of the centre of mass and the (longitudinal and transversal) spreading rates we must solve equations $(3.81)_{1,3}$ with $\overline{v}_c=0$ and (5.140). Collectively the emerging equations are

$$\begin{aligned}
&\frac{d\,\overline{x}_c}{dt}=\overline{u}_c,\\
&\frac{d\,\overline{u}_c}{dt}=\sin\zeta-C\frac{\overline{u}_c}{|\overline{u}_c|}-\frac{|\overline{u}_c|\overline{u}_c\pi g f}{\overline{\Xi}V},\\
&\frac{dg}{dt}=g',\\
&\frac{dg'}{dt}=-\left(2\frac{|\overline{u}_c|\pi g f}{\overline{\Xi}V}\right)g'+\frac{4BV}{\pi g^2 f},\\
&\frac{df}{dt}=f',\\
&\frac{df'}{dt}=-\left(\frac{C}{|\overline{u}_c|}+\frac{|\overline{u}_c|\pi g f}{\overline{\Xi}V}\right)f'+\frac{4DV}{\pi g f^2}.
\end{aligned}\tag{5.141}$$

The integration of these equations must be performed subject to the following initial conditions:

$$\begin{aligned}
&\overline{x}_c(t=0)=\overline{x}_c^0, \quad \overline{u}_c(t=0)=\overline{u}_c^0,\\
&g(t=0)=g_0, \qquad g'(t=0)=g_0',\\
&f(t=0)=f_0, \qquad f'(t=0)=f_0',
\end{aligned}\tag{5.142}$$

corresponding to a mass with initial length $2g_0$ and initial width $2f_0$. Notice that in writing (5.141) the time variable t is used instead of τ and relation $V=\overline{h}gf$ is used from (5.139).

There are many special properties of system (5.141). Some of them are listed below.

- In general, the centre of mass motion and the deformation are mutually coupled. This is due to the fact that the term $(|\overline{u}_c|\overline{u}_c \pi g f) \,/\, \overline{\Xi} V$ is composed of $\overline{u}_c$ and gf.
- Without the viscous sliding term ($\overline{\Xi} \to \infty$), the *motion* of the centre of mass of the pile *decouples* from that of the deformation. Therefore, $(5.141)_{1,2}$ and $(5.141)_{3-6}$ can be solved separately for the centre of mass motion once this is determined for the deformation and flow, respectively.
- From $(5.141)_{4,6}$ it follows that there can never be a rigid body motion (for which g and f are constant) even for finite $\overline{\Xi}$. A rigid motion would require $g' = f' = dg'/dt = df'/dt = 0$, but the statements $dg'/dt = 0$ and $df'/dt = 0$ are not possible because for $g' = 0$ and $f' = 0$ the right-hand sides of $(5.141)_{4,6}$ are positive in this case due to the presence of the terms $4BV/\pi g^2 f$ and $4DV/\pi g f^2$.
- Since g and f can never be constant, it follows from $(5.141)_2$ that the centre of mass can never be steady for finite $\overline{\Xi}$. For $\overline{\Xi} \to \infty$, $C = \sin\zeta$ is the only steady solution, which is physically very limited.

So far we have shown that the model pile has a parabolic cap shape and contour lines are elliptical. The semi-axes and the position and velocity of the centre of mass are calculated numerically. Thus, *within the context of similarity solutions*, Hutter and Greve, [176] showed that:

- *For two-dimensional spreading, a rigid body motion does not exist, no matter what the values of the bed friction angle and the coefficient of viscous drag are.*
- *A steady final velocity of the centre of the mass cannot be approached, but the motion of the centre of mass depends on the value of the* Voellmy *coefficient.*
- *The aspect ratio of the moving pile depends on the variation of the bed friction angle with position, as well as on the value of the coefficient of the viscous drag.*

These statements are rigorous inferences from (5.141). The explicit calculations show, however, that the motion of the centre of mass may reach nearly steady conditions and the corresponding longitudinal and transverse spreadings are nearly constant, so that "effective rigid steady motion" is nearly obtained. Figures 5.15 and 5.16 show this for conditions as indicated in the inset. Figure 5.15 shows temporal evolutions of g and f when the Voellmy coefficient $\overline{\Xi}$ is held constant but $\Delta = \delta_{\text{front}} - \delta_{\text{rear}}$ varies and vice versa. It is seen that both longitudinal and sidewise spreadings are affected by these variations, and in all cases except when $\Xi \geq 10^3$ nearly steady values seem to be approached when t becomes large. This indicates that the Voellmy drag and variations of the bed friction angle are very effective in attaining distinctive behaviour.

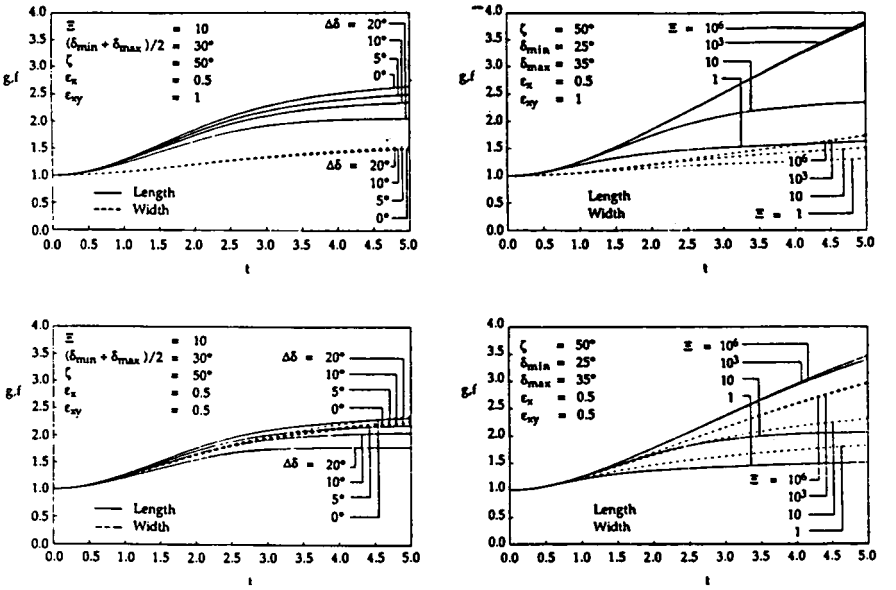

Fig. 5.15. Temporal evolution of the semi-spreads $g(t)$ (*solid line*) and $f(t)$ (*dashed line*), calculated for $\phi = 35^\circ$ and the physical parameters shown in the *inset*. In the *left panels* $\Delta = \delta_{\text{front}} - \delta_{\text{rear}}$ is varied while Ξ is held fixed, in the *right panel* it is the opposite. $(\varepsilon_x, \varepsilon_{xy}) = (0.5, 1)$ (*top*) and $(\varepsilon_x, \varepsilon_{xy}) = (0.5, 0.5)$ (*bottom*). Also note that $\varepsilon_x = [H]/[L_x]$ and $\varepsilon_{xy} = [L_y]/[L_x]$, where H is the typical avalanche height, and L_x and L_y are the typical extents of the avalanche in the x- and y-directions, respectively. (From [176].)

There must also be a strong dependence of the centre of mass motion on the VOELLMY coefficient. Figure 5.16 provides evidence for this. In the top two panels, the centre of mass position, $\overline{x}_c$, in the lower panels the centre of mass velocity, $\overline{u}_c$, (both dimensionless) are plotted against dimensionless time, t, for various values of the parameter $\overline{\Xi}$. For very large $\overline{\Xi}$ values ($\overline{\Xi} > 1000$), the centre of mass velocity is essentially linear in time and its position grows quadratically. These results are an important corroboration of our earlier calculations, which were performed without the VOELLMY term. With growing viscosity (decreasing $\overline{\Xi}$ values), the growth of the centre of mass velocity is more and more reduced. The fact that the graphs for $\varepsilon_{xy} = 1$ and $\varepsilon_{xy} = 0.5$ hardly differ is an indication that the centre of mass motion is only minimally affected by the amount of spreading. On the other hand, that the amount of spreading crucially depends on both the dry and viscous drag behaviour, demonstrates the superiority of the present model over the classical models due to VOELLMY, SALM and others.

The qualitative results gained by the analysis of similarity solutions are physically very important. One result is that with a COULOMB sliding law

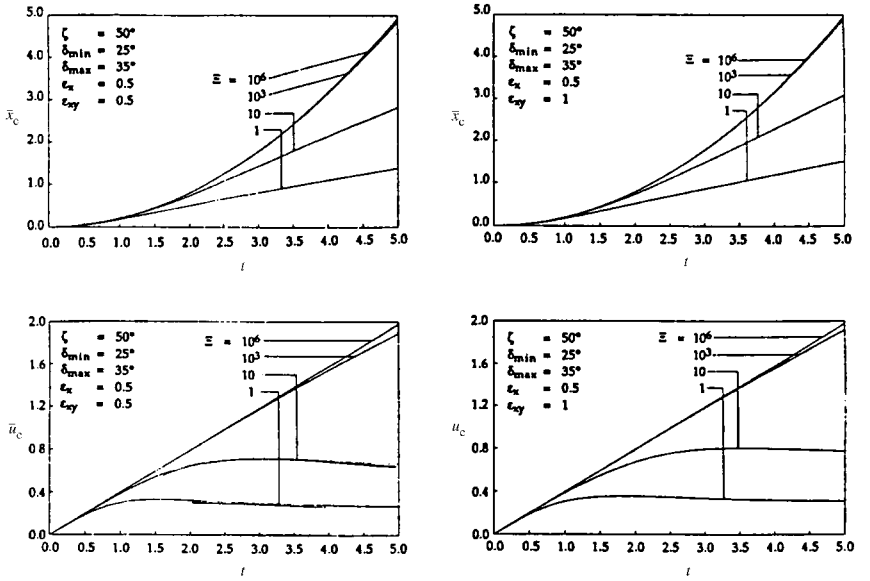

Fig. 5.16. Temporal evolution of the centre of mass position $\overline{x}_c$ and its velocity $\overline{u}_c$ calculated for $\phi = 35°$ and the physical parameters shown in the *insets*, when the VOELLMY coefficient is varied. Computations have been done for $(\varepsilon_x, \varepsilon_{xy}) = (0.5, 0.5)$ (*left*) and $(\varepsilon_x, \varepsilon_{xy}) = (0.5, 1)$ (*right*). (From [176].)

exhibiting constant friction angles, a steady state solution on an inclined plane cannot be reached. This is sometimes taken as an argument to "reject" the COULOMB friction law, calling it "physically unreasonable" since adding a velocity-dependent contribution automatically re-establishes the existence of such steady states. However, to corroborate such a steady state solution of a dry avalanche of parabolic shape by experiment has never been successful,[10] and in the field such a corroboration is hardly achieved. Thus, requesting a viscous contribution to the drag may not be experimentally substantiated. It may, however be convenient, since it provides more flexibility in matching the model with field data.

As far as the experimental reproduction of the constructed similarity solutions go, our attempts have never been successful. In chute flows neither the parabolic cap nor M-wave solutions were closely observed; only moving heaps looking like parabolic humps were observed, however with shapes breaking the symmetry in the cross-hill direction. For two-dimensional avalanches, start-

[10] In Chaps. 11–12 the motion of sand down inclined planes is experimentally studied using *particle image velocimetry*. There are indications for very long chutes at relatively small inclination angles that a steady state flow may be established far downstream. While this inference is likely, it is however, not completely convincing.

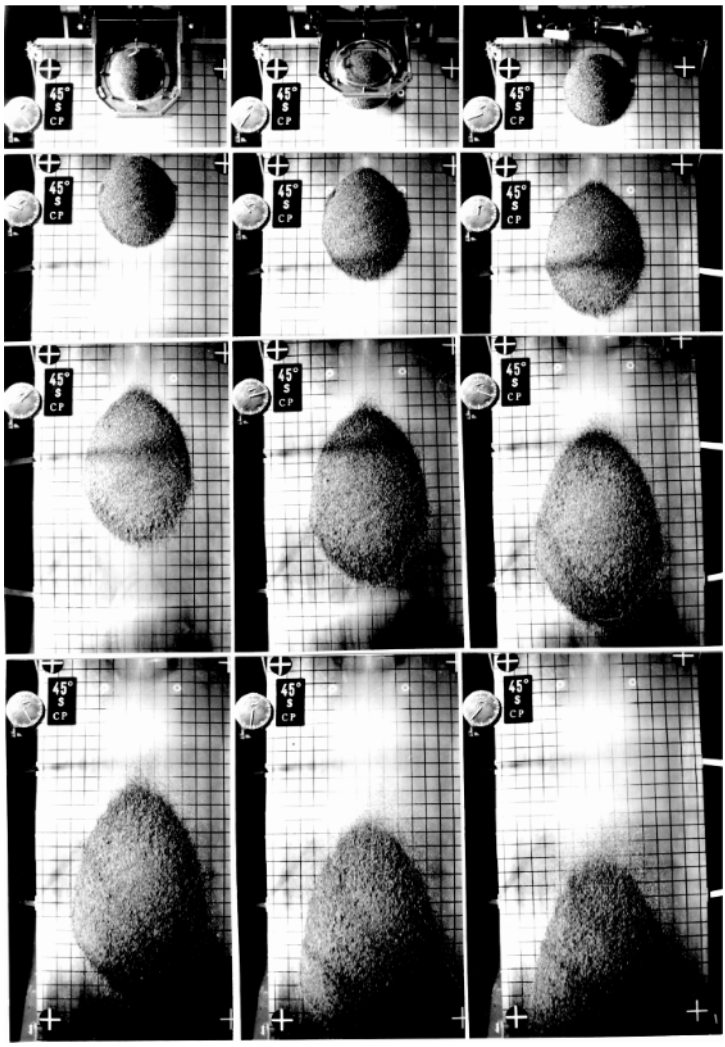

Fig. 5.17. Sequence of photographs of a moving mass of quartz sand down an inclined plane of a 45° inclination angle moving on a smooth aluminium surface. The longer arm of the clock at the *upper left corner* performs one revolution per second, so the camera takes about 10 frames per second. The motion initiates from a shutter of spherical cap geometry at rest. The *first picture* shows the granular mass immediately after the cap has been lifted by rotating it about a horizontal axis at its upper end, thus instantly freeing the granular mass. The mass develops into a droplet shape and, as time proceeds, becomes elongated with a progressively larger aspect ratio, L/B. The direction of motion is from *top* to bottom. (Courtesy of K. Hutter and C. Bucher).

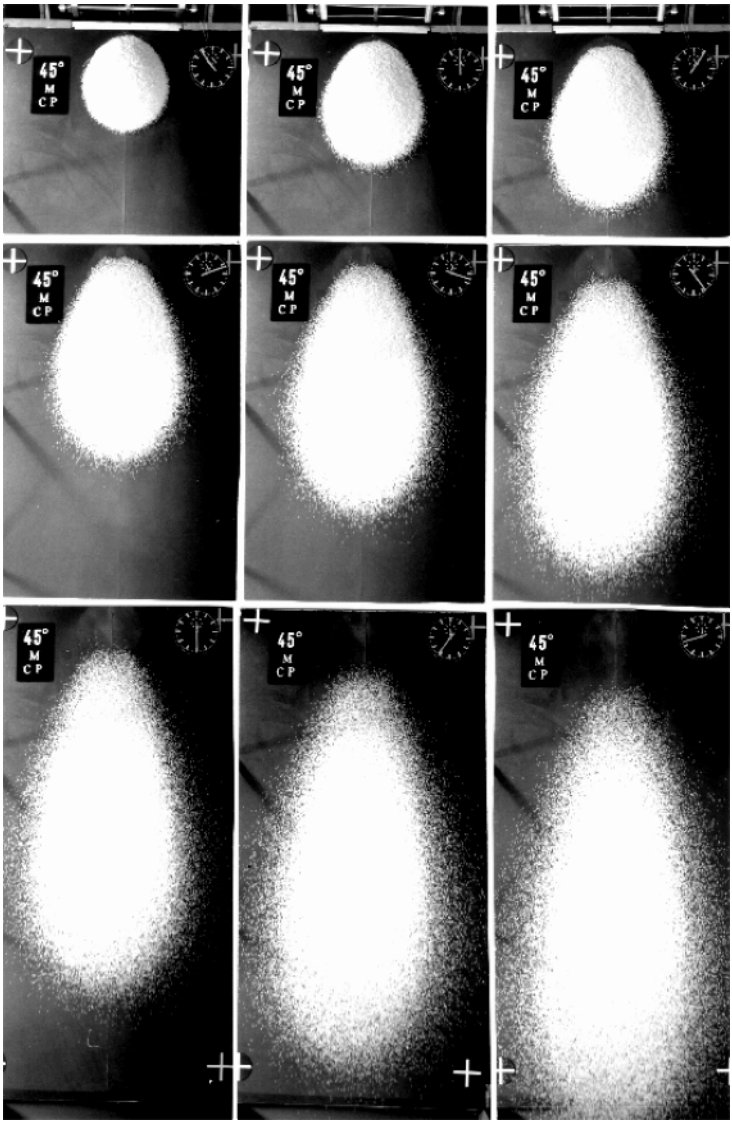

Fig. 5.18. Same as Fig. 5.17 but for a moving mass of plastic beads (Vestolen) on a sand paper coating of the inclined plane. Note the much more diffuse margins due to substantial particle bouncing because of the larger bed friction angle between the plastic particles and the sand paper bed, and the higher coefficient of restitution and a lesser compaction of the material than in Fig 5.17. Moreover, the aspect ratio of the droplets is larger than in Fig. 5.17. (Courtesy of K. Hutter and C. Bucher).

ing from a rotationally symmetric parabolic heap, tear drop-like avalanche geometries evolved, see Figs. 5.17 and 5.18, which break the double symmetry of the ellipse. A likely reason for our inability to reproduce the elliptic parabolas could be a dependence of the bed friction angle upon the position within the avalanche domain. Further research is needed to clear this point.

6 Exact Solutions for Flow Avalanches in Rotating Drums

The flow of granular materials in rotating drums is a typical example of mixing and demixing in process engineering scenarios. Many interesting and technically important phenomena can be observed in such flows. The behaviour is different depending upon whether the drum is a long cylinder extending over many particle diameters or whether it is thin, only forming a small gap between two circular disks. The character of the particle rearrangement also depends upon whether the assemblage is monodisperse or polydisperse,[1] and further factors are the filling and the presence or absence of an interstitial fluid. Dry granular flows of mixed large and small particles in long rotating horizontal cylinders tend to separate by size and form bands, separating large and small particles. The flow of dry cohesionless particles in the small gap between two co-rotating disks mix according to the avalanching motion and the embedding of the particles in the central core that performs a rigid body motion. If the avalanching motion is intermittent in a "go and stop manner", then a Catherine wheel effect is generated as shown in Figs. 2.10a,b,c. If the rotation of the cylinder is faster such that the avalanching flow at the free surface is continuous, then the deposition generates a continuous intermix between the small and large particles as shown in Fig. 2.10d.

Because of its significance in, e.g., powder mixing processes, the flow of granular materials in rotating long or short cylinders has been thoroughly analysed over the past 20 years. These studies concentrate on long or short cylinders and on continuous avalanching motion at moderately fast rotation speeds or intermittent flow at small rotation speed. Among the most detailed experimental studies of flow in a rotating cylinder that is characterised by a continuous and steady surface flow of particles are the works by Henein et al. [149] and Nakagawa et al. [291]. In the latter work, the density and velocity fields were experimentally determined by using *nuclear magnetic resonance imaging*. The authors determined the density and velocity fields across the avalanching layer. We shall return to this in Sect. 6.4. In other experimental studies, Rajchenbach [353] found *the dynamic angle of repose to be pro-*

[1] Polydisperse particle systems are particle assemblages in which particles with distinct properties are present; in monodisperse systems all particles have the same properties: size, mass and resilience.

portional to the square of the angular velocity, whereas KLEIN and WHITE [221] found it to vary with *the square root of the acceleration due to gravity* in reduced gravity experiments. According to KHAKHAR et al. [218, 219] and ORPE and KHAKHAR [307] these observations are largely unexplained.

Simulations of rotational cylindrical flow have been carried out by WALTON and BRAUN [437] for spheres and BUCHHOLTZ et al. [54] for cubic particles. Both papers report different dependencies of the dynamic angle of repose on rotation speed, inter particle friction and particle shape. Issues of transverse mixing in rotating drums have been analysed by HOGG and FÜRSTENAU [154], LEHMBERG et al. [249] and INOUE et al. [186]. Mixing at slow rotational speed, in which the cascading motion is intermittent has also been studied by METCALF et al. [281] and MCCARTHY et al. [266].

In this chapter, we will be involved with continuous "small gap" cylindrical flows. We will demonstrate how the avalanche theory can be utilised to investigate the flow mechanism and mixing behaviour in a slowly rotating partially filled drum. Exact solutions for the avalanche depth, particle paths and circuit time are constructed by including the effects of wall friction, the erosion and deposition processes and mixing phenomena in more detail. The basic concepts, notations and field equations have already been developed in Sects. 3.6 and 3.7.

6.1 A Simple Exact Solution for Steady Flow in a Rotating Drum Without Erosion and Deposition

In this section, we investigate a simple solution for the avalanche equations for two-dimensional flow of a finite mass of cohesionless granular material in a rotating drum with constant angular velocity. Here we neglect the effect of bed erosion and deposition. In other words, the granular mass only fills a small part of the gap, so that the entire mass slides along the outer wall of the gap. In Sect. 6.2 the additional effect in which a large part of the gap is filled with granular material will be treated.

6.1.1 Coordinate System, Geometry of the Drum and the Moving Mass

A Cartesian coordinate system is defined in order to describe the flow of a finite mass in a partially filled slowly rotating drum as shown in Fig. 6.1, where the x-axis connects the front, x_r, and the rear margin, $-x_r$, and the drum centre lies on the z-axis. The circular form of the drum yields the following basal topography:

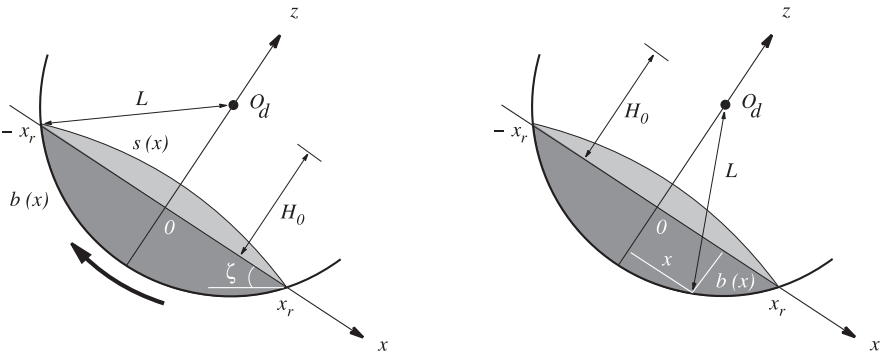

Fig. 6.1. *Left:* sketch of a Cartesian coordinate system and motion of a granular material of finite mass in a rotating drum, where L is the radius of the drum, H_0 is the distance of the drum centre, O_d, to the coordinate origin, O, and x_r is the half length of the bulk body. This coordinate system is inclined with angle ζ to the horizontal. The free surface profile and the basal topography in this coordinate system are described by $s(x)$ and $b(x)$, respectively. The light portion of the mass indicates the avalanching part, whilst the dark portion is (approximately) a rigid body part (with basal slip along the *outer circle*). *Right:* determination of the basal topography $b(x)$.

$$(H_0 - b(x))^2 + x^2 = L^2 \quad \Longrightarrow \quad b(x) = H_0 - \left(L^2 - x^2\right)^{1/2}, \tag{6.1}$$

where L is the radius of the drum and H_0 is the distance of the drum centre to the coordinate origin, i.e., to the interface of the avalanche and the rigid portion of the mass. Note that $b(x)$ is negative.

6.1.2 Avalanche Depth Determined Without Wall Friction

In a simple situation, the processes of mass evolution and avalanching motion in a rotating drum may be described by the classical smooth solution of the Savage and Hutter theory [375]. The reason for this is as follows: From observations of the bulk in experiments it is concluded that the free surface and velocity field are continuous, i.e., no discontinuity seems to develop [412, 413]. We recall that the momentum balance law (two-dimensional spatio/temporal) for the classical smooth solution is given by

$$\frac{\partial u}{\partial t} + u\frac{\partial u}{\partial x} = s_x - \beta_x \frac{\partial h}{\partial x}, \tag{6.2}$$

where s_x, the net driving acceleration, and β_x, respectively, are

$$s_x = \cos\zeta\,(\tan\zeta - u/|u|\tan\delta) - \varepsilon\cos\zeta\frac{\partial b}{\partial x}, \qquad \beta_x = \varepsilon\cos\zeta K_x. \tag{6.3}$$

Notice that all quantities appearing in the above equations, and henceforth, are in their *non-dimensional forms*. As already described in Chap. 3, h is

the avalanche thickness in the z-direction, u is the depth-averaged downslope velocity, ζ is the slope angle of the x-axis with the horizontal and K_x is the earth pressure coefficient as a function of the internal, ϕ, and basal, δ, angle of friction (see Sect. 3.4.3)

$$K_{x_{\mathrm{act/pas}}} = 2\sec^2\phi\left\{1 \mp \left(1 - \cos^2\phi/\cos^2\delta\right)^{1/2}\right\} - 1. \tag{6.4}$$

We assume a constant angular velocity of the drum. In this situation, the motion of the granular material can be viewed as in steady state (i.e., $u = u_0$) and $u/|u| = 1$. Thus, $\partial u/\partial x = 0$, and this implies that we are unable to select $K_{x_{\mathrm{act}}}$ and $K_{x_{\mathrm{pas}}}$, since $K_{x_{\mathrm{act}}} < K_x < K_{x_{\mathrm{pas}}}$. The earth pressure coefficient K_x remains undetermined, having a value perhaps between $K_{x_{\mathrm{act}}}$ and $K_{x_{\mathrm{pas}}}$. In steady state $h = h(x)$, which implies $\partial h/\partial x = dh/dx$, and $\partial b/\partial x = db/dx$. Under these conditions (6.2) and (6.3) reduce to

$$\varepsilon\left(K_x\frac{dh}{dx} + \frac{db}{dx}\right) = \tan\zeta - \tan\delta. \tag{6.5}$$

This, together with the basal topography (6.1), yields

$$\varepsilon\, K_x\frac{dh}{dx} = \tan\zeta - \tan\delta - \frac{\varepsilon\, x}{(L^2 - x^2)^{1/2}}. \tag{6.6}$$

Subject to the boundary condition $h(x_r) = 0$, the solution $h(x)$ of (6.6) is given by (see, e.g. [412])

$$\begin{aligned} h(x) = \frac{1}{\varepsilon K_x}\Big\{&(\tan\zeta - \tan\delta)x + \varepsilon(L^2 - x^2)^{1/2} \\ &-(\tan\zeta - \tan\delta)x_r - \varepsilon(L^2 - x_r^2)^{1/2}\Big\}, \quad x \in [-x_r,\, x_r]. \end{aligned} \tag{6.7}$$

This equation demonstrates the advantage exhibited by the choice of coordinate system and thus can be simplified to a great extent. The depth profile $h(x)$ must fulfil the rear margin condition $h(-x_r) = 0$, which necessarily implies that $\zeta = \delta$. This also indicates the possibility of measuring the basal friction angle by rotating drum experiments. Under the compelling condition that $\zeta = \delta$, (6.7) reduces to a very simple form

$$h(x) = \frac{1}{K_x}\Big\{\left(L^2 - x^2\right)^{1/2} - \left(L^2 - x_r^2\right)^{1/2}\Big\}, \qquad x \in [-x_r,\, x_r]. \tag{6.8}$$

This equation has two special features. Firstly, it is independent of the slope parameter ζ and the stretching parameter ε. Secondly, this implies that the thickness of the bulk body is proportional to $1/K_x$. The free surface profile is then given by $s(x) = h(x) - b(x)$. When the wall friction is neglected, the profile is symmetric with respect to $x = 0$ and the maximum height of the avalanche occurs at the centre of the drum. Together with the relation of the

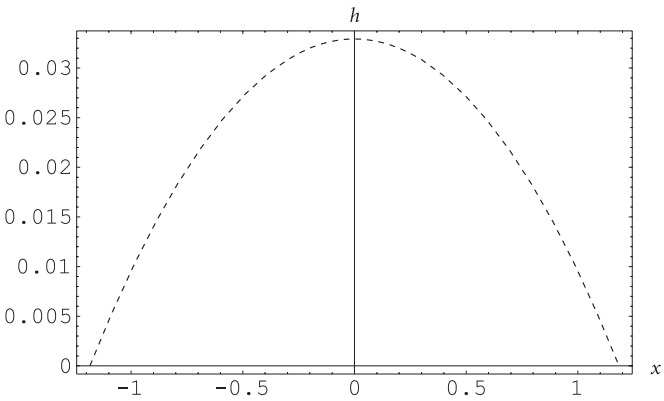

Fig. 6.2. Theoretical prediction of the avalanche thickness of a finite mass of granular material in a wall friction-free rotating drum. The result is evaluated with the compelling condition $\zeta = \delta = 31^\circ$, where the parameter values are chosen as $\varepsilon = 1$, $K_x = 0.82$, $L = 4.75$ and $H_0 = 4.6$. (From [413].)

coordinate geometry, $L^2 - x_r^2 = H_0^2$, the thickness at this centre, $x = 0$, is then given by

$$h_0 = h(0) = \frac{1}{K_x}\Big\{L - \big(L^2 - x_r^2\big)^{1/2}\Big\} = \frac{1}{K_x}\Big(L - H_0\Big). \tag{6.9}$$

Figure 6.2 demonstrates the depth profile evaluated by (6.8) in the coordinate system defined by $L = 4.75$ and $H_0 = 4.6$, where the inclination angle is equal to the basal friction angle $\zeta = \delta = 31^\circ$, and the earth pressure coefficient is $K_x = 0.82$.

Parabolic Similarity Solution We now have the possibility of obtaining a similarity solution analogous to that computed in Sect. 5.2, but for a steady flow configuration. For this we need a very large drum. With the assumption $x_r \ll L$, which is satisfied by the condition $\lambda = O(\varepsilon^\alpha)$, $0 < \alpha < 1$, of Chap. 3 and using a binomial series expansion, (6.8) can be approximated as

$$h(x) = \frac{L}{K_x}\left\{1 - \frac{x^2}{2L^2} - 1 + \frac{x_r^2}{2L^2}\right\} = \frac{x_r^2}{2LK_x}\left\{1 - \left(\frac{x}{x_r}\right)^2\right\}, \tag{6.10}$$

which forms a parabolic thickness profile [412], and is similar to the parabolic similarity solution obtained in [373, 375]. The factor $\big(x_r^2/2LK_x\big)$ on the right-hand side of (6.10) indicates that the height profile is proportional to the square of the half extent of the avalanche but inversely proportional to the radius of the drum. This is a rather trivial relation, because if the

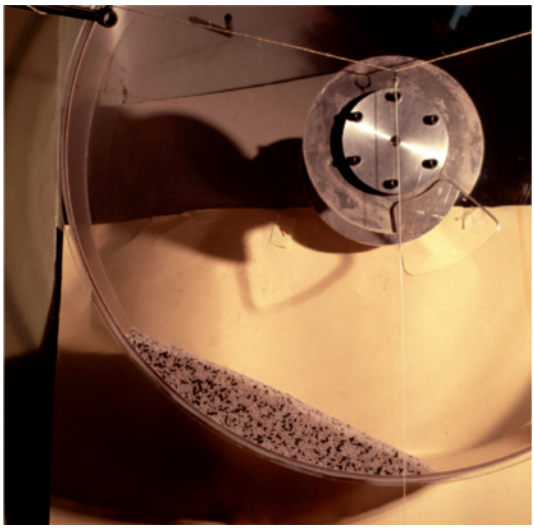

Fig. 6.3. Photograph of the rotating drum experiment with 3.5 l of Vestolen. The drum is rotated with an angular velocity of approximately 10^{-1} Hz. The dimensions of the drum are: inner width 151 mm and radius 475 mm. (From [413].)

fill level (for the definition see Sect. 6.2.2) of the granular material is below the centre of the drum, x_r increases as L decreases. The nontrivial result, however, is that $h(x)$ in (6.10) depends on K_x. Measuring $h(x)$ thus may allow determination of K_x. The rotating drum experiment with 3.5 l of Vestolen (a type of plastic particles of lens-like shape) is shown in Fig. 6.3.

6.1.3 Avalanche Depth Determined by Including Wall Friction

In real cases we need to incorporate the wall friction, which is partly responsible for the bulk drag. This kind of drag was not considered in the last section. Provided that the wall friction angle is equal to the basal friction angle and using the *hydrostatic pressure on the wall* (which contributes an additional term $-K_x \cos\zeta \tan\delta\, h/2$ on the right-hand side of $(6.3)_1$), the steady state version of (6.2) with the driving acceleration s_x, $(6.3)_1$ is then given by

$$0 = (\tan\zeta - (1 + K_x h/2)\tan\delta) - \varepsilon\frac{db}{dx} - K_x\frac{dh}{dx}. \tag{6.11}$$

This, with (6.1), reduces to

$$\varepsilon\, K_x\frac{dh}{dx} = \tan\zeta - (1 + K_x h/2)\tan\delta - \frac{\varepsilon\, x}{(L^2 - x^2)^{1/2}}, \tag{6.12}$$

which must obey the boundary conditions $h(x_r) = 0$ and $h(-x_r) = 0$. Equation (6.12) can be written in the following standard form:

$$\frac{dh}{dx} + Ph = Q, \tag{6.13}$$

where

$$P = \frac{\tan\delta}{2\varepsilon}, \quad Q = \frac{\tan\zeta - \tan\delta}{\varepsilon K_x} - \frac{x}{K_x\sqrt{L^2 - x^2}}. \tag{6.14}$$

Since P is a constant and Q is only a function of the independent variable x and does not involve h, the *linear ordinary differential equation* (6.13) has the solution (this solution is derived with the knowledge gained in any introductory course in ordinary differential equations)

$$h = A\exp\left(-\int_{-x_r}^{x} P dt\right) + \exp\left(-\int_{-x_r}^{x} P dt\right)\int_{-x_r}^{x}\left\{Q\exp\left(\int_{-x_r}^{t} P dt'\right)\right\} dt, \tag{6.15}$$

where A is a constant of integration. Subject to the boundary condition $h(-x_r) = 0$, at the upper most point of the avalanche and the solid interface, A becomes identically zero, and since P is a constant this solution has the following simple integral form (see also [413]):

$$h(x) = \left\{\int_{-x_r}^{x} Q\exp\left(P(t + x_r)\right) dt\right\}\exp\left(-P(x + x_r)\right). \tag{6.16}$$

Due to the presence of the factor $1/K_x$ in Q, as in the previous case without wall friction, the geometry of the depth profile of the avalanche explicitly depends on the value of the earth pressure coefficient. The numerical solution of $h(x)$, subject to the conditions $h(\pm x_r) = 0$, is illustrated in Fig. 6.4, where $K_x = 0.82$ and the coordinate parameters are the same as in Fig. 6.2, $L = 4.75$ and $H_0 = 4.6$.

Since the wall friction is active to drag the mass back, the inclination angle ζ is greater than the basal friction angle δ. The centre of the avalanching mass is thus shifted to the left, as expected, and located in the rear part of the bulk contrary to the case without considering the effect of wall friction.

A more detailed investigation of the steady state solutions of an avalanche of a finite mass of granular material in a slowly rotating partially filled horizontally placed (circular) cylindrical drum can be found in [412, 413], where different cases of the earth pressure coefficients are considered. In these papers, it is demonstrated that the surface curvature depends upon the numerical values of the earth pressure coefficient.

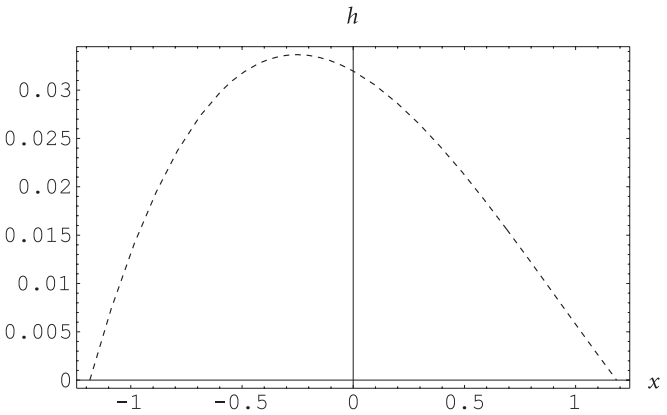

Fig. 6.4. Analytical prediction of the depth profile of the avalanching bulk of a finite mass of granular material in a rotating drum with wall friction, where $\varepsilon = 1$, $K_x = 0.82$, $L = 4.75$, $H_0 = 4.6$. The mass centre is shifted to the *left* and located in the rear part. (From [412].)

6.2 An Exact Solution for Steady Flow in a Slowly Rotating Drum with Erosion and Deposition

6.2.1 A Steady Flow Avalanche

In this section, the simple steady state solutions to the avalanching motion in a rotating drum are investigated.[2] These solutions were constructed by Gray [124]. In this section and Sect. 6.3 we will follow his procedure. The model equations have already been derived and discussed in detail in Sects. 3.6 and 3.7. It is, therefore, assumed that the solid core granular material rotates with constant angular velocity Ω_0, and that all derivatives with time are zero, $(\partial/\partial t)(\cdot) = 0$. Furthermore, the basal friction angle, δ, is assumed to have a constant value, δ_0. For the avalanche part, the coordinate system oxz is chosen (see also Sect. 3.7 and Fig. 3.13) so that its angle of inclination is $\zeta = \delta_0$. If the magnitude of the avalanche velocity is greater than $|\varepsilon\Omega_0 l|$, i.e., $(|u| > |\varepsilon\Omega_0 l|$ which implies $\operatorname{sgn}(u - \varepsilon\Omega_0 l) = 1)$, then except for the geometric contribution, $\varepsilon\cos\zeta\partial b/\partial x$, the net driving acceleration defined in (3.114) is identically equal to zero. This means that the avalanching motion is non-accelerating in the downslope direction and the *gravitational acceleration effect is cancelled out by the basal friction force*. For the classical smooth solutions (the conservation form of) the momentum balance (3.113) can be further simplified with the help of the mass balance equation (3.112), and the normal deposition rates (3.109) and (3.111), to yield the following steady state balance laws:

[2] The reader is asked to consult Sects. 3.6 and 3.7 prior to reading this section.

$$\frac{\partial}{\partial x}(hu) = \Omega_0 \left(\rho^-/\rho^+\right) \left(\varepsilon l \frac{\partial b}{\partial x} + x\right), \tag{6.17}$$

$$hu\frac{\partial u}{\partial x} + \varepsilon \frac{\partial}{\partial x}\left(K_x \cos\zeta h^2/2\right) = -\varepsilon h \cos\zeta \frac{\partial b}{\partial x}, \tag{6.18}$$

where ρ^- is the bulk density in the deposition zone and ρ^+ that in the avalanche. Usually, the model equations (6.17) and (6.18) are solved for the avalanche thickness, h, and velocity, u, for given basal angle of friction, δ, internal friction angle, ϕ, basal topography, b, and suitable initial and boundary conditions.

Note The (constitutive) parameter ρ^-/ρ^+ is included in the model equations (6.17)–(6.18) to account for the fact that the solid granular bulk material must dilate for the grains to move past each other in the fluid regime. Nevertheless, the dynamics of avalanches is not greatly affected by this parameter. Typically, the amount of dilatation is of the order of 5–10%, see, e.g., [124].

6.2.2 An Exact Solution

Here, a special class of solutions is considered in which the downslope avalanche velocity, u, is assumed to be constant,

$$u = u_0, \tag{6.19}$$

and the avalanche equations (6.17) and (6.18) are solved for the avalanche thickness, h, and the basal topography, b, provided the suitable boundary conditions and parameter values. This contrasts with other solution methods that seek values of the avalanche thickness, h, the free surface, s, and the velocity distribution, u; the present method may be considered as a "semi-inverse" technique of solution. The earth pressure coefficient, K_x, is defined in terms of du/dx, see (4.80). As for the present situation $du/dx = 0$. K_x is equal to a constant value K_0 through the avalanche region. Therefore, for constant $K_x = K_0$, the model equations (6.17) and (6.18) together with (6.19) reduce to (see [124])

$$\Lambda \frac{dh}{dx} + \varepsilon l \frac{db}{dx} + x = 0, \tag{6.20}$$

$$K_0 \frac{dh}{dx} + \frac{db}{dx} = 0, \tag{6.21}$$

where Λ is an order unity constant defined as

$$\Lambda := -\frac{\rho^+ u_0}{\rho^- \Omega_0}, \tag{6.22}$$

that incorporates the effects of the density changes from the upper part, ρ^+, to the lower part, ρ^-, of the basal interface, the constant rotation rate of the solid granular body, Ω_0, as well as the steady uniform downslope avalanche velocity, u_0. It will be shown later that for a solution with positive avalanche thickness the parameter Λ is positive. It may also be assumed without loss of generality that the constant downslope velocity is positive, $u_0 > 0$, and hence the constant angular velocity is negative, $\Omega_0 < 0$.

The point $(-a, l)$ in the solid body system is the uppermost point of the intersection between the drum wall and the avalanche free surface; it defines the top of the starting zone of the avalanche. Thus, with the *"fill level"* $l = L - H_0$, $a = \sqrt{L^2 - l^2}$ (see Figs. 3.13 and 6.1). Integrating (6.20)–(6.21) subject to the boundary conditions $h = 0$ and $b = 0$ at $x = -a$ implies

$$\Lambda h + \varepsilon l b - \frac{1}{2}\left(a^2 - x^2\right) = 0, \tag{6.23}$$

$$K_0 h + b = 0. \tag{6.24}$$

From these two equations, it follows that the avalanche height and basal topography are

$$h = h_0\left(a^2 - x^2\right)/a^2, \tag{6.25}$$

$$b = -K_0 h_0\left(a^2 - x^2\right)/a^2, \tag{6.26}$$

where the constant

$$h_0 = \frac{1}{2}a^2\left(\Lambda - \varepsilon l K_0\right) \tag{6.27}$$

is the avalanche thickness at $x = 0$. For positive order unity values of Λ, the constant h_0 in (6.27) and hence the avalanche thickness h in (6.24) is positive, provided that $\Lambda > \varepsilon l K_0$. This conforms with the assumption that Λ is a positive parameter for solutions with positive thickness of the avalanche [124].

The system of equations (6.25)–(6.26) can be used to predict the avalanche thickness h and the basal topography b, provided that the *free parameters* Λ, l and L along with a constitutive model for K_0 are known. The explicit solutions for both the avalanching as well as the rotating systems are plotted in Fig. 6.5.

Note The basal topography gradient $db/dx = 2K_0 h_0 x/a^2$ implies that a *point mass* (particle) is accelerated in the upper half (i.e., the avalanche starting zone, $x < 0$) region and decelerated in the lower half (i.e., in the avalanche deposition zone, $x > 0$) region. Similarly, the avalanche thickness gradient $dh/dx = -2h_0 x/a^2$ decelerates the avalanche in the upper half region $x < 0$ and accelerates it in the lower half region $x > 0$. An exact balance between

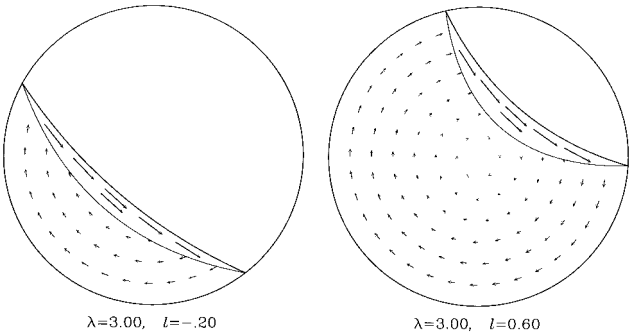

Fig. 6.5. Sketches of the steady state solutions for the flow of dry non-cohesive granular material in a partially filled and slowly rotating drum for negative and positive fill heights. In both cases, the free parameters L, K_0, respectively, are chosen to be 1 and 2.0, see [124]. The *arrows* indicate velocity vectors so as to show the relative speed and direction of the flow. Also shown are the position of the avalanche free surface and the interface between the avalanching and solid regions. (From [125].)

these competing mechanisms ensures that there is no non-zero net acceleration and the downslope avalanche velocity is constant along the entire extent of the avalanche. The mathematical description of this competition is reflected by the equation $b = -K_0 h$. This phenomenon is compatible with the assumption made before about a non-accelerating avalanche motion in the rotating drum [124].

■

6.3 Mixing in a Rotating Drum

To investigate the mixing phenomenon of a granular mixture in a rotating drum, it is necessary to know the particle[3] paths and the circuit time of each particle in the process. In this section we will deal with these aspects.

6.3.1 Particle Paths

The particle path in the solid body rotation is trivially circular once the distance from the centre of revolution is provided. However, the determination of the particle path within the avalanching flow is not straightforward and needs a detailed investigation of the balance laws, kinematic conditions, as well as interfacial conditions. The particle paths within the avalanching flow can be determined by integrating the system of ordinary differential equations

[3] The term "particle" here does not mean "grain" but the continuum mechanical particle.

$$\frac{dx}{dt} = u(x,z,t), \quad \frac{dz}{dt} = w(x,z,t), \tag{6.28}$$

subject to the initial conditions that $x = x_0$ and $z = z_0$ at the initial time $t = 0$. Notice that the time derivative d/dt is the rate of change as observed when moving along a fixed trajectory.

Since the motion is non-accelerating and the downslope velocity is constant ($u = u_0$), it trivially follows from $(6.28)_1$ that

$$x = u_0 t + x_0; \tag{6.29}$$

this formula gives the displacement at time t of the particle in the downhill direction.

There is no direct means of computing the displacement of the particle perpendicular to the x-direction. The normal velocity component w can be determined from the incompressibility relation $\partial u/\partial x + \partial w/\partial z = 0$ subject to the interfacial mass jump condition (3.101). Since the downslope velocity component is constant, the condition that the velocity field is solenoidal implies that $\partial w/\partial z = 0$, which, integrated with respect to z, implies

$$w = w^{b+}, \tag{6.30}$$

where w^{b+} is the normal velocity at the base of the avalanche (i.e., on the upper side of the singular surface) given, from (3.83), (3.109) and (3.111), by

$$w^{b+} = u_0 \frac{db}{dx} + \left(\rho^-/\rho^+\right) \Omega_0 \left(\varepsilon l \frac{db}{dx} + x\right) + O\left(\varepsilon^{1+\gamma}\right). \tag{6.31}$$

With the help of (6.22), (6.30) and (6.31), and by using (6.29), the change of variable $t = (x - x_0)/u_0$ transforms the differential equation for the normal velocity component $(6.28)_2$ into

$$\Lambda \frac{dz}{dx} = \Lambda \frac{db}{dx} - \left(\varepsilon l \frac{db}{dx} + x\right) + O\left(\varepsilon^{1+\gamma}\right). \tag{6.32}$$

Finally, integrating this with respect to x yields the height of the particle as a function of its position x

$$z = z_0 + b - \frac{1}{\Lambda}\left(\varepsilon l b + \frac{x^2}{2}\right) + O\left(\varepsilon^{1+\gamma}\right), \tag{6.33}$$

where z_0 is the initial height of the particle.

Up to now we have only used the incompressibility condition, the mass jump condition, the kinematic condition and ordering but not the momentum balance for the determination of the particle path. Next we will show how the SH-equations can be used to determine the particle paths and thus how the momentum balance enters these considerations. For more details on it, see [124].

Parameterisation of Particle Paths Due to the symmetry of the avalanche profile about the z-axis, the maximum height of the avalanche is attained at $x = 0$, and therefore all avalanche particle paths cross the z-axis. The process of tracking particles can be investigated by introducing a new parameter $\wp$. This parameter labels the particle paths that pass through the avalanching domain. Therefore, let $\wp$ be the relative height of the avalanche particle path to the maximum avalanche height, h_0, as it crosses the z-axis. With this definition, it follows that $\wp$ is equal to zero at the avalanche base and unity at the free surface and that it is linear in z, [124]. The value of $\wp$ thus uniquely labels the particle paths that pass through the avalanche region.

Substituting the definition of $\wp$ into (6.33) it follows that

$$z = b + h_0\wp - \frac{1}{\Lambda}\left\{\varepsilon l\,(b - b_0) + \frac{x^2}{2}\right\} + O\left(\varepsilon^{1+\gamma}\right), \tag{6.34}$$

where, according to (6.24), $b_0 = -K_0 h_0$ is the position of the basal interface at $x = 0$. Substituting for the basal topography from (6.26) and (6.27), (6.34) can still be simplified to yield

$$z = b + h_0\wp - h_0\left(x^2/a^2\right) + O\left(\varepsilon^{1+\gamma}\right). \tag{6.35}$$

A Closed Path In order to show that the avalanching paths form closed curves that pass through the fluid-like and solid-like regions, it is necessary to detect the points at which the particle enters into the avalanche zone from the solid body and comes back to its solid region. A particle crosses the interface between the avalanche and the solid rotating granular material when its height is equal to the local height of the basal topography, i.e., when $z = b$. Equation (6.35) in this case becomes a quadratic equation for the intersection positions and has two real and distinct roots

$$x_{b_1} = a\sqrt{\wp} =: x_b, \quad x_{b_2} = -a\sqrt{\wp} = -x_b. \tag{6.36}$$

The locations of these points are illustrated in Fig. 6.6 where they lie an equal downslope distance on either side of the z-axis. The corresponding intersection points of the normal coordinates, therefore, are given by

$$z_{b_1} = b\,(x_{b_1}), \quad z_{b_2} = b\,(x_{b_2}), \tag{6.37}$$

respectively, where b is given by (6.26). Because of the symmetry of the avalanche height about the z-axis, in other words, since the intersection points lie an equal downslope distance on either side of the origin, and since the basal interface, b, is an even function of x, the intersection points have the

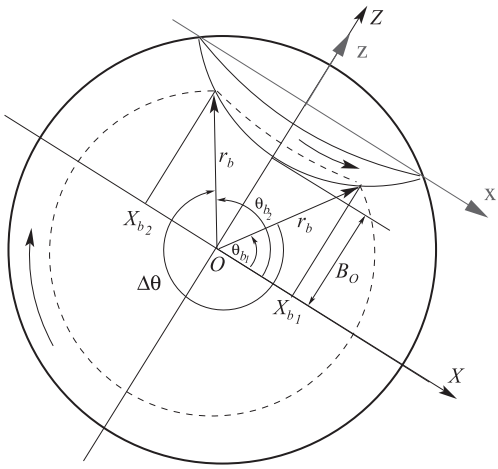

Fig. 6.6. Illustration of a closed particle path for steady granular motion inside a partially filled drum. The particle enters into the avalanching region at (r_b, θ_{b_2}) and is rapidly transported down to the wall of the drum by the avalanche. It then re-enters the solid region at (r_b, θ_{b_1}) and performs a solid body rotation and comes back to its original position (r_b, θ_{b_2}) completing a closed circuit. $\Delta\theta$ is the angle between θ_{b_1} and θ_{b_2} measured through the region of solid rotation in clockwise direction. The base of the avalanche at $X = 0$ lies at B_0. For $B_0 > 0$, a solid core develops in the centre of the drum so that the particles in this region never have contact with the avalanche and are isolated from being fluidised. (Redrawn from [125] with changes.)

same normal components $z_{b_1} = z_{b_2}$. We simply call this the common value z_b. Provided that the downslope velocity $u_0 > 0$, a granular particle will cross from the solid to the avalanche region at (x_{b_2}, z_b) and pass back from the avalanche to the solid region at (x_{b_1}, z_b). In the OXZ coordinate system these points correspond to (X_{b_2}, Z_b) and (X_{b_1}, Z_b), respectively, where $X_{b_1} = x_{b_1}$, $X_{b_2} = x_{b_2}$, and $Z_b = l + \varepsilon z_b$. Due to symmetry about the Z-axis, both of these positions lie an equal distance

$$r_b = \sqrt{X_b^2 + Z_b^2}, \tag{6.38}$$

from the axis of rotation at the centre of the drum.

Since the particles in the solid granular material are in rigid rotational motion with a constant angular speed, Ω_0, about the origin (which lies on the axis of revolution), their paths are given by the solution of the set of ordinary differential equations

$$\frac{dX^-}{dt} = -\varepsilon\Omega_0 Z^-, \quad \frac{dZ^-}{dt} = \varepsilon\Omega_0 X^-, \tag{6.39}$$

subject to the initial conditions that $X^- = X_0^-$ and $Z^- = Z_0^-$ at $t = 0$. Therefore, the particles move in circular arcs that are parameterised by

$$X^- = r\cos\theta, \quad Z^- = r\sin\theta, \tag{6.40}$$

where the azimuthal angle

$$\theta = \varepsilon\Omega_0 t + \theta_0, \quad \theta_0 = \tan\left(Z_0^-/X_0^-\right). \tag{6.41}$$

An avalanche particle path intersects the basal interface at points (X_{b_1}, Z_b) and (X_{b_2}, Z_b). In polar coordinates these points have their respective positions at (r_b, θ_{b_1}) and (r_b, θ_{b_2}), where the angles

$$\theta_{b_1} = \cos^{-1}\left(X_{b_1}/r_b\right), \quad \theta_{b_2} = \cos^{-1}\left(X_{b_2}/r_b\right). \tag{6.42}$$

It follows that after the particle has crossed from the avalanche to the solid region at (r_b, θ_{b_1}) it describes a circular arc until it reaches (r_b, θ_{b_2}), where it re-enters the avalanche region. Since both the starting and re-entry positions lie on the two end points of the same circular arc, it follows that the particle paths in the rotating drum form closed circuits that extend through both the avalanching and solid regions. Each of these closed curves are uniquely identified by the relative height $\wp$ as it crosses the z-axis in the avalanche. The exact solutions and the experimental results are illustrated for negative and positive fill levels in Fig. 6.7 [125].

Note A particularly interesting feature of the motion is that if the height of the basal topography lies above the axis of rotation at $x = 0$, a solid central core develops where the particles never enter into the avalanche, [125]. The two states of motions are thus distinguished by the height of the basal interface $B_0 = l + \varepsilon b_0$ at $x = 0$:

$$\begin{aligned} &\text{a solid core develops,} \quad \text{if} \quad B_0 > 0, \\ &\text{no solid core,} \quad \text{if} \quad B_0 \leq 0. \end{aligned} \tag{6.43}$$

For $B_0 > 0$ the radius of the central core is $B_0 = l - \varepsilon K_0 h_0$. Therefore, as the fill level increases, the size of the central core becomes progressively larger. This agrees well with the laboratory experiments. This situation is illustrated in Fig. 6.7, which shows two long time exposures of a drum partially filled with black and white poppy seeds. In the upper two panels the height of the basal interface $B_0 < 0$, which implies that all the particle paths intersect with the avalanching domain close to the free surface. In the lower two panels the height of the basal interface $B_0 > 0$, so a solid core develops where the particles are always in solid rotation.

■

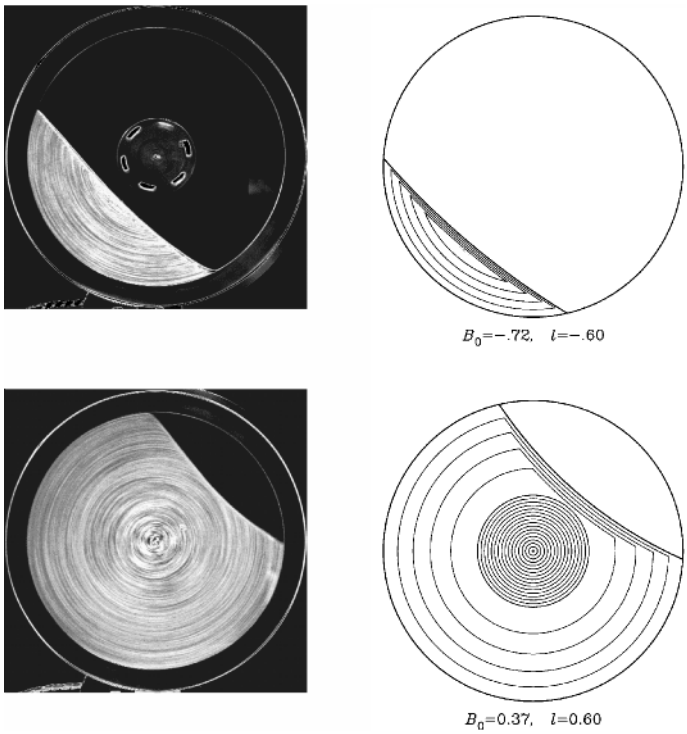

Fig. 6.7. Experiments and predictions of closed particle paths in long time exposure for negative and positive fill heights. For $B_0 \leq 0$ all the particle paths pass through the avalanche (*upper panel*). However, for $B_0 > 0$, some particles in the solid rotating region describing circular arcs never intersect with the free surface of the avalanche (*lower panel*). The diameter of the solid rotating circular disk depends on the fill level and rotation speed of the drum. (From [125].)

6.3.2 Circuit Time

To have a complete theory for mixing we further need the total time of a closed circuit, from the avalanche through the solid and back to the avalanche again. In this section, we investigate this as a closure of the theory.

The time a particle takes to complete a circuit around the drum (in the solid body and the avalanching region) has a very important consequence for the mixing of the granular material and is extremely sensitive to the particle path, $\wp$, and the fill level, l, of the drum. Since the avalanche velocity u_0 is a constant, a particle entering the avalanche at $(-x_b, z_b)$ takes a time

$$t_a = 2x_b/u_0 \tag{6.44}$$

to reach the other end of the avalanche (x_b, z_b). As the particle enters the solid region it travels along a circular arc from (r_b, θ_{b_1}) to (r_b, θ_{b_2}) in the time

$$t_s = \measuredangle / \ (-\varepsilon \Omega_0), \tag{6.45}$$

where

$$\measuredangle = \operatorname{ang}(\theta_{b_1}, \theta_{b_2}) \tag{6.46}$$

is the angle between the intersection points measured through the solid region in the clockwise sense, which lies in the range $0 \leq \measuredangle \leq 2\pi$. The factor ε^{-1} in (6.45) is the manifestation of the fact that the time spent in the solid region is much larger than the time spent in the avalanche, which implies that $t_a \ll t_s$. For convenience one may set the aspect ratio to be 1:1, which is achieved by setting $\varepsilon = 1$ in the avalanche flow solution to unstretch the coordinates. For simplicity, the angular velocity may be chosen so that the drum performs one complete revolution in a single non-dimensional time unit, i.e., $\Omega_0 = -2\pi$. It is then evident that the particles travel through the avalanche in a time $t_a \ll 1$, [125].

Finally, the total time t_t taken by a particle to perform one complete close circuit in the drum is the sum of the time spent in the avalanche, t_a, and the time spent in solid rotation t_s,

$$t_t = t_a + t_s, \tag{6.47}$$

which is equal to $2x_b/u_0 + \measuredangle / \ 2\pi$ for the aforementioned simplified situation with parameter values $\varepsilon = 1$ and $\Omega_0 = -2\pi$.

Comparison of the exact solutions of Sects. 6.2 and 6.3 with small-scale laboratory experiments was presented by GRAY in [124, 125] who investigated the mixing phenomena of differently coloured monodispersed granular particles. It is shown that the theoretical predictions agree quite well with the laboratory findings.

To summarise, this section on avalanches in rotating small cylindrical gaps is only peripherically alien to the main topic of avalanche dynamics. The exact solution of the steady motion of a finite mass of granular material sliding in a steadily rotating drum may turn out to be a solution with vanishing stretching ($\partial u/\partial x$) conditions for which the value of the earth pressure coefficient is not known. This flow state is neither active nor passive. A carefully constructed experiment, paired with the analytical solution, may provide a means of determining the earth pressure coefficient at zero stretching.

The exact steady solution for the rotating drum with erosion and deposition is an imaginable simple situation for which erosion and deposition processes arise. Even though erosion and deposition processes are generally difficult to quantise, the situation here has been shown to be simple insofar, as *no phenomenological closure statement needs to be formulated; jump conditions of mass and a statement of dilation from the deposited material to that in motion are sufficient.* This implies that the mixing of particles in avalanches can

ideally be studied under such physically simple conditions. Rotating drums have, therefore, demonstrated that they are ideal for testing the model equations of avalanching flows.

6.4 An Alternative Model Describing the Transverse Flow and Mixing of Granular Material in a Rotating Cylinder

In the previous section, the extended SH-equations were used in describing the cascading flow of granular material down the free surface of a partly filled rotating cylinder. One assumption was that the downslope velocity component within the avalanche is *constant* across the layer, and a consequence of the emerging steady equations – which, incidentally can be solved exactly – was that this depth-averaged velocity was also constant as a function of the downslope coordinate. We also saw that the results of mixing determined by this model showed good to very good agreement with observations of experiments, see Gray [124]. However, in the introduction to this chapter we also reported experiments by Nakagawa et al. [291], which do not support these findings. Khakhar et al. [218] summarise these as follows:

- "The density, i.e., solid volume fraction decreases with distance across the cascading layer, with the lowest density at the free surface.
- The cascading velocity increases linearly with the distance across the layer, except near the boundary between the bed and the layer where there is a slow variation.
- The velocity also varies along the layer and exhibits a maximum near the midpoint of the layer.
- The layer thickness is maximum near the midpoint, and the thickness at the midpoint increases with rotational speed, achieving a constant value at high rotational speeds."

Of these observational results the first three contradict the basic assumptions implied in the SH-equations. Thus, it is interesting to see how different postulates, resulting in a different theory, cope with these experimental findings. In the ensuing developments we follow Khakhar et al.

6.4.1 Model

Khakhar et al. [218] write the depth-integrated balance of mass as

$$\frac{dQ}{dx} = \frac{d}{dx}(\rho h u) = \rho_b E_b, \tag{6.48}$$

in which Q is the cascading mass flux, ρu is the depth-averaged downslope mass flux in the x-direction,

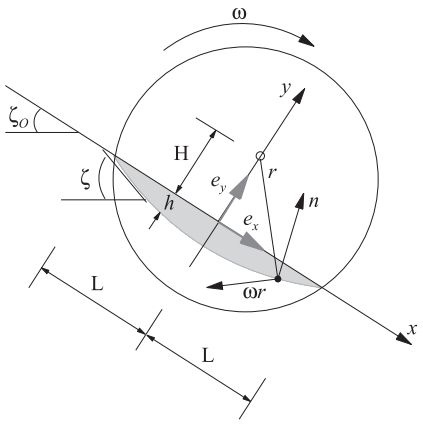

Fig. 6.8. View of the flow region showing the coordinate system and geometrical parameters of the system. Note that the unit normal vector, $\mathbf{n}$, points into the avalanche region.

$$\rho u = \frac{1}{h}\int_{-h}^{0} \rho v_x dy =: \langle \rho v_x \rangle, \tag{6.49}$$

and h is the avalanche thickness. Furthermore, ρ_b is the density of the solid core mass and E_b the entrainment rate. With reference to Fig. 6.8 it is easy to see that the velocity of the particles in the bed and the unit normal vectors perpendicular to it are

$$\begin{aligned} \mathbf{v}_b &= -\omega(H+h)\hat{\mathbf{e}}_x - \omega x \hat{\mathbf{e}}_y, \\ \hat{\mathbf{n}} &= \frac{h'\hat{\mathbf{e}}_x + \hat{\mathbf{e}}_y}{\sqrt{1+h'^2}}, \qquad \left(h' := \frac{dh}{dx}\right), \end{aligned} \tag{6.50}$$

so that

$$E_b = \mathbf{v}_b \cdot \hat{\mathbf{n}} = -\frac{h'\omega(H+h)+\omega x}{\sqrt{1+h'^2}}. \tag{6.51}$$

Because the cascading region is thin and long, we may assume that $|h'| \ll 1$. To lowest order, E_b thus takes the approximate form

$$E_b = -\omega x + O(h'\omega). \tag{6.52}$$

Consequently $dQ/dx = -\rho_b \omega x$, or after integration

$$Q = \frac{1}{2}\rho_b \omega \left(L^2 - x^2\right), \tag{6.53}$$

a formula already derived by De Gennes [111]. This shows that the mass flux is maximum at the centre (i.e., origin of the coordinate system) and vanishes at the extreme boundaries in the x-direction. The steady state depth-integrated momentum balance equation in the downslope direction can be

written as[4]

$$\frac{d}{dx}\left(\rho\langle v_x^2\rangle h\right) = \rho g h \sin\zeta_0 - \rho_b E_b [\![\mathbf{v}\cdot\hat{\mathbf{e}}_x]\!] - \tau. \tag{6.54}$$

Here, $\langle v_x^2\rangle$ is the depth-averaged x-component of the velocity square and ζ_0 is the slope angle of the coordinate system. On the right-hand side the first term is the driving force due to the acceleration due to gravity, the second term represents the impulse due to the velocity jump across the basal surface and τ is the frictional shear traction at the base. In (6.54) KHAKHAR et al. *ignore* the contribution associated with the longitudinal pressure variation. This is consistent with the earlier assumption of ignoring $O(h'\omega)$ terms in the mass balance, but the neglected term constitutes exactly the contribution in the SH-equations to be *significant*. That term alone involves the earth pressure coefficient. It follows that the MOHR–COULOMB plastic behaviour cannot be described in this model.

The velocity jump at the basal surface in the downslope direction, $[\![\mathbf{v}\cdot\hat{\mathbf{e}}_x]\!]$, takes different values for $x<0$ and $x>0$. For $x<0$, material is entrained from the bed and $[\![\mathbf{v}\cdot\hat{\mathbf{e}}_x]\!]$ is claimed to be *negligible* by the following argument: "When particles cross the interface to enter the layer, they experience an abrupt change in their tangential velocity, as mentioned above. The tangential component of the momentum of the particles entering the layer is thus difficult to estimate. However, the magnitude of the particle momentum is small (as is apparent from the experimental results of NAKAGAWA et al. [291]), and hence we assume that $[\![\mathbf{v}\cdot\hat{\mathbf{e}}_x]\!]=0$" [218]. Alternatively, the velocity jump at $x>0$ is $-[\![v_x|_{x=-h}-\omega(H+h)]\!]+O(h'\omega)\backsimeq -[\![v_x|_{x=-h}]\!]$, an approximation that is plausible, since $|v_x|_{x=-h}|\gg|\,\omega(H+h)|$.

There now remains the parameterisation of the shear stress τ. KHAKHAR et al. [218] follow JOHNSON and JACKSON [201] and write

$$\tau = \tau_f + \tau_c \tag{6.55}$$

as the sum of a frictional and collisional contribution. They write for τ_f

$$\tau_f = \rho g h \mu_s \cos\zeta_0, \tag{6.56}$$

where the coefficient of friction, μ_s is related to the static angle of repose, ζ_{0_s} by $\mu_s=\tan\zeta_{0_s}$, and set $\zeta_0=\zeta+\not{\zeta}$ with $|\not{\zeta}|=O(h')$. Thus,

$$\begin{aligned}\tau_f = \rho g h\mu_s\cos(\zeta+\not{\zeta}) &= \rho g h\mu_s\left\{\cos\zeta\underbrace{\cos\not{\zeta}}_{1} - \sin\zeta\underbrace{\sin\not{\zeta}}_{\sim\tan\not{\zeta}\,=h'}\right\}\\ &\backsimeq \rho g h\mu_s\left\{\cos\zeta-(\sin\zeta)h'\right\}.\end{aligned} \tag{6.57}$$

[4] Note that KHAKHAR et al. [218] treat ρ as a constant, even though they claim it to be a variable.

The collisional stress τ_c is written in the form derived by BAGNOLD [20]

$$\tau_c = m\lambda^2 \left(\frac{\partial v_x}{\partial y}\right)^2 \Big|_{y=-h}, \tag{6.58}$$

in which

$$m = A\rho_P D. \tag{6.59}$$

A is a constant, ρ_P is the particles' true density, D is their diameter and λ a measure of interparticle spacing. With all these simplifications the balance of linear momentum (6.54) takes the form

$$\begin{aligned}
&\text{for } x < 0: \\
&\frac{d}{dx}\left(\rho\langle v_x^2\rangle h\right) = \rho\left(a + a_1 h'\right)h - m\lambda^2\left(\frac{\partial v_x}{\partial y}\right)^2\Big|_{y=-h}, \\
&\text{for } x > 0: \\
&\frac{d}{dx}\left(\rho\langle v_x^2\rangle h\right) = \rho\left(a + a_1 h'\right)h - \rho_b\omega x v_x\big|_{y=-h} - m\lambda^2\left(\frac{\partial v_x}{\partial y}\right)^2\Big|_{y=-h},
\end{aligned} \tag{6.60}$$

where

$$\begin{aligned}
a &:= g\left(\sin\zeta - \cos\zeta_0 \tan\zeta_s\right) = \frac{g\sin\left(\zeta - \zeta_s\right)}{\cos\zeta_s}, \\
a_1 &:= g\sin\zeta\tan\zeta_s, \\
\mu_s &:= \tan\zeta_s.
\end{aligned} \tag{6.61}$$

Here, ζ_s is the bed friction angle. In deriving (6.60) and (6.61), ζ_0 on the right-hand side of (6.54) has been replaced by ζ (with an error of $O(h')$) and $\mu_s = \tan\zeta_0$ has been replaced by $\tan\zeta$ (again with an error of $O(h')$). Thus, (6.60) and (6.61) are not consistent in their h'-ordering.[5]

Equations (6.60) are not yet integrable; to that end, $\langle v_x^2\rangle$, $v_x|_{y=-h}$ and $(\partial v_x/\partial y)|_{y=-h}$ must first be expressed in terms of the depth-averaged velocity v_x and the avalanche thickness h. The approach taken is that of POHLHAUSEN [325] for the analysis of boundary layer flows. The velocity profiles correspond to solutions for steady unidirectional flow down an inclined plane, and KHAKHAR et al. [218] choose plug flow, flow of a BAGNOLD fluid and linear shearing. The velocity profiles v_x and the additional variables

$$\langle v_x^2\rangle, \quad v_x\big|_{y=-h}, \quad \left(\frac{\partial v_x}{\partial y}\right)\Big|_{y=-h} \tag{6.62}$$

corresponding to these flows are given in Table 6.1. If the expressions of the

[5] KHAKHAR et al. [218] have an error in the second term on the right-hand side of (6.60); they write $xv_x\big|_{y=-h}$ instead of $\rho_b\omega x v_x\big|_{y=-h}$.

Table 6.1. Velocity profiles v_x and corresponding values for $\langle v_x^2 \rangle$, $v_x\big|_{y=-h}$ and $(\partial v_x/\partial y)\big|_{y=-h}$ for plug flow, BAGNOLD flow and linear shearing.

Flow	v_x	$\langle v_x^2 \rangle$	$v_x\big\|_{y=-h}$	$\left(\frac{\partial v_x}{\partial y}\right)\Big\|_{y=-h}$
Plug	u	u^2	u	0
BAGNOLD	$\frac{5}{3}u\left(1-\left\|\frac{y}{h}\right\|^{3/2}\right)$	$\frac{5}{4}u^2$	0	$\frac{5}{2}\frac{u}{h}$
Linear shearing	$2u\left(1+\frac{y}{h}\right)$	$\frac{4}{3}u^2$	0	$\frac{2u}{h}$

Table 6.2. Velocity profile dependent coefficients for the momentum equation (6.64) for plug flow, BAGNOLD flow and linear shearing as given in Table 6.1. $\alpha_B := \lambda m/(\rho_b L^2)$, $\alpha_s := \lambda^2/[(\rho_b L^2)h^*]$. These two parameters are treated as fitting parameters, held constant.

Flow	$x^* < 0$			$x^* > 0$		
	C_1	C_2	C_3	C_1	C_2	C_3
Plug	1	1	0	1	0	0
BAGNOLD	$\frac{4}{5}$	1	$5\alpha_B$	$\frac{4}{5}$	1	$5\alpha_B$
Linear shearing	$\frac{3}{4}$	1	$3\alpha_s h^*$	$\frac{3}{4}$	1	$3\alpha_s h^*$

table are substituted into the momentum equations (6.60) and the resulting equations are non-dimensionalised by using the scales L, ρ_b, ω according to

$$\begin{array}{llll} x \to Lx^*, & h \to Lh^*, & Q \to \rho_b \omega L^2 Q^*, & a \to \omega^2 L a^*, \\ u \to \omega L u^*, & \rho \to \rho_b \rho^*, & H \to LH^*, & a_1 \to \omega^2 L a_1^*, \end{array} \tag{6.63}$$

in which the variables carrying an asterisk are dimensionless, then the differential equations (6.60) take the forms

$$u^* \frac{\partial u^*}{\partial x^*} = C_1 \left(a^* + a_1^* h^{*'} \right) + C_2 \frac{x^* {u^*}^2}{Q^*} - C_3 \frac{{\rho^*}^2 {u^*}^5}{{Q^*}^3}, \tag{6.64}$$

where the prime now means d/dx^* and the coefficients $C_i (i = 1, 2, 3)$ are given in Table 6.2. The first and second terms on the right-hand side constitute the net body force acting on the layer in dimensionless form (i.e., gravitational force plus frictional resistance), the third term arises due to the flow of particles into and out of the layer and the fourth term represents the dimensionless collisional stress.

Table 6.2 is informative. Firstly, the plug flow model does not include a contribution due to the collisional stress ($C_3 = 0$). Thus, its resistance to flow is due to friction alone and it is independent of the velocity (recall, the frictional resistance is contained in C_1). This contrasts with the results for the shear velocity profiles where the collisional resistance increases sharply with the average velocity. Secondly, the equations for linear shearing and BAGNOLD profiles behave qualitatively very similarly. The coefficient C_1 has values in the two cases that do not differ much from one another and since α_B and α_s, respectively, are adjustable parameters, differences in the numerical values of C_3 are less significant.

Equation (6.64) is not directly integrable since, apart from u^*, it involves $h^{*'}$ and Q^*. However, both are known, at least approximately. Q^* follows from (6.53) and $h^{*'}$ can be evaluated by differentiating $h^{*'} = Q^*/(\rho^* u^*)$. This yields

$$\begin{aligned} Q^* &= \tfrac{1}{2}\left(1 - x^{*^2}\right), \\ h^{*'} &= -\frac{x^*}{\rho^* u^*} - \frac{Q^*}{\rho^* u^{*^2}} \frac{du^*}{dx^*}. \end{aligned} \tag{6.65}$$

Note that in the evaluation of $(6.65)_2$ ρ^* is treated as a constant. With (6.65), equation (6.64) takes the form

$$\begin{aligned} &\left(1 + C_1 \frac{a_1^* Q^*}{\rho^* u^{*^3}}\right) u^* \frac{du^*}{dx^*} \\ &= \left\{ C_1 \left(a^* - a_1^* \frac{x^*}{\rho^* u^*}\right) + C_2 \frac{x^* u^{*^2}}{Q^*} - C_3 \frac{\rho^{*^2} u^{*^5}}{Q^{*^3}} \right\}. \end{aligned} \tag{6.66}$$

Analytical solutions for this equation in general cannot be found, although numerical integration seems to be straightforward. Once u^* is determined, h^* follows from $h^* = Q^*/(\rho^* u^*)$.

6.4.2 Experiments

KHAKHAR et al. [218] performed experiments; we quote the description from their paper as follows: "Transverse flow and mixing are studied experimentally using a cylinder with glass side walls; the inner curved surface is roughened by gluing sandpaper. The cylinder radius is 6.9 cm and its length is 1.5 cm. A small length is used mainly to facilitate the study of flow and mixing: the initial loading of the tracer particles is simplified, and axial variations are eliminated. The results obtained should be very similar to those for longer cylinders, because the frictional forces applied by the smooth glass walls modify the flow only slightly. The drum is driven by a computer controlled stepper motor (Compumotor) with a sufficiently small step, so that the rotation of

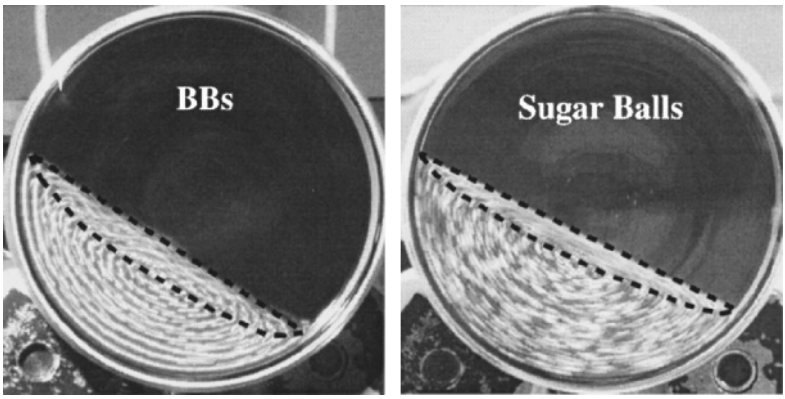

Fig. 6.9. Time exposed photograph showing *streaklines* of flow for typical cases, for different materials. The demarcation of the layer based on the streaklines is also shown by means of *dashed lines*. (From [218].)

the drum is accurately controlled and smooth. A digital camera (Kodak Mega Plus) with a resolution of 1024×1024 pixels connected to the computer is used to obtain digital images of the side of the drum. The images are then analysed to extract the required data.

The main objective of the flow experiments is to measure the layer thickness profile for different particles at different angular speeds. Time exposed digital images of the rotating drum are taken at sufficiently low shutter speeds so as to obtain particle streaks. Typical time-exposed photographs for different materials are shown in Fig. 6.9; streaklines in the fixed bed are arcs of circles and there is a nearly rectilinear flow in the moving layer substantially verifying the assumptions of the models. The layer thickness profile is obtained from a time-exposed photograph by joining the corners in the streaklines, which represent the transition between the fixed bed and the cascading layer flow. Figure 6.9 shows the layer thickness profile obtained for each case using this procedure. Each such profile is averaged over ten images. The procedure for determining the layer-bed boundary, a though somewhat subjective, gives very consistent results. For each experiment, the dynamic angle of repose (angle of the free surface when the bed rotates) and the static angle of repose (angle of the free surface at which the particles come to rest after rotation is stopped) are measured from the digital images. The length of the free surface is also measured from the images. The details of the materials used in the experiments are given in Table 6.3".

Table 6.3. Specification of the granular materials used in the flow experiments. D_p is the particle diameter, ρ_b is the bulk density of the material and ζ_s is the static angle of repose.

Material	Shape	$D_p(mm)$	$\rho_b(g/cm^3)$	$\zeta_s(deg)$
Sugar balls	Spherical	1.8	1.1	20.6
BBs	Spherical	4.5	4.4	24.6
Sugar crystals	Angular	1.0	0.84	29.1

6.4.3 Results and Discussion

The differential equation for the downslope velocity, (6.64) or (6.66), is of first-order and thus allows the satisfaction of only one constant of integration. This is determined by prescribing the boundary condition $u^* = 0$ at $x^* = -1$. A second condition for the velocity u^* at $x^* = 1$ cannot be prescribed, as its value is rather the outcome of the integration. As is evident from Table 6.2, there is no adjustable parameter for plug flow that could influence the solution. On the other hand, for the BAGNOLD and linear shearing profiles the solution of the differential equation can be influenced by adequately selecting α_B and α_s, respectively. KHAKHAR et al. [218] did this by matching the maximum velocity of the cascading layer, which approximately arises at $x^* = 0$. Velocity measurements by NAKAGAWA et al. [291] indicate that the velocity is large in the middle portion of the cascading flow, but relatively small towards the two ends, and it is compelling that $h^* = 0$ at $x^* = \pm 1$. These are the requirements that must be met by the differential equation (6.66), and it is likely that for linear shearing and BAGNOLD profiles better results can be obtained.

The dimensionless velocity u^* and the corresponding layer thickness h^* for the three different velocity profiles are shown in Fig. 6.10. The parameter values are given in the inset and correspond to typical values for the system.[6] The velocity for the plug flow case increases monotonically with distance. The reason is that the frictional resistance to flow is constant and independent of the velocity in the layer. By contrast, the flow for the linear shearing profile is strongly damped by the collisional stresses and achieves a maximum value near the midpoint of the layer $x^* = 0$. Furthermore, there is only a small difference in the velocities predicted by the simple shear flow and BAGNOLD's profile. The overall velocity is significantly higher for the plug flow case as compared to the other two. The layer thickness is consequently much smaller for the plug flow

[6] We think that these values are a bit large.

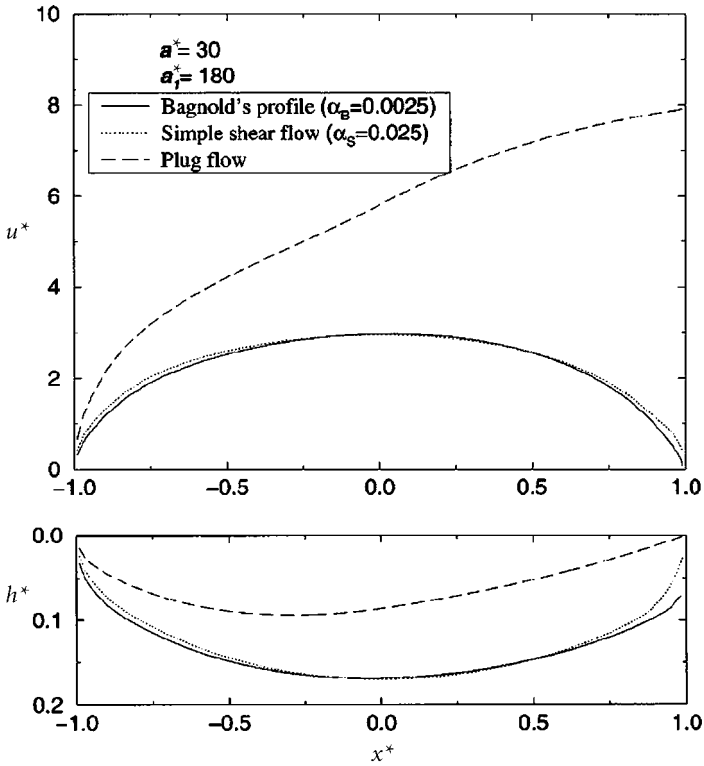

Fig. 6.10. Variation of the average velocity u^* and layer thickness h^* with distance along the layer x^* calculated using the different velocity profiles. (From [218] with changes.)

than for the shearing flows. Also note that the layer thickness profile for the plug flow is asymmetric, due to the monotonic increase in the velocity.

An estimate of the thickness of the layer at the midpoint is obtained by recognising that

$$\frac{du^*}{dx^*} \approx 0, \quad \text{and} \quad \frac{dh^*}{dx^*} \approx 0, \quad \text{at} \quad x^* = 0. \tag{6.67}$$

Using this in (6.64) yields

$$\left[C_1 a^* - C_3 \frac{{\rho^*}^2 {u^*}^5}{{Q^*}^3}\right]_{x^*=0} = 0, \tag{6.68}$$

or, since $u^* = Q^*/(\rho^* h^*), Q^*(0) = 1/2$ (from $(6.65)_1$), $\rho^* = 1$, and substituting for C_1, C_3 the values from Table 6.2, we get

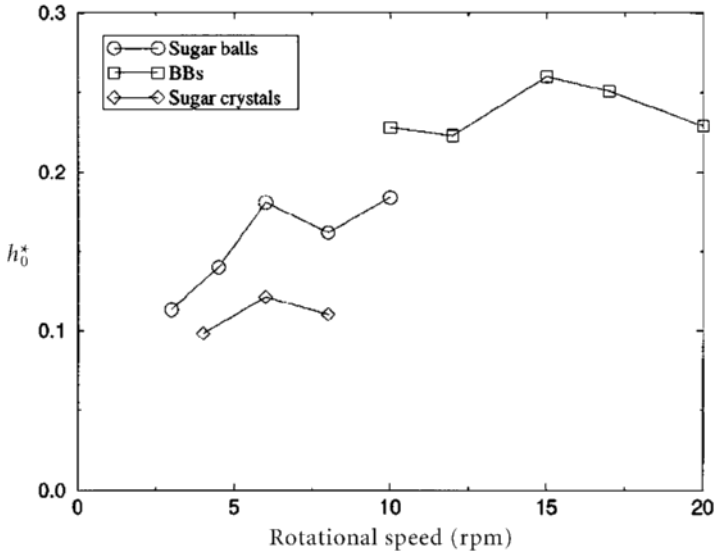

Fig. 6.11. Computed results for the variation of the experimentally measured layer thickness at the midpoint $h_0^* = h(0)/L$ with rotational speed in rpm for the different materials. Experimental parameters are taken from [218]. Experiments were performed with sugar balls, BBs and sugar crystals. (From [218].)

$$h_0^* = \begin{cases} \left(\dfrac{\alpha_s}{a^*}\right)^{1/4}, & \text{linear shearing,} \\ \left(\dfrac{25}{16}\dfrac{\alpha_B}{a^*}\right)^{1/5}, & \text{BAGNOLD profile.} \end{cases} \tag{6.69}$$

Figure 6.11 shows the values for the experimentally measured layer thickness at the midpoint h_0^* as a function of the rotational speed. Accordingly, h_0^* grows linearly with the rotational speed at low values of rpm (rotation per minute) but at rpm ≈ 20 perhaps saturating at a value of $h_0^* = 0.25$. These results do not follow RAJCHENBACH's [353] scalings that assume $(\zeta - \zeta_s) \propto \omega^2$, implying that h_0^* is independent of ω [218].

Figure 6.12 shows a comparison of the theoretical and experimental values of h_0^* for linear shearing and BAGNOLD flow. For each material the parameters α_s and α_B are adjusted so that the computed layer thickness profiles match the experimental profiles at the lowest (3–10 rpm) rotational speed. To this end, also the corresponding dimensionless parameters a^* and a_1^* are needed. Details are given in [218]. The solid lines in Fig. 6.12 are the results obtained from (6.66), and the dashed lines are obtained by using $(6.69)_1$ or $(6.69)_2$. There is good agreement between theoretical predictions and experiments. Finally, Fig. 6.13 shows a comparison between the predicted and experimental layer thickness profiles for the different materials for the smallest rota-

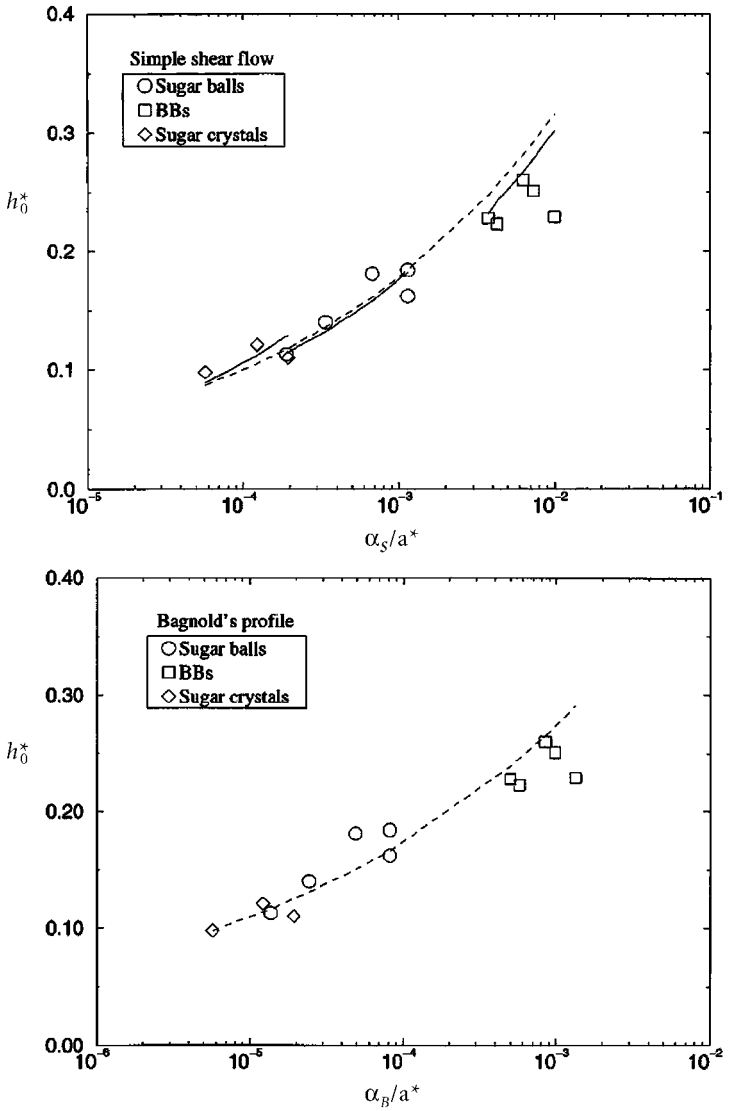

Fig. 6.12. Comparison of the theoretically predicted midpoint thickness for simple shear flow and BAGNOLD flow with experimental values. *Symbols* represent the experimental data, the *solid lines* are predictions using (6.66) and the *dashed lines* are the predictions using (6.69). (From [218].)

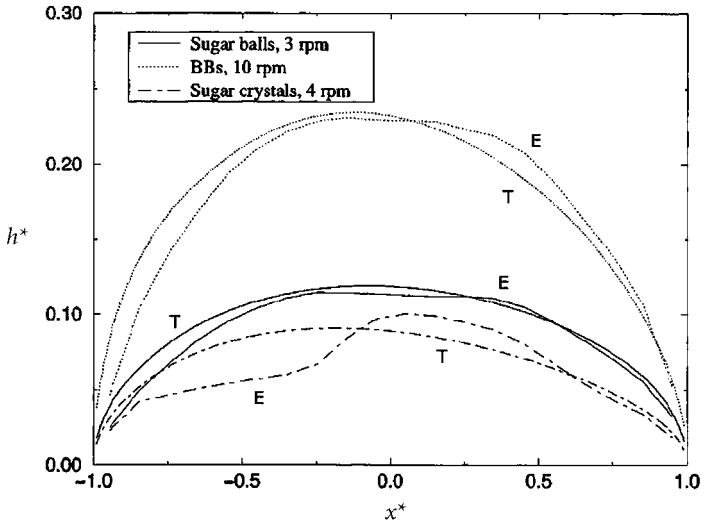

Fig. 6.13. Comparison of the experimental and theoretical layer thickness variation with dimensionless distance along the layer x^* for the lowest rotational speed (as given in the *inset*) for each material. Calculations are for simple shear flow using (6.66). Note that the experimental curves (E) are less symmetrical than the computed curves (T). (From [218].)

tional speed in each case. There is very good agreement between theory and experimental data for the sugar balls and the BBs; the agreement between theoretical prediction and experimental data for the sugar crystals is, however, not so good; here the thickness profiles deviate rather conspicuously from symmetry.

6.5 Concluding Remarks

In this chapter, two different models have been derived that are capable of describing the cascading flow of dry granular materials down the free surface of a rotating cylindrical gap. In one case, the SH-type model was the basis of the theoretical formulation, extended by entrainment statements. Uniform distribution of the velocity across the moving layer was assumed and exact solutions to the governing equations were found, in which the downslope velocity component was constant. Hence, independent of the downslope coordinate, steady layer heights were found to be symmetrically distributed and parabolic in the downslope variable. Comparison with experiments turned out to be very good, but no velocity measurements were made, so that the constancy of the downslope velocity could not be corroborated or disproved.

The concept of the second model was different. Here NMR (nuclear magnetic resonance) measurements were utilised and indicated that downslope velocities could not be assumed to be constant through the layer depth or in the downslope direction. Balances of mass and momentum and the entrainment concept were treated alike, but approximations were less accurate than in the first model insofar as the linear terms in the shallowness parameter were dropped [these are the terms of $O(h')$]. This implied that the longitudinal pressure distribution (accounting for the earth pressure normal stress) could not be accounted for. Therefore, a different stress closure had to be assumed. The basal shear stress was additively decomposed in a COULOMB frictional plus a collisional contribution for which the plug flow, linear shearing and the BAGNOLD relations were used. Employing a predescribed distribution of the downslope velocity component across the cascading layer and employing the POHLHAUSEN method to close the depth-integrated momentum equation, an explicit differential equation could be deduced for the depth integrated downslope velocity component. Applying this method to plug flow, BAGNOLD and linear shearing profiles showed that the plug flow model generated unrealistic longitudinal velocity distributions (which exhibit monotonic growth), whilst results from the other two profiles could adequately be brought together with experimental data. It was shown that the ill behaviour of the plug flow case can be traced back to the absence of the collisional stress contribution. Likewise, we can conclude from the constancy of the downslope velocity component in the first model that the plugflow assumption has not led to totally unreasonable results. The thickness distribution of the cascading region is similar to that in this model [recall that in our formulation $h^* = K(1 - x^{*^2})$, where K is a constant, see (6.10), whereas in the KHAKHAR et al. model $Q^* = (1 - x^{*^2})/2$].[7]

Our model achieves this result with an approximation that is one order higher (i.e., linear in $O(h^{*'})$) than the KHAKHAR et al. model. Furthermore, it uses a full MOHR–COULOMB stress rheology and with a plug flow assumption can reach acceptable results. By contrast, the KHAKHAR et al. model is less accurate and must, therefore, introduce collisional stress contributions and avoid plug flow profiles. Despite this success, we find it interesting that a plug flow assumption in this case generates such a physically singular behaviour.

[7] We attribute the odd behaviour of the plug flow model in the KHAKHAR et al. description to a loss of one derivative in the differential equation and a corresponding loss of a parameter in the model adjustment at one boundary. This singularity does not arise in our model.

Part III

Shock Capturing Numerical Methods and Simulations of Free Surface Flows of Shallow Avalanches Sliding Over Curved and Twisted Channels

7 Classical and High Resolution Shock-Capturing Numerical Methods in one Spatial Dimension

Numerical methods to solve the dynamical avalanche equations have been developed from simple to complex and their history reflects as much the learning experience as that of the derivation of the equations themselves. Early studies dealt with plane (chute) flows; later sidewise confinement was relaxed, two-dimensional flow was treated, and model equations for arbitrarily curved and twisted channels were derived and solved numerically. Ultimately, numerical integration of the avalanche equations on arbitrary topography is sought.

In this chapter, mostly spatial one-dimensional flow will be analysed. Physically, the chapter will thus deal with the flow of a granular mass down a narrow chute confined on either side, so that sidewise variations of the depth and velocity can be ignored, or else the moving granular mass flows down a cylindrical surface with a very wide uniform flux from above (see Fig. 7.1). Early attempts of the construction of numerical solutions of the spatially one-dimensional avalanche model equations were rather naive and grew from a great number of unsuccessful attempts. SAVAGE and HUTTER [375] constructed second-order accurate EULERian and LAGRANGEan finite difference schemes and were able to predict the confined flow of a finite mass of granular material down an inclined plane chute. The finite difference schemes were only conditionally stable and required that additional numerical diffusion be added. The LAGRANGEan scheme turned out to be preferable since it repro-

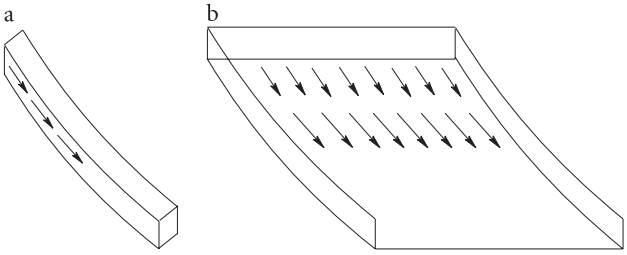

Fig. 7.1. Spatially one-dimensional flows. **a**) Narrow chute with parallel walls, **b**) flow down a wide cylindrical surface with a uniform flux from above.

duced the parabolic cap solution treated earlier, whilst the EULERian scheme did not. A great number of solutions, also for spatially two-dimensional situations was constructed. These will be discussed in detail in Chapt. 10.

Traditional schemes suffer from the disadvantage of not being able to capture possible shocks that form within a granular mass when it is, e.g., moving from an extending to a compressive regime. Modern numerical methods are capable of capturing such sudden changes. They need to be applied in avalanche dynamics to properly predict the flow. In the ensuing developments we shall first illustrate how the traditional numerical techniques using EULERian and LAGRANGEan finite difference schemes are used, after which we shall address modern numerical methods with total variation diminishing properties. In this chapter, only spatially one-dimensional configurations are analysed, i.e.,

$$\begin{aligned} &\frac{\partial h}{\partial t} + \frac{\partial}{\partial x}(hu) = 0, \\ &\frac{\partial}{\partial t}(hu) + \frac{\partial}{\partial x}\left(hu^2\right) + \frac{\partial}{\partial x}\left(\beta_x h^2/2\right) = hs_x - \varepsilon h \cos\zeta \frac{\partial b}{\partial x}, \end{aligned} \tag{7.1}$$

where $s_x = \cos\zeta\,(\tan\zeta - (u/|u|)\tan\delta)$ is the net driving acceleration and $\beta_x = \varepsilon K_x \cos\zeta$, see Sect. 3.4.3.

7.1 Classical EULERian and LAGRANGEan Approaches

The governing depth-integrated equations presented in Chaps. 3 and 4 or their one-dimensional and two-dimensional reductions for the conservation laws of mass and linear momentum, (7.1), can be solved numerically by using finite difference or other advanced schemes for several initial conditions and parameter values. Although these equations seem to be similar to the nonlinear shallow water equations, their numerical integration, in fact, turns out to be quite troublesome. There are several reasons for this:

- When a pile of a granular material is released from rest on a slope, the material near the rear end often tends to initially move up the slope. Similarly, in the deposition at the rear end material is still approaching the deposited mass; often parts of the mass at the rear end moves backwards before it comes to a rest.
- Because the motion is dominantly advective and the convective[1] acceleration terms critically decide about the stability of a numerical scheme, we must be careful to use appropriate upwinding (in the EULERian finite discretisation) to avoid numerical instabilities.
- The avalanche model equations are very close in structure to the shallow water equations, but the geometries of the avalanches are different from

[1] We use the terms "advective" and "convective" synonymously.

those of the usual water wave problem. Unlike the analogous water wave problem, the material is in contact with the bed over a small portion, and the depth is zero elsewhere. Other major mathematical and mechanical differences between the shallow water equations and the avalanche equations have been mentioned in detail in Sect. 3.4.4.

- The flow of a granular mass can be regarded as a moving interface and it embodies all the associated difficulties of such problems.

Before discussing the numerical techniques applied, we emphasise that it is very significant to realise that the scope and range of applicability of a certain software that integrates the avalanche equations depends upon which equations are in fact integrated, for example, those in conservative form (3.33)–(3.35) or those deduced from them by differentiation and substitution of mass balance (3.33), (3.43) and (3.44). Obviously, the second of these sets can only work when the avalanche velocity and thickness distribution are differentiable within the entire domain of the avalanche, whereas this need not be so for equations in conservative form, which are able to capture associated shocks. For smooth solutions, the early EULERian and LAGRANGEan schemes are applicable. Shock capturing techniques will be dealt with later.

SAVAGE and HUTTER [375] proposed two numerical finite difference schemes, one of LAGRANGEan, the other of EULERian type, to solve the spatially one-dimensional equations of motion describing the flow of an avalanche of a finite mass of granular material down a rough incline. Equations (7.1) were not used directly but transformed by differentiation into the *non-conservative* form

$$\begin{aligned} &\frac{\partial h}{\partial t} + \frac{\partial}{\partial x}(hu) = 0, \\ &\frac{\partial u}{\partial t} + u\frac{\partial h}{\partial x} + \beta_x \frac{\partial h}{\partial x} = s_x - \varepsilon \cos\zeta \frac{\partial b}{\partial x}. \end{aligned} \tag{7.2}$$

The EULERian scheme was able to reproduce the motion of the M-wave similarity solution quite well. However, even when the initial profile is something other than an M-wave, this scheme eventually forces the profile into a shape that is reminiscent of the M-wave solution. Such a behaviour is not apparent in the laboratory experiments; it may be a numerical aberration. Thus, one may conclude that the LAGRANGEan technique, in which the grid is advected with the material particles, is a natural choice for this problem. The LAGRANGEan scheme was found to be simple, efficient and able to adequately predict the observed experimental behaviour. In the following paragraphs, we will discuss these two numerical schemes for the system of (7.2).

7.1.1 EULERian Approach

Among several implicit and explicit schemes to treat hyperbolic systems[2] (see, e.g., MCDONALD and AMBROSIANO [270]), SAVAGE and HUTTER used a method similar to that of MACCORMACK [260] comprising a two-step explicit finite difference scheme. This method appeared to work best among all those that were tried. From the known solution at time $t = n\Delta$, one can predict the values of h and u at the new time $t = (n+1)\,\Delta$ by using one-sided upwind differences to approximate the first derivatives. Corrections are made in the second step to predict values using opposite one-sided differences for the first derivatives. The method is second-order accurate and stable for the appropriate timesteps.

To determine h and u, the artificial diffusive terms $\mu\partial^2 h/\partial x^2$ and $\mu\partial^2 u/\partial x^2$, respectively, (with viscosity μ) were introduced on the right-hand sides in both the mass and momentum equations (7.2) so as to dampen the oscillating effects due to sharp gradients. In one spatial dimension, in a first step the finite difference forms of the predictions for h and u at the new timestep are calculated as

$$\overline{h_i^{n+1}} = h_i^n - \frac{\Delta}{2\Delta x}\left(u_{i+1}^n h_{i+1}^n - u_{i-1}^n h_{i-1}^n\right) + \frac{\mu\Delta}{\Delta x^2}\left(h_{i+1}^n - 2h_i^n + h_{i-1}^n\right), \quad (7.3)$$

$$\begin{aligned}\overline{u_i^{n+1}} &= u_i^n - \frac{\Delta}{2\Delta x} u_i^n \left\{S\left(u_{i+1}^n - u_i^n\right) + S\left(u_i^n - u_{i-1}^n\right)\right\} \\ &\quad + \Delta\,\left(\sin\zeta - \operatorname{sgn}\left(u_i^n\right) TC\right) - \frac{\beta\Delta}{2\Delta x}\left(h_{i+1}^n - h_{i-1}^n\right) \\ &\quad + \frac{\mu\Delta}{\Delta x^2}\left(u_{i+1}^n - 2u_i^n + u_{i-1}^n\right),\end{aligned} \quad (7.4)$$

where $S = (1 - \operatorname{sgn}(u_i^n))$, $TC = \tan\delta\cos\zeta$, $\beta = \varepsilon K_{\text{act/pas}}\cos\zeta$.

The corrections for h and u at the new time are calculated in the second step by the formulas

$$\begin{aligned}h_i^{n+1} = \frac{1}{2}\Bigg[&h_i^n + \overline{h_i^{n+1}} - \frac{\Delta}{2\Delta x}\left(\overline{u_{i+1}^{n+1}}\,\overline{h_{i+1}^{n+1}} - \overline{u_{i-1}^{n+1}}\,\overline{h_{i-1}^{n+1}}\right) \\ &+ \frac{\mu\Delta}{\Delta x^2}\left(\overline{h_{i+1}^{n+1}} - 2\overline{h_i^{n+1}} + \overline{h_{i-1}^{n+1}}\right)\Bigg],\end{aligned} \quad (7.5)$$

[2] The one-dimensional first-order *quasi-linear system* of partial differential equations of the form $\frac{\partial \mathbf{w}}{\partial t} + \frac{\partial f(\mathbf{w})}{\partial x} = 0$, where $\mathbf{w}$ is the vector of conservative variables, is said to be *hyperbolic* if the JACOBIan matrix $f'(\mathbf{w})$ of the flux function $f(\mathbf{w})$ has the following property: for each value of $\mathbf{w}$ the eigenvalues of $f'(\mathbf{w})$ are real and the matrix is diagonalisable, i.e., there is a complete set of linearly independent eigenvectors.

and[3]

$$u_i^{n+1} = \frac{1}{2}\left[u_i^n + \overline{u_i^{n+1}} - \frac{\Delta t}{2\Delta x}\overline{u_i^{n+1}}\left\{\left(1 - \operatorname{sgn}\left(\overline{u_i^{n+1}}\right)\right)\left(\overline{u_{i+1}^{n+1}} - \overline{u_i^{n+1}}\right)\right.\right.$$
$$\left. + \left(1 - \operatorname{sgn}\left(\overline{u_i^{n+1}}\right)\right)\left(\overline{u_i^{n+1}} - \overline{u_{i-1}^{n+1}}\right)\right\} \qquad (7.6)$$
$$+ \Delta t\left(\sin\zeta - \operatorname{sgn}\left(\overline{u_i^{n+1}}\right)TC\right) - \frac{\beta\Delta t}{2\Delta x}\left(\overline{h_{i+1}^{n+1}} - \overline{h_{i-1}^{n+1}}\right)$$
$$\left. + \frac{\mu\Delta t}{\Delta x^2}\left(\overline{u_{i+1}^{n+1}} - 2\overline{u_i^{n+1}} + \overline{u_{i-1}^{n+1}}\right)\right].$$

In the above, the superscript n indicates the n-th timestep, whilst the subscript i denotes the i-th node point. Constant time intervals Δt and space intervals Δx are selected. Furthermore, on the right-hand side of (7.3) the second term is the *finite difference* (FD) approximation of $\partial(hu)/\partial x$, whilst the last term is the second-order FD approximation of the numerical diffusive term. Similarly, the second term on the right-hand side of (7.4) is the lowest order upwind FD representation of the convective acceleration, the second line gives the FD representation of the driving forces, whilst the third line is again the FD representation of the numerical diffusion for the velocity. The expressions for $\overline{h_i^{n+1}}$ and $\overline{u^{n+1}}$ are first approximations that are further corrected in (7.5) and (7.6) to yield the final values h_i^{n+1} and u^{n+1}. Values of μ of about 0.01 were found to be sufficient to keep the ripples near the discontinuities small without significantly smearing out the discontinuity itself. Figure 7.2 shows a series of calculations for different bed friction angles $\delta = 22°$, $\delta = 16°$ and $\delta = 10°$ but all at the same bed slope $\zeta = 32°$. The figure depicts that decreasing the bed friction angle increases the acceleration of the pile down the slope, but the rate of spread of the length of the pile remains much the same. The granular material is released from rest at time $t = 0$ with an unsymmetrical shape given by (10.4) in Chap. 10. This particular profile was chosen for comparison with the laboratory experiments performed by HUBER [160] which were the only ones known at that time.

Problems of the EULERian Approach There are several difficulties with the commonly used EULERian approach. Some of them are as follows:

- This scheme uses a fixed spatial grid that extends upstream and downstream of the moving pile.
- Even at those parts of the bed where there is no material and the depth is zero, the equations of motion (7.2) yield finite velocities upstream and downstream of the pile. This causes sudden changes in the velocities corresponding to the front and rear of the pile; a destabilising effect in numerical integrations.

[3] There is a sign mistake in front of sgn in the first line of (7.6) in the corresponding equation of SAVAGE and HUTTER [375].

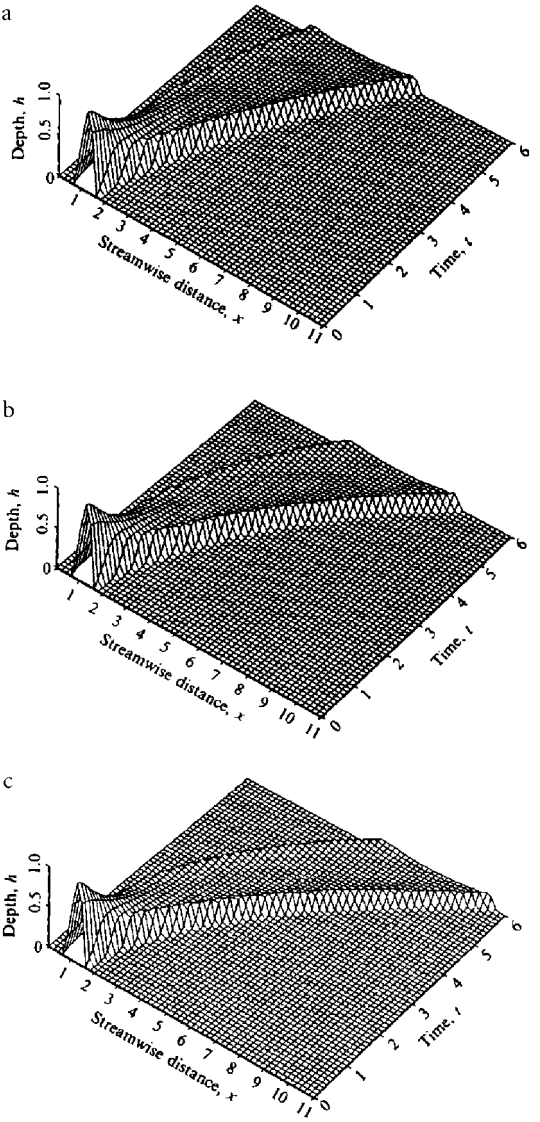

Fig. 7.2. Results obtained from MacCormack's explicit Eulerian finite difference scheme for the evolution of the motion of a finite mass of granular material starting from rest on a bed with inclination angle $\zeta = 32°$, internal friction angle $\phi = 29°$ and different bed friction angles: (**a**) $\delta = 22°$, (**b**) $\delta = 16°$, (**c**) $\delta = 10°$ and $\varepsilon = 0.3218$. (From [375].)

- Although, artificial viscosity was used to control such instabilities, in the numerical computations the velocities in the regions outside of that occupied by the pile began to affect the results in the region of the pile itself. This must have forced the pile to evolve towards the M-wave.

These faulty results led SAVAGE and HUTTER to abandon EULERian schemes and to try LAGRANGEan schemes. It was realised only much later that shock capturing EULERian integration methods were needed to obtain physically correct results.

7.1.2 LAGRANGEan Approach

A LAGRANGEan scheme was thought to be a more natural choice to overcome the difficulties of the EULERian approach. The key idea is to use a material net that follows the motion of the avalanche. This scheme involves the determination of the position of the moving margin. As shown in Fig. 7.3, the granular depth profile is divided into a number of cells, the boundaries of which are convected with the depth-averaged velocity of the granular particles as a basis for the formulation of the approach. The mesh cell boundaries are advected with the particles. Then, an index notation is set-up where i corresponds to the mesh cell centres and j corresponds to the mesh cell boundary points. The cell boundary points are defined at times $n-1$ and are designated as x_j^{n-1}. The velocities of the cell boundary points (see Fig. 7.3), are defined at the half-timesteps and are written as $u_j^{n-1/2}$.

Assume that the geometry and velocity distribution in discretised form is known at $t = (n-1)\Delta$. To determine it at $t = n\Delta$ we proceed as follows. Firstly, the new position of the cell boundaries is determined

$$x_j^n = x_j^{n-1} + u_j^{n-1/2}\Delta \qquad (j = 0, 1, 2, ..., N), \tag{7.7}$$

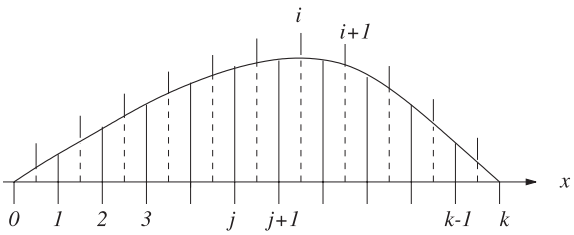

Fig. 7.3. Definition of mesh cell notation for the LAGRANGEan numerical scheme. The i indices refer to cell centres, j to cell boundaries.

from which the positions of the mid-points of the cell follow as

$$x_i^n = \frac{1}{2}\left(x_j^n + x_{j+1}^n\right) \qquad (i = 1, 2, 3, ..., N). \tag{7.8}$$

Integrating (using LEIBNIZ' rule and GAUSS' divergence theorem) the mass balance equation $(7.2)_1$ along the i-th cell yields

$$\begin{aligned} &\frac{d}{dt}\int_{x_{i-1}}^{x_i} h dx - h\left(x_i\right)\frac{\partial x_i}{\partial t} + h\left(x_{i-1}\right)\frac{\partial x_{i-1}}{\partial t} \\ &+h\left(x_i\right)u\left(x_i\right) - h\left(x_{i-1}\right)u\left(x_{i-1}\right) = 0. \end{aligned} \tag{7.9}$$

Since $u\left(x_i\right) = \partial x_i/\partial t$, we readily deduce

$$\frac{d}{dt}\int_{x_{i-1}}^{x_i} h dx = \frac{dF_i}{dt} = 0 \qquad (i = 1, 2, 3, , ..., N), \tag{7.10}$$

where F_i is the area of the i-th cell. In other words, the area of any numerically advected cell is conserved.

Approximating F_i by $h_i\left(x_i - x_{i-1}\right), \qquad i = 1, 2, 3, ..., N$, this conservation property implies

$$h_i^n\left(x_i^n - x_{i-1}^n\right) = h_i^{n-1}\left(x_i^{n-1} - x_{i-1}^{n-1}\right), \qquad i = 1, 2, 3, ..., N, \tag{7.11}$$

which determines h_i^n since all other quantities are known.

Finally, the depth-averaged momentum equation $(7.2)_2$ is used to solve for the new values of velocities at the cell boundary points. Since the left-hand side of this equation contains $\partial h/\partial x$, the boundary cells must be handled separately:

$$u_j^{n+1/2} = u_j^{n-1/2} + \Delta\left[\sin\zeta - \operatorname{sgn}\left(u_j^{n-1/2}\right)\cos\zeta\tan\delta - \varepsilon K_{\text{act/pas}}\cos\zeta P_j^n\right], \tag{7.12}$$

where

$$\begin{aligned} P_j^n &= h_0^n/(x_0^n - x_1^n), && \text{for} \quad j = 0, \\ P_j^n &= \left(h_i^n - h_{i-1}^n\right)/\left(x_i^n - x_{i-1}^n\right), && \text{for} \quad j = 1, ..., N-1, \\ P_j^n &= h_{N-1}^n/\left(x_N^n - x_{N-1}^n\right), && \text{for} \quad j = N, \end{aligned} \tag{7.13}$$

and

$$x_i^n = \frac{1}{2}\left(x_j^n + x_{j+1}^n\right), \tag{7.14}$$

$$K_{\text{act/pas}} = K_{\text{act/pas}}^{j,n} = \begin{cases} K_{\text{act}}, & \text{for} \quad u_{j+1} - u_j > 0, \\ K_{\text{pas}}, & \text{for} \quad u_{j+1} - u_j < 0. \end{cases} \tag{7.15}$$

An artificial viscosity term $\mu\partial^2 u/\partial x^2$,

$$\mu\frac{\partial^2 u}{\partial x^2} = \mu\left(u_{j+1}^{n-1/2} - 2u_j^{n-1/2} + u_{j-1}^{n-1/2}\right) / \left(x_{j+1}^n - x_{j-1}^n\right)^2 \tag{7.16}$$

is added to the right-hand side of (7.12) for the calculation at points other than the leading and trailing edge points. The artificial viscosity, μ, dampens a possible amplification of the velocity gradients and thus reduces the numerical ripples that tend to develop under certain conditions. More details regarding the justification of the introduction of the numerical diffusion can be found in ANDERSON et al. [9]. The values for the artificial viscosity μ between 0.01 and 0.03 are appropriate for the system of (7.2) [375]. The above numerical integration contains three numerical parameters, the number of cells, N, the temporal integration step, Δ , (the spatial step is related to Δ according to (7.7)) and the artificial (dimensionless) numerical viscosity, μ. The accuracy of the LAGRANGEan finite difference scheme depends on the values of these parameters. GREVE [127] has given a detailed analysis about how to select the appropriate values; he found that the results are most critically dependent upon values of μ and concluded that $N = 40$, $\Delta = 0.002$, and $\mu = 0.05$ are appropriate values for routine computations. Figure 7.4 shows the profile shapes at six different (dimensionless) times for the same initial conditions as for the EULERian integrations shown in Fig. 7.2. In the inset, the front, middle point and rear end velocities are shown. Circles mark computed values, crosses are deduced from one of HUBER's experiments [160]. Agreement is not overwhelming but it is promising. In fact, the experiments indicate movement into a smooth profile that is reminiscent of a parabolic cap and not an M-wave.

Now, we can conclude as follows: While EULERian schemes based upon MACCORMACK's [260] numerical method are able to reproduce the M-wave similarity solution, they give unreliable results for more general initial conditions. A LAGRANGEan approach in which the computational grid was advected with the material was found to be simple, efficient and reliable. However, it does not capture singularities, which is the likely reason why the M-wave solution could not be found.

SAVAGE and HUTTER [376] discretised and numerically integrated the equations of motion, written in curvilinear coordinates, for the dynamics of avalanches of granular materials from initiation to run-out along a curved bed in the form of a LAGRANGEan-type finite difference representation, where the grid is advected with the material particles.

When dealing with a curved bed and modelling the equations of motion by curvilinear coordinates, additional terms appear, mainly in the linear momentum equation, namely $\lambda\kappa u^2$, and the inclination angle ζ is a function of the downslope coordinate x, i.e., $\zeta = \zeta(x)$, see [175].

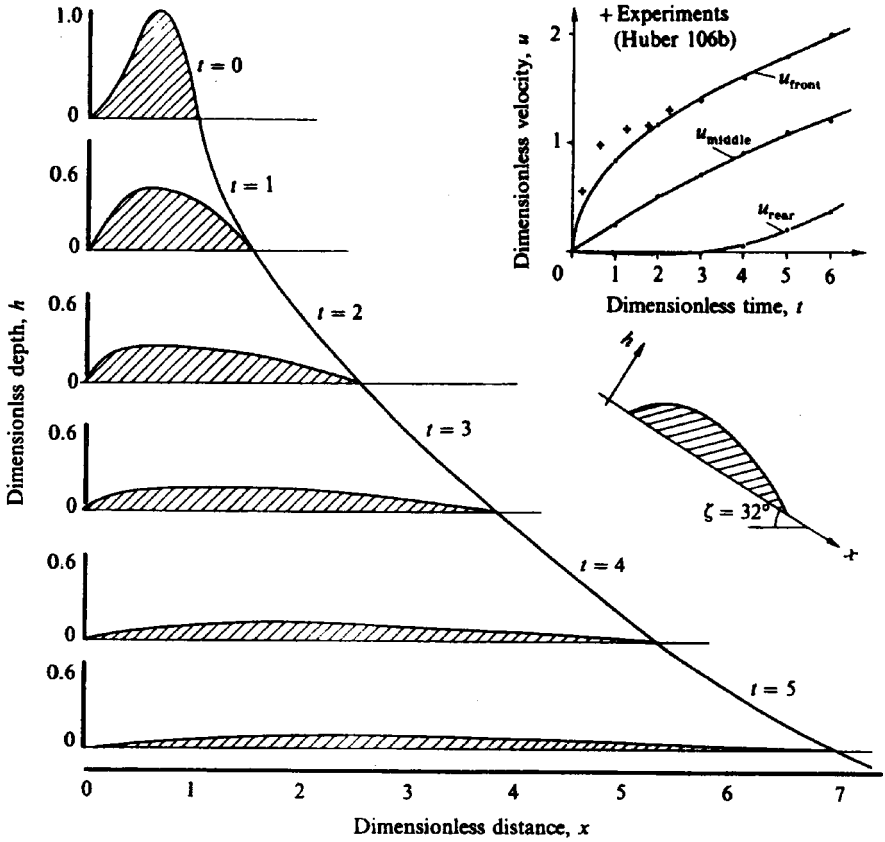

Fig. 7.4. The height h is plotted against distance x for LAGRANGEan calculations of avalanche profile shown for six different times. With increasing time the profile tends to become more parabolic. Also shown in the *inset* are the front, middle and rear end velocities. The points indicate computed values, whilst crosses are deduced by SAVAGE and HUTTER from HUBER's experiment 106*b* [160]. Computations were performed for $\zeta = 32°, \phi = 29°, \delta = 22°$ and $\varepsilon = 0.3218$. (From [375].)

GREVE and HUTTER [128] used this LAGRANGEan scheme for numerical computations of the avalanche height, velocity distribution, the front, rear and an in-between position corresponding to the maximum height, the maximum height of the avalanche for different numerical, as well as material parameter values for a motion of a granular avalanche in a convex and concave chute (see Fig. 3.6). They found good to excellent correspondence between experiments and the theory. More on this will be said in Chap. 10. This LAGRANGEan integration method has also been used in the construction of solutions to the dam break problem with COULOMB friction by KERSWELL [215].

Scrutiny of the numerical integration procedure (7.11)–(7.16) shows that the momentum equation is integrated in its non-conservative form, which itself was obtained by differentiating the conservative form of the momentum balance equation. Thus, these finite difference equations are not explicitly shock-capturing. Steep gradients and spurious oscillations of the field variables must be handled with numerical diffusion, using the latter judiciously where instability prone oscillations occur. This has been reasonably successful, but it is unsatisfactory and calls for better schemes. This will now be attempted.

7.2 Some Traditional Numerical Methods

In this section, we will present some traditional numerical schemes used in different contexts in the literature to solve hyperbolic systems of equations. We will also point out why some of these schemes are not appropriate in our case that leads to the development of high-order shock-capturing numerical methods.

7.2.1 First-Order Schemes

We start with the very simple case of a one-dimensional conservative equation. For simplicity, the x-t-plane of space and time will be discretised by choosing an uniform and stationary mesh width $\triangle x$ and a timestep $\triangle t$. However, most methods presented in this book are extendable to variable mesh grids. The discrete *mesh points* will be denoted by $(x_j,\, t^n)$ and are defined as

$$x_j = j\triangle x, \quad j = 0,\, 1,\, 2, \ldots; \quad t^n = n\triangle t, \quad n = 0,\, 1,\, 2, \ldots, \tag{7.17}$$

where the mesh cell x_j is bounded by the boundaries $x_{j-1/2}$, $x_{j+1/2}$ and $x_{j+1/2} = x_j + \triangle x/2$.

For a systematic development of numerical schemes, we start with the *homogeneous linear scalar hyperbolic advective conservation law*

$$\frac{\partial w}{\partial t} + a\frac{\partial w}{\partial x} = 0, \tag{7.18}$$

where a (the characteristic wave speed) is a positive constant. The second term $a\partial w/\partial x$ represents a *flux derivative* $\partial f/\partial x = a\partial w/\partial x$, with the *physical flux* $f = aw$, where w is a *conservative variable*. Equation (7.18) is discretised by integrating it over the space time rectangle $[x_{j-1/2},\, x_{j+1/2}] \times [t^n,\, t^{n+1}]$ to obtain

$$\int_{x_{j-1/2}}^{x_{j+1/2}} w(x,\, t^{n+1})\, dx = \int_{x_{j-1/2}}^{x_{j+1/2}} w(x,\, t^n)\, dx - \int_{t^n}^{t^{n+1}} \left\{ f(x_{j+1/2},\, t) - f(x_{j-1/2},\, t) \right\} dt. \tag{7.19}$$

All schemes presented in the following are expressed in terms of the *spatial and temporal mean values* of the conservative variable w and physical flux function f. For this reason, we define these mean values, respectively, as follows:

$$U_j^n = \frac{1}{\triangle x}\int_{x_{j-1/2}}^{x_{j+1/2}} w(x,\, t^n)\, dx, \qquad \mathcal{F}(U;\, j+1/2) = \frac{1}{\triangle t}\int_{t^n}^{t^{n+1}} f(x_{j+1/2},\, t)\, dt. \tag{7.20}$$

With these definitions, (7.19) reduces to the following discretisation in general form:

$$U_j^{n+1} = U_j^n - \frac{\triangle t}{\triangle x}\left\{\mathcal{F}\ (U;\, j+1/2) - \mathcal{F}(U;\, j-1/2)\right\}, \tag{7.21}$$

where $\mathcal{F}(U;\, j \pm 1/2)$ denote the *numerical flux functions* that are functions of the cell averages of the neighbouring cells on the cell boundaries at $x_{j+1/2}$ and $x_{j-1/2}$, respectively. We will show in the following that *these numerical fluxes may have different forms depending on the order of accuracy and types of interpolation*. If the cell averages in the numerical flux functions are taken at the time level t^n, one obtains an *explicit numerical scheme*. This allows us to determine U^{n+1} explictly, whereas using cell averages at time level t^{n+1} results in an *implicit method*. Although implicit methods are useful in solving other types of partial differential equations, they are rarely used for time-dependent hyperbolic equations. In this chapter we will only consider explicit methods. In the following derivations we will set a to be positive, unless otherwise stated explicitly. Firstly, we discuss a first-order scheme.

Upwind Method From the initial data $w_0(x) = w(x, t = 0)$ we define the data U^0 for the approximate solution as

$$U_j^0 = w_j^0(x). \tag{7.22}$$

Alternatively, this value can also be defined by cell averages $U_j^0 = \overline{w}_j^0(x)$. We then use a *time-marching procedure* to construct the approximation U^{n+1} from U^n and so on, in a several levels method. There is a wide variety of finite difference methods that can be used. In many cases, the derivatives occurring in (7.18) may simply be replaced by appropriate finite difference approximations, for example, utilising the *low-order upwind flux* approximations

$$\mathcal{F}^{UW}(U; j+1/2) = aU_j^n, \quad \mathcal{F}^{UW}(U; j-1/2) = aU_{j-1}^n. \tag{7.23}$$

For these numerical flux functions (7.21) results in the following (low) first-order *upwind* method

$$U_j^{n+1} = U_j^n - \nu(U_j^n - U_{j-1}^n), \tag{7.24}$$

where

$$\nu = a\triangle t/\triangle x. \tag{7.25}$$

Many of the high-resolution schemes for the approximation of the one-dimensional system of conservation laws are based on upwind differencing. If the conservation law is non-linear, a more complex situation occurs, particularly when there is a mixture of both right-going and left-going waves. In this case, we need to identify the direction of the "wind". The upwind method has the advantage that it does not result in any spurious oscillation near a discontinuity but it is only of first-order accuracy. As we will see later, unphysical oscillations in numerical solutions as obtained with central differences may not be encountered with the upwind method, but such schemes lead to large numerical diffusion in time-dependent problems.

7.2.2 Second-Order Schemes

The Lax–Wendroff Method A large number of second-order methods can be developed to solve the linear system (7.18) by using different finite difference approximations. Most of them are directly based on finite difference approximations of the model equations with the exception of the Lax–Wendroff method. This method is based on the Taylor series expansion of the conservative variable, where the numerical fluxes are given by

$$\mathcal{F}(U; j+1/2) = a\, U^{n+1/2}_{j+1/2}, \qquad \mathcal{F}(U; j-1/2) = a\, U^{n+1/2}_{j-1/2}. \tag{7.26}$$

Applying Taylor series expansion in time, retaining only the first-order terms and using the conservation law (7.18) yields

$$\begin{aligned} w^{n+1/2}_{j+1/2} &= w^n_j + \frac{\triangle x}{2}\left(\partial w/\partial x\right)^n_j + \frac{\triangle t}{2}\left(\partial w/\partial t\right)^n_j \\ &= w^n_j + \frac{\triangle x}{2}\left(\partial w/\partial x\right)^n_j - \frac{a\triangle t}{2}\left(\partial w/\partial x\right)^n_j . \end{aligned} \tag{7.27}$$

By virtue of (7.27) and using central differences, the value of $U^{n+1/2}_{j+1/2}$ for the numerical flux (7.26) is approximated by

$$\begin{aligned} U^{n+1/2}_{j+1/2} &= U^n_j + \frac{1}{2}\left(U^n_{j+1} - U^n_j\right) - \frac{a\triangle t}{2\triangle x}\left(U^n_{j+1} - U^n_j\right) \\ &= \frac{1}{2}\left(U^n_{j+1} + U^n_j\right) - \frac{\nu}{2}\left(U^n_{j+1} - U^n_j\right). \end{aligned} \tag{7.28}$$

Substituting (7.26) and (7.28) into (7.21) yields the Lax–Wendroff scheme in central difference form,

$$U^{n+1}_j = U^n_j - \frac{\nu}{2}\left(U^n_{j+1} - U^n_{j-1}\right) + \frac{\nu^2}{2}\left(U^n_{j+1} - 2U^n_j + U^n_{j-1}\right). \tag{7.29}$$

The TAYLOR series expansion of the form (7.29) at x_j implies that the LAX–WENDROFF method is of second-order accuracy in space. Thus, from (7.26) and (7.28), the numerical flux in (7.29) is viewed as the *high-order* LAX–WENDROFF *flux*,

$$\mathcal{F}^{LW}(U; j+1/2) = \frac{a}{2}(U_{j+1}^n + U_j^n) - \frac{a\nu}{2}(U_{j+1}^n - U_j^n). \tag{7.30}$$

Upwind Beam-Warming Method This is a one-sided version of the LAX–WENDROFF method. It is a high (second)-order approximation method with

$$U_j^{n+1} = U_j^n - \nu\left(U_j^n - U_{j-1}^n\right) - \frac{\nu}{2}(1-\nu)\left(U_j^n - 2U_{j-1}^n + U_{j-2}^n\right), \tag{7.31}$$

where the numerical fluxes are defined in the same way as in (7.26), but the value of $U_{j+1/2}^{n+1/2}$ is approximated by using (7.27) with an upwind (one-sided) method, i.e.,

$$\begin{aligned} U_{j+1/2}^{n+1/2} &= U_j^n + \frac{1}{2}\left(U_j^n - U_{j-1}^n\right) - \frac{a\triangle t}{2\triangle x}\left(U_j^n - U_{j-1}^n\right) \\ &= U_j^n + \frac{1}{2}\left(U_j^n - U_{j-1}^n\right) - \frac{\nu}{2}\left(U_j^n - U_{j-1}^n\right). \end{aligned} \tag{7.32}$$

All methods discussed so far are two-level methods. For time-dependent conservation laws, two-level methods are exclusively used. Higher-level methods involve additional difficulties, see [250].

Problems with Traditional Schemes It is well-known that traditional second-order central difference methods introduce dispersive effects that lead to unphysical oscillations in the numerical solution for physical problems with large gradients of variables. For hyperbolic equations it is often the case that the numerical oscillations are so large that a stable simulation may not be reached. For such cases, in order to avoid possible (emerging) instabilities or to suppress numerical oscillations to an "acceptable level", a certain artificial diffusion must be incorporated. In order to avoid the above problem, non-centred upstream difference schemes may be used. However, this introduces alternative difficulties – implicit numerical diffusion.

7.3 Appropriate Numerical Modelling

In all theories presented in Chaps. 3 and 4, the governing equations comprise a hyperbolic system for the avalanche thickness and bed parallel velocity, which in this spatially one-dimensional situation is the downslope velocity. In all situations the equations are very similar. Thus, common principal integration schemes can with advantage be used for all. In the following chapters, we shall demonstrate this for the different geometries illustrated in the

previous chapters as well as for some new geometric configurations. In the past decades, numerical techniques have been developed to solve the SH-type avalanche equations for typical moving boundary value problems of granular flows as illustrated in Figs. 3.7, 3.8 and 3.9. These techniques are based on LAGRANGEan *moving mesh finite difference schemes*. In these LAGRANGEan schemes, *explicit artificial numerical diffusion was incorporated to maintain stability and to make shocks diffusive*. In doing so, the quality of resolution deteriorates. In fact, the adequacy of these numerical solutions can be "challenged" because of uncontrolled spreading due to this diffusion. Without adding extra artifical diffusion, the formation of the shock resulted in numerical instabilities of the LAGRANGEan moving grid technique [227, 445]. This also occurs for the EULERian integration technique if the central difference scheme is employed [440]. Other traditional high-order difference methods with the EULERian representation are likewise susceptible to numerical instabilities and cause non-physical oscillations in regions of large gradients of the variables [439]. The usual way to deal with these types of instabilities and oscillations is also to incorporate artificial diffusion into the numerical scheme. However, if this is applied uniformly over the problem domain, and sufficient diffusion is added to dampen spurious oscillations, then the solution is smeared out elsewhere. Although traditional first-order finite difference methods, e.g., upstream schemes, are monotonic and stable due to inherent numerical diffusion, they are strongly dissipative, causing the solution to also become smeared out and often grossly inaccurate.

Successful modelling of strongly convective hyperbolic equations is one of the most challenging problems in computational fluid mechanics, particularly when large gradients of the physical variables occur, e.g., for a moving front or possibly arising shock waves in a granular avalanche. Shock formation is an essential mechanism in granular flows on an inclined surface merging into a horizontal run-out zone or encountering an obstacle when the velocity becomes subcritical from its supercritical state. It is, therefore, natural to apply conservative high-resolution numerical techniques that are able to resolve the steep gradients and moving fronts, often observed in experiments and field events but not captured by the LAGRANGEan finite difference scheme and traditional EULERian finite difference schemes. The development of high-resolution shock-capturing schemes has a long history, see, e.g., [228, 250, 412, 415, 424, 425, 440, 446]. We choose a recently developed high-resolution approach, namely the non-oscillatory central (NOC) schemes first introduced by NESSYAHU and TADMOR [294], in which different cell reconstruction techniques – the total variation diminishing (TVD) limiters [250] and an essentially non-oscillatory (ENO) cell reconstruction scheme [143] – are applied, respectively. The numerical results obtained with the high-resolution schemes are compared with and the traditional finite difference schemes. Of the numerical methods under consideration here, the NOC

scheme with the minmod limiter is demonstrated to be the most suitable for handling the problem of avalanche dynamics.

In this chapter, we will develop some high-resolution numerical methods that can essentially capture shock phenomena encountered in geophysical flows such as avalanches and debris movements over simple curved chutes in the laboratory as well as over complex non-trivial natural terrains.

7.4 Modern Numerical Methods[4]

7.4.1 Total Variation Diminishing Method

Although first-order finite difference methods are monotonous and stable, they are also strongly numerically diffusive, causing the solution to become smeared out. Second-order or higher-order techniques are less dissipative, but susceptible to non-linear, numerical instabilities that cause *non-physical oscillations. The high-resolution methods are a compromise between the traditional first-order and higher-order difference schemes.* Their central idea is, on the one hand, to avoid the introduction of under-shoots and over-shoots (numerical oscillation), and on the other hand, *to maintain the numerical diffusion as small as possible*, which is often achieved by different cell reconstruction techniques.

It is well-known that in computing discontinuous solutions, the first-order (upwind) method gives substantially smeared solutions, while the second-order method (Lax–Wendroff or beam-warming) gives spurious oscillations, see e.g., LeVeque [250]. In order to develop a method that is of higher-order and at the same time non-oscillatory and capable of capturing shocks, we need to define the powerful concept called the *total variation diminishing* (TVD) method.

We define the *total variation* (TV) of the mean value U^n as

$$TV(U^n) = \sum_{j=0}^{N-1} |U_{j+1}^n - U_j^n|. \tag{7.33}$$

The contribution $|U_{j+1}^n - U_j^n|$ at the right-hand side of (7.33) is large if values of U_{j+1}^n and U_j^n differ strongly from one another. Thus, any oscillation in the computed result increases the total variation. The TVD condition, requiring

$$TV(U^{n+1}) \leq TV(U^n), \tag{7.34}$$

[4] In writing the text of this section, we profited from Y.-C. Tai's dissertation [412]. Some parts of this section also closely follow Pudasaini [334].

provides a method that gives a solution without spurious oscillations near the discontinuities. Any numerical scheme that fulfils the TVD condition (7.34) for all grid functions U^n is called a TVD method. Therefore, any TVD method is automatically *monotonicity preserving*. This means, in particular, that oscillations of the physical quantities such as velocity jumps and other sharp gradients cannot arise near an isolated propagating discontinuity. As we will see later, another beautiful feature of the TVD requirement is that it is possible to derive higher-order accurate methods that also satisfy (7.34). It can also be shown that the true (i.e., physically relevant weak) solution to a scalar conservation law possesses this TVD property, see [250].

General Criterion for the TVD Method Let us consider a general two-sided numerical scheme of the form

$$U_j^{n+1} = U_j^n - C_{j-1/2}\left(U_j^n - U_{j-1}^n\right) + D_{j+1/2}\left(U_{j+1}^n - U_j^n\right), \tag{7.35}$$

in which $C_{j-1/2}$ and $D_{j+1/2}$ are data-dependent expressions. The scheme (7.35) is a TVD method if the following conditions are satisfied:

$$0 \le C_{j-1/2}, \quad 0 \le D_{j+1/2}, \quad 0 \le C_{j-1/2} + D_{j+1/2} \le 1, \quad \text{for all } j. \tag{7.36}$$

For a proof, see HARTEN, [143]. For example, the low-order upwind scheme (7.24) is a TVD method under the COURANT–FRIEDRICHS–LEVY (CFL) condition[5] $|a\triangle t/\triangle x| < 1$, see [66, 68], since in an upwind scheme $C_{j-1/2} = \nu = a\triangle t/\triangle x \in [0,\, 1)$ and $D_{j+1/2} = 0$, which satisfies conditions (7.36).

7.4.2 Second-Order TVD Schemes

In the following we develop some numerical methods that are second-order accurate for smooth solutions and yet give well-resolved, non-oscillatory discontinuities. The major roles are played by the TVD flux limiters and TVD slope limiters.

Flux Limiter Methods In order to achieve a better resolution of the solutions of hyperbolic conservation equations we can couple a high-order flux $\mathcal{F}_H$ (e.g., some central difference methods) that works well in the smooth regions and a low-order flux $\mathcal{F}_L$ (e.g., some monotone methods) that behaves well in

[5] In order to prevent the blow-up of the numerical scheme it is always necessary to impose the CFL condition, $|a\triangle t/\triangle x| < 1$, on the timestep. Thus, the CFL condition is an important criterion to determine the stability of a time-dependent numerical scheme. In general, a smaller timestep leads to a more stable numerical scheme. However, the number of timesteps for smaller Δt will increase, requiring more computational time for the same simulation. Therefore, it is important to select an appropriate timestep to insure a stable scheme and an efficient simulation.

the vicinity of discontinuities. The structure of this *coupling*, say F, should be such that F reduces to $\mathcal{F}_H$ for the smooth part of the solution and to $\mathcal{F}_L$ for the discontinuous part of the solution. In this section, we couple a (low) first-order upwind scheme with the (high) second-order LAX–WENDROFF scheme with the aid of a flux limiter.

The LAX–WENDROFF scheme (7.29) can be rewritten as

$$U_j^{n+1} = U_j^n - \nu\left(U_j^n - U_{j-1}^n\right) - \frac{\nu}{2}(1-\nu)\left(U_{j+1}^n - 2U_j^n + U_{j-1}^n\right), \qquad (7.37)$$

which demonstrates that the *high-order* LAX–WENDROFF *flux*, $\mathcal{F}_H$, can be viewed as consisting of the low-order upwind flux, $\mathcal{F}_L$ plus a LAX–WENDROFF *correction* $(\mathcal{F}_H - \mathcal{F}_L)$

$$\mathcal{F}_H = \mathcal{F}_L + (\mathcal{F}_H - \mathcal{F}_L)\,. \qquad (7.38)$$

The first term on the right-hand side of this equation, $\mathcal{F}_L$, corresponds to the first-order upwind scheme (7.24) and thus results in very diffusive solutions. Whereas the correction term, $(\mathcal{F}_H - \mathcal{F}_L)$, is referred to as an anti-diffusive flux (SWEBY [409]), since it will be utilised to act as an agent to capture discontinuities. The low-order flux $\mathcal{F}_L$ contains too much diffusion, which must be compensated by the correction term $(\mathcal{F}_H - \mathcal{F}_L)$, but this correction must somehow be *controlled* physically, e.g., by a TVD flux limiter.

Since the upwind method possesses the TVD property at discontinuities, by virtue of (7.38) one can define a method that uses the TVD property at discontinuities and has second-order accuracy on smooth solutions by introducing a *flux limiter* ϕ_j, that is,

$$F = \mathcal{F}_L + \phi_j\{\mathcal{F}_H - \mathcal{F}_L\}\,. \qquad (7.39)$$

The flux limiter $\phi_j = \phi(U; j)$ is chosen near unity if the data U is smooth near U_j and close to zero when there is a rapid change of the data around U_j. This means that the value of ϕ_j is exclusively determined by the smoothness of the data for the quantification. There are several ways to do this. One possibility is to observe the behaviour of the ratio of the consecutive gradients, θ_j,

$$\phi_j = \phi(\theta_j), \qquad \theta_j = \frac{U_j^n - U_{j-1}^n}{U_{j+1}^n - U_j^n}, \qquad (7.40)$$

where θ_j can be seen as a *measure of the smoothness* of the solution. This definition is a natural choice to achieve an approximate TVD condition, as we will immediately see below. Notice that this measurement breaks down near the extreme points of U when the denominator is close to zero and that θ_j becomes arbitrarily large or negative even if the solution is smooth.

Remark There are some disadvantages of the TVD method. One of them is that one cannot maintain second-order accuracy at extreme points. At these points the method is only first-order accurate. Thus, TVD methods must degenerate to first-order accuracy at extreme points.

Hybridisation Between Upwind and Lax–Wendroff Methods Now, we will establish a condition on the flux limiter ϕ_j that must be satisfied so that a hybrid approach between the upwind and Lax–Wendroff methods agrees with the TVD requirement (7.34). Let us consider the combination of first-order upwind and second-order Lax–Wendroff methods. The limited flux can be written in combination with the flux limiter as

$$F(U; j+1/2) = aU_j^n + \frac{1}{2}a(1-\nu)(U_{j+1}^n - U_j^n)\phi_j, \tag{7.41}$$

where $\phi_j = \phi_j^{LW} = 1$ generates the Lax–Wendroff method (7.30). By inspection of (7.31) and (7.41) it follows that $\phi_j^{BW} = \theta_j = (U_j^n - U_{j-1}^n)/(U_{j+1}^n - U_j^n)$ for the beam-warming scheme. This is the reason why we have defined the flux limiter by (7.40). Substituting (7.41) into (7.21) yields

$$\begin{aligned} U_j^{n+1} &= U_j^n - \nu\big(U_j^n - U_{j-1}^n\big) - \frac{\nu}{2}(1-\nu)\big\{\big(U_{j+1}^n - U_j^n\big)\phi_j - \big(U_j^n - U_{j-1}^n\big)\,\phi_{j-1}\big\} \\ &= U_j^n - C_{j-1}\left(U_j^n - U_{j-1}^n\right) + D_j\left(U_{j+1}^n - U_j^n\right), \end{aligned} \tag{7.42}$$

where

$$C_{j-1} = \nu - \frac{\nu}{2}(1-\nu)\phi_{j-1}, \quad D_j = -\frac{\nu}{2}(1-\nu)\phi_j. \tag{7.43}$$

Formula (7.42) is a TVD method if it satisfies the TVD conditions (7.36). However, this is not the case here since $D_j < 0$ for $\phi_j > 0$. Therefore, we must find some conditions on ϕ_j such that the constraints in (7.36) are satisfied with some manipulation of (7.42). For this reason, we rewrite (7.42) in an equivalent form

$$U_j^{n+1} = U_j^n - C'_{j-1}(U_j^n - U_{j-1}^n) + D'_j(U_{j+1}^n - U_j^n), \tag{7.44}$$

where the coefficients of the scheme are given by

$$C'_{j-1} = \nu + \frac{\nu}{2}(1-\nu)\left\{\frac{(U_{j+1}^n - U_j^n)\phi_j - (U_j^n - U_{j-1}^n)\phi_{j-1}}{U_j^n - U_{j-1}^n}\right\}, \; D'_j = 0. \tag{7.45}$$

The TVD condition (7.36) is satisfied by (7.45) under the restrictions

$$0 \le C'_j \le 1, \quad \text{for all} \quad j. \tag{7.46}$$

Condition (7.46) is satisfied provided that the following holds together with the CFL condition $|\nu| \le 1$:

$$\left|\frac{\phi(\theta_j)}{\theta_j} - \phi(\theta_{j-1})\right| \leq 2, \qquad \text{for all} \quad \theta_j,\, \theta_{j-1}. \tag{7.47}$$

The requirement (7.47) is satisfied only if the following two inequalities hold:

$$0 \leq \frac{\phi(\theta_j)}{\theta_j} \leq 2 \quad \text{and} \quad 0 \leq \phi(\theta_j) \leq 2, \quad \text{for all} \quad \theta_j. \tag{7.48}$$

However, the critical weakness of the TVD method is the following. If $\phi_j \leq 0$, then the slopes at neighbouring points have opposite signs. This, consequently, implies that the data has an extremum near U_j. The total variation certainly increases if the values at such points are accounted for. For this reason, the condition

$$\phi_j = \phi(\theta_j) = 0, \quad \text{for} \quad \theta_j \leq 0, \tag{7.49}$$

is imposed to be at a safe position and only the upwind method is used.

Remark It is impossible to satisfy both the higher-order accuracy and the *TVD* requirement at the critical grid values where $\phi_j < 0$. The only way out is that the higher (second)-order accuracy requirement must be given up at these critical grid values. However, any difference scheme with formal higher (second)-order accuracy at all but these critical points may be understood as having higher (second)-order resolution in the sense that the local truncation error is of order $\mathcal{O}(\Delta x)^3$ almost everywhere, and the overall higher (second)-order accuracy does not seem to be degraded in these cases, at least in the L^1-norm[6], (see [294].)

On the other hand, this is a weak point of the *TVD* method since, if the data is smooth near the extremum, one is always tempted to take the value of the flux limiter to be unity in order to use a high-order method. However, in doing so the total variation will generally increase.

■

Figure 7.5a displays the region for condition (7.48) to be satisfied. The line $\phi(\theta) = 1$ corresponds to the Lax–Wendroff method and $\phi(\theta) = \theta$ generates the second-order upwind beam-warming method. Only a part of these two lines lies in the TVD-region, so neither the Lax–Wendroff nor the beam-warming method possess the TVD-property, in general.

The best choice for ϕ is the convex combination of the ϕ^{LW} for the Lax–Wendroff method, which is simply $\phi = 1$, and the ϕ^{BW} for the beam-warming method, which is $\phi = \theta$ as follows:

[6] The L^1-norm of a vector $\mathbf{V}$ with components $V = [v_1, v_2, v_3, ..., v_n]^T$ is defined by $|\mathbf{V}|_1 = \sum_{r=1}^{n} |v_r|$.

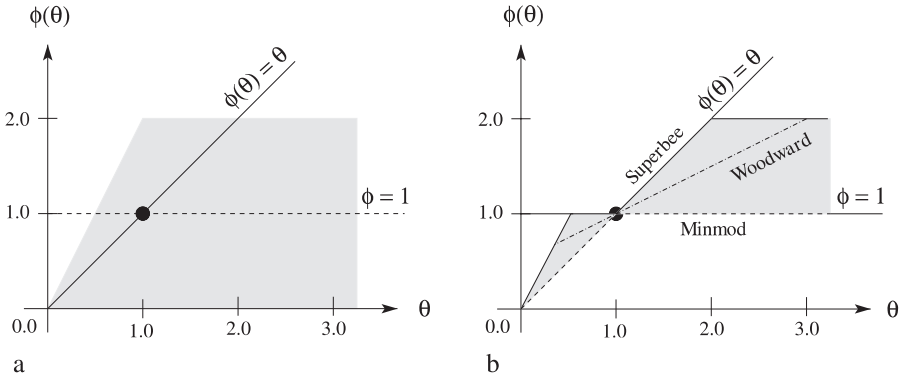

Fig. 7.5. **a**) Region (*shaded*) of values that $\phi(\theta)$ can take to possess the TVD property. **b**) Region of values $\phi(\theta)$ for the second-order TVD methods where the superbee limiter (*solid line*) is on the upper boundary, the minmod limiter (*dashed line*) lies on the lower boundary and the Woodward limiter (*dashed-dotted line*) lies between them.

$$\begin{aligned}\phi(\theta) &= (1-\psi(\theta))\,\phi^{LW} + \psi(\theta)\phi^{BW} \\ &= 1 + \psi(\theta)(\theta - 1), \qquad \text{for} \quad 0 \le \psi(\theta) \le 1. \end{aligned} \tag{7.50}$$

With conditions (7.48) and (7.50) SWEBY [409] showed that for second-order TVD, $\phi(\theta)$ is confined to lie in the region shown in Fig. 7.5b. Note that the condition $\phi(1) = 1$ is automatically imposed, which indicates that the method is of second-order accuracy for $\theta = 1$, i.e., the data is smooth.

Some Special Limiters There is no hard rule for the quantitative selection of the flux limiter $\phi(\theta)$ and it depends on the particular problem at hand. Nevertheless, its value must lie in a certain region of the $\theta - \phi$ diagram. If $\phi(\theta)$ is defined by the lower boundary of the "second-order TVD region", what results is the so-called *Minmod* limiter,

$$^{\text{Minmod}}\phi(\theta) = \max(0,\, \min(1,\, \theta)), \tag{7.51}$$

whilst the *Superbee* limiter

$$^{\text{Superbee}}\phi(\theta) = \max(0,\, \min(1,\, 2\theta),\, \min(\theta,\, 2)) \tag{7.52}$$

is obtained if $\phi(\theta)$ is defined by the upper boundary of the second-order TVD region. The *Woodward* limiter lies between them and is given by

$$^{\text{Woodward}}\phi(\theta) = \max\left(0,\, \min(2,\, 2\theta,\, 0.5(1+\theta))\right). \tag{7.53}$$

Figure 7.5b illustrates the values of $\phi(\theta)$ against θ for these three limiters. Since $\phi(\theta)$ determines the value of the *anti-diffusion flux*, different limiters

result in different diffusion. The superbee limiter which lies on the upper boundary of the second-order TVD region causes the least diffusion. The minmod limiter is the most diffusive. The Woodward limiter lies between them. In fact, the superbee limiter is not only the least diffusive, it is often anti-diffusive and hence has a tendency to steepen gradients of field variables, as we will see in the corresponding numerical results in Chap. 9. The application of these slope limiters can eliminate unwanted oscillations and gives second-order accurate reconstruction for the smooth solutions over the cell (except near critical points). One can, therefore, develop high-order resolution schemes without spurious oscillations, but with the ability to capture a possible discontinuity.

These limiters should be selected according to the physical diffusivity of the problem. For example, if we consider a linear advection hyperbolic RIEMANN problem with constant coefficient (this is problem (7.18)), we must select the most anti-diffusion flux limiter because from the exact analytical solution we know that the initial geometry is advecting with time along the characteristic direction *making the discontinuity undistorted*. As we will see in Chap. 9 while dealing with the computational results, large-scale geophysical flows such as avalanches and debris flows cannot produce such strong and sharp geometry as in the case of the aforementioned RIEMANN problem. Nevertheless, we must choose the most diffusive flux, i.e., minmod. Many other different limiters can be found in, e.g., YEE [446], but we shall not discuss them all.

7.4.3 Cell Reconstruction with Slope Limiters

We define now a so-called "slope limiter" which is an analogue of the flux limiter defined in (7.40). These slope limiters are designed in such a way that certain numerical schemes fulfil the TVD property under appropriate piecewise linear cell reconstructions.

In the above considerations we assumed $a > 0$. For $a < 0$, a similar method can be defined by again viewing the LAX–WENDROFF method as a modification of the upwind method, which is then one-sided in the opposite direction. A mathematically pleasing property is that we can unify these two methods into a single formula. This, to a great extent, helps in generalising the method to linear systems of equations and non-linear problems. Because in more general cases both negative and positive wave speeds can exist simultaneously, we now unconfine the sign of a. Thus, for a of either sign, the fluxes of the upwind and LAX–WENDROFF methods can be written as

$$\mathcal{F}^{UW}(U; j+1/2) = \tfrac{1}{2}a(U^n_{j+1} + U^n_j) - \tfrac{1}{2}|a|(U^n_{j+1} - U^n_j), \tag{7.54}$$

$$\mathcal{F}^{LW}(U; j+1/2) = \tfrac{1}{2}a(U^n_{j+1} + U^n_j) - \tfrac{1}{2}a\nu(U^n_{j+1} - U^n_j). \tag{7.55}$$

Introducing the flux limiter as in (7.39), the TVD flux for the Lax–Wendroff method is given by

$$F(U;j+1/2) = \mathcal{F}^{UW}(U;j+1/2) + \tfrac{1}{2}\phi_{j'}a(\mathrm{sgn}(\nu)-\nu)(U^n_{j+1}-U^n_j). \quad (7.56)$$

This is analogous to (7.41). The flux limiter $\phi_{j'}$ is used to determine the value of F at $x_{j+1/2}$ and $\theta_{j'}$ depends on the sign of the characteristic speed a. For both signs of a we can define $\phi_{j'}$ as

$$\phi_{j'} = \phi(\theta_{j'}), \quad \text{with} \quad \theta_{j'} = \frac{U^n_{j_a+1}-U^n_{j_a}}{U^n_{j+1}-U^n_j}, \qquad j_a = j - \mathrm{sgn}(a). \quad (7.57)$$

For $a > 0$ and $a < 0$ respectively, the TVD flux (7.56) can be realised as follows:

$$\begin{aligned} F(U;j+1/2) &= a\left\{U^n_j + \frac{1}{2}(U^n_{j+1}-U^n_j)\phi_j - \frac{\nu}{2}(U^n_{j+1}-U^n_j)\phi_j\right\} \\ &= a\left\{U^n_j + \frac{\triangle x}{2}\frac{(U^n_{j+1}-U^n_j)}{\triangle x}\phi_j - \frac{\nu\triangle x}{2}\frac{(U^n_{j+1}-U^n_j)}{\triangle x}\phi_j\right\}, \end{aligned} \quad (7.58)$$

$$\begin{aligned} F(U;j+1/2) &= a\left\{U^n_{j+1} - \frac{1}{2}(U^n_{j+1}-U^n_j)\phi_{j'} - \frac{\nu}{2}(U^n_{j+1}-U^n_j)\phi_{j'}\right\} \\ &= a\left\{U^n_{j+1} - \frac{\triangle x}{2}\frac{(U^n_{j+1}-U^n_j)}{\triangle x}\phi_{j'} - \frac{\nu\triangle x}{2}\frac{(U^n_{j+1}-U^n_j)}{\triangle x}\phi_{j'}\right\}. \end{aligned} \quad (7.59)$$

The oscillations arising in the Lax–Wendroff scheme can be interpreted geometrically as being caused by a poor choice of slopes between two grid values. This may lead to a piecewise linear reconstruction $\tilde{u}^n(x,t_n)$ with *much larger* total variation *than in the given data* U^n. This can be remedied by defining a "*slope limiter*". Let us first consider a reconstruction of the cell values by a piecewise linear function of the form

$$\tilde{u}^n(x,t_n) = U^n_j + \sigma_j(x-x_j), \quad \text{on the cell} \quad [x_{j-1/2}, x_{j+1/2}]. \quad (7.60)$$

The slope σ_j in this equation is based on the data U^n. It can be easily seen that for any choice of the slope σ_j, the mean value of the cell average $\tilde{u}^n(x,t_n)$ over $[x_{j-1/2}, x_{j+1/2}]$ is equal to the data point U^n_j. The most significant question is the choice of an appropriate slope σ_j, which will greatly influence the numerical results of the scheme.

This makes it possible to introduce the *slope limiter*

$$\sigma_j = \left(\frac{U^n_{j+1}-U^n_j}{\triangle x}\right)\phi_j. \quad (7.61)$$

With this, the numerical flux (7.56) can be rewritten as

$$F(U; j+1/2) = a\,U^n_{j_1} + \frac{1}{2}|a|\sigma_{j_1}\triangle x - \frac{a}{2}\nu\sigma_{j_1}\triangle x, \tag{7.62}$$

with

$$j_1 = \begin{cases} j, & \text{if } a > 0, \\ j+1, & \text{if } a < 0. \end{cases} \tag{7.63}$$

This means that the flux at $x_{j+1/2}$ is approximated for $a > 0$ by U_j together with σ_j and for $a < 0$ by U_{j+1} together with σ_{j+1}. Therefore, with the definition of the slope limiter (7.61), it can be seen that a piecewise linear reconstruction (7.60) over the cell $x \in [x_{j-1/2},\, x_{j+1/2}]$ is defined by the slope limiter. Also note that (7.62) reduces to the LAX–WENDROFF flux if we use (7.61) to replace σ_{j1}, whereas with $\sigma_{j1} \equiv 0$, (7.62) recovers the upwind method. This justifies the choice of the definition (7.61) as a slope limiter. The slope limiter will play a *vital role* in the remaining numerical methods to be presented. This is responsible for the order of the resolution and the entire results of the methods.

Thus, any of the flux limiters presented above can be converted into the corresponding slope limiter via (7.61) and vice versa. Also note that *slope limiters* are *geometric features* whereas *flux limiters* are their *algebraic* counterparts. Finally, the slope limiters can be viewed as an effective tool to make an appropriate piecewise linear cell reconstruction to let the numerical scheme hold the TVD property.

7.4.4 Non-Linear Conservation Law and TVD Methods

Next we will develop a second-order accurate TVD method for non-linear hyperbolic conservation laws. Consider the homogeneous non-linear scalar hyperbolic conservation law

$$\frac{\partial w}{\partial t} + \frac{\partial f(w)}{\partial x} = 0 \quad \text{or} \quad \frac{\partial w}{\partial t} + a(w)\frac{\partial w}{\partial x} = 0, \tag{7.64}$$

where $a(w) = \partial f(w)/\partial w$ is the characteristic wave speed that depends on the conservative variable w. Because of the generality of a, the problem now turns out to be more complicated than for the linear case.

In the upwind method, the physical value at the cell boundary $U_{j+1/2}$ is assumed to be one of the adjacent cell averages, either U_j or U_{j+1}. This is equivalent to using a piecewise constant reconstruction, i.e., $\sigma_j = 0$, in the flux function over the cell in the scheme. It, therefore, only gives first-order accuracy. Spatially high-order monotonic upstream schemes for conservation

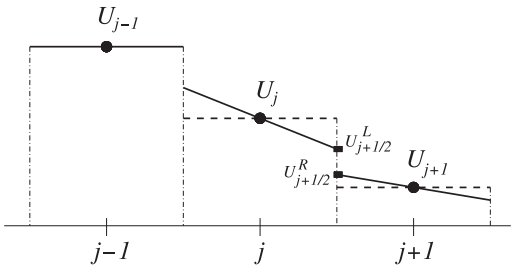

Fig. 7.6. Schematic diagram for the cell average physical values U_j (*dashed lines*) and their linear piecewise cell reconstructions (*solid lines*). For each interface (e.g., between U_j and U_{j+1}) there are two values: $U^L_{j+1/2} = U_j + U'_j/2$ from the left side of the cell and $U^R_{j+1/2} = U_{j+1} - U'_{j+1}/2$ from the right side of the cell with the corresponding approximate derivatives U'_j and U'_{j+1}, respectively.

laws (MUSCL) are introduced by applying the first-order numerical flux and replacing the arguments U_j and U_{j+1} by $U^L_{j+1/2}$ and $U^R_{j+1/2}$, respectively, as

$$U^L_{j+1/2} = U^n_j + \tfrac{1}{2}U'_j, \qquad U^R_{j+1/2} = U^n_{j+1} - \tfrac{1}{2}U'_{j+1}, \tag{7.65}$$

where U'_j denotes the slope limiter determined derivative $U'_j = \triangle x\, \sigma_j$ (see Fig. 7.6). Since the linear piecewise reconstruction is second-order accurate, MUSCL is a spatially second-order scheme, but it requires the knowledge of the characteristic variables.

7.4.5 TVD Lax–Friedrichs Method

To obtain a spatially high-order differencing scheme, a better cell reconstruction is necessary. One possibility is to apply the TVD limiters to obtain the linear piecewise reconstruction. The application of the slope limiters can eliminate unwanted oscillations and gives second-order accurate reconstruction for smooth solutions (except near the critical points) over the cell. One can, therefore, develop high-order resolution schemes without spurious oscillation, but with the ability to capture a possible discontinuity.

The main advantage of this method is its simplicity. No Riemann problems need to be solved. The Lax–Friedrichs method is defined by

$$U^{n+1}_j = \frac{1}{2}\left(U^n_{j+1} + U^n_{j-1}\right) - \frac{\triangle t}{2\triangle x}\left\{f^n_{j+1} - f^n_{j-1}\right\}, \tag{7.66}$$

where $f^n_j = f(U^n_j)$. This scheme can alternatively be written as

$$U^{n+1}_j = U^n_j - \frac{\triangle t}{2\triangle x}\left\{f^n_{j+1} - f^n_{j-1} - \frac{\triangle x}{\triangle t}\left(U^n_{j+1} - 2U^n_j + U^n_{j-1}\right)\right\}. \tag{7.67}$$

This can be realised as a scheme with the numerical fluxes of the kind

$$\mathcal{F}^{LF}_{j+1/2} = \frac{1}{2}\left\{ f_{j+1} + f_j - \frac{\triangle x}{\triangle t}\left(U^n_{j+1} - U^n_j\right)\right\},$$
$$\mathcal{F}^{LF}_{j-1/2} = \frac{1}{2}\left\{ f_j + f_{j-1} - \frac{\triangle x}{\triangle t}\left(U^n_j - U^n_{j-1}\right)\right\}. \tag{7.68}$$

This method has a *dissipation* term of the form

$$\phi^{LF}_{j+1/2} = \frac{\triangle x}{\triangle t}\left(U^n_{j+1} - U^n_j\right) = \frac{\triangle x}{\triangle t}\triangle U^n_{j+1/2}. \tag{7.69}$$

Replacing U_{j+1} and U_j by the second-order accurate $U^R_{j+1/2}$ and $U^L_{j+1/2}$ from (7.65) (which inherits the slope limiter determined derivatives) changes the first-order Lax–Friedrichs scheme into a second-order TVD Lax–Friedrichs (TVDLF) scheme,

$$U^{n+1}_j = U^n_j - \frac{\triangle t}{\triangle x}\left(\mathcal{F}_{j+1/2} - \mathcal{F}_{j-1/2}\right), \tag{7.70}$$

with the flux

$$\mathcal{F}_{j+1/2} = \frac{1}{2}\left\{ f\left(U^R_{j+1/2}\right) + f\left(U^L_{j+1/2}\right) - \frac{\triangle x}{\triangle t}\triangle U^{RL}_{j+1/2}\right\}, \tag{7.71}$$

where the *dissipative limiter* of the TVDLF scheme is given by

$$\phi^{TVDLF}_{j+1/2} = \frac{\triangle x}{\triangle t}\left(U^R_{j+1/2} - U^L_{j+1/2}\right) = \frac{\triangle x}{\triangle t}\triangle U^{RL}_{j+1/2}, \tag{7.72}$$

in which $U^R_{j+1/2}$ and $U^L_{j+1/2}$ are defined in (7.65).

7.4.6 Modified TVDLF Scheme

Although in contrast to the MUSCL scheme, the TVDLF scheme can be applied to any system of conservation laws without knowledge of the characteristic variables; the dissipative limiter (7.72) in the TVDLF scheme results in large diffusion. Tóth and Odstrčil [426] suggested that the dissipative limiter should be multiplied by the maximum Courant number $C^{\max}_{j+1/2}$ to obtain a *modified dissipative limiter*, i.e.,

$$\phi^{\mathrm{MLF}}_{j+1/2} = C^{\max}_{j+1/2}\phi^{\mathrm{LF}}_{j+1/2} = \left(C^{\max}_{j+1/2}\frac{\triangle x}{\triangle t}\right)\triangle U^{RL}_{j+1/2} = a^{\max}_{j+1/2}\triangle U^{RL}_{j+1/2}, \tag{7.73}$$

with

$$a^{\max}_{j+1/2} = \max\left\{ a^{\max}(U^R_{j+1/2}),\, a^{\max}(U^L_{j+1/2})\right\}, \tag{7.74}$$

where $a^{\max}_{j+1/2}$ is the associated maximum wave speed of the hyperbolic equation. Therefore, the modified TVDLF (MTVDLF) flux is expressed by

$$\mathcal{F}^{\text{MLF}}_{j+1/2} = \frac{1}{2}\left\{f(U^R_{j+1/2}) + f(U^L_{j+1/2}) - a^{\max}_{j+1/2}\triangle U^{RL}_{j+1/2}\right\}, \tag{7.75}$$

where the superscript MLF stands for the *dissipative limiter* of the modified TVD Lax–Friedrichs scheme.

Up until now we have discussed the methods that are second-order only in space. We can improve the numerical model further by using the Hancock *predictor step*, see e.g., [426], which can be used to introduce an *intermediate state* "$U^{n+1/2}_j$" in order to obtain a method that is second-order accurate in space as well as time; explicitly,

$$U^{n+1/2}_j = U^n_j - \frac{\triangle t}{2\triangle x}\left\{f\left(U^n_{j+1/2}\right) - f\left(U^n_{j-1/2}\right)\right\}, \tag{7.76}$$

in which the flux arguments are taken to be $U^n_{j\pm1/2} = U^n_j \pm \dfrac{\triangle x}{2}\sigma_j$. The full scheme (*corrector step*) then takes the form

$$U^{n+1}_j = U^n_j - \frac{\triangle t}{\triangle x}\left\{\mathcal{F}^{\text{MLF}}\left(U^{n+1/2}_{j+1/2}\right) - \mathcal{F}^{\text{MLF}}\left(U^{n+1/2}_{j-1/2}\right)\right\}, \tag{7.77}$$

where $\mathcal{F}$ is defined in (7.75). Note that no dissipative limiter appears in the predictor step (7.76). The left and right values, ${U^{n+1/2}_{j+1/2}}^L$ and ${U^{n+1/2}_{j+1/2}}^R$ arising in (7.77) can be computed by first-order Taylor series expansion at the grid point $(x_j,\, t^n)$ and approximated, respectively as,

$${U^{n+1/2}_{j+1/2}}^L = U^n_j \quad + \frac{\triangle t}{2}\left(\partial U/\partial t\right)^n_j \quad + \frac{\triangle x}{2}\sigma^n_j \quad = U^{n+1/2}_j + \frac{\triangle x}{2}\sigma^n_j \quad , \tag{7.78}$$

$${U^{n+1/2}_{j+1/2}}^R = U^n_{j+1} + \frac{\triangle t}{2}\left(\partial U/\partial t\right)^n_{j+1} - \frac{\triangle x}{2}\sigma^n_{j+1} = U^{n+1/2}_{j+1} - \frac{\triangle x}{2}\sigma^n_{j+1}. \tag{7.79}$$

Thus, we see that the main idea of the MTVDLF method is to avoid the dissipative limiter but still maintain second-order accuracy.

7.5 NOC Schemes

Nessyahu and Tadmor [294] developed the one-dimensional non-oscillatory central differencing (NOC) scheme, which is a *second-order accurate* extension of the classical Lax–Friedrichs scheme [246] but with high-resolution

(higher-order), obeying the TVD requirement. In this scheme, the TVD limiter is used for the cell reconstructions. If the cell reconstruction is computed, numerical integrations with the NOC schemes can be realised. A main concept of the NOC schemes is the use of a *staggered grid*, which is a *predictor corrector method* and consists of two steps. At time $t^{n+1} = t^n + \Delta$, the cell averages $U_{j+1/2}^{n+1}$ are evaluated over the bounded region $[x_j, x_{j+1}]$ (see Fig. 7.7). As a consequence, the *boundaries* of the cells at the new time level are the *centres* of the cells at the old time level. At these boundary points, the piecewise polynomial reconstruction of the cell averages at the old time level t^n is smooth, and it remains so for $t < t^{n+1}$ under an appropriate restriction of the timestep. Therefore, the flux across the boundaries of the cells at the new time level may be evaluated by TAYLOR extrapolations using the differential equation and standard quadrature rules. Here we use the *midpoint rule* in time to achieve temporally second-order accuracy.

Let us consider the general one-dimensional hyperbolic differential equation

$$\frac{\delta w}{\delta t} + \frac{\delta f(w)}{\delta x} = s(w), \tag{7.80}$$

where $s(w)$ is the source term. Integrating (7.80) over the rectangle $[x_j,\, x_{j+1}] \times [t^n,\, t^{n+1}]$ gives

$$\begin{aligned}\int_{x_j}^{x_{j+1}} w(x,\, t^{n+1})\, dx = \int_{x_j}^{x_{j+1}} w(x,\, t^n)\, dx - \int_{t^n}^{t^{n+1}} (f(x_{j+1},\, t) - f(x_j,\, t))\, dt \\ + \int_{x_j}^{x_{j+1}} \int_{t^n}^{t^{n+1}} s(x,\, t)\, dt\, dx.\end{aligned} \tag{7.81}$$

This is discretised by

$$\begin{aligned}\triangle x\, U_{j+1/2}^{n+1} =& \frac{\triangle x}{2} \left(U_{j+1/4}^n + U_{j+3/4}^n\right) - \triangle t \left(f_{j+1}^{n+1/2} - f_j^{n+1/2}\right) \\ &+ \frac{\triangle t\, \triangle x}{2} \left(s_{j+1/4}^{n+1/2} + s_{j+3/4}^{n+1/2}\right),\end{aligned} \tag{7.82}$$

where $U_{j+1/2}$ is interpreted as the cell average over $[x_j,\, x_{j+1}]$. Dividing by Δ, this reduces to a scheme of the type

$$\begin{aligned}U_{j+1/2}^{n+1} = \frac{1}{2} \left(U_{j+1/4}^n + U_{j+3/4}^n\right) - \frac{\triangle t}{\triangle x} \left(f_{j+1}^{n+1/2} - f_j^{n+1/2}\right) \\ + \frac{\triangle t}{2} \left(s_{j+1/4}^{n+1/2} + s_{j+3/4}^{n+1/2}\right),\end{aligned} \tag{7.83}$$

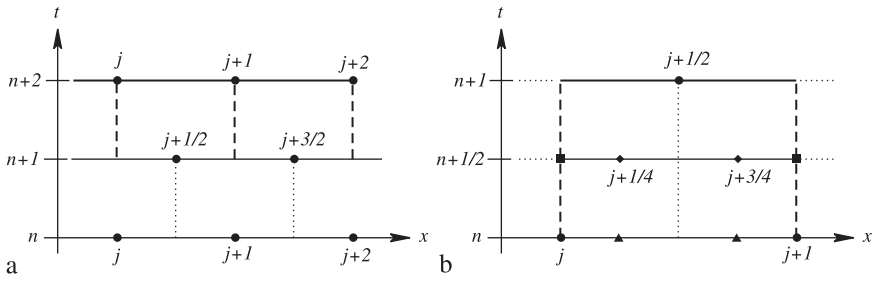

Fig. 7.7. Diagram of the NOC scheme. **a**) Grid points computed in the NOC method. **b**) NOC computational diagram. • indicate the grid points at time level n, $n+1$ and $n+2$. ■ represents the positions where the fluxes $\mathcal{F}$ at time level $n+1/2$ are approximated, ♦ the source terms s and ▲ denotes the quarter and three-quarter points, e.g., $U^n_{j+1/4}$, $U^n_{j+3/4}$.

as illustrated in Fig. 7.7b. Using the TVD slope limiter σ^n_j for the j-th cell at time t^n, the values of $U^n_{j+1/4}$ and $U^n_{j+3/4}$ are determined by the *reconstruction* over the j-th and $(j+1)$-th cell, i.e.,

$$U^n_{j+1/4} = U^n_j + \frac{\triangle x}{4}\sigma^n_j, \quad U^n_{j+3/4} = U^n_{j+1} - \frac{\triangle x}{4}\sigma^n_{j+1}. \tag{7.84}$$

The integral of the transport flux f is approximated by the physical values at $(x_j,\, t^{n+1/2})$ and $(x_{j+1},\, t^{n+1/2})$, i.e.,

$$f^{n+1/2}_j = f\left(U^{n+1/2}_j\right), \qquad f^{n+1/2}_{j+1} = f\left(U^{n+1/2}_{j+1}\right), \tag{7.85}$$

together with the following approximations for the arguments:

$$U^{n+1/2}_j = U^n_j + \frac{\triangle t}{2}\left(\partial U/\partial t\right)^n_j, \;\; U^{n+1/2}_{j+1} = U^n_{j+1} + \frac{\triangle t}{2}\left(\partial U/\partial t\right)^n_{j+1}. \tag{7.86}$$

Similarly, the integral of the source s is approximated at $(x_{j+1/4}, t^{n+1/2})$ and $(x_{j+3/4}, t^{n+1/2})$, respectively, by

$$s^{n+1/2}_{j+1/4} = s\left(U^{n+1/2}_{j+1/4}\right), \quad s^{n+1/2}_{j+3/4} = s\left(U^{n+1/2}_{j+3/4}\right), \tag{7.87}$$

the grid values are approximated by the cell reconstructions

$$\begin{aligned} U^{n+1/2}_{j+1/4} &= U^n_j + \frac{\triangle t}{2}\left(\partial U/\partial t\right)^n_j + \frac{\triangle x}{4}\sigma^n_j, \\ U^{n+1/2}_{j+3/4} &= U^n_{j+1} + \frac{\triangle t}{2}\left(\partial U/\partial t\right)^n_{j+1} - \frac{\triangle x}{4}\sigma^n_{j+1}. \end{aligned} \tag{7.88}$$

Finally, the temporal derivative $\left(\partial U/\partial t\right)^n_j$ in (7.86) and (7.88) is determined by using the conservation law (7.80) as follows:

$$(\partial w/\partial t)_j^n = -\,(\partial f/\partial x)_j^n + s_j^n = -a_j^n\,\sigma_j^n + s_j^n, \tag{7.89}$$

where

$$(\partial f/\partial x) = (\partial f/\partial w)\,(\partial w/\partial x)\,, \quad a = \partial f/\partial w, \quad \sigma = \partial w/\partial x. \tag{7.90}$$

The CFL Condition Substituting the TVD *cell reconstruction* by the *midpoint rule* and using the one-step scheme, (7.83) reduces (with $s = 0$) to

$$U_{j+1/2}^{n+1} = \frac{1}{2}\left(U_j^n + U_{j+1}^n\right) - \frac{\triangle t}{\triangle x}\left(f_{j+1}^n - f_j^n\right), \tag{7.91}$$

which satisfies the TVD requirement (7.34) under the CFL condition

$$\frac{\triangle t}{\triangle x}\left|\frac{f_{j+1} - f_j}{U_{j+1} - U_j}\right| \le \frac{1}{2}, \quad \Longrightarrow \quad \frac{\triangle t}{\triangle x}\,|a^{\max}| < \frac{1}{2}, \quad \text{for all} \quad j, \tag{7.92}$$

where $a^{\max}$ is the maximum wave speed. NESSYAHU and TADMOR [294] showed by some numerical examples that with the CFL condition (7.92) the NOC scheme (7.83) possesses the TVD property for a homogeneous scalar conservative law $\partial w/\partial t + \partial f(w)/\partial x = 0$.

7.6 Alternative Numerical Schemes

In this chapter we have dealt with numerical finite difference representations of the spatially one-dimensional avalanche equations (7.2), or equivalently (7.5)–(7.6). Our procedure was "historical", presenting the early EULERian and LAGRANGEan schemes, identifying with them the difficulties and ranges of inadequate application and then moving to modern shock-capturing finite difference methods.

The EULERian method applied to the non-conservative form of the model equations was integrated for a finite mass of granular material moving down an inclined plane chute and generated solutions that were hardly trustworthy. The subsequent LAGRANGEan integration method generated solutions for the same problem, which were closer to the shapes of the evolving granular piles. Both integration methods required incorporation of additional numerical diffusion for stability. The LAGRANGEan integration method, appearing to be the more trustworthy one of the two, was subsequently used for a number of avalanching flows down inclines, and curved chutes, see e.g. Chap. 10, but a rational reason for its preference over the EULERian scheme was not identified.

This step came with the replacement of these classical finite difference methods by the modern EULERian finite difference method and the recognition that the equations ought to be written in conservative form and non-oscillatory total variation diminishing schemes should be used. These methods are apt for hyperbolic partial differential equations, because they capture

shocks if such discontinuities develop within the domain of a moving granular pile. We presented non-oscillatory central difference schemes that obey the total variation diminishing property, but we did not at the same time also present results of the performances of these schemes. Such results have been presented by TAI [412] and are somewhat academic, but since the finite difference methods are sound, i.e., have proven convergence and stability properties, the numerical results are trustworthy.

There is yet another difficulty that one encounters when dealing with finite domain *moving boundary value problems*, such as the motion of a finite mass of granular material with vanishing height at the front and rear margins. This requires special handling of the boundary conditions, since in a EULERian description the front and rear margins may not lie at grid points. The *special* finite difference approximations at these boundary locations are called front tracking methods. For the spatially one-dimensional case, they were introduced by TAI et al. [415], and very good performance was also demonstrated.

The modern numerical methods for hyperbolic partial differential equations of this chapter are based on finite difference methods as originally developed by NEUMANN and RICHTMYER [295] and LAX and WENDROFF [247], and combine the finite difference approximated flux terms. An alternative approximation was proposed by GODUNOV [115, 116]. In his method exact solutions at the cell boundaries are computed for piecewise constant initial values that are subsequently smeared over each cell. These special initial value problems are the so-called RIEMANN problems, and they are solved exactly or approximately. The considered temporal step is limited by the COURANT–LEVY–FRIEDRICHS (CLF) condition, which avoids collisions of waves that are generated at the boundaries. HARTEN et al. [145] and RODIONOV [359] improved on the accuracy of the GODUNOV procedure.

Such a GODUNOV scheme with second-order accuracy, using a LAGRANGEan grid has been used by KOSCHDON and SCHÄFER and KOSCHDON [228, 229] and was applied, among others, to the one-dimensional SH-equations. As was previously also done by TAI [412], the comparison between numerical and exact solutions was demonstrated for the parabolic cap solution, see Chap. 5, and the dam break problem. The accuracy for the parabolic cap solution is about the same for the two integration methods, but the results for the dam break problem seem better with TAI's shock-capturing EULERian integration technique.

As a final remark on numerical technique, we would also like to mention numerical integration procedures used by SARTORIS and BARTELT and CHRISTEN et al. from EISLF, Davos [61, 368]. These are the avalanche dynamics program for the particle of snow, and upwind finite difference schemes for

dense snow avalanche flows, respectively. For physical modelling they use the improved VOELLMY model.

Using SAINT VENANT type equations with COULOMB basal friction, and no COULOMB material behaviour, but a hydrodynamic isotropic fluid pressure inside the body, BOUCHUT et al. [38] presented a hydrostatic reconstruction scheme. By adequately combining the conservation laws of mass and momentum an energy-type balance law was derived, which, for weak solutions becomes an inequality that may be used as an entropy inequality to select the physically acceptable solutions. MANGENEY et al. [264, 265] used this kinetic scheme to simulate the spreading of a granular cylindrical heap on a horizontal plane. A summary of a great number of balanced schemes is given by BOUCHUT [39].

7.7 Summary

In this chapter, we have presented numerical schemes for classical as well as modern computational methods to solve one-dimensional avalanche equations and that are, in general, applicable to the hyperbolic conservation laws. As for the classical methods we have discussed advantages and disadvantages of both EULERian and LAGRANGEan finite difference schemes. A peculiar characteristic of hyperbolic (avalanche) equations (partial differential equations) is that they are associated with internal shock formation when the flow changes from the supercritical to subcritical state. This means that the field variables, e.g., the depth and velocity profiles, possess jump discontinuities if such flows hit obstacles on their way or if they encounter sudden changes in the topography over which the slides take place. The classical EULERian scheme is not able to capture the generation and propagation of such discontinuities, whereas the LAGRANGEan scheme is too diffusive because it needs artificial diffusion to be imposed to numerically dampen non-physical oscillation. In order to develop a modern shock-capturing scheme, which in fact is able to resolve these problems, we have discussed first-order and second-order traditional schemes, such as first-order upwind, and second-order LAX–WENDROFF and upwind beam-warming schemes. These methods are either numerically diffusive or instable and cause non-physical oscillations. A high resolution method is a compromise between them. A total variation diminishing high resolution shock-capturing numerical scheme with different flux limiters was presented. Slope limiters were employed for cell reconstruction. Finally, non-oscillatory central difference numerical schemes with different limiters were constructed, which can be used to solve granular and debris flows equations. In Chap. 8 this modern numerical scheme will further be extended to two-dimensional avalanche equations written in their most general forms. We have also presented a discussion on several alternative numerical schemes that can be applied in solving hyperbolic conservation laws.

8 Two-Dimensional Shock-Capturing Schemes for Avalanching Flow

In this chapter, we extend the procedures that were applied in the last chapter to spatially one-dimensional flows to two dimensions. Our own early numerical solution procedures were second-order LAGRANGEan finite difference methods and thus did not have total variation diminishing properties and required explicit additional numerical diffusion. This was kept as small as possible and only became substantial in the transition regime from dilating to compressing flow configurations (or vice versa). In Sect. 8.1, we shall briefly give a survey of the literature of this LAGRANGEan integration method, but not the entire method, because today more suitable shock-capturing schemes are used. Section 8.2 deals with non-oscillatory finite difference schemes in the EULERian description, whilst Sect. 8.3 applies these to the extended avalanche-equations. We also review briefly other shock-capturing integration techniques. In the Sect. 8.4 a summary is presented.

8.1 The Two-Dimensional LAGRANGEan Techniques

The LAGRANGEan integration technique is particularly attractive for two-dimensional avalanche problems, because the grid is advecting, which makes the handling of marginal lines, along which the avalanche thickness must vanish, easy. Moreover, the LAGRANGEan integration technique with second-order accuracy in the spatial finite difference operators and leapfrog integration procedure in time yields accurate results whenever only dilational or only compressional flow conditions prevail.

The above-mentioned numerical integration scheme was developed in the avalanche context by KOCH et al. and WIELAND et al. [227, 445]. A finite difference approximation is presented that handles two-dimensional problems numerically accurately. It applies for the model equations of un-confined flow of granular avalanches along a partly curved surface that is flat laterally (see Fig. 3.8). In the scheme of [227] the granular material is divided into triangular prisms with flat tops. For stability and simplicity each triangle has its own constant height. Figure 8.1 displays a typical discretisation. In order to model the experimental results, this discretisation is fit to the initial

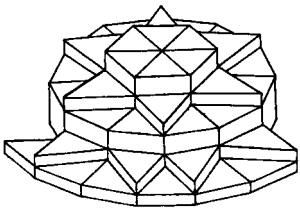

Fig. 8.1. Triangulation of a granular mass with cylindrical triangular elements (*prisms*) having constant heights. (From [227].)

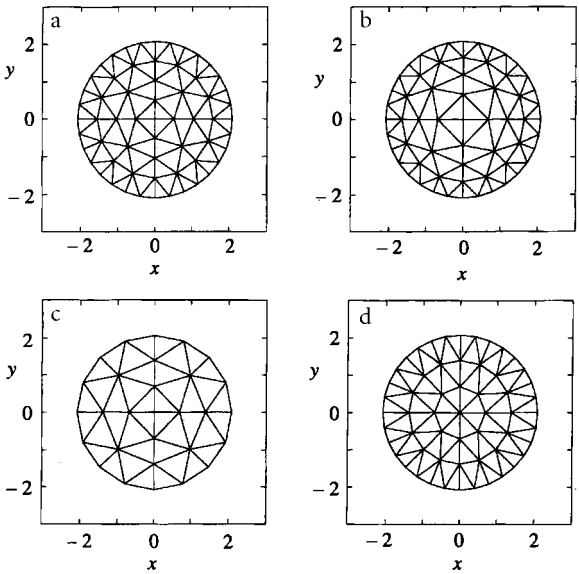

Fig. 8.2. The initial circular surface of the granular material with the inclined bed is filled with a number of triangular elements (*prisms*). (**a**) Triangulation with 88 elements arranged in four rings of approximately equal width. (**b**) Same as in (**a**) but the outer rings are smaller than the interior rings to better account for approximation of the steep radial gradient of the height at the margin. (**c**) Triangulation with 40 elements arranged in three rings. (**d**) Same as in (**c**) but with 80 elements. (From [227].)

form of the experimental granular material. Figure 8.2 shows the projections of the numerical grid onto the Cartesian plane. We are not going to deal with this in detail but only wish to present some results computed by this method. For a detailed study the reader is reffered to [227].

GRAY et al. [123] improved and extended the two-dimensional LAGRANGEan numerical scheme of KOCH et al. [227] to solve the system of equations derived to investigate the motion of free surface flow of granular avalanches over complex basal topography. WIELAND et al. [445] implemented a mixed-

type finite-volume finite difference scheme, explicit in time and a spatially two-dimensional LAGRANGEan scheme to solve the aforementioned depth-averaged equations of motion designed by GRAY et al. [123]. The avalanche is discretised into a finite number of triangular elements, which form a grid that moves and deforms with the motion of the avalanche as shown in the Fig. 8.3. The set of points used to generate this grid reflects the initial experimental configuration of the avalanche. The authors have explicitly discussed the numerical scheme and showed convincing agreement with several different laboratory experiments that will be discussed later in Chap. 10.

8.2 The Two-Dimensional NOC Schemes

The finite difference scheme presented in the remainder of this chapter will be fixed EULERian. Only in the final reviewing section shall we also address LAGRANGEan techniques.

8.2.1 Description

The one-dimensional non-oscillatory central differencing (NOC) scheme of NESSYAHU and TADMOR [294] (as discussed in the previous chapter) is a second-order accurate extension of the classical LAX–FRIEDRICHS scheme [246]. Its two-dimensional scheme was first proposed by JIANG and TADMOR [200] and was also modified by LIE and NOELLE [251]. This scheme was applied to numerical simulations of granular avalanche flows by TAI [412], TAI et al. [415], GRAY et al. [126], WANG et al. [440], CHIOU et al. [60] and PUDASAINI and others [334, 336, 339, 340, 341, 342, 343].

Since in numerical schemes only values of the cell averages are available, with the concept of high-resolution methods the distribution of the physical variables over the cell is reconstructed. As in the one-dimensional case, the two-dimensional NOC scheme is a *predictor–corrector* method that consists of two steps. (*i*) The grid values are predicted according to the non-oscillatory reconstructions from the given cell averages. (*ii*) At the second corrector step, a *staggered averaging* is introduced, together with the predicted mid-values, to determine the full evolution of these averages. This results in a high-order, non-oscillatory central scheme. The key feature of this scheme is that the staggered averages at $(x_{p\pm1/2}, y_{q\pm1/2}, t^{n+1})$ are computed by the cell averages at (x_p, y_q, t^n), see Fig. 8.4a. Our main aim in this chapter is to extend this scheme to a system of non-homogeneous two-dimensional shallow avalanche equations.

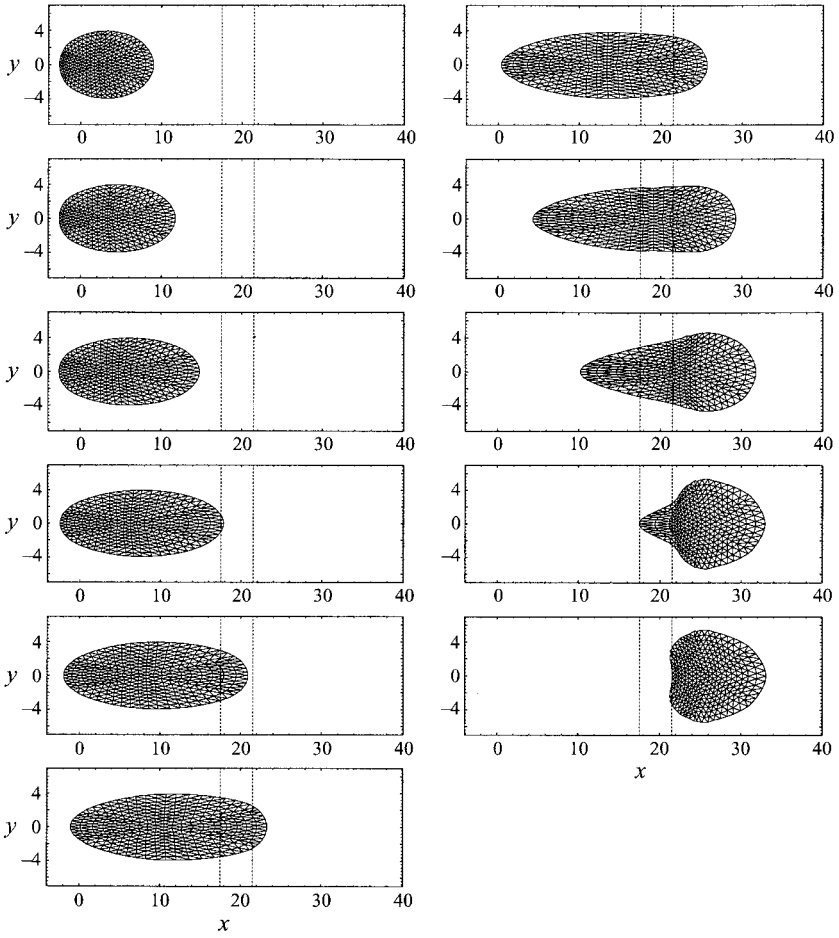

Fig. 8.3. Dimensionless deformations and displacements of a ten-ring numerical grid used to simulate the avalanche experiment V05 (Vestolen). The flow is *from left to right*, at first down on an inclined plane, then (*between the dashed vertical lines*) into the horizontal plane *on the right*. The image sequence is shown at dimensionless times $t = 3.1, 4.1, 5.1, 6.0, 7.0, 8.0, 9.1, 11.1, 13.2, 15.2, 17.2$. The *vertical dashed lines* at $x = 17.5$ and $x = 21.5$ indicate the beginning and the end of the transition zone, with a 40^0 inclined channel *to the left* and the horizontal run-out plane *to the right*. (From [445].)

Let us start with the general two-dimensional conservation law

$$\frac{\partial w}{\partial t} + \frac{\partial f(w)}{\partial x} + \frac{\partial g(w)}{\partial y} = s(w), \tag{8.1}$$

subject to prescribed initial data, $w(x,\, y,\, t=0) = w_0\,(x,\, y)$. Let $C_{p,q}$ be the (p,q)-th cell-covered region,

$$C_{p,q} = \left\{ (x,\, y) \,\middle|\, |x - x_p| \leq \frac{\triangle x}{2},\ |y - y_q| \leq \frac{\triangle y}{2} \right\}. \tag{8.2}$$

Moreover, let $U^n_{p,q}$ denote the cell average over this region at time t^n, and

$$\widetilde{w}_{p,q}(x,\, y,\, t^n) = U^n_{p,q} + \sigma^x_{p,q}(x - x_p) + \sigma^y_{p,q}(y - y_q), \text{ for } (x,y) \in C_{p,q}, \tag{8.3}$$

be a piecewise linear reconstruction over the cell, where $\sigma^x_{p,q}$ and $\sigma^y_{p,q}$ denote the discrete slopes of U in the x- and y-directions, respectively, which are determined by a TVD limiter [250], or a central, essentially non-oscillatory (ENO) cell reconstruction [143]. In the TVD schemes they are the TVD slope limiters and in the ENO schemes they are the mean slopes of the high-order interpolations over the cells.

The piecewise linear cell reconstructions are at most of second-order accuracy. With the help of ENO schemes it is possible to construct a polynomial approximation over the cell that is accurate pointwise to higher-order. The ENO schemes were first developed by Harten [143], who approximated the cell reconstructions by an essentially non-oscillatory high-order accurate polynomial interpolation of a piecewise smooth function from its cell averages. Thus, it is a generalisation of the TVD method of piecewise linear cell reconstructions. The second-order ENO scheme results in a piecewise linear cell reconstruction, equivalent to a TVD method with a cell reconstruction determined by the minmod limiter. In what follows, the third-order quadratic ENO cell reconstruction is employed, for details see [143, 412, 440]. Let $U_{p+1/2,\,q+1/2}$ denote the *staggered average* over $C_{p+1/2,\,q+1/2}$. Integration of (8.1) over $C_{p+1/2,\,q+1/2} \times [t^n,\, t^{n+1}]$ yields

$$\begin{aligned}
U^{n+1}_{p+1/2,\,q+1/2} = {} & \frac{1}{\triangle x \triangle y} \int_{x_p}^{x_{p+1}} \int_{y_q}^{y_{q+1}} w(x,\, y,\, t^n) dx\, dy \\
& - \frac{1}{\triangle x \triangle y} \int_{t^n}^{t^{n+1}} \int_{y_q}^{y_{q+1}} \left(f(x_{p+1},\, y,\, t) - f(x_p,\, y,\, t) \right) dy\, dt \\
& - \frac{1}{\triangle x \triangle y} \int_{t^n}^{t^{n+1}} \int_{x_p}^{x_{p+1}} \left(g(x,\, y_{q+1},\, t) - g(x,\, y_q,\, t) \right) dx\, dt \\
& + \frac{1}{\triangle x \triangle y} \int_{t^n}^{t^{n+1}} \int_{x_p}^{x_{p+1}} \int_{y_q}^{y_{q+1}} s(x,\, y,\, t) dx\, dy\, dt.
\end{aligned} \tag{8.4}$$

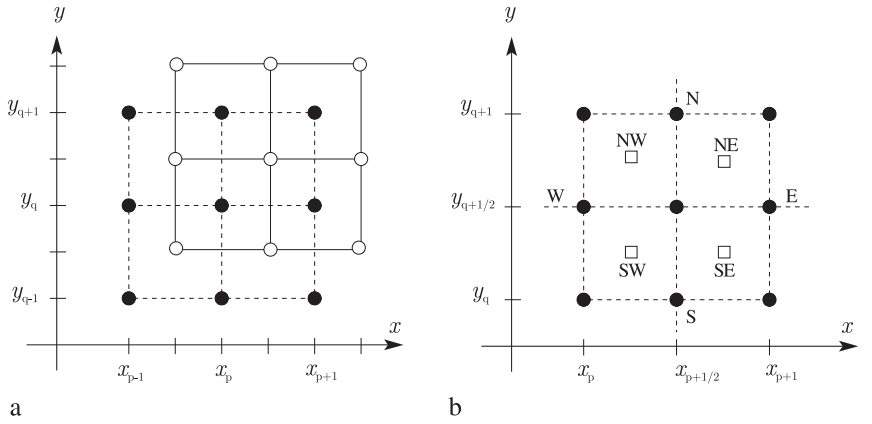

Fig. 8.4. **a**) The two-dimensional NOC scheme and the staggered grid. The staggered averages at $(x_{p\pm1/2}, y_{q\pm1/2}, t^{n+1})$, denoted by $\circ$, are computed by the averages at (x_p, y_q, t^n), represented by $\bullet$. **b**) The two-dimensional NOC scheme and a floor plan of the staggered grid. The cell $C_{p+1/2,\,q+1/2}$ consists of four intersecting cells with $C_{p,q}$, $C_{p+1,q}$, $C_{p+1,q+1}$ and $C_{p,q+1}$, denoted by $C^{SW}_{p,q}$, $C^{SE}_{p+1,q}$, $C^{NE}_{p+1,q+1}$ and $C^{NW}_{p,q+1}$, respectively. $\bullet$ indicates the computed cell centre and $\square$ denotes the centre of the intersecting cell. The numerical fluxes are considered on the values across the corresponding faces, east (E), north (N), west (W) and south (S), respectively.

The first integral on the right-hand side of this equation can be split into four parts as follows:

$$\int_{x_p}^{x_{p+1}} \int_{y_q}^{y_{q+1}} w(x,\,y,\,t^n)\,dx\,dy = \iint\limits_{C^{SW}_{p,q}} w(x,\,y,\,t^n)\,dx\,dy + \iint\limits_{C^{SE}_{p+1,q}} w(x,\,y,\,t^n)\,dx\,dy$$
$$+ \iint\limits_{C^{NE}_{p+1,q+1}} w(x,\,y,\,t^n)\,dx\,dy + \iint\limits_{C^{NW}_{p,q+1}} w(x,\,y,\,t^n)\,dx\,dy. \tag{8.5}$$

These contributions come from the four intersecting cells, viz., $C^{SW}_{p,q}$, $C^{SE}_{p+1,q}$, $C^{NE}_{p+1,q+1}$ and $C^{NW}_{p,q+1}$. These cells are defined as

$$\begin{aligned} C^{SW}_{p,q} &:= C_{p+1/2,q+1/2} \cap C_{p,q}, \\ C^{SE}_{p+1,q} &:= C_{p+1/2,q+1/2} \cap C_{p+1,q}, \\ C^{NE}_{p+1,q+1} &:= C_{p+1/2,q+1/2} \cap C_{p+1,q+1}, \\ C^{NW}_{p,q+1} &:= C_{p+1/2,q+1/2} \cap C_{p,q+1}, \end{aligned} \tag{8.6}$$

respectively (see Fig. 8.4b).

Starting with the intersection cell $C^{SW}_{p,q}$ at the south west corner, using the reconstructed polynomial in (8.3) together with the discrete slopes $\sigma^x_{j,k}$ and $\sigma^y_{j,k}$ of U in the x- and y-directions, respectively, we may derive

$$\begin{aligned}
&\frac{1}{\triangle x \triangle y}\int_{x_p}^{x_{p+1/2}}\int_{y_q}^{y_{q+1/2}} w(x,\, y,\, t^n)dx\, dy \\
&= \frac{1}{\triangle x \triangle y}\int_{x_p}^{x_{p+1/2}}\int_{y_q}^{y_{q+1/2}} \left(U^n_{p,q} + \sigma^x_{p,q}(x - x_p) + \sigma^y_{p,q}(y - y_q)\right) dx\, dy \\
&= \frac{1}{4}U^n_{p,q} + \frac{\triangle x}{16}\sigma^x_{p,q} + \frac{\triangle y}{16}\sigma^y_{p,q}. \qquad (8.7)
\end{aligned}$$

Following this procedure and continuing in a counterclockwise direction, it follows that

$$\begin{aligned}
&\frac{1}{\triangle x \triangle y}\int_{x_{p+1/2}}^{x_{p+1}}\int_{y_q}^{y_{q+1/2}} w(x,\, y,\, t^n)dx\, dy \\
&\qquad = \frac{1}{4}U^n_{p+1,q} - \frac{\triangle x}{16}\sigma^x_{p+1,q} + \frac{\triangle y}{16}\sigma^y_{p+1,q}, \qquad (8.8) \\
&\frac{1}{\triangle x \triangle y}\int_{x_{p+1/2}}^{x_{p+1}}\int_{y_{q+1/2}}^{y_{q+1}} w(x,\, y,\, t^n)dx\, dy \\
&\qquad = \frac{1}{4}U^n_{p+1,q+1} - \frac{\triangle x}{16}\sigma^x_{p+1,q+1} - \frac{\triangle y}{16}\sigma^y_{p+1,q+1}, \qquad (8.9) \\
&\frac{1}{\triangle x \triangle y}\int_{x_p}^{x_{p+1/2}}\int_{y_{q+1/2}}^{y_{q+1}} w(x,\, y,\, t^n)dx\, dy \\
&\qquad = \frac{1}{4}U^n_{p,q+1} + \frac{\triangle x}{16}\sigma^x_{p,q+1} - \frac{\triangle y}{16}\sigma^y_{p,q+1}. \qquad (8.10)
\end{aligned}$$

Next, we compute the four numerical fluxes corresponding to the points $x_{p+1}, x_p, y_{q+1}, y_q$ in (8.4) on the east and west surfaces (associated with the flux function f), and north and south (associated with the flux function g) surfaces, respectively (see Fig. 8.4b). They are approximated by the *midpoint quadrature rule* for second-order accuracy of the temporal integral and *second-order rectangular rule* for the spatial integration across the corresponding face. The flux along the east face is then given by

$$\begin{aligned}
&\frac{1}{\triangle x \triangle y}\int_{t^n}^{t^{n+1}}\int_{y_q}^{y_{q+1}} f(x_{p+1},\, y,\, t)dy\, dt \\
&= \frac{1}{2}\frac{\triangle t}{\triangle x}\left\{f(x_{p+1},\, y_q,\, t^{n+1/2}) + f(x_{p+1},\, y_{q+1},\, t^{n+1/2})\right\} \\
&= \frac{1}{2}\frac{\triangle t}{\triangle x}\left\{f\left(U^{n+1/2}_{p+1,q}\right) + f\left(U^{n+1/2}_{p+1,q+1}\right)\right\}. \qquad (8.11)
\end{aligned}$$

Analogously, the other three fluxes in a counterclockwise direction are, respectively, given by

$$\frac{1}{\triangle x \triangle y}\int_{t^n}^{t^{n+1}}\int_{x_p}^{x_{p+1}} g(x,\, y_{q+1},\, t)dx\, dt = \frac{1}{2}\frac{\triangle t}{\triangle y}\left\{g\left(U_{p,q+1}^{n+1/2}\right) + g\left(U_{p+1,q+1}^{n+1/2}\right)\right\}, \tag{8.12}$$

$$\frac{1}{\triangle x \triangle y}\int_{t^n}^{t^{n+1}}\int_{y_q}^{y_{q+1}} f(x_p,\, y,\, t)dy\, dt = \frac{1}{2}\frac{\triangle t}{\triangle x}\left\{f\left(U_{p,q}^{n+1/2}\right) + f\left(U_{p,q+1}^{n+1/2}\right)\right\}, \tag{8.13}$$

$$\frac{1}{\triangle x \triangle y}\int_{t^n}^{t^{n+1}}\int_{x_p}^{x_{p+1}} g(x,\, y_q,\, t)dx\, dt = \frac{1}{2}\frac{\triangle t}{\triangle y}\left\{g\left(U_{p,q}^{n+1/2}\right) + g\left(U_{p+1,q}^{n+1/2}\right)\right\}. \tag{8.14}$$

8.2.2 Predictor Step

The conservation law (8.1) is employed to evaluate the values of $U_{j,k}^{n+1/2}$ for $j = p,\, p+1,\ k = q,\, q+1$ in (8.11)–(8.14):

$$\begin{aligned} U_{j,k}^{n+1/2} &= U_{j,k}^{n} + \frac{\triangle t}{2}\left(\frac{\partial w}{\partial t}\right)_{j,k}^{n} \\ &= U_{j,k}^{n} - \frac{\triangle t}{2}\left(\frac{\partial f(w)}{\partial x}\right)_{j,k}^{n} - \frac{\triangle t}{2}\left(\frac{\partial g(w)}{\partial y}\right)_{j,k}^{n} + \frac{\triangle t}{2} s\left(U_{j,k}^{n}\right) \\ &= U_{j,k}^{n} - \frac{\triangle t}{2}\left(\sigma^f\right)_{j,k}^{n} - \frac{\triangle t}{2}\left(\sigma^g\right)_{j,k}^{n} + \frac{\triangle t}{2} s\left(U_{j,k}^{n}\right), \end{aligned} \tag{8.15}$$

where σ^f and σ^g are one-dimensional discrete slopes of the fluxes f and g in the x- and y-directions, respectively, which are determined by the non-oscillatory TVD limiters or ENO interpolations. Alternatively, they can also be represented by the corresponding JACOBIans,

$$\left(\sigma^f\right)_{j,k}^{n} = \left(\frac{\partial f(w)}{\partial w}\right)_{j,k}^{n} \sigma_{j,k}^{x}, \qquad \left(\sigma^g\right)_{j,k}^{n} = \left(\frac{\partial g(w)}{\partial w}\right)_{j,k}^{n} \sigma_{j,k}^{y}, \tag{8.16}$$

where $\sigma_{j,k}^{x}$ and $\sigma_{j,k}^{y}$ are the discrete slopes of U in the x- and y-directions, respectively, see JIANG and TADMOR [200]. Nevertheless, herein we will employ only the JACOBI*an-free* approach [294].

There remains now the integration of the source term. This integration also combines contributions from the four intersecting cells, and it is approximated by the *values at the centres* of the four intersecting cells, $(x_{p+1/4}, y_{q+1/4}, t^{n+1/2})$, $(x_{p+3/4}, y_{q+1/4}, t^{n+1/2})$, $(x_{p+3/4}, y_{q+3/4}, t^{n+1/2})$ and $(x_{p+1/4}, y_{q+3/4}, t^{n+1/2})$, see Fig. 8.4b,

$$\begin{aligned}
&\frac{1}{\triangle x \triangle y}\int_{t_n}^{t^{n+1}}\int_{x_p}^{x_{p+1}}\int_{y_q}^{y_{q+1}} s(x,\, y,\, t)dx\, dy\, dt \\
=&\frac{\triangle t}{4}\Big\{s(x_{p+1/4},\, y_{q+1/4},\, t^{n+1/2}) + s(x_{p+3/4},\, y_{q+1/4},\, t^{n+1/2}) \\
&\quad + s(x_{p+3/4},\, y_{q+3/4},\, t^{n+1/2}) + s(x_{p+1/4},\, y_{q+3/4},\, t^{n+1/2})\Big\} \\
=&\frac{\triangle t}{4}\left\{s\left(U^{n+1/2}_{p+1/4,q+1/4}\right) + s\left(U^{n+1/2}_{p+3/4,q+1/4}\right)\right. \\
&\quad \left. + s\left(U^{n+1/2}_{p+3/4,q+3/4}\right) + s\left(U^{n+1/2}_{p+1/4,q+3/4}\right)\right\}. \qquad (8.17)
\end{aligned}$$

A Taylor series expansion is used to evaluate the values of $U^{n+1/2}_{p+1/4,q+1/4}$ at the southwest intersecting cell

$$\begin{aligned}
U^{n+1/2}_{p+1/4,q+1/4} &= U^{n+1/2}_{p,q} + \frac{\triangle x}{4}\left(\frac{\partial w}{\partial x}\right)^n_{p,q} + \frac{\triangle y}{4}\left(\frac{\partial w}{\partial y}\right)^n_{p,q} \\
&= U^{n+1/2}_{p,q} + \frac{\triangle x}{4}(\sigma^x)^n_{p,q} + \frac{\triangle y}{4}(\sigma^y)^n_{p,q}\,, \qquad (8.18)
\end{aligned}$$

where $U^{n+1/2}_{p,q}$, defined in (8.15), is employed. Continuing in a counterclockwise direction and repeating the last equation, it follows that

$$U^{n+1/2}_{p+1/4,q+1/4} = U^{n+1/2}_{p,q} + \frac{\triangle x}{4}(\sigma^x)^n_{p,q} + \frac{\triangle y}{4}(\sigma^y)^n_{p,q}\,, \qquad (8.19)$$

$$U^{n+1/2}_{p+3/4,q+1/4} = U^{n+1/2}_{p+1,q} - \frac{\triangle x}{4}(\sigma^x)^n_{p+1,q} + \frac{\triangle y}{4}(\sigma^y)^n_{p+1,q}\,, \qquad (8.20)$$

$$U^{n+1/2}_{p+3/4,q+3/4} = U^{n+1/2}_{p+1,q+1} - \frac{\triangle x}{4}(\sigma^x)^n_{p+1,q+1} - \frac{\triangle y}{4}(\sigma^y)^n_{p+1,q+1}\,, \qquad (8.21)$$

$$U^{n+1/2}_{p+1/4,q+3/4} = U^{n+1/2}_{p,q+1} + \frac{\triangle x}{4}(\sigma^x)^n_{p,q+1} - \frac{\triangle y}{4}(\sigma^y)^n_{p,q+1}\,. \qquad (8.22)$$

8.2.3 Corrector Step

Collecting all the results from (8.7)–(8.10) and (8.11)–(8.14), we can summarise as follows. The two-dimensional NOC scheme consists of the *first-*

order predictor steps (8.15), (8.19)–(8.22) and the *second-order corrector* steps,

$$
\begin{aligned}
U^{n+1}_{p+1/2,\,q+1/2} &= \frac{1}{4}\left\{U^n_{p,q} + U^n_{p+1,q} + U^n_{p+1,q+1} + U^n_{p,q+1}\right\} \\
&+\frac{\triangle x}{16}\left\{\sigma^x_{p,q} - \sigma^x_{p+1,q} - \sigma^x_{p+1,q+1} + \sigma^x_{p,q+1}\right\} \\
&+\frac{\triangle y}{16}\left\{\sigma^y_{p,q} + \sigma^y_{p+1,q} - \sigma^y_{p+1,q+1} - \sigma^y_{p,q+1}\right\} \\
&-\frac{\triangle t}{2\triangle x}\left\{f\left(U^{n+1/2}_{p+1,q}\right) + f\left(U^{n+1/2}_{p+1,q+1}\right) - f\left(U^{n+1/2}_{p,q}\right) - f\left(U^{n+1/2}_{p,q+1}\right)\right\} \\
&-\frac{\triangle t}{2\triangle y}\left\{g\left(U^{n+1/2}_{p,q+1}\right) + g\left(U^{n+1/2}_{p+1,q+1}\right) - g\left(U^{n+1/2}_{p,q}\right) - g\left(U^{n+1/2}_{p+1,q}\right)\right\} \\
&+\frac{\triangle t}{4}\left\{s\left(U^{n+1/2}_{p+1/4,q+1/4}\right) + s\left(U^{n+1/2}_{p+3/4,q+1/4}\right)\right. \\
&\left.+ s\left(U^{n+1/2}_{p+3/4,q+3/4}\right) + s\left(U^{n+1/2}_{p+1/4,q+3/4}\right)\right\}
\end{aligned}
\tag{8.23}
$$

for the cell mean value at $(x_{p+1/2},\, q_{q+1/2},\, t^{n+1})$. This results in a high-order accurate non-oscillatory scheme. As in the one-dimensional case, presented in Chap. 7, the non-oscillatory behaviour of this scheme also strongly depends on the reconstructed discrete slopes, σ^x, σ^y, σ^f and σ^g.

The CFL Condition A "realistic" geometric CFL restriction for the scheme given by (8.15) and (8.23) is

$$
\max\left(\frac{\triangle t}{\triangle x}\frac{\partial f}{\partial w},\, \frac{\triangle t}{\triangle y}\frac{\partial g}{\partial w}\right) \leq 1/2. \tag{8.24}
$$

This condition was confirmed by the numerical tests by Jiang and Tadmor [200] with the simple linear advection equation, $\partial w/\partial t + \partial w/\partial x + \partial w/\partial y = 0$.

8.3 Two-Dimensional Shock-Capturing Methods Applied to the Extended Avalanche Equations

In this section, we will apply the two-dimensional NOC scheme developed in Sect. 8.2 to the two-dimensional extended model equations for flow avalanches down curved and twisted channels derived by Pudasaini and Hutter [335] as a generalisation of the SH-equations. For this purpose, let us consider the model equations (4.89)–(4.91) of Chap. 4 in conservative form. These equations can be written in compact vectorial form (see (4.98)), as follows:

$$\frac{\partial \mathbf{w}}{\partial t} + \frac{\partial \mathbf{f}(\mathbf{w})}{\partial x} + \frac{\partial \mathbf{g}(\mathbf{w})}{\partial y} = \mathbf{s}(\mathbf{w}), \tag{8.25}$$

where $\mathbf{w}$ denotes the vector of conservative variables, $\mathbf{f}$ and $\mathbf{g}$ represent the transport fluxes in the x- and y-directions, respectively, and $\mathbf{s}$ denotes the source term. They are

$$\mathbf{w} = \begin{pmatrix} h \\ m_x \\ m_y \end{pmatrix}, \ \mathbf{f} = \begin{pmatrix} m_x \\ m_x^2/h + \beta_x h^2/2 \\ m_x m_y/h \end{pmatrix}, \ \mathbf{g} = \begin{pmatrix} m_y \\ m_x m_y/h \\ m_y^2/h + \beta_y h^2/2 \end{pmatrix}, \ \mathbf{s} = \begin{pmatrix} 0 \\ h s_x \\ h s_y \end{pmatrix}, \tag{8.26}$$

where the source terms in the momentum balance equations, s_x and s_y, the parameters β_x and β_y are defined in (4.92)–(4.94), and the equations are computed in the conservative variables h, $m_x = hu$ and $m_y = hv$.

By virtue of (8.23), the cell average $\mathbf{w}_{p+1/2,\,q+1/2}^{n+1}$ at $\left(x_{p+1/2}, y_{q+1/2}, t^{n+1}\right)$ is given by

$$\begin{aligned}
&\mathbf{w}_{p+1/2,\,q+1/2}^{n+1} \\
&= \frac{1}{4}\left\{\mathbf{w}_{p,q}^{n} + \mathbf{w}_{p+1,q}^{n} + \mathbf{w}_{p+1,q+1}^{n} + \mathbf{w}_{p,q+1}^{n}\right\} \\
&+ \frac{\triangle x}{16}\left\{\mathbf{w}_{p,q}^{x} - \mathbf{w}_{p+1,q}^{x} - \mathbf{w}_{p+1,q+1}^{x} + \mathbf{w}_{p,q+1}^{x}\right\} \\
&+ \frac{\triangle y}{16}\left\{\mathbf{w}_{p,q}^{y} + \mathbf{w}_{p+1,q}^{y} - \mathbf{w}_{p+1,q+1}^{y} - \mathbf{w}_{p,q+1}^{y}\right\} \\
&- \frac{\triangle t}{2\triangle x}\left\{\mathbf{f}\left(\mathbf{w}_{p+1,q}^{n+1/2}\right) + \mathbf{f}\left(\mathbf{w}_{p+1,q+1}^{n+1/2}\right) - \mathbf{f}\left(\mathbf{w}_{p,q}^{n+1/2}\right) - \mathbf{f}\left(\mathbf{w}_{p,q+1}^{n+1/2}\right)\right\} \\
&- \frac{\triangle t}{2\triangle y}\left\{\mathbf{g}\left(\mathbf{w}_{p,q+1}^{n+1/2}\right) + \mathbf{g}\left(\mathbf{w}_{p+1,q+1}^{n+1/2}\right) - \mathbf{g}\left(\mathbf{w}_{p,q}^{n+1/2}\right) - \mathbf{g}\left(\mathbf{w}_{p+1,q}^{n+1/2}\right)\right\} \\
&+ \frac{\triangle t}{4}\left\{\mathbf{s}\left(\mathbf{w}_{p+1/4,q+1/4}^{n+1/2}\right) + \mathbf{s}\left(\mathbf{w}_{p+3/4,q+1/4}^{n+1/2}\right)\right. \\
&\qquad \left. + \mathbf{s}\left(\mathbf{w}_{p+3/4,q+3/4}^{n+1/2}\right) + \mathbf{s}\left(\mathbf{w}_{p+1/4,q+3/4}^{n+1/2}\right)\right\}.
\end{aligned} \tag{8.27}$$

Here, $\mathbf{w}_{j,k}^{x}$ and $\mathbf{w}_{j,k}^{y}$ for $j = p,\, p+1$ and $k = q,\, q+1$ are the mean discrete deviators (derivatives) over the cell in the x- and y-directions, respectively,

$$\mathbf{w}_{j,k}^{x} = \boldsymbol{\sigma}_{j,k}^{x}, \qquad \mathbf{w}_{j,k}^{y} = \boldsymbol{\sigma}_{j,k}^{y}. \tag{8.28}$$

Applying the conservation law (8.25), the cell average at time level $t^{n+1/2}$, as in (8.15), is given by

$$\mathbf{w}_{j,k}^{n+1/2} = \mathbf{w}_{j,k}^{n} + \frac{\triangle t}{2}\left(\frac{\partial \mathbf{w}}{\partial t}\right)_{j,k}^{n}, \tag{8.29}$$

where the temporal derivative is approximated by

$$\begin{aligned}\left(\frac{\partial \mathbf{w}}{\partial t}\right)_{j,k}^{n} &= -\left(\frac{\partial \mathbf{f}}{\partial x}\right)_{j,k}^{n} - \left(\frac{\partial \mathbf{g}}{\partial y}\right)_{j,k}^{n} + \mathbf{s}\left(\mathbf{w}_{j,k}^{n}\right) \\ &= -\left(\sigma^{\mathbf{f}}\right)_{j,k}^{n} - \left(\sigma^{\mathbf{g}}\right)_{j,k}^{n} + \mathbf{s}\left(\mathbf{w}_{j,k}^{n}\right). \end{aligned} \tag{8.30}$$

Here $\sigma^{\mathbf{f}}$ and $\sigma^{\mathbf{g}}$ are the one-dimensional discrete slopes of the fluxes in the x- and y-directions, respectively.

For our problem, the earth pressure coefficients, K_x and K_y arising in the fluxes (via $\mathbf{f}$ and $\mathbf{g}$) $\beta_x = -\varepsilon g_z K_x$ and $\beta_y = -\varepsilon g_z K_y$, can be determined by the velocities on the adjacent cells with the ad hoc definitions (4.80) and (4.81),

$$(K_x)_{p,q} = K_x(u_{p+1,q},\, u_{p-1,q}), \tag{8.31}$$

$$(K_y)_{p,q} = K_y(u_{p+1,q},\, u_{p-1,q},\, v_{p,q+1},\, v_{p,q-1}). \tag{8.32}$$

Here u and v are the velocities in the x- and y-directions, respectively, which are determined by the definition of the conservative variables,

$$u_{p,q} = (m_x)_{p,q}/h_{p,q}, \quad v_{p,q} = (m_y)_{p,q}/h_{p,q} \quad \text{for} \quad h_{p,q} \neq 0. \tag{8.33}$$

Remark Equations (8.33) indicate that the scheme given by (8.27) suffers from the trivial solution, $0 = 0$, at $h = 0$ for the momentum balance equation. There are two remedies to this problem. (*i*) A first choice is the addition of a very thin layer of material over the entire computational domain. (*ii*) Alternatively, one may set all the physical variables equal to zero outside the avalanche domain.

■

Using the cell reconstructions and the predicted values (8.29), the arguments for the source term in (8.27) are given by

$$\begin{aligned}
\mathbf{w}_{p+1/4,q+1/4}^{n+1/2} &= \mathbf{w}_{p,q}^{n+1/2} + \frac{\triangle x}{4}\mathbf{w}_{p,q}^{x} + \frac{\triangle y}{4}\mathbf{w}_{p,q}^{y}, \\
\mathbf{w}_{p+3/4,q+1/4}^{n+1/2} &= \mathbf{w}_{p+1,q}^{n+1/2} - \frac{\triangle x}{4}\mathbf{w}_{p+1,q}^{x} + \frac{\triangle y}{4}\mathbf{w}_{p+1,q}^{y}, \\
\mathbf{w}_{p+3/4,q+3/4}^{n+1/2} &= \mathbf{w}_{p+1,q+1}^{n+1/2} - \frac{\triangle x}{4}\mathbf{w}_{p+1,q+1}^{x} - \frac{\triangle y}{4}\mathbf{w}_{p+1,q+1}^{y}, \\
\mathbf{w}_{p+1/4,q+3/4}^{n+1/2} &= \mathbf{w}_{p,q+1}^{n+1/2} + \frac{\triangle x}{4}\mathbf{w}_{p,q+1}^{x} - \frac{\triangle y}{4}\mathbf{w}_{p,q+1}^{y}.
\end{aligned} \tag{8.34}$$

They are analogous to (8.19)–(8.22).

The CFL Condition As in (7.92), this NOC scheme must obey the CFL condition

$$\frac{\triangle t}{\triangle x}\,|c^{\max}| < \frac{1}{2}, \qquad \text{for all} \quad p,\, q, \tag{8.35}$$

with the global maximum wave speed

$$c^{\max} = \max_{\text{all } p,q} \left(|u_{p,q}| + \sqrt{\beta_x h_{p,q}}\,,\; |v_{p,q}| + \sqrt{\beta_y h_{p,q}} \right) \tag{8.36}$$

over the entire computational domain. For methods how to compute the wave speeds, we refer to (4.105).

In Chap. 9, we will implement the numerical scheme of this section to solve the two-dimensional avalanche equations (4.89)–(4.91) for a number of cases: (*i*) different topographies, (*ii*) different parameter values, (*iii*) different numerical methods and (*iv*) different cell reconstructions.

Discussion on Alternative Numerical Schemes As with the spatially one-dimensional case, additional alternative shock-capturing and shock-tracking schemes have been and are still being developed in the current literature. The discussion presented here follows immediately that of Sect 7.6. Multi-dimensional versions of Godunov-type schemes with relaxation and kinetic solvers are described in Bouchut [39]. The motion of the numerical grid allows the description of flows in variable numerical domains. Godunov developed his method on moving grids by adequately discretising the corresponding conservation laws [116]. A number of publications deals with the motion of the grid within a given finite volume solver. On this basis, Thomas and Lombard [420] developed their geometric conservation law, which determines the enlargement of the controlling volume that is generated by the motion. Farhat et al. [96] propose a discretised form of the conservation law on a moving grid that agrees with that of Godunov. The corresponding explicit schemes with second-order accuracy are presented by Baumann [29] and Azarenok et al. [18]. Koschdon [229] reproduces results of granular flows down an inclined channel merging into a horizontal plane and states that the results agree well with the experiments of Wieland et al. [445]. Similarly, Vollmöller employed the wave propagation method to predict the sand flow down channels [431].

8.4 Summary

At the beginning of this chapter, we briefly discussed the two-dimensional Lagrangean finite difference scheme. This was motivated by the fact that for two-dimensional avalanche problems one can easily handle the advecting margin of the avalanche along which its depth must vanish. However, this

technique is only well-suited for dilational or compressional flow situations, but not when the flow prevails rapid changes in depth and velocity profiles during the motion. In such situations, the method is oscillatory and produces non-physical results. It is necessary to add numerical diffusion into the model equations in order to control instabilities. To accurately solve the hyperbolic model equations describing the avalanching debris flows, a shock-capturing scheme is needed. For this reason, we presented in detail NOC schemes with appropriate slope limiters for cell reconstructions. This is a high resolution shock-capturing scheme and satisfies the TVD requirement of conservative variables, a method that gives a solution without spurious oscillations near the discontinuities. This scheme employs a two-step method, expressed by two predictor corrector steps. Finally, the extended avalanche equations of Chap. 4 are put into a two-dimensional shock-capturing TVD-NOC scheme.

9 Avalanche Simulations over Curved and Twisted Channels

In this chapter, we will implement the numerical schemes developed in Chap. 8 into a computer code in order to simulate avalanching masses. We will make use of the two-dimensional avalanche equations (4.89)–(4.91) proposed by PUDASAINI and HUTTER [335] for a number of cases: (*i*) different numerical methods, (*ii*) different cell reconstructions, (*iii*) different topographies, (*iv*) different parameter values and (*v*) flow down a basal surface with humps.

9.1 Performance of Various Numerical Schemes

In order to identify the best numerical scheme that ideally fits the problem of avalanche dynamics, we first consider a very simple geometric situation in which the basal topography varies only in the downhill direction but is laterally flat. Let us consider the model equations (4.89)–(4.91). By setting $\theta = 0^\circ$ (where θ appears through η and ζ via the net driving force components (4.93)–(4.94), and the factors β_x and β_y in (4.92)), we obtain a torsion-free master curve. Indeed, if we set the parameter $\theta = 0^\circ$, we obtain a topography that varies only in the downhill direction and is flat in the cross-slope direction.

In this section, a simulation example of an avalanche of finite granular mass sliding down an inclined plane and merging continuously into a horizontal plane is presented. A hemispherical shell holding the material together at the upper end of the chute is suddenly released so that the bulk material commences to slide on an inclined flat plane at 35° into a horizontal run-out plane connected by a smooth transition. The computational domain is the rectangle $x \in [0, 30]$ and $y \in [-7, 7]$ in dimensionless length units, where the inclined section lies in the interval $x \in [0, 17.5]$ and the horizontal region lies where $x \geq 21.5$ with a smooth change of the topography in the transition zone, $x \in [17.5, 21.5]$. The inclination angle is prescribed as

$$\tilde{\zeta}(x) = \begin{cases} \tilde{\zeta}_0, & 0 \le x \le 17.5\,, \\ \tilde{\zeta}_0(1-(x-17.5)/4), & 17.5 < x < 21.5\,, \\ 0^\circ, & x \ge 21.5\,, \end{cases} \tag{9.1}$$

with $\tilde{\zeta}_0 = 35^\circ$. The simulation is performed with an internal angle of friction $\phi = 30^\circ$ and a bed friction angle $\delta = 30^\circ$. The material is suddenly released at $t = 0$ from the hemispherical shell with an initial radius of $r_0 = 1.85$ in dimensionless length units. The centre of the cap is initially located at $(x_0, y_0) = (4, 0)$, see Fig. 9.1. The results of the numerical simulations will be tested against laboratory avalanche experiments in Chaps. 10 and 12.

9.1.1 Numerical Performances

Figures 9.2 and 9.4–9.8 illustrate the thickness contours of the avalanche body at nine time instances as the avalanche slides on the inclined plane into the horizontal run-out zone, obtained with different numerical schemes (for more details see [334, 440]). If the traditional *central difference scheme* is applied to simulate the avalanche flow, stable numerical simulations cannot be performed. For such cases, in order to suppress *numerical oscillations* and avoid possible emerging instabilities, *artificial diffusion* must be incorporated.

Figure 9.2 shows numerical results obtained with the central difference scheme where the artificial diffusion term $\mu_x \partial^2 \mathbf{w}/\partial x^2 + \mu_y \partial^2 \mathbf{w}/\partial y^2$ is added to the right-hand sides of (8.25) with viscosities $\mu_x = \mu_y = 0.02$. For smaller viscosities the simulation becomes unstable. The central difference schemes, as well as many other traditional higher-order difference methods, introduce *dispersive effects* that are susceptible to numerical instabilities and lead to unphysical oscillations in the numerical solution. These are usually located behind the advancing front and are damped with growing distance from the front (for $t = 3$ to $t = 12$ in Fig. 9.2), although for this case certain artificial diffusion has been incorporated. The corresponding three-dimensional evolution of the avalanche geometry at three different dimensionless times $t = 6$, 9, 12 is shown in Fig. 9.3. The unphysical oscillations behind the moving front are obvious. If sufficiently large artificial diffusion is added to dampen the spurious oscillations, a solution without superimposed numerical oscillations can be reached. However, in such cases, the corresponding solution will be highly diffusive, similar to that obtained with the first-order accuracy upstream scheme (Fig. 9.4), in which additional diffusion is inherent. Although traditional first-order finite difference methods, e.g., the first-order upstream scheme, are monotonic without numerical oscillations and stable, they are strongly dissipative, causing the solution to become smeared out and often grossly inaccurate. Due to the dissipative nature of the upstream difference scheme, the simulated granular flow spreads out over a much wider area than that with high-order difference schemes. At some time levels, e.g., for $t = 9$

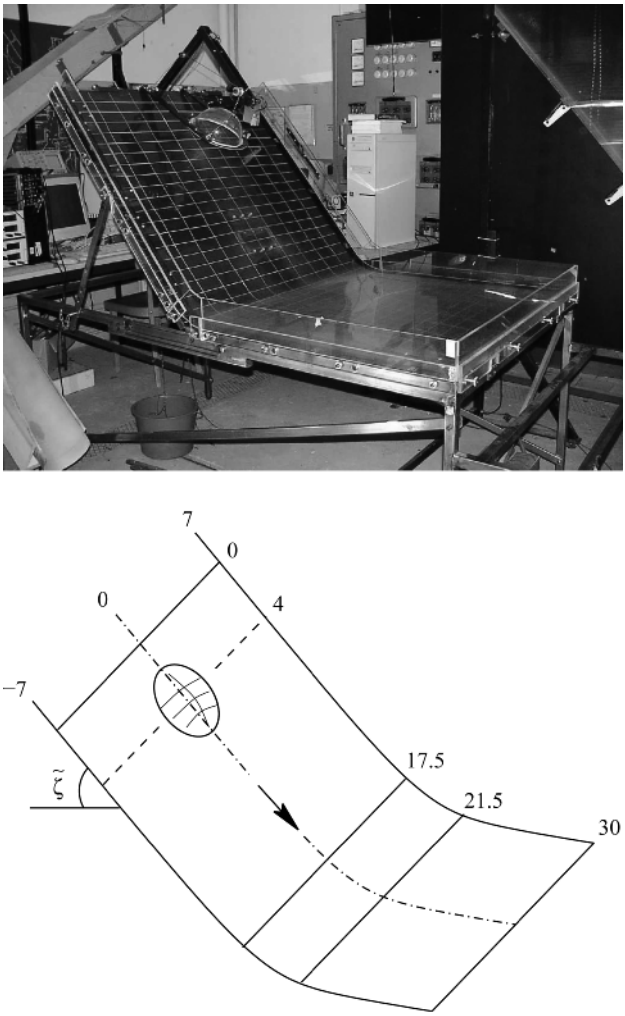

Fig. 9.1. *Top*: Laboratory avalanche chute consisting of upper inclined, middle continuous transition and lower horizontal parts. At the top of the inclined part, a hemispherical cap is mounted to hold the initial granular mass. *Bottom*: Idealised bottom topography to test the various numerical schemes with scalings in dimensionless form.

and $t = 18 - 24$ in Fig. 9.4, the extents of the granular mass exceed the computational domain. Thus, to study the numerical solution of this scheme more deeply, a relatively large (lateral) computational domain should be chosen.

The numerical results obtained by the use of the NOC scheme with different cell reconstruction methods – three TVD limiters: superbee, Woodward and minmod – as well as the third-order ENO cell reconstruction are shown in

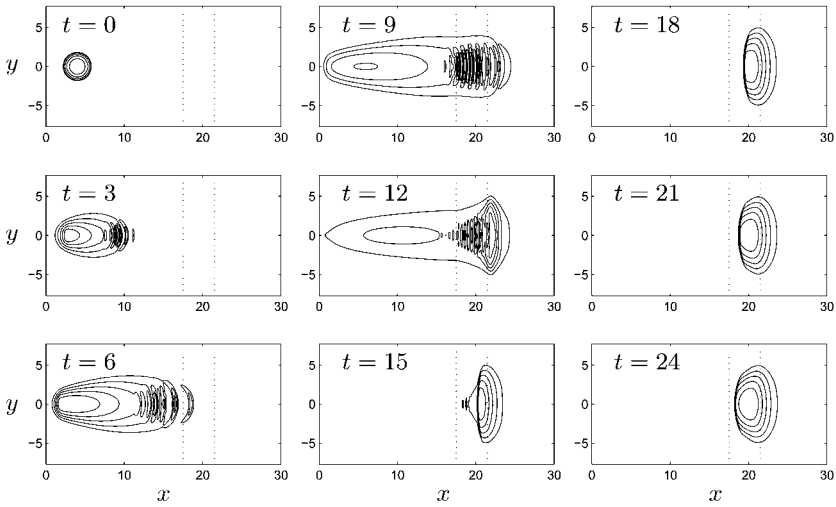

Fig. 9.2. Thickness contours of the avalanche at nine different dimensionless times $t = 0, 3, 6, 9, 12, 15, 18, 21, 24$, obtained with the *traditional central difference scheme*. The transition zone from the inclined plane to the horizontal plane lies between the two *dotted lines*. In order to achieve a stable simulation, the artificial numerical diffusion term $\mu_x \partial^2 \mathbf{w}/\partial x^2 + \mu_y \partial^2 \mathbf{w}/\partial y^2$ must be incorporated in (8.25) with viscosities $\mu_x \geq 0.018$, $\mu_y \geq 0.018$. Here we choose $\mu_x = \mu_y = 0.02$. Nevertheless, large numerical oscillations still exist. (From [440]).

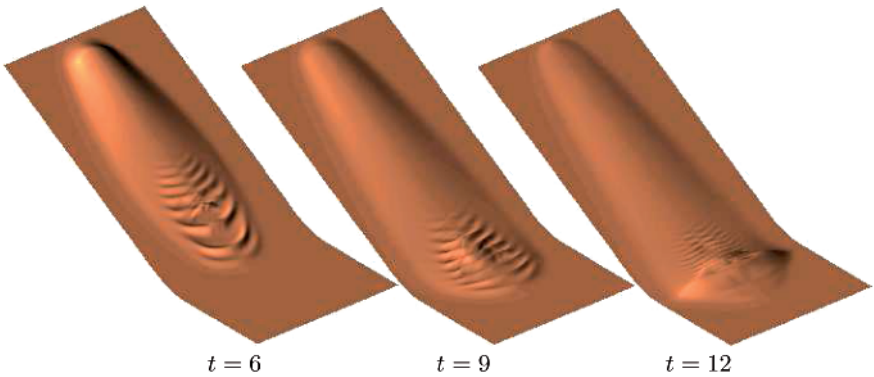

Fig. 9.3. Three-dimensional geometries of the avalanche at three different dimensionless times $t = 6, 9, 12$, obtained with the *traditional central difference scheme* as in Fig. 9.2. Considerable numerical oscillations can be observed. (From [440].)

Figs. 9.5–9.8. Because the superbee limiter is the least diffusive among the second-order TVD limiters, the solution with this limiter still exhibits oscillations (for $t = 9$ and $t = 12$ in Fig. 9.5). In fact, the superbee limiter is often anti-diffusive, i.e., it has a tendency to steepen gradients. The deposition in

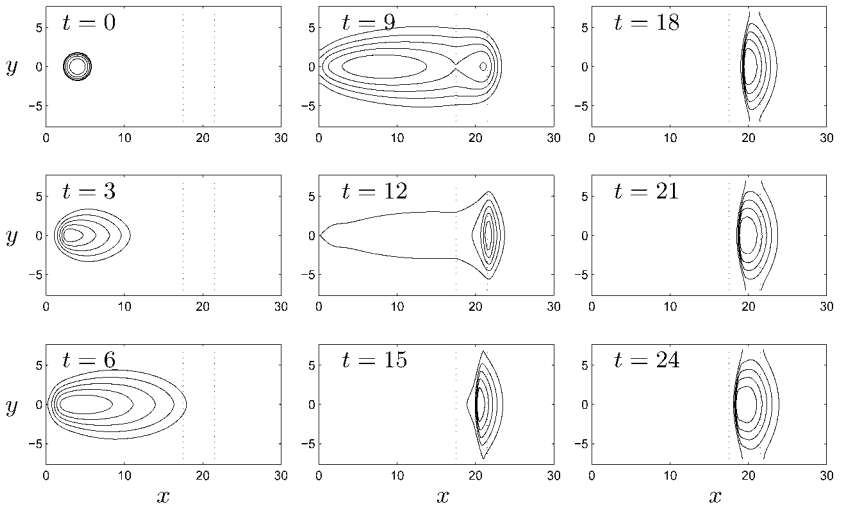

Fig. 9.4. Thickness contours of the avalanche at nine different dimensionless times $t = 0, 3, 6, 9, 12, 15, 18, 21, 24$, obtained with the *traditional first-order upstream difference scheme*. The *zone between the two dotted lines* is the transition zone from the inclined plane to the horizontal plane. The scheme is obviously very diffusive. (From [440].)

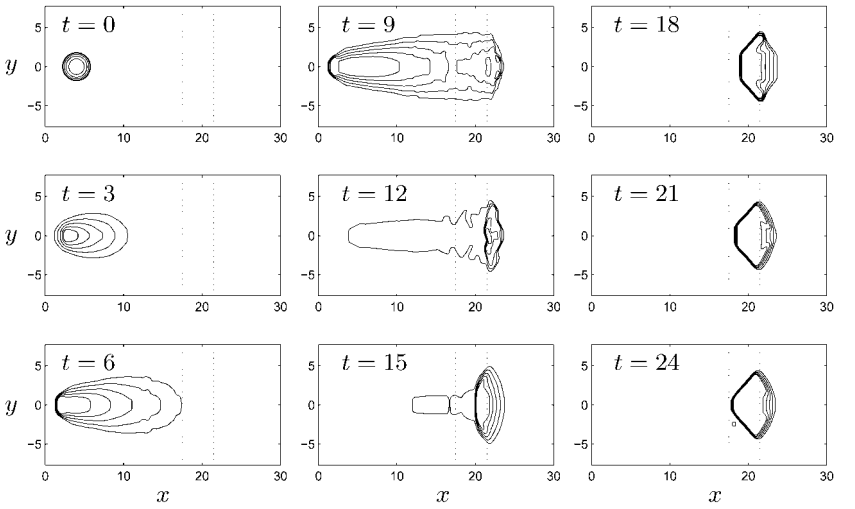

Fig. 9.5. Thickness contours of the avalanche at nine different dimensionless times $t = 0, 3, 6, 9, 12, 15, 18, 21, 24$, obtained with the *NOC scheme* and the *superbee limiter*. The *zone between the two dotted lines* is the transition zone from the inclined plane to the horizontal plane. Because the superbee limiter is the least diffusive or even anti-diffusive, some numerical oscillations still occur and even large gradients are recorded. (From [440].)

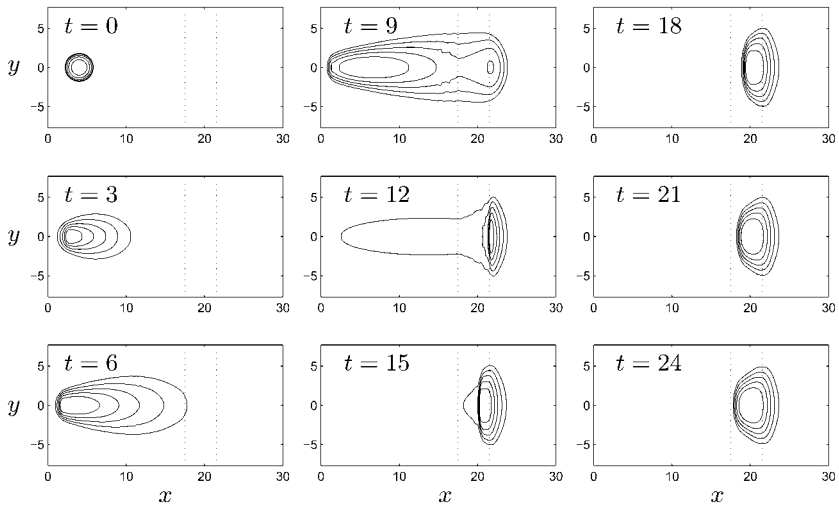

Fig. 9.6. Thickness contours of the avalanche at nine different dimensionless times $t = 0$, 3, 6, 9, 12, 15, 18, 21, 24, obtained with the *NOC scheme* and the *Woodward limiter*. The *zone between the two dotted lines* is the transition zone from the inclined plane to the horizontal plane. With this TVD limiter satisfactory numerical results can be achieved, although some small oscillations still exist. (From [440].)

Fig. 9.5 for $t = 18 - 24$ has a steepened border in comparison with the results in Figs. 9.6–9.8, obtained with other high-resolution schemes.

The NOC schemes with the Woodward TVD limiter (Fig. 9.6), the ENO cell reconstruction (Fig. 9.7) or the minmod TVD limiter (Fig. 9.8) show fairly similar results, where few numerical oscillations occur and simultaneously numerical dissipation is negligibly small. However, we recommend application of the NOC scheme with the minmod TVD limiter to simulate the granular avalanche flow described by the extended SAVAGE–HUTTER theory, because in some other test examples, e.g., with a larger inclined angle of the chute plane, some small numerical oscillations are also visible in the solutions obtained with the Woodward limiter and the ENO cell reconstruction.

From Figs. 9.6–9.8 it can be seen that, once the cap is opened, the avalanche accelerates downslope due to gravity and extends until the front reaches the horizontal run-out zone. The front comes (almost) to rest when $t > 9$, but part of the tail accelerates further down, and the avalanche body contracts. Once the velocity changes from supercritical to subcritical, a shock wave develops around the end of the transition zone at $x = 21.5$ for $t = 12$. With the approaching mass from the tail, the shock wave propagates backwards from $t = 12$ to $t = 24$. At $t = 24$, the shock front reaches almost the beginning of the transition zone at $x = 17.5$, and the final deposition of the granular mass is nearly attained.

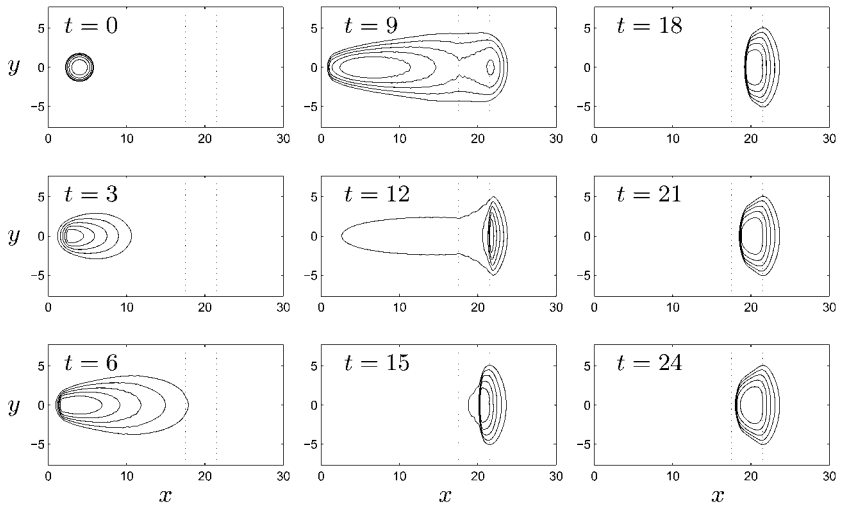

Fig. 9.7. Thickness contours of the avalanche at nine different dimensionless times $t = 0$, 3, 6, 9, 12, 15, 18, 21, 24, obtained with the *NOC scheme* and the *third-order ENO cell reconstruction*. The *zone between the two dotted lines* is the transition zone from the inclined plane to the horizontal plane. This scheme can provide fairly satisfactory numerical results. (From [440].)

Figure 9.9 illustrates the depth profiles of the granular flow along the central line $y = 0$ simulated by the NOC scheme with the minmod limiter for the same times as in Fig. 9.8. The granular mass released from the cap extends on the inclined plane until the front reaches the horizontal run-out zone. Here, the basal friction is sufficiently large to bring the front of the granular flow to rest. At this stage, a *surge wave* is created at $t = 12$, which moves a short distance upward, as can clearly be seen by comparing the humps for $t = 12$ to $t = 24$. A more direct overview of the granular avalanche flow can be obtained from the evolution of the three-dimensional avalanche geometries displayed in Fig. 9.10.

Choice of Numerical Scheme We have seen that the NOC scheme with the minmod TVD limiter demonstrates the best numerical performance for simulating avalanche dynamics among all other limiters and the ENO cell reconstructions. For this reason, in the remainder of this book, we will implement only the NOC scheme together with the minmod limiter for the numerical simulations of avalanches over different bed topographies and parameter values.

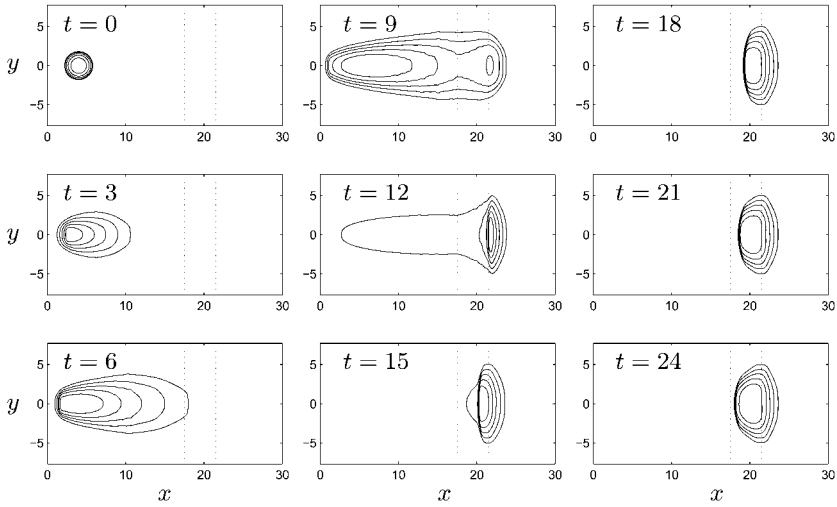

Fig. 9.8. Same as in Fig. 9.7 but with the *NOC scheme* and the *minmod limiter*. The scheme is demonstrated to be the most favourable in treating these hyperbolic avalanche equations, including the cases with various other parameters. (From [440].)

9.2 Effects of Topographic Variations

9.2.1 Constant Cross-Slope Curvature

In order to further test the model equations (4.89)–(4.91) of Chap. 4, we consider an idealised mountain subregion in which the non-twisted talweg is defined by the slope function

$$\tilde{\zeta}(x) = \begin{cases} \tilde{\zeta}_0, & 0 \le x \le x_l, \\ \tilde{\zeta}_0\left(\dfrac{x_r - x}{x_r - x_l}\right), & x_l \le x \le x_r, \\ 0^\circ, & x \ge x_r, \end{cases} \tag{9.2}$$

where $\tilde{\zeta}_0 = 45^\circ$ is the straight upper part of the talweg that merges into a horizontal run-out plane as shown in Fig. 4.13a, and $x_l = 11.5$ and $x_r = 14.5$ are the (non-dimensional) initial and final points of the continuous transition. The azimuthal angle θ (which includes the cross-slope curvature) is confined to the interval $[-14.32^\circ, 14.32^\circ]$ and the non-dimensional distance of the master curve to the talweg is set equal to $z_T = 20$, corresponding to $y \in [-5, 5]$, see Fig. 4.13b. A hemispherical cap with non-dimensional radius $R_0 = 0.98$ holding the granular material in it is placed at $(x_0, y_0) = (3.0, 0.0)$ of the chute and suddenly released. The values of the material parameters are chosen as $\delta = 33^\circ$ and $\phi = 43^\circ$, which correspond to *marble chips* of mean diameter 2–4 mm.

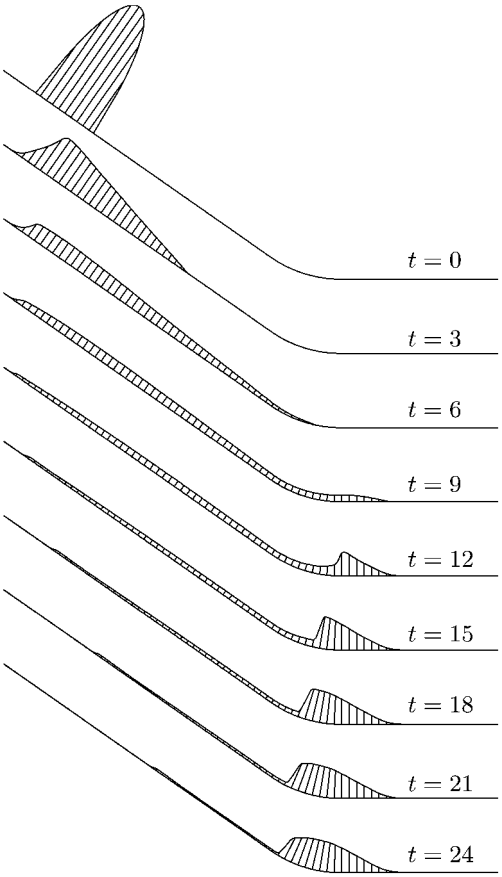

Fig. 9.9. Avalanche thickness along the central line of the flow, $y = 0$, at different dimensionless times obtained with the *NOC scheme* and the *minmod limiter*. Since the deposited height of the avalanche is very small compared to the length, the height is four times exaggerated. As the front reaches the run-out zone and comes to rest, the rear part of the avalanche accelerates further and the avalanche body contracts. When supercritical flow merges into a region of subcritical flow, a shock wave develops, which moves upward. Here we do not explicitly see the volume preserving of the material since we have plotted only the central section of the avalanche in the vertical plane that contains the talweg. (From [440].)

Figure 9.11 depicts the thickness contours of the avalanching body, as computed by PUDASAINI et al. [340], at ten non-dimensional time steps in a *doubly curved channel* in the downhill direction (see Fig. 4.13). The bulk body commences to slide and deform continuously along the chute as long as the bed friction resistive force is smaller than the downslope component of gravity. The first four panels in this figure clearly show that, once the cap is opened, the avalanche accelerates and spreads rapidly in the downslope direction due

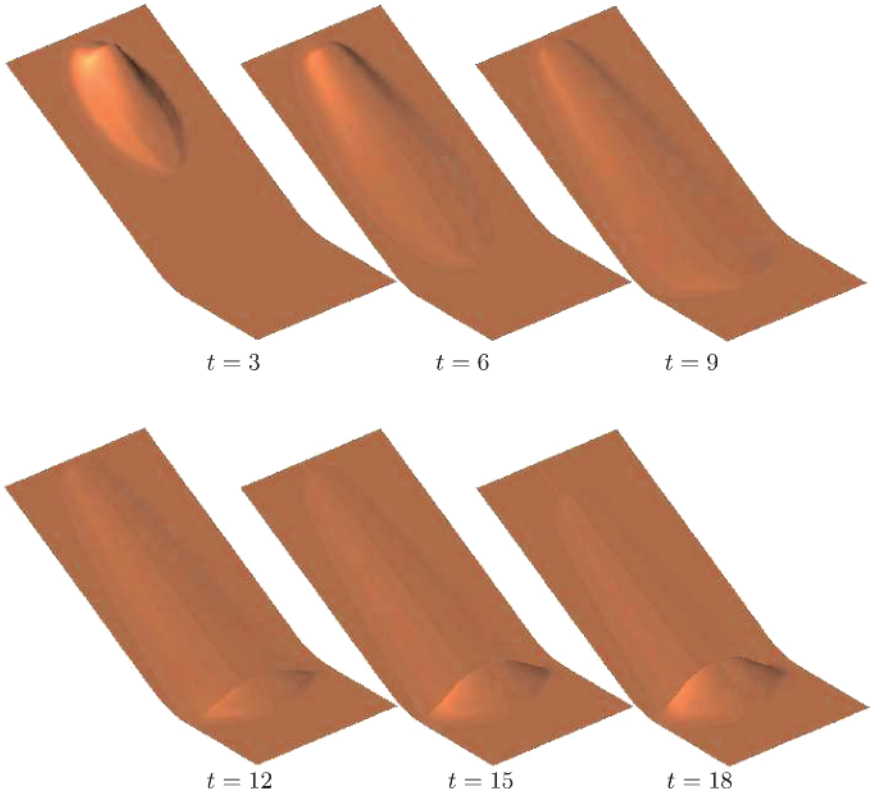

Fig. 9.10. Three-dimensional geometries of the avalanche at six different dimensionless times $t = 3, 6, 9, 12, 15, 18$, obtained with the *NOC scheme* and the *minmod limiter* as in Figs. 9.8 and 9.9. (From [440].)

to the channelling effect in the cross-slope direction. The avalanche decelerates rapidly as soon as it enters the run-out zone, from the fourth panel for $t > 4.5$. Due to the continued mass flux from the tail, its front is then able to spread out laterally as seen in panels 5–7 for $t = 6.0, 7.5, 9.0$.

After $t = 7.5$, due to the channelling effect of the cross-section, the tail of the avalanche reduces in width, but the head expands in width in the run-out zone. The curvature of the transition zone induces a shock associated with the height of the avalanche that is moving upstream from time $t = 9.0$ onward. The avalanche comes to rest after $t = 13.5$. The first three panels of Fig. 9.11 indicate that due to the dilatation, the granular body is extending in all directions, although mainly in the downhill direction. Although the front is descending rapidly, the tail moves upward in the beginning because of the earth pressure. At $t = 4.5$, the front reaches the transition zone, while the tail also starts to move downward. At $t = 6.0$, the front part of the body has fully

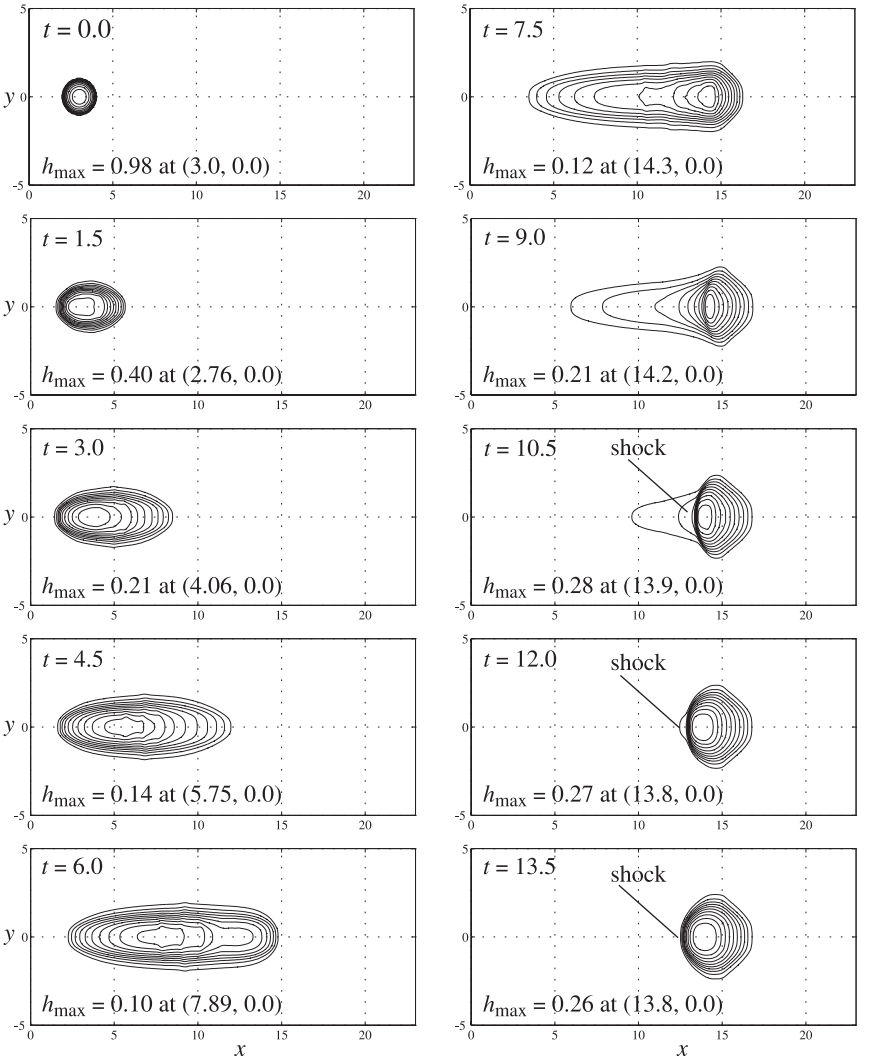

Fig. 9.11. A sequence of numerical snapshots of the avalanching motion of a granular material with internal and basal friction angles $\phi = 43^\circ$ and $\delta = 33^\circ$, for different time slices. Contours of equal thickness are plotted at ten time intervals using "unrolled" projected non-dimensional curvilinear coordinates (x, y). The transition zone lies between $x = 11.5$ to $x = 14.5$. The 45° inclined section lies on the left and the horizontal part lies on the right of each panel. The talweg of the valley is indicated by the line $y = 0$. The panels thus demonstrate the deformation and settling of avalanches in doubly curved (both in the downslope and cross-slope directions) channels. (From [340].)

reached the transition zone. Therefore, the mass at the front is contracting due to the effect of the passive earth pressure coefficient, but the mass in the tail is still extending. At $t = 7.5$, deposition of the mass starts near the vicinity of the lower end of the transition zone. Owing to the effect of the curvature, the flowing body starts contracting longitudinally but extending laterally. After $t = 9.0$, a steep surface (height) gradient starts to develop on the tail side of the avalanche. *Although the front of the body is almost at standstill, the mass from the tail is continuously flowing down and is deposited on the tail side of the body. This is the main mechanism for the development of the shock front moving upstream.* The physical explanation for this is that from the front there is a strong resistive force from the bed that prevents the body from sliding further. Thus, mass arriving from the upper part of the channel must be deposited at the back of the body. Consequently, the stopped body must extend upward. The last three panels show the continuous development of the upward moving shock. At the same time, there is almost no motion at the front. Due to the partial lateral confinement, the extension of the body in the cross-slope direction is almost negligible.

As determined by PUDASAINI et al. [340], Fig. 9.12 depicts the channelling effects for different channel widths. Parameter values are as in Fig. 9.11. The contours represent the final deposits of the avalanches for four different channel curvatures. As the value of the parameter θ (azimuthal angle) increases, the lateral curvature increases and the width of the channel decreases. The values of $\theta = 0°$, $15°$, $25°$ and $45°$ correspond to the non-dimensional distances (representing the radius of curvature of the lateral bed profile) ∞, 19.1, 11.46 and 6.4, respectively, while the range of y is kept fixed as before, i.e., $y \in [-5, 5]$. Consequently, with the increase of θ, the granular materials tend to accumulate around and along the talweg of the channel, the geometries of the deposited piles change, and both the pile heights and the run-out distances increase considerably. This effect is directly associated with the lateral component of the gravitational acceleration (g_y), which depends on the lateral curvature (this was always zero in previous extensions of the theory).

Dispersion of the Masses In order to analyse the dispersion of the avalanching mass quantitatively, we consider the total volume of the granular body ($V = \int h(x, y)\, dx\, dy$) and define the centre of mass as follows:

$$(\overline{x},\ \overline{y}) = \left(\frac{1}{V} \int x\, h(x, y)\, dx\, dy,\ \underbrace{\frac{1}{V} \int y\, h(x, y)\, dx\, dy}_{= 0 \text{ by symmetry}} \right). \tag{9.3}$$

The dispersion of the deformable granular body can then be computed by the following standard deviation formula (where "dis" stands for dispersion):

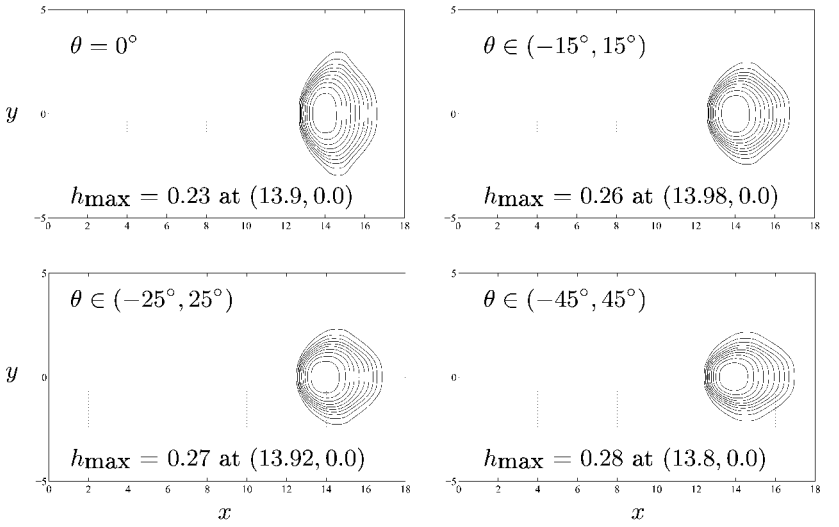

Fig. 9.12. *Channelling effects*: Parameter values are as in Fig. 9.11. The contours represent the final deposits of identical avalanche masses for four different channel widths corresponding to the parameter θ. As the value of the parameter θ (*azimuthal angle*) increases, the width of the channel decreases. Consequently, the granular materials tend to accumulate around and along the talweg of the channel, the geometries of the deposited piles are changed, and both the pile heights and the run-out distances increase. (From [340].)

$$(x_{\mathrm{dis}},\, y_{\mathrm{dis}}) = \left(\sqrt{\frac{1}{V}\int (x-\overline{x})^2\, h(x,y)\, dx\, dy},\ \sqrt{\frac{1}{V}\int (y-\overline{y})^2\, h(x,y)\, dx\, dy} \right). \tag{9.4}$$

Tables 9.1 and 9.2 represent data sets for the centre of mass and the dispersion of the sliding and deforming granular body for different non-dimensional time steps and azimuthal angles. Other parameter values are as in Fig. 9.12. Analysing these tables we draw the following conclusions: (*i*) The centre of mass is almost independent of the azimuthal angle θ at all times. The dispersion along the downhill direction first increases then decreases but the dispersion in the crosshill direction increases monotonically for all values of θ. (*ii*) In general, the dispersion along the downhill direction increases as θ increases, but this relation is reversed for the dispersion in the cross-slope direction, as expected. (*iii*) Since the channel is flatter around the talweg and has larger cross-slope gradients at the outer rims along the downhill direction than elsewhere, dispersion relations in both directions are more pronounced in the two panels in the first row than in the two panels in the last row of Fig. 9.12; this is exactly what is quantitatively shown in Table 9.2.

Table 9.1. The centre of mass of the avalanching body at different non-dimensional time steps t and azimuthal angles θ. The first and the second coordinates in each column represent the centre of mass in the x- and y-directions, respectively, as predicted by (9.3).

	$\theta = 0^\circ$	$\theta \in (-15^\circ, 15^\circ)$	$\theta \in (-25^\circ, 25^\circ)$	$\theta \in (-45^\circ, 45^\circ)$
$t = 3.0$	(4.7, 0.0)	(4.7, 0.0)	(4.6, 0.0)	(4.7, 0.0)
$t = 6.0$	(8.8, 0.0)	(8.7, 0.0)	(8.7, 0.0)	(8.8, 0.0)
$t = 9.0$	(13.0, 0.0)	(13.0, 0.0)	(12.9, 0.0)	(13.0, 0.0)
$t = 12.0$	(14.3, 0.0)	(14.3, 0.0)	(14.3, 0.0)	(14.3, 0.0)
$t = 13.5$	(14.4, 0.0)	(14.4, 0.0)	(14.4, 0.0)	(14.4, 0.0)

Table 9.2. Same as in Table 9.1 but for the dispersion as predicted by (9.4). (From [340].)

	$\theta = 0^\circ$	$\theta \in (-15^\circ, 15^\circ)$	$\theta \in (-25^\circ, 25^\circ)$	$\theta \in (-45^\circ, 45^\circ)$
$t = 3.0$	(1.60, 0.75)	(1.60, 0.72)	(1.59, 0.70)	(1.63, 0.67)
$t = 6.0$	(2.99, 0.95)	(3.00, 0.81)	(2.98, 0.76)	(3.04, 0.69)
$t = 9.0$	(2.53, 1.09)	(2.55, 0.89)	(2.57, 0.82)	(2.59, 0.73)
$t = 12.0$	(0.97, 1.18)	(1.01, 0.97)	(1.04, 0.91)	(1.10, 0.84)
$t = 13.5$	(0.86, 1.20)	(0.91, 1.00)	(0.95, 0.95)	(1.02, 0.89)

9.2.2 Variable Cross-Slope Curvature

Until now, only numerical results of an avalanche of finite granular mass sliding down an inclined surface have been demonstrated, where there exists no variation of topography in the cross-slope direction. The cross-sectional basal surface was circular. In nature, avalanches often occur in a valley; for such cases lateral variations of the topography should be considered. In the previous section, we considered the case where the bed topography had a constant cross-slope curvature forming a uniform cylindrical channel. In this section, we deal with a more general case where the bed topography contains variable curvature also in the cross-slope direction. The cross-slope curvature can be made variable by defining the parameter θ as a function of x and y. Let us consider a bed topography of which upper part is a cylindrical channel merging continuously into an open flat run-out zone according to

$$\theta(x,y) = \begin{cases} y/z_T, & 0 \le x \le x_l, \\ (y/z_T) f(x), & x_l \le x \le x_r, \\ 0^\circ, & x \ge x_r. \end{cases} \tag{9.5}$$

Here, z_T is the distance between the master curve and the talweg in the upper inclined part of the channel (hence a constant), and $f(x) = \sin\tilde{\zeta}(x)/\sin\tilde{\zeta}_0$, where $\tilde{\zeta}_0$ is the inclination angle of the upper part of the channel. This implies that $f = 1$ at x_l and $f = 0$ at x_r. Thus, the continuous transition of the parameter θ from its higher value (y/z_T) in the upper part to the zero value in the open run-out zone constitutes a *three-dimensional channel* that has variable curvature both in the longitudinal as well as the lateral direction.

For the numerical simulation we choose the parameter values as follows: $x_l = 15$ and $x_r = 20$ are the (non-dimensional) initial and final points of the continuous transition. The azimuthal angle θ (which includes the cross-slope curvature) in the upper part of the channel is confined to the interval $[-45^\circ, 45^\circ]$ and the non-dimensional distance is set equal to $z_T = 7.6$, corresponding to $y \in [-6, 6]$, see Fig. 4.13b. A hemispherical cap with non-dimensional radius $R_0 = 1.75$ holding the granular material in it is placed at $(x_0, y_0) = (5.0, 0.0)$ of the chute and suddenly released. The values of the material parameters are chosen as $\delta = 27^\circ$ and $\phi = 37^\circ$, which correspond to *Vestolen*, a sort of plastic particle of lens-like shape and 4 mm diameter, on *drawing paper*. The inclination angle of the upper part of the channel relative to the horizontal is $\tilde{\zeta} = 50^\circ$.

It is interesting to make a comparative study of the avalanching motion among the three channels: (*i*) a cylindrical channel merging into the run-out zone maintaining constant cross-slope curvature (i.e., constant channel width), (*ii*) a channel with continuously varying cross-slope curvature given by (9.5) so as to form an open divergent channel continuously transitting to the horizontal run-out area, and (*iii*) a rolled surface (see Figs. 3.8, 4.1 and 9.1) curved downslope as before but entirely flat laterally. As computed by Pudasaini [334], the dynamics of the avalanche in the channel with a constant cross-slope curvature is presented in Fig. 9.13. Since there is a strong lateral curvature forming a narrow channel, the granular material is not able to spread considerably in the cross-slope direction. However, such a lateral spread is pronounced a bit just after the release (non-dimensional time, $t = 1.5, 3$) and just before the deposit (non-dimensional time, $t = 10.5, 12, 15$, due to the effect of the downhill curvature) of the bulk material. Therefore, the dynamics is mainly dominated by the extension and contraction of the avalanching and deforming body parallel to the direction of the talweg of the channel.

By contrast, the dynamics is completely different for the flow in the channel with variable cross-slope curvature. Results are presented in Fig. 9.14.

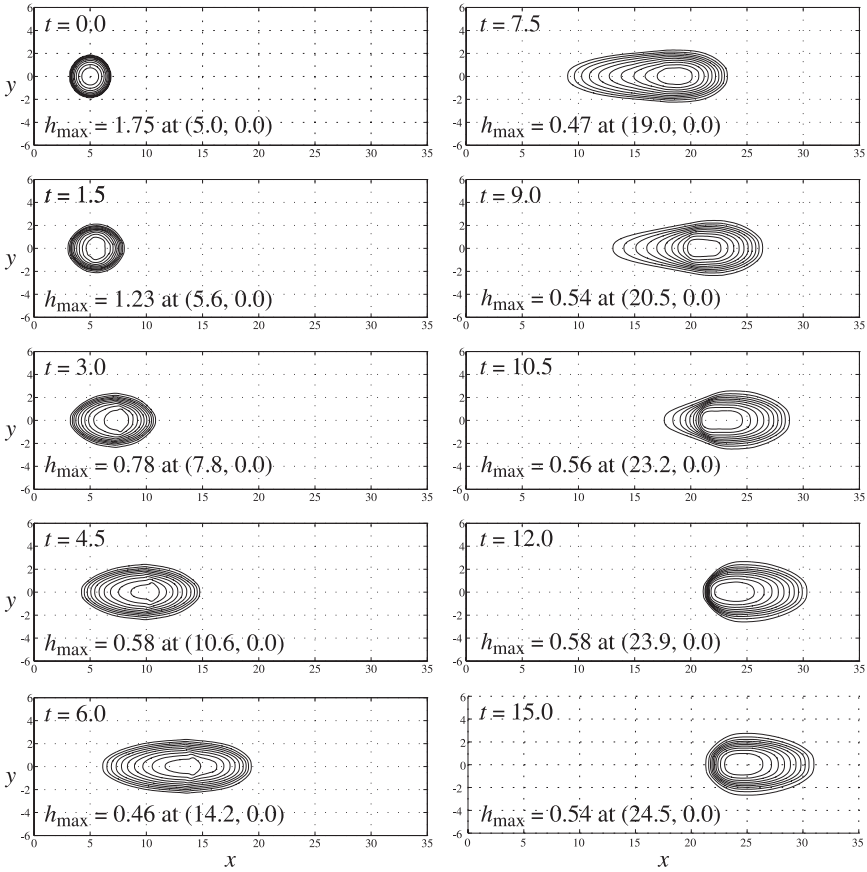

Fig. 9.13. A sequence of numerical snapshots of an avalanching motion of a granular material with internal and basal friction angles $\phi = 37^\circ$ and $\delta = 27^\circ$, for different time points. The contours of equal thickness are plotted at ten time intervals using "unrolled" projected non-dimensional curvilinear coordinates (x, y). The transition zone lies between $x = 15$ to $x = 20$. The 50° inclined section lies on the left and the horizontal part lies on the right of each panel. The talweg of the valley is indicated by the line $y = 0$. The panels thus demonstrate the deformation and settling of avalanches in doubly curved (both in the downslope and cross-slope directions) channels. (From [334].)

The channel width remains constant in the range $x \in [0, 15]$. It is flattened continuously in the range $x \in [15, 20]$ and, afterward, the section of the bed topography is a part of the horizontal plane. Before $t = 6$ the contours representing the avalanche geometry are the same as in Fig. 9.13. The results are completely different after time $t = 7.5$. Since the channel is continuously open and ultimately, in the horizontal run-out area, completely flattened in the lateral direction, the avalanching body spreads rapidly in the lateral di-

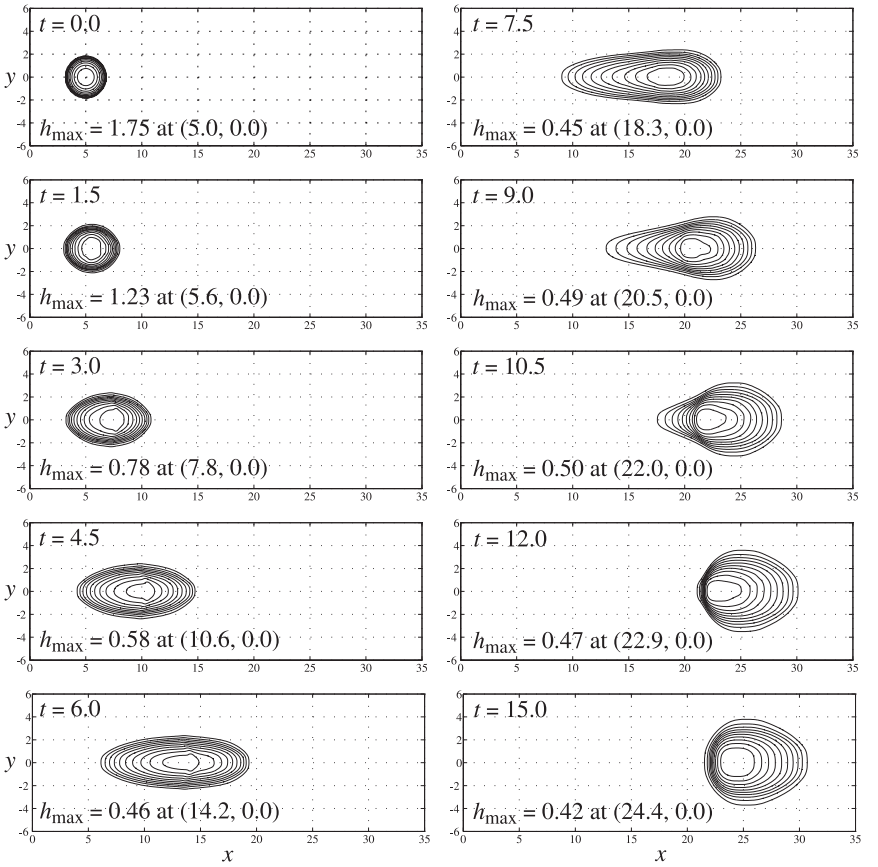

Fig. 9.14. Same as in Fig. 9.13 but with variable lateral curvature given by (9.5) so that the upper cylindrical channel merges continuously into an open fan-like horizontal run-out zone. (From [334].)

rection. However, there is not such a big difference in the dispersion in the longitudinal direction.

Similarly, Fig. 9.15 records the motion of an avalanche over a bed topography curved downslope as before but completely flat in the cross-slope direction, i.e., with zero lateral curvature over the entire flow domain. Since the channel is unconfined in the lateral direction, the avalanching mass is continuously extending in the lateral direction until it comes to rest. Also, the body is extending in the downhill direction until it reaches the continuous transition zone. Afterwards, as in the other cases, the body starts decelerating and comes to rest. A more detailed comparison of the final deposits is presented in Fig. 9.16, see PUDASAINI [334]. It shows the final deposits at time $t = 15$ of

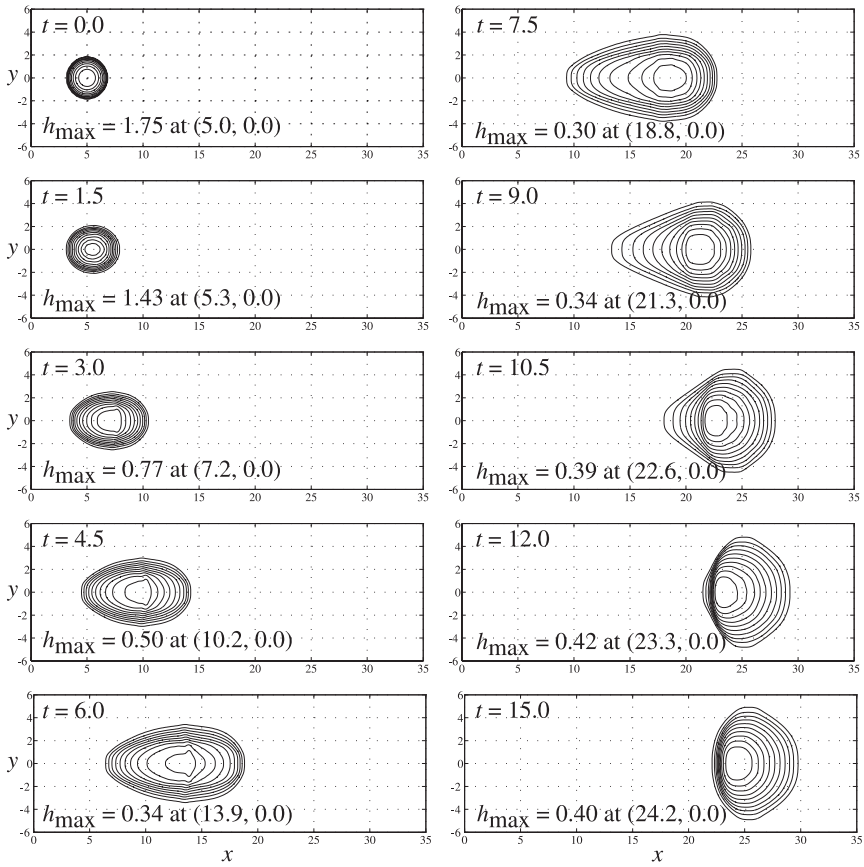

Fig. 9.15. Same as in Fig. 9.14 but with zero lateral curvature. (From [334].)

Figs. 9.13, 9.14–Fig. 9.15. These comparisons thus demonstrate and highlight the effects of the bed topographies on the final depositions of the avalanches.

9.3 Superimposed Basal Topography

Until now, we used only the downslope and cross-slope coordinates to form a three-dimensionally varying basal topography that is actually just a reference topography. In real applications we need to include detailed local information about the elevation of the mountain subregion, for instance through GIS digital elevation data. This is usually done by superimposing a basal topography over a reference surface that may be curved or flat both in the lateral and longitudinal directions.

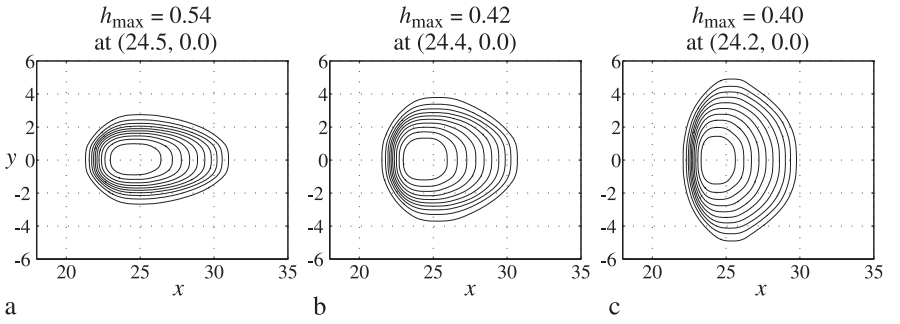

Fig. 9.16. Effects of the topographic variation of an avalanche track in the deposits of avalanches. Comparison of the final deposits of an avalanche for a constant cross-slope curvature, $\theta \in (-45°, 45°)$: (**a**) corresponding to Fig. 9.13, a variably flattened bed topography given by (9.5); (**b**) corresponding to Fig. 9.14 and a completely flat bed topography in the cross-slope direction; (**c**) corresponding to Fig. 9.15. (From [334]).

Below we consider a basal topography varying in the cross-slope direction, which is defined by its elevation $b(x, y)$ above a reference surface without lateral variation:

$$b(x,y) = b_0 \left(1 - \cos\left(\frac{\pi}{4}\frac{y}{(B/2)}\right)\right) \sin\tilde{\zeta}(x), \quad \text{for } y \in [-7, 7]. \tag{9.6}$$

Here, $B = 14$ is the width of the computational domain, and multiplication by $\sin\tilde{\zeta}$ ensures that this elevation is smoothly transited from the inclined reference surface (with its maximum) to zero value on the horizontal run-out plane where the lateral elevation ceases, as in Fig. 3.9. The basal topography over which the avalanche flows has a channelling effect on the inclined section of the chute. Two values, $b_0 = 2$ and $b_0 = 10$, are chosen corresponding to maximum elevations at the lateral boundary of the computational domain on the inclination of the basal surface $b^{\max} = 0.34$ and $b^{\max} = 1.68$; they indicate mean lateral inclinations of 2.8° and 13.5°, respectively. Other parameter values are taken from Sect. 9.1. Numerical results are depicted in Figs. 9.17 and 9.18. It is surprising that a fairly small lateral curvature can exert obvious influences on avalanche geometries, as we can see by comparing Fig. 9.17 (*left panel*) and Fig. 9.18 (*upper panels*) for $b^{\max} = 0.34$ with Figs. 9.8 and 9.9 for $b^{\max} = 0$, respectively. A comparison of Fig. 9.8 with Fig. 9.18 and Fig. 9.9 with Fig. 9.17 shows that partial confinement of the avalanche in the inclined parabolic-type section of the chute prevents lateral spreading and strongly channelises the flow. With the increase in the lateral confinement, granular materials tend to accumulate around the talweg as a result of the lateral channelling. Consequently, the granular flow becomes thicker and longer along the talweg.

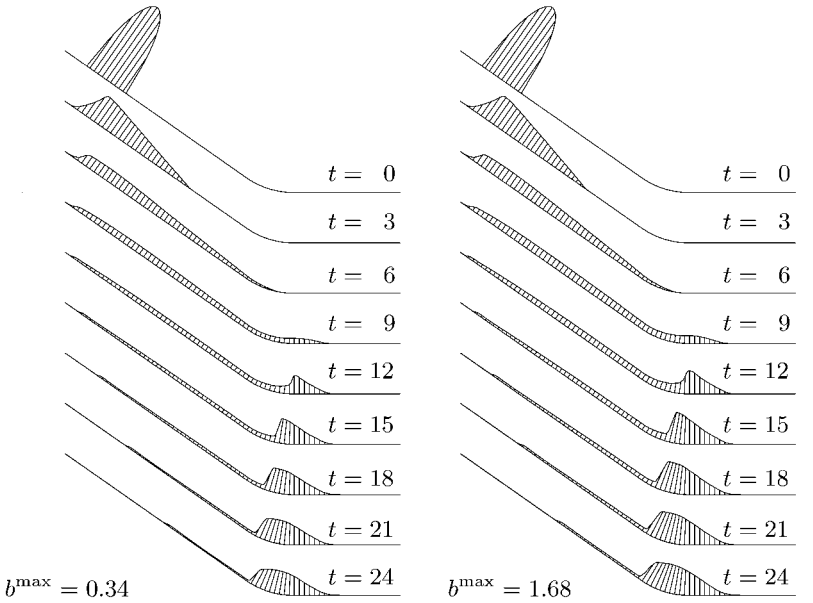

Fig. 9.17. Avalanche thickness along the central line of the flow, $y = 0$. The bottom topography varies in the cross-slope direction according to (9.6) with $b_0 = 2$ (*left panel*), corresponding to a maximum dimensionless elevation $b^{\max} = 0.34$ at the lateral boundaries $y = \pm 7$ within the top inclined region, and $b_0 = 10$ (*right panel*), corresponding to $b^{\max} = 1.68$. (From [440].)

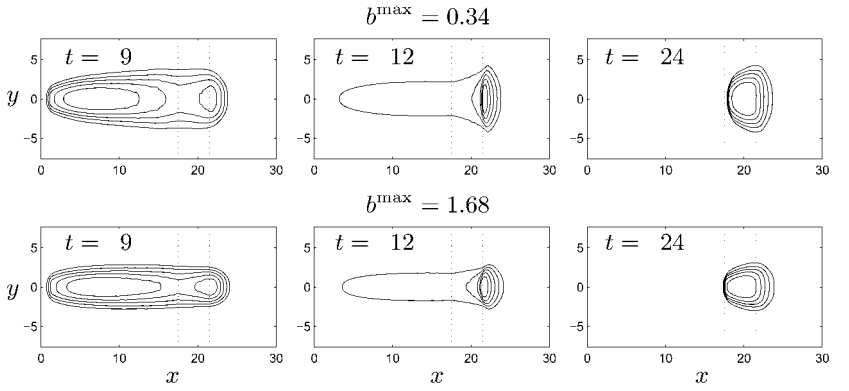

Fig. 9.18. Thickness contours of the avalanche. The bottom topography varies in the cross-slope direction according to (9.6) with $b_0 = 2$ (*upper panels*), corresponding to a maximum dimensionless elevation $b^{\max} = 0.34$ at the lateral boundaries $y = \pm 7$ within the top inclined region, and $b_0 = 10$ (*lower panels*), corresponding to $b^{\max} = 1.68$. (From [440].)

It should be pointed out that (3.33)–(3.38) described in Chap. 3 are only suitable for a shallow topographic elevation $b = b(x, y)$ above the reference surface $z = 0$. This reference surface (or equivalently the downslope inclination angle $\tilde{\zeta}$) changes only as a function of the downslope coordinate x and there is no lateral variation in the cross-slope y-direction. For a large lateral variation of the basal topography the extended model (4.89)–(4.91) for rapid shear flows of dry granular masses, proposed by PUDASAINI and HUTTER [335] is more suitable, because there the talwegs may be arbitrarily curved and twisted and the channel geometry may also be more flexible. The equations as derived by BOUCHUT and WESTDICKENBERG [40] refer to the true topography and are, therefore, better-suited to natural conditions. They, however, do not use MOHR–COULOMB material response but isotropic hydrodynamic pressure and thus present difficulties in adequately modelling motions and depositions.

9.4 Avalanches Sliding Down Curved and Twisted Channels

Our main intention while developing the avalanche theory in Chap. 4 was to be able to include the simultaneous effects of curvature and torsion in the dynamics of an avalanching mass over generally curved and twisted mountain topography. One might expect that there must be not only the effect of curvature but also that of torsion on the entire dynamics and the deposit of an avalanche when it slides down over a curved and twisted terrain. The model equations (4.89)–(4.91), proposed by PUDASAINI and HUTTER [335], should be able to predict the flow of an avalanche over a non-uniformly curved and twisted channel where the cross-slope curvature (or the channel width) may vary. This section is devoted to numerical simulations and their physical explanations and analysis over such topographic configurations. The main target is the analysis of the joint effects of curvature, torsion, cross-slope curvature, i.e., the channel width, and the "centrifugal" force[1] in the dynamics of the avalanching body sliding down more general channels and topographies. This is a *new aspect* in the field of avalanche research, not previously touched upon. On the one hand, the simulations, to be presented in the following, will *disclose the related peculiarities of the physics* and thus uncover fundamental insights into the dynamical behaviour of avalanches; as a consequence, the study will allow us to judge about the applicability of the new model equations presented in Chap. 4. On the other hand, the simulations will open a wide spectrum of possibilities for applied scientists involved in hazard mapping, risk management and public safety. This then will lead to

[1] In the strict sense "centrifugal" is the wrong terminology; what we mean here is the radial acceleration effects operating in a curvilinear coordinate system.

the implementation of the theory to realistic mountain topography together with GIS elevation data of some specific mountain subregions.

9.4.1 Flows Through Uniformly Curved and Twisted Channels

As an example, we consider a helically curved and twisted channel. On the one hand, this is an academic *test example* that can be (relatively) easily verified by laboratory experiments. On the other hand, there are many industrial applications of granular flows in process engineering scenarios where such flow configurations are practically used. For this reason, we consider a *helix* as a talweg, so as to form a helically curved and twisted channel. For a more detailed discussion, see PUDASAINI et al. [334, 341, 342].

Let us consider a circular helix described by

$$\mathbf{R}(\vartheta) = (A\cos\vartheta, A\sin\vartheta, -B\vartheta)\,, \tag{9.7}$$

where ϑ is the azimuthal angle. The arc length x, curvature κ, torsion τ and pitch $\mathcal{P}$ of the helix are given by

$$x = \left(A^2+B^2\right)^{1/2}\vartheta, \quad \kappa = \frac{A}{(A^2+B^2)}, \quad \tau = -\frac{B}{(A^2+B^2)}, \quad \mathcal{P} = 2\pi B, \tag{9.8}$$

respectively. Based on (9.7) a helically curved and twisted channel is formed as in Sect. 9.2.1. The lateral section of the topography is the intersection of a plane perpendicular to the talweg of the channel and the channel itself. Here, this section is a circular arc, but note that when dealing with variable channel widths the curvature of this arc changes with the width of the channel. One expects the flowing granular mass to deviate continuously outward from the central line (i.e., the talweg) of the channel due to the radial acceleration induced by the slope-fitted curvilinear coordinates.

Figure 9.20 displays thickness contours of an avalanche sliding down a helically curved and twisted channel (see Fig. 9.19 (a)) with uniform curvature and torsion given by (9.8) and a constant cross-slope channel width.[2] The parameter values are $A = 300$ and $B = 300$, so that the channel is inclined relative to the horizontal at 45°; the internal and bed friction angles are $\phi = 33°$ and $\delta = 27°$, respectively. The radius of curvature in the cross-slope direction is $z_T = 128$ and $\theta \in (-44.8°, 44.8°)$ corresponding to $y \in [-100, 100]$. The mass held initially by a hemispherical cap centred at $(23, 0)$ with radius 6.5

[2] All figures shown for helical chutes are geometrically distorted. The graphs are vertical projections of the chute and granular heaps whose circular-annular geometry is stretched to become straight. Thus, a segment of the annular ring becomes a rectangle whose top edge is the chute outside and the bottom edge the chute inside boundary. This graphical representation is chosen because it is relatively easy to program.

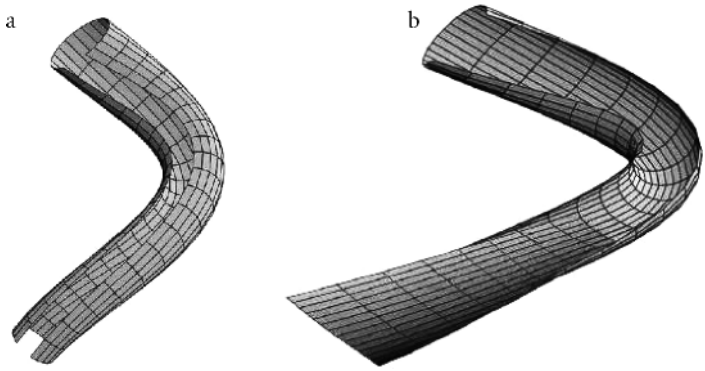

Fig. 9.19. a) A curved and twisted channel with uniform curvature and torsion. **b**) A curved and twisted channel with non-uniform curvature and torsion. The channel merges continuously into the flat horizontal run-out zone. (From [342].)

is suddenly released with zero initial velocity. The contours are plotted at the time steps $15, 18, 21, 24, 27, 28.5$, respectively, only in the vicinity of the flow domain where the granular mass occupies a subregion of it. We also adopt this idea for the plotting of consecutive figures of this section. As time increases, the avalanching mass spreads less laterally, but it rapidly moves outwards from the centreline of the channel in the front much more than in the back. This is because the speed of the front is much larger than that of the tail. Such behaviour of the deforming mass is the joint effect of the curvature, torsion, and the radial acceleration that is modelled in the theory (4.89)–(4.94) through the gravitational acceleration components g_x, g_y, g_z and the net driving force components s_x, s_y, which include the curvature and torsion of the talweg, the bed topography and the cross-slope curvature of the channel. The mass is always extending and accelerating in the downslope direction, because the channel does not merge into transition and run-out zones. In the following, we will deal with cases in which the transition and run-out zones are included in the geometrical part of the model.

9.4.2 Avalanching Flows Through Non-Uniformly Curved and Twisted Channels

In reality, channels may be arbitrarily curved and twisted with variable cross-slope curvature and channel width. In particular, realistic avalanche tracks go from steep to flat regions, where they come to a halt. The geometry must play a crucial role to make the body stand still. The concave curvature of the mountainside increases the bed friction and consequently forces the avalanche to slow down and eventually come to rest. In this section we will present avalanche simulations through curved and twisted channels having run-out zones. However, we will pay particular attention to the different forms in

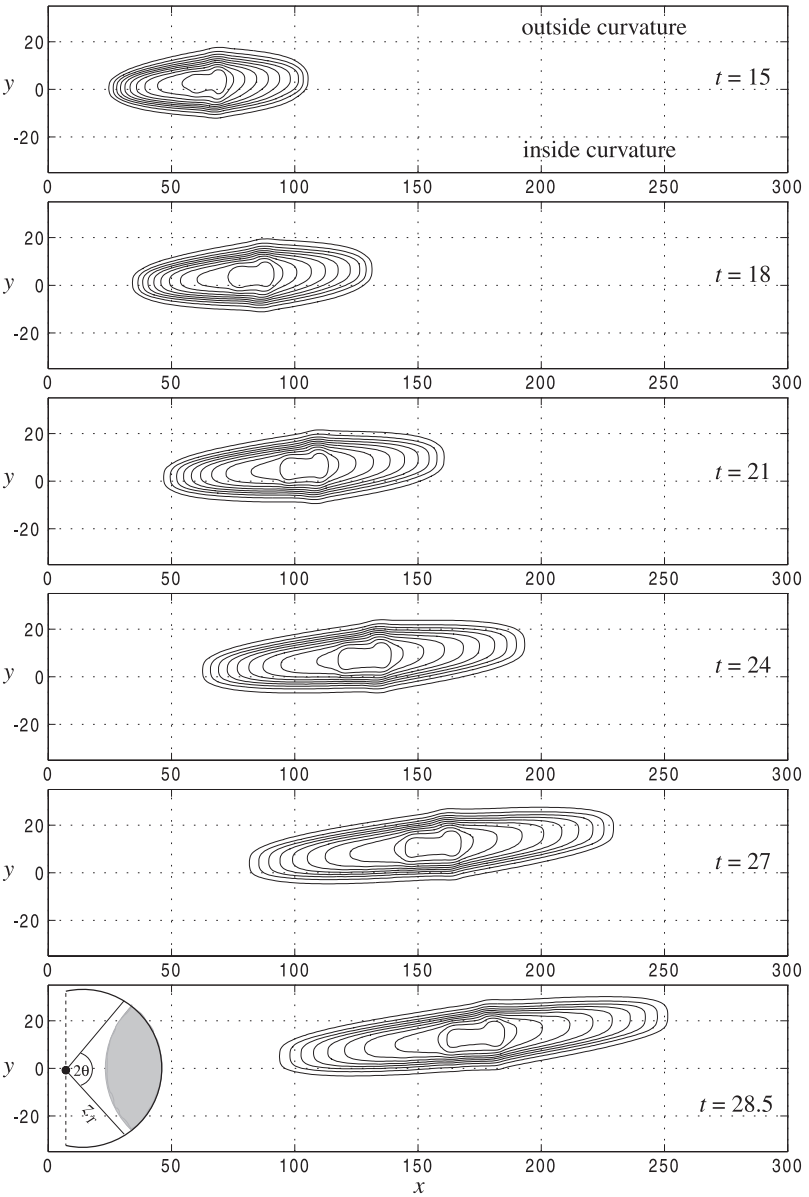
outside curvature
inside curvature
t = 15
t = 18
t = 21
t = 24
t = 27
t = 28.5
y
x
2θ
r_c

Fig. 9.20. Height contours of an avalanching motion in a helically curved and twisted channel with uniform curvature and torsion and a constant circular cross-slope channel width. The plane rectangles are in reality helically curved and twisted in the x-direction and circularly curved in the y-direction. Parameter values: the radii of curvature and torsion are 26, friction angles are $\phi = 33^\circ$ and $\delta = 27^\circ$, respectively. The mass held by a hemispherical cap centred at $(23, 0)$ with radius 6.5 is suddenly released with zero initial velocity. The *inset in the last panel* shows schematically the circular cross-section and a cross-cut of the avalanching mass. (From [341].)

which this transition from the steep inclined helical channel to the horizontal run-out is executed. PUDASAINI et al. [334, 341, 342, 344] have presented a more detailed and extended analysis for flows down such non-trivial channels.

(I) Variable Pitch[3] One geometric model is such that the pitch defined in (9.8) can be modified as

$$B(x) = \begin{cases} B_0, & 0 \le x \le x_l, \\ B_0\left(\dfrac{x_r - x}{x_r - x_l}\right)^2, & x_l \le x \le x_r, \\ 0, & x \ge x_r, \end{cases} \tag{9.9}$$

so that prior to the left end point, x_l, of the continuous transition zone, the chute is exactly the same as that used in the previous part of this section. However, there is a continuous decrease of the pitch from x_l to x_r. Then, for $x \ge x_r$ the pitch is always zero and thus, the subsequent channel forms a channelised circular run-out. Of course, physically this can only be realised if $(x_{\text{final}} - x_r) < 2\pi A$, where x_{final} is the end point of the talweg in the run-out zone.

Avalanche simulations for this case are presented in Fig. 9.21. The chosen parameter values are as in Fig. 9.20, and $B_0 = 300, x_l = 250$ and $x_r = 350$. The different forms in Fig. 9.21 are presented only for the time slices after the avalanche entered the transition zone. Before that the flow is the same as displayed in Fig. 9.20 ($t = 15$ to $t = 28.5$). Since the pitch of the channel continuously decreases for $x > x_l$, from $t = 35$ onward, the granular mass tends to slow down and turn smoothly towards the central line of the channel. Corresponding to the decrease of the pitch, the inclination angle of the chute with the horizontal plane also continuously decreases. Ultimately, the channel merges into a horizontal circularly curved channel, thus forming a gully-type channelised run-out zone. Beyond $t = 28.5$ (Fig. 9.20), the sidewise pressure from the channelised bed topography exceeds the force due to the radial acceleration. This occurs more effectively at the front than in the rear part,

[3] Later we will refer to this as case (I), etc.

because the velocities are now smaller there than in the rear part. This leads to a continuous rotation of the body towards the centre of the channel. This sidewise pressure is so strong that after $t = 60$, the mass crosses the talweg of the channel and heads towards the opposite side. Finally, the body comes to rest at time $t = 70$.

(II) Variable Curvature and Torsion Next, consider a channel where the curvature and torsion are redefined with the new expression for A in (9.8) given as

$$A(x) = \begin{cases} A_0, & 0 \le x \le x_l, \\ A_0 \exp[(x - x_l)^a], & x_l \le x \le x_r, \\ A_0 \exp[(x_r - x_l)^a], & x \ge x_r, \end{cases} \tag{9.10}$$

where a is an exponent that determines the intensity of decrease of the curvature and torsion. For the simulations we have set $a = 1$ and $A_0 = 300$, so that before the transition ($x < x_l$) the channel is the same as in the previous case (Fig. 9.21). Equation (9.10) tells us that the radius of the curvature and the torsion of the channel increase rapidly as the arc-length x becomes larger than x_l. Before this transition point, the channel has uniform radius of curvature, torsion and pitch. This increase forces the channel to quickly merge (approximately) into a lesser and lesser curved and eventually straight, horizontal channel. This horizontal portion of the channel also forms the run-out zone for the avalanche.

The results of the avalanche simulation for this configuration are presented in Fig. 9.22. There are large differences in the avalanche motions in Figs. 9.21 and 9.22, especially in the run-out zones. For the present case, since the radius of curvature and the torsion increase rapidly from $x = x_l$, the avalanche quickly turns back to the central line of the channel and suddenly comes to rest, much earlier and much closer to the transition zone than in Fig. 9.21. It is also interesting to observe that in Fig. 9.22 the deposit between $t = 60$ and $t = 70$ still seems to spread slightly in all directions.

The differences manifest themselves for $t > 35$. In particular, for $t = 40$, the pile in Fig. 9.21 has left the transition zone by about one-third of its mass, whereas it is still almost inside the transition zone in Fig. 9.22. This can be physically understood. The increasing radius of curvature of the channel axis in the transition zone for case (II) reduces the local slope angle of the channel axis much faster than for case (I), so that within the transition zone of case (II) the avalanching mass encounters deposition prone conditions more quickly than in case (I). Comparing the thickness contours for $t \ge 45$ in the two figures shows that the run-out distance of the avalanche mass is greatly affected.

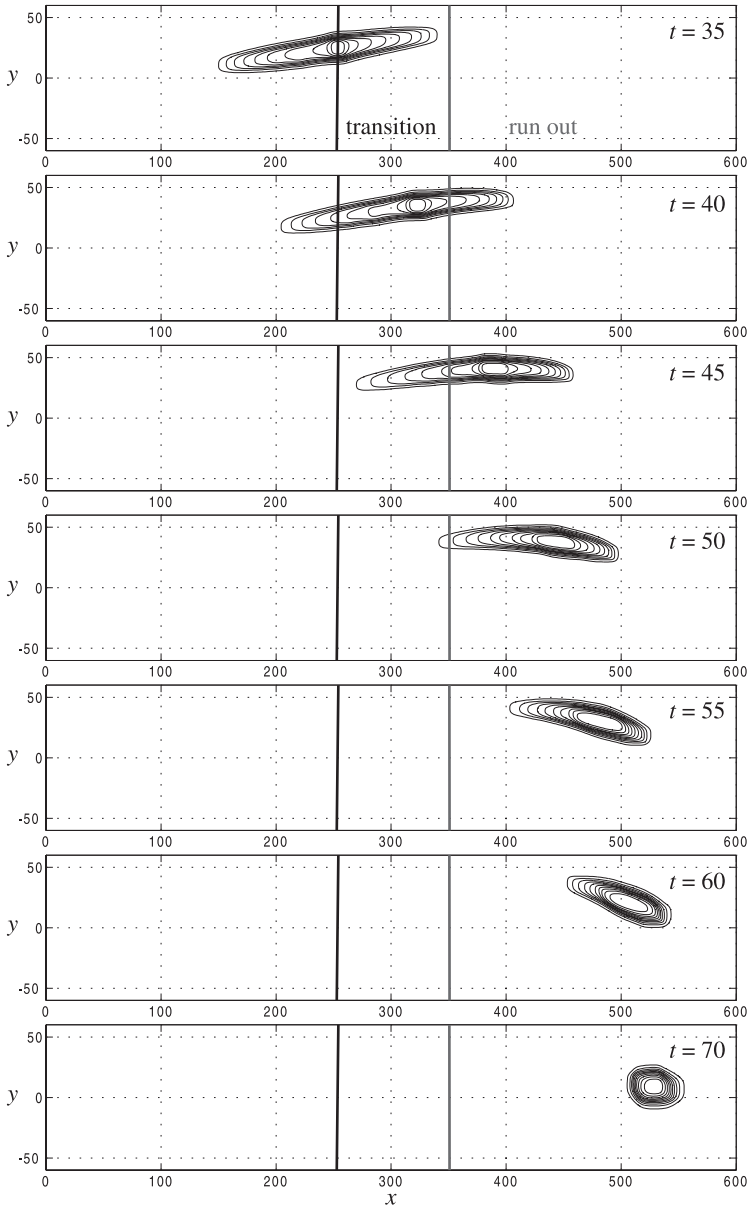

Fig. 9.21. Avalanche motion in a helically curved and twisted channel with variable pitch and a constant cross-slope channel width. Parameter values: the internal and bed friction angles are $\phi = 33^\circ$ and $\delta = 27^\circ$, respectively. The mass, held by a hemispherical cap centred at $(23, 0)$ with radius 6.5, is suddenly released with zero initial velocity. *Contour lines* are plotted at the time steps $35, 40, 45, 50, 55, 60, 70$, respectively. The transition zone lies between $x_l = 250$ and $x_r = 350$. (From [341].)

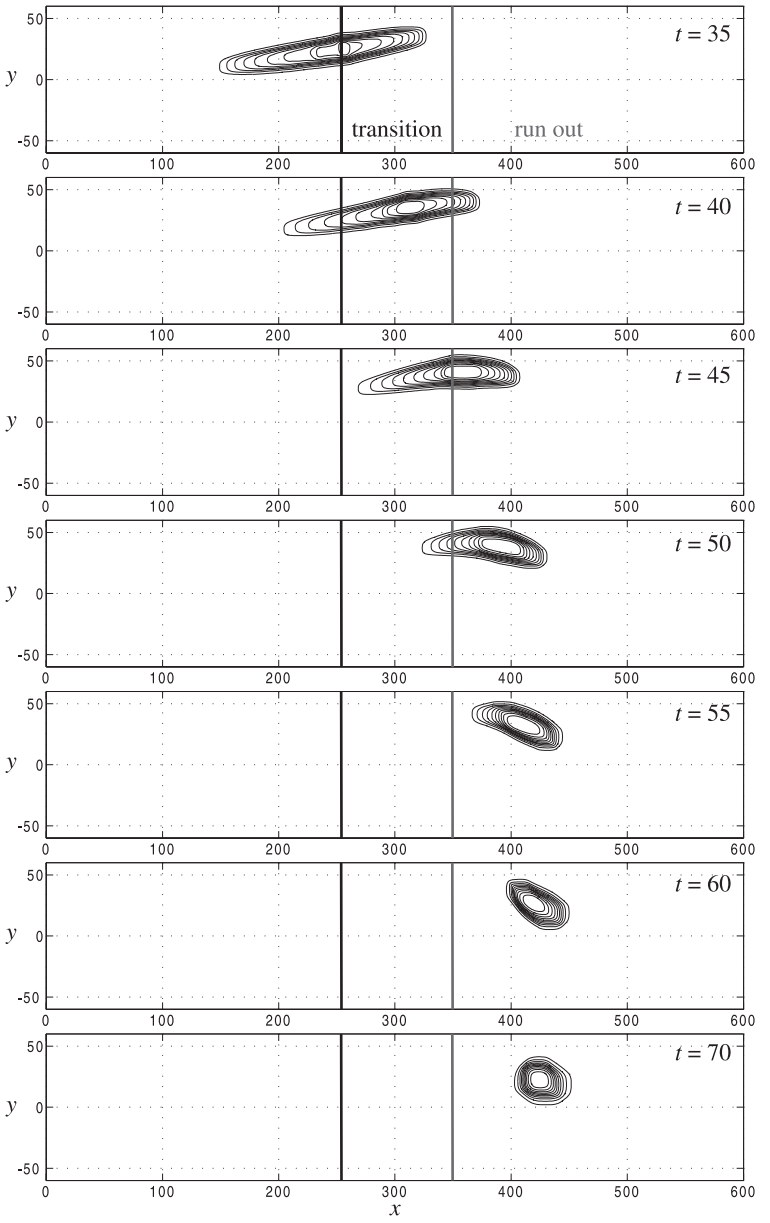

Fig. 9.22. Avalanche motion in a "helically" curved and twisted channel with decreasing curvature and torsion and a constant cross-slope channel width. Parameter values: the radius of curvature and the torsion are given by (9.8) and (9.10), and the internal and bed friction angles are $\phi = 33^\circ$ and $\delta = 27^\circ$, respectively. The *contours* are plotted at the time steps $35, 40, 45, 50, 55, 60, 70$. The transition zone lies between $x_l = 250$ and $x_r = 350$. (From [341].)

(III) Decreasing Pitch and Variable Cross-Slope Curvature Real channels may be diverging or converging (with respect to their channel width or cross-slope curvature) in the downhill direction. Therefore, the avalanche theory must be able to deal with more general channels and natural valleys or gullies with generally varying cross-slope curvature. At this point, we simulate the avalanche motion in a channel where the pitch, B, is defined by (9.9), as for case (I), and the parameter A is constant, but now we vary the channel width starting from the left boundary of the transition zone where the pitch starts to decrease. This can be achieved by defining a channel that merges continuously into an open flat run-out zone according to

$$\theta(x,y) = \begin{cases} y/z_T, & 0 \le x \le x_l, \\ (y/z_T)f(x), & x_l \le x \le x_r, \\ 0^\circ, & x \ge x_r. \end{cases} \tag{9.11}$$

Here, z_T is the distance between the master curve and the talweg in the upper inclined part of the channel (hence a constant), and the function defining the cross-slope curvature is given by

$$f(x) = \left(1 - \frac{(x - x_l)}{(x_r - x_l)}\right)^2. \tag{9.12}$$

Thus, the continuous transition of the parametric function θ from its higher value (y/z_T) in the upper part to its zero value in the open run-out zone constitutes a three-dimensional channel having variable pitch and variable curvature both in the longitudinal and the lateral directions. Figure 9.23 depicts the contours of the avalanche motion from its transition to the open run-out zone, where only the outward half part of the channel is plotted, because in this and in the following cases (for $t \le 35$) the granular masses appear only in this half part of the channel. The graphs describe the deformation of the avalanche disclosing its subtle reaction to the different geometry of the run-out region. Although the pitch is decreasing, after reaching the transition zone, the avalanching body heads radially outwards of the flat run-out zone until it comes to rest close to the outside edge of the chute. The main mechanism for this is that, as soon as the mass enters the run-out zone, the radial acceleration decreases rapidly, but since the chute is flattening out in the cross-slope direction, the decreasing radial acceleration must keep the mass further and further away from the centreline. The direction and the process of the deposition is in conformity with physical intuition and expectation.

(IV) Decreasing Curvature and Torsion, and Variable Cross-Slope Curvature A further interesting geometrical model is a channel whose curvature and torsion decrease from the beginning of the continuous transition zone as described by (9.10). The channel opens and merges continuously into the horizontal plane as described by (9.11) and (9.12), but $B = B_0$ is kept

fixed. This case is more important in geophysical applications because curvature and torsion often decrease as one enters into the horizontal run-out zone of a mountain valley. The avalanching motion from the transition to the run-out zone in such a channel is presented in Fig. 9.24. The principal mechanism for the deformation and the deposition of the mass is analogous to case (III) (i.e., Fig. 9.23), but it stops earlier in time and at a shorter run-out distance than before. Given the results of cases (I) and (II), this was to be expected.

Figures 9.21–9.24 already demonstrate the significant role of the details of the topography, however, this comparison takes a particularly striking form if the final deposits are repeated in one common place. Thus, in Fig. 9.25 the deposits of the four different model cases (I)–(IV) are repeated to emphasise the significant influence of the geometry of the avalanche track on the travel distance, location and distribution of the deposited masses.

9.5 Sensitivity to Phenomenological Parameters

In the above sections the numerical results of the various schemes were compared with respect to different topographies. In this section, we will investigate the effects of the internal and bed friction angles if their values are varied.

Internal and Bed Friction Angles In Figs. 9.26 and 9.27, the sensitivity of the extended SH-equations to the internal angle of friction, ϕ, and the bed friction angle, δ, is examined by depicting the evolutions of the avalanching body at various dimensionless time points in a vertical plane along the central line of the flow. The topographic description and other parameters are as in Sect. 9.1 (see (9.1) and Fig. 9.1). Comparing the numerical results for $\phi = 30^\circ$ (right panels), $\phi = 32^\circ$ (middle panels) and $\phi = 37^\circ$ (left panels) of Fig. 9.26 shows that the avalanche flow is robust against variations of the internal angle of friction. In contrast, the geometries of the avalanching bodies are fairly sensitive to variations of the bed friction angle, as shown by comparing the numerical results for $\delta = 30^\circ$ (left panels), $\delta = 28^\circ$ (middle panels) and $\delta = 23^\circ$ (right panels), respectively, in Fig. 9.27. With a decrease of the bed friction angle, the granular body becomes more fluidised. Consequently, the run-out zone and the run-out distance are larger and the deposit becomes shallower than for deposits obtained with large values of the bed friction angle. From these simulations we infer the following: although the geometry and the shape of the deposit of an avalanche also depend on the internal angle of friction, the fluidity of the sliding mass is very sensitive to a change of the bed friction angle. This means that *one must be very careful when supplying the correct bed friction angle as an input parameter of the model*

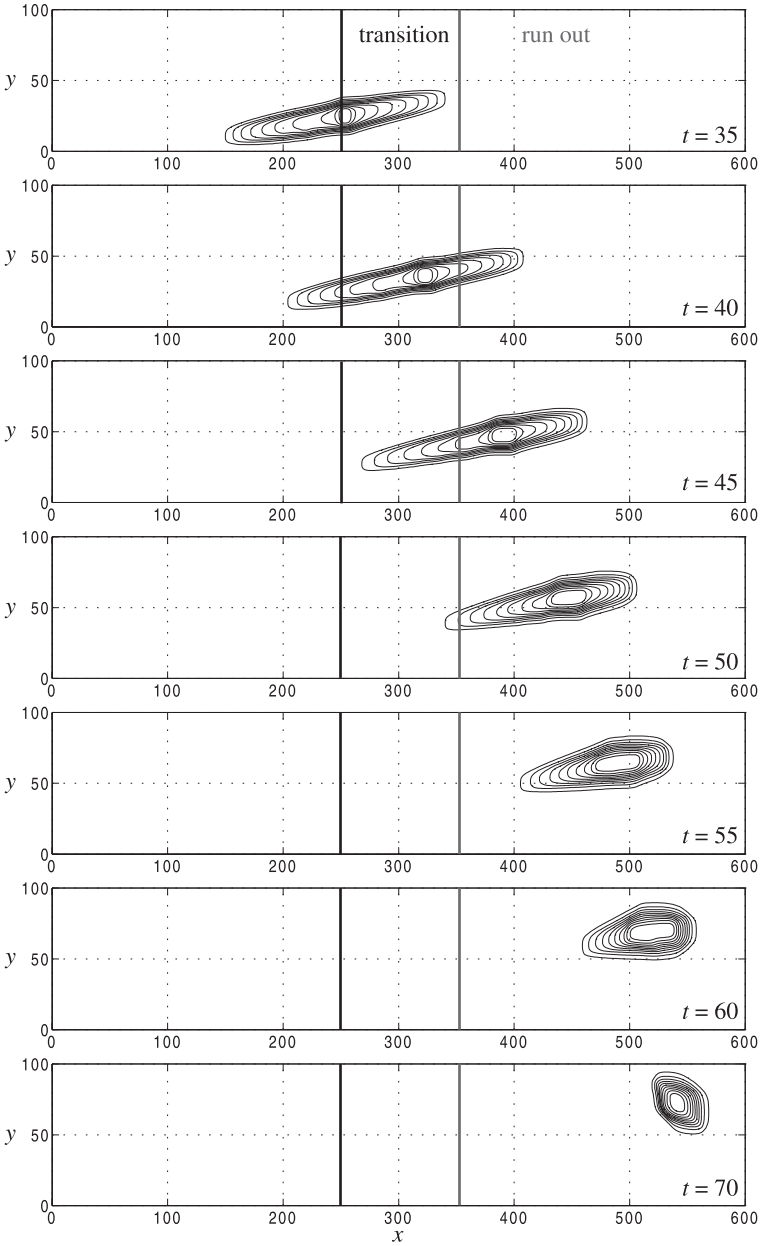

Fig. 9.23. Avalanche motion in a "helically" curved and twisted channel with decreasing pitch and increasing cross-slope channel width. Parameter values: the radius of curvature and the torsion are given by (9.8), (9.9) and (9.11), the internal and bed friction angles are $\phi = 33^\circ$ and $\delta = 27^\circ$, respectively. The contours are plotted for the time steps $35, 40, 45, 50, 55, 60, 70$. The transition zone lies between $x_l = 250$ and $x_r = 350$. (From [341].)

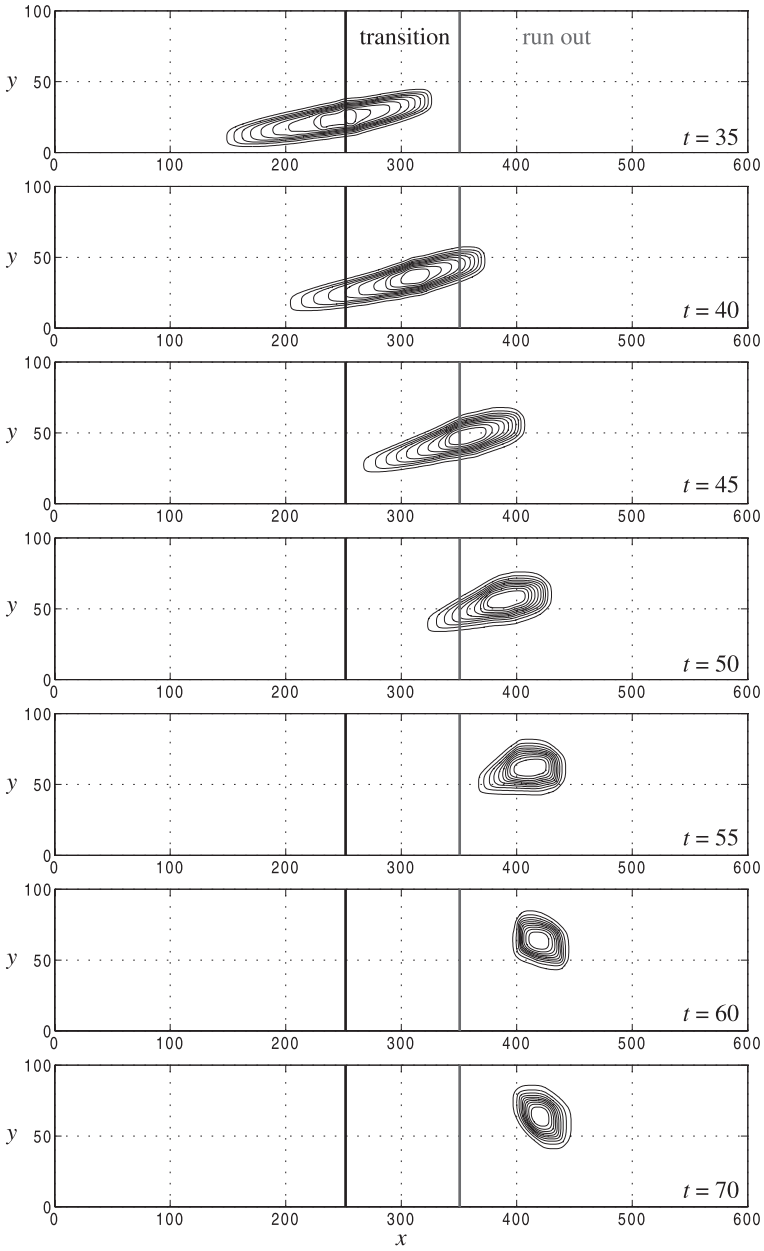

Fig. 9.24. Avalanche motion in a "helically" curved and twisted channel with decreasing curvature and torsion and increasing cross-slope channel width. Parameter values: the radius of curvature and the torsion are given by (9.8), (9.10), and (9.11), the internal and bed friction angles are $\phi = 33^\circ$ and $\delta = 27^\circ$, respectively. The contours are plotted at the time steps $35, 40, 45, 50, 55, 60, 70$, respectively. The transition zone lies between $x_l = 250$ and $x_r = 350$. (From [341].)

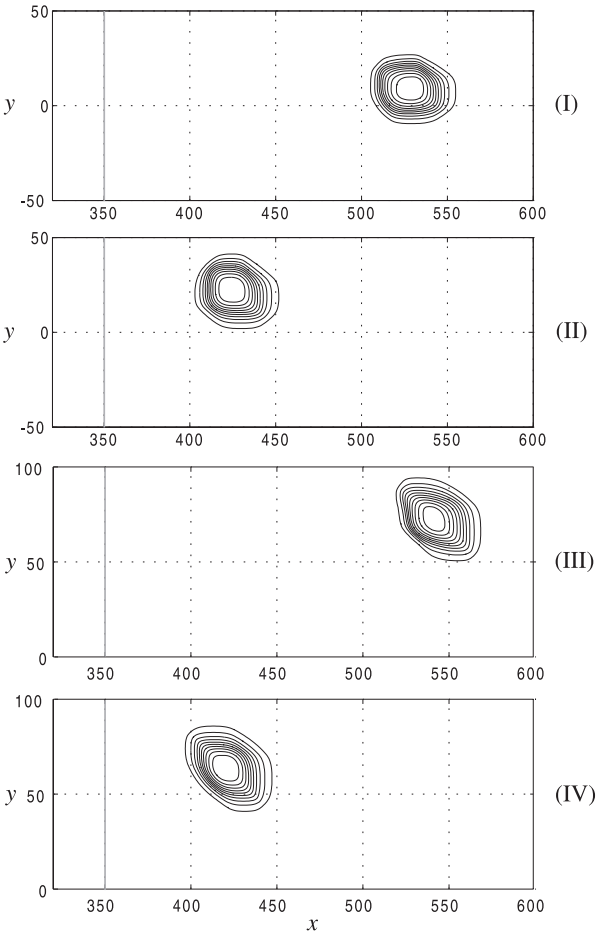

Fig. 9.25. Granular deposits in the run-out zones at non-dimensional time $t = 70$, reproduced from Figs. 9.21 (case (I)), 9.22 (case (II)), 9.23 (case (III)) and 9.24 (case (IV)).

but one can less carefull with the internal angle of friction. Otherwise, the computed results are less reliable in comparison to reality.

9.6 Pressure Dependence of the Friction Angles

A pressure dependence of the internal angle of friction is known to represent the *quantification* of the *pore space* dependence of the internal friction, see [238]. Such a dependence has also been observed in wall friction experiments for the bed friction angle, see [328, 417]. Thus, we must assume $\delta = \delta(p)$

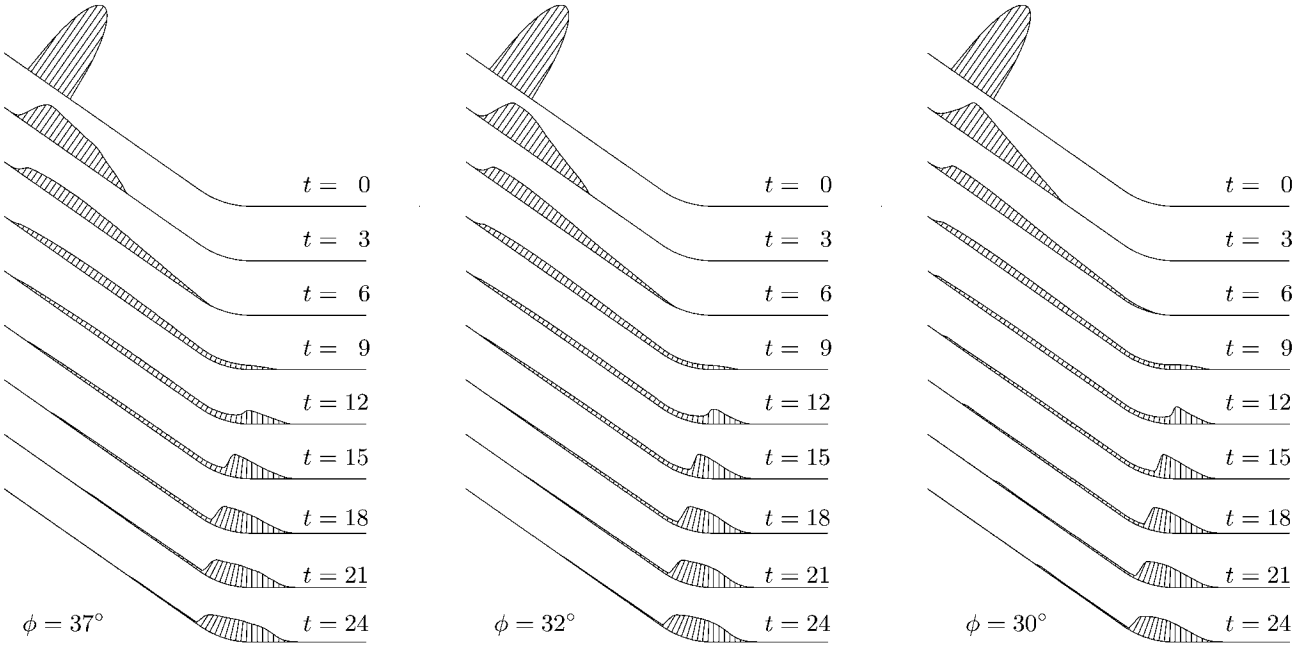

Fig. 9.26. Avalanche thickness along the central line of the flow, $y = 0$, at different dimensionless times $t = 0,\ 3,\ 6,\ 9,\ 12,\ 15,\ 18,\ 21,\ 24$ for three different internal friction angles ϕ: $\phi = 37°$ $(left)$, $\phi = 32°$ $(middle)$ and $\phi = 30°$ $(right)$. The bottom friction angle remains unchanged, i.e., $\delta = 30°$. (From [440].)

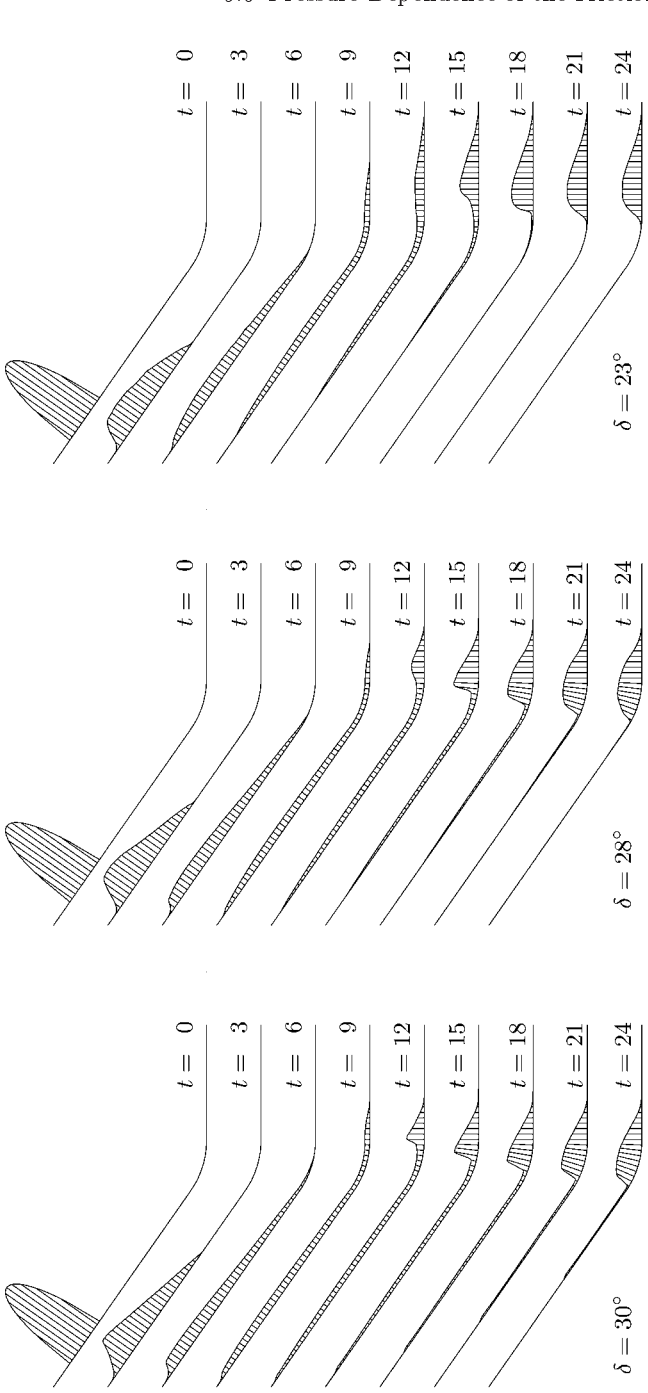

Fig. 9.27. Avalanche thickness along the central line of the flow, $y = 0$, at different dimensionless times $t = 0, 3, 6, 9, 12, 15, 18, 21, 24$ for three different bottom friction angles δ: $\delta = 30^\circ$ $(left)$, $\delta = 28^\circ$ $(middle)$ and $\delta = 23^\circ$ $(right)$. The internal friction angle remains unchanged, i.e., $\phi = 30^\circ$. (From [440].)

and $\phi = \phi(p)$, where p is the pressure. However, since the SH-type theory has only manifested a weak dependence of the avalanche geometry on the values of ϕ as demonstrated in Sect. 9.5, we shall ignore pressure dependence of ϕ, and $\phi =$ constant. Experiments indicate a decrease of the bed friction angle with pressure [238, 328, 417]; the simplest parameterisation is linear and according to [339] we choose

$$\delta = \delta_0 - \frac{\delta_0 - \delta_1}{p_1} p, \tag{9.13}$$

where δ_0 is the pressure-independent bed friction angle and δ_1 is its value at $p = p_1$. Scaling p and p_1 according to

$$p = \varrho g[H]\hat{p}, \quad p_1 = \varrho g[H_1], \tag{9.14}$$

(9.13) takes the form

$$\delta = \delta_0 \left\{ 1 - \frac{[H]}{[H_1]} \frac{\delta_0 - \delta_1}{\delta_0} \hat{p} \right\}, \tag{9.15}$$

where $\hat{p}$ at the base,

$$\hat{p} = \left(-g_z + \lambda \kappa \eta u^2 \right) h, \tag{9.16}$$

is the dimensionless pressure, see (4.93) and (4.94). Formula (9.15) is remarkable in the following respect: *the pressure-dependent term is not scale-invariant* because it involves the factor $[H]/[H_1]$. We shall choose the following notation and study its influence upon the avalanche motion:

$$\Pi = \frac{[H]}{[H_1]} \frac{\delta_0 - \delta_1}{\delta_0}. \tag{9.17}$$

This parameterisation of the bed friction angle δ destroys the scale invariance of the avalanche equations. According to practitioners the avalanche dynamics and the run-out distance must be mass-dependent for extremely large natural events, typically larger than 10^6 m^3 in volume.

9.6.1 Mass-Dependent Bed Friction Angle

In order to test the mass dependence of the dynamics and deposits of the avalanche, we consider an ideal mountain subregion where the talweg is defined by the slope function (9.2), where $\tilde{\zeta}_0 = 50°$ is the straight upper part of the talweg that merges into a horizontal run-out as shown in Fig. 4.13a, and $x_l = 13$ and $x_r = 17$ are the initial and the final points of the continuous transition. The azimuthal angle θ varies in the interval $[-17.9°, 17.9°]$, which accounts for a (shallow) circular variation (cross-slope curvature) of the bed topography in the lateral direction, and the non-dimensional distance $z_T = 16$ corresponds to $y \in [-5, 5]$, see Fig. 4.13b. A hemispherical cap with radius

$R_0 = 1.85$ holding the granular material in it is placed at $(x_0, y_0) = (5.0, 0.0)$ of the chute and suddenly released. The phenomenological parameters are chosen as $\delta_0 = 27°$ and $\phi = 37°$, which corresponds to *Vestolen* on *drawing paper*.

At first, the bed friction angle δ is considered to be pressure-independent and it is assumed to be constant, $\delta = \delta_0 = 27°$ corresponding to $\Pi = 0$ in (9.17). Figure 9.28a depicts the evolution of the avalanching body at ten non-dimensional time steps in a vertical plane containing the talweg of the valley. For more details see PUDASAINI et al. [339]. The first four panels clearly show that once the mass is released, the avalanche accelerates and spreads rapidly in the downslope direction due to the channelling effect in the cross-slope direction, the gravity and the dilatation. Although the front descends rapidly, the tail moves a bit upward (second panel) because of the fluidisation of the mass and the support of the material from the downhill (front) side. At $t = 4$ the front reaches the transition zone and the tail also starts to move downward. At $t = 6$, the front part of the body has fully reached the transition zone. Therefore, the mass at the front is contracting due to the effect of the passive earth pressure coefficient, but the mass in the tail is still extending. At $t = 7$, the mass in the vicinity of the lower part of the transition zone starts to be deposited and, owing to the effect of the curvature, the flowing body is contracting. For $t > 8$, a steep surface (height) gradient develops on the tail side of the avalanche. Although the front of the body is almost at standstill, the mass from the tail is still continuously flowing down and being deposited on the tail side of the body. This leads to the shock front moving upstream. The physical explanation for this is that from the front there is a strong resistive force from the bed, which prevents the body from advecting further. Thus, whatever comes from the upper part of the channel must be deposited on the back of the body. Consequently, the mass body must extend upward. The last four panels show the continuous development of the upcoming shock, while there is no simultaneous motion at the front.

9.6.2 Scale Effects Due to the Pressure Dependence of δ

As an example, the value of the parameter Π is taken to be 0.4, which corresponds to the reference values $\delta_1 = 20°$ and $H/H_1 = 1.6$. Figure 9.28b collects a series of numerical results for the same data as in Fig. 9.28a but with the pressure-dependent bed friction angle (9.15). The granular body is more fluidised as this angle decreases. Consequently, the run-out distance is larger and the height of the deposit is shallower than for a constant bed friction angle. The last panels indicate that the front of the avalanche for a variable bed friction angle is about 20% farther away than for a constant bed friction angle. Similarly, the maximum pile height of the final deposit for a

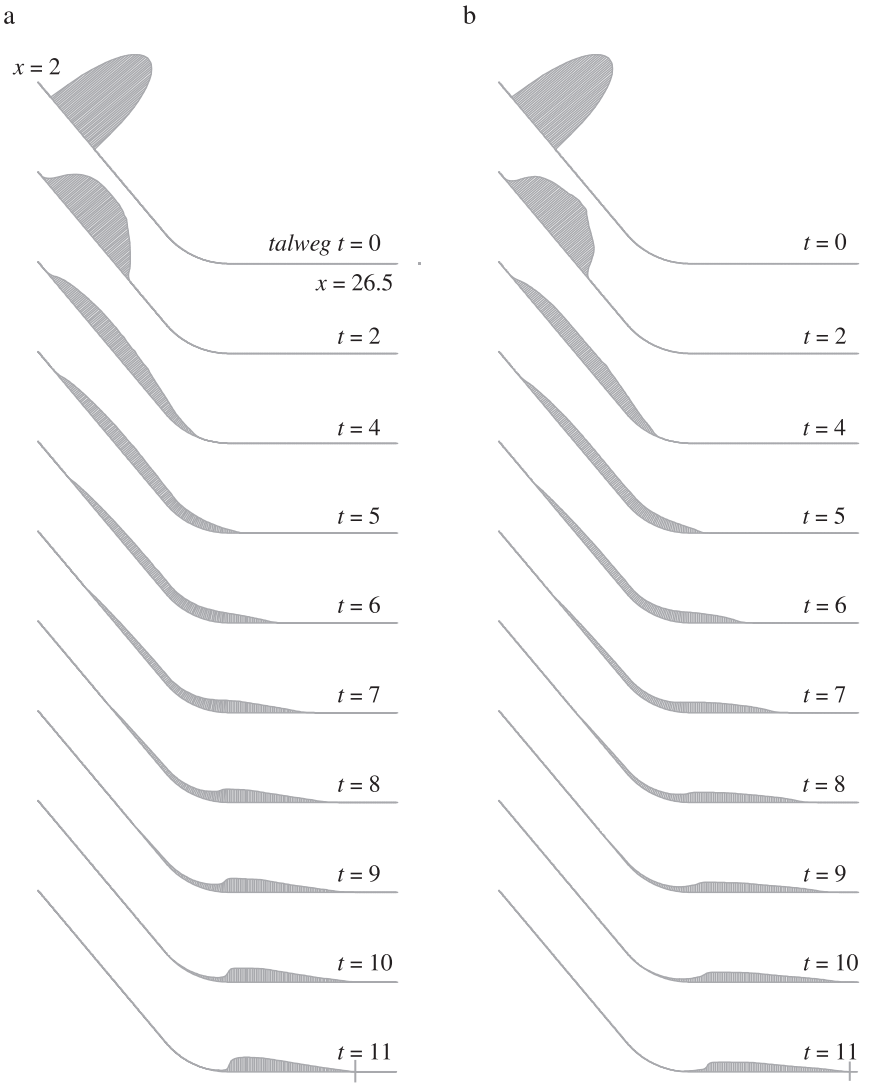

Fig. 9.28. **a**) A series of numerical simulations of avalanche motion with internal and basal friction angles $\phi = 37°$ and $\delta = 27°$, for different time points. The avalanche thickness is plotted using the curvilinear coordinate x, which runs from left to right along the talweg of non-dimensional length 26.5. Here we do not explicitly see the volume preserving of the material since we have plotted only the central section of the avalanche in the vertical plane containing the talweg. The remaining mass spreads in the sidewise direction. **b**) Same as in **a**) but with a pressure-dependent bed friction angle. In this case, the avalanche body is more fluidised, the travel distance (indicated by | in the last panels) increases and the height of the deposit decreases considerably. (From [339].)

variable bed friction angle is about 25% less than in the previous case. These conclusions are also applicable right after the release of the mass, but the comparison is more pronounced as time elapses. Due to the excess fluidity, the formation of the shock is weaker in the last four panels of Fig. 9.28b.

9.7 Formation of Shocks

The previous sections dealt with the application of the shock-capturing numerical scheme (TVD, mainly with minmod limiter) to the extended SH-equations, but the focus was not emphatically on capturing two-dimensional shock formations. This will be done now. The basal topography is shown in Fig. 9.29; the reference surface consists of a plane, inclined at $\zeta = 40°$, that merges into a horizontal run-out zone with $\zeta = 0°$ by a cylindrical transition zone. Superposed on the inclined section of the chute is a shallow parabolic cross-slope topography, $z^b(y) = y^2/(2R)$ with $R = 110$ cm, thus channelising the avalanche in its downhill motion. The inclined parabolic channel lies in the range $0 < x < 215$ cm and the run-out zone lies in the range $x > 245$ cm, between which a transition zone smoothly joins the two regions. At $x = 160$ cm, a circular bump with parabolic height profile is positioned. It is symmetrically arranged, has a base radius of 15 cm and a central height that can be varied to study the obstructing effect of this bump (see Fig. 9.29). In the transition zone, 215 cm $< x <$ 245 cm, the topography changes according to

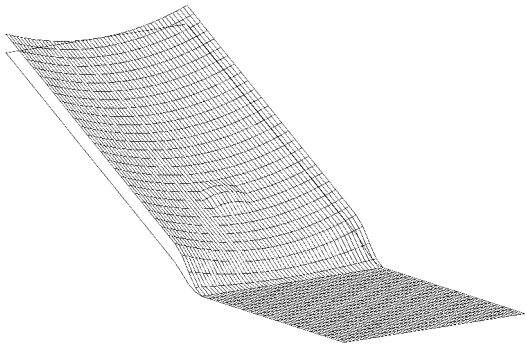

Fig. 9.29. Basal topography for the test problem describing two-dimensional shock formation. A simple reference surface is defined consisting of an inclined plane that is connected to a horizontal run-out zone by a transition zone. Superposed on the reference surface is a shallow parabolic cross-slope topography, which forms a channel that partly confines the avalanche motion. The parabolic channel is restricted to the inclined range. It is connected with the horizontal run-out zone by a smooth transition zone. A small parabolic hill lies in the channel centre of the inclined portion and constitutes a partial obstruction. (Courtesy of Y.-C. Tai).

$$\tilde{\zeta}(x) = \begin{cases} \tilde{\zeta}_0, & 0 \le x \le 215 \text{ cm}, \\ \tilde{\zeta}_0[1 - (x - 215)/40], & 215 < x < 245 \text{ cm}, \\ 0^\circ, & x \ge 245 \text{ cm}, \end{cases} \tag{9.18}$$

where $\tilde{\zeta}_0 = 40^\circ$. The simulation is performed with an internal angle of friction, $\phi = 37^\circ$ and a bed friction angle, $\delta = 32^\circ$. The material is suddenly released from a hemispherical shell with radius $r_0 = 32$ cm. It is so fitted to the basal chute topography that the projection of the line of intersection onto the reference surface is approximately elliptical in shape. The major axis of the ellipse is 32 cm long and the maximum height of the cap above the reference surface is 22 cm. Computations were made for circular bumps with two different central heights, $h^{(1)}_{\text{central}} = 0.5$ cm and $h^{(2)}_{\text{central}} = 1.5$ cm, respectively.

Figure 9.30 (top panels) shows the depth contours for the bump with small height. It displays the results for a sequence of non-dimensional times, from the release of the material ($t = 0$) until the avalanche comes to rest ($t = 22.5$). As soon as the material is released, the avalanche accelerates and extends, where the acceleration in the downslope direction is obviously dominant ($t = 2.5$). Because of the back pressure, the rear part of the avalanche moves slightly backwards at the initial stage of the motion. Due to the curvature in the cross-slope direction, the extension in the y-direction is limited in the channel region (see $t = 5.0$ to $t = 10$). The bump partly holds the material up ($t = 0.5$ to $t = 12.5$), but immediately below the hill and on either side of it two knolls form. Furthermore, behind the bump the reduction of inflowing mass causes a dent to form. Basically, the material accelerates until it reaches the horizontal run-out zone. With increasing basal drag the front comes to rest ($t = 12.5$ to $t = 22.5$), but part of the tail accelerates further. At this stage the avalanche body contracts. Once the supercritical velocity becomes subcritical, a shock wave (steep surface gradient) is formed. This occurs just after the end of the transition zone at approximately $x = 26$ dm ($t = 15$). With the approaching mass from the tail, the shock wave propagates backward ($t = 15$ to $t = 20$), i.e., as time proceeds, this shock wave propagates upstream. At $t = 22.5$ the avalanche comes to rest.

The velocities inside the avalanche body are illustrated in Fig. 9.30 (bottom panels), at the same times as the avalanche geometries in Fig. 9.30 (top panels). The arrows denote the direction of the velocity and their lengths indicate the speed. The velocity of the elements with depth $h < 0.1$ cm are not shown here. Although the bump holds the material back slightly, and side knolls are formed around it and a dent behind it, the velocity is not (significantly) affected by these features ($t = 5.0$ to $t = 12.5$). The material is obviously accelerated in the downslope direction. The front comes to rest in the run-out zone, but part of the tail accelerates further ($t = 10$ to $t = 22.5$). At $t = 15$ a jump in velocity obviously takes place in the transition zone, which corresponds to the steep surface gradient in Fig. (9.30) (top panels).

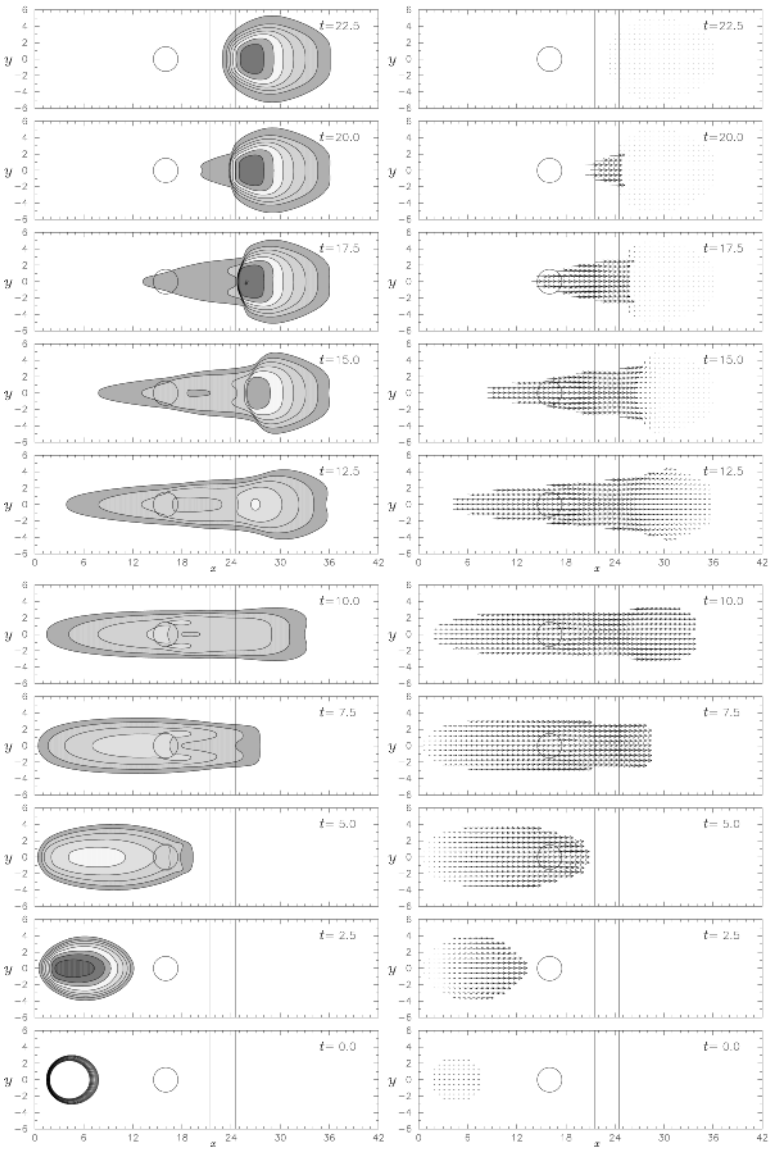

Fig. 9.30. *Top panels*: depth contours of the simulated results at a series of non-dimensional times, from the release of the material ($t = 0$) until the avalanche comes to rest ($t = 22.5$). The length unit is in dm. *Bottom panels*: velocities of the avalanche body at the same times; the *arrows* denote the direction of the velocity and their lengths indicate the speed. (Courtesy of Y.-C. Tai).

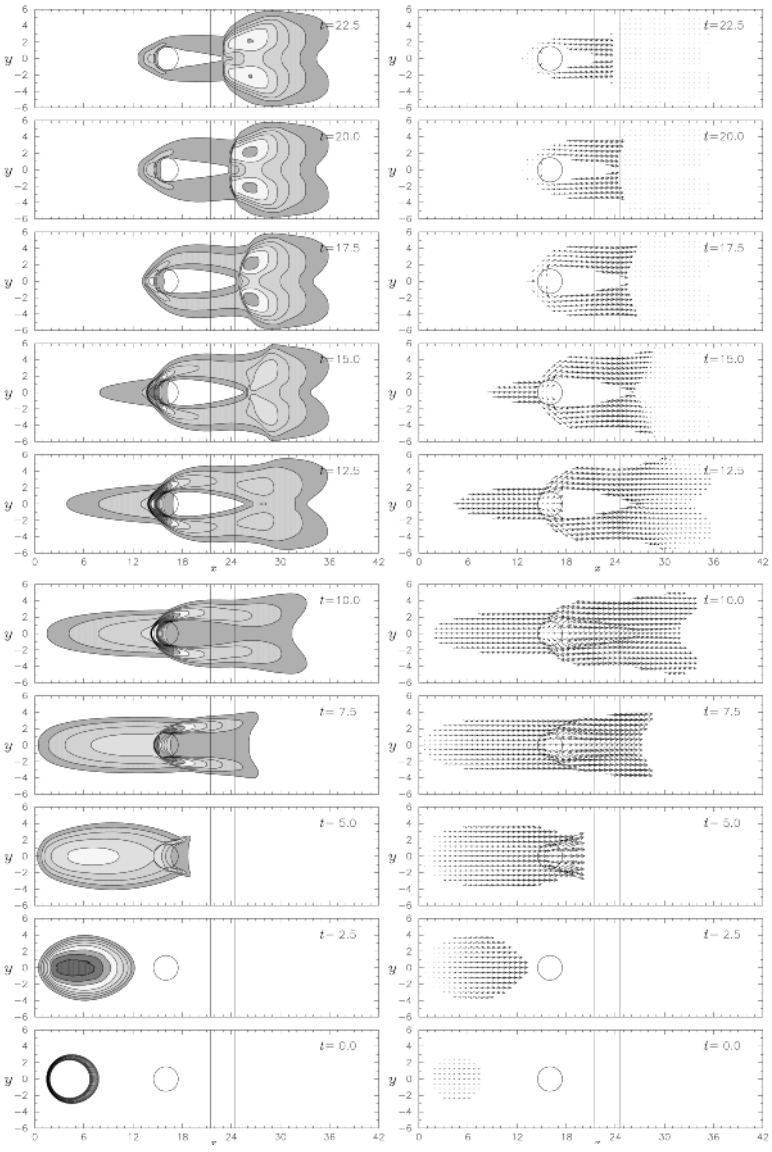

Fig. 9.31. *Top panels*: with increased height of the parabolic hill in the channel of the inclined portion, the flow is divided into two parts. The shock travels upslope around the obstacle and into the transition zone. At large time $t \geq 12.5$ granular vacua are formed below the parabolic hill. *Bottom panels*: velocities of the avalanche body at the same times; the *arrows* denote the direction of the velocity and their lengths indicate the speed. (Courtesy of Y.-C. Tai).

With the mass approaching from the tail, the jump propagates backwards ($t = 15$ to $t = 20$). At $t = 22.5$ the avalanche comes to rest. As a typical result, the bump is evidently not sufficiently strong to generate an internal shock in its immediate vicinity. The flow over it and around it remains continuous. The discontinuities are rather generated by the transition into the horizontal run-out zone.

This situation changes drastically if the height of the bump is increased so that it becomes a more substantial obstruction. Results of the evolution of the same avalanche on an otherwise identical chute but now with a bump of $h^{(2)}_{\text{central}} = 1.5$ cm are shown in Fig. 9.31. Before the moving granular mass reaches the bump results are identical to those of Fig. 9.30, but they change dramatically afterwards ($t \geq 5.0$). The bump induces a shock at the upper part and along the sides, forming lobes of higher elevation ($t = 7.5$). At $t = 12.5$, a small region of zero particle coverage develops in the lower part of the bump. This granular vacuum grows with increasing time and then covers the rear part of the bump (a large region below it), but as the material moves into the horizontal run-out zone the vacuum decreases. At $t = 12.5$, this granule-free region has a carrot-like form. The substantial mass flow around the bump exerts a considerable effect on the mass distribution within the deposition. The mass now spreads more to the sides, and two hills are formed that are due to the increased flow of mass down the two side lobes than in Fig. 9.30. This also makes the granular mass in the horizontal part move out farther to the left and right than the centre. Quite obvious is also the slower flow as compared to Fig. 9.30. At $t = 22.5$, when the granular mass has come to rest in Fig. 9.30 with a small height bump, there is still considerable flow for the large bump case. Furthermore, the evolution of the shock, although still present in the rear part of the deposit is somewhat weaker here than in Fig. 9.30.

In short, these two examples show that the geometry of the track may have a decisive effect not only on the evolving distribution of the granular mass, but also the flow field; internal shocks may or may not form, a fact that influences both the velocity and the mass field distributions.

9.8 Summary

In this chapter, we presented avalanche simulations over different topographies where the talweg was curved only in the downhill direction, or it was curved and twisted in an analytically prescribable way. This means that the theory developed in Chap. 4 can, in principle, be applied to (almost) any kind of topography[4] – from a simply inclined plane to very complicated arbitrarily

[4] Restrictions are only given by the fact that the shallowness assumption is satisfied and that the avalanche does not lift from the base.

curved and twisted channels, from initiation to the deposits in the run-out zones.

Similarly, we presented simulations for different phenomenological parameters, for pressure-dependent and pressure-independent bed friction angles, for flows along the reference surfaces and flows in superimposed channels, for diverging, converging and uniform channels, for flow with obstruction, and so on. All these simulations revealed quite reasonable and physically justifiable results for avalanching debris flows of granular materials. However, the model equations must still be tested with experiments. With this proviso, therefore, we may conclude that the theory presented in Chap. 4 can describe the avalanching motion for diverse situations, mainly with respect to the topography. This thus proves the applicability of the theory under realistic configurations for flows of granular materials in transportation phenomena in process engineering and in geophysical contexts. More importantly, we must compute the functional relations describing the curvature and torsion of the talwegs, as well as the function describing the cross-slope geometry of the mountain terrains from GIS digital elevation data. Once this has been achieved, we can use the model computer code to simulate avalanching debris down complicated mountain topographies. In this way, the model serves the purpose of constructing hazard maps and the protection of life and property. The next step is now a thorough comparison with experiments.

Part IV

Experimental Validation of the Theoretical Prediction with Different Measurement Techniques

10 Experimental Findings and a Comparison with the Theory

10.1 Why Are Laboratory Experiments Performed? What Can be Inferred from Them?

In earlier chapters, a number of laboratory experiments were reported to demonstrate that the class of SH-models was predicting features that are in fact observed in realistic situations. Such cases were the avalanching motions of dry particles in small-gap drums, in which the re-ordering of the particles in the gap was well-reproduced by the theory at least for a number of revolutions of the drum. Nothing was said about how to perform the experiments and how reliable the inferences were. It was simply recognised, on the basis of visual coincidence, that the model equations reproduced the process of the granular motion in the drum very well.

Furthermore, *since all model equations derived in Chaps.* 3 *and* 4 *on the basis of realistic assumptions are scale-invariant, the theoretical model can be tested with any size of physical model as long as scale effects are not manifest in the physical model.* Scale effects will obviously play a role when either avalanche models are so small that, for instance, the grain size is no longer very small as compared to the avalanche height or when the avalanche is too large such that the pressure distribution over depth is no longer close to hydrostatic – an assumption inherently incorporated not only in all extensions of the SH-equations but also in all other models known to the authors, see [26, 74, 75, 76, 191, 267, 272, 273, 274, 302, 303, 315, 316, 323, 342, 361, 362, 365, 430].

It has also already been mentioned that direct field observations of the catastrophic motions of avalanches are extremely difficult to make; in fact there are only a limited number of field observations that would permit a partial verification of theoretical models (see, e.g., Gubler [134], Norem et al. [302, 303], Issler [190]). In addition, comparison of models with results from field events is often aggravated because these events can be extremely complex in terms of the kinds and sizes of materials that are present, as well as the bed and avalanche geometries that might be involved. Moreover, controlled observations of catastrophic debris flows are not known, because their inception is largely unpredictable and even more dangerous than snow

avalanches. Laboratory experiments permit a control of material properties, bed geometries and initial conditions, and thus facilitate a comparison of theory with experiment.

In the hope of isolating the simplicities inherent in the response behaviour of rapidly flowing granular materials, HUTTER and co-workers (see the reference list below) performed well-defined laboratory experiments and compared their results with the findings from model computations. Later, similar laboratory experiments were also conducted by IVERSON et al. [194], MCDOUGALL and HUNGR [273, 274] and others. Laboratory experiments were also performed with the principal focus of identifying the frictional behaviour. Among these are, e.g., the experiments of POULIQUEN and POULIQUEN and FORTERRE, [329, 330]. A satisfactory fit of a theory with laboratory data, however, does still not imply that the theory is adequate to describe large-scale processes in nature. Apart from the idealisations of the laboratory experiment, scale effects might falsify the conclusions. Finding a satisfactory agreement between theory and experimental results at the small-scale constitutes a step in the direction of treating the full problem.

Three classes of problems have been analysed:

- *Flows of a finite mass of granular material within a narrow straight or curved chute situated in a vertical plane.* This flow is nearly, but not exactly, plane because the two side walls confine the material and slow its velocity in boundary layers near walls. This side boundary effectively increases the friction and is the cause for the deviation of the flow from being purely plane. A spatially one-dimensional version of the avalanche model equations is employed in this case and accounts for the deviation from strict one-dimensionality by adjusting the bed friction angle accordingly. Experiments have been performed for chutes with flat beds by HUBER [160]; exponentially curved beds by KOCH [225], HUTTER and KOCH [175], chutes consisting of a straight inclined portion, a curved part and a horizontal part by PLÜSS [324], HUTTER et al. [172, 179], and chutes of with a concavely and convexly curved bed by GREVE [127], GREVE and HUTTER [128].
- *Flows of a finite mass of granular material down a surface in three-dimensional space, providing no or at most limited sidewise confinement to the moving granular mass* were considered in the second stage. These surfaces are either *inclined planes* or *rolled surfaces* that are curved in the direction of steepest descent but flat perpendicular to this direction. Experiments were performed for inclined planes and surfaces consisting of an inclined plane in the upper part, a cylindrically curved transition zone and a horizontal plane in the run-out and deposition zones by GREVE et al. [129] and KOCH et al. [227]. The next conceivable complication is to replace the inclined plane by a weakly parabolic channel with a straight talweg in the direction of steepest descent merging into the horizontal

plane where the deposition is expected. GRAY et al. [123] and WIELAND et al. [445] performed laboratory experiments on such topographies. Still a further complication arises if the talweg does not follow the direction of steepest descent of the inclined reference plane but performs a sidewise meandering so that an avalanche in a channel following this talweg is guided and partially mimics this sidewise displacement. Experiments on such bed profiles have been conducted by GRAY and HUTTER [121]. The situation closest to an avalanche flow in a *corrie* is a channel-type topography where the talweg forms a smooth curve in three-dimensional space that exhibits both curvature and twist (or torsion). A helicoidal talweg is an example of this and was considered by PUDASAINI et al. [337]. A more general system for corrie-type channels with arbitrary curvature and torsion is due to PUDASAINI and HUTTER, [335].[1] IVERSON et al. [194], on the other hand, performed table-top experiments of avalanching flow down a surface mimicking a natural terrain close to an inclined plane with topographic variations not favouring channelling of the flow. MCDOUGALL and HUNGR [273, 274] in their laboratory experiment mimic the flow changing direction from a side channel into a main channel with different direction.

- *Flows that disclose the hyperbolic nature of the governing equations* are those for which internal *shocks* are formed. These, for instance, comprise flows of a granular material down an inclined plane encountering obstructions or moving from a steep slope at supercritical speed into a shallow run-out zone where subsonic flow prevails. This transition is associated with a "hydraulic jump", i.e., a sudden increase in avalanche depth and associated decrease of the streamwise velocity. A similar situation arises when a granular avalanche with supercritical speed approaches an inclined wall (e.g., perpendicular to the basal topography) and is diverted to the side, or can be seen in the flow around an obstruction, see, e.g., [59, 60, 411]. We have seen in Chap. 9 that shock-capturing numerical schemes are capable of identifying such discontinuities.

In this chapter, we shall show that all these phenomena can be well-reproduced with the equations presented in Chaps. 3 and 4. Our treatment will present qualitative details, so that the reader, in principle, will be able to perform his/her own experiments.

[1] As this book goes to press, such laboratory experiments are underway by S.-S. HSIAU from the National Central University at Chung-Li, Taiwan and the authors, but to report results would be premature here.

10.2 Chute Flow Experiments

10.2.1 Experimental Set-Up

Experiments have been performed by HUTTER et al. [179] in a 100 mm wide chute of variable length slightly greater than 4000 mm. The chute was made of two straight portions (one inclined, the other horizontal) that were connected by a curved replaceable segment so as to adjust the angle of inclination from 40° to 60° (first-type experiments). Alternatively, the bed consisted of a flexible strip of Makrolon (a material similar to plexiglass but softer and more flexible, second-type experiments, so as to form an exponentially curved chute). This bed was formed to follow the trace of a prescribed shape, i.e., an exponential curve (HUTTER and KOCH [175]). A third type of experiment was performed down a curved chute with an intermediate bump (GREVE and HUTTER [128]). The back wall of the chute was made of a PVC, whilst the front wall was made of clear and transparent plexiglass through which the moving granular pile could be photographed.

Figure 10.1 shows the arrangement of the set-up for the first type of experiments, the technical details being described in the figure caption. The situation for the second type of experiments was analogous but not exactly the same. Important for the present purposes is that the motion of a finite mass of granular material was followed from initiation to run-out and the material, its total mass, the chute geometry and the roughness of the bed were varied.

The motion of the pile of granular material was observed through the transparent front wall, and it was video-filmed and photographed by a 50 mm camera with a high-speed motor drive capable of operating at nominally 6, 12.5 and 15 frames per second, respectively. The distance of the camera from the chute varied from 3.5 m to 5 m. Generally, the camera was positioned as close to the chute as possible, the minimum distance being dictated by the requirement that the chute be photographed in its entire length. A clock, accurate to 0.01 s, was also positioned such that it was visible on the photographs.

Figure 10.2 gives a sketch of the laboratory test apparatus as used for the chutes with exponentially curved beds $\zeta = \zeta_0 \exp(-ax)$, where a is a curve parameter ($a = 0.1$). Figure 10.3 shows the chute with the bed made of Makrolon and the distance scale that was taped on the front plexiglass wall and the back wall. Figure 10.4a is a photograph of the plate confining the granular material with its rotating mechanism, whilst Fig. 10.4b shows it in operation when 3 l of plastic beads were released.

The tests were performed for the seven different sorts of granular materials shown in Fig. 10.5(a)–(g), glass beads of 3 mm and 5 mm nominal diame-

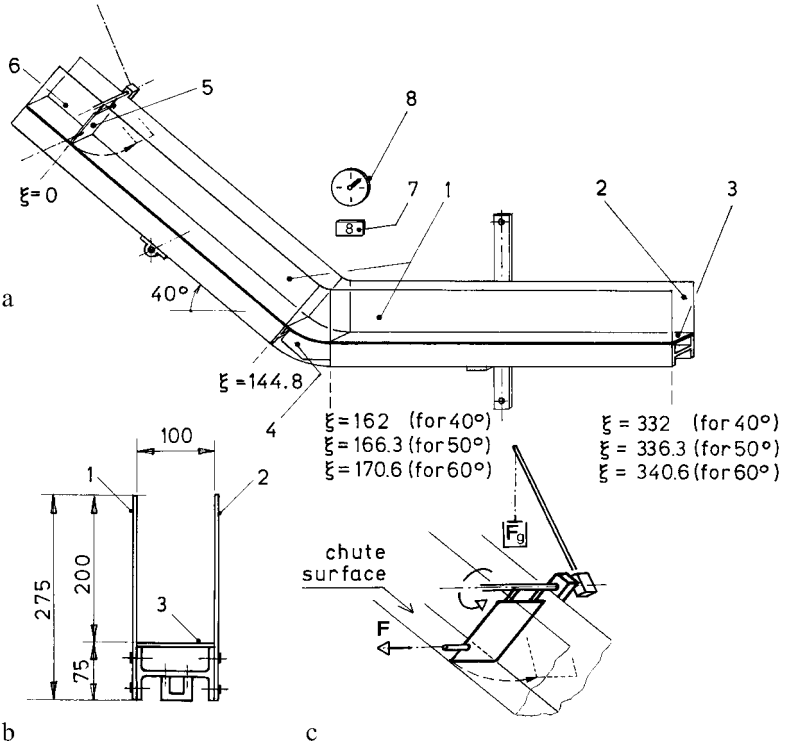

Fig. 10.1. **a**) Perspective view of the chute with a 40° inclination angle. 1: frontal side wall made of plexiglass. 2: rear side wall made of PVC. 3: basal surface (either PVC, or coated by drawing paper or sandpaper). 4: curved chute element. 5: shutter or gate that may rotate about a horizontal axis upon removing a bolt. 6: space to fill in the avalanche material. 7: number identifying the experiment. 8: clock with a minute scale, but its arm performs one revolution per second. **b**) Cross-sectional cut through the chute. *Scales* are in mm. 1: frontal side wall (plexiglass). 2: rear side wall (PVC). 3: basal surface (PVC, coated by drawing paper, sandpaper or Makrolon). **c**) Detail of the operating mechanism of the shutter consisting of an aluminium blade, an axle and a lever arm carrying a weight F_g. F bolt to release the shutter from its rest position, F_g weight generating fast rotation of the blade about the indicated horizontal axle. The rotation speed can be increased by enlarging the weight. (From [179].)

ters, plastic particles (Vestolen of lense-type shape, 2.8 mm diameter, 4 mm height), quartz granulates of 3 mm and 5 mm mean diameter and two fractions of marble chips with rough shapes and typical diameters of 3 mm and 5 mm. These materials differ from one another in important physical properties: quartz has a high mass density as well as a large internal angle of friction; alternatively, the glass beads have a similarly high mass density but a small internal angle of friction. On the other hand, the plastic particles

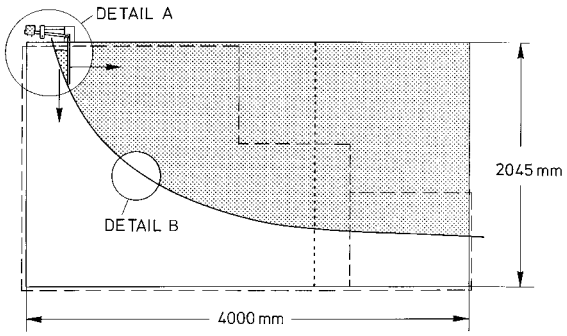

Fig. 10.2. Overview of the laboratory test apparatus showing the dimensions of the back wall (*solid and dotted lines*) and the front plexiglass wall (*dashed line*). The basal surface of the chute follows an exponential curve. Dimensions are in mm. Details A and B are shown in Figs. 10.3 and 10.4. (From [175].)

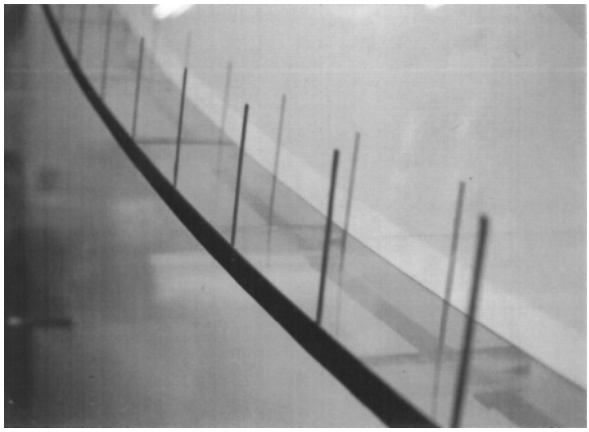

Fig. 10.3. Detail B in Fig. 10.2 showing the chute made of Makrolon (a kind of plexiglass, but softer). Visible on the front plexiglass and the rear walls is the distance scale (distance of markers: 5 cm). (From [175].)

have a small mass density and an internal angle of friction that lies between those of the glass beads and the quartz chips. Finally, all these materials differ considerably in the coefficient of restitution.

The effects of the bed roughness were examined by performing experiments with different bed linings of Makrolon, drawing paper and no. 120 SIA sandpaper, respectively. In all these cases, the sidewall smoothness was kept small in an attempt to maintain the two-dimensional flow as far as possible.

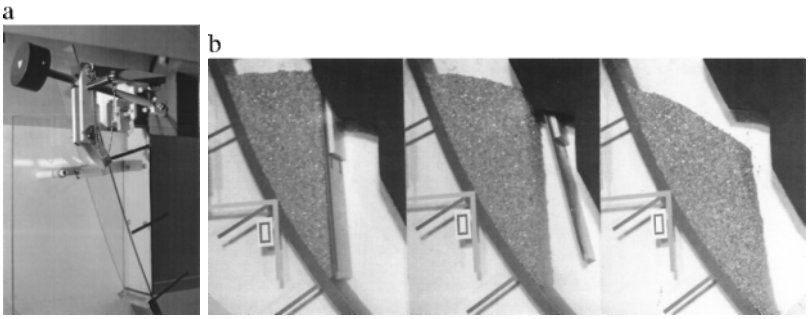

Fig. 10.4. **a**) Detail A in Fig. 10.2 showing the vertical plate confining the granular material. By pulling the bolt, the plate rotates about a horizontal axle in the counter-clockwise direction. **b**) The release of 3 l of plastic beads in a chute having 60° initial slope angle. The nominal speed with which the shots were taken was 15 frames per second. (From [175]).

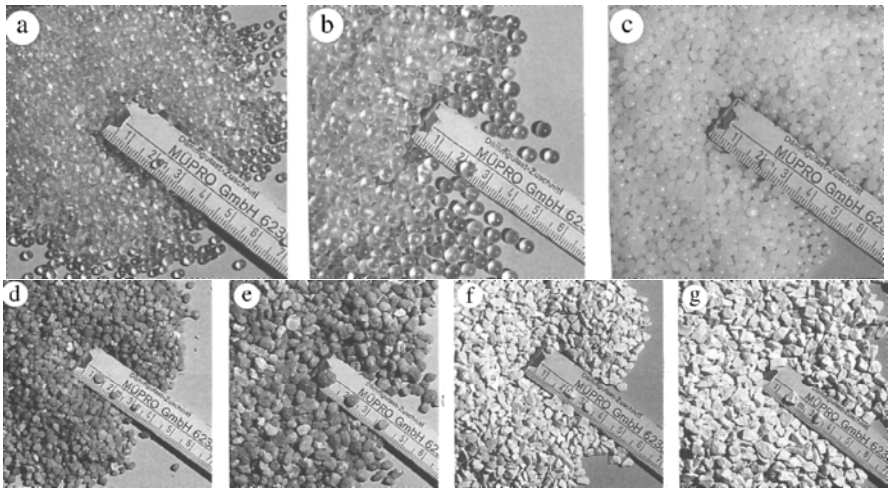

Fig. 10.5. Samples of the granular materials: **a**) glass 0 (3 mm); **b**) glass 1 (5 mm); **c**) Vestolen; **d**) quartz 0 (3 mm); **e**) quartz 1 (5 mm); **f**) marble 0 (3 mm); **g**) marble 1 (5 mm). (From [175].)

10.2.2 Experimental Procedure

A large number of experiments (> 100) was conducted by varying the following parameters:

- *Bulk volume:* for material at its densest packing: 1.5, 2.5 and 3.0 l and other volumes in special cases.
- *Initial geometry of the pile*: wedge-type, roof-like and parabolic initial shapes were used, but it was found that the initial shape of the pile had

relatively little influence upon the development of the avalanche at later stages.[2] Therefore, experiments were conducted only with wedge-like initial shapes.
- The seven *different sorts of granular materials* shown in Fig. 10.5.
- *Basal bed linings* consisting of Makrolon, drawing paper and no. 120 SIA sandpaper were used.
- *Different chute forms*: (*i*) chutes consisting of a straight inclined part with a curved segment merging into a straight horizontal portion; (*ii*) two exponentially curved chutes with different initial slope angles; (*iii*) a chute with a concave bed smoothly going through a convexly curved segment (bump) were considered.

Most experiments were performed repeatedly. Results from such experiments differed little from one another when they were performed consecutively, but could differ when a number of experiments had been performed one after another. The reason for this behaviour was the fact that the bed lining Makrolon and drawing paper changed the roughness with the number of experiments.

Figures 10.6 and 10.7 display the motions of two avalanches from initiation to run-out. The figures are compositions from individual consecutive photographs. The clock indicates the time when each photograph was taken; the long arm performs one revolution per second, so consecutive photographs in Fig. 10.6 are approximately 0.15 s apart from one another.

In experiment no. 97, a mass of 2000 g Vestolen particles moves down the chute with an inclination angle of 50° and basal roughness of no. 120 SIA sandpaper. The first photograph in Fig. 10.6 shows the pile of particles shortly after its release by the shutter. As seen from the consecutive photographs, the mass spreads very quickly. The front reaches the curved part of the chute before the rear end has barely started to move. The mass seems to spread further even when its front has already travelled quite a distance into the horizontal portion, even though signs of deceleration and particle deposition can already be seen as soon as the avalanche front has reached the horizontal part of the chute.

The photographs do not give any indication of very violent particle motion in the interior parts of the moving pile. Thus the flow there seems to be primarily "laminar".[3] Alternatively, the immediate front and especially a considerable portion of the tail shows substantial agitation of the particles, see the front of the avalanche in the last panel on the left in Fig. 10.6 and the rear of the avalanche in the panels on the right. Evidently, the shear due to basal friction causes enough fluidisation and the particle collisions generate considerable

[2] Notice that in two dimensions the initial shape influenced the shape of the pile.

[3] The term "laminar" is used to characterise particle motions subject more to rubbing friction between the particles than bouncing.

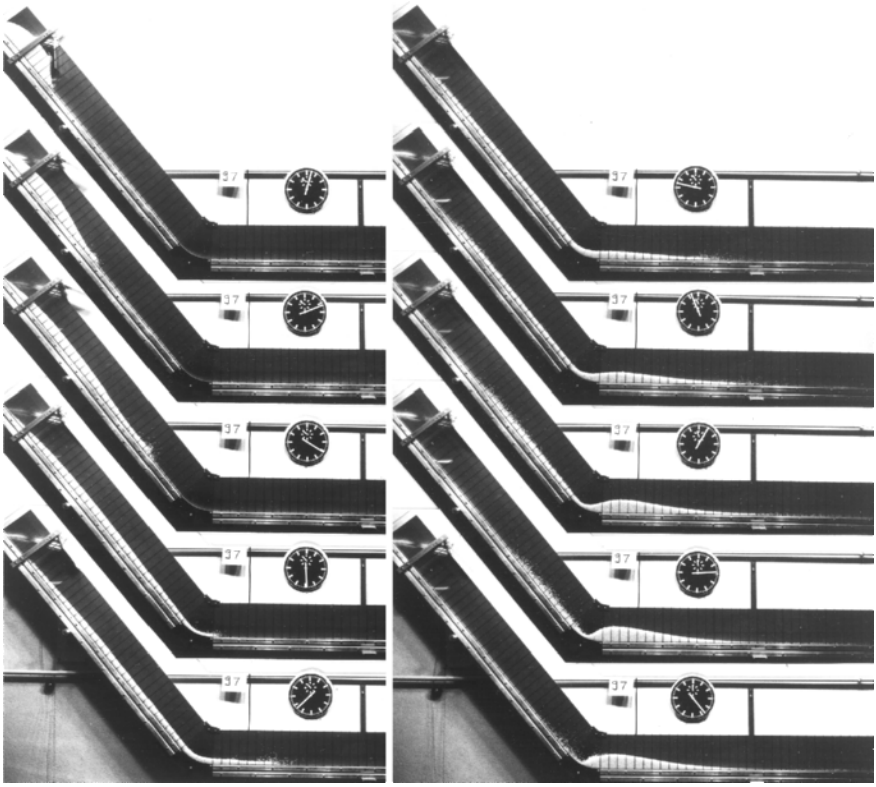

Fig. 10.6. Series of snapshots (experiment no. 97) of a mass of 2000 g of plastic particles (Vestolen) moving down a chute with an inclination angle of 50° and a bottom surface coated by no. 120 SIA sandpaper. The inclined portion is 170 cm long, the curved part has a radius of 24.5 cm. The *black lines* on the frontal plexiwall mark increments of 5 cm and the long leg of the clock performs one revolution per second. (From [179].)

dispersion and dilatation. Other experiments show less activation at the front and the tail.

Figure 10.7 shows an analogous situation for a mass of 3 l quartz 0 particles, moving down an exponentially curved chute. The photographs show consecutive shots of a moving and deforming pile from initiation to rest. Such photographs (in large prints) can be used to determine the evolution of the geometry of the granular avalanche as it moves down the curved chute; however, rather than tracing the entire geometry in each print, we shall present the following set of variables (see Fig. 10.8a): x_r, the rear end of the pile; x_f, the front end of the pile; $x_{\max}$, position where the moving pile is thickest; $H_{\max}$, the height of the pile at the position of $x_{\max}$ – all as functions of time.

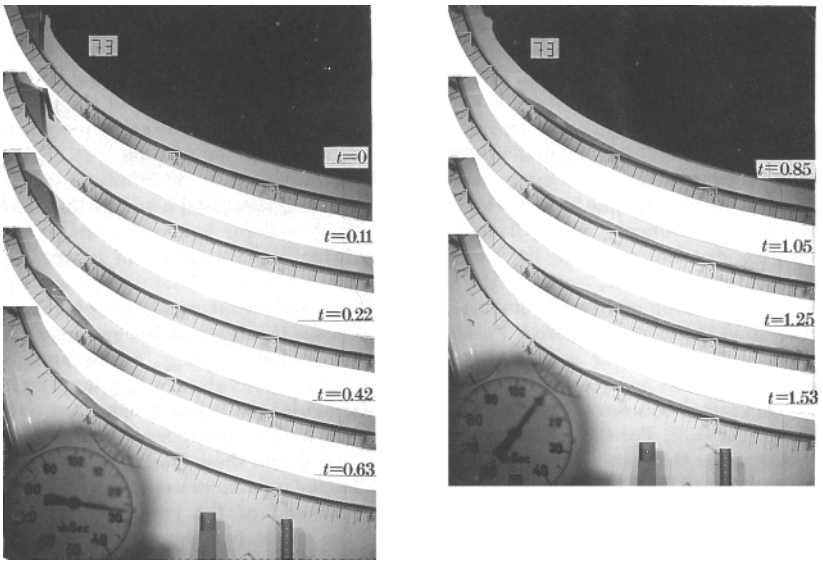

Fig. 10.7. Series of photographs (experiment 73) taken at different dimensionless times of a granular material (3 l of quartz 0 particles) moving down the exponentially curved chute, the bed of which is roughened by drawing paper and the initial slope angle is 60°. Times of the individual photographs are shown in seconds as inferred from the clock bearly seen in the *lower left*. (From [175].)

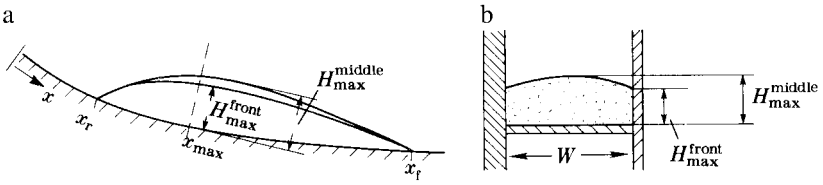

Fig. 10.8. a) Front view of the avalanche geometry during motion. The coordinate x is the arc length measured along the base of the chute; x_r, x_f and $x_{\max}$ denote the position at the rear end, the front end and where the avalanche depth is at a maximum. **b**) Cross-sectional view of the granular avalanche at the position $x_{\max}$, identifying $H_{\max}^{\text{middle}}$ and $H_{\max}^{\text{front}}$. (From [175].)

How reliably these data are derived and how the physical quantities can be determined from enlarged prints of the photographs is explained in detail in [175, 179]. For instance, the front, x_f, and rear, x_r, positions as viewed through the front plexiglass wall are different from corresponding positions in the middle of the chute. As sketched in Fig. 10.8, the maximum height as well as its position, $x_{\max}$, varied according to whether it was referred to the middle of the chute, $H_{\max}^{\text{middle}}$, or its value at the front wall, $H_{\max}^{\text{front}}$. Figure 10.9a shows the rear end of a granular pile in its deposit, the parabolic-like curve

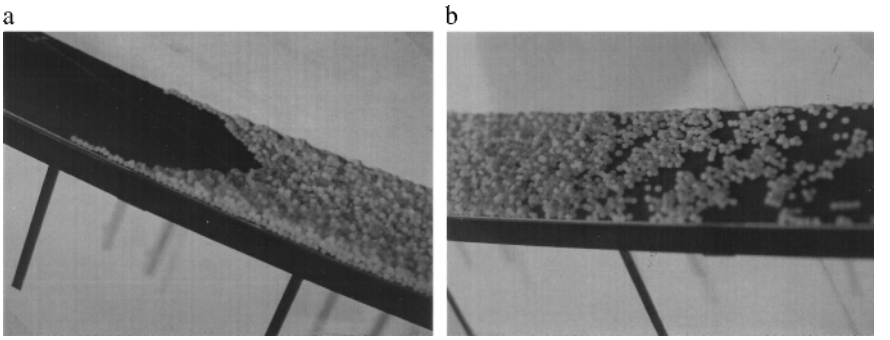

Fig. 10.9. **a**) Photograph of the rear end of the granular avalanche (experiment 73) at rest, showing the parabolic-type distribution of the rear end across the width of the chute. **b**) Leading edge of the settled granular avalanche (experiment 73) showing the large spread of the particles. (From [175].)

of the arrangement of the last granules being the manifestation of increased friction at the confining side walls; similarly, at the front, the particles are spread over wide distances (see Fig. 10.9b).

Among the more difficult variables that had to be determined experimentally are the *time of the onset of the motion* ($t = 0$) and the *time at which the granular pile comes to rest* ($t = T$). The former can best be determined by using close-ups of the video films of the shutter confining the granular material. Under the assumption that the opening of the plate takes place with a constant speed of rotation (see Fig. 10.4b), the time of the opening of the shutter can be extrapolated backwards from the two consecutive frames, taking into account that the video camera was operating at a nominal speed of 25 frames per seconds. Analogously, the time when the avalanche comes to rest, defined as the time when the particles at x_r come to rest, was determined by quadratic extrapolation from the last three shots when the rear end was still in motion and the end position x_r at rest.

Using this procedure, a great number of experiments were conducted, about 100 for the chute arrangement shown in Figs. 10.1 and 10.6 and more than 30 for the exponentially curved chute of Fig. 10.7. Not all experiments were analysed in detail, but a careful description of a comparison of experiments and the corresponding theoretical numerical results for about 30 experiments are provided in [179, 175]. A subset thereof will be discussed below.

10.2.3 Measurement of Phenomenological Coefficients

The theoretical formulation of the avalanche theory requires knowledge of the values of the internal angle of friction, ϕ, and the bed friction angle,

δ; these were determined for the materials together with some estimates of the coefficient of restitution. Of course their determination for laboratory granular avalanches is different from that in the fields. We report here about procedures taken for the laboratory avalanches.

Internal Friction Angle The *static internal angle of friction* is generally identified with the *angle of repose* of a wedge-type pile of the granular material that is deposited on a rough horizontal plane. Results depend to a certain extent on how the material is poured to form the wedge. Repeating the experiment several times and working with wedges held between two parallel walls and of different size to eliminate size effects, led to mean angles of repose between 30° and 47° with deviations of the individual measurements from the mean of at most 4° for the seven materials with which experiments were conducted.

Dynamic internal friction angles are smaller than their static counterparts. HUNGR and MORGENSTERN [161, 162] found in their annular shear cell experiments that the dynamic friction angle was about 4° less than the angle of repose. As a consequence, we reduced the effective internal friction angles from the wedge measurements by 2° or 3°. Fortunately, as we will see later, computations indicate that the computed results are not critically sensitive to the values of ϕ except when the bed friction angle δ is close to the internal angle of friction ϕ, so a very accurate determination of ϕ is not so important.

Bed Friction Angle The other parameter that appears in the theory is the bed friction angle δ_0 (the reason for the index 0 will soon become apparent). Two different experimental procedures are employed, the first one adequate to determine the bed friction angle without including the side-wall-boundary layer effect for chute flows, the second with it. To determine δ_0, the "true" bed friction angle, a small cylindrical container of 70 mm diameter was made out of paper and placed on a tilting plane apparatus filled with the granules to a certain height. The paper ring was lifted about half a particle diameter to eliminate the contact with the plate (see Fig. 10.10). The plate was then gradually inclined until a gentle push on the side of the cylinder containing the granular material resulted in its continued motion down the incline. The corresponding tilt angle was taken to be the bed friction angle δ_0. Repeating this experiment for each material and each bed lining (three to four times) gave values for δ_0 between 20.0° and 40.0° with errors not larger than 2°. Values are listed in Table 10.1.[4]

[4] There are, obviously, professionally better-established methods to determine the internal and bed friction angles. The above are the poor scientist's methods; every geotechnical institute possesses standard instruments by which shear and normal stresses in a layer of granular material can be correlated to determine the internal or bed friction angles, also for much larger forces than those exhibited above.

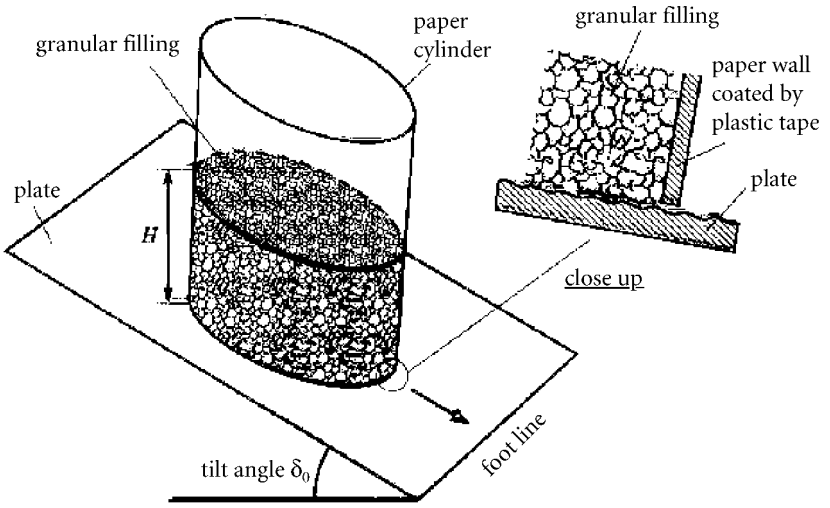

Fig. 10.10. Experimental arrangement to determine the bed friction angle.

Influence of Wall Friction As is evident from Fig. 10.9 there are side wall effects in chute flows; a simple approximate way to account for the side wall friction effects is to make use of an effective bed friction coefficient $\tan\delta_{\text{eff}}$ as suggested by ROBERTS [358] and SAVAGE [369]. According to these authors, the effective bed friction angle can accurately be expressed as a linear function of the depth to width ratio, namely

$$\delta_{\text{eff}} = \delta_0 + k\frac{H}{W}h = \delta_0 + \varepsilon k_{\text{wall}} h; \quad k_{\text{wall}} = \left(\frac{H}{W}\right) k, \tag{10.1}$$

where H is the characteristic height scale, W is the width and h the dimensionless depth of the flow. In the experiment δ_{eff} is measured as a function of height, see Fig. 10.11, and k_{wall} is computed according to

$$k_{\text{wall}} = \frac{(\delta_{\text{eff}} - \delta_0)}{\varepsilon h}. \tag{10.2}$$

To find the effective bed friction angle, the arrangement of Fig. 10.12 was used. A box made of styrofoam plates and without side walls[5] was placed between a copy of the chute and filled with the granular material to height H such that neither its front nor its rear end plates could touch the side walls or the bed. Then the entire arrangement was tilted as for the first experiment with the cylinder. Experiments were again performed several times and results are collected in Table 10.1.

[5] This material and arrangement was chosen to minimise the weight of the box; it should be negligible in comparison to the weight of the granular filling.

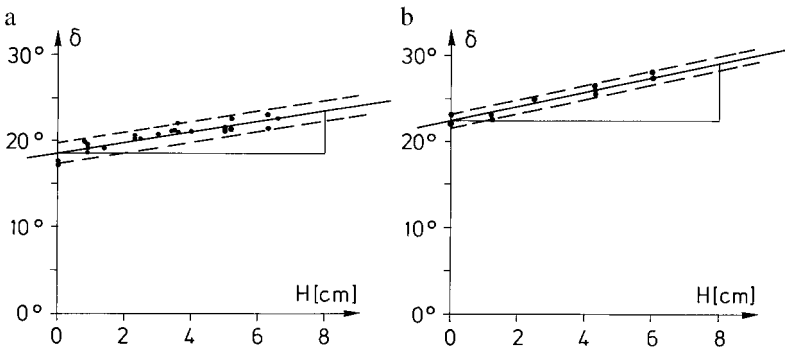

Fig. 10.11. Effective bed friction angle δ plotted against depth H (in cm) for (**a**) glass 0 on a Makrolon lining and (**b**) marble 0 granules on a Makrolon lining. *Points* represent the experimental findings, *solid lines* give the best fit linear dependence, with *dashed lines* showing the variance. The values of δ_0 and δ_{wall} arising in (10.1) and the variation Δ (the indicated band width) are: for (**a**), δ_0 =18.5°, Δ =1.2°, $k_{\text{wall}} = 9.19°$; for (**b**), $\delta_0 = 22.3°$, Δ = 0.8°, $k_{\text{wall}} = 12.6°$. (From [175].)

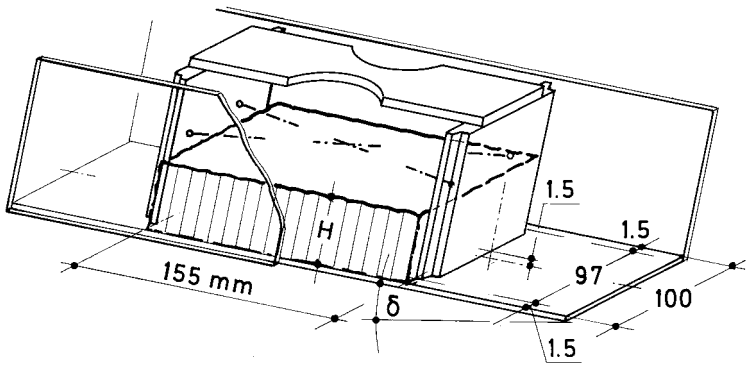

Fig. 10.12. Box with crosswise tightened strings for stabilisation, placed between the back and front walls of the chute and positioned on a strip lined with Makrolon. The box is uniformly filled with the granular material to the depth H. The tilting angle δ at which the box, including the granular material inside it, commences to move is defined as the effective bed friction angle. Dimensions are in millimetres. (From [175].)

Bulk Density and Coefficient of Restitution Values for bulk densities depend heavily on the amount of packing that is achieved. Two methods were applied, first by filling a measuring cylinder to its 500 ml mark and determining its density ρ_1 (defined as a dense packing) and then slightly shaking the cylinder with the material and measuring the density $\rho_2 > \rho_1$, yielding an even closer packing of the granular material. Repeating this experiment led to mean values and errors, also listed in Table 10.1. The coefficient of restitution gives information about the elasticity of the encounters between

the particles and the bed linings. Thus, it was determined according to

$$e = \sqrt{h_r/h_0}, \tag{10.3}$$

where h_0 is the height from which a particle at rest falls onto a plane and h_r is the corresponding height of rebouncing. Values of the coefficient of restitution were obtained as averages from 50 repetitions and more, but errors were still 5% to 10%. The results in Table 10.1 show what one would expect, that the rougher the plate and the surfaces of the particles, the smaller the coefficient of restitution.

10.2.4 Results

Results will be shown for flows of a finite mass of granular materials down different chutes as discussed above, however, only a small number of the experiments conducted and compared with theoretical results will be presented. A large number of additional illustrations of this comparison, corroborating the convincing performance of the theory given in [128, 175, 179].

Straight Chute Flow down a straight chute was already discussed in brief in Chap. 7. SAVAGE and HUTTER, [375] used a EULERian code to predict the evolution of a finite mass of granular material down an inclined chute.

Figure 7.2 shows a series of calculations all at the same bed slope $\zeta = 32^\circ$ but for different bed friction angles 22°, 16° and 10°. As the bed friction angle decreases, the acceleration of the pile down the slope increases, whereas the rate of spread of the length of the pile remains much the same. For these, numerical simulations, an asymmetrical initial shape of the granular material was used that started from rest at time $t = 0$ with the shape given by

$$h(x) = 0.879897 \sin\left[\pi\,(x - 0.6)\,\right] - 0.3 \sin\left[2\pi\,(x - 0.6)\right], \quad 0.6 < x < 1.6. \tag{10.4}$$

This initial profile was chosen for comparison with the laboratory experiments of HUBER [160]. It is seen to evolve into the M-wave shape, see Chap. 5 and [375].

As was already suggested in Chap. 7, it seems unlikely that a given heap at rest will asymptotically develop into an M-wave, virtually irrespective of what its initial geometry might have been. This was the reason for developing a LAGRANGEan scheme for which different solutions arose despite the fact that the same initial profile was used. Thus, unless otherwise stated, in this chapter, we will discuss the comparison of the experimental findings with the LAGRANGEan numerical simulations of the theory.

Predictions of HUBER's experiment no. 106b [160] using the LAGRANGEan scheme are shown in Fig. 7.4, and were based upon the initial depth profile

Table 10.1. Material constants of several granular materials. d is the mean grain diameter; $l_{\max}$ is the maximum length of a grain found in a sample of approximately 200 particles; ρ_1 and ρ_2 are bulk densities, ρ the true density, δ_1, δ_2, δ_3 are the bed friction angles on a Makrolon, drawing paper and sandpaper bed lining and e_1, e_2, e_3 the corresponding coefficients of restitution. δ_0 and k_{wall} were determined for a Makrolon bed lining; compare the main text for the definition of δ_0. Here, ϕ is the internal friction angle and all angles are in degrees, and d and $l_{\max}$ are in mm. The numbers in the even lines (given in left column by $\pm$) indicate the errors for the numbers immediately above. (Data taken from [175].)

Granulates	d	$l_{\max}$	$\rho_1/(gl^{-1})$	$\rho_2/(gl^{-1})$	$\rho/(gl^{-1})$	ϕ	δ_1	δ_2	δ_3	δ_0	k_{wall}	e_1	e_2	e_3
Glass 0	3	3.7	1784	1632	2730	31.0	20.5	22.0	23.5	18.5	9.0	0.85	0.48	0.67
$\pm$			15			2.0	1.5	1.5	1.0		2.0	0.03	0.03	0.05
Glass 1	5	5.4	1619	1574	2730	29.0	20.0	$--$	$--$	17.5	11.0	0.74	$--$	$--$
$\pm$			10			1.5	2.0				2.0	0.03		
Vestolen	4	4.0	552	540	540	37.0	23.0	23.5	36.0	17.5	11.0	0.75	0.61	0.54
$\pm$			10			2.0	2.0	1.0	2.0		2.0	0.03	0.04	0.06
Quartz 0	3	5.0	1562	1426	2600	44.0	25.5	30.5	39.0	21.0	12.0	0.79	0.54	0.7
$\pm$			20		150	2.5	2.0	1.5	2.0		2.0	0.03	0.04	0.1
Quartz 1	5	8.0	1572	1418	2600	43.0	25.0	28.0	$--$	21.1	11.5	0.72	0.58	$--$
$\pm$			15		150	3.0	1.5				2.0	0.04	0.05	
Marble 0	3	5.5	1447	1342	2500	47.0	27.0	$--$	$--$	23.3	12.5	0.74	$--$	$--$
$\pm$			40		200	3.0	1.5				2.0	0.03		
Marble 1	5		1495	1334	2500	45.5	26.0	$--$	$--$	21.7	12.0	0.68	$--$	$--$
$\pm$			35		200	4.0	1.0				2.0	0.03		

given by (10.4) with the measured quasi-static bed friction angle $\delta = 22°$ and the estimated dynamic internal friction angle $\phi = 29°$. The figure shows the profile shapes at six different (dimensionless) times. Also shown in the inset are the front, middle and rear end velocities. The circle marks are computed values and the cross marks are deduced values from HUBER's laboratory experiments involving the motion of gravel released from rest on a rough inclined plane. Although in these experiments the continuum approximation breaks down at large times when the gravel layer is only a few particle diameters thick, the general features of the development of the gravel mass give reason to assume that these are the correct solutions. Of course, this must be verified. The above descriptions of numerical solutions obtained with the EULERian and LAGRANGEan codes require further comment. By mere observation and comparison of experiments conducted in the laboratory with avalanches consisting of a cohesionless granular pile it was concluded that the M-wave type solutions obtained with the EULERian scheme were false results, not corresponding to a physically realizable situation, whilst the results obtained with the LAGRANGEan scheme were physically more realistic. This interpretation was corroborated only once EULERian TVD schemes were developed, as we have seen in Chap. 7 where the parabolic cap solution can be reproduced with any EULERian scheme obeying the TVD conditions. Solutions constructed with these schemes from initial continuous humps all developed into shapes that were close to those obtained with the LAGRANGEan scheme as displayed in Fig. 7.4, see [412, 415].

Straight Chute with Horizontal Run-out Let us now concentrate on experiments of the type displayed in Fig. 10.6; these concern the motion of a pile of plastic beads down a bed made up of a straight, inclined portion, a curved part and a horizontal part. The numerical simulations are presented here for conditions as described in the caption of Fig. 10.6, and the physical parameters ϕ, δ (for no. 120 SIA lining, i.e., sandpaper) are given in Table 10.1. It is found that the predicted temporal evolutions of the rear and front ends of the pile of granular material, as well as the shape, agree quite well with those of the laboratory experiments [175]. The trailing and leading edges of the granular avalanches indicate that their computed counterparts react sensitively to variations in the bed friction angle but not to those of the internal angle of friction. Furthermore, a weak velocity dependence of the bed friction angle, δ, is also seen to have a small, but negligible effect on these variables. Comparison of the experimental results with computational findings for many (more than 20) combinations of the masses of the granular materials and bed lining showed that the theoretical predictions and experimental results agree satisfactorily.

Figure 10.13 shows just one comparison between the positions of the front, x_f, the trailing edge, x_r, and the maximum height positions, x_s, (top panel) as obtained by the experiment and the model for conditions as detailed in the

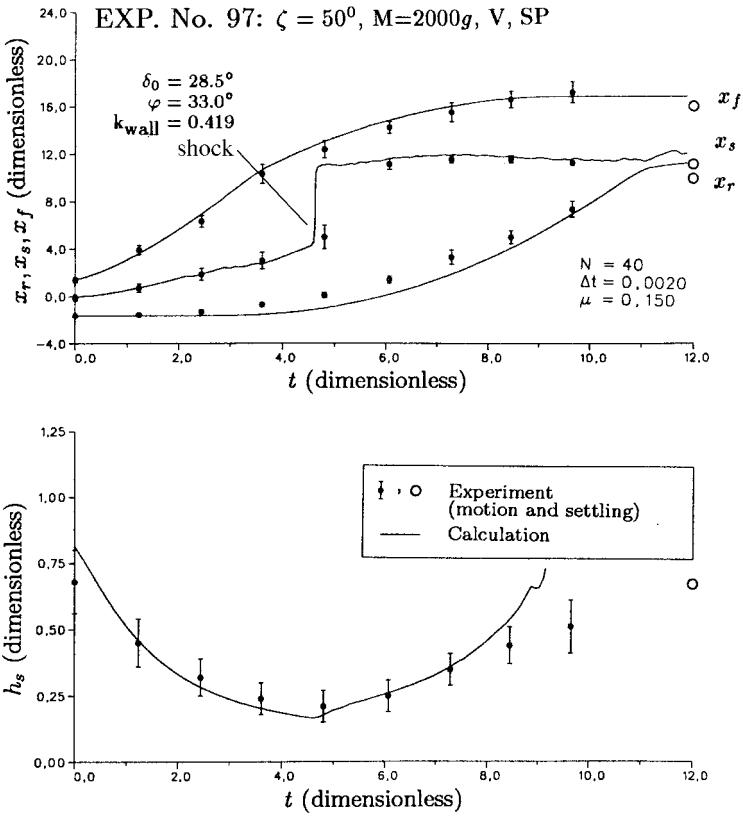

Fig. 10.13. Comparison of the theoretical predictions and experimental measurements of the (dimensionless) leading edge, x_f, the trailing edge, x_r and the position where the maximum height, x_s, arises (*top figure*) and the (dimensionless) maximum height, h_s, (*bottom figure*) plotted against the (dimensionless) time for experiment no. 97. Data points, taken from large prints of photographs, are shown as *full circles* with estimated *error bars*; direct readings of the positions x_f, x_s and x_r of the settled masses are shown as *open circles*. Computed results are shown as *solid curves*, obtained for a bed friction angle δ_0, an internal angle of friction, ϕ, and κ_{wall} as indicated in the *inset*. Also shown are the material (V = Vestolen), its mass M, the bed lining (SP = sandpaper), and bed inclination angle ζ. The parameters N, Δ and μ are the number of grid points, the time step and the diffusivity of the numerical scheme. The laboratory data have been made dimensionless with $L = 15$ cm and $H = 15$ cm corresponding to $\varepsilon = 1$. (From [179].)

inset and the figure caption. The symbols (full circles with error bars) are inferred from the photographs, the solid lines represent the computational results. The lower panel in Fig. 10.13 displays the corresponding results for the maximum height. It is seen that the front and trailing edges are reasonably well-reproduced by the model. The computed positions of the maximum

height also show a relatively sudden jump of the position x_s of the maximum height that obviously cannot be reproduced by the photographs; it arises at $t \approx 4.6$ when the front of the avalanche reaches the horizontal part and when the flow changes from an extensional to a compactive state. The final position of the avalanche in the settling zone of x_f, x_s, x_r (open circles) is also satisfactorily reproduced, as is the maximum height, even though there seem to be some deviations at times immediately before standstill. Of special interest is the temporal development of the position, x_s, of the maximum height within the avalanche. The computational evolution $x_s(t)$ clearly shows the occurrence of an internal shock at $t = 4.6$. This demonstrates that the LAGRANGEan scheme used here, is capable of reproducing large gradients, well in agreement with the measurement.[6] There are a large number of analogous experiments showing a similar agreement between experimental findings and computational results, see [179].

Exponentially Curved Chute A comparison of theoretical results and experiments was also conducted for the motion of a finite mass of a granular material down an exponentially curved chute (Fig. 10.7). HUTTER and KOCH [175] gave a detailed account on the experiments themselves and their exploitation; here we only give a brief account, not addressing the fine tunings needed in a trustworthy evaluation. Since slope changes for exponentially curved chutes are less abrupt than for straight inclined chutes merging into the horizontal via a curved segment, it is expected that all fields will also change more smoothly, in particular the change from dilating to contracting flow. This will most likely imply that agreement of computational results with experimental findings will look more convincing here than with earlier chute experiments. This is indeed so, as we shall soon see.

The bed friction angle was taken as accounting for wall friction as in (10.1) with $\delta_0(x)$ being a function of position along its track,

$$\delta_0(x) = \begin{cases} -0.0461\,(x-9)^2 + 29, & x < 18.3, \\ 25, & x \geq 18.3, \end{cases} \tag{10.5}$$

because the bed turned out to be worn out when the experiments were made. Several different but equally plausible initial profiles were selected.

[6] This jump is the manifestation of the internal shock that is formed when the velocity changes from supercritical to subcritical and can arise as a sharp transition only for a truly hyperbolic system of equations. The LAGRANGEan numerical integration scheme of Sect. 7.1.2 cannot capture such a shock, as it is diffusive and additional numerical diffusion has been introduced to stabilise it where large gradients occur with the adoption of a mesh refinement at these locations to properly capture the diffusive shock. We shall see later when shock-capturing integration methods are used that this shock is a real jump of the thickness.

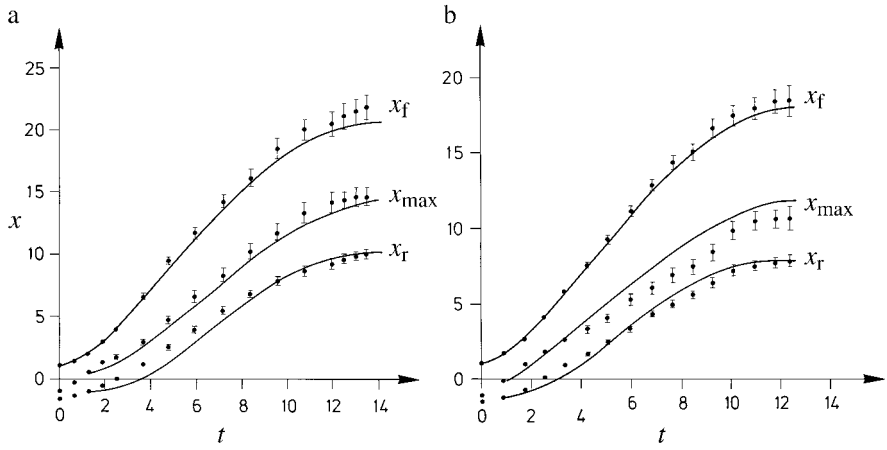

Fig. 10.14. Experimental measurements and theoretical predictions of x_r, x_f and $x_{\max}$ as functions of dimensionless time for (**a**) experiment 66 and (**b**) experiment 73. Data points are shown with *error bars*. Internal and bed friction angles are reduced from their static counterparts listed in Table 10.1. In (**a**) $\zeta_0 = 60°$, $a = 0.1$, $\varepsilon = 1$, $\delta_0 = 26°$, $\phi = 33°$, $k_{\text{wall}} = 11°$. In (**b**) $\zeta_0 = 60°$, $a = 0.1$, $\varepsilon = 1$, $\delta_0 = 29°$, $\phi = 40°$, $k_{\text{wall}} = 12°$. (From [175].)

Here we present results of when the initial condition was defined from the first photograph in which the avalanche was already moving. The pile depth was read in these cases at 10 to 15 positions and a polynomial interpolation was used to construct the computational initial profile. The initial time could then simply be determined from the photograph and the initial streamwise velocity was linearly interpolated between u_r and u_f, and the initial velocities at the rear and front ends, respectively.

Figure 10.14 compares experimental measurements and theoretical predictions of the evolution of the leading and trailing edge positions x_f, x_r, as well as the position, $x_{\max}$, where the maximum height of the granular avalanche occurs for experiments 66 (3 l of Vestolen particles on a basal bed lined with drawing paper) and 73 (3 l of quartz 0 particles on a basal bed lined with drawing paper). The data points are shown with error bars. Agreement in the prediction of the evolution of x_r, x_f and $x_{\max}$ between theory and observation is good with some deviations for x_r at the early stages and for $x_{\max}$.

Figure 10.15 compares the observed and computed non-dimensional velocities at the front, u_f and the rear, u_r, and at the position where the height is a maximum, $u_{\max}$. Agreement between theory and experiments for the velocities is less convincing than for positions, mainly because the velocities inferred from the photographic prints are fraught with larger errors. This is the reason why we need to implement sophisticated measuring techniques for

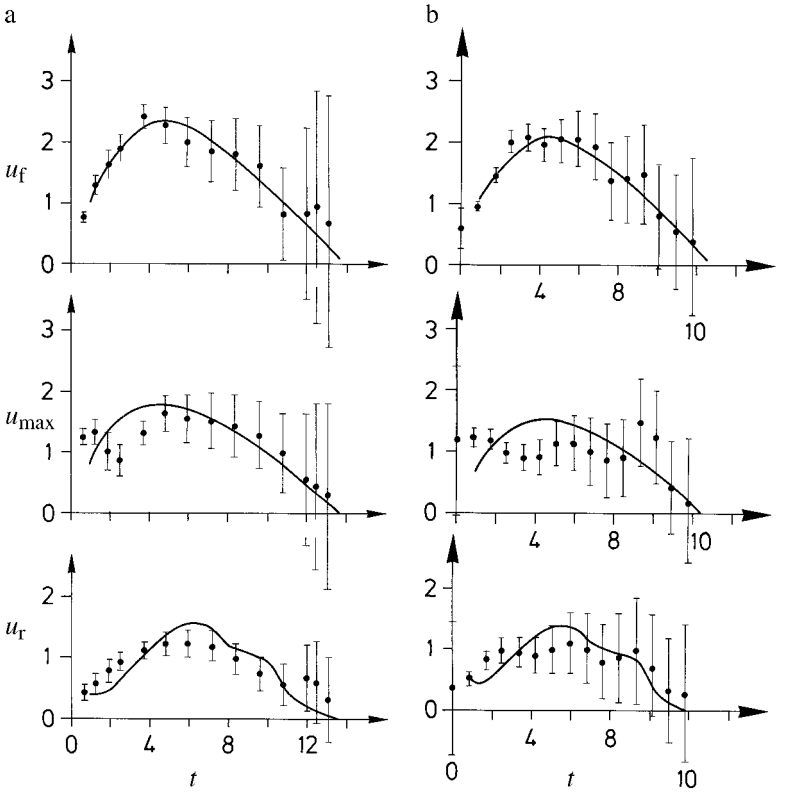

Fig. 10.15. Evolution of the dimensionless velocities at the front u_f (*top*), at the position where the avalanche depth has a maximum u_{max} (*middle*) and at the trailing edge u_r (*bottom*) as deduced from experiment and theory under the same conditions as in Fig. 10.14. (**a**) Results for experiment 66, (**b**) for experiment 73. (From [175].)

the determination of the velocity field. We will address these in Chaps. 11 and 12.

Comparisons of other variables as deduced from the experiments and derived from the theory are equally convincing for the two experiments selected. Figure 10.16 displays the evolution with time of the maximum height, h_{max} within the granular pile for both experiments 66 and 73.

10.2.5 Variable Bed Friction Angle (Position-Dependent)

It was mentioned before that repeated experiments wore down the bed and resulted in a position dependence of the bed friction angle. A curve fit to the measured bed friction angle $\delta_0(x)$ was given in (10.5); this was used

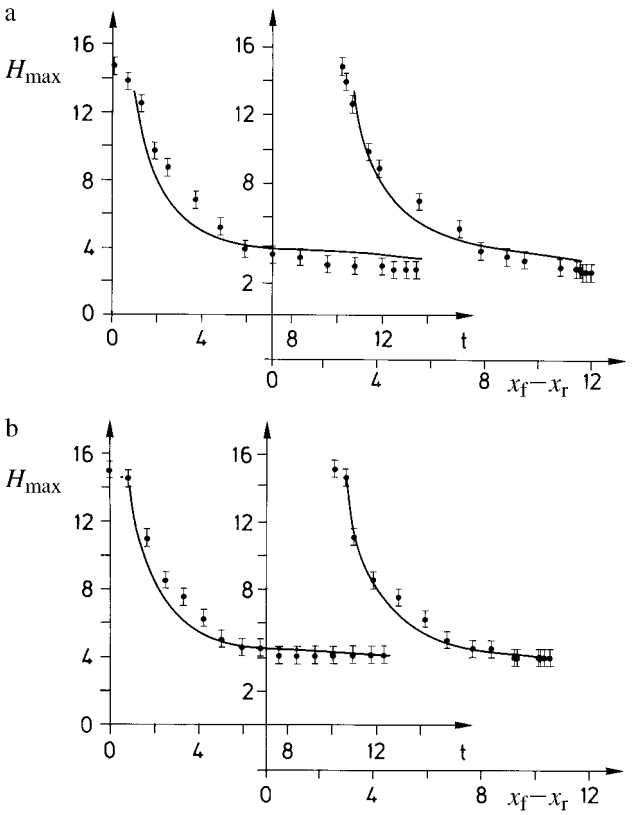

Fig. 10.16. Experimental measurements and theoretical predictions of the maximum height plotted against dimensionless time and avalanche length, respectively, for (**a**) experiment 66, (**b**) experiment 73. The computations are for (**a**), $\zeta_0 = 60°$, $a = 0.1$, $\varepsilon = 1$, $\delta_0 = 26.5°$, $\phi = 32°$, $k_{\text{wall}} = 11°$; in (**b**), $\zeta_0 = 60°$, $a = 0.1$, $\varepsilon = 1$, $\delta_0 = 29°$, $\phi = 40°$, $k_{\text{wall}} = 12°$. (From [175].)

in evaluations of the effective bed friction angle and in computations and reproductions of experiment 37 (3 l of quartz 0 on Makrolon bed lining). Figure 10.17 shows a comparison of experiments with computational predictions for x_r, x_f and $x_{\max}$ for both a variable δ_0 (according to (10.5)) and a constant $\delta_0 = 28°$. The computational results hardly differ from each other and the agreement between theory and experiment is excellent. Thus, consideration of the variability of the bed friction angle is not needed in this example.

The above comparison between observational results and theoretical predictions involved only three experiments. This is not sufficient to be able to claim adequacy of the theoretical model. We performed many more comparisons both for straight chutes with horizontal run-out and for exponentially curved chutes. Results are summarised in [175, 179]. Here we list a few additional

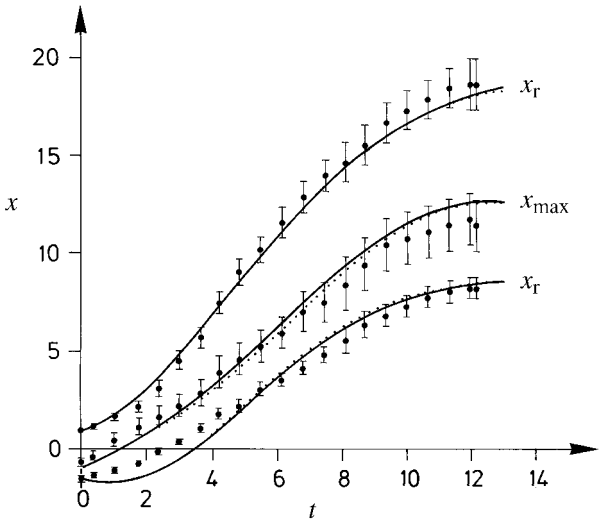

Fig. 10.17. Experimental measurements and theoretical predictions of x_r, x_f and $x_{\max}$ as functions of dimensionless time for experiment 37 (3 l of quartz 0 granules and a bed lining of Makrolon). Computations were done by using the law (10.5) for the bed friction, once with a constant value $\delta_0 = 28°$ (*dotted lines*) and once for a variable δ_0 (*solid lines*). Differences in the results are small. Aspect ratio, $\varepsilon = 1$; friction angles $\phi = 41°$; $\delta_0 = 28°$; $k_{\text{wall}} = 12°$; chute parameters $\zeta_0 = 60°$, $a = 0.1$. (From [175].)

results obtained for the exponential chute. Table 10.2 lists the conditions for eight experiments and Fig. 10.18 shows the comparison between experimental findings and computational results. Agreement in these eight experiments is generally very good.

10.2.6 Chutes with a Convex Curved Bump

The above results indicate that the agreement between theoretical predictions and laboratory experiments is good and seems to be somewhat better for the chute with an exponentially curved bed than the chute with a straight inclined part, connected by a short and sharply curved element merging into a straight horizontal part. These results, as promising as they are, could nevertheless be challenged by avalanche practitioners, the argument being that agreement between theoretical predictions and laboratory experiments might be less satisfactory in chutes with a convex curved "bump". In these cases, depending on the internal and basal friction angles, and the bed curvature and total mass, a single initial mass of granular material might settle in one of the following forms: (*i*) deposition of all the material above the bump, (*ii*) deposition of all material below the bump and (*iii*) splitting of the entire mass into two depositions, one above and the other below the bump. Greve

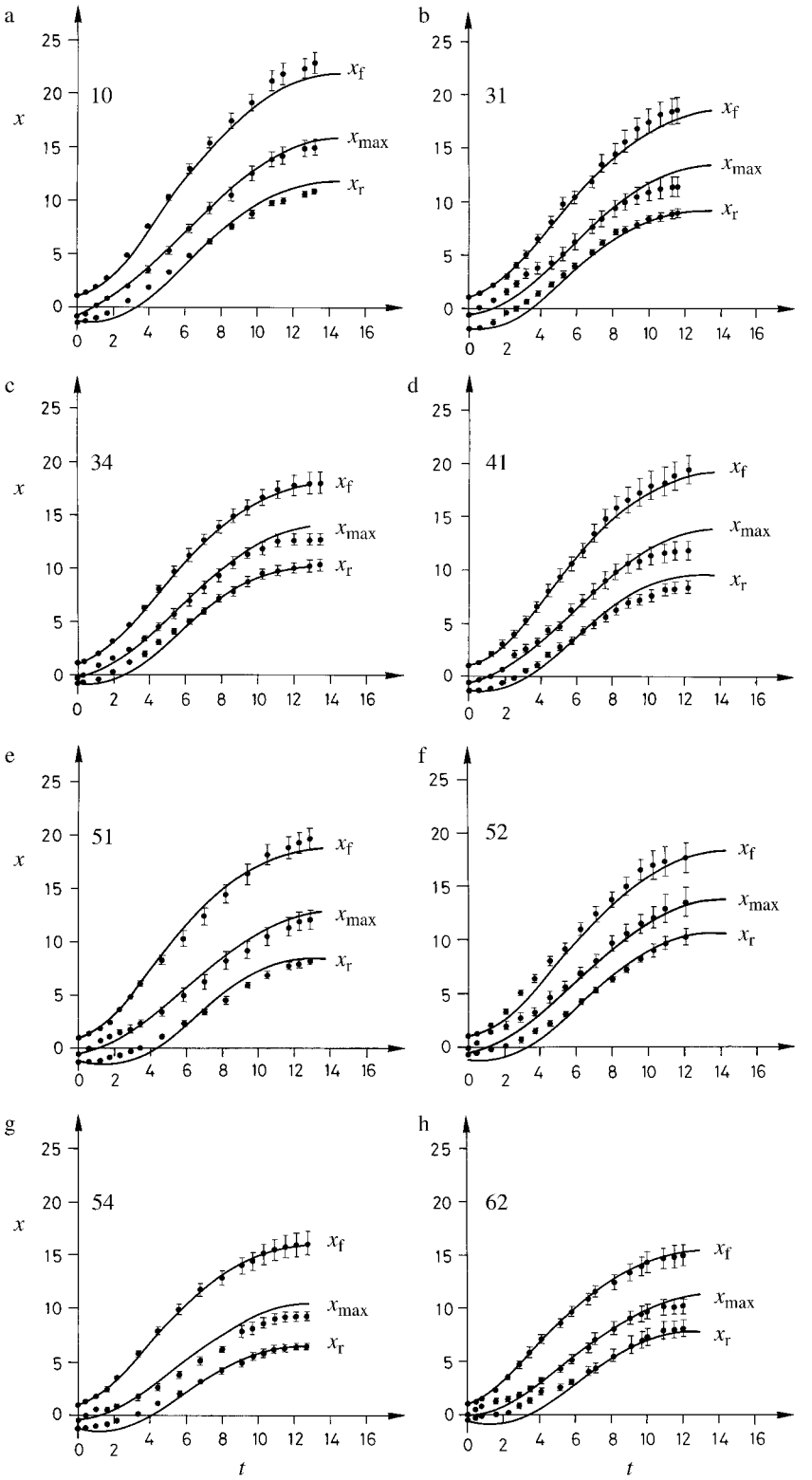
a
b
c
d
e
f
g
h
10
31
34
41
51
52
54
62
x
t
x_f
x_{max}
x_r
0 2 4 6 8 10 12 14 16
0 5 10 15 20 25

Fig. 10.18. Experimental measurements and theoretical predictions of x_r, x_f and $x_{\max}$ plotted as functions of dimensionless time t for experiment no. (**a**) 10, (**b**) 31, (**c**) 34, (**d**) 41, (**e**) 51, (**f**) 52, (**g**) 54, (**h**) 62, listed in Table 10.2. For all calculations $a = 0.1$ and $\varepsilon = 1$. Data points are shown with *error bars*. All graphs demonstrate a satisfactory agreement between experiment and theory. (From [175].)

Table 10.2. Experimental conditions for granular avalanches sliding down the exponentially curved chute of Fig. 10.7, where M = Makrolon, D = drawing paper, all angles are in degrees and volume in litres. These data are employed to produce the eight different panels in Fig. 10.18.

Exp. no.	Granular material	Bed material	Volume	Initial slope, ζ_0	Internal friction angle, ϕ	Bed friction angle, δ	Wall fiction angle, k_{wall}
10	Vestolen	M	3	60	32	25	10
51	Vestolen	D	3	54	32	25.5	11
52	Vestolen	D	1.5	54	32	25.5	11
34	quartz 0	D	1.5	60	40	27.5	12
62	quartz 0	D	1.5	54	40	29	11
54	quartz 0	D	3	54	40	29	11
31	marble 0	M	3	60	43	27	12.5
41	quartz 1	D	3	60	39	27	11.5

[127] and Greve and Hutter [128] demonstrate that agreement between theoretical predictions and observations in the laboratory is very good. They chose the same granular materials and chute properties as described earlier in this chapter (see Table 10.1), but constructed a particular form of the chute with a partly convex and partly concave geometry (see Fig. 10.19). A total of 48 experiments was conducted under the following conditions and by varying the following parameters:

- bulk volume of the material at its densest packing: 1.5 l and 3.0 l;
- the seven different sorts of materials shown in Fig. 10.5;
- basal bed linings consisting of drawing paper and no. 120 SIA sandpaper;
- one particular form of the chute: in the dimensionless coordinate x (equal to arc length), the slope angle ζ is expressed as

$$\zeta(x) = \zeta_0 \exp(-0.1x) + \zeta_1 \xi / \left(1 + \xi^8\right) - \zeta_2 \exp\left(-0.3\,(x + 10/3)^2\right), \quad (10.6)$$

with

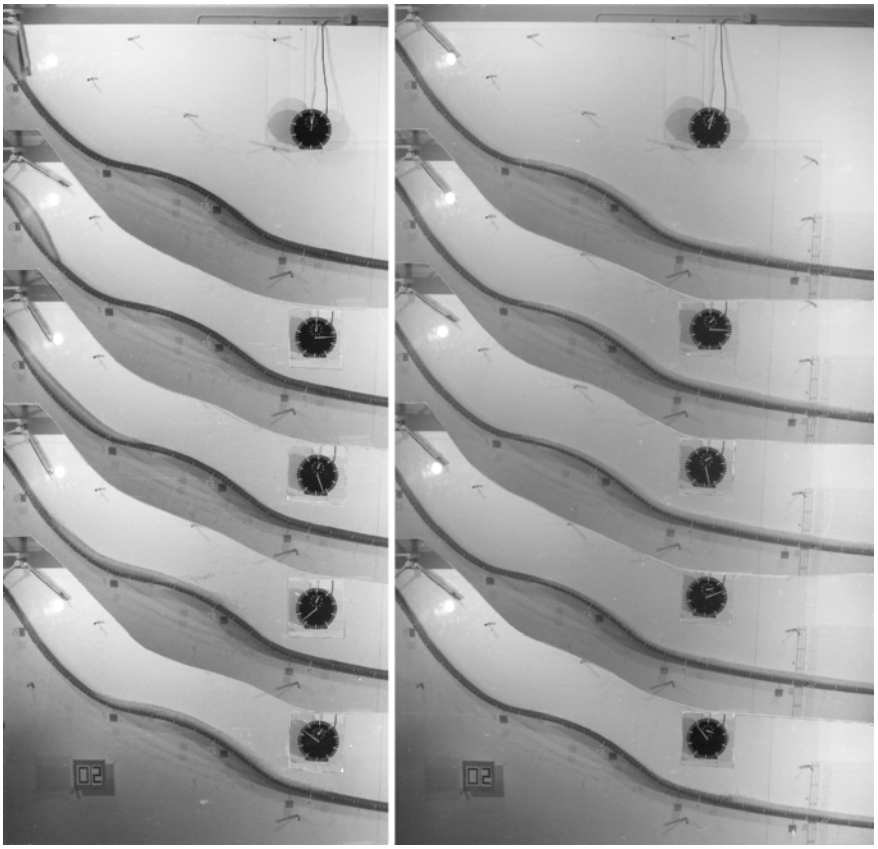

Fig. 10.19. Series of photographs (experiment no. 02, taken at different dimensionless times) of a granular material (3 l of glass beads with 5 mm diameter on no. 120 SIA sandpaper) moving down a concave and convex bed. (From [128].)

Fig. 10.20. Experimental (*dashed lines*) and theoretical (*solid lines*) dimensionless avalanche profiles $h(x,t)$ plotted in each panel for fixed dimensionless times (when the photographs were taken) in dimensionless temporal steps ≈ 2.5 (viz. the time sequence starting from the *top panel* and ending in the *bottom panel* is $t = 0, 2.5, 4.93, 7.60, 10.10, 12.53, 15.12, 17.71, 20.21, 22.80, 25.39$) for experiment no. 29 in which 1.5 l of plastic beads (Vestolen) were used on a bed lined with drawing paper for which $\delta_0 = 26.5^\circ$, $\phi = 37.0^\circ$ and $\kappa_{\text{wall}} = 11.0^\circ$. The numerical parameters chosen were $N = 40$, $\Delta = 0.002$ and $\mu = 0.05$. The *inset* shows the geometry of the bed with the dimensionless length scale along the bed profile that is unrolled in the panel as the horizontal axis. The *diamond symbols* denote the segment of the bed with convex curvature. (From [128].)

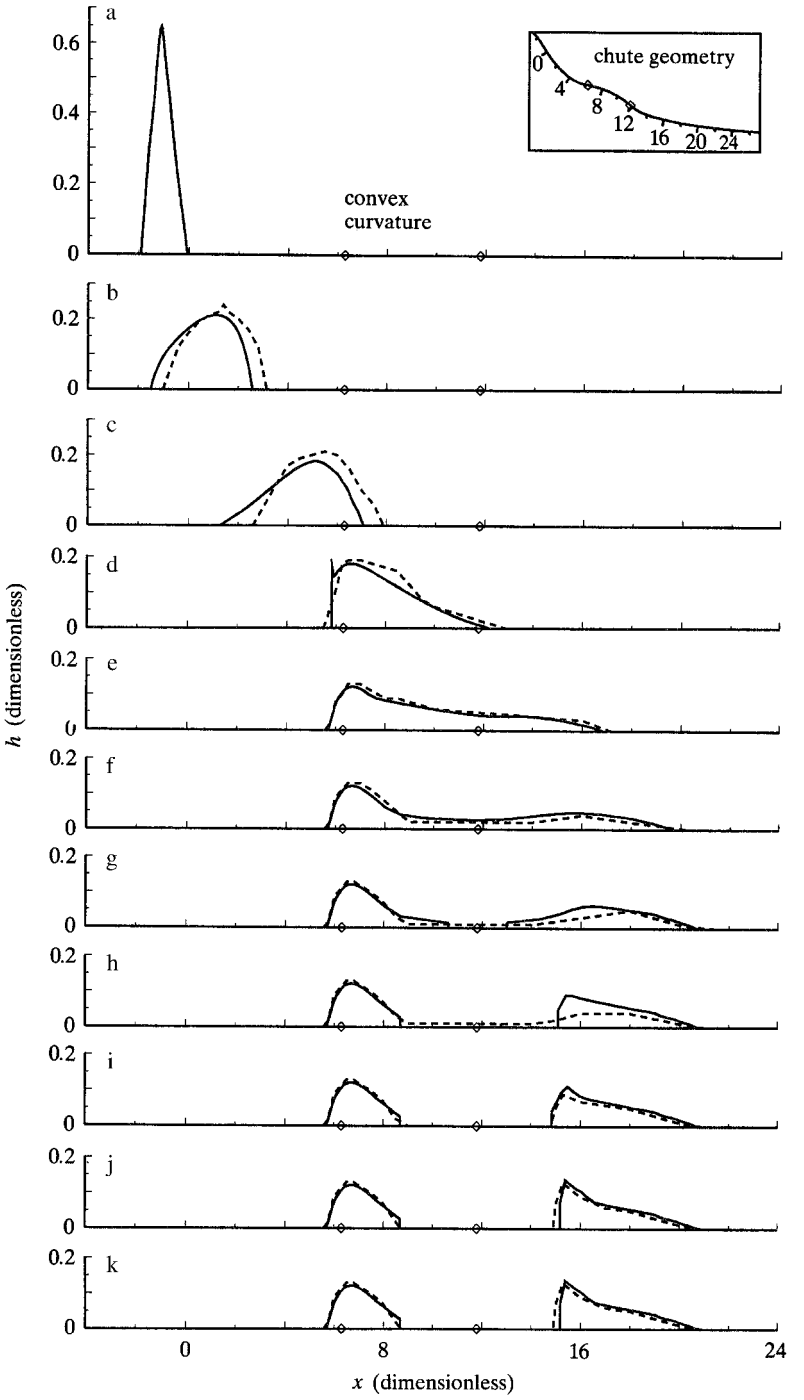
a
b
c
d
e
f
g
h
i
j
k
0.6
0.4
0.2
0
chute geometry
0
4
8
12
16
20
24
convex
curvature
h (dimensionless)
0
8
16
24
x (dimensionless)

$$\xi = \frac{4}{15}(x - 9) \tag{10.7}$$

and

$$\zeta_0 = 60^\circ, \quad \zeta_1 = 31.4^\circ, \quad \zeta_2 = 37^\circ, \tag{10.8}$$

in which non-dimensionalisation has been implemented by choosing for L, H, R 150 mm each.

Comparison of the experimental findings with computational results proved to lead to very good agreement between experiment and theory. A comparison of the experimentally determined avalanche geometries against the theoretical predictions at the times when the snapshots were taken is summarised for one experiment in Fig. 10.20. It is noteworthy that the model computations reflect the measured avalanche profiles surprisingly well, for all times of the experimental duration, including such details as the profile shapes and the separation of the single granular masses into separate piles. Therefore, we can conclude that the chute flow of cohesionless granular material along a bed topography with convex and concave curved segments is well-predicted by the model equations.

10.2.7 Limitation of the Model

The above is a report where comparisons of theory and experiment are successful. This is, because the prerequisites of the model were generally satisfied. For the exponential or "bumpy" chute geometries, the bed curvature was small in comparison to the avalanche length. This was, however, not so for the chute in which the straight inclined and horizontal arms were connected by a curved segment. In this case, the dimensionless curvature was not $O(\varepsilon^\gamma)$, $0 < \gamma < 1$, but $O(1)$ or even larger. Nevertheless, in all experiments the results led to satisfactory agreement between theoretical results and laboratory experiments [179].

In all experiments for which a comparison with theoretical results is reported here, the numerical values for the internal, ϕ, and bed, δ_0, friction angles, are sufficiently distinct. Results for experiments where ϕ and δ_0 were rather close to one another, so that the total bed friction angle often formally exceeded the internal angle of friction are reported in [175]. In these circumstances, we used $\delta = 0.999\phi$. With $\delta \approx \phi$, the basal surface is no longer dynamically different from any internal surface of the granular pile. We suspect, but have not been able to support this with an explicit proof, that the basal surface no longer acts as a clear and distinct sliding surface and that the velocity distribution is not as uniform over depth and now has a substantial shear layer. This problem clearly warrants further study.

There have also been cases where computed and measured travel times or travel distances differed from one another. The causes for this failure can

not in all these cases be attributed to the internal and bed friction angles being close to each other. A small total mass paired with a high coefficient of restitution allowed the particles to bounce over large parts of the granular pile, so that a considerable amount of energy was stored in the fluctuating motion. This would make it plausible that in these cases, experimental travel times are considerably smaller than in their computed counterparts. The exact causes, however, are still not known.

10.3 Avalanche Flow Without Side Confinement

The confined chute flow models presented so far constitute a first attempt to describe real avalanche flows but are certainly not realistic enough for flow avalanches moving down steep mountain slopes. For that purpose, two-dimensional extensions are needed as developed in Chap. 3. The first models of this class, e.g., [127, 174, 242], were still spatially one-dimensional; the evolving avalanche geometry was computed by double averaging and the results were compared with corresponding data from laboratory experiments, but this comparison was not convincing. The experiments were conducted with granular avalanches on an unconstrained inclined plane connected to a horizontal run-out plane by a curved cylindrical element (see Figs. 4.1 and 10.21). The likely reason for the poor coincidence was the fact that calculations were based on a set of equations obtained from the three-dimensional equations by performing both depth and width averages. This, paired with the satisfactory results obtained when the width average is not performed, implies that *double averages should be avoided*, see [242].

10.3.1 Experimental Set-Up

A set of experiments without side confinement was performed on the surface shown in Fig. 10.21, consisting of an inclined and horizontal plate connected with a cylindrical element. Its surface was either fairly smooth plastic Makrolon, or it was covered with drawing paper or sandpaper SIA no. 120. The time was again measured with an analogue clock, and the material was filled into a hemispherical cap at densest packing. The motion was initiated by tilting the cap as shown in Figs. 2.26a and 10.21, and the moving mass was photographed from the front. The rectangular grid drawn on the sliding surface facilitated evaluation and interpretation of enlarged prints. Numerically simulated time sequences for this case are plotted in Fig. 10.22.

Inclined Plane Here we present numerical results for an avalanche on an inclined plane. The calculations are based on a LAGRANGEan finite difference scheme.

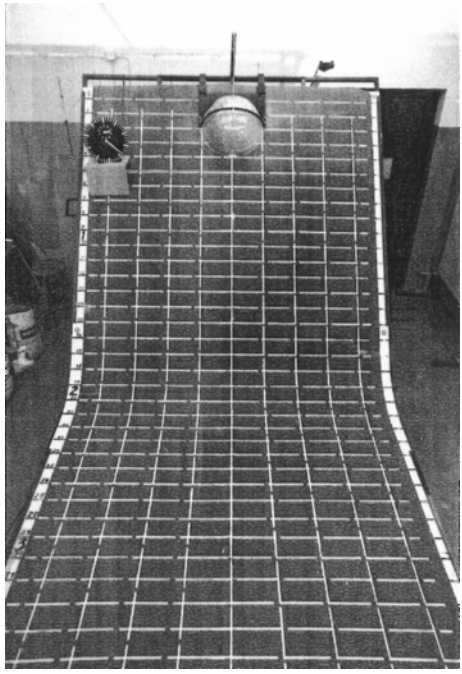

Fig. 10.21. Photograph of the longitudinally curved laboratory slide. Here, the slide is lined with sandpaper SIA no. 120 carrying a 20×10 cm grid. The granular material is filled in a hemispherical cap and released by tilting the cap (*top middle*). The arm of the clock performs one revolution per second. (From [241].)

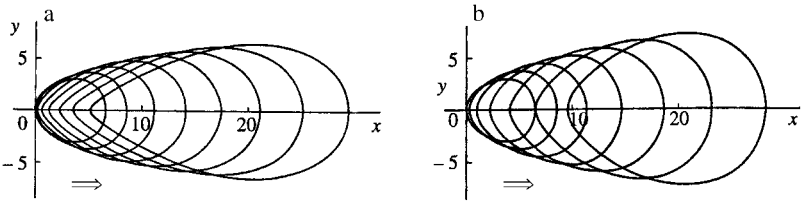

Fig. 10.22. (**a**) Numerically simulated time sequences $t = 0, 1, 2, 3, 4, 5, 6, 7$, for the basal profile of an avalanche moving on an inclined plane with an inclination angle $\zeta = 45°$. The other parameters are: dimensionless volume $V = 13.6$, bed friction angle $\delta = 29°$, internal friction angle $\phi = 39°$. The positions and time are given in dimensionless form. (**b**) The same, but the time sequence up to only 7 units and $\delta = 10°$. The *double arrow* shows the flow direction. (From [129].)

Figure 10.23 depicts temporal sequences for the basal profile of an avalanche with a total dimensionless volume 13.6 on an inclined plane with an inclination angle $\zeta = 45°$. The initial profile consists of a half-egg-shaped body representing the approximate shape of an originally hemispherical avalanche

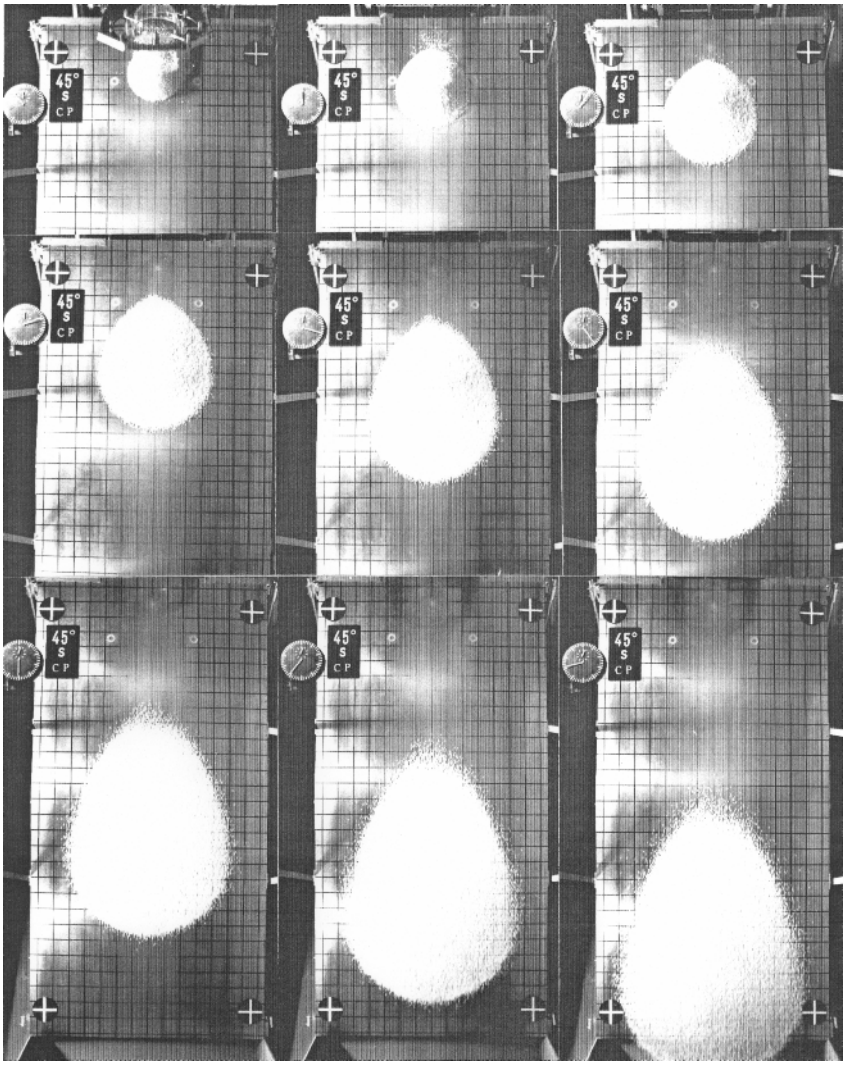

Fig. 10.23. Sequence of photographs of a moving mass of plastic beads (Vestolen) down an inclined plane of a 45° inclination angle moving on a smooth aluminium surface. The arm of the clock at the *upper left corner* performs one revolution per second so the camera takes about 10 frames per second. The motion initiates from a shutter of hemispherical cap geometry at rest. The *first picture* shows the granular mass immediately after the cap has been lifted by rotation about a horizontal axis at its upper end, thus instantly freeing the granular mass. The mass develops into a droplet shape and, as time proceeds, becomes elongated with a progressively larger aspect ratio, L/B. Direction of motion from *top to bottom*. (From [129].)

some tenths of a second after its release with ϕ and δ as prescribed in the figure caption. The originally circular circumference develops into a tear drop with a blunt front and a more pointed rear end. Furthermore, the tear drop shape of the granular avalanche is blunter when the bed friction angle is small than when it is big. Thus, sidewise spreading is obviously increasingly hampered by enlarged friction. This can be made more convincing by plotting the aspect ratio "typical length to typical width", L/B, for a fixed time after the onset of the motion for different values of δ. The aspect ratio grows with increasing bed friction angle δ. This is exactly what observations also reveal. Figures 10.23 and 10.24 show a sequence of snapshots of plastic beads moving down a plane of 45° inclination angle on a smooth aluminium surface (Fig. 10.23) and a rough surface coated by sandpaper (Fig. 10.24). The two granular piles have the same mass and start from rest with the shape of a hemispherical cap. The two figures also indicate that the basal friction angle is very significant for the identification of the pile geometry. A smooth base gives rise to little agitation of the particles, a rough base obviously leads to violent bouncing of the particles. The question therefore arises as to how the outer boundary of the experimental avalanche should be defined. This question will be addressed later. Figure 10.25 compares the experimental and numerical results for the motion of a pile of plastic beads (Vestolen) down an inclined aluminium plane of 45° inclination angle. The experimental marginal contours are represented by strokes that are indicative for a range of boundary positions (error bars), marking the margin of a mono layer of particles. The computational results are shown by solid curves, linearly interpolated between points that are the outcome of the computations. The outer curves mark the numerical avalanche margin with vanishing height, the inner one defines the contour with height $h = 3.5$ mm, agreeing with the approximate magnitude of the diameters of the granular particles. The motion in this figure is from left to right, and only that part of the inclined plane is shown that exhibits the entire moving mass. The first plot in panel (a) shows the state from which the numerical scheme is started. Further comparisons are given by Koch [226].

10.3.2 Rolled Surfaces

Experiments were also conducted on slides comprising an inclined plane merging into a horizontal plane via a cylindrically curved segment, see Lang et al. [241], Koch [226] and Koch et al. [227]. Figure 10.26 shows a sequence of snapshots of an experiment with quartz granules moving on a surface consisting of sandpaper SIA no. 120. The avalanche again starts from a state of rest from a hemispherical cap; its initial motion consists of a dilatation both in the downhill and sidewise directions until the avalanche enters the curved part of the slide where it contracts, particularly in the streamwise direction and eventually comes to rest in the horizontal plane. Figure 10.27 shows a comparison

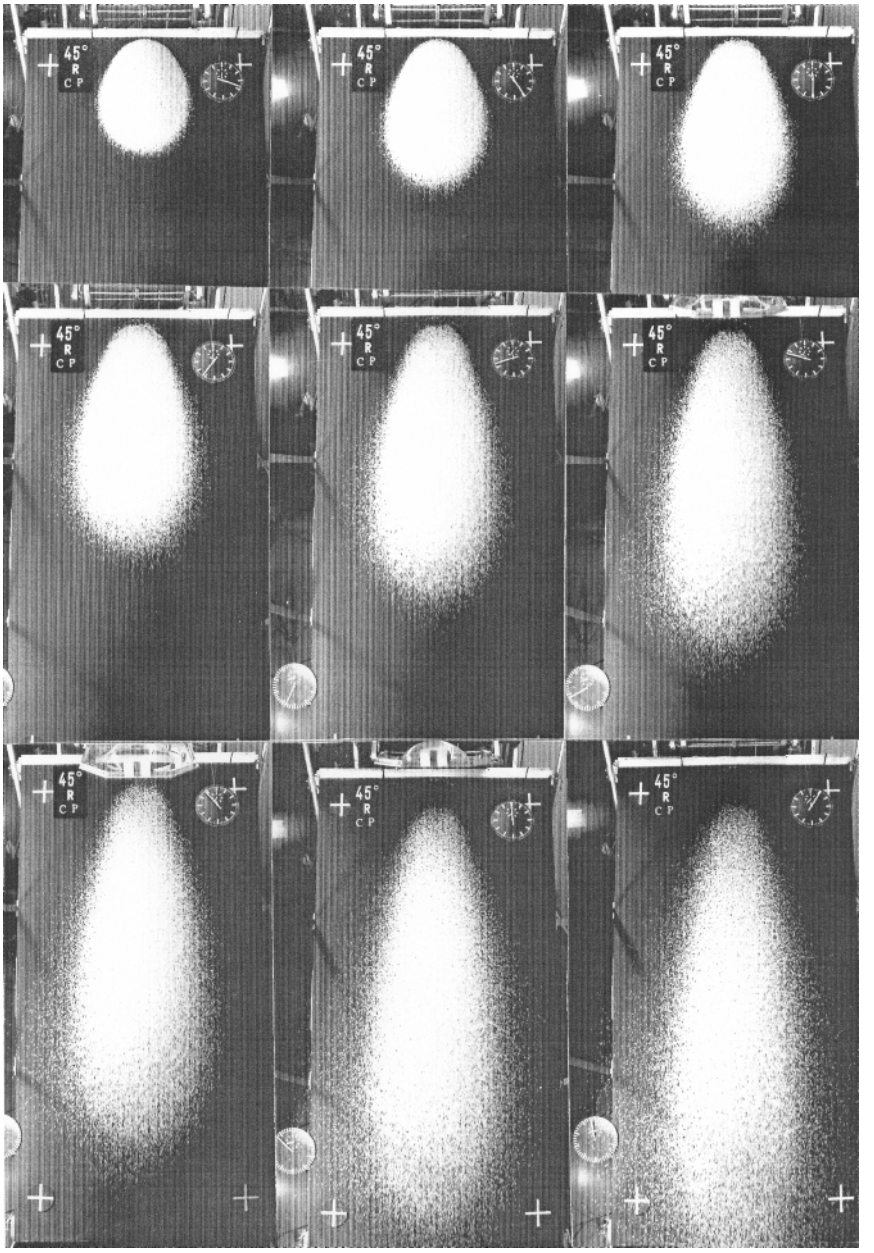

Fig. 10.24. Same as in Fig. 10.23 but the motion takes place on a surface coated by sandpaper no. 120 SIA. Note that because of the larger bed friction angle as compared to Fig. 10.23, the shape is less blunt and the aspect ratio is larger. Furthermore, it is difficult to identify the outer contour margin because of the particles' higher collisional agitation. Direction of motion from *top to bottom*. (From [129].)

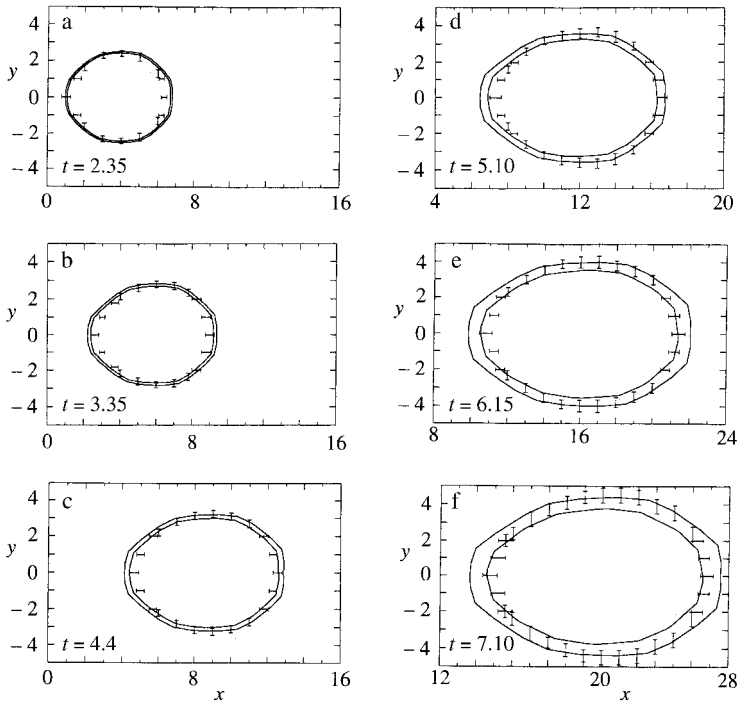

Fig. 10.25. Time series of numerical and experimental positions of an avalanche on an inclined plane in an experiment with plastic beads. The x- and y-coordinates are downhill and sidewise, respectively, and the direction of motion is from *left to right*. Only that portion of the slide is shown where the granular pile is momentarily positioned. *Solid lines* indicate theoretical avalanche margins, at height $h = 0$, and $h = 3.5$ mm; *symbols* represent the experimental margin indicating the location where the ground is fully covered by a mono layer of particles. The variables x, y and t are all dimensionless and the time series is $t = 2.35, 3.35, 4.4, 5.10, 6.15, 7.10$. (From [227].)

between experiments and numerical predictions for an experiment conducted with marble chips on a bed lined with SIA no. 120 sandpaper. The motion in the figure is from left to right and symbols are as before. Agreement between experiment and theory immediately after the release ($t = 4.0$) is very good. As the avalanche moves down, the agreement remains good for $t \leq 6.09$. For $t \geq 8.39$, the experimental positions of the margin points, indicated by the error bars, are again well-predicted by the theory, except for the trailing edge where the outer numerical contour stays a bit behind. Even the rather strong lateral spreading at the leading edge in the run-out zone where the avalanche comes to rest is rather well-described by the theory. The spreading of the experimental 50% areal coverage contours (dashed lines) cannot be predicted by the model, since it is based on a continuum mechanical description that

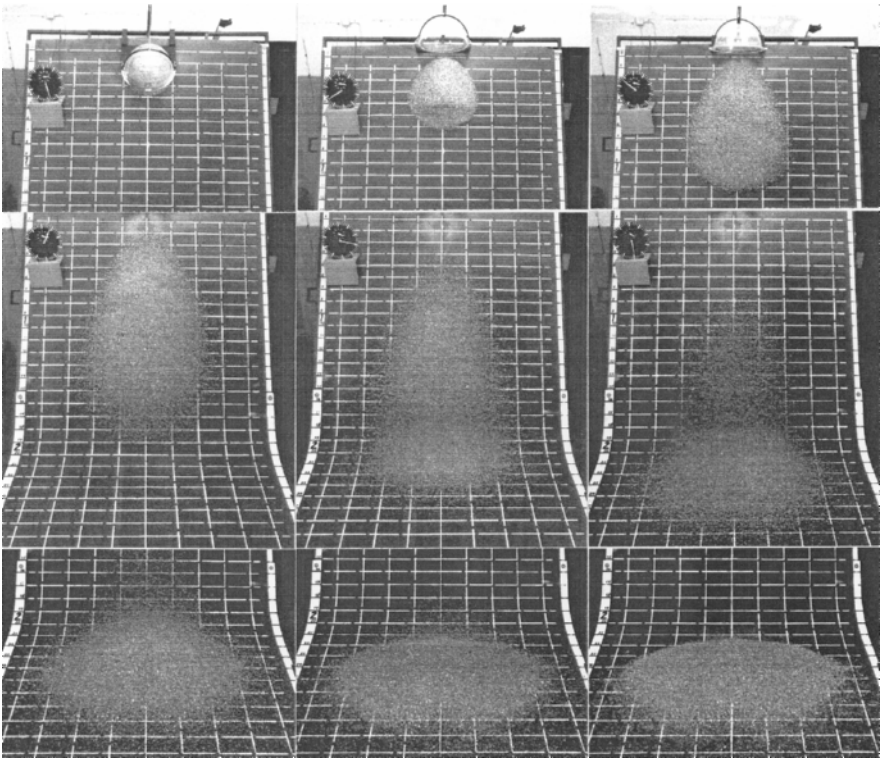

Fig. 10.26. Sequence of snapshots of an experiment with quartz granules on a partly curved slide coated with SIA no. 120 sandpaper. Time interval between subsequent shots is approximately 0.2 s and ≈ 1.98 in dimensionless representation. The inclination angle in the acceleration zone is $\zeta_0 = 45°$, the friction angles are $\delta = 29°$ and $\phi = 39°$. (From [227].)

is certainly violated in this domain. To summarise, the agreement between the motion of the experimental granular avalanches and the numerical calculations performed with the two-dimensional LAGRANGEan finite difference scheme of the model equations is surprisingly good [227].

Further comparisons were performed for different materials and different bed linings (see KOCH [226] and KOCH et al. [227]) with similarly convincing results. Only the relatively large spreading due to the bouncing of individual particles is somewhat concerning. It is less violent in snow avalanches, because the coefficient of restitution is considerably smaller for snow than for the experimental particles.

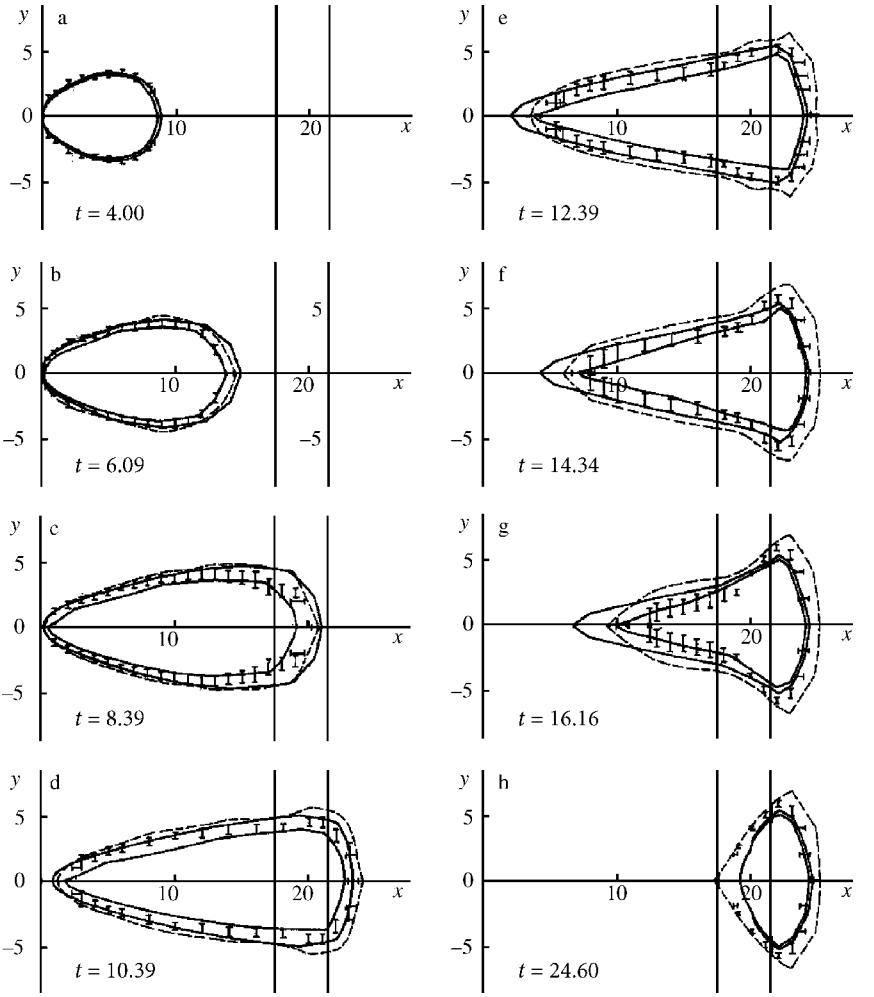

Fig. 10.27. Time series of numerical and experimental positions of an avalanche on a curved bed with marble chips. The motion is from *left to right* and the horizontal axis is the unrolled arc length along the steepest descent. Each panel represents a snapshot of the in-surface projection of the moving pile in consecutive order numbered from (**a**) to (**h**). The slide is plane and inclined at $\zeta = 45^\circ$ to the left of the *first vertical line* and to the right of the *second vertical line* lies the horizontal plane; in between the cylindrical transition zone. *Solid lines* represent the computed contour at zero height and the height of one particle diameter. *Symbols* represent the location in the experiment where the bed is covered at least by one particle and *dashed lines* indicate, where, experimentally, the bed is half covered by particles and half free (50% areal coverage). The variables x, y and t are all dimensionless. The bed and internal angles of friction are $\delta = 35^\circ$ and $\phi = 42^\circ$, respectively. (From [227].)

10.4 Channelised Avalanche Flows

Chutes provide maximum confinement, almost giving rise to plane flow, sliding surfaces without sidewise curvature exhibiting no confinement; channelised flow, for which the sliding surface has a sidewise curvature lies in between these two extremes. Flow down a sliding surface that is a straight parabolic channel down an inclined plane merging into a horizontal plane may be considered a first step towards the description of a granular flow over complex basal topography. Figure 10.28 shows such a model and experiment for a table-top demonstration. A laboratory experiment on a chute with a geometry much like that in Fig. 10.28 has been performed to test the validity of the theoretical model in this more complicated situation. A simple reference surface is defined, which consists of an inclined plane ($\zeta = 40°$) that is connected to a horizontal run-out zone ($\zeta = 0°$) by a cylindrical transition zone (see Fig. 3.9). The x-axis is aligned with the direction of steepest descent of the reference surface and the y-axis points in the cross-slope direction. Superposed on the inclined section of the chute is a shallow parabolic cross-slope topography, $b = y^2/(2R)$ with $R = 110$ cm, which forms a channel that partly confines the avalanche motion. The inclined parabolic chute lies in the range $x < 175$ cm, the plane run-out zone lies in the range 215 cm $< x <$ 320 cm and the transition zone smoothly joins these two regions. The partly confined chute channels the flow and results in significantly longer maximum run-out distances than in an unconfined chute. Below we discuss the results of Gray et al. [123].

The experiment (V02) was performed with quartz chips of a mean diameter of 2–4 mm (quartz 0), an internal angle of friction, $\phi = 40°$ and a basal friction angle, $\delta = 30°$. The granular material was released from rest on the parabolic inclined section of the chute by means of a cap having the form of a hemispherical surface and fitted to the basal chute topography. Figure 10.29 shows that, once the cap is opened, the avalanche accelerates and spreads rapidly in the downslope direction, while it is channelled by the parabolic cross-slope profile. As the avalanche enters the run-out zone, it decelerates rapidly and is able to spread out laterally once the partial confinement of the topography ceases. The avalanche comes to rest after 1.79 s.

Figure 10.30 shows a comparison of the marginal curves of the experimental avalanche with the computed topography (shaded area), demonstrating that the computed speeds of the rear part of the avalanche are considerably underpredicted. The last panel in Fig. 10.30 also shows that the experimental avalanche has come to rest while the rear part of the computed avalanche is still in motion. The most likely cause for this slow tail motion is that the basal sliding law is considerably more complicated than simple Coulomb dry friction with a constant bed friction angle.

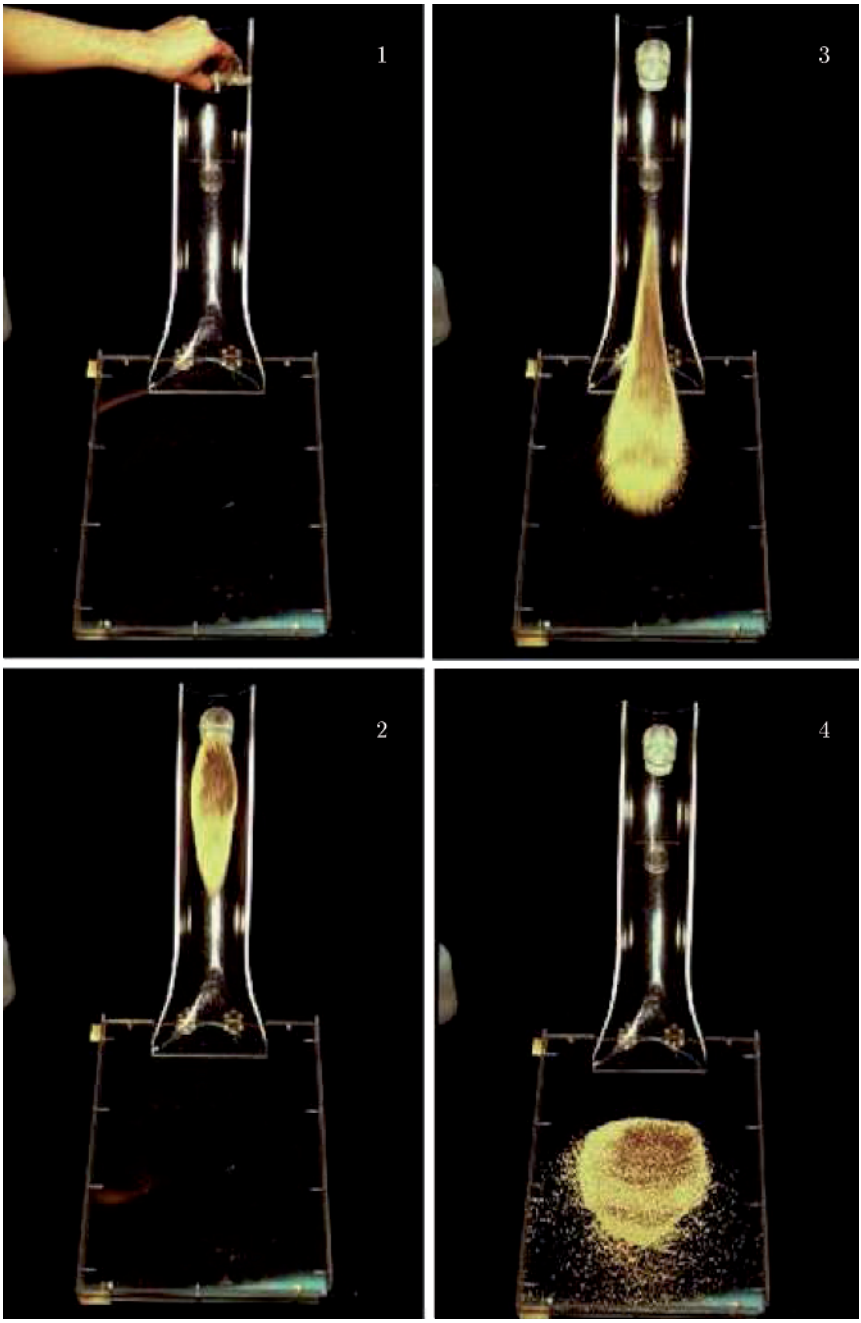

Fig. 10.28. Plexiglass model of a straight parabolic channel at a given inclination angle merging into a plane. Avalanching motion of a bidisperse granular material from beginning to deposit. (For more details, see Fig. 2.6). (From [411].)

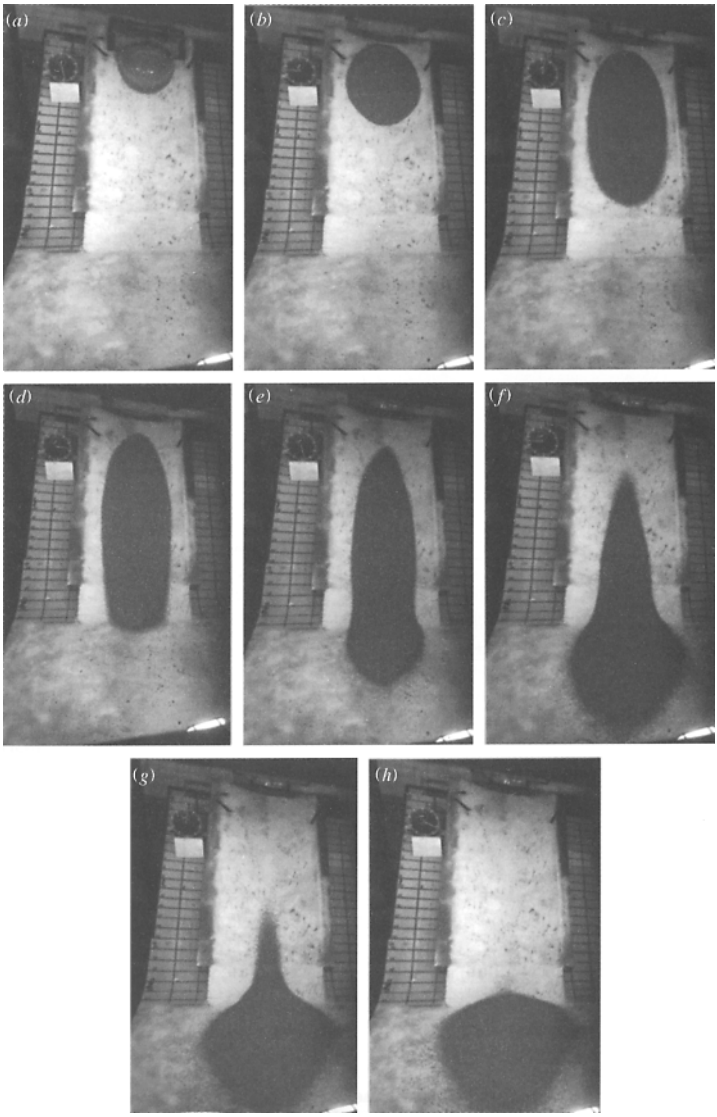

Fig. 10.29. An experimental image sequence from experiment V02 showing the deformation of the avalanche at approximately equally spaced time intervals of 0.25 s. The sequence begins at (**a**) and ends at (**h**). The parabolic channel and run-out plane are constructed from sheet steel and the smooth transition is made from wood and modelling plaster. The entire chute is painted to give it an even finish. The *sparkles in dark colour* are necessary requirements for photogrammetric processing. (From [123].)

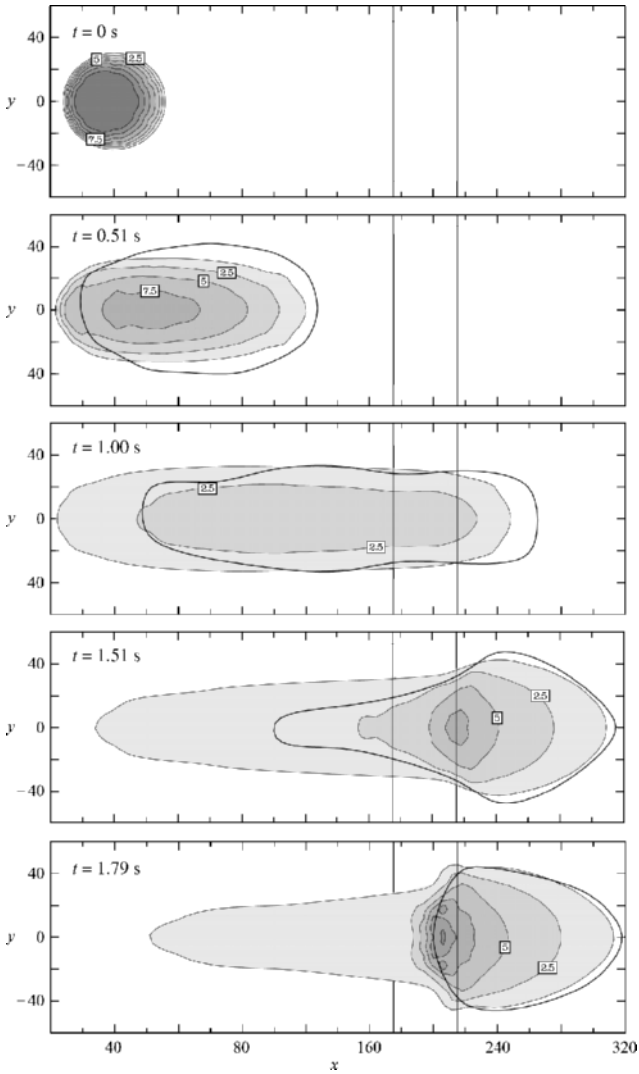

Fig. 10.30. The computed avalanche thickness is illustrated at five time intervals using "unrolled" projected curvilinear coordinates (x, y). Contours of equal thickness are indicated in cm and thickness ranges are *differently shaded*. The time is indicated in the *top left-hand corner* and all lengths are in cm. The *solid lines* at $x = 175$ cm and $x = 215$ cm indicate the position of the transition zone. The 40° inclined parabolic section lies on the *left* and the horizontal plane on the *right* of each panel. The line $y = 0$ is the talweg. The *thick solid line* indicates the position of the avalanche edge in the laboratory experiment (V02), determined from photographs. (From [123].)

In order to demonstrate that a change in the bed friction sliding law can at least qualitatively bring theory and experiment into agreement, the numerical computations have been repeated using a variable bed friction angle. In the front quarter of the avalanche the bed friction angle is constant as before, but linearly reduced in the rear according to

$$\delta = \begin{cases} \delta_0, & x \geq x_f - \dfrac{1}{4}(x_f - x_r), \\ \delta_0 - m_\delta \left((x_f - x) - \dfrac{1}{4}(x_f - x_r) \right), & x < x_f - \dfrac{1}{4}(x_f - x_r), \end{cases} \tag{10.9}$$

where $\delta_0 = 30^\circ$ is the constant bed friction angle, $m_\delta = 10^\circ\ \mathrm{m}^{-1}$ is the bed friction reduction factor and x_f and x_r are the positions of the front and the rear of the avalanche, respectively. The avalanche thickness distributions computed by using the modified bed friction relation (10.9) are illustrated in Fig. 10.31. The reduced bed friction angle in the avalanche tail allows the rear of the avalanche to accelerate more rapidly under the action of gravity and the agreement with the experimental boundary is considerably better.

Wieland et al. [445] performed a series of laboratory experiments on the channelised free surface and the variable bed friction angle (10.9) as described above. They extensively discussed the experimental procedures, the basal topography, initial conditions and measurements, as well as numerical techniques. Here, we will explain one of these experiments and its comparison with numerical computations. For example, experiment (V05) was performed with round plastic beads (Vestolen) with a mean diameter of 2–3.5 mm, a basal angle of friction, $\delta = 27^\circ$, and an internal angle of friction, $\phi = 33^\circ$. The experimental pictures are similar to those of Fig. 10.29, so we will not repeat them here. In Fig. 10.32, the computed thickness is illustrated at the time steps as shown in this figure, and the bottom right panel shows a comparison with the final thickness distribution, which agrees very well with that predicted (immediately) above.

The above-reported comparisons between experiments and numerical predictions were conducted using the Lagrangean integration technique for the (3.33), (3.43) and (3.44) in non-conservative form. Agreement has been good even for cases in which rapid changes, i.e., steep gradients in the topography of the moving avalanche occurred. An example is experiment V04, performed with marble chips with a mean diameter of 2–4 mm. These have quite a pointed geometry and their surface is considerably rougher than that of the plastic beads. As a result, there is much more interparticle and basal friction, which is reflected in the higher internal, $\phi = 43^\circ$, and basal, $\delta = 33^\circ$, friction angles.

Figure 10.33 shows computed results of avalanche thicknesses for the avalanche from initiation to run-out demonstrating in the panel for $t = 16.8$ and

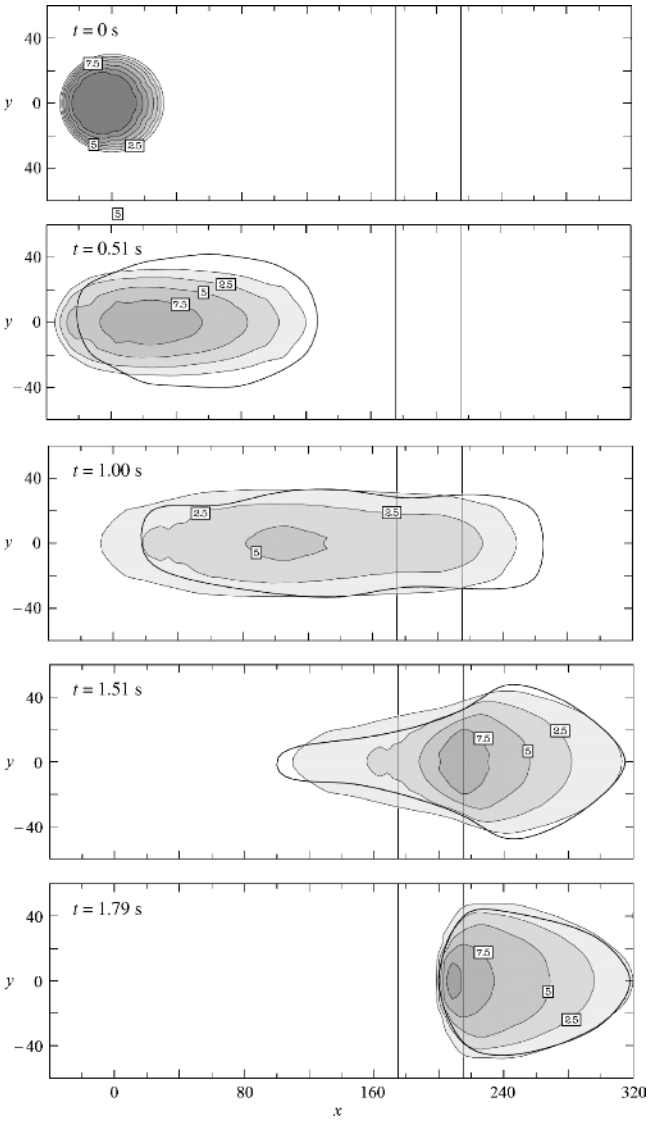

Fig. 10.31. Same as in Fig. 10.30, but avalanche thickness are computed by using the modified basal angle of friction (10.9) and a comparison with the experimental avalanche boundary (V02). (From [123].)

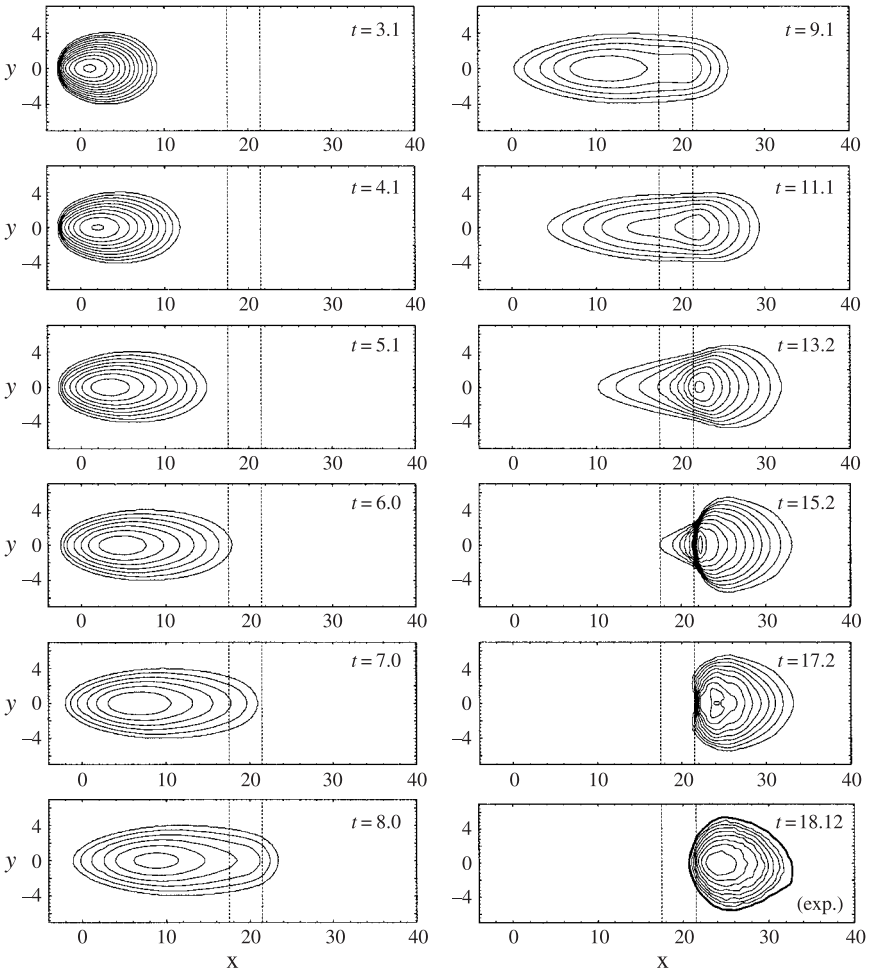

Fig. 10.32. Computed dimensionless avalanche thicknesses for experiment V05 (Vestolen) are illustrated using contour intervals. The *vertical dashed lines* at $x = 17.5$ and $x = 21.5$ indicate the position of the transition zone with the 40° inclined channel to the *left* and the horizontal run-out plane to the *right*. In the *bottom right panel* the thickness distribution of the experimental avalanche is illustrated, which agrees very well with that predicted (immediately) above. (From [445].)

$t = 18.7$ that gradients of the topography in the rear part of the avalanche are very steep, most likely the sign of an internal shock. Thus, in further work shock-capturing integration techniques are used, see Chap. 12. The numerical scheme can also be used to demonstrate that sidewise confinement (here caused by the parabolic profile) narrows the geometry of the avalanche both in motion and at rest as evidenced in Fig. 10.34.

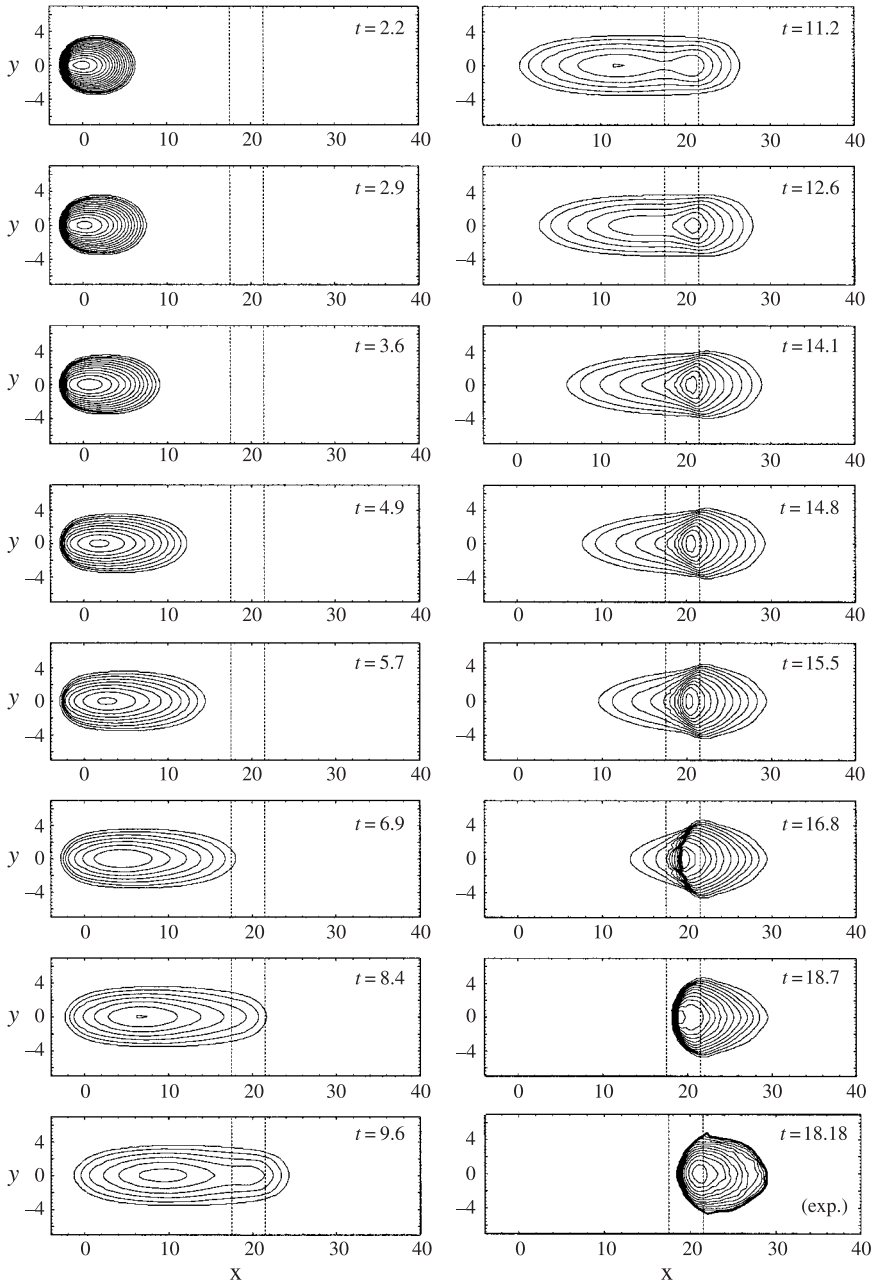

Fig. 10.33. Computed dimensionless avalanche thicknesses for experiment V04 (marble) are illustrated as in Fig. 10.32 using contour intervals. The final experimental thickness distribution is shown *bottom right*. (From [445].)

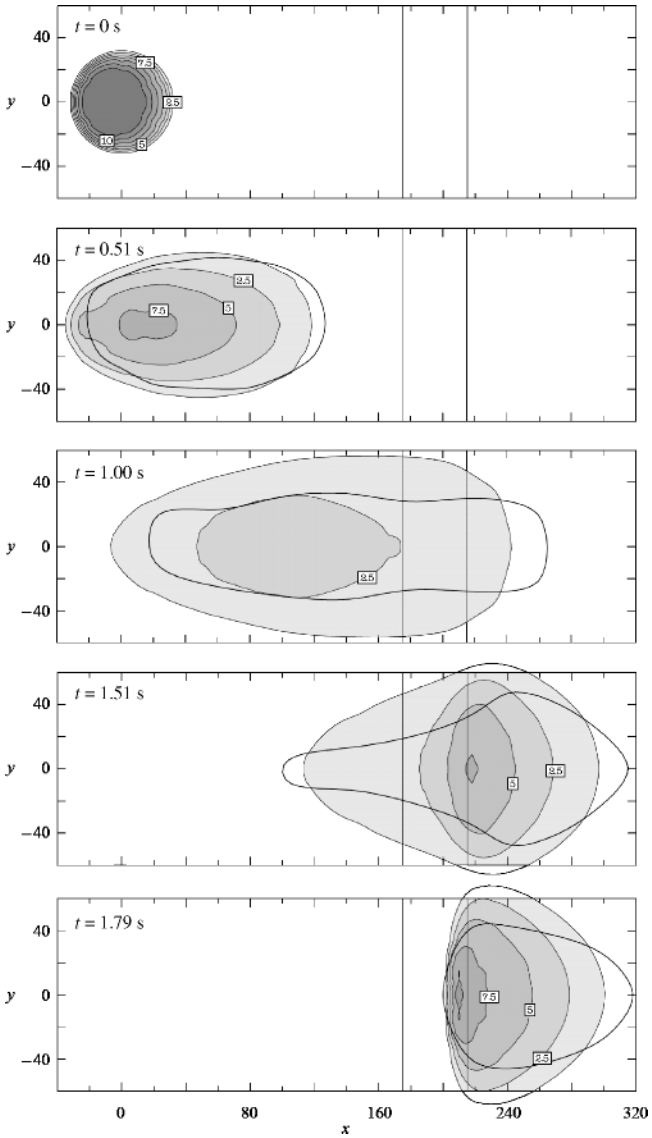

Fig. 10.34. Computed avalanche thickness on a chute without lateral confinement illustrated at a sequence of time steps. The *thick solid line* shows a comparison with experiment (V02), which has lateral confinement. (From [123].)

Shallow Water (Avalanche) Model It was pointed out earlier that the SH-equations or any one of their extensions are very similar in form to the shallow water equations of fluid mechanics. The theory differs, naturally, with respect to the coordinate system, the nature of the forcing terms and the drag relations. However, the major differences lie in the assumed constitutive properties and basal topographies. One-dimensional hydraulic avalanche models of this kind were put forward by EGLIT [87], but no numerical solutions have been performed in either one or two dimensions. It is, therefore, of considerable interest to determine how well the shallow water equations can describe the flow of granular avalanches over complex topography.

A two-dimensional shallow water avalanche model can be obtained by setting $K_x = K_y = 1$ and performing the computations under otherwise identical conditions. This was done for the conditions of experiment V02 and results of the computations are shown in Fig. 10.35. It is evident from this figure that under rapid dilatational motion the computed and experimental avalanche shapes do not differ considerably from one another; however the contracting computed avalanche differs substantially from that of the experiment. The travel distance is too short and the avalanche spread too wide. COULOMB *frictional behaviour is, therefore, very significant in catching the correct dynamical behaviour of the avalanche.*

It is worth mentioning that selecting earth pressure coefficients unequal to unity (i.e., $K_x \neq 1 \neq K_y$) is tantamount to accepting normal stress effects in the constitutive relationship. Following the retaining wall analogy, we assume that the smaller active value is associated with extensive motions and the larger passive value is associated with compressive motions with a jump traction between the two states when the downslope divergence is zero. This is assumed to be the standard behaviour in soil plasticity. It is interesting that an alternative hydraulic formulation with $K_x = 1 = K_y$ was suggested in the early Soviet/Russian literature by GRIGORIYAN et al. [130, 131, 132, 133], KULIKOVSKIY and EGLIT [230] and EGLIT [84, 87, 88, 90, 91]. This latter formulation was again taken up by GRAY et al. [126] who state that "to date, there is no compelling experimental evidence to suggest that such a sharp stress transition [the jump] actually takes place ...". They further state that "GRAY et al. [123] and GRAY [124] have found that this simpler model also gives promising results in steep flows and in industrial rotating drum flows". They then show computations of their numerical solutions with their experiments for granular bores and flows past a wedge-type obstacle, but no flow close to and forming the deposition in the run-out zone. Our own computations for the cases analogous but not identical to GRAY et al. [126], using $K_x \neq 1 \neq K_y$, show similar results in the rapid flow regime, see, e.g., Chap. 12, to GRAY et al., but we also reproduce the depository geometries, as shown in the last panel of Fig. 10.35 (corresponding to the experimental curve). We have no conclusive arguments to offer for this behaviour, but argue that

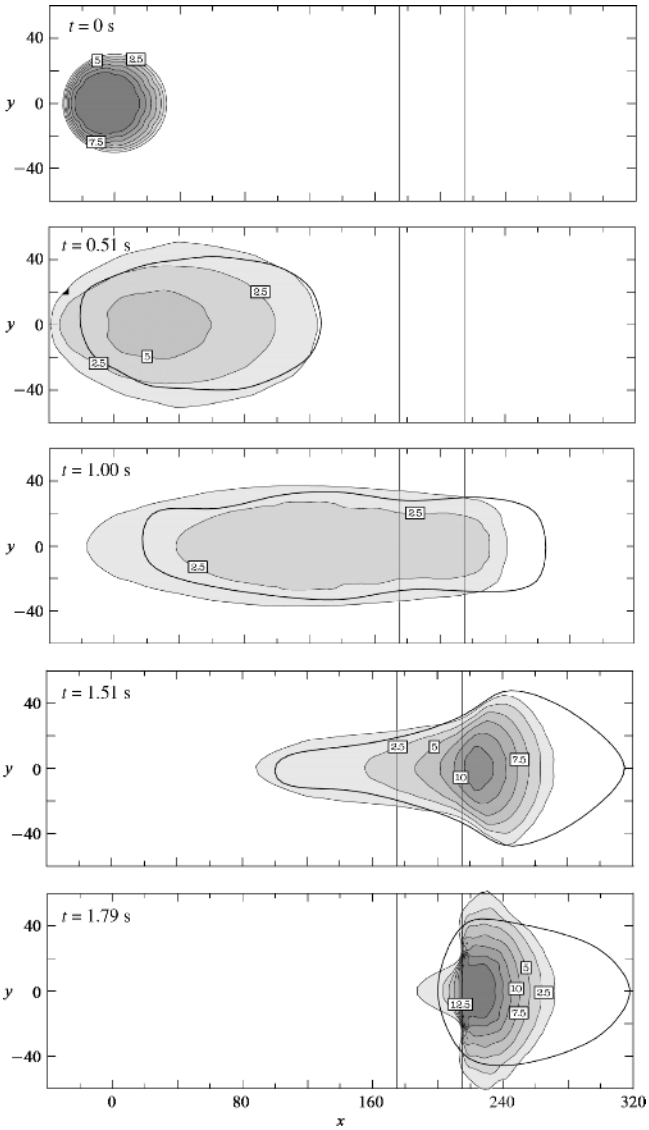

Fig. 10.35. Computed avalanche thickness using the shallow water avalanche model illustrated at a sequence of time steps for which V02-experiment photographs are plotted in *dark lines*. (From [123].)

normal stress effects are likely to play a significant role when the avalanche transits into the depository mode. Here, further research is certainly required.

A Laboratory Gully Model So far all talweg geometries were curves in vertical planes following the direction of steepest descent. This allowed the fastest downhill motion into the run-out zone. Figure 10.36 shows a laboratory gully for simulations of granular avalanches where the talweg deviates sinusoidally from the direction of steepest descent. The parabolic channel merges after 240 cm into the horizontal plane in the foreground and thereby gives up the parabolic profile. A mixture of sand and gravel (40 kg) is released from a hemispherical plexiglass cap and moves down the gully, obviously while being diverted by the sidewise sinusoidal deviation of the talweg from the direction of steepest descent. The early longitudinal stretching and the formation of a tail that still moves when the front of the avalanche has already settled down are typical. Figure 10.37 displays a comparison of this experiment with computational results, also using the LAGRANGEan integration technique developed in GRAY et al. [123]. Comparison between theory and experiment is fair to good.

10.5 Avalanches Across Irregular Three-Dimensional Terrain

The above laboratory experiments were all concerned with "academic" (laboratory) situations, i.e., idealised geometries of basal topographies that allow not only straightforward chute construction in the laboratory but also controlled performance of experiments and, perhaps, easy identification of causes for the observed behaviour. The ultimate test of the theory is, however, obtained with the motion of granular materials across irregular three-dimensional terrain. There are complications associated with such flows; the experimental techniques are generally more involved and the results more difficult to explain, since certain peculiar behaviour may not be correlated to a single identifiable cause. Such laboratory experiments have been conducted at the Cascade Volcano Observatory of the US Geological Survey (USGS) by IVERSON and associates on two different scales: (*i*) table-top experiments of approximately 1.2 m length (see Fig. 10.38) and (*ii*) outdoor flume experiments of 95 m length and 31° inclination plus approximately 10 m horizontal deposition area. In a series of papers, both dry and water-saturated granular materials were analysed, [74, 75, 191, 192, 194]. Here we only report on the table-top experiments conducted with dry granular materials. Analogous experiments were also performed by MCDOUGALL and HUNGR, PATRA et al. and PITMAN et al. [273, 274, 313, 322]. Some of their findings will also be reported here.

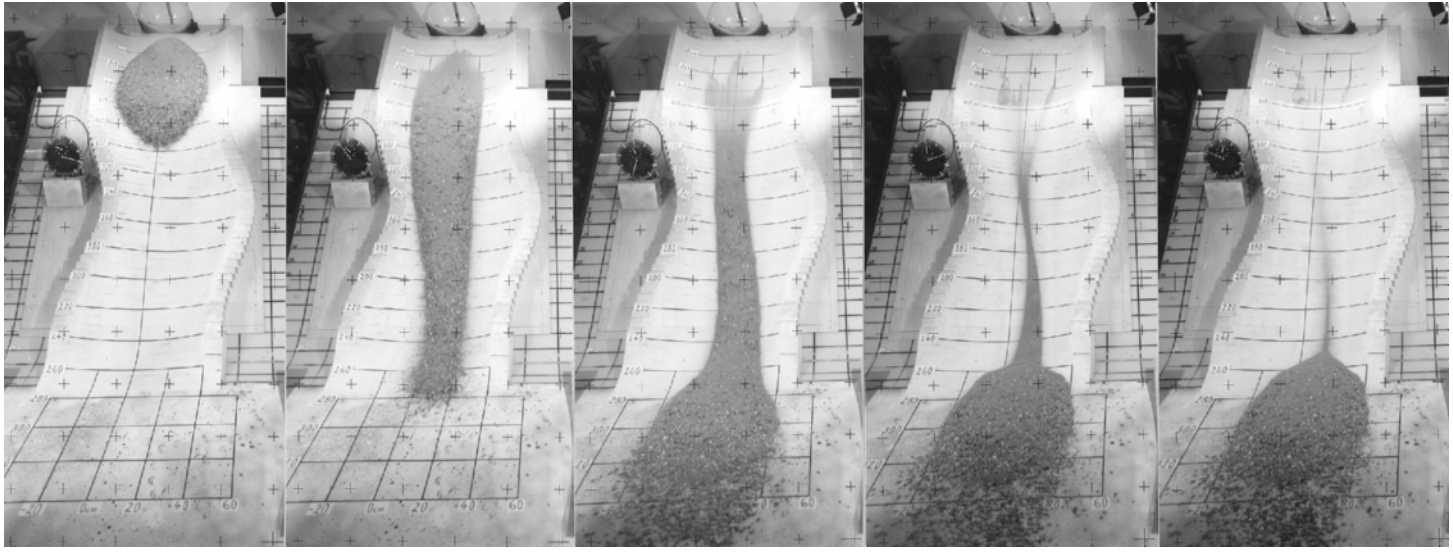

Fig. 10.36. Laboratory gully for simulations of granular avalanches. On a plane inclined by 40° against the horizontal a parabolically shaped channel is mounted where the talweg deviates sinusoidally from the direction of steepest descent. A mixture of 40 kg sand and gravel is released from a plexiglass hemispherical cap at the upper edge of the channel. A clock on the left in the pictures measures the time; its arm performs one revolution per second. The photographs show five shots of the moving avalanche. Note that the originally well-mixed gravel mass is demixed with the coarse particles in the front and the small ones in the rear. (From [121].)

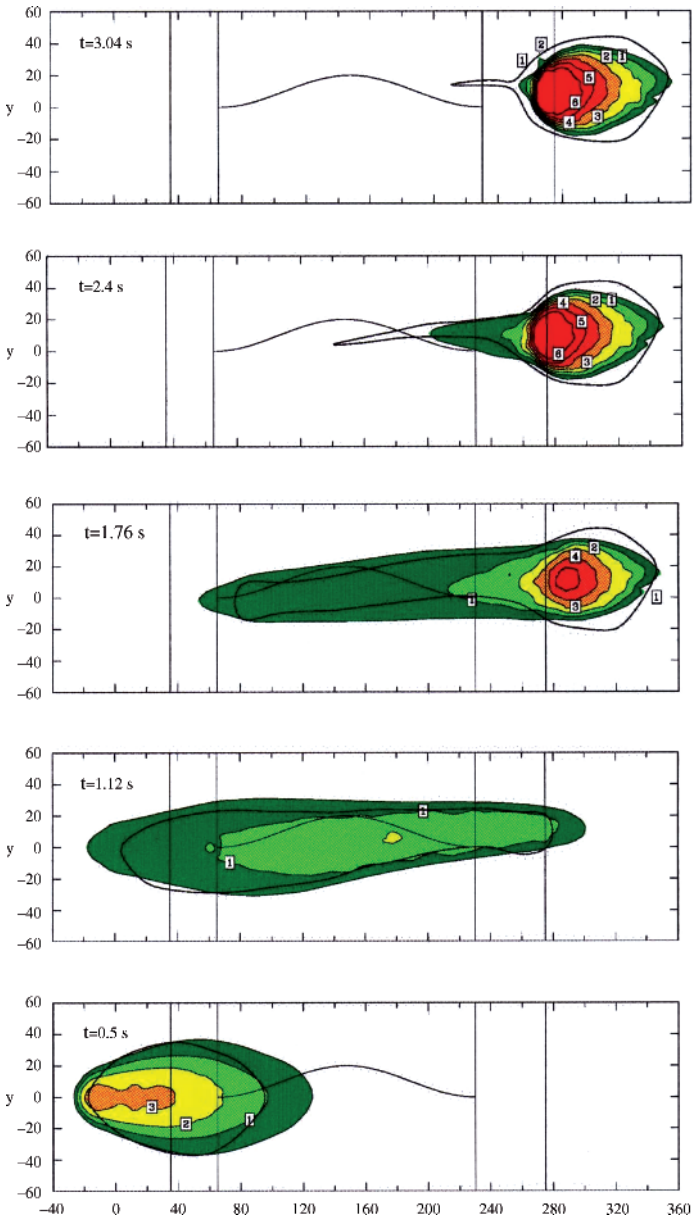

Fig. 10.37. Plane view of the unrolled chute of Fig. 10.36 with the avalanche motion from *top* to *bottom*. The *horizontal lines* show where the sinusoidal talweg begins (above at $x = 65$ cm), ends (at $x = 230$ cm) and where the horizontal plane begins (below $x = 275$ cm). The times in the panels indicate the moments since the avalanche was released from rest. The graphs show the topographies in different shadings (with numbers indicating the thickness in cm), as obtained via numerical computations. The *black solid line* shows the margins of the avalanche piles as declared from the photographs. (From [121].)

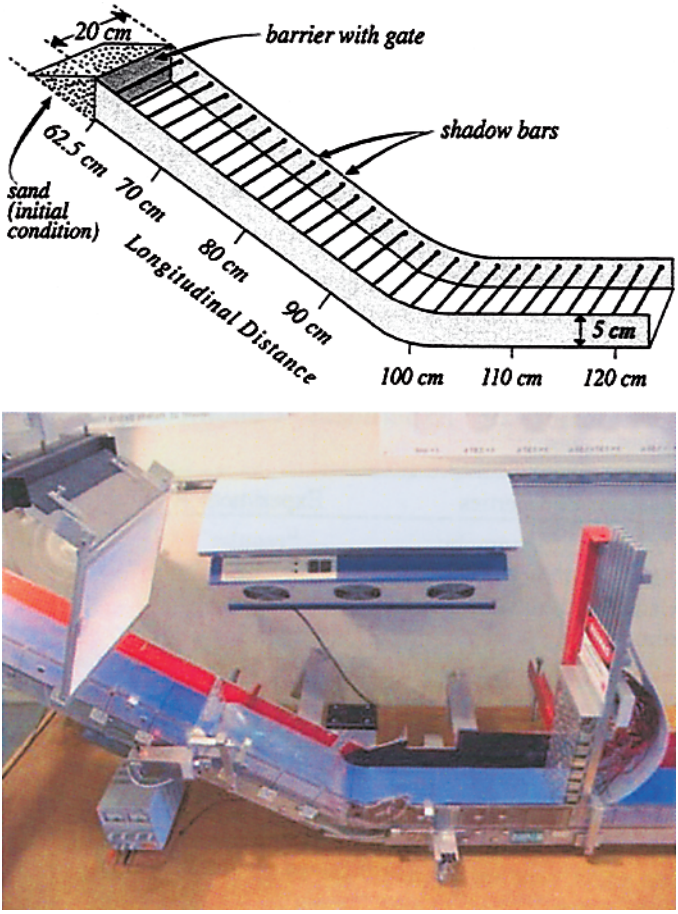

Fig. 10.38. Schematic (*top*) and photograph (*bottom*) of the miniature flume used by IVERSON et al. to construct dry avalanche experiments. (From [74, 194].)

10.5.1 The Table-Top Experiments

IVERSON and collaborators used data from small-scale experiments of dry sand. They employed a rectangular flume with a bed of 31.6° inclination, merging via a curved section with a 10 cm radius of curvature into a horizontal run-out surface. In each experiment dry quartz sand with grain diameters $\approx$ 0.5 mm was placed behind a vertical wall, positioned 37.5 cm upslope from the entrance to the horizontal run-out plate. The sand was arranged behind the gate to form a triangular cone (i.e., wedge-shape) with a horizontal surface and then discharged suddenly by opening a spring loaded gate. In one type of experiment the gate spanned the entire flume of 20 cm width,

and in a second type it spanned a slot, 4 cm to 12 cm wide in the centre of the flume. Two bed linings were used. One was simply a planar inclined surface merging into a horizontal plane, and the three dimensionality of the flow was reached by releasing the material through a slot gate smaller than the flume width. In the other, the steep part of the flume was fitted with a custom-formed insert that provided an irregular surface. Rotation of the insert enabled experimentation with two distinct topographic configurations of the chute and the kind of materials used as surface coatings. Precautions had to be taken to avoid electrostatic adhesive forces between the grains and the bed linings. Details as to how the gate, holding the material in its initial position, was opened to initiate the motion are not presented here.

The data acquired in the avalanche experiment consisted of sequential photographic snapshots of the avalanche geometry, recorded in vertical photographs. The three-dimensional geometry of the avalanching masses was mapped by using the following cartographic technique. Horizontal sheets of light from refracted laser beams were projected onto the bare bed (for calibration reasons) and the moving granular mass at 5 mm intervals. The form of the illuminated lines allowed, via post-data processing, the construction of the digitised height distribution of the moving granular mass at the time slices when photographs were taken[7] (see Fig. 10.39).

In what follows we only report on a fraction of the results reported in Denlinger and Iverson [74] and Iverson et al. [194]. Figure 10.40 illustrates results for the flow of quartz grains with 0.1–0.5 mm diameter down an inclined plane from an initial wedge-shaped silo through a 4 cm wide gate in the middle of the 20 cm wide flume. The left column displays isopachs (lines of equal thickness) at 1 mm intervals as revealed from the experiments, the right column shows those computed from the theory and its numerical implementation.[8] "The narrow gate impeded sand discharge and caused pro-

[7] In our own experiments we used methods of photogrammetry but the implied experimental method did not achieve sufficient accuracy except in the standstill deposit, see Wieland et al. [445]. The light sheet method was also used by McDonald and Anderson and Pouliquen and Forterre [271, 330].

[8] The theoretical model on which the numerical method is based does not match the SH-type equations (see [74]). For instance, the equations are referred to the horizontal and vertical directions of a Cartesian coordinate system and define the shallowness with respect to the vertical direction. For this reason, the hydrostatic pressure assumption in the z-direction cannot be maintained, and vertical acceleration needs to accommodate for the fact that the flow is guided by the inclined surface. Furthermore, Denlinger and Iverson [74] use an earth pressure closure different from ours. All these differences make it rather difficult to identify the true differences of the two models. Computationally, Denlinger and Iverson use a shock-capturing finite volume/finite element procedure in which the flux discretisation is based on a wave propagation form of Godunov's method as outlined by LeVeque [250]. This difference in the

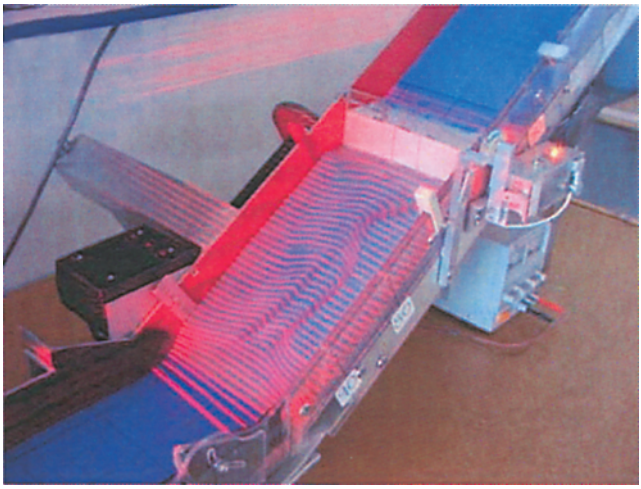

Fig. 10.39. Miniature flume used by IVERSON et al., illuminated from the left by horizontal light sheets. Each light sheet generates an illuminated line on the surface of the topography from which the topography of the moving granular avalanche can be constructed. (From [194].)

nounced cross-slope momentum transport as the flow converged and thus divided while passing through the gate opening. Frictional energy dissipation associated with this convergence and divergence caused the flow to move [as a slow thin sheet]" [192]. Completion of the deposit required approximately 5 s, which is relatively long and due to the slow and continuous mass release from the granular wedge through the gate. DENLINGER and IVERSON [74] state that the model predictions compare well with the results. We quote from their paper [194]:

"Flow timing, depth and depositional pattern all match approximately. The largest discrepancies between model predictions and data occur as a result of very thin flow (≈1 grain diameter thick), where the COULOMB continuum model is inappropriate. For example, much of the upward tapering margin of the measured deposit resulted from accumulation of saltating grains, which are not simulated by the model. Despite such discrepancies the final deposit shape and time of deposition shown in Fig. 10.40 exhibit relatively small errors. Model predictions for the narrow gate leave sand stranded behind the vertical barrier at 62.5 cm, just as measured in experiments. However, the model predicts that the heap of sand behind the gate undergoes smoothing and stretching due to numerical creep that results from imperfect balancing of static driving and resisting forces. The same numerical creep allows a trickle

numerical solution procedure in comparison to our own is probably less critical than the differences in the theoretical approaches.

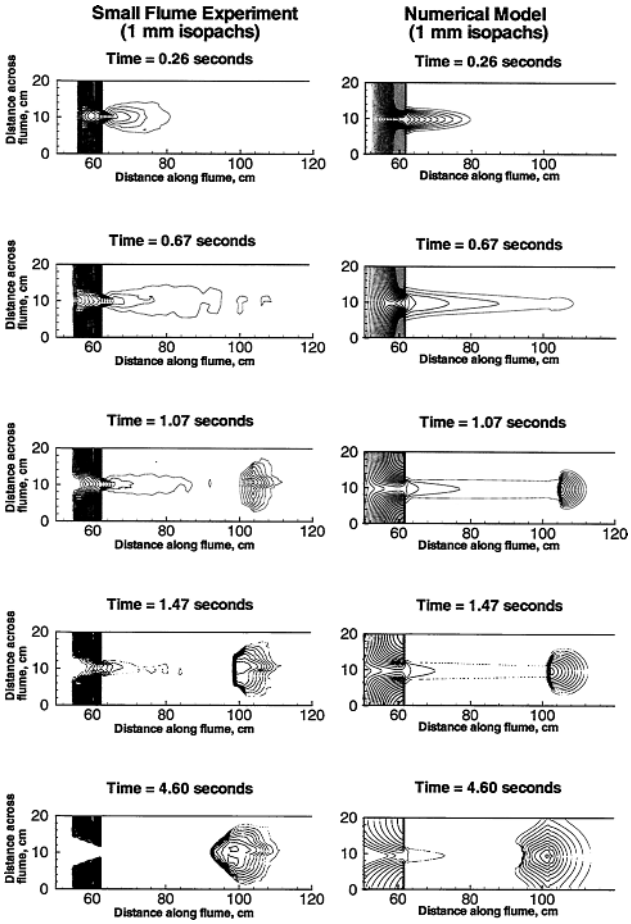

Fig. 10.40. Maps of sand comparing experimental data and model predictions for flow of dry sand released instantaneously from a 4 cm gate in the experimental set-up of Fig. 10.38. The basal surface was an inclined plane (31.6°) merging into a horizontal plane. The gate opened at time zero and contours depict 1 mm isopachs of sand thickness normal to the bed. The *left column* shows the experimental results and the *right column* the computed ones. (From [74].)

of sand to escape from behind the barrier even after deposition has effectively ceased, but this shortcoming has little effect on the final deposit geometry".

Judging visually the isopach sequences of Fig. 10.40 between the experiments and the numerical output, it is probably fair to say that the principal characteristics of the avalanche evolution are adequately reproduced by the model. The final deposition of the computed avalanche is larger in its areal extent in the computational results than in the experiment. The cause for this might

be that the erosion of the wedge and the funnel formed immediately above the gate must be different in the experiment and the computations. A better judgement of the performance of the model will most likely result from controlled initial conditions.

In Fig. 10.41 we compare computational results from our model equations (PUDASAINI et al. [342]) with the measurement data of DENLINGER and IVERSON [74] where the gate of the channel spanned the entire flume of 20 cm width in which 1 mm contour isopachs are plotted normal to the bed surface. Comparison is made at five time slices that include the entire avalanche motion. The most important aspects of the model performance can be seen when comparing the panels on the left and right columns. In both cases, it took 1.5 s for the mass to complete deposition. Predicted timing, depth, geometry, front and tail positions, and final deposit of the granular sand fit almost exactly with the measured data of DENLINGER and IVERSON. Conspicuous boundary layer effects, mainly in the tail side of the debris body, can be seen at time 0.93 s in the experimental result. Otherwise, this effect is small or likely to be negligible. Shocks form at the tail side of the body in the deposits, as seen at times 0.93 s and 1.50 s in the experimental panels. They are accurately predicted by our model simulations. Qualitatively, similar results were also obtained by DENLINGER and IVERSON, [74].

IVERSON et al. [194] also conducted experiments with the miniature flume when its steep part was filled with an urethane insert that provided an irregular basal surface. Their paper reports on two experiments with grain diameters of 0.5–1.0 mm and 0.25–0.5 mm and head gate widths of 12 cm and 4 cm, respectively. We only report here about the second experiment and give the results from computations. Except for the addition of the irregular topography in the steep part of the flume, experimental conditions are the same as stated before.

Figure 10.42 shows time slices of the avalanche evolution for the experiment (left) and as determined by the authors' numerical implementation (right); details are described in the figure caption. Model predictions match many of the details as well as the overall behaviour of the avalanche in experiment. The effects of topographic forcing on the three-dimensional form, and lateral limits of the avalanche are well-predicted, especially at early times. At $t \geq 1.0$ s "differences in the geometry of observed and computed deposits result largely from dispersal of the distal margin due to sand saltation in the experiments" [194].

IVERSON et al. [194] express their opinion that their model offers advantages over the SH-equations through the more flexible three-dimensionality and their use of continuous change of the earth pressure coefficients. They also state that "the accuracy of their predictions lends support to the SAVAGE and HUTTER [375] hypothesis that a simple COULOMB proportionality ($\tau =$

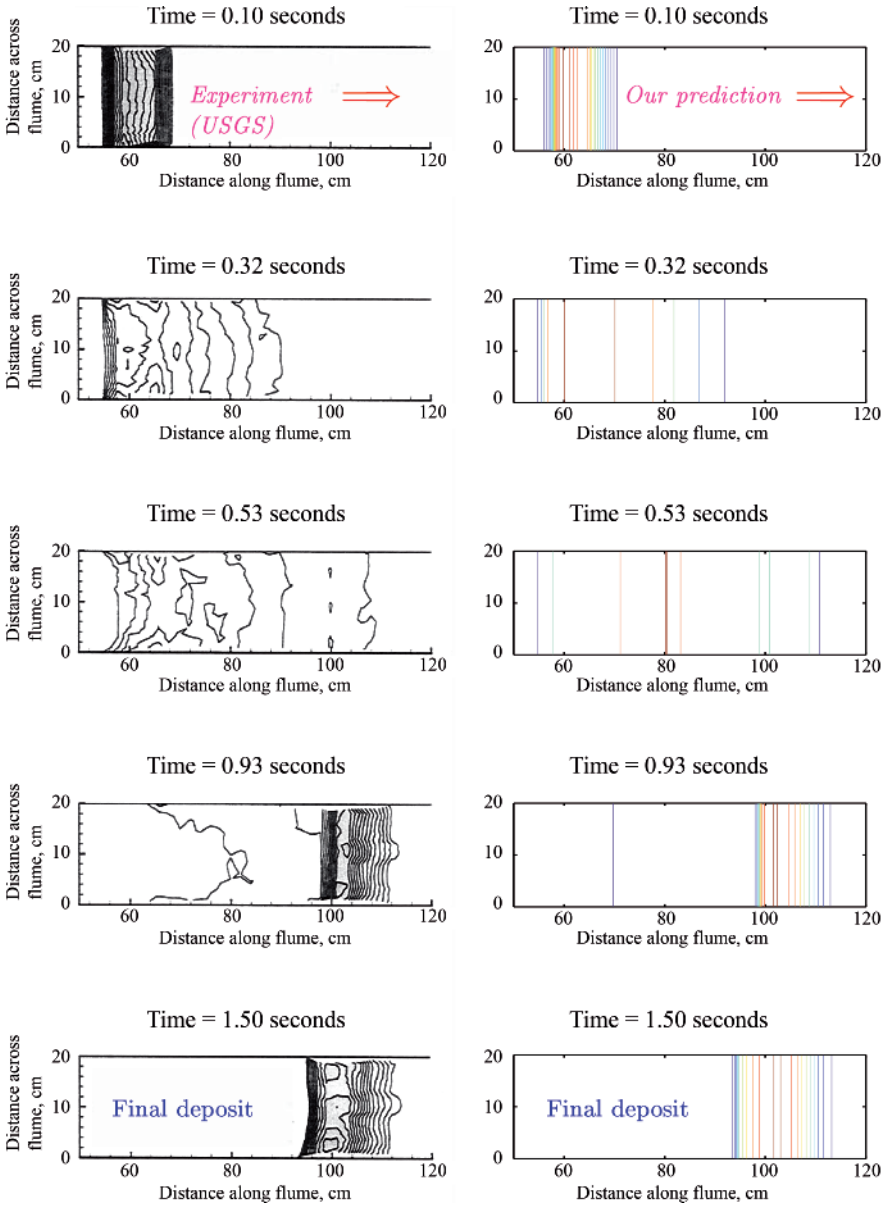

Fig. 10.41. Maps of sand comparing experimental data and model predictions for flow of dry sand released instantaneously from a 20 cm gate in the experimental set-up of Fig. 10.38 (*top panel*). The basal surface was an inclined plane (31.6°) merging into a horizontal plane. The gate opened at time zero and contours depict 1 mm isopachs of sand thickness normal to the bed. The *left column* shows the experimental results [74], the *right column* the computed ones [342]. (From [74] and [342].)

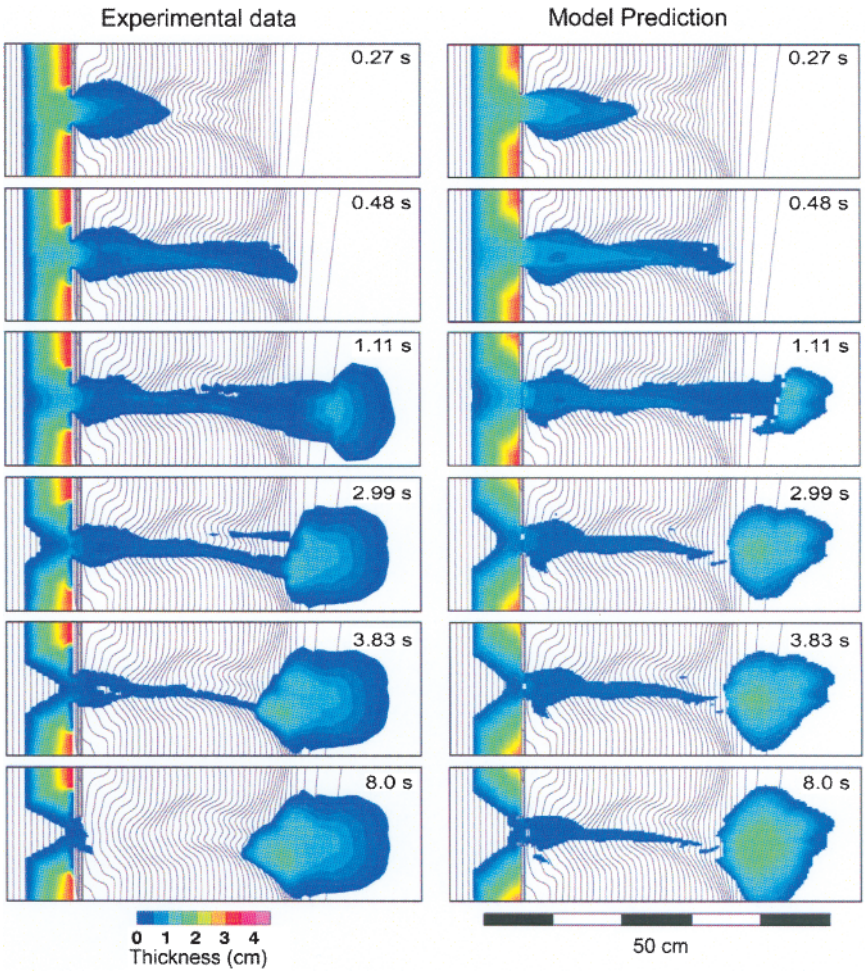

Fig. 10.42. Isopach maps of the vertical avalanche thickness h, comparing data (*left*) and model predictions (*right*) for experiment (B) in IVERSON et al. [194]. The aperture width of the flume is 4 cm, the shape of the quartz grains is rounded with 0.25–0.5 mm diameter, the sand mass is 476.5 g, the basal friction angle of the sand on urethane is $22.45 \pm 0.66°$ and the internal friction angle is $39.39 \pm 0.23°$. The head gate is opened at $t = 0$ s. (From [194].)

$\sigma \tan \phi$) between shear stress τ and normal stress σ is a robust feature of granular avalanches. This finding may seem surprising", since typical shear rates in this experiment are $u/H \approx 200\ \mathrm{s}^{-1}$, which is considerably larger than shear rates that may be typical of most geophysical avalanches (IVERSON and VALLANCE [193]) and are far longer than the shear rates of classical quasi-static COULOMB behaviour. This finding also agrees with the corresponding

findings of Ancey and Meunier [7] deduced from snow avalanche back analyses and discounts the conjectural approach of Gray et al. [126], who advocate a classical hydraulic approach.

10.5.2 Further Verification of the Model Equations

The Geotechnical Engineering Group at UBC Almost simultaneously with the developments of the model equations of the research group at the US Geological Survey, Hungr and associates from the University of British Columbia developed their own continuum model and verified it with laboratory experiments and with a back analysis of the Frank Slide, Turtle Mountain, Canada, that claimed 70 lives in 1903. Papers of significance are [163, 164, 165, 166, 167, 168, 169, 273, 274]. The derivation of the model equations that reduce essentially to the SH-type equations are presented by McDougall and Hungr in [273]. This paper also presents the integration scheme for numerically computing avalanche flow on arbitrary topography and compares the results with photographs from laboratory avalanches and a large-scale landslide. McDougall and Hungr aim at the derivation of a model obeying the following requirements [273]:

- "The model should allow for non-hydrostatic, anisotropic[9] internal stress, which may be controlled by an internal rheology different from the basal rheology.
- It should allow for entrainment of material along the slide path.
- It should allow selection of a variety of material rheologies, which can vary along the slide path and/or within the slide mass.
- It should permit very long displacements and possible branching or decoupling of the slide mass.
- It should be user-friendly and efficient in order to facilitate rapid back-analysis and extensive calibration against real events."

Their paper is an attempt towards this end; they acknowledge that the models of Iverson [191], Iverson and Denlinger [192] and Denlinger and Iverson [74] that incorporate constitutive relationships adapted from grain-fluid mixture theory have successfully simulated controlled flume experiments, but they also express their desire for a simpler semi-empirical approach based on the concept of the "equivalent fluid", defined by Hungr [163] and used tacitly,

[9] What is meant here is the deviation of the total stress from the isotropic fluid stress that is expressible as a pressure alone. This is contrary to the assumption of fluid behaviour in the Russian literature [84, 85, 86, 87, 130, 131, 132, 230] and in the more recent literature, Gray et al. [126]. This requirement of an anisotropic stress tensor exhibiting normal stress effects is deeply rooted in experimental evidence of soil mechanics and has indirectly also been corroborated by the results displayed in Fig. 10.35 [123].

e.g., by a number of other researchers (see, e.g., SOUSSA and VOIGHT [401], O'BRIEN et al. [305], RICKENMANN and KOCH [355]).

The derivation of the governing equations follows an ad hoc engineering approach, uses in each point a local Cartesian coordinate system, employs the hydraulic pressure assumption and incorporates entrainment of material from the ground. Interestingly, in the hydrostatic pressure assumption, perpendicular to the base the centripetal acceleration due to the downhill velocity is accounted for. MCDOUGALL and HUNGR [273] consider with this exactly the dominant term of the CHRISTOFFEL symbols arising due to the curvilinearity of the coordinates. It agrees with the curvature term that survives in our formulation, when the shallowness approximation is introduced and only first-order and second-order terms in the shallowness parameter are retained.

The stress parameterisation in MCDOUGALL and HUNGR's [273] model is based on RANKINE's earth pressure theory and expresses $\sigma_{xx}, \sigma_{yy}, \tau_{xy}, ...$ in terms of σ_{zz} via

$$\sigma_{xx} = K_x \sigma_{zz}, \quad \sigma_{yy} = K_y \sigma_{zz}, \quad \tau_{xy} = K_{xy} \sigma_{zz}, ... \tag{10.10}$$

The earth pressure coefficients $K_x, K_y, K_{xy}, ...$ are defined by the tangential strain state prevailing within the deforming landslide. This strain state is described by the symmetric part of the (x, y)-components of the velocity gradient

$$\mathrm{symgrad}_{(x,y)}(u, v) = \begin{pmatrix} \dfrac{\partial u}{\partial x} & \dfrac{1}{2}\left(\dfrac{\partial u}{\partial y} + \dfrac{\partial v}{\partial x}\right) \\ \mathrm{sym} & \dfrac{\partial v}{\partial y} \end{pmatrix},$$

which approximately equals

$$\mathrm{symgrad}_{(x,y)}(u, v) \approx \begin{pmatrix} \dfrac{\partial u}{\partial x} & \sim 0 \\ \sim 0 & \dfrac{\partial v}{\partial y}, \end{pmatrix} \tag{10.11}$$

so that $K_{xy} \cong 0$. It follows that σ_{yy} is close to a principal stress, implying the same earth pressure coefficient as in all formulations of the SH-type equations considered in this book. The earth pressure coefficients used by MCDOUGALL and HUNGR now take forms for which asymptotic values are those of our theory. Nevertheless, the two formulations still differ slightly in the following respect. In the formulation of PUDASAINI and HUTTER and PUDASAINI et al. [335, 342] the approximation (10.11) is employed for x pointing in the direction of the talweg and y perpendicular to it, thereby ignoring the shearing γ_{xy}. Thus, the xy-shearing is assumed to be small in comparison to the stretchings $\partial u/\partial x$ and $\partial v/\partial y$. MCDOUGALL and HUNGR employ a more local

criterion for which their γ_{xy} is assumed to be negligible. Both procedures are approximations, but they are not the same. More correct than both would be to compute locally the eigenvalues and eigenvectors of $\mathrm{symgrad}_{(x,y)}(u,v)$ and to define these as directors for a local coordinate system and afterwards rotate everything back to whichever orthogonal coordinate system used. HUTTER has explicity spelled this out in [184].

The discretisation of the equations used by MCDOUGALL and HUNGR [273] is a LAGRANGEan integration technique as demonstrated in Chaps. 7 and 8. Their model follows the same discretisation approach as ours, but employs *a meshless technique* in which mass conservation is implicitly satisfied by interpolation. The method is based on smoothed particle hydrodynamics, which was developed for the simulation of astrophysical phenomena, see LUCY [256], GINGOLD and MONAGHAN [114], and has been adapted for depth-averaged analysis of free surface flows, see WANG and SHEN [438]. For reviews, see, e.g., BENZ [32] and MONAGHAN [286, 287]. We shall not go into any details here.

MCDOUGALL and HUNGR checked their program against the classical dam break problem (STOKER [405]), its generalisation that accounts for bed slope and basal friction (MANGENEY et al. [263]) and one of the two-dimensional experiments of GRAY et al. [123]. They found very good agreement with the analytical solutions of the first two and good coincidence with the experiment for the latter. They state that, since their model is not shock-capturing and a shock arises in the experiment, improvement may be achieved by adequately altering the numerical software.

Their laboratory experiment was a deflection run-out experiment conducted with dry polystere beads. In their own words [273]: "The material was released from a box onto a chute with variable slope (to control the approach velocity), ran out onto a 20° approach slope and was defected by a dyke oriented obliquely to the flow direction. The deflection angle, α_1 (plan angle between the initial direction of motion and the intersection of the dyke and approach planes), and the dyke dip angle, α_2, were variable. The sliding surface of smooth sheet metal was marked with a 10 cm square grid. A photograph of the laboratory apparatus is shown in Figure 10.43.

A simulation of an experiment configured with $\alpha_1 = 60°$ and $\alpha_2 = 33°$ is shown in Figure 10.44. The box used to contain and release the material at start-up could not be replicated by a digital three-dimensional sliding surface, due to its infinitely sloping sidewalls. Therefore, an imaginary release chute and the initial distribution of material were used by the model. By trial and error, the position, width and velocity of the simulated flow front were synchronised with the experiment at the start of the 20° approach slope. The model was calibrated to match the maximum run-up distance on the dyke plane using a frictional rheology with $\delta = 20°$ and $\phi = 25°$. These friction

Fig. 10.43. Photograph of the laboratory apparatus at the University of British Columbia used for deflected run-out experiments. (From [273].)

angles are within a small range of values measured in separate laboratory tests by placing a conical pile of beads on a sheet metal plane and, respectively: (*i*) measuring the tilt angle that initiates basal sliding and (*ii*) measuring the angle of repose of the material itself. The model accurately simulates the position of the flow front and the general trajectory of the flow along the dyke plane.

With rheological parameters calibrated on the basis of the previous test ($\delta = 20°$ and $\phi = 25°$), the model was used to predict the maximum run-up distances observed using three other experimental configurations. A comparison of observed and predicted maximum run-up distances is shown in Fig. 10.45. The calibrated model produces accurate predictions of maximum run-up distance, as well as the position and distribution of slide material at that instant. This is important as it demonstrates the ability of the calibrated model to make accurate first-order predictions of landslide motion involving geometries different from that used for calibration" [273].

McDougall and Hungr also performed a back analysis of a real, historic landslide to see whether the model equations adequately reproduced the soil mass movement in the landslide. They use the *Frank Slide* in Canada. We again quote from their paper [273].

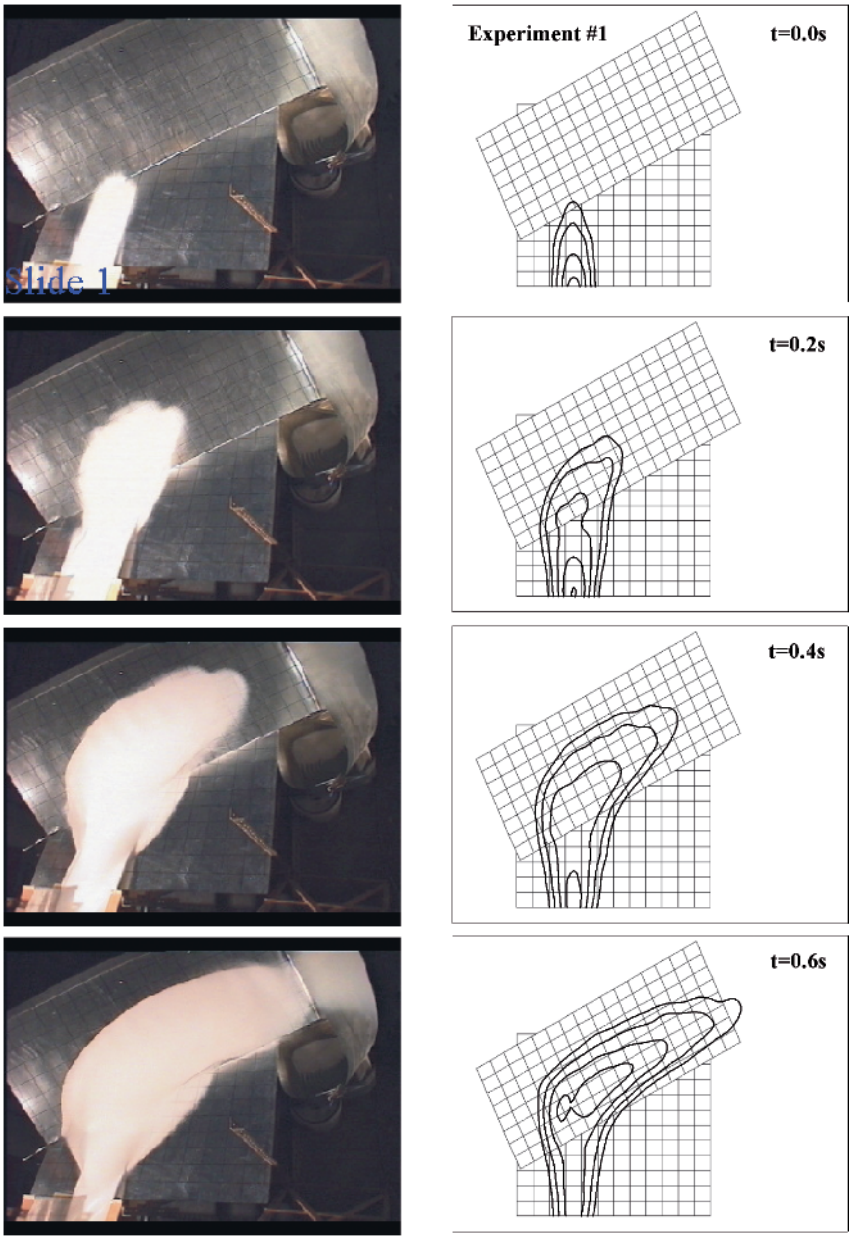

Fig. 10.44. Analysis of a deflected run-out experiment using $\alpha_1 = 60°$ and $\alpha_2 = 33°$. The experimental and simulated flow positions are shown at 0.2 s intervals and the flow depth contours are at 10 mm intervals. The planes are marked with a 10 cm square grid. (From [273].)

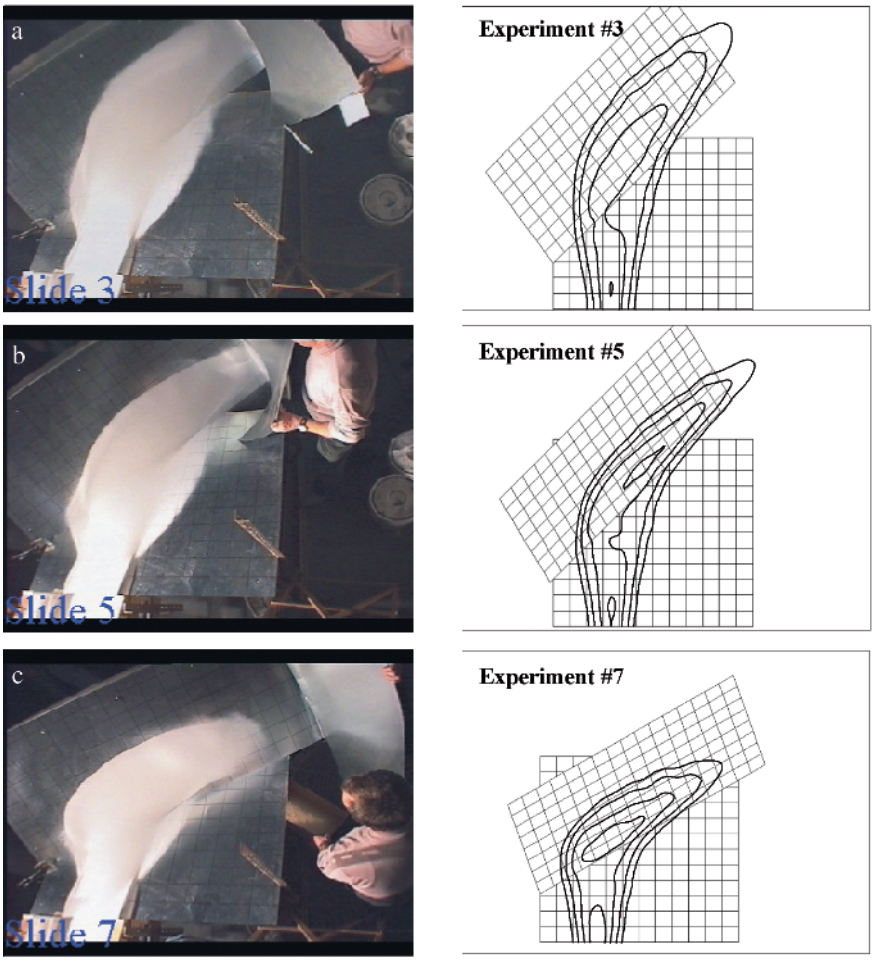

Fig. 10.45. Comparison of observed and predicted maximum run-up distances using three other experimental configurations: **a**) $\alpha_1 = 45°$ and $\alpha_2 = 33°$ **b**) $\alpha_1 = 45°$ and $\alpha_2 = 45°$ **c**) $\alpha_1 = 60°$ and $\alpha_2 = 45°$. The experimental and simulated flow positions are shown at the point of maximum run-up on the dyke plane and the flow depth contours are at 10 mm intervals. The planes are marked with a 10 cm square grid. (From [273].)

"On April 29, 1903 approximately 30 million m^3 of rock descended Turtle Mountain into the Crowsnest River valley, partially burying the town of Frank, Alberta and killing about 70 people. It was Canada's worst landslide disaster (Evans [95]).

The analysis of the Frank Slide presented below is preliminary, in that no attempt was made to optimise the input data and the calibration of the model,

or to describe the detailed results. The simulation is shown in Fig. 10.46. A detailed digital elevation model of the present-day topography was provided by the Geological Survey of Canada. With reference to historical photos and maps, the topography of the deposition zone was modified to approximate the preslide condition, by removing approximately 30 million m^3 from the area according to estimated deposit depths. The starting position of the 30 million m^3 slide mass was similarly estimated. This modification, while subjective, is not unduly significant for the performance of the frictional model, as the introduced elevation changes affect the slope of the mean energy line of the model by less than 1%.

The model provided a good match of the general extent and distribution of the final deposit using a frictional rheology with $\delta = 14°$ and $\phi = 40°$. The low value of the bulk basal friction angle implies the presence of pore water pressure in the flowing material. This result is in close agreement with the analysis of the Frank Slide reported by HUNGR and EVANS [164].

The results of the preliminary analysis resemble the real event in a number of ways. The flow comes to rest within 100 s. It spreads thinly across the opposite side of the valley and banks slightly right. The bulk of the flow is deposited proximally on the opposite side of the Crowsnest River, while the distal flow margin is influenced by the terraced valley topography, running up and back down the slopes and depositing on the terraces. More detailed evaluation of these results, tests with different rheologies and further calibration of the model could undoubtedly yield even better correspondence with the prototype" [273].

In a companion paper [274], MCDOUGALL and HUNGR incorporated effects of entraining loose material into the moving avalanche from the bottom. If $M = \rho V$ is the rate of mass entrained per unit area at the base (M has the dimension of density $\times$ velocity and V that of a velocity), then this quantity enters the balance of mass as a source term and a similar term, multiplied with $\mathbf{v}$, enters the momentum balance equations as a resisting force (because the entrained mass must be accelerated). Parameterisation of M is the crucial closure condition of this model; indeed we regard it as one of the grand unsolved problems of landslide/avalanche dynamics. MCDOUGALL and HUNGR motivate their parameterisation from early turbulent closure conditions in jet, plume and boundary layer flows, and write

$$V = E\left(|\mathbf{v}|h\right), \tag{10.12}$$

where $|\mathbf{v}|$ is the modulus of the depth-averaged velocity and h is the avalanche depth, whilst E is a parameter that they assume as a function of space.

The event is the 1999 Nomash River rock slide-debris avalanche in British Columbia. This landslide began with the collapse of 300,000 m^3 of crystalline limestone, with the head scarp located about 430 m above the river on the

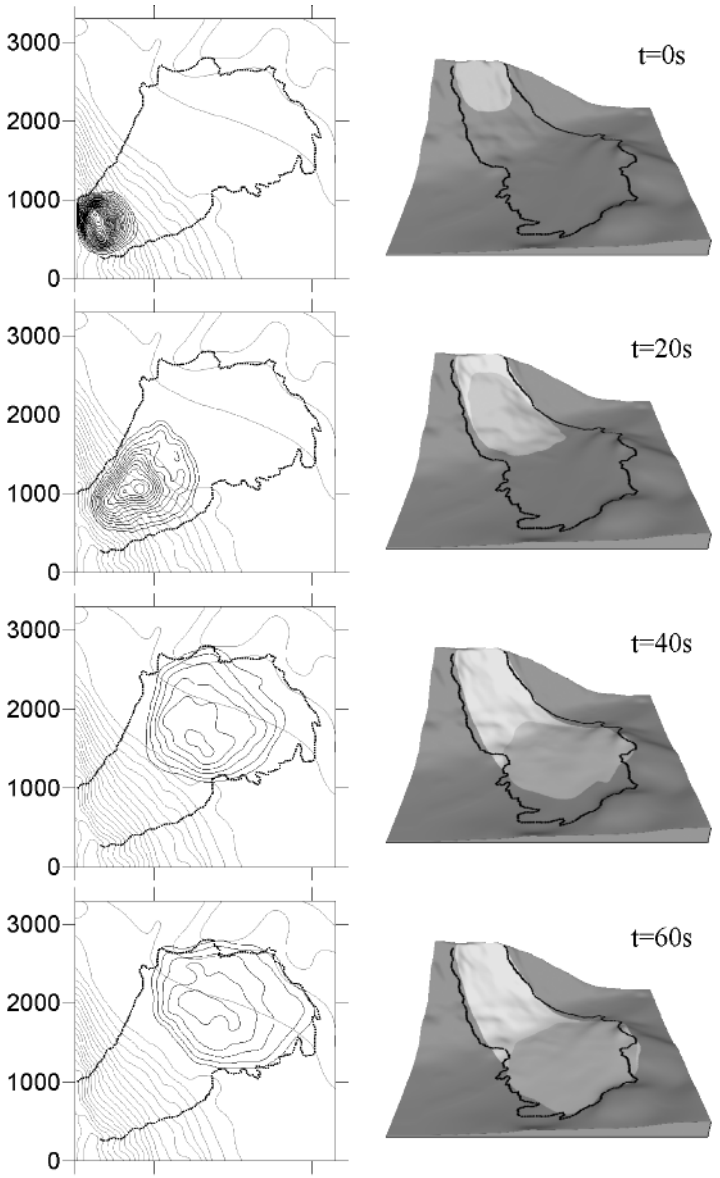

Fig. 10.46. Analysis of the Frank Slide. Plane and oblique views of the simulated flow position at 20 s intervals. The flow depth contours are at 5 m intervals and the sliding surface contours are at 50 m intervals. The *thick solid line* indicates the extent of the real event (digitised from Canada Department of Mines, 1917 [58]). (From [273].)

Fig. 10.47. Oblique aerial views of the 1999 Nomash River rock slide-debris avalanche in British Columbia, Canada (photographs courtesy of D. Ayotte). *Top* photograph looking down valley, *bottom* photograph showing the erosion in the track. (From [274].)

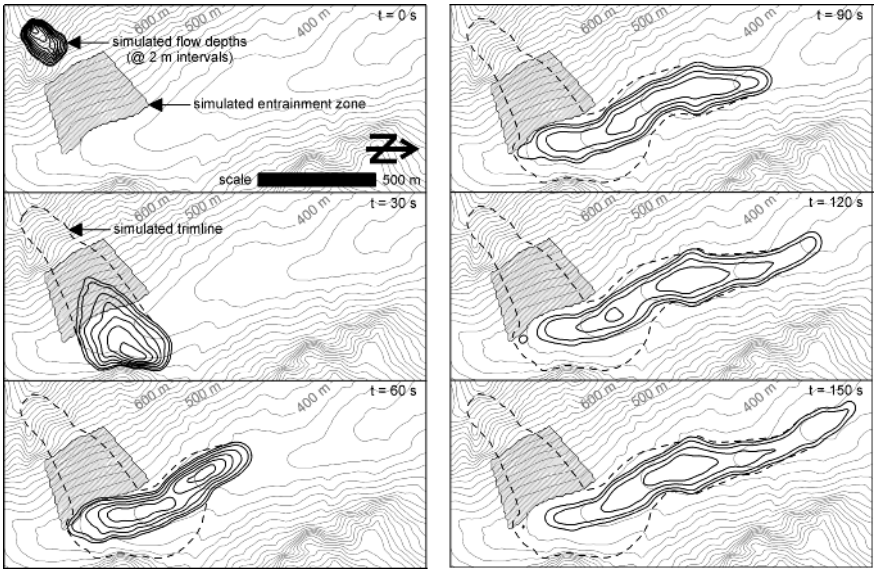

Fig. 10.48. Simulation of the Nomash River landslide accounting for entrainment of material from the source slope. The surface elevation contours are shown at 20 m intervals. *Dashed lines* show the computed trimline. (From [274].)

western side of the narrow V-shaped glacial valley (see Fig. 10.47). A dry granular avalanche of this magnitude is *likely* not to be able to run down the entire valley for more than a kilometre, but will form a "steep talus-like deposit at the foot of the source slope" [274] as has been corroborated by McDougall and Hungr's computations for the entrainment-free case. Thus, *an entrainment region had to be introduced for which the true distribution of the parameter E had to be estimated such that an additional run-out of 360,000 m^3 of saturated, fine-grained surfacial deposits would be mobilised.* By trial and error McDougall and Hungr found $E = 1.9 \times 10^{-3}$ m^{-1} applied in the quadrilateral grey zone of Fig. 10.48, which shows both the simulated and the observed trimlines.

A disadvantage of this model is that the entrainment constant E was determined from estimated observations of entrained mass. These estimates are bound to be inaccurate and tuned to some extent to generate the desired results. This will remain so until a reliable entrainment model is given that allows quantification from the material in the ground prior to a possible avalanche event. Here one has learned that entrainment may change the run-out significantly.

The Geophysical Mass Flow Group Model The interdisciplinary Geophysical Mass Flow Group (GMFG) of the New York State University at

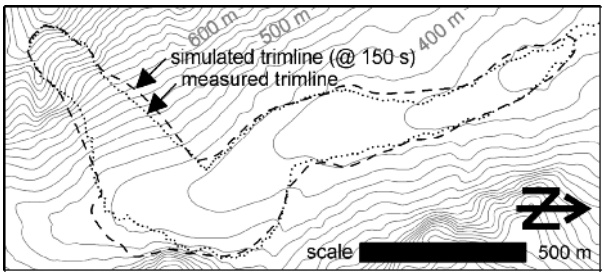

Fig. 10.49. Comparison of simulated and measured trimlines for the Nomash River landslide. The surface elevation contours are shown at 20 m intervals. (From [274].)

Buffalo, consisting of mathematicians, numerical analysts, engineers, geologists and geographers, designed models for dry as well as water-saturated granular avalanches, developed their own computational software TITAN2D [467] and applied it to situations of laboratory scale as well as field avalanches. In a series of papers [313, 318, 320, 321, 322, 323, 386, 387, 423] they introduced their model to the interdisciplinary science community.

Their avalanche model for dry granular avalanches is identical to that of IVERSON and others [74, 75, 191, 192, 194] and differs in its essential physics from the extended SH-model in the fact that it "preserves the rotational symmetry" by setting

$$\sigma_{xx} = \sigma_{yy} = K_{\text{act/pas}}\sigma_{zz} \tag{10.13}$$

and selecting the branch of the earth pressure coefficient according to whether

$$\frac{\partial u}{\partial x} + \frac{\partial v}{\partial y} \tag{10.14}$$

is positive or negative. In other words, the two earth pressure coefficients for σ_{xx} and σ_{yy} have the same value. They state that the earth pressure coefficients in our formulation violate the objectivity requirements. This is correct, but we believe the statement emphasises the different point. Many approximations of objective physical models may become inobjective by the very approximation, e.g., linear elasticity. So let us try to state the differences more clearly: *the difference of the stress closure in this book (including* MCDOUGALL *and* HUNGR*'s closure) and that of the groups at the GMFG is that the former allow stress anisotropies or normal stress effects, whereas the latter do not; (in this regard) they are closer to a hydrodynamic model.* [10]

[10] Of course, there are also other differences. For instance, the (x, y)-coordinates in this book are not measured in the principal directions of the two-dimensional rate of the strain tensor. They are only nearly so, if the downhill velocity component is much larger than the cross-slope velocity component. Similarly, the

PITMAN et al. [322] look at a granular flow down an inclined plane abruptly merging at 1000 m into a horizontal surface. They show pictures from computational results, but do not compare them with experimental findings. They also state that with TITAN2D they can well reproduce the two-dimensional similarity solutions of HUTTER et al. [177]. Somewhat more explicit is a comparison of their computational predictions and a laboratory experiment reported in PATRA et al. [313]. Their laboratory experiments were conducted using sand flows released on a masonite plane. The following statement is taken from their paper: "It measured 190 cm × 60 cm, and consisted of two parts. The first section was tilted at angles of 23.9°–44.3° with an adjustable mount. Particles were released instantaneously on the upper part of this section either from a smaller spherical or a larger cylindrical container. The tilted section was joined to a second section that dipped from 1°–2° downstream. The mass released from the spherical cap was $\sim$ 43 g, that from the cylindrical container was $\sim$ 425 g. Particles were playground sand grains sieved so that only 177–250 μm fraction was used. The basal friction angle for the material was tested by a number of methods to lie at 18°–29°. The large variance resulted from differences in the test methodology. The basal maximum angle of stability was 36°. Both the internal friction angle and the internal maximum angle of stability were 37.3°. The propagation of the sand was measured by videotaping while a horizontal grid was projected onto the plane to aid in visualisation. Video frames were then grapped with a digital frame grabber, and the sand propagation was measured directly from the frames by measuring the lateral spreading, as well as the advance of the head and tail of the flowing mass. Because of the difficulty in ascertaining the edge of the flow during time steps when the material was thinly spread, and because of geometrical distortions, the error in the measurements of positions of the flow is estimated to range from 1− $\sim$ 2.5 cm.

A typical experiment proceeded as follows (Fig. 10.50). The video camera was started and the operator then filled the starting container with sand as the base was placed flush to the test plane. The container was removed with a smooth motion to avoid undue disturbance of the particles. The test mass then began propagation downslope, with the head initially moving at a noticeably greater speed than the tail, which appeared to be stationary for a short time. The sand grains spread laterally as well as downstream, so that the mass rapidly attained a teardrop shape. With time, this teardrop shape elongated and spread laterally, although the tail did ultimately propagate downstream. Once on the lower test section, the particles in the head began to deposit in a teardrop shape that was noticeably less elongated in the downstream direction than the actively propagating mass. The final disposition of

(x, y)-coordinates of the USGS and GMFG groups are horizontal, but should be locally tangent to the basal surface. Therefore, requesting rotational invariance relative to these coordinates is as inappropriate as may be the violation of the objectivity of the SH-procedure.

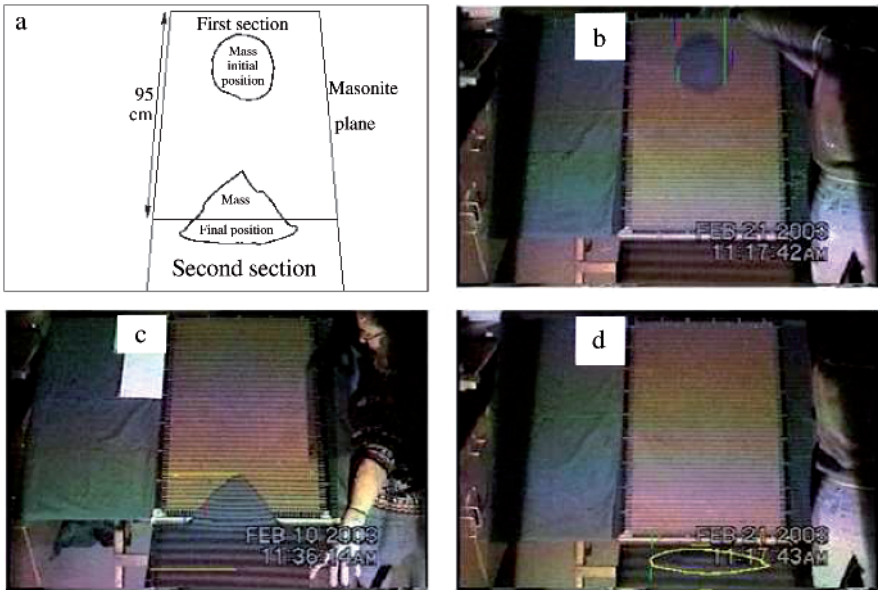

Fig. 10.50. Experimental set-up and example runs. **a**) Schematic diagram traced from an image showing the positions of masonite planes and sandpile masses. The angle of the plane was measured with a digital construction level. **b**) Starting of experiment at 44.3° with a mass of 425.3 g. Image taken 0.23 s after start of experiment. **c**) Final position of the sandpile from experiment at 31.8°, with a mass of 425.11 g. Image taken 3.13 s after start of experiment. **d**) Final position of the sandpile from experiment at 44.3° (as part b). Image taken 1.26 s after start of experiment. Note the shorter time to the final position, and more distal final position than in part c. The final sandpile is outlined in yellow for visualisation. (From [313].)

the mass resembled a conic section with its base on the lower test section and its apex at some height on the upper test section that depended on the slope angle of the upper test section. The only exception to this geometry was in experiments at angles within the range of the basal friction angle, in which case the mass was arrested on the upper test section" [313].

Patra et al. [313] also show comparison of their table-top experiments with numerical output. Figures 10.51a,b show this sample comparison of the flow simulations with the experiments for the case of a $\sim$ 425 g mass and slopes of 38.5°. They state that the plots show good qualitative comparison of the evolving pile shape, speed and run-out distance, if an offset of +0.35 is applied to the numerical results. When compared with earlier findings, the results of Fig 10.51 are at best fair. Reasons by Patra et al. are given but not scrutinised. Since the basic physics of the model of the USGS and GMFG groups are similar, and since the results of the comparisons between the

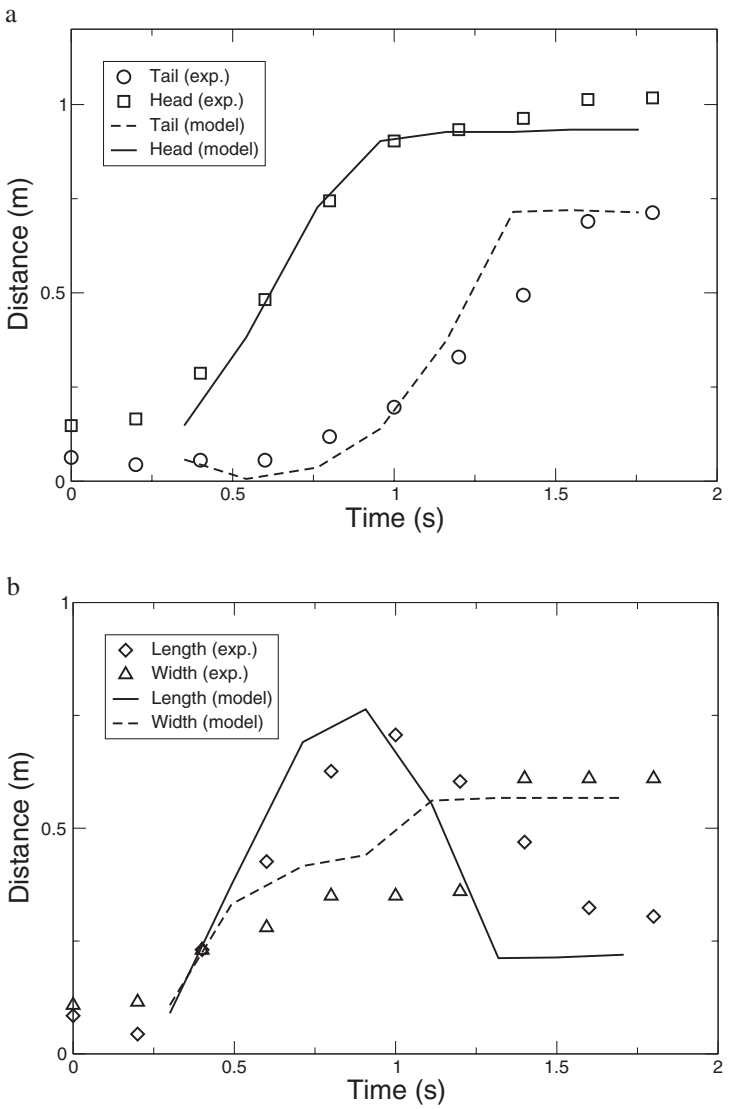

Fig. 10.51. Simulated and experimental observations of the front and tail of a pile of granular material sliding down a flat plane inclined at 38.5°. The propagation of the experimental and numerical flows matches well with a time offset of 0.3 s added to the numerical flow. **a**) Propagation in the downslope direction as indicated by the position of flow head and tail. **b**) Propagation in the cross-slope direction as indicated by the width, and extension and elongation of the pile as indicated by the difference in head and tail positions. (From [313].)

model and computations of our models and the model of McDougall and Hungr are more detailed and appear to be more convincing, a benchmark comparison would be helpful.

The group GMFG (University at Buffalo) has also performed computations of mass flow from volcanoes on real topography. One example is the spreading of an avalanche down the mountain flanks of Volcan de Colima in Mexico, the other is the flow down Little Tahoma Peak on Mount Rainier, Washington. However, no comparison with independently determined debris depositions from a real event has been made so far.

11 Particle Image Velocimetry for Free Surface Flow Avalanches

11.1 Introduction

Following the numerical simulations and the results from the experiments presented in the previous chapters, we continue with the validation of the theory by means of modern and different laboratory avalanche experiments. In this chapter we will particularly focus on *velocity measurements*. The velocity and depth distributions are crucial in describing the dynamics and drawing inferences about the flow behaviour of an avalanche. Our primary task in this and the following chapter is the measurement of these quantities and their comparison with theoretical predictions. We are mainly interested in measuring velocity distributions for unsteady free surface flows of finite mass avalanches.

The experimental method that will be described and applied here is the so-called *particle image velocimetry* (PIV) technique with which the velocity field of the surface in a granular avalanche can be measured. This is an *optical* measuring system. The basic idea is as follows: A part of or the whole surface of a flowing granular avalanche is illuminated twice, at time t and time $t+\Delta t$. Then the two pictures, called "frame A" and "frame B", are captured by a CCD (charge coupled devices) camera. "Displacements" of identifiable points of the moving avalanche are calculated by comparing frame A and frame B via pattern recognition. The velocity of such a point is simply its displacement divided by the time difference Δt between both frames.[1]

We intend to implement the PIV system to measure dynamical quantities such as the velocity distribution and geometry of an unsteady and free surface flow of granular avalanches over curved surfaces. In the following we consider the flow without lateral confinement on an inclined plane that merges continuously into the horizontal run-out zone. To measure the velocity of such an avalanche, which is released from a hemispherical cap and flows down an inclined surface, a two-dimensional PIV system is used. Particularly, we are interested in the magnitude of the *surface velocity* over the avalanche. Furthermore, we intend to obtain information about the velocity profile through

[1] Note that some parts of this chapter closely follow [83, 334].

the depth by simultaneous measurement of the velocity from the surface and the base of the chute. The form of the velocity profile through the depth influences the factor in front of the non-linear convective terms in the equations of motion. This factor is unity if the profile is uniform and $6/5$ if it is parabolic, see [183]. In addition, knowledge about this depth profile provides general information of the physics of granular materials. It may, for example, help us to answer the question as to under which flow conditions the granular material behaves more fluid-like or more solid-like and how these conditions can be best mathematically described [83, 334]. Another important information is the development of the velocity field at the onset of the avalanche motion and during its settling in the deposition zone where the avalanche comes to rest. The former flow situation may provide information about the initial conditions, which are particularly important for numerical simulations, whereas the latter is of practical importance for determining the run-out distance.

11.2 Particle Image Velocimetry (PIV) Technique

At first, we briefly review some basic theoretical aspects of the PIV system. Some details are taken from Eckart et al., Raffel et al. and Pudasaini et al. [83, 334, 343, 352] and TSI's manual for PIV [468]. The PIV system is an optical system that essentially interprets differences in light intensities as a pattern. The use of a transparent fluid is the common case in PIV. To generate a pattern in the transparent fluid, small non-transparent *tracer particles* are seeded in the fluid. The PIV theory is based primarily on two important concepts: Firstly, the *image intensity field* and, secondly, the *cross-correlation function*. The function describing the pattern mathematically is the image intensity field. Particular spots of brightness are interpreted as grey-scale patterns that, in general, move. Such a moving pattern can most easily be detected by comparing two consecutive frames captured by a camera. Then, the second task of the system is to decide which displacement (and hence velocity) is "correct" among a certain set of possible displacements. This can be mathematically accomplished by constructing the cross-correlation function between two consecutive brightness distributions. To this end, it is necessary to detect both a pattern on frame A and frame B, and the difference between the patterns obtained from the two frames.

The *geometric imaging* scheme is sketched in Fig. 11.1. The whole region of interest (here the light sheet) in the three-dimensional physical space with coordinates $\mathbf{X}, \mathbf{Y}, \mathbf{Z}$ is subdivided into smaller regions, the so-called "interrogation volumes". Such a volume is mapped with the imaging lens onto the "interrogation area" in the two-dimensional image plane with the coordinates $\mathbf{x}, \mathbf{y}, \mathbf{z}$. For simplicity, in the following the phrase "interrogation spot" will be used for either interrogation volume or interrogation area.

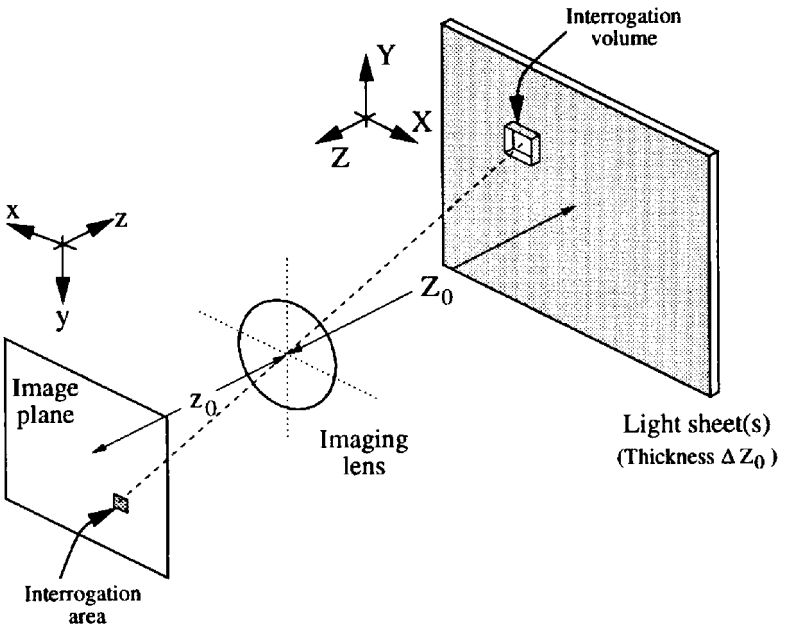

Fig. 11.1. Sketch of the geometric imaging arrangement. (From [352].)

11.2.1 Image Intensity Field

For each of the interrogation spots, the image intensity field assigns to each point in the image plane a scalar value that quantifies the light intensity of the corresponding point in the physical space. This light intensity depends on many factors, in particular the illumination, but also on the physical properties of the lens and the camera. However, for a series of experiments these latter influences can be kept constant. The *image intensity field* maps the light energy of an individual particle in physical space (i.e., the tracer particles in the observed region of the flow) into an intensity value in the image plane. Mathematically, this function can be viewed as a transformation between two spaces. It is basically a convolution of the transfer function responsible for the determination of the "effective" light energy of one particle and the point spread function describing the optical behaviour of the lens.

The image intensity fields $I(\mathbf{x}, \mathbf{\Gamma})$ and $I'(\mathbf{x}, \mathbf{\Gamma} + \mathbf{D})$ at times t and $t + \Delta t$ are defined, respectively, as follows:

$$I(\mathbf{x}, \mathbf{\Gamma}) = \sum_{i=1}^{N} V_0(\mathbf{X}_i)\, \tau(\mathbf{x} - \mathbf{x}_i), \tag{11.1}$$

$$I'(\mathbf{x}, \mathbf{\Gamma} + \mathbf{D}) = \sum_{j=1}^{N} V_0'(\mathbf{X}_j + \mathbf{D})\, \tau(\mathbf{x} - \mathbf{x}_j - \mathbf{d}), \tag{11.2}$$

where $\mathbf{\Gamma} = (\mathbf{X}_1, \mathbf{X}_2, ..., \mathbf{X}_N)$ denotes the positions of the N different (tracer) particles in the (three-dimensional) physical space, $\mathbf{x}$ the position in the (two-dimensional) image plane, $\mathbf{D}$ the displacement in the physical space ($\mathbf{D} = \mathbf{X}_i' - \mathbf{X}_i$), $\mathbf{d}$ the displacement in the image plane, V_0 the transfer function and τ the point spread function of the lens.

In this way, one obtains a field of numbers in the interrogation area for each pixel and each instant of time. These numbers may be considered as grey values, and the whole set may be interpreted as a *grey scale pattern* [83]. It is in general moving and/or deforming (i.e., a function of time). However, it is common practice to assume that all points in this spot are assigned the same velocity, i.e., this pattern moves "rigidly" within the interrogation spot.

11.2.2 Cross-Correlation Function

The cross-correlation function $R_{II}(\mathbf{s}, \mathbf{\Gamma}, \mathbf{D})$ is defined as the *convolution*

$$R_{II'}(\mathbf{s}, \mathbf{\Gamma}, \mathbf{D}) = \frac{1}{\alpha_I} \int_{\alpha_I} I(\mathbf{x}, \mathbf{\Gamma})\, I'(\mathbf{x} + \mathbf{s}, \mathbf{\Gamma} + \mathbf{D})\, \mathrm{d}\mathbf{x}$$

$$= \frac{1}{\alpha_I} \sum_{i,j} V_0(\mathbf{X}_i)\, V_0'(\mathbf{X}_j + \mathbf{D}) \int_{\alpha_I} \tau(\mathbf{x} - \mathbf{x}_i)\, \tau(\mathbf{x} - \mathbf{x}_j + \mathbf{s} - \mathbf{d})\, \mathrm{d}\mathbf{x}, \tag{11.3}$$

where α_I denotes the interrogation area and $\mathbf{s}$ the separation vector in the correlation plane. The function $R_{II'}$ essentially calculates possible displacements by correlating all "grey values" from the first frame (intensity field I) with all "grey values" from the second frame (intensity field I'), where the separation vector is the independent variable that is to be varied. To make this clear, consider a simple example as illustrated in Fig. 11.2. Suppose that three particles are located at $\mathbf{x}_1$, $\mathbf{x}_2$ and $\mathbf{x}_3$ in an interrogation spot at time t, i.e., picture I in Fig. 11.2a. By the time $t + \Delta t$, they have moved to positions $\mathbf{x}'_1$, $\mathbf{x}'_2$ and $\mathbf{x}'_3$ in picture I' of Fig. 11.2a. In passing we note that $\mathbf{x}'_2$ is not inside the interrogation spot. This is called "loss of pairs". However, the cross-correlation function $R_{II'}$ shown in Fig. 11.2b is calculated by taking *all* possible displacements *regardless* of whether the correct particles are correlated with each other or not, i.e., if the particle at $\mathbf{x}_1$ has moved to $\mathbf{x}'_3$, then the displacement is $\mathbf{x}'_3 - \mathbf{x}_1$ and so on. Four of the six possible displacements occur only once, but $\mathbf{x}'_1 - \mathbf{x}_1 = \mathbf{x}'_3 - \mathbf{x}_3 = \mathbf{d}$ occurs twice. Thus, the displacement $\mathbf{d}$ is the most likely displacement.

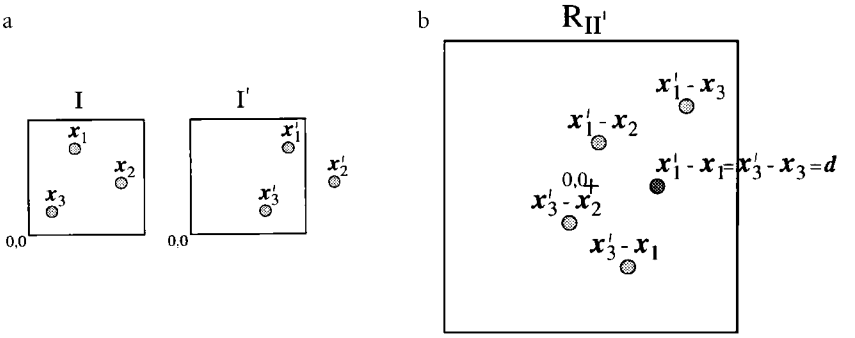

Fig. 11.2. **a**) Image intensity fields I and I' at times t and $t' = t + \Delta t$, respectively. **b**) The corresponding cross-correlation of all possible displacements. (From [352].)

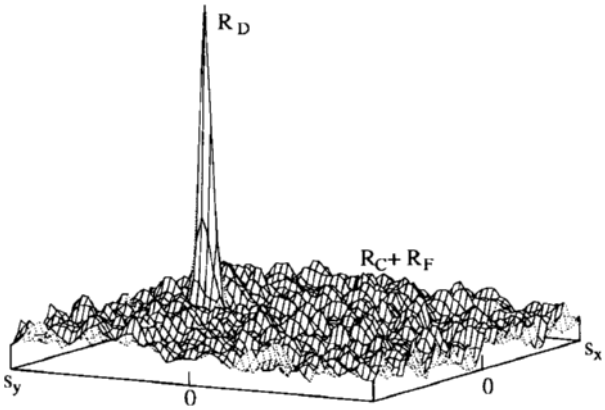

Fig. 11.3. An example of the cross-correlation plane illustrating the correlation of identical particle images R_D and the errors $R_C + R_F$. (From [352].)

$R_{II'}$ can be decomposed into three parts (see [211]):

$$R_{II'}(\mathbf{s}, \mathbf{\Gamma}, \mathbf{D}) = R_D(\mathbf{s}, \mathbf{\Gamma}, \mathbf{D}) + (R_C(\mathbf{s}, \mathbf{\Gamma}, \mathbf{D}) + R_F(\mathbf{s}, \mathbf{\Gamma}, \mathbf{D})), \quad (11.4)$$

where R_D is the correlation of identical particle images (terms $i = j$), R_C the convolution of the mean intensities (terms $i \neq j$) and R_F the fluctuating noise (terms $i \neq j$). This means that $R_C + R_F$ produce the errors, whereas R_D is the correct value that is sought. Figure 11.3 shows an image of the cross-correlation plane. R_D corresponds to the highest value of $R_{II'}$ in the correlation plane called "first peak". The coordinates s_x and s_y are the separations in the x- and the y-directions, respectively. This picture can be read as follows: The most likely displacement is the displacement $d = (s_x(R_D), s_y(R_D))$, where $s_{x,y}(R_D)$ denote the coordinates of R_D in the cross-correlation plane. The quality of this measurement is usually estimated by determining the ratio of the value of the first peak divided by the value of

the second tallest peak (called first noise peak, the tallest peak of the "noise" $R_C + R_F$): A high ratio means high and a low ratio means low reliability of the measurements.

11.2.3 Spatial Resolution

It is to be noted that *only one* displacement vector is calculated within one interrogation spot. The velocity vector is simply the displacement vector divided by the time delay Δt between two frames. It must hence be viewed as an average velocity vector of the particles inside the interrogation spot. To increase the *spatial accuracy*, especially for flows with strong displacement gradients, the interrogation spot size must be chosen sufficiently small. Common values are 32×32 and 64×64, for example. If the camera resolution is 1280×1024 pixels and the observed region fits the whole image zone, then $1280/32 \times 1024/32 = 1280$ and $1280/64 \times 1024/64 = 320$ velocity vectors are calculated for interrogation spot sizes of 32×32 and 64×64, respectively, see e.g., [468].

11.2.4 Summary of the PIV System

The mathematical procedure of the PIV system can be summarised as follows, see, e.g., Eckart et al. and Pudasaini et al. [83, 334]:

- Subdivide the whole area/image into interrogation spots.
- Calculate the image intensity fields at time t and $t + \Delta t$ for one interrogation spot.
- Calculate the correlation between these image intensity fields for one given separation.
- The cross-correlation plane is built by the correlation values of all possible separations.
- The most likely displacement is the separation for which the correlation function has the highest value.
- Repeat the procedure for each interrogation spot.

11.3 Experimental Set-Up for Granular Avalanches

In this section, the PIV set-up for granular avalanches flowing down inclined surfaces is described. Firstly, the "usual" PIV set-up for transparent fluids is introduced. Subsequently, it becomes clear that there are specific problems occurring for (usually) "non-transparent" granular materials. For granular avalanche experiments we use plexiglass chutes. There are some particular problems with their usage, which will also be discussed in this section. However, plexiglass chutes are used because they can be easily deformed to make

different channels and the velocity fields can be measured simultaneously from above and below the chute.

11.3.1 Transparent Fluids and the Usual PIV Set-Up

Firstly, we briefly review the usual set-up in a wind tunnel. A sketch is given in Fig. 11.4. The major device of the PIV system is the CCD camera. Together with lenses this is called *imaging optics*. For illumination, a laser, light sheet and a mirror are needed. To control and trigger the laser and the camera, a synchroniser and a PC with evaluation and post-processing software should be installed. The transparent fluid must be seeded with tracer particles so that the camera and the software can detect some pattern.

11.3.2 Set-Up for Granular Avalanches

The set-up for granular materials differs from that described above in the following respects: For non-transparent materials, laser light sheets can obviously not be used for illumination. Therefore, we employed computer controllable flashes equipped with a diffuser. In order to guarantee (nearly) the same brightness on both frames, the intensity and the duration of the flashes were adjustable. From Fig. 11.4 it is clear that for "usual PIV" the velocity distribution of the tracer particles inside the flow is measured. However, for "granular PIV" this is not possible. Alternatively, we measure the velocity of granular particles of an avalanching flow at the surface or at some boundary and the base, i.e., from below the plexiglass chute. It is advantageous

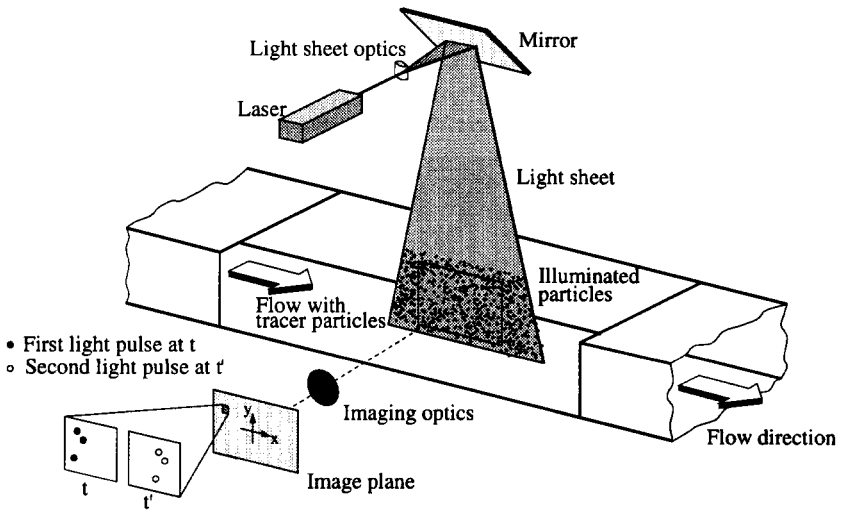

Fig. 11.4. Usual PIV set-up in a wind tunnel with tracer particles. (From [352].)

with granular particles that the *optical surface structure*, which is *produced by illumination* of the surface of the avalanche, is already sufficient to detect the motion. This means that we do not need to add tracer particles in the bulk material. However, the flash illumination in connection with the plexiglass chutes used may produce different kinds of illumination errors, which will be discussed later in greater detail. Furthermore, the region outside the support of the avalanche in the chute can be disregarded in the evaluation and post-processing stage so as to eliminate (or to minimise) such errors.

11.3.3 Technical Details

It is appropriate to describe the technical details of the electronic equipments employed in the experiments. We use a system of the company TSI, see [468]. It includes two charge coupled devices (CCD cameras) of type TSI PIVCAM 13-8, two NIKON wide-angle lenses NIKKOR AF 28mm f/2.8D (called WA lenses), see [332], a synchroniser and a PC including the INSIGHT PIV software. For illumination, we used two or four flashes (depending upon whether one or two cameras were used) of the type METZ MECABLITZ 60 CT-4, see [331]. As has already been explained, two flashes for one camera are needed since a camera captures two frames. Because the time delay between frames A and B is rather short, one might think it is sufficient to use one flash for illuminating both pictures. For two reasons this is not possible. Firstly, *it is nearly impossible to trigger and adjust one flash such that the brightness on both pictures would be the same.* Secondly, *the shutter of the second frame is opened for a relatively long time due to technical reasons, which would result in distortions if only one flash were used. The motion can, in general, not be frozen in time and the second picture would become blurred* [83, 334]. Hence, proper adjustment of the flashes is mandatory. The system is also supplemented by superwide-angle zoom lenses of type NIKON NIKKOR AF 18–35 mm f/3.5 $\sim$ 4.5D IF (called WAZ lenses), see also [332]. In fact, these lenses were used in all experiments because of their greater variability and quality compared to the WA lenses. As explained in Sect. 11.2.3, the CCD camera (which we used) has a resolution of 1280×1024 pixels and a colour depth of 12 bits ($2^{12} = 4096$ different grey values). Furthermore, its highest temporal resolution is four double frames per second. The time delay between the first and the second frame depends on the range of the velocity values. We chose it to be in the order of 1 μs.

11.4 Experimental Peculiarities Arising for Granular Materials

As in any other measuring system, PIV is subjected to certain measurement uncertainties that cause errors. Some of them are specific for granu-

lar avalanches and some are of general relevance. There are two main error sources for granular PIV: Inappropriate surface structure of the avalanche and/or the background and imperfect illumination due to shadows, reflections, etc., see also ECKART et al. and PUDASAINI [83, 334]. Both are specific for granular avalanches. Because of their exceptional importance, they will be discussed in the following in more detail.

11.4.1 General Errors

Below we point out some error sources of general relevance arising both in transparent and non-transparent fluids:

- Motion perpendicular to the picture plane (two-dimensional measurements): This is only of importance for locations where strong gradients of the height arise, e.g., in the flow inception and deposition zones of laboratory avalanches. However, even in this situation the influence is rather small in comparison with the main error sources.
- Displacement gradients arising within the interrogation spot: The pattern is not only shifted, but also deformed. This error is of limited importance at fixed boundaries of the domain.
- The angle between the observation plane and the camera may not always be 90°: This is a big error source when the chute is relatively large and the space available for the experimental set-up is small. This is also a considerable problem for curved, and curved and twisted chutes and channels. In this case, many cameras are needed, each for a small portion of the flow domain or identical experiments where shifted camera positions must be performed.
- Distortion due to the usage of extreme wide-angle lenses and short distances between camera and observation plane: As in the previous case, this causes problems for large chutes and small available experimental space.

11.4.2 Particular Errors for Granular Flows

Error Due to Light Reflection There are still many other problems for granular PIV, e.g., light reflections from the chute or from the laboratory environments. Reflections can, in general, be avoided by either choosing an appropriate position of the flashes or using indirect flashing that does not point directly to the chute but is directed towards a white paper or screen reflecting the light of the flash to the chute. This well-known procedure diffuses the light such that the chutes are, in general, illuminated with no or very few reflections [83, 334].

Error from Electrostatic Charging Another specific problem, in the case of fine materials flowing over plexiglass or plastic chutes is electrostatic

charging. This is more pronounced for two-dimensional channelised flows from a silo or flows down confined channels than for three-dimensional free surface flows. Electrostatic charging can be minimised by using an anti-electrostatic charging spray or ionising airgun. Alternatively, electrostatic forces may be minimised by avoiding minute experimental set-ups and designing larger scale models.

Optical Surface Properties The optical surface properties are of utmost importance. To illustrate this, velocity measurements of two plates at rest are compared [83]. One plate is covered with sand, the other one with a varnish. Whereas the surface of the former is optically well-structured, the surface of the latter is rather homogeneous, see Fig. 11.5.

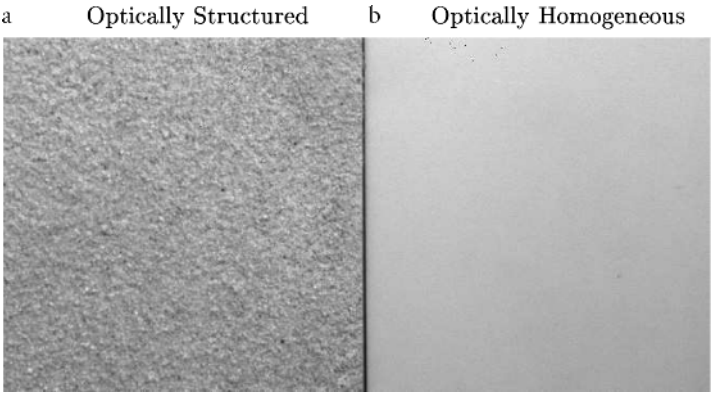

Fig. 11.5. Two different surfaces at rest, coated with **a**) sand and **b**) varnish. (From [83].)

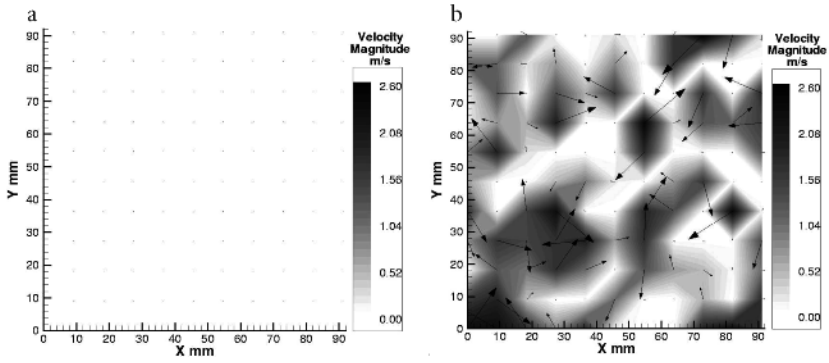

Fig. 11.6. Measured velocity for **a**) sandpaper, corresponding to Fig. 11.5a and, **b**) varnish, corresponding to Fig. 11.5b. (From [83].)

The velocity distribution corresponding to these cases is given in Fig. 11.6. Whereas the velocity for the "sand plate" is measured correctly, that of the varnished plate is not: the in-plane velocities are more or less randomly distributed in magnitude and orientation, which is clearly wrong. Evidently, with an optically homogeneous (i.e., non-structured) background, erroneous velocity vectors may be produced; this may deteriorate the entire quality of the measurements. It is thus recommended to choose also the background appropriately, i.e., with an optical structure if possible. However, this is not possible when plexiglass chutes are used. Nevertheless, in many situations we can either eliminate or minimise such errors by disregarding the grain-free zone of an avalanche in the post-processing operations.

Illumination Another main error source is illumination. If laser light sheets can be used, the quality of the illumination may, in general, be good. However, we are compelled to use alternative illumination techniques such as flashes to illuminate the surface of non-transparent materials. Figures 11.7 and 11.8 show frame A and frame B of one double frame for different positions by flash A and flash B. The object is sandpaper at rest. To illustrate the effect in a drastic way, the position of the flashes are chosen exaggeratedly badly. The illumination of subregions on the sandpaper for frames A and B is not the same in Fig. 11.7, but it is fairly uniform in Fig. 11.8. Note that illumination differences between different regions on the sandpaper are of minor importance; crucial is the comparison of the same subregion in frame A with that in frame B.

Figure 11.9 displays the inferred velocity distribution of the sandpaper for the different positions of the flashes. It clearly shows that inappropriate positions of the flashes lead to significant measurement errors. Notice that the error produced here is not of a random nature, as was the case in the last paragraph. The direction of the "faulty velocity" distribution in Fig. 11.9a somehow reflects the axis and orientation of the flash illumination.

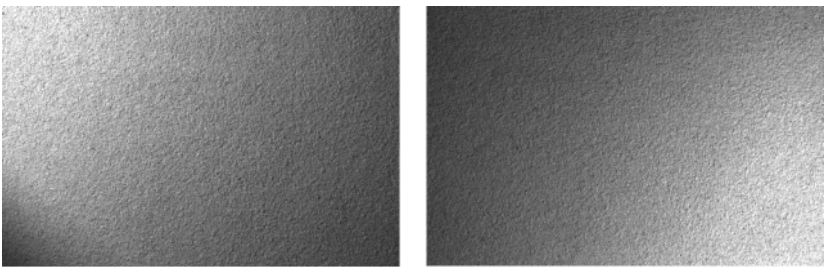

Fig. 11.7. Flash A *upper left corner*, flash B *lower right corner* of the observed region of a sandpaper surface at rest. (From [83].)

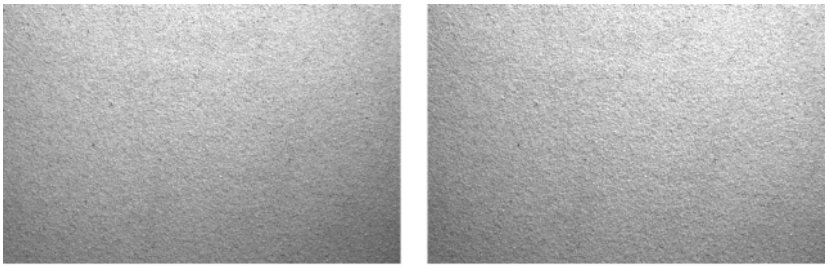

Fig. 11.8. Flashes as close to each other as possible, illuminating a sandpaper surface at rest in a fairly homogenuous way. (From [83].)

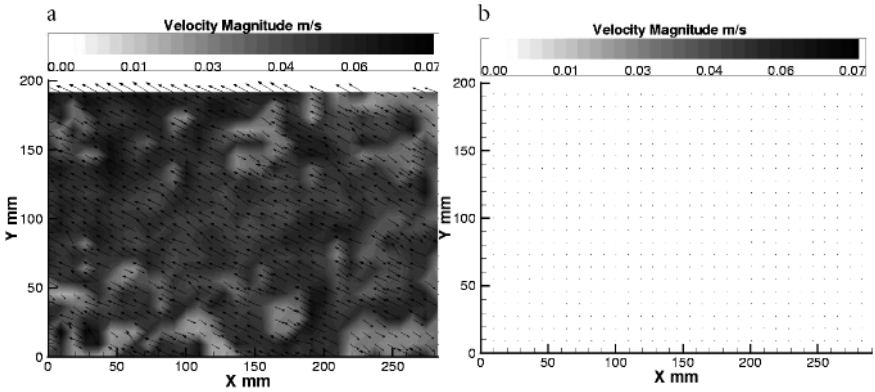

Fig. 11.9. Measured velocity of sandpaper **a**) for illumination as in Fig. 11.7 and **b**) for that in Fig. 11.8. (From [83].)

Testing the PIV System In this paragraph, a simple method to estimate systematic errors of the measured velocity values of the granular PIV system is described. Specifically of interest is the deviation of velocity values at the surface from those at the bottom at the same spatial locations (which may also include the influence of the plexiglass) and the deviation of the velocity values from one another in the whole region either at the surface or at the bottom. This will be dealt with in greater detail in the next chapter when measuring the velocity distribution of a free surface flow of an avalanche over a curved plexiglass chute.

Towards this end, a set-up with two cameras, a plexiglass chute and a "rigid avalanche" is used (see Fig. 11.10). One camera is placed below the chute, capturing pictures through the plexiglass, the other one is above it. If the sandpaper is released, double frames of both cameras are taken simultaneously; frames A are shown in Fig. 11.11 and the measured velocity distributions are given in Fig. 11.12. Note that the range of the colour bars is from

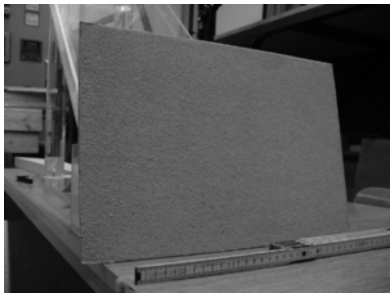

Fig. 11.10. The "rigid avalanche". A thick piece of rigid paper (0.3 mm thickness) with sand on both sides. (From [83].)

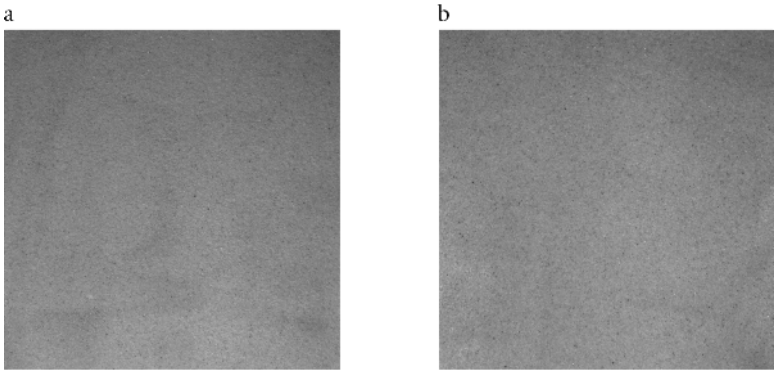

Fig. 11.11. Frame A of **a**) the bottom and **b**) the surface camera (not mirrored). Motion is from top to bottom. (From [83].)

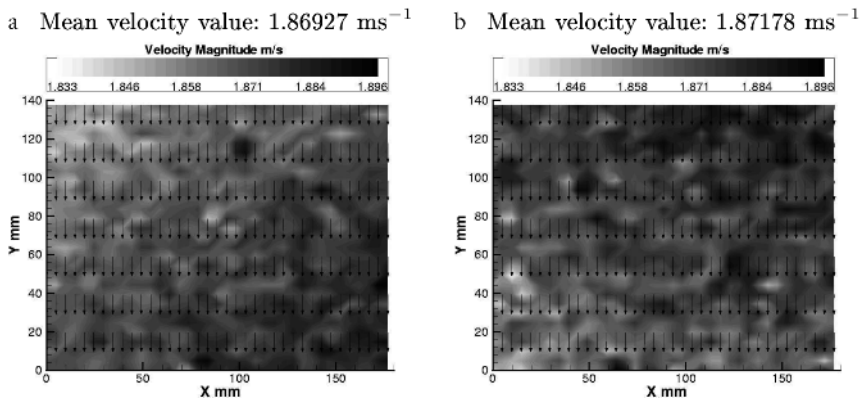

Fig. 11.12. Measured velocity of **a**) the bottom and **b**) the top surface of the sandpaper (not mirrored). Motion is from top to bottom. (From [83].)

the lowest (1.833 ms^{-1}) to the highest (1.898 ms^{-1}) measured value and *raw data* were used, i.e., no filters (see Sect. 11.5) were applied to the data shown in Fig. 11.12. The deviation between the mean surface and the mean bottom velocity is only 0.13%. However, the deviation between the smallest and the largest velocity value in either panel a) or b), is approximately 3.5%. This shows once again that surface properties and illumination that are responsible for the velocity variations are the main error sources, whereas the influence of the plexiglass is negligible.

11.5 Post-Processing and Evaluation

At the instant when the material is suddenly released, i.e., by lifting the cap or head gate, by which it is held, a sequence of pictures is captured. The most important information that can be obtained from granular PIV measurements is the surface velocity distribution. After capturing this, the interesting portions of the pictures are subject to calculation and validation processes to obtain the velocity (done by the software). A cross-correlation algorithm utilising *fast* FOURIER *transform* (FFT) is used [468]. The spot size of the interrogation windows is either 32×32 pixels (no oversampling) or 32×16 (double oversampling). After filtering possible errors, the processed data are exported to suitable plot programs for post-processing operations.

In a PIV system, the raw data may be subjected to a so-called validation procedure to eliminate possible faulty data. This is done by filters. There are different filters, but two of them are important for avalanche flows, namely the *range filter* and the *standard deviation filter*. With the range filter, the permissible range of velocity values can be adjusted. Sometimes selection of this range depends on personal experience. It is to be mentioned that the avalanche always flows from top to bottom, say in the negative y-direction. This clearly suggests restriction of the velocity values in the y-direction to negative values. By definition, the standard deviation filter eliminates all velocity values that are not within a certain distance to the mean velocity. It can only be applied if the velocity values not differ extremely from one another. In our case, the flow field is almost homogeneous, and thus the standard deviation filter provides a good choice for eliminating random errors. The blanks areas were interpolated by a mean neighbourhood filter.

However, in the next chapter we do not use these filters and thus need not validate the data for the free surface flow of the avalanche. The reason for this is that we select a grain free region (outside the boundary) of the avalanche and delete it from processing, so that (almost) no faulty data remains. In the following, we will use this technique in order not to use artificially interpolated data. This also increases the reliability of the measurements.

11.6 PIV with Multi-Cameras

Finally, we explain how PIV measurements are made with many cameras. Multi-cameras are used mainly for three purposes: (*i*) One camera is put below and the other one above the chute to measure simultaneously at the same locations the velocities at the base and the surface of the avalanche, respectively. These measurements serve as additional experimental results from which one may decide whether or not the velocity profile is uniform through depth. (*ii*) Two cameras can also be used to obtain the three-dimensional stereographic images and the velocity fields. (*iii*) In the case of large, curved, and curved and twisted channels, one must make use of a series of cameras so as to guarantee good measurements of several subdivided flow regions. (*iv*) If a limited number of cameras, e.g., just a single one, available, one may alternatively, perform repetitive experiments under identical conditions but different camera positions. This requires that conditions do not change from one experiment to the next. This may have to be checked carefully, especially with regard to the frictional properties of the chute, i.e., the bed friction angle. We will mainly be concerned with points (*i*) and (*iii*).

11.7 Particle Tracking Velocimetry (PTV) Measuring Technique

Pudasaini et al. [344] introduced an alternative measuring technique called *particle tracking velocimetry* (PTV) to measure the velocity field of free surface flow in granular avalanches down curved and twisted channels. This technique is a predecessor of the PIV technique. The basic idea of this system is as follows: A series of images of a part or the whole body (i.e., the region of interest) of the surface of a flowing granular avalanche is captured by using CCD camera(s). Then two consecutive images (say frames A and B) are selected to determine the velocity of tracer particles appearing on the free surface. The addition of an adequate amount of tracer particles with sufficient colour contrast against background particles is a necessary integral part of any PTV system. This is where PTV differs from PIV, which, for any type of granular flows, needs no tracer particles, see Pudasaini et al. [343]. Displacements of identifiable tracer particles of the moving avalanche are calculated by comparing frames A and B through grey value recognition across the boundaries of the tracer particles and the background bulk body. The displacement divided by the time difference Δt between both frames gives the velocity of a tracer particle. The PTV system works, particularly, for non-transparent fluids such as sand, gravel, quartz or other granular materials. We call this PTV system "granular PTV". Velocity fields of the tracer particles detected by this system at the free surface of the flow are assumed to be representatives of the real velocity field. This means that the velocity of

other particles (constituting the main bulk body) in the immediate vicinity of a tracer particle is the same or almost the same, because the background material and the tracer particles are the same material with different colours.

Technical Overview At this stage, we describe the technical details of the electronic equipment employed in the experiments. Because the PTV system is limited to non-transparent fluids, only the flow surface can be recorded and analysed by an image processing system. This system consists of a JAI CV-A11 CCD camera, a frame grabber (Matrox, Meteor II) and an IBM compatible personal computer. The shutter speed of the camera is usually controlled between 1/2000 and 1/10,000 seconds. The typical space resolution is 648×492. For a shorter shutter time, the image becomes sharper. The quality of the image taken by the camera is sensitive to the source and direction of the light. A typical distance of the camera from the channel is 100 cm. A 300 W tungsten halogen light was used as the continuous light source. Every image of the motion is digitised to grey levels (ranging from 0 to 255; 8 bits) through an image grabber and stored in a computer file.

PTV Methodology The particle tracking method is employed to measure velocity fields. In an usual shear cell experiment, the minimum amount of tracer particles needed is about 5%, but for rapid motions such as avalanches a larger amount of tracer particles should be used. The amount of tracer particles thus depends on the speed of the flow and the gradients of the flow variables. Pudasaini et al. [344] used 10% identical black sand particles acting as tracer particles against the main bulk of white granular particles. From two consecutive images, the displacement of each tracer particle is identified by the autocorrelation technique (see, e.g., Natarajan et al., [293]; Hsiau and Shieh, [158]). A set of consecutive images is shown in Fig. 11.13. Firstly, a small window with $n_{1x} \times n_{1y}$ pixels is allocated around an identified tracer particle in the first image. A larger window with $n_{2x} \times n_{2y}$ pixels is drawn in the second image. This latter window must be sufficiently large to include all possible locations of the tracer particle in the next time step. The first window is then shifted in the streamwise and transverse directions by δs_i and δs_j pixels each time, which are multiplied with the corresponding pixel value of the second window to get the autocorrection value $c = c(\delta s_i, \delta s_j)$:

$$c(\delta s_i, \delta s_j) = \sum_{i=1}^{n_{1x}} \sum_{j=1}^{n_{1y}} P_1(i,j) P_2(i + \delta s_i, j + \delta s_j), \tag{11.5}$$

where i and j indicate the pixel coordinates in the images and P_1 and P_2 are the pixel values in the two image windows. When the maximum autocorrelation value c occurs, the shifts of δs_i and δs_j are used to calculate the displacement of the tracer particle (see, e.g., Natarajan et al. [293], Hsiau and Jang [157]). The errors of velocity measurements are within 7%.

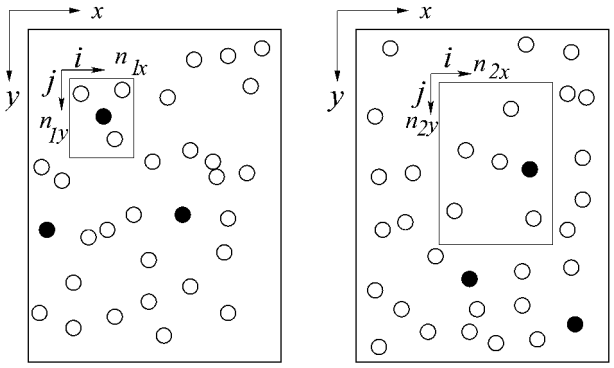

Fig. 11.13. Two consecutive frames captured by using a CCD camera during the motion of granular flow. *White circles* represent the main background bulk material and the *dark particles* are tracer particles. A small window with $n_{1x} \times n_{1y}$ pixels is allocated around an identified tracer particle in the *left image*. A larger window with $n_{2x} \times n_{2y}$ pixels is drawn in the *right image*, so as to include all possible locations of the tracer particle in the immediate next time step.

Improved PTV In order to improve the accuracy of the usual PTV methodology, HSIAU and SHIEH [158] calculated the corrections of the grey level deviations in the x- and y-directions by the following equations:

$$c_x(\delta s_i, \delta s_j) = \sum_{i=1}^{n_{1x}} \sum_{j=1}^{n_{1y}} \Big\{ [P_1(i+1,j) - P_1(i,j)] \times [P_2(i+1+\delta s_i, j+\delta s_j) - P_2(i+\delta s_i, j+\delta s_j)] \Big\} \tag{11.6}$$

and

$$c_y(\delta s_i, \delta s_j) = \sum_{i=1}^{n_{1x}} \sum_{j=1}^{n_{1y}} \Big\{ [P_1(i,j+1) - P_1(i,j)] \times [P_2(i+\delta s_i, j+1+\delta s_j) - P_2(i+\delta s_i, j+\delta s_j)] \Big\}. \tag{11.7}$$

The total correlation value $R = R(\delta s_i, \delta s_j)$ was decided by the sum of these three correlation values $c(\delta s_i, \delta s_j)$, $c_x(\delta s_i, \delta s_j)$ and $c_y(\delta s_i, \delta s_j)$, multiplied by the corresponding weighting factors k, k_x and k_y

$$R(\delta s_i, \delta s_j) = kc(\delta s_i, \delta s_j) + k_x c_x(\delta s_i, \delta s_j) + k_y c_y(\delta s_i, \delta s_j). \tag{11.8}$$

Tracer displacements in two consecutive images were then determined from δs_i and δs_j when the maximum value of R occurred. Because the deviation of

the grey value at the interface between the tracer particle and the background ones is more significant, it is easier to locate the tracer boundary. In typical experiment, the ratio of $c(\delta s_i, \delta s_j)$, $c_x(\delta s_i, \delta s_j)$ and $c_y(\delta s_i, \delta s_j)$ should be about 60:2.45:2.45. Therefore, 2, 49 and 49 were chosen as the weighting factors for k, k_x and k_y respectively ($1/60{:}1/2.45{:}1/2.45 \approx 2{:}49{:}49$). The accuracy of this modified method is $> 98.5\%$ [158].

12 Avalanche Experiments Using the PIV Measurement Technique

In this chapter, we will measure the efficiency of the extended avalanche theory of Pudasaini and Hutter [335] presented in Chap. 4 [335]. There are two ways to check the validity of a theory. On the one hand, one can apply the theory in real practice and "measure the distance between the theory and the reality", e.g., in some large-scale (natural) geophysical debris or avalanche flows. On the other hand, the performance of the theory can be judged by comparing well-controlled laboratory experiments against the theoretical prediction of the model equations via their numerical solutions.

There are many factors that directly or indirectly influence the correspondence between theory and experiments:

1. Laboratory circumstances: the experimental set-up and the measurement techniques are concerned with the technical part of the correspondence.
2. Similarly, the numerical method is responsible for solving the model equations appropriately without losing the underlying physics of these equations.
3. The theoretical model is always the heart of the description of any physical process.

Because the model equations are generally constructed with ample physical insight together with some advanced mathematical computations, one normally considers them to possess the capacity of reflecting the natural phenomenon with high precision. However, this must be verified by experiments. In this chapter, we will corroborate the physical adequacy of the model equations, the efficiency of the numerical method and their harmony with the laboratory experiments performed under essentially well-controlled circumstances. We use an advanced measurement technique. Ultimately, it will be demonstrated that for the prediction of the avalanche geometry and velocity through time, the theory, numerics and experimental results are in very good agreement.

As explained in the last chapter, we will make use of the particle image velocimetry technique to measure the dynamics of the *velocity distribution* of the avalanching flow down a curved chute. The other important variable in the

model equations is the evolution of the *avalanche geometry* from initiation to the run-out zone until it comes to rest as a deposit. We will present results of both the velocity and the height of the free surface flow of avalanches through a comparison of the experimental findings against theoretical predictions. To our knowledge, such results (in such detail by making direct comparisons with the theoretical predictions) have not been presented before. For more details on results presented in this chapter we refer the reader to PUDASAINI et al. [334, 343].

12.1 Experimental Details

Chute Geometry and Arrangement We performed several series of experiments over a curved chute as shown in Fig. 12.1.[1] consists of three different parts connected together. The inclination angle of the upper inclined plane portion is 45°; it merges continuously into the horizontal run-out zone. Specifically, the details are as follows: (*i*) upper inclined zone: length 1560 mm, (*ii*) middle continuous transition zone: (curved) length 370 mm, (*iii*) lower horizontal run-out zone: length 2250 mm. The width of all three parts is 1600 mm. Experimental images are taken separately in all three zones by repeating experiments under (essentially) identical conditions and laboratory circumstances to assure the quality and reliability of the measurements. It should also be noted that, if one includes the entire flow region, i.e., the whole chute, in a single capture, the image and the data will be highly distorted because the chute is very large and curved. In the upper right part of the chute, an electric analogue clock with two arms is mounted: the long arm performs one complete revolution in one second, whereas one unit of the short arm stands for one second. In the middle of the top of the inclined portion, a cap cut from a sphere is mounted to hold the initial mass of the granules. The cap is made of plexiglass with the supporting frame made of steel, and can instantly be lifted. This motion in the opening process is a rotation about a horizontal axis. The opening of the cap, the flashes, the cameras, the clock and the PC are all synchronised.

Initial Conditions Two kinds of caps are separately used to hold the granular materials at the middle-top of the chute (see Fig. 12.1). The caps are called "small-cap" and "big-cap", respectively, depending on their capacity (volume). Both caps are skull caps of different hemispheres. For the small-cap, the upper part, above 30° latitude, of a hemispherical cap of radius 195 mm is cut and used to hold the initial pile of the granular material. The radius of the base of the cap thus constructed is 170 mm. The big-cap is

[1] This chute was built by the workshop personnel H. HOFFMANN, H. WIENER and C. BONK of the Department of Mechanics, Darmstadt University of Technology.

Table 12.1. Details of the granular materials used in different experiments. For rice the mean diameter means the mean length of the major axis. (From [334]).

	Quartz	Yellow sand	Rice	Caps
Mean diameter (mm)	5	0.5	7	––
Mass (kg)	8.72	8.91	8.30	Small
Mass (kg)	29.30	––	––	Big
ϕ	35°	30°	40°	––
δ	23°	21°	22°	––

constructed analogously from a hemisphere of radius 300 mm. The radius of the base of this cap is 260 mm. Note that this cap is the upper part of the corresponding hemisphere above 30° latitude measured from the horizontal. This design of the caps prevents the granules from a free fall motion at the front and the top of the heap at the time of release. These caps can instantly be lifted by applying a relatively heavy load connected by a rope from the forehead of the cap to its opposite side (back of the chute) without disturbing the flow. This motion in the opening process is a rotation about a horizontal axis. Furthermore, with this choice the rear part of the heap does not initially move backward. Therefore, we can define the initial computational velocity to be $(u_0, v_0) = (0, 0)$. Other conditions concerning the internal and bed friction angles, and initial mass are listed in Table 12.1.

Materials A series of experiments was conducted for three different types of dry granular materials with small and big caps, separately. The experiments were repeated for all three zones of the chute under essentially the same conditions. The materials used for the experiments were: quartz, yellow sand and rice (long ellipsoidal). Table 12.1 presents the necessary information for the materials. Of the many experiments, only selected results are presented.

Control and Synchronisation The lifting of the cap, opening of the camera shutter, blinking of the flashes, starting of the clock and the connection of these devices with the computer are all synchronised.[2] All are controlled and operated simultaneously. Such controls and synchronisations are *crucial* in determining the *real-time* of different *snaps* and positions of the avalanching mass. The real-time elapse determined in this way is then used to find the correspondence between the experiment and the theoretical prediction.

[2] The electronic instrumentation for this was built by the electronic technician K. Polster of the Laboratory of the Department of Mechanics, Darmstadt University of Technology.

Velocity Measurements As explained in the last chapter, the velocity of the avalanching and deforming granular material is measured by the PIV measurement technique using instrumentation of the company TSI. The velocity field of the particles at the free surface and the bottom of the avalanche are measured. This provides information about the adequacy of one assumption of our theory, which deals with depth-averaged equations.

Non-Dimensional Parameters and Length Scales The model equations contain two non-dimensional parameters, ε and λ. They are associated with the geometry of the avalanching material and the chute. Provided that the chute geometry and initial conditions are similar, the model equations (4.89)–(4.91) predict the same avalanche flow irrespective of whether it is in a small-scale laboratory run or a geophysical avalanche in a large-scale mountain environment. This is a consequence of the scale invariance of the equations and, e.g., assumes that no pressure-dependent or velocity-dependent bed friction angle is used. To achieve a possibly greater generality and a real feeling for the physical variables, both the experimental and the computed results are presented in dimensional variables. The appropriate physical variables for a particular application can then be constructed by applying the (back) transformation of the scalings (4.23). To make a correspondence between the theory and the experiments we must define a non-dimensionalisation of the physical variables. We chose the same length scale in all x-, y- and z-directions, i.e., $L = H = 100$ mm and $\mathcal{R} = 100$ mm. These length scales correspond to the characteristic lengths, the initial heights of the respective granular piles kept in the caps, providing $\varepsilon = H/L = 1$ and $\lambda = L/\mathcal{R} = 1$. This preserves the aspect ratio of the physical avalanche and makes it easier to interpret the results.

Single Constituent Granulates In the theory, we treat the granular mixture as a single constituent. In reality, it is almost impossible to find geomaterials that consist of a single constituent medium. Sand, quartz or rice, whatever we use for a laboratory run, contain some dust, powder and small grains either because the material was not properly washed or abrasion occurs during the experiment. After several runs the situation becomes even worse. During the flow of an avalanche, small particles move towards the bottom and the rear part of the avalanche, whereas the larger grains are carried to the surface and collected near the front of the avalanche. This is a consequence of kinetic sieving during the dynamics of the avalanche, see Chap. 2. Therefore, it is not so easy to control the friction angle between the avalanching material and the chute and between the grains themselves. This could make the bed friction angle position-dependent. Nevertheless, in all experiments we tried to maintain the possible optimal choice by cleaning the chute with anti-static spray after each experiment and filling the caps homogeneously. Therefore, one should always recall, while comparing the experimental results with the

theory, that such factors may also be responsible for possible discrepancies between theory and experiments.

12.2 Measurement of Avalanche Depth Profiles

The temporal and spatial variations of the velocity distribution and the depth geometry describe the dynamics of the avalanche. If their prediction by the theory is correct, then there must be a good correspondence between the avalanche depth predicted by the theory with that measured by the experiment at any instant of time. In particular, we are interested to acquire knowledge of the depth profile of the deposit of the avalanche in the run-out zone. Its correct determination is very important in real applications. There are two reasons for this. Knowing the actual run-out distance (area) and the height profile of the deposit one can easily divide avalanche prone mountain terrains and valleys into danger zones of different degrees, i.e., one can construct the hazard map of the specific site. On the other hand, if there is good agreement between the theory and the experimental measurement of the height profile in the deposit, then one can easily infer the reliability and efficiency of the theory over the entire avalanche path. In this way, the theory can be used to predict the velocity distribution, depth profile, impact pressure, strain rate and other related quantities as an avalanche slides down a mountain side.

For these reasons, we measured the depth profiles of the deposits of avalanches of different materials. The depth profile of each avalanche deposit is measured very carefully with a penetrometer. In regions of large gradients of the granular pile heights the density of points is increased. For each experiment, the depth measurements are taken at (about) 200 points. The data are interpolated and the geometries thus obtained are compared with the computed geometries of the theoretical predictions. Note also that the determination of the avalanche margin at each time step is very easy and can be identified by the margin of the velocity field recorded by the PIV measurements.

Determination of the Avalanche Boundary If the mass is relatively large, the granular particles are small and regular, the chute surface is smooth, the opening of the shutter holding the pile in its initial position is very fast and it can be lifted approximately perpendicularly to the chute, and the other mechanisms are also appropriately used, then, the demarcation between the grain free and the avalanche covered zone is easy. Under such circumstances, the granular body cannot spread unsystematically near its boundary and the mass distribution around and along the boundary is fairly continuous. Otherwise, dispersion of the grains along the boundary is inevitable. Consequently, it is very difficult to define the boundary. If the boundary cannot be determined properly, e.g., because of the bouncing of the particles, one cannot

establish a reliable and accurate correspondence between the theoretical prediction and the experimental measurements. In all measurements we define a contour as the boundary of the avalanche if it passes through those points of the chute that are approximately covered (in height) at least by a single grain of the granular material. Also note that the determination of such boundaries is relatively easy for experiments with the big-cap and with sand, but it is difficult for small-cap experiments conducted with quartz particles.

12.3 Validation of the Theory

The aim is to validate of the theory by some laboratory experiments. In this section, we will present some selected results of unsteady free surface avalanche flow of granular materials in a laboratory chute against theoretical prediction, see PUDASAINI et al. [334, 343]. In particular, we will demonstrate how well the theoretical prediction of the velocity distribution of an unsteady avalanche flow down a curved chute compares with the PIV-measured velocity field of the particles at different parts of the free surface.

12.3.1 Experiments Using Small-Cap and Quartz Particles

Figure 12.1 depicts a series of experimental snapshots of an avalanche in the laboratory taken with a digital video (DV) camera. The bulk material consisting of quartz granulates is held inside the hemispherical cap that is pressed to the bottom at the upper edge of the inclined plane. The first panel shows a photograph before the cap is lifted, defining the initial condition of the avalanche, the second panel describes the circumstances right after opening the cap. As soon as the cap is removed, the bulk material is continuously extending, mostly in the direction of steepest descent. Panel three captures the fully developed flow in which the entire granular mass lies in the upper inclined zone. Comparing the first and second panels, one can see that the front of the avalanche accelerates faster than its tail. The reason for this is that the entire heap is under a passive state of stress before the cap is lifted. Immediately after the release of the cap, the front part of the heap no longer suffers a surface stress from the confining cap, and an active state of earth pressure is established. The remaining grains still feel the stresses from their neighbours (this is passive stress) until the wave front that separates the active from the passive states has reached the upper part. Thus, the motion of the frontal part of the pile is ahead of that in the rear portion. Moreover, the initial surface slope triggers the downhill motion, whereas that in the rear part acts in the uphill direction. In panel four, the avalanche front has entered the transition zone. The front of the avalanche has just crossed the front boundary of the transition to the deposition zone. Due to the downslope curvature of the chute topography in the transition zone, the avalanching front starts

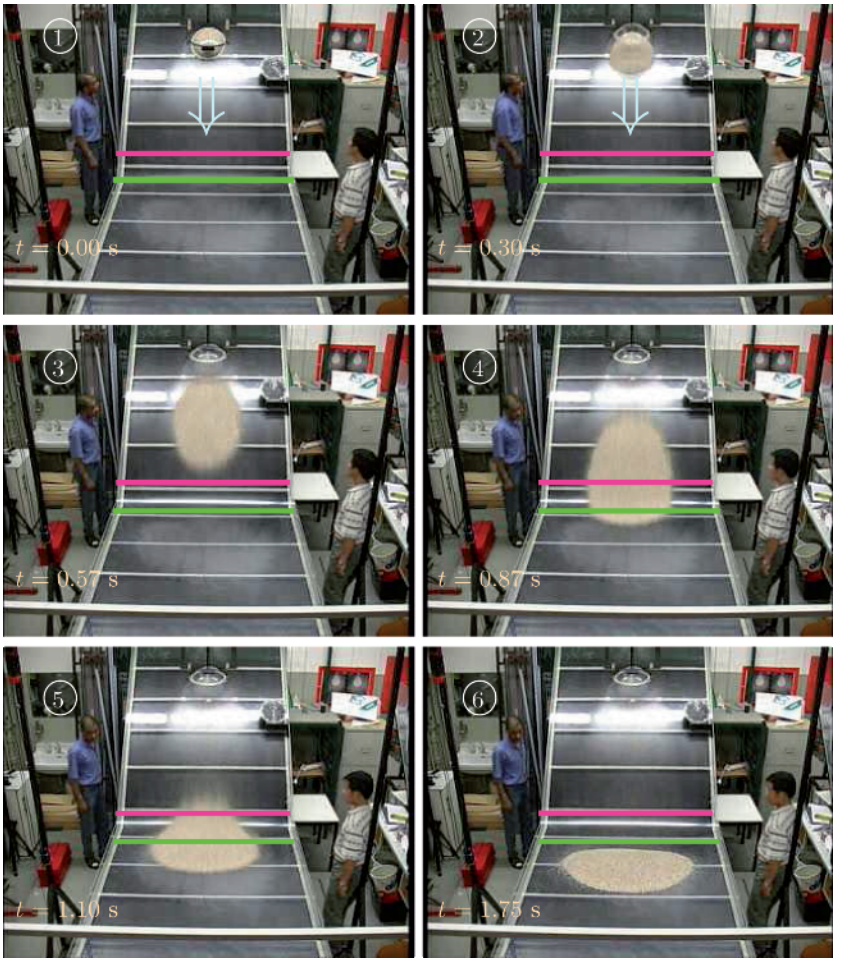

Fig. 12.1. Overview of the laboratory avalanche chute with six snapshots of a sand avalanche showing the spreading mass from initiation (*first panel*) to deposition (*sixth panel*), lasting approximately 1.75 seconds. The chute (4000 mm long and 1600 mm wide) is made of plexiglass. The upper plane part is inclined at 45°; it merges into a short cylindrical element with rear boundary at 1560 mm and front boundary at 1930 mm from the top of the chute. These boundaries are indicated by red and green lines, respectively. It is followed by the horizontal run-out plane. The sand is initially held in a hemispherical cap that is quickly tilted upward to release the material, which here is quartz of 4 mm nominal diameter. On the upper right edge of the chute an analogue clock indicates the time. The *arrows in the first two panels* show the direction of the downhill motion, the *circled numbers* indicate the consecutive orders of the snapshots and the real times are shown in the *lower left corners*. Note the somewhat blurred margins of the piles due to collisions. The persons are: *left*: S.P. Pudasaini, *right*: S.-S. Hsiau. (From [343].)

decelerating. Therefore, the mass in the front is contracting in the downhill direction due to the effect of the passive earth pressure, but the mass in the tail is still extending. The deposition of the mass commences in the vicinity of the lower end of the transition zone. The fifth panel captures a snap of the avalanche at a time when the major part of the body lies in the run-out zone and the body approaches its rest position. The rear material is now hindered from freely moving forward; it dilates in the cross-slope direction and begins to broaden its deposition. The far end part of the tail consists mainly of the fine granulates and powder is an inevitable constituent of the bulk material. The final panel shows the deposit of the avalanche, which lies entirely in the horizontal run-out zone of the chute. Although (immediately before the deposit) the front of the body is almost at standstill the mass from the tail is still flowing down and deposited on the tail side of the body. A steep surface (height) gradient is thus developed on the tail side of the avalanche. Occasionally, this steep backward slope is slightly weakened in the last phase of the motion by a backward motion of the top granules to re-establish the local angle of repose. The deposit is of convex shape, more or less but not quite "ellipsoidal" with the major axis along the lateral direction. Actually, in all panels the flowing granular body is fairly compact with only slightly diffusive margins due to particle bouncing, so that the continuum assumption seems to be justified. The shape of the body depends on the material properties, i.e., internal and bed friction angles, the chute geometry, the geometry of the material in its initial position and the initial conditions. The motion of the bulk and the deforming body from panel one to panel six defines the *complete dynamics* of the avalanche as a rapid free surface motion of dry granular material from initiation to deposit.

12.3.2 The PIV Measurement and Validation of the Theory

One of the dynamical aspects of an avalanche is its velocity distribution. It is very helpful for practitioners to have a proper knowledge of the velocity field in order to estimate the stagnation and impact pressures (on obstructions and infrastructures), stress and strain rate, and so on along the track of an avalanche sliding down a mountain topography. From a structural engineering and planning point of view, one must know the velocity field properly in order to adequately design buildings, roadways and rail transportation in mountainous regions and properly predict the tractions on obstructing buildings that may be hit by an avalanche. Of equal importance is to know the velocity field of flowing granular materials and fine granulates through various channels in process engineering scenarios to predict the flow dynamics. In this regard, we now present some results concerning the velocity field obtained by using the PIV measurements of an avalanche of quartz particles flowing down a curved chute (see Fig. 12.1) and compare it with the theoretical prediction.

We will see in the following that there is rather good agreement between theory and measurements.

Before presenting a detailed comparison between theory and measurements, some remarks are in order. In fact, the ensuing figures show the full frames captured by the camera(s) (see panels on the right of Fig. 12.2). This implies that consecutive pictures correspond to different experiments and repetitions under identical external conditions. Also note that the different colours in these pictures represent the magnitudes of a kind of mean velocity distribution in the corresponding regions determined by the contours computed from the real data of the velocity magnitudes. The magnitudes of the velocity fields are shown in colour bars on the right of each picture. It should, therefore, be clear that the real range of the actual velocity field may be somewhat larger than that presented by the colour coding. Since we plotted the mean velocity for both the measurements and theoretical predictions, there is no question of inconsistency. As we increase the number of contours, the range of the colour bars may also increase. Furthermore, the arrows indicate the directions, and their lengths represent the relative magnitudes of the actual velocity vectors in each panel.

Figure 12.2 depicts the comparison between the theoretical predictions (left panels) and PIV measurements (right panels) of an avalanche of quartz particles sliding and deforming down a curved plexiglass chute, as shown and explained in Fig. 12.1 (from PUDASAINI et al. [334, 343]). The comparison is presented at five consecutive times as indicated in the upper left corners of each panel, immediately after the onset of the motion of an avalanche until it almost reaches the deposit in the horizontal run-out zone.

The two uppermost panels of Fig. 12.2 present the theoretical versus the experimental results at the time 0.38 s. The flow is fully developed, unsteady and the granular mass lies entirely on the inclined upper zone of the chute. The motion is mainly in the downhill direction, with some sidewise spreading, accelerating, and the velocity field is symmetric about the central line ($y = 0$) of the chute. The colour bars on the right of each picture indicate the magnitudes of the velocity fields in ms^{-1}. Differences are only seen in the curvature of the lines separating the differently coloured velocity regions. The likely reason for this difference is that the shear stresses τ_{xy} parallel to the sliding surface are ignored in our theory but may be active in the experiment. Apart from this, comparison of the two panels shows excellent agreement between theory and experiment for both the geometry (boundary) and the velocity distribution of the avalanche of quartz particles for this time step.

The second row contains the theoretical and experimental results at time 0.63 s. A trace of a boundary layer effect along the margins can be seen in the experimental panel. As soon as the mass crosses the upper boundary of the transition zone (horizontal red line), the flow switches from its supercrit-

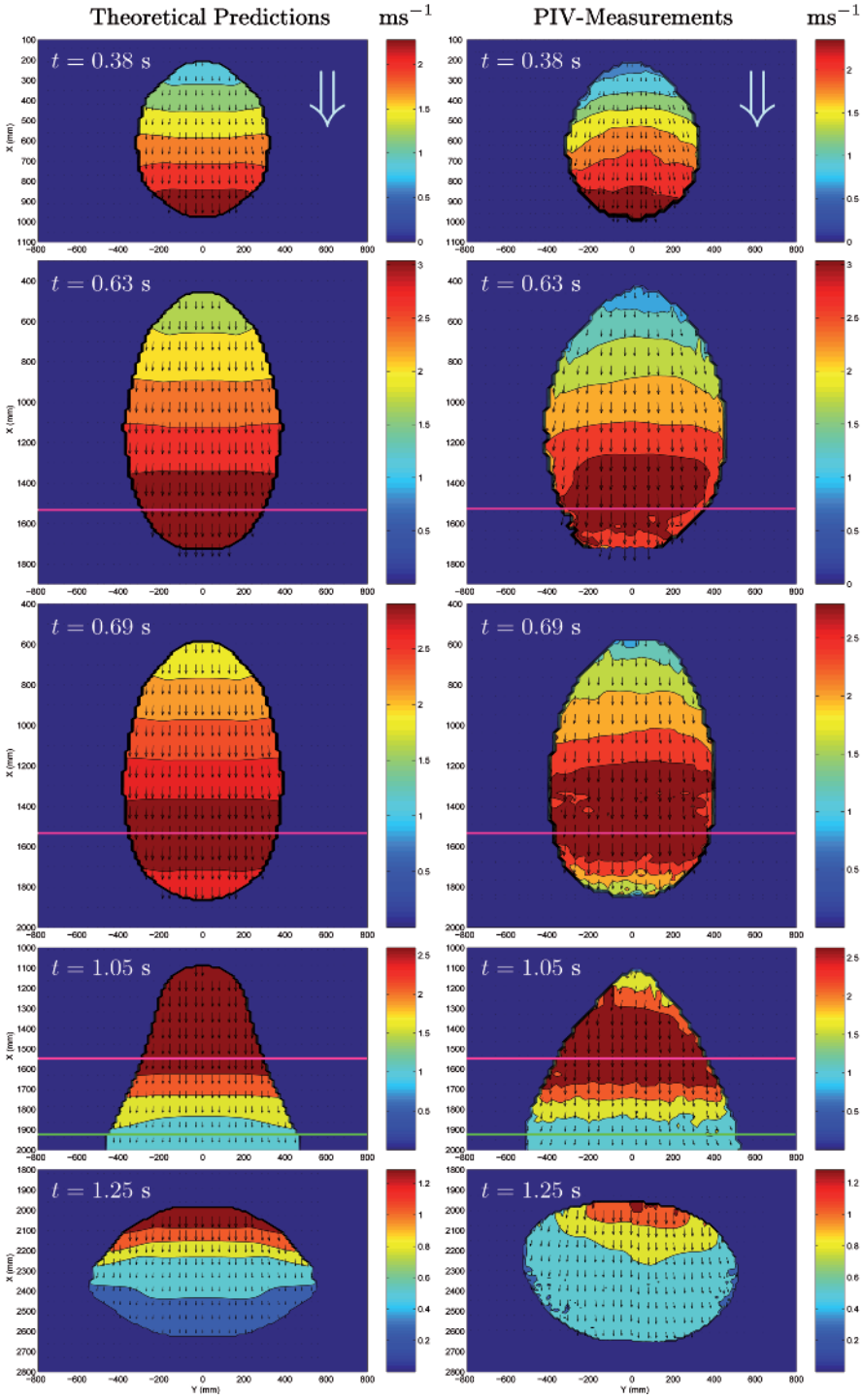
Theoretical Predictions
ms^{-1}
PIV-Measurements
ms^{-1}
$t = 0.38$ s
$t = 0.63$ s
$t = 0.69$ s
$t = 1.05$ s
$t = 1.25$ s
X (mm)
Y (mm)

◀

Fig. 12.2. Comparison between pile geometries and the velocity distributions at the surface according to the theoretical prediction (*left panels*) and the PIV measurements (*right panels*). The experimental configuration is explained and presented in Fig. 12.1. Very good agreement between theory and experimental measurements of the velocity distribution is seen. (From [343].)

ical to the subcritical state, and the mass starts decelerating. This is seen in both panels, but most clearly in the experimental one, in which the velocity reduction at the front tip of the margin seems to be somewhat larger than in the computed panel. Otherwise, the measured pile is slightly wider than the computed one, and in the rear the computed pile is rounder than the measured pile. The slight asymmetry of the measured pile cannot be explained. This asymmetry seems to disappear as the pile moves on. Apart from this, there is very good correspondence between the prediction of the theory and the PIV measurements.

At time 0.69 s (panels of row three) a large portion of the mass has entered into the transition zone. At this time, the transition of the flow from the supercritical to the subcritical state can be clearly seen in both panels. As explained before, this is the effect of the curvature of the chute in the downhill direction. Although the body is contracting around its front, it is still extending in its rear part. Comparing the experimental and computed velocity distributions and the pile geometries, it is seen that the symmetry of the experimental avalanche pile is almost established. As in the previous panels, one can see very good correspondence between theory and experiment.

A special situation is presented in the fourth row (time 1.05 s) in the sense that these panels only show the rear part of the pile (only this part was covered by the camera). Furthermore, the panels exhibit the motion of the avalanche in three parts: the upper inclined zone, the middle transition zone and the lower run-out zone. A close look at the lower parts of both panels reveals that the granular body is contracting around its front in the run-out zone. Since the chute is laterally unconfined, the granular mass is extending in the cross-slope direction near the front. This spreading is symmetric about the central line. The longitudinal earth pressure is increasing (passive pressure state), and this information is propagating upstream. This can clearly be observed, if we compare these panels with the panels of the third row, because the magnitude of the velocity field has considerably decreased. On the other hand, the cross-slope earth pressure is decreasing (active pressure state). This information is also propagating upstream. As soon as the mass enters the run-out zone, the velocities of the particles decrease rapidly. Consequently, the mass is extending in the lateral direction. Although the rear margin is far more pointed in the experimental pile than in its computed

counterpart,[3] comparison of the theoretical prediction with the experimental result nevertheless still reveals very good agreement.

The last panel describes the state of the avalanching mass just before it comes to rest at time 1.25 s. The entire mass of the body now lies in the horizontal run-out zone. Although the particles around the rear ends are still considerably in motion, those near the front of the body are close to rest. Note that, although the colour distribution does not seem to correspond exactly to each other between theory and measurement, their numerical values agree quite well. The discrepancy in the shape of the pile body is also due to the contour plotting because it neglects that part of the body that has very small velocity magnitude. Apart from this, the lateral and longitudinal spread of the body and velocity distributions between the theoretical predictions and the experimental measurements are both in very good agreement.

12.3.3 Evolution of the Avalanche Geometry

We have seen in the last section that the PIV measurements can obviously be used to determine the avalanche boundary, and thus the areal coverage, during the motion. Since the applied technique is only apt for the velocity measurements, we cannot use it to determine the three-dimensional evolution of the avalanche geometry. For this, we need to apply some other techniques such as digital photogrammetry. One of the most important aspects in avalanche dynamics is the determination of the run-out area and the height profile of the avalanche in its deposit. This is so, because with this information we can construct the hazard map and estimate the impact pressures on obstructions in the run-out zone. The evolution of the three-dimensional geometry along the entire track is not so vital. For this reason, we measured the avalanche height in the deposit using a penetrometer. Figure 12.3 displays the contours of the depths of the avalanche in the deposition area both for the theoretical prediction and the experimental measurement at times $t \geq 1.35$ s when the avalanche is at rest, see also Pudasaini et al. [334, 343]. It is clearly seen that the lateral and longitudinal run-out distances, the over all run-out zone, as well as the height profiles are well-predicted by the theory.

12.3.4 Multi-CCD Cameras and Velocity Shearing

The avalanche equations developed by us and presented in Chap. 4 to predict the velocity and evolution of the avalanche geometry is based on realistic

[3] The source for this is unknown and we can only muse about possible causes: local fines may reduce the bed friction angle, decreased bed friction at the rear margin, which seems to be evident from the colours at the immediate rear end of the experimental avalanche.

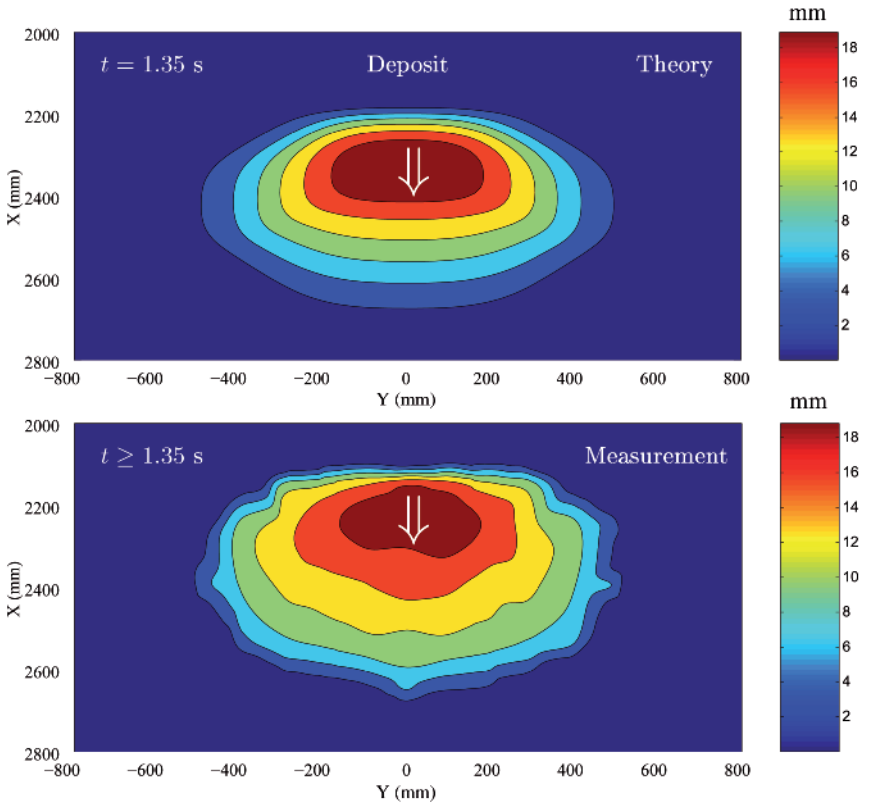

Fig. 12.3. Final deposit of the avalanche. The *contours in the upper panel* represent the computed avalanche heights and the *contours in the lower panel* represent the measured heights, both in the horizontal run-out zone. The experimental result is well-predicted by the theory. (From [343].)

assumptions. One of them concerns the velocity distribution. We assumed that the velocity profile is almost uniform through the depth of the avalanche. This assumption may not be adequate right after the release, in the vicinity of obstructions and close to the deposit where both the height and vertical component of the velocity field may change considerably, in some cases even abruptly. Therefore, assuming uniform velocity is a good approximation only when there is a smooth boundary. However, along the main flow path or along the track of the avalanche, the concept of a uniform velocity distribution through its depth should be a fairly reasonable assumption. We analysed the images just before the transition zone so as to have both a fully developed unsteady flow and good quality and resolution of the images. Also note that, for simplicity, only a rectangular portion of the avalanche containing the central line of the chute (the left boundary in Fig. 12.4) is taken into account.

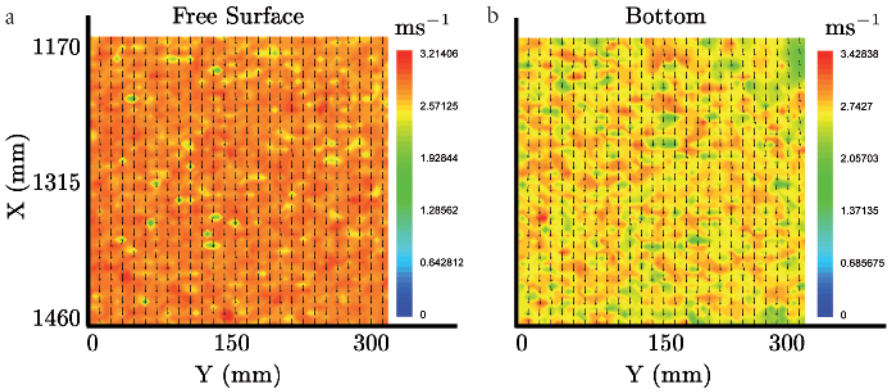

Fig. 12.4. Velocity distribution: **a**) at the free surface, **b**) at the bottom. The actual topographic location of the chute is shown in length units in mm. The left velocity field is computed from the image captured by the CCD camera from the top (free surface) and the right field is its counterpart computed from the image captured simultaneously by another CCD camera from the opposite side (bottom) of the plexiglass chute. For a better visualisation the right field is mirrored about the central line of the chute. (From [343].)

Two cameras were placed and aligned parallel to the normal of the chute surface about 1000 mm distance from the chute on both sides. Since we used a plexiglass chute, images from either side of the chute was possible (to capture). The measured velocity distributions from the top and bottom of the chute show that the difference between the top and bottom mean velocities is about 5%, providing the physical justification of the assumption on the velocity profile through the depth of the avalanche. We computed the relative difference between the top and bottom velocities with the following expression:

$$\text{relative difference} = \frac{\int_A (v_{\text{top}} - v_{\text{bottom}})\, dA}{\sqrt{\int_A v_{\text{top}} dA}\ \sqrt{\int_A v_{\text{bottom}} dA}}, \tag{12.1}$$

where A is the area of the image zone, v_{top} and v_{bottom} the velocity at the top and bottom, respectively. The difference in the mean between the top and bottom velocity fields is computed by

$$\text{relative difference in mean} = \frac{\overline{v}_{\text{top}} - \overline{v}_{\text{bottom}}}{\sqrt{\overline{v}_{\text{top}}}\ \sqrt{\overline{v}_{\text{bottom}}}}, \tag{12.2}$$

where $\overline{v}_{\text{top}}$ and $\overline{v}_{\text{bottom}}$ are the mean values of the velocities at the top and bottom, respectively.

Furthermore, in the following, we will also discuss standard deviations at the top and bottom of the flow, respectively.

Figure 12.4a depicts the velocity measurement at the free surface of a fully developed avalanche of quartz particles initially kept in a cut of the hemispherical cap (small cap) as explained earlier (details are taken from PUDASAINI et al. [334, 343]). Similarly, Fig. 12.4b displays the velocity field at the bottom of the avalanche measured from the opposite side of the plexiglass chute. For better visualisation this field is mirrored about the central line $y = 0$ of the chute. Mean values at the top and bottom are 2.79 ms^{-1} and 2.65 ms^{-1}, respectively. Therefore, the mean deviation between the top and bottom velocities is 5.1% [from (12.2)]. Standard deviations for the top and bottom velocity profiles are 0.24 ms^{-1} and 0.32 ms^{-1}, respectively. Another important aspect is the relative difference between the top and bottom velocities, computed in relation with the corresponding values at the top and bottom of the flow, which is found to be 9% [from (12.1)]. This value is larger than the mean deviation between the top and bottom velocities computed separately. The reason for this are large errors at some points on the bottom data. This analysis indicates that, although the absolute maximum value of the velocity field in the right figure is a bit larger than in the left one, the mean velocity at the free surface is slightly larger than the mean velocity at the bottom. The non-realistic larger absolute values in the right figure emerge from the measurement errors. There are two main error sources. Firstly, the chute is a bit scratched. These scratches produce random reflections. Secondly, reflections are also due to the horizontal metal bars (the supports of the chute). These reflections artificially increase the magnitudes of the velocity field. However, there is no problem of this kind for the image taken from the top of the chute. The higher value of the standard deviation (for the right figure) also manifests the random fluctuation of the velocity field due to these reflections. Otherwise, a comparison between these two figures reveals that for the fully developed motion of an avalanche, the velocity distribution through the depth is highly uniform.

Finally, we would like to mention the following results based on simulations of model equations with and without inclusion of the velocity shearing. In order to study the effects of the velocity shearing, we introduced momentum correction factors in the momentum balance equations and concluded that *a depth-averaged model based on uniform velocity profiles provides a fair description of the dynamics of flow avalanches even on rather rough beds* [183].

12.4 Is There a Terminal Velocity on Inclined Planes?

12.4.1 Background

The question as to whether the basal drag can be described by a dry COULOMB-type law alone or must be complemented by a velocity-dependent contribution has been disputed ever since VOELLMY presented his avalanche

model, which in fact contained both [430]. We have also seen in Chap. 5 that introducing a viscous contribution to the basal drag changes the qualitative behaviour of the flow of a granular mass down an inclined chute considerably. Once again: for flows down an inclined plane, COULOMB friction alone with constant friction angles leads to an ever accelerating flow far downstream, whilst a viscous sliding law yields a steady flow far downstream, as does a flow subject to a combination of a COULOMB-dependent and velocity-dependent drag. Steady flow can also exist for COULOMB drag alone, but then it must be down a chute with a curved base, or the bed friction angle must be velocity-dependent [373].

Measurements have been performed on inclined planes at low inclination angles smaller than 30° by POULIQUEN and POULIQUEN and FORTERRE [329, 330], which indicate that the drag is velocity-dependent. Our own measurements and comparisons with computational results, using the extended avalanche equations, however, never indicated that the introduction of the velocity-dependent term was necessary (see, e.g., Chaps. 10 and 12). Our own experiments were consistently carried out for granular flows on steep slopes with inclination angles larger than 30°. Moreover they were conducted on relatively smooth beds, whilst POULIQUEN's experiments were done on bumpy beds and may for that reason have led to shearing conditions that affected not only the base via sliding, but a considerable layer of the entire avalanche depth. We studied latter point [183] by accounting for this shearing in the model equations, and was found through a series of avalanche computations that in almost all situations it had a negligible effect on the geometry of the deposits. However, the question as to whether a velocity-dependent drag is important still remains unsettled.

One may ask, whether this question can be settled experimentally. An attempt was made to this end by ECKART et al. [83] in an experimental study, using PIV, of flows of a cohesionless granular material down inclined planes. In fact, they studied the flow from a silo through its outlet slit down plexiglass planes of 30°, 35°, 40° and 45° inclination, 650 mm, 1850 mm, 2850 mm lengths, 260 mm width, and photos were taken from above, the side and below.

One of the tasks in this section is to find indications of a terminal velocity of the avalanche. Another challenging question is the dependence of the flow behaviour on the inclination angle. Different flow behaviour of the avalanche may define a "(phase) transition", where the flow behaviour changes significantly, for example, from more fluid-like to more solid-like behaviour (see also [330]).

12.4.2 Remarks on Experimental Procedures

When sand moves on plexiglass surfaces uncontrollable forces due to electrostatic charging may develop. To minimise these, an anti-static spray was applied before each experiment. Furthermore, it was checked whether variations in the measured velocities between identical repetitions of the experiments would remain small, and indeed they did. Experiments were conducted with cohesionless sand of a nominal particle diameter of 0.5 mm and roundish shape. The (static) basal friction angle of the sand on plexiglass is 20°.

Pictures were taken from the side and above. For those taken from the side, the camera had a distance between 400 mm and 600 mm from the chute. The visible section corresponds to a rectangular domain of 100 mm × 200 mm. Note also that for all measurements taken from the side through the plexiglass, only the velocity at the boundary was measured, which in general is different from the internal velocity away from the boundary. In all these pictures, the avalanche flows from left to right. For the pictures taken from the top, the camera had a distance of 100–200 mm from the chute. In this case, the avalanche always flows from the top of the picture to the bottom. For data analysis, the raw data were subjected to a validation procedure using range and mean filters to eliminate the faulty data.

12.4.3 Results

Free Surface Velocities We start our discussion with surface velocity measurements obtained near the outlet for inclination angles of 30°, 35°, 40° and 45°, which are presented in Fig. 12.5. In each panel velocity vectors (in black) and the velocity magnitude (in colour) are shown, in one case in shades of grey. The colour scale is always chosen according to the maximum velocity measured in this particular experiment. The measurements were taken approximately 0.5 s after release, when the whole chute is covered by material. The visible region is 450 mm downstream from the outlet, which is at $y = 0$. Here it can be clearly seen that the qualitative behaviour of the flow is the same for all inclination angles investigated. This can be concluded from the relative distribution of the velocity magnitude, which is nearly the same for all panels. The avalanche accelerates downstream; the maximum velocities of each experiment are reached at the bottom of all pictures. Furthermore, the velocity distribution in the cross-slope direction (i.e., in the x-direction, note that the x- and y-directions are interchanged in this section) is quite uniform in all panels. From this, we conclude that the boundary effects due to the confining side walls are relatively small and restricted to very thin layers in the direct vicinity of these walls.

Next, we turn to the end of the long chute (see Fig. 12.6). Here the velocity was measured at the end of the chute (i.e., $y = 0$ means 1850 mm down-

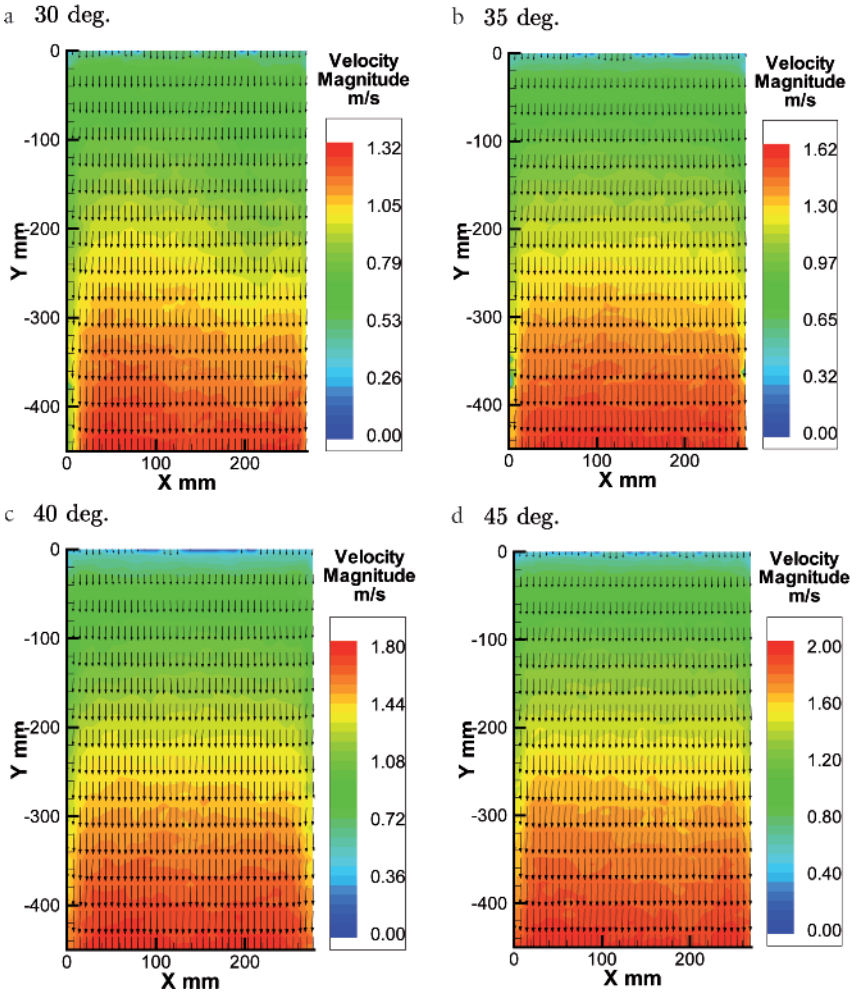

Fig. 12.5. Measured surface velocity near the outlet ($y = 0$) for four different inclination angles. Motion is from *top* to *bottom*. (From [83].)

stream from the outlet), where the visible region corresponds to a domain of 730 mm. The pictures were taken approximately 0.75 s after release. Once again, velocity vectors and the velocity magnitude are given in panels (a)–(d) for inclination angles of 30°, 35°, 40° and 45°. It can be seen that the velocity values in Fig. 12.6 are larger than those in Fig. 12.5; the avalanche has

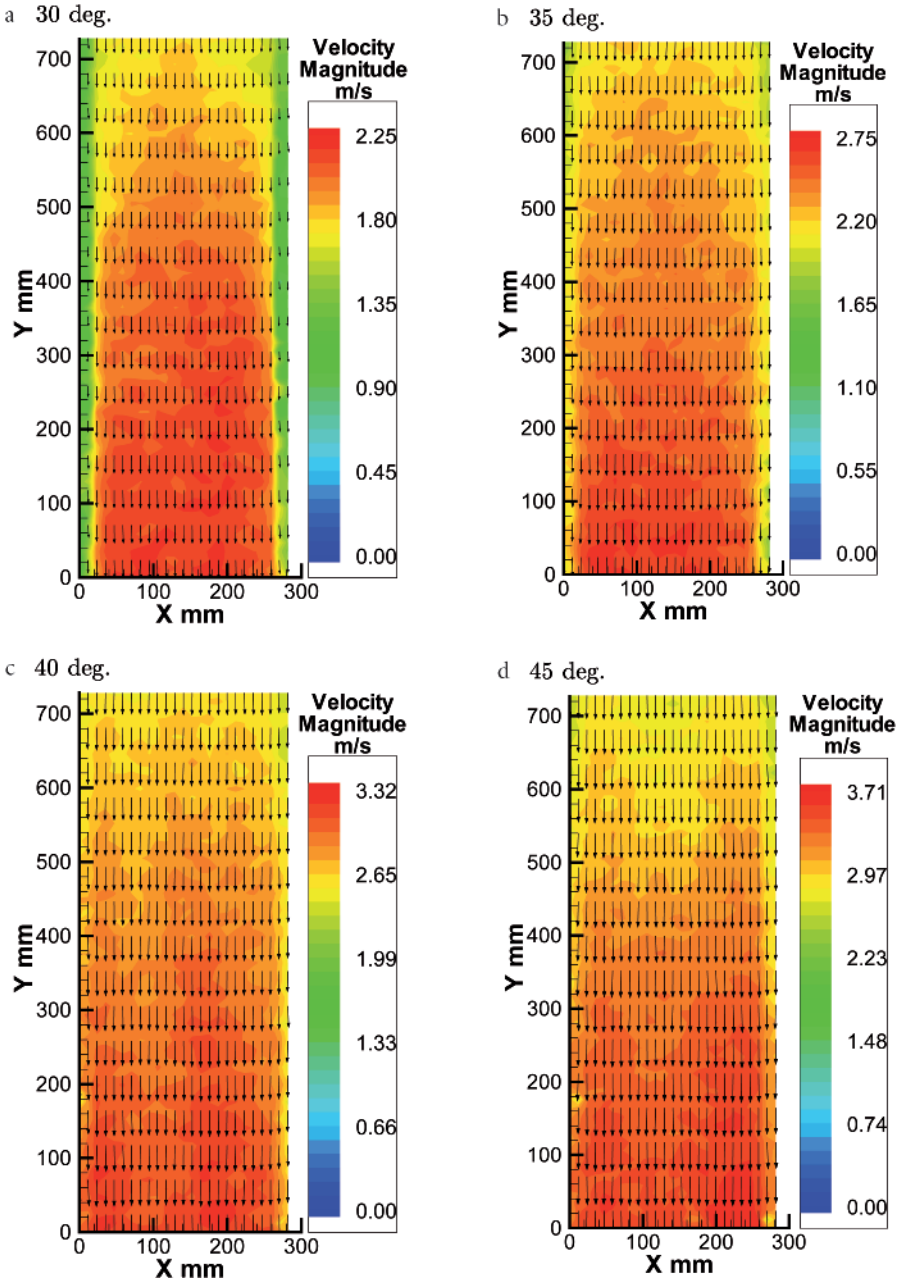

Fig. 12.6. Measured downslope surface velocity near the outlet for four different inclination angles. Motion is from *top* to *bottom*. (From [83].)

clearly accelerated further downstream.[4] However, the velocity differences in each panel decrease compared to those in Fig. 12.5.

The velocity distribution in panel (a) for an inclination angle of 30° differs slightly from that of the other panels. On the one hand, pronounced side boundary layers can be seen where the velocity differs significantly from the velocity in the middle of the chute. The material in these boundary layers has a velocity of approximately 1.35–1.5 ms^{-1} and seems to accelerate more slowly or at least with some delay as compared to the bulk in the middle of the chute. Recall that the maximum velocity in panel (a) of Fig. 12.5 was 1.32 ms^{-1}. The boundary effects for the other inclination angles are less pronounced. On the other hand, there are slightly "darker" regions in panel (a) than in the other panels, which means that the distribution of the velocity magnitude in this panel is slightly different from those in the other ones.

Let us now turn to the measurements obtained for an extra long chute (2.85 m), which are presented in Fig. 12.7. The axis $y = 0$ corresponds to a distance of 2850 mm downstream of the outlet, the visible region is 720 mm. Now, a significantly different behaviour can be observed, in particular in panel (a), where the results for an inclination angle of 30° are presented. Firstly, *the maximum velocity is not located at the end of the chute as is to be expected, but is more or less randomly distributed* in this picture. The velocity magnitude does not change much within this picture except perhaps in the boundary layer. It is worth noting that the maximum velocity in panel (a) of Fig. 12.7 is nearly the same as in panel (a) of Fig. 12.6 (long chute). From these results it can be concluded that a rate-dependent drag law must probably be included in depth-integrated theories. This behaviour for panel (a) of Fig. 12.7 is not seen in panels (b)–(d), and the velocity is significantly increased in comparison with panels (b)–(d) of Fig. 12.6 (long chute). However, to examine this clearly, even longer chutes would be needed. We may now summarise and clarify the results of Figs. 12.5, 12.6 and 12.7. This is done in Fig. 12.8, where we present cross-slope-averaged values of the velocity magnitude from Figs. 12.5, 12.6 and 12.7.

The most remarkable information that can be inferred by comparing panels (a)–(d) of Fig. 12.8 is that the behaviour for an inclination angle of 30° differs significantly form the other ones. It shows that for travel distances beyond 2–3 m the avalanche no longer accelerates but seems to come to a steady state (terminal velocity). Note that the scale of the vertical axis in panels (a)–(d) is chosen according to the maximum velocity for this particular inclination

[4] Note that the colour distribution in Fig. 12.6 is slightly distorted as compared to Fig. 12.5 (i.e., the mean colour is shifted to higher velocities) to be able to show flow details.

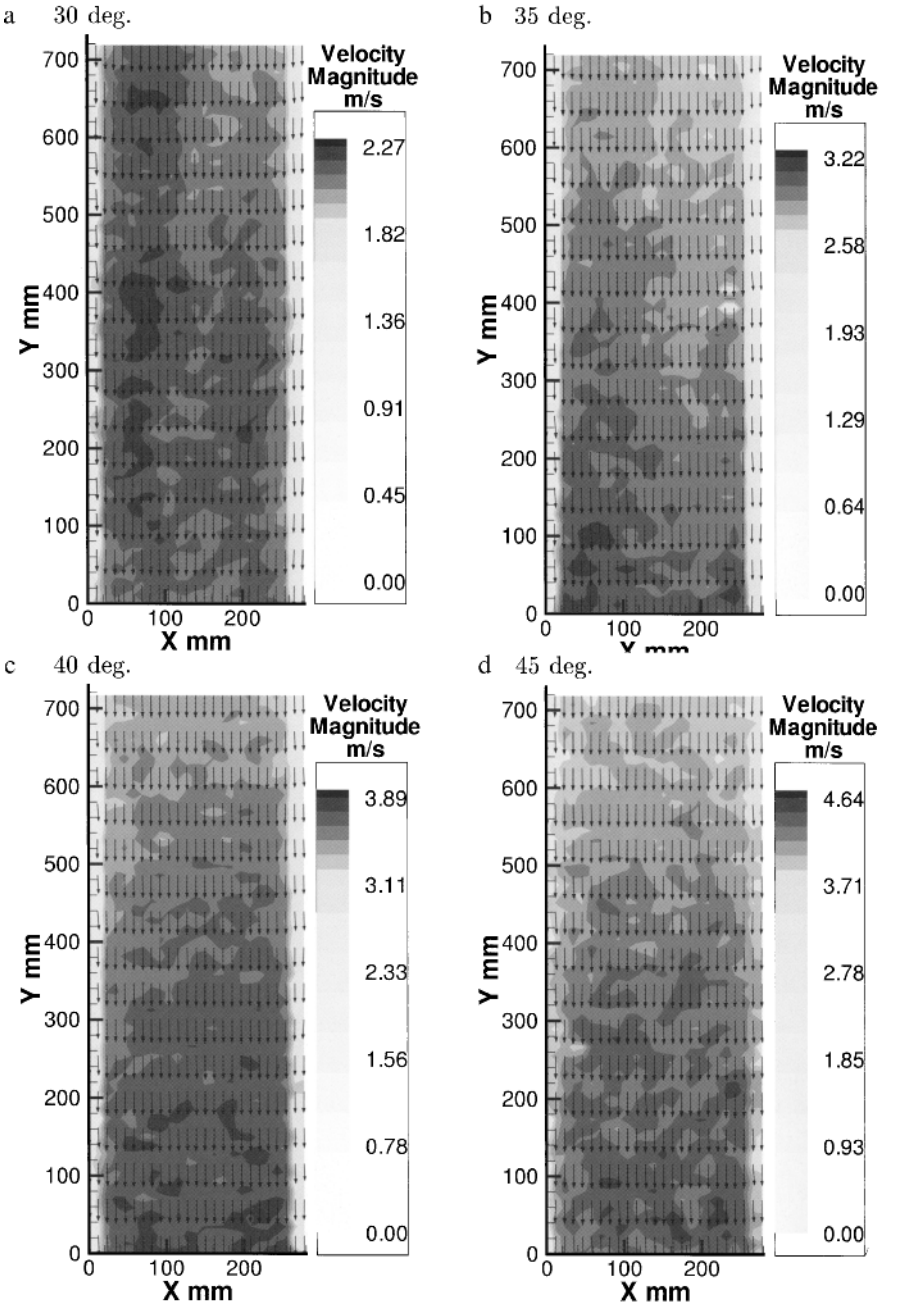

Fig. 12.7. Measured surface velocity at the end of the extra long chute for four different inclination angles. Motion is from *top* to *bottom*. (From [83].)

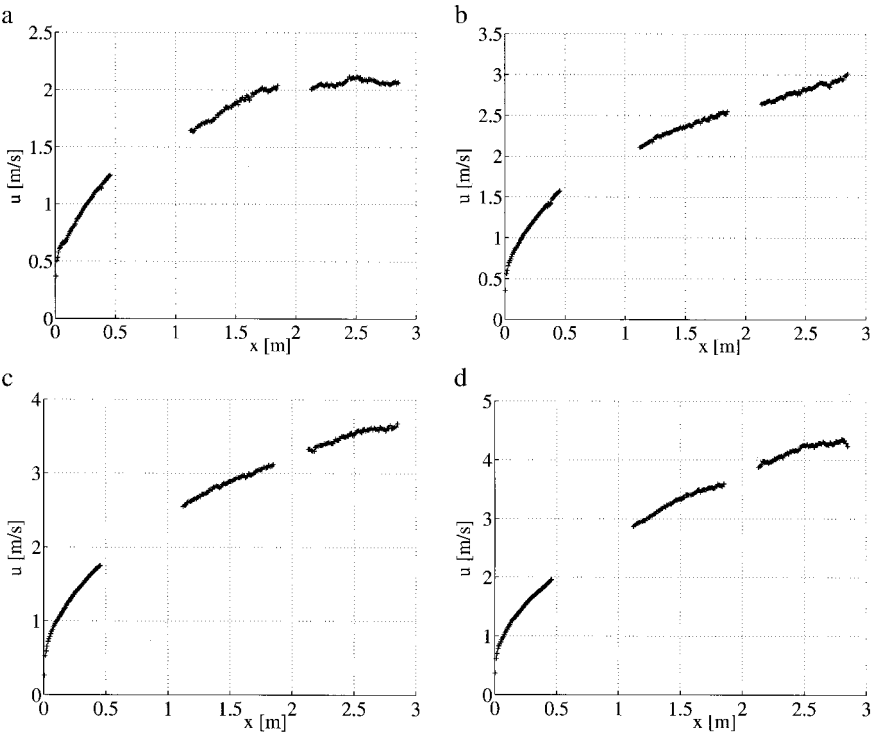

Fig. 12.8. Cross-slope-averaged velocity values calculated from the experimental results for (**a**) 30°, (**b**) 35°, (**c**) 40° and (**d**) 45°. (From [83].)

angle. The curves for the inclination angles of 35°, 40° and 45° are rather similar in shape.

In summary, we conclude that for granular flows on steep planes with inclination angles larger than 30° a terminal velocity was not reached within a chute length of approximately 3 m. For a chute inclination of 30°, however, there are indications that within 3 m steady flow conditions are reached. This agrees both with observations of Pouliquen [329] in his own laboratory experiments with small inclination angles ($\leq 30°$), deductions for field data of snow avalanches by Ancey and Meunier [7] and our own observations. This problem obviously warrants further study.

Velocity measurements have also been made from the side of the chute through the plexiglass walls both immediately below the head gate from the silo (Fig. 12.9) and near the end of of the short chute (Fig. 12.10).

Observations from the Side It can be seen in Fig. 12.9 that (in the vicinity of the outlet) there is a region where the material at the bottom nearly sticks

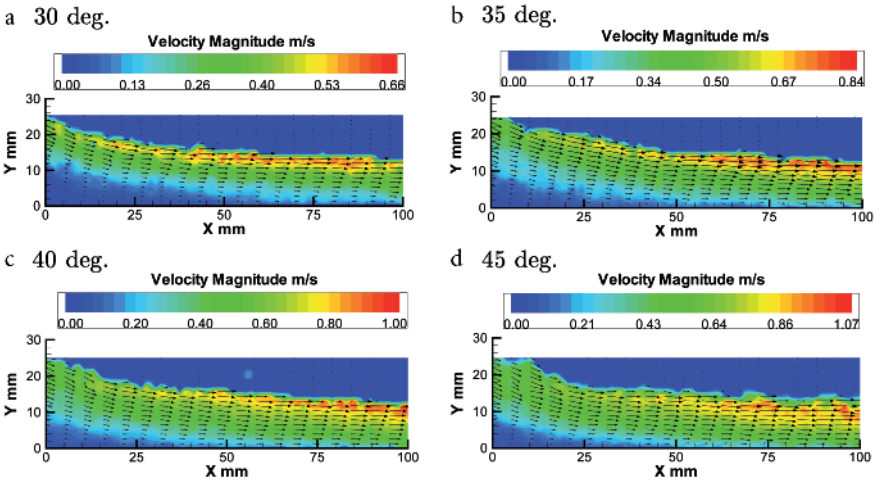

Fig. 12.9. Velocity measurements from the side at the outlet for different inclination angles. Motion is from *left* to *right*. (From [83].)

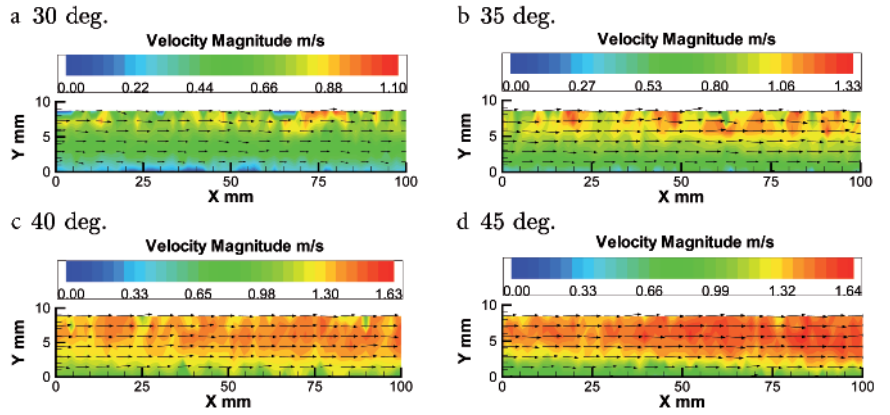

Fig. 12.10. Velocity measurements from the side near the end of the short chute for four different inclination angles. Motion is from *left* to *right*. (From [83].)

to the bed (called a "dead zone"), while the material at the top is already flowing: the material is vertically divided into (at least) two regions, where the upper region slips over the lower region. This fits quite well with the observations and descriptions of creeping flows of soils as shown in [436]. However, the panels of Fig. 12.9 show only the onset of the flow. The velocity profile is clearly not constant through depth. Comparisons of the velocity measurements that were taken for different inclination angles show that the dead zone increases if the inclination angle decreases. Indeed, if we were to further decrease the angle, the dead zone material would remain stagnant

on the chute whilst the complete upper layer would flow down. A similar behaviour is also reported in [329, 330].

There is an obvious qualitative interpretation of the fact that the velocity profiles close to the left end show a pronounced dependence across the layer depth with zero velocity at the base and a much more uniform distribution close to the right end. The free surface exerts no shear resistance to the surface particles and so they are accelerated first. It takes some time (i.e., the distance from the left to the right) until this information has reached the bottom. This is obviously faster for the steeper chute inclinations than for the shallow ones. The initial shearing is larger, but at a distance of 50 to 100 mm from the outlet it is small and the deviation of the velocity profiles from uniformity is considerably reduced.

In the velocity measurements of Fig. 12.10 near the end of the short chute, it can be seen that the velocity is to a good approximation uniform through depth. Recall (also from the surface velocity measurements) that the velocity at the confining plexiglass wall is not the same as inside the flow region, hence the velocity distribution through depth also cannot be the same as in the middle. However, ECKART et al. and PUDASAINI et al. [83, 334, 343] also performed experiments with two cameras, one from above the other from below and corroborated equality of the surface and basal velocities at an interior region to within very small experimental differences.

12.4.4 Summary

In this section, we presented and discussed the experimental results of sand avalanches flowing down inclined rectangular plexiglass chutes. Surface, basal and sidewall velocities were measured with a PIV system. Although the PIV system was originally not designed for the flow of granular avalanches, it provides a good measuring technique for visible regions of the flow. The major difference of the granular PIV to usual PIV is the use of flash lights instead of laser light sheets, which cause a more or less inhomogeneous illumination. Careful positioning and use of the flashes are required to reduce measurement errors. Sand avalanches possess enough surface structure for the system to easily detect a moving pattern, i.e., no seeding (tracer particle) is needed.

Surface measurements of the avalanche for inclination angles of 35°, 40° and 45° showed nearly the same qualitative behaviour. The avalanche accelerates downstream on all chutes and the maximum velocity is higher for larger inclination angles. However, for the smallest inclination angle of 30° an onset of a terminal velocity on the longest chute (approximately 3 m) was detected. In this case, the avalanche did not accelerate any further. This shows a significantly different behaviour in comparison with results for other inclination angles.

It is perhaps premature to draw definite inferences from this result, because it only points at a peculiar behaviour but does not explore it in its full extent. Two different physical behaviours are imaginable: (*i*) a possible "phase" transition where the granular flow changes significantly when starting from slopes that have inclination angles smaller than, say 30°, from the other regime at inclination angles larger than 30°; (*ii*) a more complex frictional behaviour than COULOMB-type (e.g., COULOMB plus a viscous-type behaviour) for sliding on slopes on all inclination angles. The presently known experimental results do not seem to support either of the two possibilities. Further experiments are needed on even longer inclines to see whether, asymptotically, constant velocities are reached.

For the measurements taken from the side of the channel and the experiment carried out with two cameras (one below and one above the chute) we showed that the velocity distribution through depth is fairly uniform except in a limited region very close to the outlet. Thus, the assumption of a uniform velocity distribution through depth is reasonable, at least for the flows investigated here. At high velocities we observed small boundary layers in the vicinity of the confining walls, whilst in the interior the velocity remained uniform across the channel. The boundary layers were more pronounced for smaller inclination angles and for longer distances down the chute.

12.5 Concluding Remarks

One of the most fundamental questions related to the avalanche theory presented in this book is: are these model equations really able to simultaneously predict flow properties such as the velocity and flow depth in chutes and channels? Several results can be found in the literature concerning the geometric deformation of the granular pile from initiation to deposit. They are reported in Chap. 10 and involve chute flows as well as two-dimensional flows over various topographies. However, comparison between the theory and the experimental results for both the dynamics of the velocity field and the geometry of the avalanche along the channel and in the run-out zone are scarce in the existing literature. In fact, we only know of velocity measurements in an exponentially curved channelised chute as reported in [175]. There, only the velocities at the front, at the position where the avalanche depth has a maximum and at the trailing edge were measured. However, the results were not complete and not convincing as far as velocities are concerned, because of the large errors incurred by the measuring technique (see Fig. 10.15). To improve on velocity measurements and to make it complete was one of the purposes of this chapter.

Both the velocity distribution and the evolution of the avalanche boundary from its initiation to the deposit on the run-out zone and the depth profile of

the deposit, were measured. We introduced and used the PIV measurement technique to measure the velocity field of non-transparent granular particles at the surface and the bottom of free surface flows of non-uniform and unsteady motions of avalanches over a chute curved in the main flow direction and merging continuously into the horizontal run-out zone. The results are presented for different regions of the chute and for different times. We were able to demonstrate excellent agreement between the theoretical predictions and experimental measurements. This, ultimately, proves the applicability of the theory and efficiency of the numerical method, and establishes a very good correlation between theory, numerics and experiments.

We further presented results on velocity variations along inclined planes of different lengths to see whether a uniform flow released from rest would reach a steady velocity. However, measurements performed along four different chutes with different lengths did not clearly indicate that the granular flow down an inclined plane reaches steady conditions. Thus, the necessity of a velocity-dependent drag does not seem to be compelling.

Mention should also be made of work by TISCHER et al. [423], who also used PIV-measuring techniques to analyse the kinematics of sand avalanches on inclined beds with inclination angles ζ in the interval $\zeta_r < \zeta < \zeta_m$, where ζ_r is the angle of repose and ξ_m is the maximum angle of stability, beyond which sand grains start to move along the side of a heap. They released a continuous grain flow from a bulb pipette on an inclined plane that is either rough, solid and immobile, or consists of a loose layer of sand and observed different behaviour in the two cases. The PIV technique applied by them is similar to ours. Since the purpose of TISCHER et al. was the description of the observed flow, and no theory or model description was provided, details are not presented here. Finally, since our PIV results seem to indicate a steady terminal velocity when the inclination is below 30°, which is obtained also by POULIQUEN, it is equally appropriate to call upon FÉLIX AND THOMAS' work [98] on the relation between dry granular flow regimes and morphology of the deposit. With classical laboratory experiments – not using PIV – these authors show that the frontal velocity of a finite width granular mass (they use glass beads) down an inclined plane from a steady upstream finite width source, reaches a constant. Since their inclination angle is 20°, this result seems to reinforce the statement, spelled out above, that the frictional behaviour is different for $\zeta < 30°$ than for $\zeta > 30°$. A clear understanding still awaits to be found.

Part V

Avalanche Protection and Defence Structures

13 Protection Against Snow Avalanche Hazards

The main purpose of research on *avalanche dynamics* is the issue of *avalanche protection* in mountainous regions that are frequently targeted by such natural calamities. For mountainous countries or regions, such as Austria, Canada, France, Iceland, Italy, Japan, Nepal, Norway, Russia, Switzerland and the United States, to name a few, an effective avalanche warning service is crucial to safeguard densely populated areas and traffic lines, and to provide ski area operators, off-piste skiers and mountaineers with up-to-date information on the current snow and avalanche situation. Since historic times people of the Alps have developed and used different avalanche protection measures on the sloping faces of the mountains above their settlements, agricultural farms, and other important objects. There is no unique way or method for avalanche protection. It may depend on the slope, slope orientation, topography, snow cover, vegetation, and the nature of the object needing protection, i.e., whether it is a single object, a road, a highway, a railway track, a house, a small village or a whole town. Another important factor may be whether the protection measures are to be taken on a steep slope of a mountain (the starting area), with the intention of preventing the avalanche from being formed; or in the likely travelling zone of an avalanche, rockslide and landslide to influence, i.e., redirect or slow the motion to its standstill.

The technology of avalanche protection has primarily been developed in the context of snow avalanches and much less in the area of landslide, debris or pyroclastic flows from volcanoes. The literature on the subject can be found basically in reports of specialized institutions and less in scientific communications, and is therefore not readily available, either, e.g., because these reports are written in the local language of the institution, or the documents are simply internal reports for the specialists or the contracting agencies committing the study. In snow avalanche research, such institutions are the Swiss Federal Institute of Snow and Avalanche Research (EISLF), Davos; in France CEMAGREF and Meteo France; in Norway the Norwegian Geotechnical Institute (NGI) in Oslo and in Iceland the Icelandic Meteorological Office. We only know of a single book that is explicitly devoted to the practical aspects of avalanches and protection from them, see Ancey [5], and the lecture notes by Salm et al. [367].

Avalanche defence structures are commonly used, but they are restricted to the protection of settlements (towns and villages or simply isolated single buildings), industrial sites and major highways. These structures are generally very expensive, and this expense can only be justified if the defence structures protect something very important such as human lives and property.

In this chapter, we will give a brief introduction into these techniques, which have been in use in the Alps (e.g., Austria, Switzerland, France) for many decades already, and have in recent years been extensively employed in Iceland after the avalanche accidents in Súðavík (1995) and Flateyri (1998). They present an advanced technique, specially designed from a structural engineering point of view.

13.1 Types of Avalanche Protection

13.1.1 Avalanche Initiation and Protective Measures

The potential threat of any avalanche depends on the strength and structure of each layer of snow within a snowpack. Each layer is different because different precipitation events and weather histories create different types of snow crystals, as well as varying structures and amounts of snow. As time goes by, a *snowpack* becomes "a multi-layered history of storms and weather". A weak layer is formed whenever snow crystals do not bond tightly and are loosely packed together, thereby creating an unstable layer. In snow, such weak layers are often associated with *depth hoar* that is formed by recrystallisation processes due to thermodynamic phase change conditions. The dominant factor that determines how threatening an avalanche is, is how deeply the weak layer of snow within the snowpack is buried. Generally, *the deeper a weak layer is buried, the more unstable the snowpack above it will be.* This is so, because the temperature of the snow grows with increasing depth and thus causes thermodynamic conditions in its vicinity that favour the formation of larger crystals with fewer bonds. An avalanche in this instance is called a slab avalanche and occurs when any form of stress or trigger (which includes new or windblown snow, skiers, a loud noise and explosives used for avalanche control or seismic activities that may produce an extra shear stress of several hundred Pa over some time duration) causes snow to break off in a single large plate. Subsequently, the slab or plate fractures and slips down the slope of the mountainside as a granular piece or cloud of snow mass, with the result of being potentially dangerous. While *it is difficult to predict exactly when or where an avalanche will occur*, detailed monitoring and investigation of the snowpack, weather conditions and past avalanche occurrences are likely to provide the necessary information to forecast avalanche cycles. The threat of most snow avalanches is confined to rather well-defined avalanche tracks or channels. Snow avalanches have a large potential to destroy natural resources,

man-made structures, and transportation and communication links. However, the removal of the forest cover from steep slopes in snow belts having high accumulation can create potentially destructive snow movement zones. While it is difficult to control the complete effects of large avalanches, it is possible to reduce the frequency and effects of small ones by the application of snow avalanche protection measures.

Usually, an avalanche path consists of three parts: the starting zone, the track, and the run-out zone. Some avalanche paths have an airblast zone below the run-out zone. Snow accumulates at the starting zone, which is the critical area for snow avalanches. The areas adjacent to the starting zone, especially on the windward side are also critical. Therefore, it is necessary to consider all high elevation forests and mountains within or adjacent to the starting zone for delineation as potential avalanche areas. Little can be done to stop the damage caused by huge and fast avalanches, but a protective buffer in the run-out zone is usually effective in controlling small and slow avalanches of dense flow type.

Mountainous regions may be categorised according to "red, yellow and green zones", with red being dangerous, where housing and any form of construction is strictly prohibited, and yellow being less dangerous but potentially not safe, where certain safety precautions and housing codes apply. Therefore, the yellow zone implies that avalanches are possible but adequate protection in the form of barriers of housing are maintained. The green zone is generally safe. However, this division is only a very rough way of zoning avalanche prone mountain slopes. It should be noted that hazard mapping is now carried out for many mountainous regions, if not all. Different designations, criteria and colour codes are being used by different countries in constructing their hazard maps. Effective long-term preventive measures to reduce avalanche fatality include *hazard mapping, land use planning, development of protective forests*, as well as *installation of defence structures*. Short-term measures include *avalanche forecasting*, *avalanche warnings, artificial releases of snow masses, road and rail closures* and *evacuations*. Some governments in Europe have already invested heavily in such avalanche protection measures because of their demonstrated cost effectiveness. Over the past 50 years, for example, about 1.5 billion Swiss francs (about 1 billion €) has been invested in protective structures in Switzerland, in addition to the resources devoted to forecasting, hazard zoning and protective forests.

Avalanche projects aimed at protecting human habitats can be regarded as part of the infrastructure of mountain areas. Protective structures must be of high quality and receive regular maintenance to ensure that they continue to provide reliable protection for a considerable time in the future [455].

13.1.2 Early Efforts

FRASER speculates that the first defence structure may have been a deflection wall built above the Swiss village of Leukerbad after a devastating avalanche in 1518 killed 61 inhabitants in this village [102]. However, avalanche protection structures became popular in the Alps only in the late 1880s when these mountain ranges became more densely inhabited and the Swiss railway system had been established. It has already been mentioned in Sect. 1.3.1 that blasts were used in World War II to release avalanches as an instrument of death. "During the fighting in the Alps, armies aimed their cannons not on the opposing armies but on the slopes above them, and the avalanches rained down in torrents of death" [13]. Military weapons, such as explosives (grenades and artillery), have been used in Europe since 1930 for controlled avalanche release and protection. In the United States, avalanche control was started for the purpose of mining by blasting during the mining era of the late 19th century.

13.1.3 Modern Methods of Avalanche Defence and Protection

There are two quite different ways of controlling avalanches – *active* and *passive*. One is to attack a slope to cause it to slide when intended and it can do no harm. This is referred to as an active attack, usually done by explosives so as to check the stability of the snow by giving it a massive jolt. Such active control is most commonly used along highways and in ski areas. The other is avalanche defence by preventing a slope from sliding, called passive control. If the sliding takes place, this measure is still more important to channel the avalanche where it can do no harm or to stop it before it can cause damage.

In this section, we will mainly focus on passive controls. These are the solid, somehow permanent, structures built to control avalanches. There are *three general types of avalanche defence structures,* depending on the position of the avalanche path. In the starting zone, the structures are designed to hold the snow in place; as a result an avalanche should never occur. The other types of structures are installed in the main track or the run-out zone to divert the flow or to dissipate its destructive power. The final types of avalanche defence structures are designed to alter the snow deposition patterns; they are built above an avalanche path, either on the opposite windward slope or on the ridge of a mountain itself.

Supporting Structures in the Starting Zones These are rigid and heavy structures built of concrete, steel, aluminium, wood, or a combination of these materials. They are designed *to anchor the snow in its place.* They are built in parallel lines, stretching along the contours of the initiation zone. There are three types of support structures. Two of them are of rigid types. Those

Fig. 13.1. Snow bridges in the Swiss Alps. **a**) Heavy structures made of concrete or steel are located at the top of a mountain, the starting zone of avalanches. (From [13], courtesy RICHARD L. ARMSTRONG). **b**) Wooden bridges illustrating how they hold the snow in place. (From [4] and Swiss Federal Institute of Snow and Avalanche Research, SLF, Davos.)

having horizontal bars are called *snow bridges*, as shown in Fig. 13.1, and those having vertical bars are called *snow rakes*. The final type of support structures are *flexible supports*. They are snow nets consisting of flexible cables hung on tubular steel posts.

Supporting structures are costly to build and maintain. In the Alps it is not unusual that millions of Euros must be invested in supporting structures for a single starting zone, when the avalanche threatens a town below. Much of the expense goes into the cost of the construction materials, mostly concrete, cement and steel, but are also, due to the very complicated mountain topography, and into transportation costs by helicopters.

Deflecting and Dissipating Structures These kinds of defence structures are located in the track and run-out zones to divert, retard and stop a moving avalanche before it hits what is to be protected. These structures are usually massive and made of concrete, rock and steel because they must withstand huge dynamic forces. However, dams and breaking mounds are also made from earth and boulders. The deflection angles of these structures should be small (normally no more than 15–20°) because walls built at sharper angles to the flow are likely to be over run by the fast moving dry snow avalanches (see Figs. 13.15 and 13.16). In addition, the stresses normal to the structure against which it has to be designed are this way kept small.

Earthen cone-shaped mounds are frequently built in the lower part of the track and the run-out zone to retard and dissipate the destructive power of an avalanche, as shown in Fig. 13.2. Once such protections have effectively

Fig. 13.2. Cone-shaped mounds placed close to the run-out zone for avalanche protection. (From [4] and Swiss Federal Institute of Snow and Avalanche Research, SLF, Davos.)

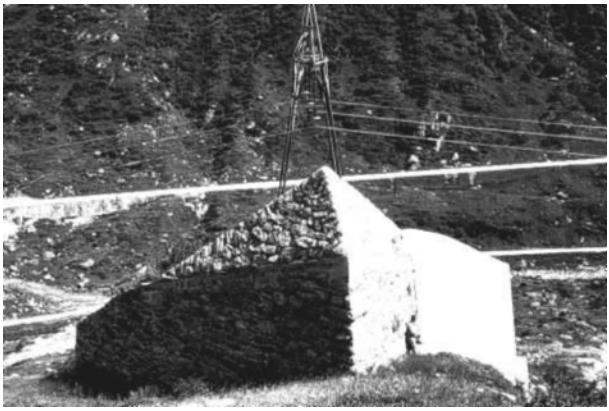

Fig. 13.3. Defensive structure as an integral part of an object. A pole of an electric line protected by a tetrahedral wedge. (From [4] and Swiss Federal Institute of Snow and Avalanche Research, SLF, Davos.)

stopped an avalanche, it is necessary to bulldoze the deposit of the debris from around the mounds to make them work well for subsequent avalanches. Defensive structures can also be built directly uphill as an integral part of an object, like a building, a historic monument or a tower that need protection (see Fig. 13.3). A good example of such structures are splitting triangular

Fig. 13.4. A snow shed gallery, protecting a motorway from being damaged or interrupted by avalanches in Switzerland. (From [4] and Swiss Federal Institute of Snow and Avalanche Research, SLF, Davos.)

and prism-like wedges. We will discuss this kind of protection structure in more detail in Sect. 13.3.

In Switzerland, it is common practice to build *sheds* and *galleries* along mountain highways and railways to protect them from avalanches. This is an advanced technique, often and worldwide used, where the sheds are roofs built close to the angle of the slope of the mountain and allow avalanches to cross over them without interrupting public traffic (see Fig. 13.4). However, in the design of such sheds the corresponding impact forces have to be taken into account. These sheds are so expensive that a 100 m shed costs as much as €1.5 million in Switzerland.

Structures Installed Above the Starting Area By building appropriate structures just above the starting zone of avalanches it is possible to alter the snow accumulation and thus reduce the amount of deposit in the starting zone. This results in a reduction of the size and number of avalanches. One method is to keep snow out of the starting zone by erecting *snow fences* on the windward slope upstream of the starting zone, so as to deposit the drifting snow right downwind of the fence instead of letting it accumulate in the starting zone. The erection of fences, however, is a rather tricky measure, since the local aerodynamic conditions change because of the fences that may alter the depositions of the transported snow in an unwanted manner. Gauer gives an account of the complexity of this problem [110].

13.2 Avalanche Protection in Different Countries

13.2.1 Avalanche Protection in Switzerland

Different avalanche protection measures such as supporting structures and shed galleries have been in operation or used in Switzerland for many years. The task of supporting structures is to prevent large avalanches or at least to limit snow motions, but experience shows that they are never completely eliminated to a harmless magnitude. Fully developed avalanches cannot be stopped completely by supporting structures. The first task is to produce an overall increase in the *stability*[1] of the flowing avalanche by additional *compressive stresses* and to reduce the *shear stresses* in the weak layer by the defence structure. The second task consists in limiting the size of the snow masses that have been set in motion and in retarding and catching them. The principal calculation and the design of supporting structures are explained in the "Swiss Guidelines for Avalanche Control in the Starting Zone" [407]. These guidelines are the basis for all designs and applications of supporting structures in Switzerland.

According to these guidelines, mountain slopes at an inclination of 30° to 50° are generally considered to be in the range that justifies the construction of defence measures. *The primary location for supporting structures is below the highest fracture line* that is observed by the experts or is expected from experience. The continuous arrangement of structures in lines with lengths between 20 m and 50 m is preferred. The height of a structure is decisive for the avalanche safety during situations of intense snow accumulation and for the design of the structures. The structures have to withstand the maximum *static and dynamic snow pressures*. Furthermore, they must reduce the velocities of small avalanches together with the roughness of the supporting plane. In Switzerland, the vertical height of the structures must correspond at least to the extreme snow depth with a return period of 100 years. Typical structure heights used in the Swiss Alps are 3 m to 4 m.

The costs for these supporting structures, as explained previously, are high. Usually, one hectare costs more than 1 million Swiss francs, but these supporting structures in the starting zones have been used for avalanche control for about 120 years. Until 1996, supporting structures with a total length of approximately 470 km had been built. At present, steel and concrete snow-bridges and flexible snow net systems are most commonly used. The snow pressure loads are up to 100 kNm^{-1}. This manifests the required strength of these defence structures. Supporting structures are suitable to prevent extremely destructive avalanches with long return periods and long run-outs. In

[1] The term "stability" is used in the avalanche community differently than in the mathematical or engineering literature. It here means something like "probability of the snow not to slide down".

Switzerland, *expensive supporting structures are widely used to protect zones or objects that are difficult to evacuate or to close* (like town and village settlements, industrial areas, motorways and railways that were built a long time ago in the run-out of extreme avalanches) during high avalanche hazard [464].

13.2.2 Avalanche Protection in France

Avalanche Protection Screens and Nets Avalanche protection *screens* and *nets* are widely used in France (see Fig. 13.5). These nets are *flexible structures* mounted in areas where avalanches begin. They prevent the snow mantle from breaking off by braking the snow slide. They can also resist small avalanches that may occur between two rows of nets, as well as rockfalls. Such nets are used in avalanche protection mainly because of (*i*) a considerably lower investment and (*ii*) a better fit into the surrounding scenery with landscape. On the other hand, this type of defensive equipment may be installed on all types of ground, on a sound bedrock or on loose soil, but what is expected is that the average snow depth is about 3 m to 5 m on stiff slope. Specific avalanche protection nets and screens can be designed and are being produced, including particular specifications depending on environmental conditions.

Rock Protection Nets Rockslides and rockfalls are also common phenomena in mountainous regions. In France, *rock protection nets*, made of flexible structures are used to prevent fatalities caused by natural hazards such as rockslides. Such screens are made of metallic nets linked to energy squanderers. Tubular stands keep the entire system perpendicular to the slope. The nets are equipped with energy absorption systems. They are able to disperse the kinetic energy of falling or sliding rocks until they definitely stop. The

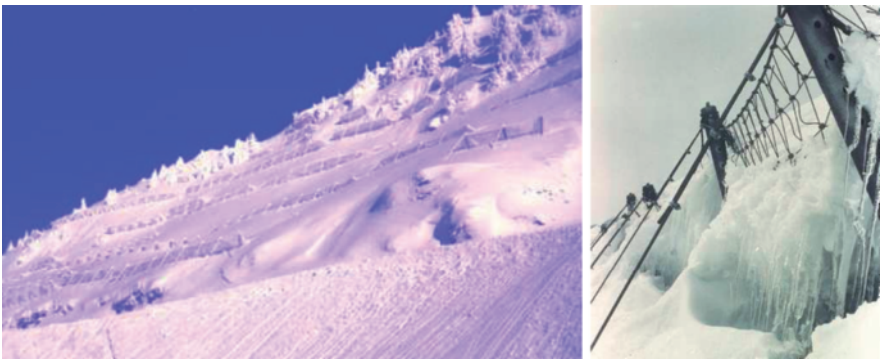

Fig. 13.5. Avalanche protection screens and nets used in France. (From [463].)

nets allow a 500 kJ to 5000 kJ retention, representing a 10 ton rock falling at 31.7 ms^{-1} (114 kmh^{-1}), see [463].

13.2.3 Avalanche Protection in Iceland

Avalanche accidents have had a major effect on the development of avalanche research in Iceland. In December 1974, catastrophic avalanches in Neskaupstaður killed 12 people. Following that accident, a committee was established in Neskaupstaður and a year later a report was completed with plans for cooperation over the whole country for protection against avalanche danger. In January 1995, an avalanche struck Súðavík, killing 14 people (see Fig. 13.6). In October of the same year, another one fell on the village Flateyri causing the death of 20 people. The three catastrophic avalanches, all of which fell during the night on people sleeping in their houses, in the Westfjords that occurred during three winters in the years 1994 and 1995 had a major influence on avalanche work in Iceland. The direct economic loss due to avalanches and landslides in the last 26 years alone is estimated to be around 3.8 billion IKR.[2] If the cost of re-location and defence structures is added to this economic loss, the direct cost of avalanches and landslides in Iceland exceeds 6 billion IKR. Jóhannesson also mentions in [204] that if the death of a person in an avalanche or landslide accident is included in the economic

Fig. 13.6. Súðavík in August 1995. The main part of the village in Súðavík was moved after the avalanche accident. The old houses were bought by the authorities and new ones were built in a different area, which is considered safe. (From [458].)

[2] At present 1 Euro = 73 IKR.

loss as 100 million IKR per fatal accident, the total cost of avalanche and landslide accidents in Iceland in the last 26 years together with the cost of avalanche protection totals more than 13 billion IKR! All of these avalanches had longer run-out distances than thought possible in those areas according to the methods for making hazard maps at that time. It was then realised that the avalanche history should be reviewed and the run-out zones estimated by some reliable measures. The Icelandic Meteorological Office made a report in 1996 with suggestions on avalanche protection measures and estimation of their costs for all avalanche endangered towns [458].

In 1996, experts in those hazard areas installed avalanche retaining structures under Icelandic conditions and standards because *the snow in Iceland is much heavier than in Alpine countries.* In preparation for building avalanche defence structures, dozens of *snow stakes* were installed in the starting zones above various villages.

In Flateyri two deflecting dams were built in August 1998 to protect the village against avalanches from the two gullies. The *dams* are connected at the top and farther down the slope an additional *catching dam* connects the two *main dams.* Together, the three dams form the shape of an "A" as seen in Fig. 13.7, [393]. For more details, see also [458].

Fig. 13.7. Flateyri, the deflecting dams in August 1998. Two deflecting dams have been built to protect against avalanches from the two gullies. The dams are connected at the top and farther down the slope is a catching dam. Together the three of them form the shape of an "A". (From [458].)

13.2.4 Snow Avalanche Protection in Austria

A major avalanche hazard in the history of Austria occurred in January 1954, when 56 people were killed in the town of Blons in Vorarlberg State. The avalanche that struck Galtür in the Paznaun valley was the first to hit the village in living memory. Local records showed that the last avalanche to hit Galtür was back in 1689 and wiped out the village and killed 250 people. Since avalanches had not attacked Galtür for over 300 years, it was considered a less dangerous zone until it was hit again in 1999 killing more than 30 people.

Galtür was placed in the yellow (i.e., potentially less endangered) zone until 1999. Austria has invested more than €60 million in the Paznaun Valley and €20 million in Galtür alone, in avalanche prevention over 50 years. *Metal* and *concrete barriers (bridges and racks)*, as used in Switzerland, were placed above the timber line and positioned in many rows on avalanche prone slopes. However, the avalanche that devastated Galtür rushed down an unprotected slope [456].

In addition, the relatively high avalanche activity that has occurred in the past half century and may in part be due to global warming, has led to an impetus in Austria in avalanche research, in particular the development of improved mathematical descriptions of mixed flow powder snow avalanches and their applications to field events, see [449, 450] and the account of the history of snow and avalanche research in Austria in Chap. 1.

13.2.5 Snow Avalanche Barriers in North America

As in the European Alps, snow avalanche barriers are also used in the prevention of snow avalanches in North America. Although these types of systems are extensively used throughout Europe, a new system, called the *Brugg (cables) system,* which uses a combination of *flexible nets* and *high yield anchors* (which have also been routinely used in the Alpine regions for many years), is probably installed only in North America. The first system of this kind in the world was installed in at the Washington State Snoqualmie Pass. The placement of the system is pre-engineered by avalanche experts and structural engineers to pinpoint the exact locations on the slope where the system is to be installed. The system, which is particularly useful in forest areas, is probably one of the largest snow avalanche barriers installed in the world [459] (see Fig. 13.8). This is a highly effective and proven system. The system was installed to protect houses threatened by snow avalanches.

Remark In Sect. 1.4.2 we presented a short account of the history of avalanche research of most avalanche prone countries. This historic description also incorporates avalanche fatalities and means of avalanche protection

Fig. 13.8. Installing snow avalanche barrier posts for the Brugg System. (From [459].)

and includes countries like Switzerland, France, Austria, Iceland, Norway, USSR (former) and Russia, USA, Canada and Japan. Thus, readers more interested in avalanche hazards and protection measures are also referred to Sect. 1.4.2.

■

13.3 Laboratory Experiments: A Means to Design Defence Structures

The avalanche equations presented in Chaps. 3 and 4 have been demonstrated to be an adequate mathematical model for snow flow avalanches that are relatively dry and dense granular flows. Since the equations are scale-invariant and because agreement with experiments is good, laboratory experiments can be used to test realistic flows with and without obstructions. Therefore, principles of similitude can be applied and physical models be constructed for the design of avalanche protection structures. Experimental techniques can also be used in the optimal design of flow around avalanche protection structures in mountainous regions. Laboratory experimental techniques can be used effectively in the design of avalanche protection constructions and in the determination of potential avalanche endangered zones of inhabited regions [411].

13.3.1 Laboratory Models and Experiments

Consider an obstruction designed to protect a structure from being hit by an avalanche. The model object selected for protection is the *Schneefernerhaus* at the Zugspitze, Germany, which is an old hotel that has been renovated and transferred into a research laboratory for environmental and climatological research (see Fig. 13.9a). The building is situated at 2700 m above sea level on a steep mountain slope, but that is flat in the cross-slope, inclined approximately at an angle of 45°. It was planned to erect a number of masts equipped with meteorological instruments on the roof of the building. The building must be protected against avalanche impact throughout the year. Several avalanches pass every year and occasionally flow over the building so that a protection for a 100 year event is thought necessary.[3] According to expert studies, a large avalanche with a 100 year recurrence is a snow layer of slightly more that 8 m depth moving down the mountain. In a first study of protecting the building against such an event, a tetrahedral wedge (pyramid) was designed that should divert the flow and guide the snow to pass the building on either side. Figure 13.9a shows a photograph of the Schneefernerhaus. Experiments in situ being out of the question, it was decided to perform laboratory experiments. The mountain flank was modelled as an inclined plane of a 45° slope angle, made of metal and plexiglass, respectively, and the model Schneefernerhaus and wedge were cut from plastic and wooden blocks, depending on the scale. Figure 13.9b shows one of the laboratory models. A tetrahedral wedge was positioned above the building

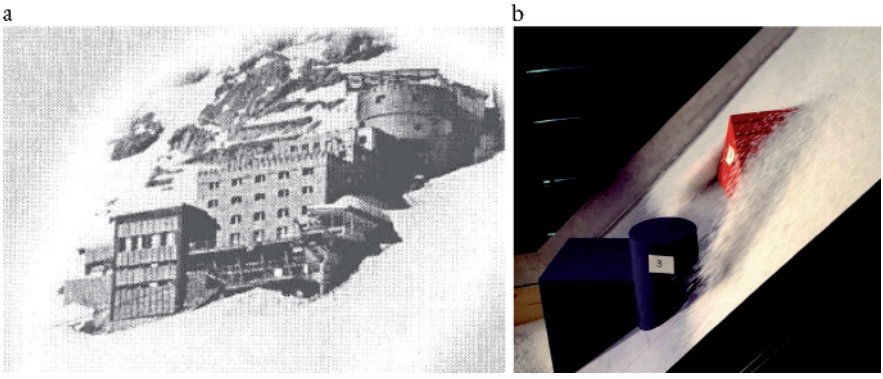

Fig. 13.9. a) *Schneefernerhaus* at the Zugspitze in the German Alps, at 2700 m on a rather planar mountain slope inclined at an angle of approximately 45°. **b**) A model reproduction together with a tetrahedral-wedge-type avalanche protection structure. (From [411].)

[3] An avalanche of large size hit the hotel in 1963 and killed 14 people, who were on the roof.

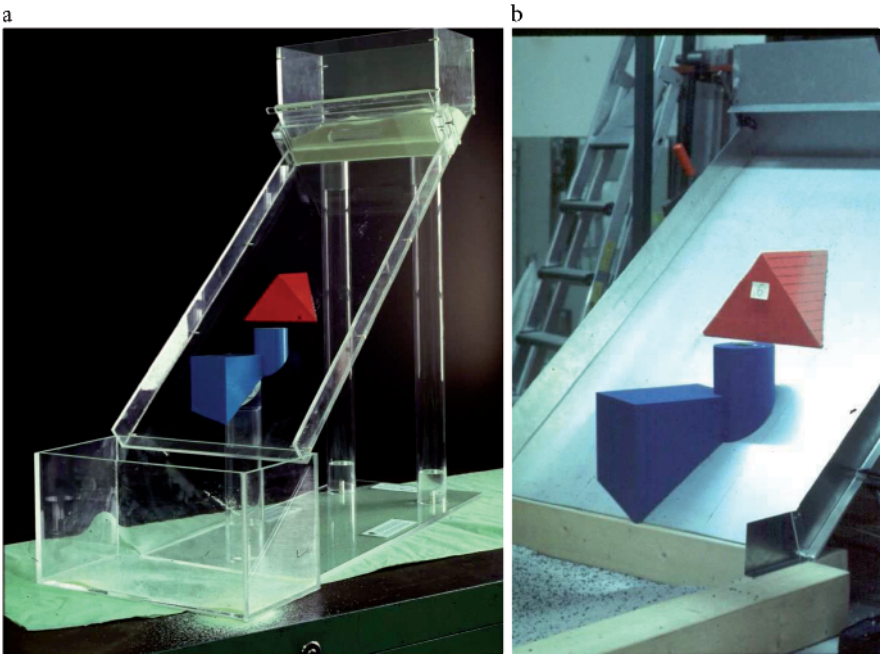

Fig. 13.10. *Schneefernerhaus* in an incline and the avalanche protection wedge as its integral part. Scales: **a**) 1:300, **b**) 1:100. (From [411].)

at an optimal distance by trial and error. The experiments were performed with two models of scales 1:100 and 1:300, respectively. Plastic beads of 2.5 mm and semolina and white sugar of approximately 0.8 mm in diameter, respectively, were used as "dry snow" for the laboratory simulation. These materials gave internal and basal angles of friction of approximately 35–45° and 15–25°, which lie in the range appropriate for snow.

Figures 13.10a,b shows the experimental set-up in the two scales mentioned above. Figure 13.11 displays three consecutive snapshots of the motion of a layer of semolina down the slope, past and around the wedge and the Schneefernerhaus at three different stages. The snow depth here corresponds to the motion of an 8 m layer. It can clearly be seen how the side flanks of the wedge divert the flow. A shock is formed at the wedge tip that extends on both sides of the flanks of the wedge.

An obvious advantage of the model experiments is the fact that various different event scenarios can be tested, and thus the effectiveness of the structure estimated. A frequent scenario is when a layer of new snow is deposited on a hard and stable layer of old snow, and this new layer becomes unstable

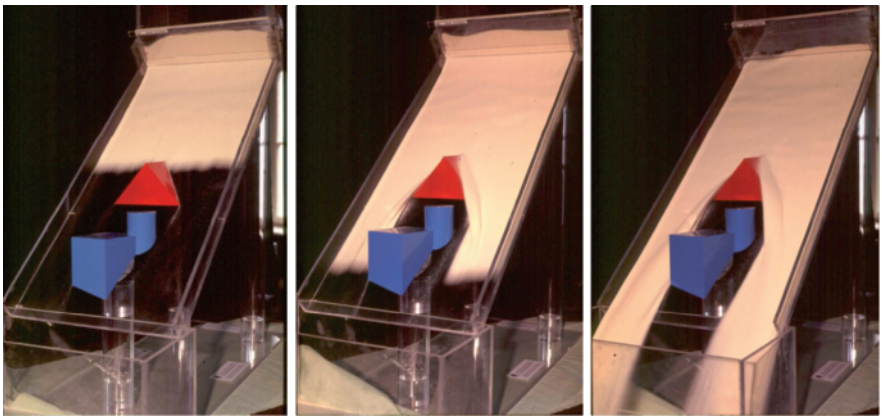

Fig. 13.11. Flow of a layer of semolina, discharged by opening the gate of the silo at the top of the chute, which is inclined at 45° angles. The flow goes past the tetrahedral wedge and around the building that must be protected. (From [411].)

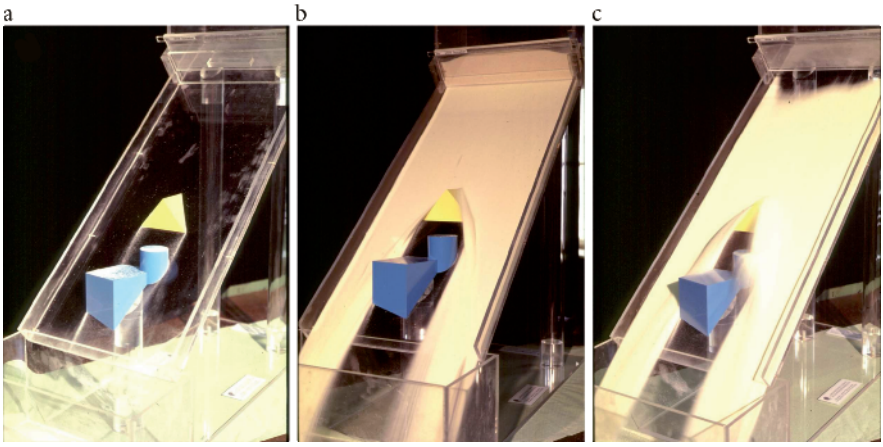

Fig. 13.12. **a**) Model *Schneefernerhaus* accompanied by a tetrahedral protection wedge against avalanches. In these experiments, it is assumed that 5 m hard snow is stably deposited and the plexiglass surface corresponds to the upper level of this snow cover. Motion of **b**) a 3 m and **c**) an 8 m layer of "snow" (semolina). (From [411].)

and forms an avalanche. Such a case is illustrated in Fig. 13.12. In this case, the plexiglass surface is identified with the upper surface of the hard layer; here it corresponds to a 5 m deep layer, and the flowing granular mass has been designed to represent 3 m and 8 m new snow layers, thus amounting, at most, to a total of 13 m snow cover. It is evident that the wedge suffices for the first scenario but does not sufficiently shield the building for the second, which was neither intended nor achieved.

13.3.2 Simulation of Avalanche Protection

The avalanche model equations of Chaps. 3 and 4 have been applied in the design of avalanche protection constructions as discussed above [412]. To describe the flow in the situation of the Schneefernerhaus is really a great challenge. There are many reasons for this. Below the pyramid wedge the flow forms a vacuum with a grain-free region. In a first test example, the wedge is interpreted as an integral part of the basal surface. Figure 13.13 displays the photograph and a result from the simulation with the model equations for the steady flow past the tetrahedral wedge (pyramid) as an avalanche defence structure.[4] The triangular lines represent the tetrahedral wedge and the computed flow thickness is given in contours of dimensionless length scale at the dimensionless time unit $t = 10$, when the flow is *nearly*

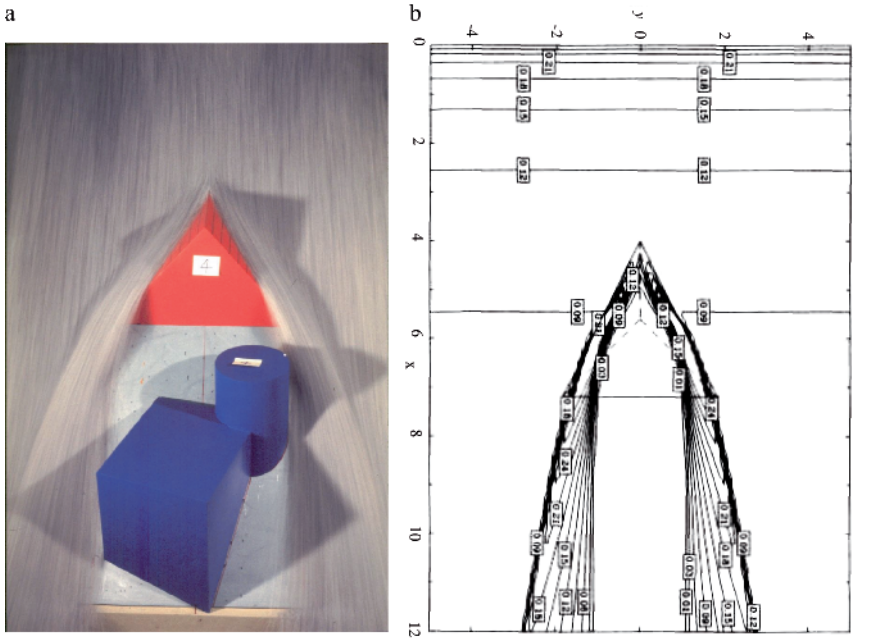

Fig. 13.13. **a**) Photograph of the steady flow past an avalanche defence structure (pyramid). **b**) The defence structure is represented by *triangular lines*. The computed dimensionless flow thickness contours of equal thickness are illustrated at the dimensionless time unit $t = 10$, when the flow is nearly stationary. (From [412].)

[4] The formulation of the boundary value problem in this situation does not in all respects correspond to the experimental performance of the flow. For instance, panel a) in Fig. 13.13 shows two subregions of ballistic (free flight) motion that was computationally not reproduced. Given such deviations of the real flow and its computed analogue the agreement is convincing.

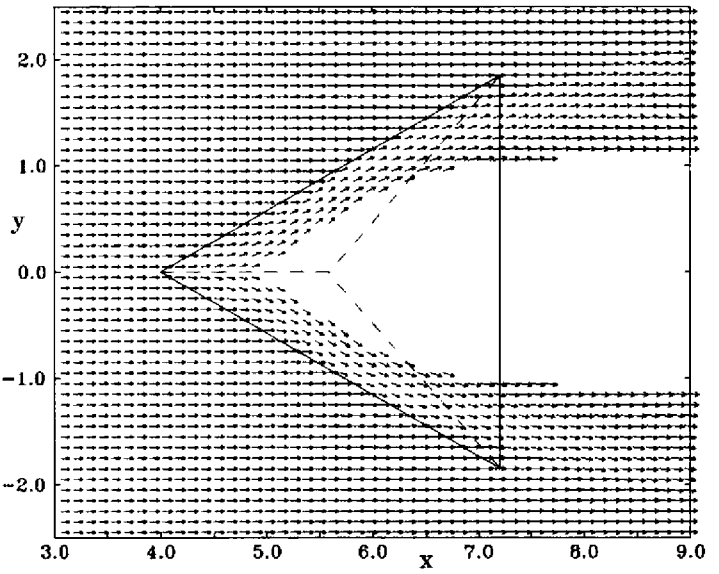

Fig. 13.14. Local view of the velocity field around the defence structure (tetrahedral wedge) obtained by a numerical simulation. The *arrows* and their lengths, respectively, are representative of the directions and the speed of the velocity. (From [412].) TAI

stationary. At the tip of the defence structure an oblique shock is formed. This can be clearly seen from the streamlines in the photography, as well as in the corresponding contour plot obtained from the numerical simulation. Behind (i.e., below) the pyramid, the mass rapidly spreads in the lateral direction and thus an *expansion fan* is formed, which is well-described by the contour plot. A *grain-free zone*, which is viewed as the protected region, is developed behind the defence structure.

Figure 13.14 depicts the velocity field of the flow around the pyramid. It is seen that the pyramid arrests the flow and diverts it to either side of it. The arrows and their lengths are indicative of the directions and the speed of the velocity, respectively. Below the pyramid the flow accelerates and the downslope velocity becomes dominant again.

Similar experiments have also been performed in the Laboratory of the Department of Mechanics, Darmstadt University of Technology. GRAY et al. [126] report on flows around a tetrahedron arranged upside down and CHIOU [59] conducted a great number of experiments against and around obstructing walls and tetrahedra of different size.

13.3.3 A Structural Protection Technique by Deflection

Rapidly flowing granular masses, such as snow avalanches or rockslides are diverted and redistributed by structural devices such as fences and walls. These are classical constructions for the protection of valuable structures on a mountainside. Here, we consider some simple *deflection structures*. If a uniform layer of rapidly flowing granular material down an inclined plane encounters a vertical wall forming an angle α with the direction of steepest descent, as shown in Fig. 13.15, then a straight triangular shock is formed at an angle β. Although the protected region is a function of angle α, this angle must not exceed a certain critical value depending on the strength of the material of the deflecting device and its structural design. Also notice that the angle β depends on the basal topography, the material property of the flowing mass and the angle α. Above the shock, the undisturbed flow is supercritical with a given height h_1 and velocity u_1; behind the shock it is subcritical with a different thickness $h_2 > h_1$ and different velocity $u_2 < u_1$. The situation is analogous to the subcritical and supercritical flows in the hydraulics of free surface channel flow. If the retaining wall is curved, the

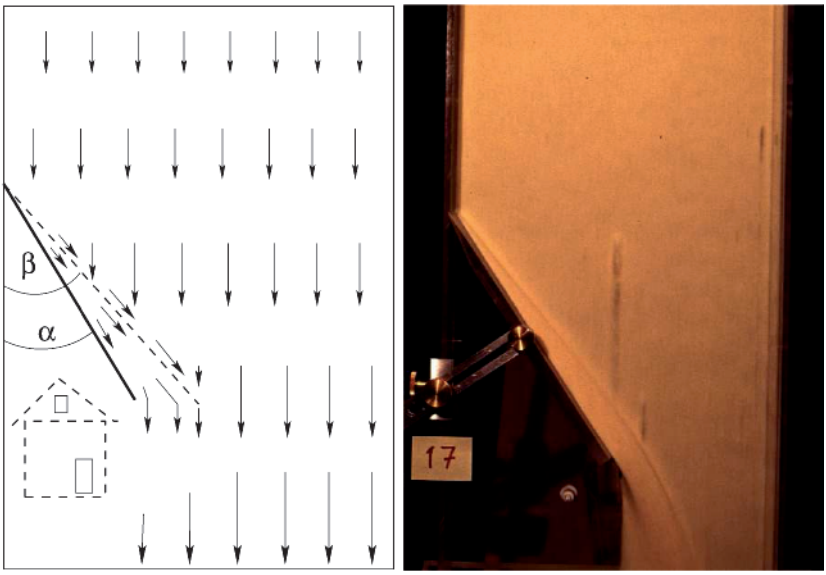

Fig. 13.15. A steady layer of granular material with thickness h_1 and the supercritical downstream velocity u_1 is moving down an inclined plane. As the flow encounters a straight vertical wall inclined at an angle α, the induced cross-flow generates a straight triangular shock that is inclined at an angle β with layer thickness $h_2 > h_1$ and velocity $u_2 < u_1$. *Arrows* indicate the direction and (relative) magnitude of the velocity field. Also shown is the protection of a house below the avalanche. *Left:* sketch, *right:* experiment. (Right picture: From [411].)

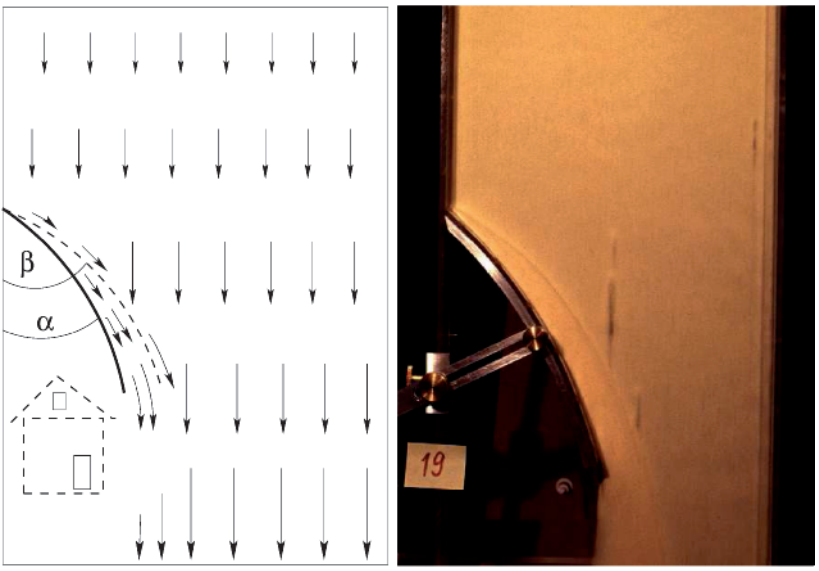

Fig. 13.16. Similar to Fig. 13.15 but for the curved deflecting structure. (Right picture from [411].)

steady shock that is formed will also be curved (see Fig. 13.16). This means that *the nature of the shock depends on the topography and the shape of the deflecting structure itself.* The downstream flow behaviour can be computed if the upstream conditions (velocity, height and pressure) are given. The determination of the impact pressure at the deflecting wall is very important from a structural point of view. The concept discussed here can also be extended for slopes of varying topography, as well as for complicated structures, see [59].

13.4 Conclusion

A review has been given in this chapter about the various protective measures that are taken in various countries to protect the people in avalanche prone regions from being directly exposed to their dangers. While a potential danger cannot, in general, be completely avoided, a partial reduction is possible. In many cases, an understanding of the mechanisms is already a substantial step towards its removal.

One step towards this goal is the modelling of the avalanche processes from (basic) *first physical principles.* This has led, on the one hand, to the construction of the SH-theory and its various extensions dealt with in this book. On the other hand, this model and its validation by laboratory experiments

has opened up a new and innovative method of analysis for the study of avalanche flows by physical model experiments. Since our model equations are scale-invariant and agreement of the theoretical-numerical results with laboratory experiments under fairly varied conditions range from good to excellent (see Chaps. 10 and 12), physical models and their results provide us with trustworthy results that can be transferred from the laboratory scale to a scale in nature. Therefore, such experiments ought to be performed more often than presently done, especially when protective measures against potential avalanche dangers are to be designed.

One should not forget that even if no avalanches occur in potentially avalanche prone regions for years or decades, the threat remains, and we must be prepared to face the avalanche danger. Research on avalanche hazard protection must be done continuously. Protection measures against avalanches must be carried out in endangered areas, so that gradually it will be safer to live in the avalanche prone towns and villages. Even when protection structures are completed, future observation of the snow cover, its metamorphisms and the weather outlook is vital in order to warn against the avalanche danger. Protections can only reduce risk and will never be able to provide complete safety. It is extremely important to be aware of the remaining risk. Gradually people have seen that avalanches can strike where there is no previous history of occurence. Realising the possibility of danger, that knowledge can be used for protection against it. On the one hand, continuous further research for more advanced avalanche protection and mappings should be conducted, while on the other hand people must be educated about avalanches and the signs of avalanche danger, which is very important for the well-being of the inhabitants in the areas of avalanche danger, as well as the people travelling and enjoying outdoor winter sports.

14 Summary and Outlook

For the convenience of the reader, we shall in this chapter briefly outline a summary of what we believe to have covered in this book and also provide an outlook to future activity.

There remain two questions to be answered: What has been achieved so far and what should be done in future? The answer to the first question is relatively easy but very important in order to give an overall impression about the up-to-date achievements, as well as the specific, significant and novel and lofty outcomes presented in this book. A straightforward answer to the second question seems to be a little difficult, but from past experience, knowing today's needs and technology we can infer what can be and what must be done in future. Firstly, to provide continuity to the work that has been done until now, and secondly, to utilise the achievements obtained so far in real applications directly related to the security and benefits of the public. For the continuation of the research activities and the implementation of the results thus obtained as predictive tools of avalanche behaviour, it is required in practice to use the most advanced technology both in understanding the physics of the flow by means of well-controllable laboratory and field experiments and in corroborating most advanced and sophisticated theoretical tools available in different configurations that are compatible with the need of the people and are close to reality. Such tasks may be related to geophysical flows at large-scale and catastrophic deformations and movements of earth materials such as landslides, rockslides, debris and snow avalanches down the slopes of mountains. Understanding the mechanisms of the initiation and dynamics of the flows from the breaking and release of the masses to the depositions is extremely important for hazard mapping of mountainous regions, for the prevention, reduction and mitigation of the natural hazards causing devastating damage of property and claiming the lives of the people on a large scale. Alternatively, one can make use of these theoretical and experimental facilities to analyse also the flows of powders and fine granulates in silos, hoppers, and the transportation of different kinds of bulk materials such as cereals, ceramics, dyestuffs, electronic materials, pills and capsules, just to name a few, through different and specific channels in the food producing, chemical process and pharmaceutical industries. The prediction of such flows

basically helps the production and quality control of these materials to meet the standards set by the authority concerned.

Let us review the knowledge as we see it *at present* and then contemplate activities that may or ought to be done *in future*.

14.1 Knowledge at Present

We mainly focus on dry granular materials. Let us now go back to the first question. We were mainly involved in doing three things successively:

- the collective and systematic *presentation of the classical and new general theories* for avalanching granular flows that can be used both in geophysics and process engineering,
- *implementation of reliable and sophisticated numerical methods* that can appropriately solve the model equations thus developed without losing the underlying physics of the theory,
- and, finally, *providing the proof that the theoretical predictions of the model equations can well be reproduced by the laboratory experiments,* so as to pave ways to real applications in different scenarios.

14.1.1 Theory

Concerning the theory, the following points are worth emphasising: We have presented and discussed the most widely used avalanche theories in practice ranging, from the classical mass point model of Voellmy [430] to the early depth-integrated continuum mechanical model due to Savage and Hutter [375, 376] to recent extensions and a generalisation of this model proposed by Pudasaini and Hutter [335]. In this endeavour, competing models are also discussed. Major attention is paid to the systematic evolution of these hydraulic avalanche equations. The new and generalised model equations developed in Chap. 4, are formally analogous to those of previous derivations under much simpler situations. For torsion-free and flat cross-slope (reference) bed topography, these equations reduce to the much simpler equations proposed by Gray et al. and Wieland et al. [123, 445] as special cases. Furthermore, the new theory can reproduce all previous model equations of the Savage–Hutter-type theory as particular cases. Analysis of the motion of avalanches in channels with different cross-slope curvatures and widths is now possible, see [341]. For the first time, we were able to include the simultaneous *effects of the curvature and torsion* of the channel axis and cross-sectional curvature in the avalanche motion, which could not be achieved explicitly by any previous models. This should be realised as one of the major advantages and achievements of these new model equations. The applicability of

the present model equations is, therefore, much broader than in the previous cases. The advantage of this formulation of a depth-averaged avalanche model lies in its flexibility of application. The flow down an inclined plane or within a channel with its axis in a vertical plane (which may be curved) can be described, as can the flow down complicated mountain valleys with arbitrarily curved and twisted talwegs and bed topographies. It is this last application that motivated us to derive the new model. Thus, the theory provides an entirely new direction in the field of avalanche and debris flow research. It also opens a large spectrum of applications in different industrial and geophysical problems. We simply mention at this point that PUDASAINI et al. [342] extended the aforementioned single-phase cohesionless dry granular avalanche model equations over generally curved and twisted channels to a two-phase fluid-solid mixture of debris material.[1]

14.1.2 Numerics

Another challenge has been to solve the model equations. The first step towards the full understanding of the theory is the simulation of the model equations for some specific and particularly interesting, somehow academic engineering problems. The results emerging from these simulations indicate the basic and fundamental capabilities of the entire theory. Since the model consists of non-linear hyperbolic partial differential equations with discontinuous coefficients, we should not solve them with classical numerical methods. These require the use of additional numerical diffusion and may thus smear out rapid changes of the values of the physical variables. We have seen that their approximate preservation requires a tricky and balanced application of artificial numerical diffusion that, however, may not work satisfactorily

[1] These remarks require the following clarification. In the literature, depth-integrated equations of motion are often derived by referring their coordinate-dependent version to a Cartesian coordinate system with two horizontal axes and one vertical axis rather than a coordinate system that follows the local topography, see [191, 192, 321, 323]. Such a procedure defines shallowness differently, and in particular, requires among other things that the slopes are not steep. Nevertheless, those authors apply their equations up to very high slopes. True, the curvilinear coordinates employed by PUDASAINI and HUTTER [335] do not exactly follow the true topography either, but only approximately and more closely than when horizontal-vertical Cartesian coordinates are used. A direct comparison between the different approaches is difficult and perhaps not possible, but – discounting other differences, e.g., the use of different numerical techniques and softwares for the integration of the equations – the procedure followed by us is certainly more accurate. Equations founded on the true topography would be the ideal modelling basis. BOUCHUT and WESTDICKENBERG [40] have derived them for hydraulic equations with basal friction. A worthwhile understanding could be a benchmark problem in which the different approaches are compared.

under all circumstances. To avoid any spurious oscillations and include naturally induced shock phenomena of the hyperbolic equations, we introduced shock-capturing numerical schemes. To this end, NOC schemes with TVD-limiters were implemented. The numerical sensitivity analysis reveals that the NOC method with the minmod limiter provides the best performance for the avalanche flows.

One of the most interesting aspects of avalanche dynamics is the study of avalanching motion over different bed structures and the effect of topography on their motion and deposits. For this purpose, a large number of simulations are presented for different topographic configurations. The first part of the simulations is concerned with a very simple bed topography that is laterally flat but curved and merges into the horizontal run-out zone along the down-hill direction. One of the most basic and fundamental questions related to the new equations derived in Chap. 4 is: are these model equations really able to predict flows in chutes and channels that simultaneously incorporate curvature and torsion effects of the bed topography? In other words, can we really use these equations to predict the flow dynamics of debris and avalanches down arbitrarily curved and twisted mountain valleys and natural gullies from initiation to deposit? To answer these questions, we performed several numerical tests for avalanching masses down curved and twisted bed topographies. Uniformly curved and twisted channels, as well as channels incorporating a continuous transition zone merging into the horizontal run-out zones were considered. Both confined and unconfined transition zones with constant and variable inclination angle of the topography were taken into account. In one instance, the topographies used were based on helical talwegs. As the "arts" of the theory can be seen in the simulations, these computations reveal the fantastic and fascinating results that we were imaging while developing the theory. They demonstrate the combined effects of curvature, torsion and the radial acceleration associated with the bed topography. Thus, we were able to quantify the intrinsic effects of the topography on the dynamics of flow avalanches. Such sophisticated studies have not been carried out before, and it was possible here only with the new model equations.[2]

14.1.3 Experiments

A scientific work on a physical process, whatever it may be, should be verified by observations on the natural object or some suitable experiments conducted in the laboratory. It should not merely be based on some computations, manipulations, reasonings and logics that are not physically verified. Practitioners and engineers use or tend to use model equations that have already been

[2] There are some experimental works that show that extended theory [335] is well able to reproduce the flow in helical channels merging into a horizontal plane, see Pudasaini et al. [344].

proven to be able to reproduce experimental facts either in the laboratory or in the field. Thus, in order to acquire confidence in new model equations it is vital to corroborate them by direct observation. In this spirit, we performed several laboratory experiments for different materials in order to check the validity of the theory. The two most important variables that should be known in the determination of the motion of an avalanche are probably the *mass transport* or *depth-averaged velocity distribution* and the *evolution of the avalanche boundary* from its initiation to the deposit in the run-out zone and the depth profile of the deposit.

We have explicitly explained different measurement techniques and tools to perform laboratory experiments. A large number of laboratory experiments with increasing complexity have been conducted. Results were obtained and compared with the theoretical predictions of the model equations. Simple to complex topographies incorporating bumps and side walls and sidewise confinements were taken into account. Several granular materials were used for the experiments. Deposits of the avalanches were measured. In some instances, highspeed photo cameras and video cameras were used, from which one can identify the geometry, the front and rear positions and the position of the maximum height of the pile; the velocity of the front and rear part of the avalanching motion.

We also used the modern measurement technique, PIV, to measure the velocity field of the particles at the free surface and the bottom of the free surface and unsteady motion of an unconfined avalanche over a chute curved in the main flow direction and merging continuously into the horizontal run-out zone. This technique is discussed in detail and implemented by Eckart et al. and Pudasaini et al. [83, 334, 343]. Only selected results were presented here to show how the method works in reality. We presented the results for different regions of the chute. We were looking for the correspondence and harmony between the theory, the adequacy of the numerics and the demonstration of the experimental facts. We were able to demonstrate that there are good to excellent agreements between the theoretical predictions of the model equations and the experimental measurements. This, ultimately, proves the applicability of the theory and efficiency of the numerical method and code, and establishes a nice and strong correlation among theory, numerics and experiments. We also reported such successful comparisons done by others.

The proof of the adequacy of the model equations by hindcast analysis of real events is an order of magnitude more complicated and because of less reliable input also less convincing. Here, the breaking mass of soil must be estimated from the site investigations of the deposited materials and carved surface of the likely breaking zone and eroded channel walls. Trimlines bounding the affected region must also be estimated by geological investigations from the after-the-fact studies. We have reported about attempts to compute the motion of the mass of granular material for hindcast analysis of the Frank Slide

in Canada. Results are convincing. Thus, the usefulness of the computations cannot be denied.

14.2 Attempts in Future

Now we address the second and final question posed at the beginning: What should be done in future? Our experience says that there are still many challenges to be met in the field of avalanche and debris flow research. Here we will focus only on the part of the problem related to dynamics. The main intention of research in this field should be directed towards modelling and solving the real problems so as to minimise the casualties and hazards induced by natural catastrophes such as avalanches and debris disasters. This includes knowledge and understanding of the release mechanisms of avalanching masses, the reliable prediction of the motion from initiation to run-out, the evaluation of impact forces of the moving masses on the objects they may encounter, the estimation of the likelihood of an avalanche prone region to be hit by a moving mass, etc. This list involves more than the scientific techniques provided in this book, but what has been tackled here is a vital step towards the solution of the overall theme. Within the limited scope, here is an outlook.

14.2.1 Application in Nature

The next and immediate goal should be to perform additional numerical simulations on realistic topographies with the purpose of providing a general purpose software for practitioners involved in the prediction of avalanche run-out in mountainous regions. The approach is to use GIS from which DEM can be deduced and digitised realistic topographies in mountainous regions realised. With GIS particular avalanche prone subregions can be selected. From a preselected release of a finite mass of gravel or snow at a breaking zone the flow from initiation to run-out can be determined. This step requires numerical integration via avalanche purpose-built software incorporating a shock-capturing TVD scheme. Its output could, in a final step, be used in visualisation software to identify endangered zones. A multitude of applications could then be investigated with the software. A comparison with observational data in the field such as photographs from helicopters, or a digital video camera positioned at a fixed station, may then become possible. From these computational results one can easily estimate the impact pressures on obstructions and infrastructures along the track and in the deposit, which is very useful for civil and forest engineers, rural planers and authorities from municipalities responsible for the safety preservance in populated mountain regions. Moreover, the results should ultimately be applied

to construct hazard maps in the mountain ranges with the aim of avalanche warning, reduction, mitigation and prevention of the hazards.

A number of prime and fundamental works in this direction has been and is being done. One example of this kind is the reanalysis of site events by McDougall and Hungr [273, 274], another is the implementation of the Savage–Hutter equations to the bottom dense-flowing part of the avalanche in the computational SAMOS model by Zwinger and Zwinger et al. Known as GMFG research group from the University at Buffalo, the State University of New York, researchers here are using GIS technology with parallel adaptive numerical simulations. They are also involved in improving the model equations by incorporating erosion and deposition processes [313, 321, 322, 323]. Iverson and Denlinger from USGS are dealing with the modification of the existing models and computations of avalanching flows across irregular three-dimensional terrains [74, 75, 191, 192, 194]. Their aim is to further test the ability of these models to predict the behaviour of (ideal) dry granular flows down such topographic surfaces that may provide an important step towards the full understanding of the dynamics of rapid and massive mass movements across irregular terrains. These are only a few examples. However, the research is oriented in the right direction.

14.2.2 Application in the Laboratory

Laboratory experiments can be used not only for the corroboration of the theoretical-numerical results, but equally as an alternative to test on a small-scale the behaviour of an avalanching mass at a larger scale, as it occurs in nature. This method is particularly apt, because the SH-equations and many of their present extensions, such as the model equations proposed by Gray et al. and Pudasaini and Hutter [123, 335] have been found to be scale-independent. Thus, whenever the physical conditions are such that these model equations may be adequate, laboratory experiments may be advantageous for the computational approach. Furthermore, the effect of obstructions in an avalanche track can easily be studied by laboratory experiments. Moreover, with adequate pressure and shear gauges being used at walls of obstructions, such laboratory experiments may even be suitable to gain information about the forces exerted by avalanches on obstructing structures. Besides, laboratory experiments should be amply used to broaden the information on the corroboration of the theory. Also to be mentioned here is that Iverson and Denlinger performed several experiments for avalanching granular and debris flows in relatively long flume. Iverson et al. [194] also conducted indoor small-scale experiments down irregular prototype terrain. The intention of these experiments was to test the theory for the situation of a realistic bottom topography, to perform experiments under controlled conditions and thus to have optimal conditions for a comparison. Small-scale indoor exper-

iments have also been performed by McDougall and Hungr [273, 274], Patra et al. and Pitman et al. [313, 322].

14.2.3 Advancing the Numerics

Determination of the front and the entire boundary of the free surface flow of avalanches is very important. From this one can probably more efficiently predict the front and boundary of the avalanche in time, which may also be useful to increase the accuracy of the velocity distributions and the evolution of the avalanche geometry along its path and in the deposit. For this reason, one needs to develop a two-dimensional shock-capturing scheme that can be utilised for the moving boundary problem of the avalanche to determine the margin locations. For this, one should either incorporate the shock-capturing capability in a Lagrangean moving grid scheme or develop new numerical methods in which the Lagrangean method can somehow be inserted into the NOC schemes that we have implemented here. Alternatively, finite volume and finite element methods can also be implemented together with the finite difference method as proposed by Denlinger and Iverson [75] and Koschdon and Schäfer and Koschdon, [228, 229]. Similarly, Patra et al. and Pitman and others implemented a parallel adaptive mesh finite volume computational method based on a Godunov solver to simulate avalanche and debris flows [313, 321, 323]. However, whatever method is used, it must be able to describe the physics of avalanches and debris flows to a reliable, reasonable, acceptable and applicable level. Every advancement in the numerical methods must be applied from laboratory to real-scale events and thus be judged in practice.

14.2.4 More Advanced Measurement Techniques and Experiments

As usual, the final step should be related to the experimental phenomena. There are lots of things to be done. One may categorise avalanche and debris flow experiments into four divisions: small-scale indoor experiments (described in detail in this book), large-scale outdoor but well-controllable experiments (done by the Japanese and others, see, e.g., [213, 275, 297]), artificially triggered large-scale field experiments and naturally released events that can automatically be monitored from measuring stations (see [134, 190]). All are very important. They may have some common and some disjoint properties. Here we mainly focus on the small-scale laboratory experiments.

From the technical side, one should use high speed CCD cameras so as to capture a larger number of experimental images during the flow of the avalanche. One may then obtain a better correspondence between theory and experiments. On the other hand, the PIV measurement facility should be utilised to analyse avalanching flows over more complicated topographies. One can

remodel the chute topography to include sidewise curvature, either uniform or non-uniform. The chute channel may either be diverging or converging in its main flow direction. Further complicated aspects would be to add more CCD cameras and perform experiments for the flows over curved and twisted channels, as discussed above. The most interesting aspect would be the determination of the flow velocity by the PIV measurement system for the flow of a granular mass sliding down a (more general) prototype mountain topography consisting of some realistic obstructions, with the principle of down-scaling, in the laboratory environment, and then to use the measured results to predict the flow dynamics in the field.

The other aspect of the experiment should be the correct determination of the avalanche geometry during its entire evolution over irregular topography. Fundamental work in this direction has been recently started, e.g., by Denlinger and Iverson and Iverson et al. [75, 194]. They implemented a new method of laser assisted cartography to map the three-dimensionally deforming avalanches over a non-smooth benchtop avalanche chute. In this technology, horizontal sheets of light from refracted laser beams were used to superpose topographic contours on the chute bed and the moving free surface of the avalanche. A similar method was already used earlier by McDonald and Anderson and Pouliquen and Forterre [271, 330]. The other aspect could be the use of digital photogrammetry technique to map the three-dimensionally deforming avalanche body and compare the results obtained by other techniques. Such experiments should be done for several prototype flumes and chutes with different irregularities, for different granular materials and for different initial conditions. The conclusions of these experiments will then be of great importance to safely apply the model equations to real flow situations in nature.

References

1. E.E. Adams, R.L. Brown: A mixture theory for evaluating heat and mass transport processes in nonhomogeneous snow. *Continuum Mech. Thermodyn.* **2**, 31–63 (1990)
2. E. Akitaya: Studies on depth hoar. In: *Snow Mechanics.* (IAHS-AISH Publication, No. 114) (Proceedings of Grindelwald Symposium, April 1–5, 1974), 42–48 (1975)
3. P.M. Allen, D.J. Tildesley: *Computer Simulation of Liquids.* (Oxford University Press, Oxford, 1987)
4. W. Ammann, O. Buser, U. Vollenwyder: *Lawinen.* (Birkhäuser, Basel 1997)
5. C. Ancey (ed): Guide Neige et Avalanches: Connaissances, Pratiques, Sécurité, 2nd edition. (Édisud Aix-en-Provence, 1998) [http://lhe.epfl.ch]
6. C. Ancey: Snow avalanches. In: N.J. Balmforth, A. Provenzale (eds): *Geomorphological Fluid Mechanics* (Springer, Berlin Heidelberg New York 2001) pp 319–338
7. C. Ancey, M. Meunier: Estimating bulk rheological properties of flowing avalanches from the field data. *Journal of Geophysical Research* **109**, No. F1, F01004 10.1029/2003JF000036 (2003)
8. C. Ancey: *Dynamique des Avalanches.* (Press Polytechniques Universitaires Romandes, Lausanne, 2006)
9. D. Anderson, J. Tannehill, R. Pletcher: *Computational Fluid Mechanics and Heat Transfer* (New York and London, McGraw-Hill, 1984)
10. M.I. Anisimov: *Sneg I snezhnye obvaly* [Snow and snow cover collapses] (Moscow, Academy of Sciences of the USSR, 1958)
11. Anonymous 1: *Sneg I snezhnye obvaly v Khibinakh* [Snow and snow cover collapses in Khibiny mountains] (Leningrad, Gidrometeoizdat, 1938)
12. Anonymous 2: *Kadastr lavin SSSR*, 1–20 (Leningrad, Gidrometeoizdat, 1984–1991)
13. B. Armstrong, K. Williams: *The Avalanche Book* (Fulcrum Golden, CO 1986)
14. Th. Arnalds, K. Jónasson, S. Sigurðsson: Avalanche hazard zoning in Iceland based on individual risk. *Ann. Glaciol.* **38**, 285–290 (2004)
15. W.R. Ashby: General system theory and the problem of the black box. In: Mittelstaedtt (ed): *Regelungsvorgänge in lebenden Wesen* (München, 1961) pp. 51–62
16. M. Atwater: *The Avalanche Hunters* (Macrae Smith, Philadelphia, PA 1968)

17. H. Aulitzky: Stand des Lawinenschutzes und der Lawinenforschung – Aufgaben von wachsender Bedeutung. Universität für Bodenkultur, Wien, Heft 7 (1977)
18. B.N. Azarenok, S.A. Ivanenko, T. Tang: Godunov's scheme and moving adaptive grids. *Report on Applied Mathematics* (2002)
19. H. Bader, R. Haefeli, E. Bucher: *Snow and Its Metamorphism* [Der Schnee und Seine Metamorphose]. *Translation 14, January 1954, Snow, Ice and Permafrost Research Establishment, U.S. Army.* (1954)
20. R.A. Bagnold: Experiments on a gravity free dispersion of large solid spheres in a Newtonian fluid under shear. *Proc. R. Soc. A* **225**, 49–63 (1954)
21. R.A. Bagnold: Auto-suspension of transported sediment: turbidity currents. *Proc. R. Soc. A* **265**, 313–319 (1962)
22. S. Bakkehøi, H. Norem: Comparing topographical and dynamical run-out models by ideas of "nearest neighbour method". 2nd Avlanche Dynamics Workshop in Innsbruck. Preliminary (1993)
23. S. Bakkehøi, H. Norem: Sammenlikning av metoder for beregning av maksimal utløpsdistanse for snøskred [Comparison of methods for calculation of maximum avalanche runout distance]. Norwegian Geotechnical Institute, Report 581200-30 [in Norwegian] (1994)
24. J.P. Bardet, I. Vardoulakis: The asymmetry of stress in granular media. *Int. J. Solids Struct.* **38**, 353–367 (2001)
25. P. Bartelt, U. Gruber: Development and calibration of a Voellmy-fluid dense snow avalanche model based on a finite element method. Swiss Federal Institute for Snow and Avalanche Research, Internal Report No. 714 (Davos 1997)
26. P. Bartelt, B. Salm, U. Gruber: Modelling dense snow avalanche flow as a Criminale-Ericksen-Filby fluid without cohesion. Swiss Federal Institute for Snow and Avlanche Research, Internal Report No. 717 (Davos 1997)
27. P. Bartelt, B. Salm, U. Gruber: Calculating dense-snow avalanche runout using a Voellmy fluid model with active/passive longitudinal straining. *J. Glaciol.* **45**, 242–254 (1999)
28. P. Bartelt, O. Buser: The principle of minimum entropy production and snow structure. *J. Glaciol.* **50**, 342–352 (2004)
29. K. Baumann: *Godunov-Typ Verfahren für die Gleichungen der Hydrodynamik auf bewegten Gitter.* PhD Dissertation, Technische Universität Karlsruhe (1997)
30. Z.P. Bazant, G.S. Zi, D. McClung: Size effect law and fracture mechanics of the triggering of dry snow slab avalanches. *J. Geophys. Res.* SOL EA **108**, (B2)2119 (2003)
31. P. Beghin: *Etude des bouffées bidimensionnelles de densité en éconlement sur pente avec application aux avalanches de neige poudrense.* PhD Dissertation, Université P. Fourier, Grenoble (1979)
32. W. Benz: Smooth particle hydrodynamics: a review. In: J.R. Buchler (ed): *The Numerical Modelling of Nonlinear Stellar Pulsations* (Kluwer–Dordrecht 1990) pp 269–288
33. H. Björnsson: Snow avalanche studies in Iceland. In: *Avalanches. Glaciological Data Report GD-1* (World Data Center A for Glaciology, University of Colorado, Boulder, CO 1977) pp 39–42

34. H. Björnsson: Avalanche activity in Iceland, climatic conditions, and terrain features. *J. Glaciol.* **26**(94), 13–23 (1980)
35. V.P. Blagoveshchenskiy, M.E. Eglit: Matematicheskoe modelirovanie vlijanija parametrov lavinnih ochagov I fizicheskih svoistv snega na dvizhenije lavin [Mathematical modelling of the effect of the parameters of avalanche sources and physical properties of the snow on the dynamics of avalanches]. *Materialy Glyatsiologicheskikh Issledovaniy* [Data of Glaciological Studies] **53**, 108–112 [In Russian with English summary] (1985)
36. V.P. Blagoveshchenskiy, E.M. Mironova, M.E. Eglit: Calculation of avalanche parameters in little-studied mountain areas. *Materialy Glyatsiologicheskikh Issledovainiy* [Data of Glaciological Studies] **79**, 36–40 [Russian with English summary] (1995)
37. A. Boillot, A.K. Prasad: Optimization procedure for pulse separation in cross-correlation PIV. *Exp. Fluids* **21**, 87–93 (1996)
38. F. Bouchut, A. Mangeney-Castelnau, B. Perthame, J.-P. Vilotte: A new model of Saint Venant and Savage–Hutter type for gravity driven shallow water flows. *C.R. Acad. Sci. Paris série I* **336**, 531–536 (2003)
39. F. Bouchut: *Nonlinear stability of finite volume methods for hyperbolic conservation laws, and well-balanced schemes for sources* (Frontiers in Mathematics series) (Birkhäuser, Basel 2004)
40. F. Bouchut, M. Westdickenberg: Gravity driven shallow water models for arbitrary topography. *Comm. Math. Sci.* **2**, 359–389 (2004)
41. J. Boussinesq: *Théorie Analytique de la Chaleur. Vol. 2.* (Gathier-Villars Paris 1903)
42. R.M. Bowen, C.-C. Wang: *Introduction to Vectors and Tensors: Volume 1 – Linear and Multilinear Algebra* (Plenum Press, New York 1976)
43. R.M. Bowen, C.-C. Wang: *Introduction to Vectors and Tensors: Volume 2 – Vector and Tensor Analysis* (Plenum Press, New York 1976)
44. A.N. Bozhinskii, K.S. Losev: Osnovy lavinovedeniya. Leningrad, 1987 (published by the Swiss Federal Institute of Snow Avalanche Research, SLF, Davos) [In English as] *Fundamentals of avalanche study.* (SLF, Mitteilung Nr. 55) (1998)
45. A.P. Breu: *Segregation und Strukturenbildung in granularer Materie.* PhD Dissertation, Universität Bayreuth (Shaker Verlag, Aachen 2004)
46. L. Brillouin: *Tensors in Mechanics and Elasticity.* (Academic Press, New York 1964)
47. R.L. Brown: A thermodynamic study of materials representable by integral expansions. *Int. J. Eng. Sci.* **14**(11), 1033–1046 (1976)
48. R.L. Brown: A fracture criterion for snow. *J. Glaciol.* **19**(81), 111–121 (1976)
49. R.L. Brown: Pressure waves in snow. *J. Glaciol.* **25**(91), 99–107 (1980)
50. R.L. Brown: An analysis of non-steady plastic shock waves in snow. *J. Glaciol.* **25**(92), 279–287 (1980)
51. R.L. Brown: A volumetric constitutive law for snow based on a neck growth model. *J. Appl. Phys.* **51**(1), 161–165 (1980)
52. G. Brugnot: Recent progress and new applications of the dynamics of avalanches. In: *Proc. Snow in Motion Symp.* (Intl. Glaciol. Soc. 1979)
53. V. Buchholtz, T. Pöschel: Numerical investigations of the evolution of sandpiles. *Physica A* **202**, 390–401 (1994)

54. V. Buchholtz, T. Pöschel, H.-J. Tillemans: Simulation of rotating drum experiments using non-circular particles. *Physica A* **216**, 199–212 (1995)
55. H. Buggisch, R. Stadtler: On the relation between shear rate and stresses in one-dimensional steady flow of moist bulk solids. In: *Proc. World Congress Particle Technology, Part III, Mechanics of Pneumatic and Hydraulic Conveying and Mixing* (Nürnberg, 16–18 April, 1986) pp 187–202
56. O. Buser, M. Bütter, W. Good: *Avalanche forecast by the nearest neighbour method* (IAHS, publ. no. 162) (1987)
57. C.S. Campbell: Rapid granular flows. *Ann. Rev. Fluid Mech.* **22**, 57–92 (1990)
58. Canada Department of Mines: Map 57A. (Frank, Alberta 1917)
59. M.-C. Chiou: *Modelling Dry Granular Avalanches Past Different Obstructions: Numerical Simulations and Laboratorical Analyses.* PhD Dissertation, Darmstadt University of Technology, Germany (2005)
60. M.-C. Chiou, Y. Wang, K. Hutter: Influence of obstacles on rapid granular flows. *Acta Mechanica* **175**, 105–122 (2005)
61. M. Christen, P. Bartelt, U. Gruber: Aval-1D: An avalanche dynamics program for the particle. IPR Publication. Proceedings of International Congress INTERPRAEVENT 2002 in the Pacific Rim. Vol. 2 (Matsumoto, Japan 2002) pp 715–725
62. T. Chu, G. Hill, D.M. McClung, R. Sherkat: Experiments on granular flows to predict avalanche run-up. *Canad. Geotechn. J.* **32**, 285–295 (1995)
63. V. Chugunov, J.M.N.T. Gray, K. Hutter: Group theoretic methods and similarity solutions of the Savage–Hutter equations. In: K. Hutter, N. Kirchner (ed): *Dynamic Response of Granular and Porous Materials under Large and Catastrophic Deformations.* (Springer, Berlin Heidelberg New York 2003)
64. G.D. Cody, D.J. Goldfarb, G.V. Storch, Jr, A.N. Norris: Particle granular temperature in gas fluidized beds. *Powder Technol.* **87**, 211–232 (1996)
65. C. Cole: Modified spouted beds: practical fluidized bed combustion of lightweight particulate cellulose fuels. In: *National Conference on Bulk Materials Handling* (Melbourne, 1996)
66. R. Courant, K.O. Friedrichs, H. Levy: Über die partiellen Differenzengleichungen der mathematischen Physik. *Math. Ann.* **100**, 32–74 (1928)
67. R. Courant, D. Hilbert: *Methods of Mathematical Physics. I and II* (Interscience Publishers, London 1962)
68. R. Courant, K.O. Friedrichs, H. Levy: On the partial differential equations of mathematical physics. *IBM J.* **11**, 215–234 (1967)
69. E.M. Danilova, M.E. Eglit: The motion of chute avalanches. *Materialy Glyatsiologicheskikh Issledovaniy* [Data of Glaciological Studies] **31**, 65–74 [In Russian with English summary] (1977a)
70. E.M. Danilova, M.E. Eglit: The motion of snow avalanches under conditions of limiting friction. *Izv. Akad. Nauk SSSR Mekh. Zhidk. Gaza* **5**, 30–37 [English transl. In *Fluid Dynamics* **12**] (1977b)
71. W.B. Dade, H.E. Huppert: Long-runout rockfalls. *Geology* **26**, 803–806 (1998)
72. W.R. Dean: Note on the motion of fluid in a curved pipe. *Phil. Mag.* **4**(7), 208–223 (1927)
73. W.R. Dean: The stream-line motion of fluid in a curved pipe. *Phil. Mag.* **5**(7), 673–695 (1928)

74. R.P. Denlinger, R.M. Iverson: Flow of variably fluidised granular masses across three-dimensional terrain. II: Numerical predictions and experimental tests. *J. Geophys. Res.* **106**, 552–566 (2001)
75. R.P. Denlinger, R.M. Iverson: Granular avalanches across irregular three-dimensional terrain. I: Theory and computation *J. Geophys. Res.* **109**, No. F1, F01014 10.1029/2003JF000085 (2004)
76. J.D. Dent, T.E. Lang: Modelling of snow flow. *J. Glaciol.* **26**(94), 131–140 (1980)
77. J.D. Dent, T.E. Lang: *Experiments on the mechanics of flowing snow.* (Cold Reg. Sci. Tech., **5**(3), 253–258 (1982))
78. J.D. Dent: *A biviscous modified Bingham model for snow avalanche motion.* PhD Dissertation Montana State University (1982)
79. J.D. Dent, T.E. Lang: A biviscous modified Bingham model of snow avalanche motion. *Ann. Glaciol.* **4**, 42–46 (1983)
80. J.D. Dent, K.J. Burrel, D.S. Schmidt, M.Y. Louge, E.E. Adams, T.G. Jazbutis: Density, velocity and friction measurements in a dry-snow avalanche. *Ann. Glaciol.* **26**, 247–252 (1998)
81. H.B. Dwight: *Tables of integrals and other mathematical data.* (Macmillan, London 1968)
82. W. Eckart, S. Faria, K. Hutter, N. Kirchner, S.P. Pudasaini, Y. Wang: Continuum description of granular materials, Spring School at the Department of Structural and Geotechnical Engineering, Polytechnical Institute, Turin, Italy, 8–12 April (2002)
83. W. Eckart, J.M.N.T. Gray, K. Hutter: Particle image velocimetry (PIV) for granular avalanches on inclined planes. In: K. Hutter, N. Kirchner (ed): *Dynamic Response of Granular and Porous Materials under Large and Catastrophic Deformations* (Springer, Berlin Heidelberg New York 2003)
84. M.E. Eglit: Theoretical approaches to the calculation of the motion of snow avalanches. In: *Itogi Nauki, Moscow, VINITI, 60–97.* (English translation in *Glaciological Data Report* GD-16, 63–118, 1974)
85. M.E. Eglit, E.I. Sveshnikova: Matematicheskoe modelirovanie snezhnih lavin [Mathematical modeling of snow avalanches]. *Materialy, Glyatsiologicheskikh Issledovaniy* [Data of Glaciological Studies] **38**, 79–84 [In Russian with English summary] (1980)
86. M.E. Eglit: Calculation of the parameters of avalanches in the region of braking and halting. *Materialy Glyatsiologicheskikh Issledovaniy* [Data of Glaciological Studies] **53**, 35–39 [In Russian with English summary] (1982)
87. M.E. Eglit: Some mathematical models of snow avalanches. In: M. Shahinpoor (ed): *Advances in mechanics and the flow of granular materials, Vol. 2* (Clausthal-Zellerfeld and Gulf Publishing Company, Houston TX 1983) pp 577–588
88. M.E. Eglit: Teoreticheskie pdkhody k raschetu dvizheniia snezhnikh lavin. [Theoretical approaches to avalanche dynamics]. In: *Itogi Nauki, Moscow, VINITI, Gidrologiia Sushi. Glatsiologiia* (1967), 69–97. English transl. in: *Glaciological Data Report* DG-16 1984, Soviet Avalanche Research – Avalanche Bibliography Update: 1977–1983. (World Data Center A for Glaciology [Snow and Ice], University of Colorado, Boulder CO, 63–116, 1984)

89. M.E. Eglit, N.N. Vel'tishechev: Issledovanije matematicheskih modelei snezhnopilevoi lavini [Investigation of mathematical models of powder-snow avalanche]. *Materialy Glyatsiologicheskikh Issledovaniy* [Data of Glaciological Studies] **53**, 116–120 [In Russian with English summary] (1985)
90. M.E. Eglit: Mathematical and physical modelling of powder-snow avalanches in Russia. *Ann. Glaciol.* **26**, 281–284 (1998a)
91. M.E. Eglit: Mathematical modeling of dense avalanches. In: *25 Years of Snow Avalanche Research at NGI* (Anniversary Conference, Voss, Norway 12–16 May, 1998, Proceedings *NGI Publications 203*) (Norwegian Geotechnical Institute, Oslo, 1998b)
92. T.H. Ellison, J.S. Turner: Turbulent entrainment in stratified flows. *J. Fluid Mech.* **6**, 432–448 (1959)
93. T. Erismann: Flowing, rolling, bouncing, sliding: synopsis of basic mechanisms. *Acta Mech.* **64**, 101–110 (1986)
94. T. Erismann, G. Abele: *Dynamics of Rockslides and Rockfalls*, (Springer, Berlin Heidelberg New York 2001)
95. S.G. Evans: Landslides. In: G.R. Brooks (ed): *A Synthesis of Geological Hazards in Canada*. (*Geological Survey of Canada Bulletin* **548**, 2001) 43–79
96. C. Farhat, P. Geuzaine, C. Grandmont: The discrete geometric conservation law and the nonlinear stability of ALE schemes for the solution of flow problems on moving grids. *J. Comp. Phys.* **174**, 669–694 (2001)
97. R. Farwig: Existence of avalanching flows. In: K. Hutter, N. Kirchner (eds): *Dynamic Response of Granular and Porous Materials under Large and Catastrophic Deformations*. (Springer, Berlin Heidelberg New York 2003)
98. G. Félix, N. Thomas: Relation between dry granular flow regimes and morphology of the deposits: formation of levées in pyroclastic deposits. *Earth Planet Sci. Lett.* **221**, 197–213 (2004)
99. W. Flaig: *Der Lawinen-Franzjosef* (Gesellschaft alpiner Bücherfreunde, München, 1941)
100. W. Flaig: *Lawinen* (Brockhaus, Wiesbaden 1955)
101. C. Fraser: *The Avalanches Enigma* (John Murray Publishers Ltd., London 1966)
102. C. Fraser: *Avalanches and Snow Safety* (John Murray Publishers Ltd., London 1978)
103. Y. Fukushima, G. Parker, H.W. Pantim: Prediction of ignitive turbidity currents in Scripps Submarine Canyon. *Marine Geology* **67**, 55–81 (1985)
104. Y. Fukushima, G. Parker: Numerical simulation of powder snow avalanches. *J. Glaciol.* **36**(123), 229–237 (1990)
105. T. Fukuzawa, E. Akitaya: Depth-hoar crystal growth in the surface layer under high temperature gradient. *Ann. Glaciol.* **18**, 39–45 (1993)
106. D. Gammack, P.E. Hydon: Flow in pipes with non-uniform curvature and torsion. *J. Fluid Mech.* **433**, 357–382 (2001)
107. R. García-Rojo, H.J. Herrmann, S. McNamara (ed): *Powders and Grains 2005*. Proceedings of the Fifth International Conference on Micromechanics of Granular Media, Stuttgart, Germany. (A.A. Balkema, Rotterdam 2005)
108. P. Gauer: Bewegung einer Staublawine längs eines Berghangs. Diploma Thesis, Fachbereich Mechanik (III), Technische Hochschule Darmstadt, Germany (1994)

109. P. Gauer: A model of powder snow avalanches. In: F. Sivardière (ed): *Proc. of the Colloquium on the Contribution of Scientific Research to Safety with Snow, Ice and Avalanches.* (Chamonix, France, May 30–June 3, 1995) (ANENA Editions du CEMAGREF, Antony, France 1995)
110. P. Gauer: *Blowing and Drifting Snow in Alpine Terrain: A Physically-Based Numerical Model and Related Field Measurements.* PhD. Dissertation, Department of Mechanical and Process Engineering, ETH Zürich, Switzerland (1999)
111. P.-G. de Gennes: Reflections on the mechanics of granular matter. *Physica A* **261**, 267–293 (1998)
112. M. Germano: On the effect of torsion on helical pipe flow. *J. Fluid Mech.* **125**, 1–8 (1982)
113. M. Germano: The Dean equations extended to a helical pipe flow. *J. Fluid Mech.* **203**, 289–305 (1989)
114. R.A. Gingold, J.J. Monaghan: Smoothed particle hydrodynamics: theory and application to non-spherical stars. *Monthly Notices of the Royal Astronomical Society* **181**, 375–389 (1977)
115. S.K. Godunov: Finite difference methods for numerical computation of discontinuous solutions of the equations of fluid dynamics. *Mat. Sb.* **47**, 271–306 (1959)
116. S.K. Godunov: *Numerical solution of multidimensional problems in gas dynamics.* (Nauka, Moscow 1976)
117. A.G. Goff, G.F. Otten: Fiziko-mekhanicheskie svoistva snezhnogo pokrova [Physical-mechanical properties of snow cover]. In: M.I. Anisimov (ed): *Sneg I snezhnye obvaly* [Snow and snow cover collapses]. (Academy of Sciences of the USSR, Moscow 1958)
118. J. Goguel: Scale dependent rockslide mechanics. In: B. Voight (ed): *Rockslides and Avalanches, Vol. 1.* (Elsevier, Amsterdam 1978) pp 167–189
119. I.S. Gradshteyn, I.M. Ryshik: *Tables of Integrals, Series and Products.* 4th ed. (Academic Press, New York 1980)
120. J.M.N.T. Gray, K. Hutter: Pattern formation in granular avalanches. *Continuum Mech. Thermodyn.* **9**, 341–345 (1997)
121. J.M.N.T. Gray, K. Hutter: Physik granularer Lawinen. *Physikalische Blätter* **54**, 37–43 (1998)
122. J.M.N.T. Gray, Y.C. Tai: On the inclusion of a velocity-dependent basal drag in avalanche models. *Ann. Glaciol.* **26**, 277–280 (1998)
123. J.M.N.T. Gray, M. Wieland, K. Hutter: Gravity-driven free surface flow of granular avalanches over complex basal topography. *Proc. R. Soc. A* **455**, 1841–1874 (1999)
124. J.M.N.T. Gray: Granular flow in partially filled slowly rotating drums. *J. Fluid Mech.* **441**, 1–29 (2001)
125. J.M.N.T. Gray: Rapid granular avalanches. In: K. Hutter, N. Kirchner (ed): *Dynamic Response of Granular and Porous Materials under Large and Catastrophic Deformations.* (Springer, Berlin Heidelberg New York 2003) pp 1–40
126. J.M.N.T. Gray, Y.-C. Tai, S. Noelle: Shock waves, dead zones and particle free regions in rapid granular free surface flows. *J. Fluid Mech.* **491**, 160–181 (2003)
127. R. Greve: *Zur Ausbreitung einer Granulatlawine entlang gekrümmter Flächen.* Diploma Thesis, Darmstadt University of Technology, Darmstadt, Germany (1991)

128. R. Greve, K. Hutter: Motion of a granular avalanche in a convex and concave curved chute: experiments and theoretical predictions. *Phil. Trans. R. Soc. A* **342**, 573–600 (1993)
129. R. Greve, T. Koch, K. Hutter: Unconfined flow of granular avalanches along a partly curved surface. I: Theory. *Proc. R. Soc. A* **445**, 399–413 (1994)
130. S.S. Grigoriyan, M.E. Eglit, Yu.L. Yakimov: A new formulation and solution of the problem of the motion of a snow avalanche. *Trudy Vycokogornogo Geofizicheskogo Istituta* **12**, 104–113 [In Russian] (1967)
131. S.S. Grigoriyan, A.V. Ostroumov: *On the mechanics of the formation and collapse of mountainous slag heaps.* (Report No. 1724. Inst. Mekh. Moskov. Gos. Univ., Moscow) [In Russian] (1975a)
132. S.S. Grigoriyan, A.V. Ostroumov: *Calculation of the parameters of the motion and the force action on an avalanche dike "Tubri"* (Nizhnyaya Svanetiya). (Report No. 1695, Inst. Mekh. Moskov. Gos. Univ., Moscow) [In Russian] (1975b)
133. S.S. Grigoryan: Novii zakon trenija I mehanizm krupnomasshtabnih gornih obvalov I opolznei [A new law of friction and mechanism for large-scale slag heaps and landslides]. Dokl. Akad. Nauk SSSR 244(4), 846–849; English transl. in: *Soviet Phys. Dokl.* **24**, 110–111 (1979)
134. H.-U. Gubler: Measurements and modelling of snow avalanche speeds. In: B. Salm, H.-U. Gubler (ed): *Avalanche Formation, Movement and Effects.* (IAHS Publ. 162, September 14–19, 1986) (IAHS, 1987) pp 405–420
135. A. Hachikubo: Numerical modeling of sublimation on snow and comparison with field measurements. *Ann. Glaciol.* **32**, 27–32 (2001)
136. W. Haeberli, C. Huggel, A. Kääb, S. Oswald, A. Polkvoj, I. Zotikov, N. Osokin: The Kolka-Karmadon rock/ice slide of 20 September 2002 – an extraordinary event of historical dimensions in North Ossetia (Russian Caucasus). *J. Glaciol.* **50**, 533–546 (2004)
137. P.K. Haff: Grain flow as a fluid-mechanical phenomenon. *J. Fluid Mech.* **134**, 401–430 (1983)
138. P.K. Haff, B.T. Werner: Computer simulation of the mechanical sorting of grains. *Powder Technol.* **48**, 239–245 (1987)
139. K.M. Hákonardóttir, A.J. Hogg, T. Jóhannesson, G.G. Tómasson: A laboratory study of the retarding effects of braking mounds on snow avalanches. *J. Glaciol.* **49**(165), 191–200 (2003)
140. K.M. Hákonardóttir: *The Interaction Between Snow Avalanches and Dams.* PhD Dissertation, School of Mathematics, University of Bristol, England (2004)
141. D.M. Hanes, D.L. Inman: Observations of rapidly flowing granular-fluid materials. *J. Fluid. Mech.* **150**, 357–380 (1985)
142. C.B. Harbitz: *Snow Avalanche Modelling, Mapping and Warning in Europe* (SAME), Report of the Fourth European Framework Programme: Environment and Climate. C.B. Harbitz (ed) (NGI, Norway 1998)
143. A. Harten: High resolution schemes for hyperbolic conservation laws. *J. Comput. Phys.* **49**, 357–393 (1983)
144. A. Harten, S. Osher, B. Engquist, R. Chakravarthy: Some results on uniformly high-order accurate essentially nonoscillatory schemes. *Appl. Numer. Math.* **2**, 347–377 (1986)

145. A. Harten, P.D. Lax, B. van Leer: On upstream differencing and Godunov-type schemes for hyperbolic conservation laws. *SIAM-Rev.* **25**(1), 35–61 (1988)
146. A. Heim: Der Bergsturz von Elm. *Deutsch. Geol. Gesell. Zeitschrift* **34**, 74–115 (1882)
147. A. Heim: Bergsturz und Menschenleben. *Beiblatt zur Vierteljahresschrift der Naft. Ges. Zürich* **20**, 1–218 (1932)
148. D. Helbing, H.J. Herrmann, M. Schreckenberg, D.E. Wolf (Ed.): *Granular and Traffic Flow 1999: Social, Traffic, and Granular Dynamics.* (Springer, Berlin Heidelberg New York 2000)
149. H. Henein, J.K. Brimacombe, A.P. Watkinson: Experimental study of transverse bed motion in rotary kilns. *Metall. Trans. B* **14**, 191–205 (1983)
150. F. Hermann: *Experimente zur Dynamik von Staublawinen in der Auslaufzone.* (Mitteilung Nr. 107 Versuchsanstalt für Wasserbau, Hydrologie und Glaziologie, ETH Zürich) (1990)
151. F. Herrmann, K. Hutter: Laboratory experiments on the dynamics of powder-snow avalanches in the run-out zone. *J. Glaciol.* **37**(126), 281–295 (1991)
152. H.J. Herrmann, S. Luding: Modeling granular media on the computer. *Continuum Mech. Thermodyn.* **10**, 189–231 (1998)
153. E. Hestnes: *Skredfare i arealbruksammenheng. Studietur i Island. 30.07–05.08.1984.* (Norwegian Geotechnical Institute, Oslo, Report no. 58030-3) (1985)
154. R. Hogg, D.W. Fuerstenau: Transverse mixing in rotating cylinders. *Powder Technol.* **6**, 139–148 (1972)
155. E.J. Hopfinger: Snow avalanche motion and related phenomena. *Ann. Rev. Fluid Mech.* **15**, 47–76 (1983)
156. K. Hsü: On sturzstorms – catastrophic debris streams generated by rockfalls. *Geol. Soc. Am. Bull.* **86**, 129–140 (1975)
157. S.S. Hsiau, H.W. Jang: Measurements of velocity fluctuations of granular materials in a shear cell. *Exp. Therm. Fluid Sci.* **17**(3), 202–209 (1998)
158. S.S. Hsiau, Y.M. Shieh: Fluctuations and self-diffusion of sheared granular material flows. *J. Rheol.* **4**, 1049–1066 (1999)
159. X.H. Huang, M.H. Garcia: Perturbation solution for Bingham-plastic mudflows. *J. of Hydraul. Eng.* **123**(11), 986–994 (1997)
160. A. Huber: *Schwallwellen in Seen als Folge von Felsstürzen.* (Mitteilung No. 47, der Versuchsanstalt für Wasserbau, Hydrologie und Glaziologie an der ETH, Zürich) (1980)
161. O. Hungr, N.R. Morgenstern: Experiments on the flow behaviour of granular-materials at high-velocity in an open channel. *Geotechnique* **34**, 405–413 (1984)
162. O. Hungr, N.R. Morgenstern: High-velocity ring tests on sand. *Geotechnique* **34**, 415–421 (1984)
163. O. Hungr: A model for the runout analysis of rapid flow slides, debris flows, and avalanches. *Canadian Geotech. J.* **32**, 610–623 (1995)
164. O. Hungr, S.G. Evans: Rock avalanche runout prediction using a dynamic model. In: K. Senneset (ed): *Landslides.* (Proceedings of the 7th International Symposium on Landslides, Trondheim, Norway). (Balkema, Rotterdam 1996) pp 233–238

165. O. Hungr: Some methods of landslide hazard intensity mapping. In: R. Fell, D.M. Cruden (ed): *Proceedings of the Landslide Risk Workshop* (Balkema, Rotterdam 1997) pp 215–226
166. O. Hungr, S.G. Evans, M. Bovis, J.N. Hutchinson: Review of the classification of landslides of the flow type. *Environ. Eng. Geosci.* **7**, 221–238 (2001)
167. O. Hungr: Analytical models for slides and flows. In: *Proceedings of the International Symposium on Landslide Risk Mitigation and Protection of Cultural and Natural Heritage, Kyoto.* (Kyoto, 2002) pp 559–586
168. O. Hungr, R. Dawson, A. Kent, D. Campbell, N.R. Morgenstern: Rapid flow slides of coal mine waste in British Columbia, Canada. In: S.G. Evans, J.V. DeGraff (eds): *Catastrophic Landslides: Effects, Occurrence and Mechanisms.* (Geological Society of America), *Reviews in Engineering Geology* **15**, (2002) pp 191–208
169. O. Hungr: Rock avalanche motion: process and modeling. In: *Proceedings of NATO Symposium on Massive Rock Slope Movements.* (Kluwer, Dordrecht, 2004)
170. K. Hutter, F. Szidarovszky, S. Yakowitz: Plane steady shear flow of a cohesionless granular material down an inclined plane: a model for flow avalanches, Part I. Theory. *Acta Mech.* **63**, 87–112 (1986a)
171. K. Hutter, F. Szidarovszky, S. Yakowitz: Plane steady shear flow of a cohesionless granular material down an inclined plane: a model for flow avalanches, Part II. Numerical results. *Acta Mech.* **65**, 239–261 (1986b)
172. K. Hutter, C. Plüss, N. Maeno: *Some implications deduced from laboratory experiments on granular avalanches.* (Mitteilung No. 94 der Versuchsanstalt für Wasserbau, Hydrologie und Glaziologie an der ETH, Zürich) (1988)
173. K. Hutter, Y. Nohguchi: Similarity solution for a Voellmy model of snow avalanches with finite mass. *Acta Mech.* **82**, 99–127 (1990)
174. K. Hutter: Two- and three-dimensional evolution of granular flow – theory and experiments revisited. *Acta Mech.* **1**[Suppl], 167–181 (1991)
175. K. Hutter, T. Koch: Motion of a granular avalanche in an exponentially curved chute: experiments and theoretical predictions. *Phil. Trans. R. Soc. A* **334**, 93–138 (1991)
176. K. Hutter, R. Greve: Two-dimensional similarity solutions for finite-mass granular avalanches with Coulomb-type and viscous-type frictional resistance. *J. Glaciol.* **39**(132), 357–372 (1993)
177. K. Hutter, M. Siegel, S.B. Savage, Y. Nohguchi: Two-dimensional spreading of a granular avalanche down an inclined plane. I. Theory. *Acta Mech.* **100**, 37–68 (1993)
178. K. Hutter, K.R. Rajagopal: On flows of granular materials. *Continuum Mech. Thermodyn.* **6**, 81–139 (1994)
179. K. Hutter, T. Koch, C. Plüss, S.B. Savage: Dynamics of avalanches of granular materials from initiation to runout. Part II: Experiments. *Acta Mech.* **109**, 127–165 (1995)
180. K. Hutter: Avalanche Dynamics. In: V.P. Singh (ed): *Hydrology of Disaster.* (Kluwer, Dordrecht 1996) pp 317–394
181. K. Hutter, B. Svendsen, D. Rickenmann: Debris flow modeling: a review. *Cont. Mech. Thermodyn.* **8**, 1–35 (1996)
182. K. Hutter, K. Jöhnk: *Continuum Methods of Physical Modeling* (Springer, Berlin Heidelberg New York 2004)

183. K. Hutter, Y. Wang, S.P. Pudasaini: The Savage–Hutter avalanche model. How far can it be pushed? *Phil. Trans. R. Soc. A* **363**, 1507–1528 (2005)
184. K. Hutter: Debris and mudflows: Are we asking the correct questions? What are the deficits? In: E. Minor (ed): *Mitteilung Nr. 7./8. der Versuchsanstalt für Wasserbau, Hydrologie und Glaziologie an der ETH Zürich* (ETH Zürich, 2005) pp 1–15
185. H. Hwang, K. Hutter: A new kinetic model for rapid granular flow. *Continuum Mech. Thermodyn.* **7**, 357–384 (1995)
186. I. Inoue, K. Yamaguchi, K. Sato: Motion of a particle and mixing process in an horizontal drum mixer. *Kagaku Kogaku* **34**, 1323 (1979)
187. F. Irgens, B. Schieldrop, C.B. Harbitz, U. Domaas, R. Posahl: Simulations of dense snow avalanches on deflecting dams. *Ann. Glaciol.* **26**, 265–271 (1998)
188. D. Issler: Modelling of snow entrainment and deposition in powder-snow avalanches. *Ann. Glaciol.* **26**, 253–258 (1998)
189. D. Issler, P. Gauer, M. Barbolini: Continuum models of particle entrainment and deposition in snow drift and avalanche dynamics. In: H.-D. Alber, R. Balean, R. Farwig (eds): *Models of Continuum Mechanics in Analysis and Engineering.* (Shaker Verlag, Aachen 1998) pp 58–80
190. D. Issler: Experimental information on the dynamics of dry-snow avalanches. In: K. Hutter, N. Kirchner (eds): *Dynamic Response of Granular and Porous Materials under Large and Catastrophic Deformations.* (Springer, Berlin Heidelberg New York 2003) pp 109–160
191. R.M. Iverson: The physics of debris flows. *Rev. Geophys.* **35**, 245–296 (1997)
192. R.M. Iverson, R.P. Denlinger: Flow of variably fluidised granular masses across three-dimensional terrain. I: Coulomb mixture theory. *J. Geophys. Res.* **106**, 537–552 (2001)
193. R.M. Iverson, J.W. Vallance: New views of granular mass flows. *Geology* **29**, 115–118 (2001)
194. R.M. Iverson, M. Logan, R.P. Denlinger: Granular avalanches across irregular three-dimensional terrain: II: Experimental tests. *J. Geophys. Res.* **109**, No. F1, F01015 10.1029/2003JF000084 (2004)
195. J.T. Jenkins, S.B. Savage: A theory for the rapid flow of identical, smooth, nearly elastic particles. *J. Fluid Mech.* **130**, 186–202 (1983)
196. J.T. Jenkins, M.W. Richman: Grad's 13-moment system for a dense gas of inelastic spheres. *Arch. Rat. Mech. Anal.* **87**, 355–377 (1985)
197. J.T. Jenkins, M.W. Richman: Boundary conditions for plane flows of smooth, nearly elastic, circular discs. *J. Fluid Mech.* **171**, 53–69 (1986)
198. J.T. Jenkins: Hydraulic theory for a frictional debris flow on a collisional shear layer. In: B. Straughan, R. Greve, H. Ehrentraut, Y. Wang (eds): *Continuum Mechanics and Applications in Geophysics and in the Environment.* (Springer, Berlin Heidelberg New York 2001) pp 113–125
199. J.T. Jenkins, L. La Ragione: Particle spin in anisotropic granular materials. *Int. J. Solids Struct.* **38**, 1063–1069 (2001)
200. G.S. Jiang, E. Tadmor: Nonoscillatory central schemes for multidimensional hyperbolic conservation laws. *SIAM J. Sci. Comput.* **19**, 1892–1917 (1998)
201. P.C. Johnson, R. Jackson: Frictional-collisional constitutive relations for granular materials with application to plane shearing. *J. Fluid Mech.* **176**, 67–93 (1987)

202. T. Jóhannesson, K. Lied, S. Margreth, F. Sandersen: An overview of the need for avalanche protection measures in Iceland. *Reykjavík, Icel. Meteorol. Office, Rep. R96004* (1996)
203. T. Jóhannesson: Icelandic avalanche runout models compared with topographic models used in other countries. In: E. Hestnes (ed): *25 years of Snow Avalanche Research.* (Publication nr. 203, Oslo, NGI, 1998) pp 43–52
204. T. Jóhannesson: Accidents and economic damage due to snow avalanches and landslides in Iceland. In: *International LACDE conference* (Reykjavík, 28–30 August, 2000)
205. T. Jóhannesson: Run-up of two avalanches on the deflecting dams at Flateyri, north-western Iceland. *Ann. Glaciol.* **32**, 350–354 (2001)
206. T. Jóhannesson, Th. Arnalds: Accidents and economic damage due to snow avalanches and landslides in Iceland. *Jökull* **50**, 81–94 (2001)
207. T. Jóhannesson: Field observations and laboratory experiments for evaluating the effectiveness of avalanche defence structures in Iceland. Main results and future programme. In: F. Naaim-Bouvet (ed): *Proceedings of the International Seminar on Snow and Avalanches Test Sites* (Grenoble, France, 22–23 November 2002). (Grenoble, Cemagref, 2003) pp 99–109
208. Ó. Jónsson, S. Rist, J. Sigvaldason: *Skriðuföll og snjóflóð. III. Snjóflóðaannáll. [Snow avalanches and landslides. III. A chronicle of snow avalanches.]* (Bókaútgáfan Skjaldborg, Reykjavík 1992)
209. K. Jónasson, S. Sigurðsson, Th. Arnalds: Estimation of Avalanche Risk. *Reykjavík, Icel. Meteorol. Office, Rep. R99001* (1999)
210. L.A. Kanaev: Problemy klassifikatsii lavin [Problems of avalanche classification], *Trudy SANIGMI* [Proceedings SANIGMI], **71**(152), 11–24 (1980)
211. R.D. Keane, R.J. Adrian: Theory of cross-correlation analysis of PIV images. *Appl. Sci. Res.* **49**, 191–215 (1992)
212. S. Keller: *Physikalische Simulation von Staublawinen – Experimente zur Dynamik im dreidimensionalen Auslauf.* PhD Dissertation, Swiss Federal Institute of Technology, Zürich, Switzerland, October, 1995. (Mittlg. Versuchsanstalt für Wasserbau, Hydrologie und Glaziologie, Swiss Federal Institute of Technology, Zürich, Nr. **141**) (1995)
213. S. Keller, Y. Ito, K. Nishimura: Measurements of the vertical velocity distribution in ping-pong ball avalanches. *Ann. Glac.* **26**, 259–264 (1998)
214. P.E. Kent: The transport mechanism in catastrophic rockfalls. *J. Geol.* **74**, 79–83 (1965)
215. R.R. Kerswell: Dam break with Coulomb friction: A model for granular slumping? *Physics Fluids* **17** 057101 (2005)
216. C.J. Keylock: Snow avalanches. *Prog. Phys. Geog.* **21**(4), 481–500 (1997)
217. C.J. Keylock, D.M. McClung, M.M. Mágnusson: Avalanche risk mapping by simulation. *J. Glaciol.* **45**(150), 303–314 (1999)
218. D.V. Khakhar, J.J. McCarthy, Troy Shinbrot, J.M. Ottino: Transverse flow and mixing of granular materials in a rotating cylinder. *Physics Fluids* **9**, 31–43 (1997)
219. D.V. Khakhar, A.V. Orpe, J.M Ottino: Surface granular flows: Two related examples. *Adv. Complex Sys.* **4**, 407–417 (2001)
220. Y. Kishino (ed): *Powder and Grains 2001*: Proceedings of the Fourth International Conference on Micromechanics of Granular Media, Sendai, 21–25, May 2001 (A.A. Balkema, Rotterdam 2001)

221. S.P. Klein, B.R. White: Dynamic shear of granular material under variable gravity conditions: *AIAA J.* **28**, 1701 (1990)
222. E. Klingbeil: *Tensorrechung für Ingenieure* (Hochschultaschenbücher), (Bibliographisches Institut, Mannheim 1966)
223. Chr. Krülle: On structure-formation phenomena in granular matter: Transition, transport and segregation. Habilitationsschrift, Fakultät für Mathematik und Physik, Universität Bayreuth (2004)
224. D. Kobayashi: *Studies of snow transport in low-level drifting snow.* Contributions from the Institute of Low Temperature Science Series A No. 24. (Institute of Low Temperature Science, Hokkaido University Sapporo, Japan, July, 1972)
225. T. Koch: *Bewegung einer Granulatlawine entlang gekrümmten Bahn.* Diploma Thesis, Darmstadt University of Technology, Darmstadt, Germany (1989)
226. T. Koch: *Zwei- und dreidimensionale Granulatlawinen, ihre dynamische Beschreibung: Theory Numerik und Experiment.* PhD Dissertation, Darmstadt University of Technology, Darmstadt, Germany (1994)
227. T. Koch, R. Greve, K. Hutter: Unconfined flow of granular avalanches along a partly curved chute. II: Experiments and numerical computations. *Proc. R. Soc. A* **445**, 415–435 (1994)
228. K. Koschdon, M. Schäfer: A Lagrangian-Eulerian finite-volume method for simulating free surface flows of granular avalanches. In: K. Hutter, N. Kirchner (ed): *Dynamic Response of Granular and Porous Materials under Large and Catastrophic Deformations.* (Springer, Berlin Heidelberg New York 2003) pp 83–108
229. K. Koschdon: *Numerische Simulation des dynamischen Verhaltens granularer Medien.* PhD Dissertation, Darmstadt University of Technology, Darmstadt, Germany (Shaker Verlag, Aachen 2004)
230. A.G. Kulikovskiy, M.E. Eglit: A two-dimensional problem on the motion of a snow avalanche along a slope with smoothly changing properties. *Prikl. Mat. Mekh.* **37**, 837–848 [English transl. in *J. Appl. Math. Mech.* **37**, 792–803 (1973)] (1973)
231. A.G. Kulikovskiy, E.I. Sveshnikova: Model dlja rascheta dvizhenija pilevoi snezhnoi lavini [A model for calculation of motion of powder snow avalanche]. *Materialy Glyatsiologicheskikh Issledovaniy* [Data of Glaciological Studies] **31**, 74–80 [In Russian with English summary] (1977)
232. D. Kröner: *Numerical Schemes for Conservation Laws* (Teubner, Stuttgart 1997)
233. E. Lachapelle: *The ABC of Avalanche Safety* (Highlander, Colorado 1961)
234. E. LaChapelle: The avalanche review. In: E. LaChapelle (ed): *The Alta Avalanche Study Center* **2**(6), 7 (1984)
235. E. LaChapelle: *Secrets of the Snow: Visual Clues to Avalanche and Ski Conditions* (University of Washington Press, Washington 2001)
236. B. Lackinger: Überlegungen zur österreichischen Schnee- und Lawinenforschung unter Berücksichtigung von Sicherheitsaspekten. In: P. Baumgartner, E. Rabofsky (ed): *Sicherheit im Bergland.* (Jahrbuch 1985, 1985) pp 208–216
237. E. Lajeunesse, A. Mangeney-Castelnau, J.P. Vilotte: Spreading of a granular mass on a horizontal plane. *Physics Fluids* **16**, 2371–2381 (2004)
238. W.T. Lambe, R.V. Whitman: *Soil Mechanics* (Wiley, New York 1979)

239. T.E. Lang, J.D. Dent: Scale modelling of snow avalanche impact on structures. *J. Glaciol.* **26**(94), 189–196 (1980)
240. T.E. Lang, J.D. Dent: Review of surface friction, surface resistance and flow of snow. *Rev. Geophys. Space Phys.* **20**(1), 21–37 (1982)
241. R.M. Lang, B.R. Leo, K. Hutter: Flow characteristics of an unconstrained non-cohesive granular medium down an inclined, curved surface: Preliminary experimental results. *Ann. Glaciol.* **13**, 146–153 (1989)
242. R.M. Lang: *An Experimental and Analytical Study on Gravity-Driven Free Surface Flow of Cohesionless Granular Media.* PhD Dissertation, Darmstadt University of Technology, Darmstadt, Germany (1992)
243. J. Latham, J. Montagne: The possible importance of electrical forces in the development of snow cornices. *J. Glaciol.* **9**(57), 375–384 (1970)
244. W.F. St. Lawrence: *A Structural Theory for the Deformation of Snow.* PhD Dissertation, Montana State University (1977)
245. W.F. St. Lawrence, T.E. Lang: A constitutive relation for the deformation of snow. *Cold Reg. Sci. Tech.* **4**, 3–14 (1981)
246. P. Lax: Weak solutions of nonlinear hyperbolic equations and their numerical computation. *Comm. Pure Appl. Math.* **7**, 159–193 (1954)
247. P.D. Lax, B. Wendroff: Systems of conservation laws. *Comm. Pure Appl. Math.* **13**, 217–237 (1960)
248. F. Legros: The mobility of long-runout landslides. *Eng. Geol.* **63**(3–4), 301–331 (2002)
249. J. Lehmberg, M. Hehl, K. Schügerl: Transverse mixing and heat transfer in a horizontal drum mixer. *Powder Technol.* **18**(2), 149–163 (1977)
250. R.J. LeVeque: *Numerical Methods for Conservation Laws.* (Birkhäuser, Basel 1990)
251. K.A. Lie, S. Noelle: An improved quadrature rule for the flux-computation in staggered central difference schemes in multidimensions. *J. Sci. Comp.* **18**, 69–80 (2003)
252. K. Lied, S. Bakkehøi: Empirical calculations of snow-avalanche run-out distance based on topographic parameters. *J. Glaciol.* **26**, 165–177 (1980)
253. K. Lied, R. Toppe: Calculation of maximum snow avalanche runout distance based on topographic parameters identified by digital terrain models. *Ann. Glaciol.* **13**, 164–169 (1989)
254. K.F. Liu, C.C. Mei: Approximate equations for the slow spreading of a thin sheet of Bingham plastic fluid. *Phys. Fluids A* **2**(1), 30–36 (1989)
255. D.H. Lorenzen: *Mission Mars. Die sensationellen Entdeckungen der neuen Raumsonden.* (Kosmos, Stuttgart 2004)
256. L.B. Lucy: A numerical approach to the testing of the fission hypothesis. *Astrophys. J.* **82**(12), 1013–1024 (1977)
257. R.M. Lueptow, A. Akonur, T. Shinbrot: PIV for granular flows. *Exp. Fluids* **28**, 183–186 (2000)
258. C.K.K. Lun, S.B. Savage, D.J. Jeffrey, N. Chepurniy: Kinetic theories for granular flows: inelastic particles in couette flow and slightly inelastic particles in general flow field. *J. Fluid Mech.* **140**, 223–256 (1984)
259. M. Mabssout, M. Pastor: A two-step Taylor–Galerkin algorithm applied to shock wave propagation in soils. *Int. J. Numer. Anal. Meth. Geomech.* **27**, 685–704 (DOI: 10.1002/nag.292) (2003)

260. R.W. MacCormack: An efficient explicit-implicit characteristic method for solving the compressible Navier–Stokes equations. *SIAM-AMS Proc.* **11**, 130–155 (1978)
261. N. Maeno, K. Nishimura: Numerical computation of snow avalanche motion in a three-dimensional topography. *Low Temerpature Science, Ser. A* **46**, 99–110 (1987)
262. M.M. Magnússon: The buildup of the avalanche section of the Icelandic Meteorological Office. In: *Proceedings of the International Snow Science Workshop 1998.* (The Washington State Department of Transportation, 1998) pp 132–139
263. A. Mangeney, P. Heinrich, R. Roche: Analytical solution for testing debris avalanche numerical models. *Pure Appl. Geophys.* **157**(6–8), 1081–1096 (2000)
264. A. Mangeney-Castelnau, J.P. Vilotte, M.O. Bristeau, B. Perthame, F. Bouchut, C. Simeoni, S. Yerneni: Numerical modelling of avalanches based on Saint Venant equations using a kinetic scheme. *J. Geophys. Res.* SOL EA **108**, (B11)2527 (2003)
265. A. Mangeney-Castelnau, F. Bouchut, E. Lajeunesse, A. Aubertin, J.P. Vilotte, M. Pirulli: On the use of Saint-Venant equations for simulating the spreading of a granular mass. *J. Geophys. Res.* **110**, B09103 (2005)
266. J.J. McCarthy, J.E. Wolf, T. Shinbrot; G. Metcalfe, J.M. Ottino: Mixing of granular materials in slowly rotated containers. *American Institue Chemical Engineers J.* **42**, 3351–3353 (1996)
267. D.M. McClung, K. Lied: Statistical and geometrical definition of snow avalanche runout. *Cold Reg. Sci. Technol.* **13**, 107–119 (1987)
268. D. McClung: Avalanche fatalities in Himalayan mountaineering. *Ameri. Alpine J.* **23**(55), 138–145 (1981)
269. D. McClung: Size scaling for dry snow slab release. *J. Geophys. Res.* SOL EA **108**, (B10)2465 (2003)
270. B.E. McDonald, J. Ambrosiano: High-order upwind flux correction methods for hyperbolic conservation laws. *J. Comp. Phys.* **56**, 448–460 (1984)
271. R.R. McDonald, R.S. Anderson: Constraints on eolian grain flow dynamics through laboratory experiments on sand slopes. *J. Sediment. Res.* **66**, 642–653 (1996)
272. S. McDougall, O. Hungr: Objectivities for the development of an integrated three-dimensional continuum model for the analysis of landslide runout. In: D. Rickenmann, C.L. Chen (eds): *Proceedings of the 3rd International Conference on Debris-Flow Hazards Mitigation: Mechanics, Prediction and Assessment.* (Millpress, Rotterdam 2003)
273. S. McDougall, O. Hungr: A model for the analysis of rapid landslide motion across three-dimensional terrain. *Canad. Geotech. J.* **41**(6), 1084–1097 (2004)
274. S. McDougall, O. Hungr: Dynamic modelling of entrainment in rapid landslides. *Canad. Geotech. J.* **42**(5), 1437–1448 (2005)
275. J. McElwaine, K. Nishimura: Ping-pong ball avalanche experiments. *Ann. Glaciol.* **32**, 241–250 (2001)
276. C.C. Mei, M. Yuhi: Slow flow of a Bingham fluid in a shallow channel of finite width. *J. Fluid Mech.* **431**, 135–159 (2001)
277. S. Melin: Simulation of sound propagation in granular media on the Connection Machine. *Int. J. Mod. Phys. C* **4**, 1103–1107 (1993)

278. M. Mellor: *Avalanches.* In: Part III-A 3d, Cold Regions Science and Engineering, Cold Regions Research and Engineering Lab., Corp of Engineers, U.S. Army, Hanover, N.H. 1968)
279. J. Melosh: The physics of very large landslides. *Acta Mech.* **64**, 89–99 (1986)
280. C. Mercier: Sur une representation des surfaces toroidales: applications aux equilibres magnetohydrodynamiques. *Fusion Nucleaire* **3**(94), 89 (1963)
281. G. Metcalfe, T. Shinbrot, J.J. McCarthy, J.M. Ottino: Avalanche mixing of granular solids. *Nature* **374**, 39–41 (1995)
282. E.M. Mironova: Computation of avalanche flows based on a two-dimensional hydraulic model. *Materialy Glyatsiologicheskikh Issledovaniy* [Data of Glaciological Studies] **53**, 113–115 [In Russian with English summary] (1985)
283. E.M. Mironova: *Mathematical modelling of the motion of water flows, snow avalanches, and floods.* Candidate's Dissertation, Moscow [In Russian] (1987)
284. E.M. Mironova, M.E. Eglit: The set of software for numerical modelling of snow avalanches, mudflows and water flows. *Materialy Glyatsiologicheskikh Issledovaniy.* [Data of Glaciological Studies] **63**, 161–165 [In Russian with English summary] (1988)
285. L.S. Mohan, P.R. Nott, K.K. Rao: A frictional Cosserat model for the flow of granular materials through a vertical channel. *Acta Mechanica* **138**, 75–96 (1999)
286. J.J. Monaghan: Particle methods for hydrodynamics. *Comput. Phys. Rep.* **3**, 71–124 (1985)
287. J.J. Monaghan: Smoothed particle hydrodynamics. *Annu. Rev. Astron. Astr.* **30**, 543–574 (1992)
288. B.R. Morton, G.I. Taylor, S.J. Turner: Turbulent gravitational convection from maintained and instantaneous sources. *Proc. R. Soc. A* **234**, 1–23 (1956)
289. P. Mougin: *Restauration des montagnes.* (Imprimerie Nationale, Paris 1931)
290. W. Munter: 3×3 *Lawinen: Risikomanagement im Wintersport.* (Pohl and Schellhammer, Garmisch-Partenkirchen 2003)
291. M. Nakagawa, S.A. Altobelli, A. Caprihan, E. Fukushima, E.-K. Jeong: Noninvasive measurements of granular flows by magnetic resonance imaging. *Exp. Fluids* **16**, 54–60 (1993)
292. T. Nakamura, H. Nakamura, O. Abe, A. Sato, N. Numano: A newly designed chute for snow avalanche experiments. In: B. Salm, H.-U. Gubler (eds): *Avalanche Formation, Movement and Effects.* (IAHS Publ. 162, September 14–19, 1986), (IAHS, 1987) pp 441–451
293. V.V.R. Natarajan, M.L. Hunt, E.D. Taylor: Local measurements of velocity fluctuations and diffusion coefficients for a granular material flow. *J. Fluid Mech.* **304**, 1–25 (1995)
294. H. Nessyahu, E. Tadmor: Non-oscillatory central differencing for hyperbolic conservation laws. *J. Comput. Phys.* **87**, 408–463 (1990)
295. J. von Neumann, R. Richtmyer: A Method for the numerical calculation of hydrodynamic shocks. *J. Appl. Phys.* **21**, 232–237 (1950)
296. K. Nishimura, N. Maeno: Contribution of viscous forces to avalanche dynamics. *Ann. Glaciol.* **13**, 202–206 (1989)
297. K. Nishimura, S. Keller, J. McElwaine, Y. Nohguchi: Ping-pong ball avalanche at a ski jump. *Granul. Matter* **1**(2), 51–56 (1998)
298. K. Nishimura, N. Maeno, K. Kawada, K. Izumi: Structures of snow cloud in dry-snow avalanches. *Ann. Glaciol.* **18**, 173–178 (1993)

299. K. Nishimura, H. Narita, N. Maeno, K. Kawada: The internal structure of powder-snow avalanches. *Ann. Glaciol.* **13**, 207–210 (1989)
300. Y. Nohguchi: Three-dimensional equations for mass centre motion of an avalanche of arbitrary configuration. *Ann. Glociol.* **13**, 215–217 (1989)
301. Y. Nohguchi, K. Hutter, S.B. Savage: Similarity solutions for granular avalanches of finite mass with variable bed friction. *Continuum Mech. Thermodyn.* **1**, 239–265 (1989)
302. H. Norem, F. Irgens, B. Schieldrop: Continuum model for calculating snow avalanches. In: B. Salm, H.-U. Gubler (eds): *Avalanche Formation, Movement and Effects.* (IAHS Publ. 162, September 14–19, 1986). (IAHS, 1987) pp 263–279
303. H. Norem, F. Irgens, B. Schieldrop: Simulation of snow avalanche flow in runout zones. *Ann. Glaciol.* **13**, 218–225 (1989)
304. H. Norem: *The Ryggfonn project, summary report 1981–1995.* (A/S, report A952-1, 1995)
305. J.S. O'Brien, P.Y. Julien, W.T. Fullerton: Two-dimensional water flood and mudflow simulation. *J. Hydr. Engrg.* **119**(2), 244–261 (1993)
306. T. Ohtsuki, Y. Takemoto, T. Hata, S. Kawai, A. Hayashi: Molecular dynamics study of cohesionless granular materials: Size segregation by shaking. *Int. J. Mod. Phys. B* **7**, 1865–1872 (1993)
307. A.V. Orpe, D.V. Khakhar: Scaling relations for granular flow in quasi-tow-dimensional rotating cylinders. *Phys. Rev. E* **64**, 031302, 1302-1-13 (2003)
308. A.V. Ostroumov: *A model of the motion of snow avalanches of chute type.* Candidate's Dissertation, Moscow [In Russian] (1972)
309. G. Parker, Y. Fukushima, H.M. Pantin: Self accelerating turbidity currents. *J. Fluid Mech.* **171**, 145–181 (1986)
310. M. Pastor, M. Quecedo, J.A. Fernández Merodo, M.I. Herrores, E. Gonzalez, P. Mira: Modelling tailings dams and mine waste dumps failures. *Géotechnique* **52**(8), 579–591 (2002)
311. M. Pastor, J.A. Fernández Merodo, E. González, P. Mira, T. Li, X. Liu: Modelling of landslides (I) Failure mechanisms. In: F. Darve, I. Vardoulakis (ed): *CISM Courses Series Degradations and Instabilities in Geomaterials* (CISM Courses and Lectures, No. 461) (Springer, Wien 2004) pp 287–318
312. M. Pastor, M. Quecedo, E. Gonzalez, M. Isabel Herreros, E. González, J.A. Fernández Merodo, P. Mira: Modelling of landslides. (II) Propagation of fast catastrophic landslides. In: F. Darve, I. Vardoulakis (eds): *CISM Courses Series Degradations and Instabilities in Geomaterials.* (CISM Courses and Lectures, No. 461) (Springer, Wien 2004) pp 319–367
313. A.K. Patra, A.C. Bauer, C.C. Nichita, E.B. Pitman, M.F. Sheridan, M. Bursik, B. Rupp, A. Weber, A. Stinto, L. Namikawa, C. Renschler: Parallel adaptive numerical simulation of day avalanches over natural terrain. *J. Volcanol. and Geoth. Res.* **139**(1–2), 1–21 (2005)
314. R.I. Perla, M.Jr. Martinelli: *The Avalanche Handbook*, USDA Forest Service, Fort Collins, Colorado, 1976
315. I.P. Perla, T.T. Cheng, D.M. McClung: A two-parameter model of snow avalanche motion. *J. Glaciol.* **26**(94), 197–207 (1980)
316. I.P. Perla, K. Lied, K. Kristensen: Particle simulation of snow avalanche motion. *Cold Reg. Sci. Technol.* **9**, 191–202 (1984)
317. L. Piegl, W. Tiller: *The NURBS Book.* 2nd edition. (Springer 1997)

318. E.B. Pitman: The mechanics of particle-fluid flow at high solids volume Fraction. In: A. Rosato, D. Blackmore (Ed.): *Proc. IUTAM Symposium on Segregation in Granular Materials.* (Kluwer, Boston 2000) pp 241–254
319. E.B. Pitman, C. Nichita: Numerical simulation of small particles in a fluid. In: *Proc. APM 2000 Summer School, St. Petersburg, Russia, 2002*, pp 155–163
320. E.B. Pitman, A. Patra, A. Bauer, M. Sheridan, M. Bursik: Computing debris flows and landslides: towards a tool for hazard risk evaluation. In: T. Hou, E. Tadmor (ed): *Hyperbolic Problems: Theory, Numerics, Applications* (Springer, Berlin Heidelberg New York 2002) pp 807–818
321. E.B. Pitman, C.C. Nichita, A.K. Patra, A.C. Bauer, M. Bursik, A. Weber: A Numerical Study of Granular Flows on Erodible Surface. *Discret Cont. Dyn. S. – Series B* **3**, 589–599 (2003)
322. E.B. Pitman, A. Patra, A. Bauer, C. Nichita, M. Sheridan, M. Bursik: Computing granular avalanches and landslides. *Physics Fluids* **15**, 3638–3646 (2003)
323. E.B. Pitman, L. Le: A two-fluid model for avalanche and debris flows. *Phil. Trans. R. Soc. A* **363**, 1573–1601 (2005)
324. C. Plüss: *Experiments on Granular Avalanches.* Diplomarbeit, Abt. X, Eidg. Techn. Hochschule, Zürich (1987)
325. K. Pohlhausen: Zur näherungsweisen Integration der Differentialgleichung der laminaren Grenzschicht. *ZAMM* **1**, 252–268 (1921)
326. V.V. Popovnin, D.A. Petrakov, O.V. Tutubalina, S.S. Chernomorets: The 2002 glacial catasptophe in North Ossetia. [In Russian] 2002
327. T. Pöschel, C. Saluena, T. Schwager T: Scaling properties of granular materials. *Phys. Rev. E* **64**, art. no. 011308 Part 1 (2001)
328. J.G. Potyondy: Skin friction between soils and construction materials. *Geotechnique* **11**, 339–353 (1961)
329. O. Pouliquen: Scaling laws in granular flows down rough inclined planes. *Physics Fluids* **11** (3), 542–548 (1999)
330. O. Pouliquen, Y. Forterre: Friction law for dense granular flows: application to the motion of a mass down a rough inclined plane. *J. Fluid Mech.* **453**, 133–151 (2002)
331. Product information *Metz Mecablitz* (2000)
332. Product information *Nikon Nikkor Objektive* (2000)
333. S.P. Pudasaini, J. Mohring: Mathematical model and experimental validation of free surface size segregation for polydisperse granular materials. *Granul. Matter* **4**, 45–56 (2002)
334. S.P. Pudasaini: *Dynamics of Flow Avalanches Over Curved and Twisted Channels: Theory, Numerics and Experimental Validation.* PhD Dissertation, Darmstadt University of Technology, Germany (2003)
335. S.P. Pudasaini, K. Hutter: Rapid shear flows of dry granular masses down curved and twisted channels. *J. Fluid Mech.* **495**, 193–208 (2003)
336. S.P. Pudasaini, K. Hutter: Granular Avalanche Model in Arbitrarily Curved and Twisted Mountain Terrain: a Basis for the Extension to Debris Flow. In: D. Rickenmann, C.-L. Chen (eds): *Debris-Flow Hazards Mitigation: Mechanics, Prediction and Assessment, Vol. 1.* (Millpress, San Francisco 2003) pp 491–502
337. S.P. Pudasaini, W. Eckart, K. Hutter: Gravity-driven rapid shear flows of dry granular masses in helically curved and twisted channels. *Math. Mod. Meth. Appl. Sci.* **13**(7), 1019–1052 (2003)

338. S.P. Pudasaini, K. Hutter, W. Eckart: Gravity-driven rapid shear flows of dry granular masses in topographies with orthogonal and non-orthogonal metrics. In: K. Hutter, N. Kirchner (eds): *Dynamic Response of Granular and Porous Materials under Large and Catastrophic Deformations* (Springer, Berlin Heidelberg New York 2003) pp 43–82
339. S.P. Pudasaini, Y. Wang, K. Hutter: Porous Effects in the Description of the Dynamics of Granular Avalanches. In: J.M. Huyghe, P.A. C. Raats, S.C. Cowin (eds): *IUTAM Proceedings on Physicochemical and Electromechanical Interactions in Porous Media.* (Springer, Berlin Heidelberg New York 2005) pp 81–89
340. S.P. Pudasaini, Y. Wang, K. Hutter: Dynamics of avalanches along general mountain slopes. *Ann. Glacol.* **38**, 357–362 (2005a)
341. S.P. Pudasaini, Y. Wang, K. Hutter: Rapid motions of free surface avalanches down curved and twisted channels and their numerical simulation. *Phil. Trans. R. Soc. A*, **363**, 1551–1571 (2005b)
342. S.P. Pudasaini, Y. Wang, K. Hutter: Modelling debris flows down general channels. *Natural Hazards and Earth System Sciences* **5** (2005c)
343. S.P. Pudasaini, S.-S. Hsiau, Y. Wang, K. Hutter: Velocity measurements in dry granular avalanches using particle image velocimetry technique and comparison with theoretical predictions. *Physics Fluids* **17**(9) (2005)
344. S.P. Pudasaini, Y. Wang, L.-T. Sheng, S.-C. Tai, S.-H. Chou, S.-S. Hsiau, K. Hutter: Avalanching granular flow down curved and twisted channels: Theory and particle tracking velocimetry (PTV) experiments. Preprint, Department of Mechanics, Darmstadt University of Technology (2005)
345. M. Quecedo, M. Pastor: Journal element modelling of free surface flows on inclined and curved beds. *J. Comput. Physics* **189**, 45–62 (2003)
346. M. Quecedo, M. Pastor, M.I. Herreros: Numerical modelling of impulse wave generated by fast landslides. *Int. J. Numer. Meth. Engng.* **59**, 1633–1656 (DOI: 10.1002/nme.934) (2004)
347. M. Quecedo, M. Pastor, M.I. Herreros, J.A. Fernández Merodo: Numerical modelling of the propagation of fast landslides using the finite element method. *Int. J. Numer. Meth. Engng.* **59**, 755–794 (DOI: 10.1002/nme.841) (2004)
348. M.R. de Quervain: Avalanche problems of Iceland. Analysis and recommendation for further action. *(Davos, Eidg. Inst. für Schnee- und Lawinenforschung, Rep. G75.51)* (1975)
349. M. de Quervain, R. Meister: 50 years of snow profiles on the Weissfluhjoch and relations to the surrounding avalanche activity (1936/37-1985/86). In: B. Salm, H.-U. Gubler (eds): *Avalanche Formation, Movement and Effects.* (IAHS Publ. 162, September 14–19, 1986). (IAHS, 1987) 161–181
350. E. Rabofsky: Entwicklung des Wissenstandes über Lawinen in Österreich. In: P. Baumgartner, E. Rabofsky (Ed.): *Sicherheit im Bergland* (Jahrbuch, 1985) pp 193–204
351. E. Rabofsky: *Ziele der Lawinenforschung in Österreich.* (Auftrag des Bundesministeriums für Wissenschaft und Forschung, Z1.5.085/2-23/1976) (1977)
352. M. Raffel, C. Willert, J. Kompenhans: *Particle Image Velocimetry.* (Springer, Berlin Heidelberg New York 1998)
353. J. Rajchenbach: Flow in powders: From avalanches to continuous regime. *Phys. Rev. Lett.* **65**, 2221–2225 (1990)

354. O. Reynolds: On the dilatancy of media composed of rigid particles in contact. *Phil. Mag. Ser.* **5**(20), 469–481 (1885)
355. D. Rickenmann, T. Koch: Comparison of debris flow modelling approaches. In: C.-L. Chen (Ed.): *Proceedings of the 1st International Conference on Debris-Flow Hazards Mitigation: Mechanics, Prediction and Assessment* (ASCE, New York 1997)
356. G.H. Ristow: Molecular dynamics simulations of granular materials on the Intel iPSC/860. *Int. J. Mod. Phys. C* **3**, 1281–1293 (1992)
357. G.H. Ristow: Particle mass segregation in a two-dimensional rotating drum. *Europhys. Lett.* **28**, 97–101 (1994)
358. A.W. Roberts: An investigation of the gravity flow of noncohesive granular materials through discharge chutes. *SMSE Trans., J. Eng. Ind.* **91**, 373–381 (1969)
359. A.V. Rodionov: Methods of increasing the accuracy in Godunov's scheme. *J. Comput. Math. Math. Phys.* **27**(12), 1853–1860 (1987)
360. G.G. Saatchan: Sneg I snezhnye obvaly [Snow and snow cover collapses]. *Trudy Tbilisskogo Instituta Sooruzhenii* [Transactions of the Tbilisi Institute of Constructions] **27**, 1–59 (1963)
361. B. Salm: Contribution to avalanche dynamics. In: *IAHS AISH Publ. 69.* (IAHS, 1966) 199–214
362. B. Salm: On nonuniform, steady flow of avalanching snow. In: *International Association of Scientific Hydrology (General Assembly of Bern* 1967 – *Snow and Ice).* (IAHS Publication 79) (1968) 19–29
363. B. Salm: A constitutive equation for creeping snow. In: *IAHS AISH Publ. 114* (1975) 222–235
364. B. Salm: Mechanical properties of snow. *Rev. Geophys. Space Phys.* **20**(1), 1–19 (1982)
365. B. Salm, A. Burkard, H.U. Gubler: Berechnung von Fliesslawinen; eine Anleitung für Praktiker mit Beispielen. *(Mitteilungen des Eidgenössischen Inituts für Schnee- und Lawinenforschung 47)*, (Davos 1987)
366. B. Salm, H. Gubler: Measurement and Analysis of dense flow of avalanches. *Ann. Glaciol.* **6**, 26–34 (1985)
367. B. Salm, B. Zam, V. Bigger: Vorlesung: Schnee, Lawinen und Lawinenschutz. ETH Zürich. Mimeographed Notes (Davos, EISLF, 1987)
368. G. Sartoris, P. Bartelt: Upwinded finite difference schemes for dense snow avalanche modeling. *Int. J. Numer. Meth. Fluids* **32**, 799–821 (2000)
369. S.B. Savage: Gravity flow of cohesionless granular-materials in chutes and channels. *J. Fluid Mech.* **92**, 53–96 (1979)
370. S.B. Savage: Granular flows down rough inclines – review and extension. In: J. Jenkins, M. Satake (eds): *Mechanics of Granular Materials: New Models and Constitutive Relations.* (Elsevier, Amsterdam 1983) pp 261–282
371. S.B. Savage, S. McKeown: Shear stresses developed during rapid shear of concentrated suspensions of large spherical-particles between concentric cylinders. *J. Fluid Mech.* **127**, 453–472 (1983)
372. S.B. Savage, M. Sayed: Stresses developed by dry cohesionless granular-materials sheared in an annular shear cell. *J. Fluid Mech.* **142**, 391–430 (1984)
373. S.B. Savage, Y. Nohguchi: Similarity solutions for avalanches of granular-materials down curved beds. *Acta Mech.* **75**, 153–174 (1988)

374. S.B. Savage: Flow of granular materials. In: P. Germain, M. Piau, D. Caillerie (eds): *Theoretical and Applied Mechanics.* (Elsevier, Amsterdam 1989) pp 241–266
375. S.B. Savage, K. Hutter: The motion of a finite mass of granular material down a rough incline. *J. Fluid Mech.* **199**, 177–215 (1989)
376. S.B. Savage, K. Hutter: Dynamics of avalanches of granular materials from initiation to runout. Part I: Analysis. *Acta Mech.* **86**, 201–223 (1991)
377. P.A. Schaerer, A.A. Salway: Seismic and impact-pressure monitoring of flowing avalanches. *J. Glaciol.* **26**(94), 179–187 (1980)
378. H. Schaffhauser: Aufgaben und Ziele der Lawinenforschung seit 1985. In: F. Rühm (ed): *Waldforschung an der FBVA 1984–1994.* (FBVA, 1985) 77–82
379. A.E. Scheidegger: On the prediction of the reach and velocity of catastrophic landslides. *Rock Mech.* **5**, 231–236 (1973)
380. T. Scheiwiller, K. Hutter: Lawinendynamik, Übersicht über Experimente und theoretische Modelle von Fliess- und Staublawinen. *(Mitteilung Nr. 81 Versuchsanstalt für Wasserbau, Hydrologie und Glaziologie, ETH Zürich)* (1982)
381. T. Scheiwiller: *Dynamics of powder snow avalanche.* (Mitteilung Nr. 81 Versuchsanstalt für Wasserbau, Hydrologie und Glaziologie, ETH Zürich) (1986)
382. M. Schneebeli, M. Laternser, P. Föhn, W.J. Ammann: *Wechselwirkungen zwischen Klima, Lawinen, und technischen Massnahmen.* (VDF, Zürich 1998)
383. J. Selby: Rock slopes. In: R. Anderson (Ed.): *Slope stability.* (Wiley, New York 1987) pp 475–504
384. I.V. Severskii, V.P. Blagoveshchenskii: Otsenka lavinnoi opasnosti gornoiterritorii [Estimation of avalanche danger of a mountain region]. (Alma-Ata, Nauka, 1983)
385. M.F. Sheridan, J.L. Macias: Estimation of risk probability for gravity-driven pyroclastic flows at Volcano Colima, Mexico. *J. Volcanol. Geoth. Res.* **66**, 251–256 (1995)
386. M.F. Sheridan, C.L. Bloebaum, T. Kesavadas, A.K. Patra, E. Winer: Visualization and communication in risk management of Landslides. In: C.A. Brebbia (ed): *Risk Analysis III.* (WIT Press Southampton, 2002) pp 691–701
387. M.F. Sheridan, A.J. Stinton, A.K. Patra, E.B. Pitman, A.C. Bauer, C. Nichita: Evaluating TITAN2D mass flow using the 1963 Little Tahoma Peak Avalanches. *J. Volcanol. Geoth. Res.* **139**(1–2), 89–102 (2005)
388. M. Shoda: An experimental study on dynamics of avalanching snow. In: *Proceedings of the International Symposium on Scientific Aspects of Snow and Ice Avalanches.* (April 5-10, 1965, Davos, Switzerland), (IASH-AIHS, Publication, No. 69, 1966) pp 215–229
389. R.L. Shreve: Shermann landslide Alaska. *Science* **154**, 1639–1643 (1966)
390. H. Shimizu, T. Huzioka: Internal strains and stresses of snow cover on slopes. In: *Snow Mechanics: Proceedings of Grindelwald Symposium.* (April 1–5, 1974), (IAHS-AISH Publication, No. 114, 1975) pp 321–331
391. W. Siemes, L. Hellmer: Die Messung der Wirbelschichtviskosität mit der pneumatischen Rinne. *Chem. Eng. Sci.* **17**, 555–571 (1962)
392. F. Sigurðsson, K. Jónasson, Th. Arnalds: Transferring avalanches between paths. In: E. Hestnes (Ed.): *25 years of Snow Avalanche Research.* (Publikation nr. 203), (NGI, Oslo 1998) pp 259–263
393. F. Sigurðsson, G.G. Tómasson, F. Sandersen: Avalanche defences for Flateyri, Iceland. From hazard evaluation to construction of defences. In: E. Hestnes

(Ed.): *25 years of Snow Avalanche Research.* (Publikation nr. 203), (NGI, Oslo 1998) pp 254–258
394. H.P. Sigurðsson, T. Jóhannesson, H. Gubler, K. Kristensen, E. Lied, P. Gauer: *Temporary installation of a CW-Doppler radar at the Ryggfonn full-scale avalanche test site in western Norway.* Reykjavík, Icel. Meteorol. Office, Rep. G04025 (2004)
395. J.E. Simpson: *Gravity Currents in the Environment and the Laboratory* (Cambridge University Press, Cambridge, 1997)
396. V.P. Singh: Disasters: Natural or Man-made. In: V.P. Singh (Ed.): *Hydrology of Disaster.* (Kluwer, Dordrecht 1996) pp 1–18
397. *Sino-Geotechnics, Research and Development Foundation, Taipei, Taiwan* **57** (1996)
398. I.S. Sokolnikoff: *Tensor Analysis Theory and Applications.* (Wiley, New York 1951)
399. L.S. Solove'v, V.D. Shafranov: Plasma confinement in closed magnetic system. *Rev. Plasma Phys.* **5** (1970)
400. T. Sonar: *Mehrdimensionale ENO-Verfahren* (Teubner, Stuttgart 1997)
401. J. Soussa, B. Voight: Continuum simulation of flow failures. *Geotechnique* **41**, 515–538 (1991)
402. R. Stadler, H. Buggisch: Influence of the deformation rate on shear stress in bulk solids: theoretical aspects and experimental results. In: *Reliable Flow of Particulate Solids.* (EFCE Publication Series No. 49), (Bergen, Norway 1985)
403. R. Stadler: *Stationäres, schnelles Fliessen von dicht gepackten trockenen und feuchten Schüttgütern.* PhD Dissertation, University Karlsruhe, Karlsruhe, Germany (1986)
404. S. Steinemann: Experimentelle Untersuchungen zur Plastizität von Eis: Beiträge zur Geologie der Schweiz. *Hydrologie* **10** (1958)
405. J.J. Stoker: *Water Waves.* (Interscience, New York 1957)
406. S. Straub: *Schnelles granular Fließen in subaerischen pyroklastischen Strömen.* PhD Dissertation, Bayerische Julius-Maximilians-Universität Würzburg, Germany (1994)
407. Swiss Guidelines. Original title: "Richtlinien für den Lawinenverbau im Anbruchgebiet". BUWAL, WSL, Eidg. Institut für Schnee- und Lawinenforschung, 1990.
408. G.K. Sulakvelidze: K voprosu ob obrazovanii I dvizhenii snezhnykh lavin [On formation and movement of snow avalanches], *Trudy institua fiziki I geofiziki AN GruzSSR* [Transactions of the Institute of Physics and Geophysics of the Academy of Sciences of Georgian Soviet Socialist Republic] **11**, 101–110 (1949)
409. P.K. Sweby: High resolution schemes using flux limiters for hyperbolic conservative laws. *SIAM J. Numer. Anal.* **21**(5), 995–1101 (1984)
410. Y.C. Tai, J.M.N.T. Gray: Limiting stress states in granular avalanches. *Ann. Glaciol.* **26**, 272–276 (1998)
411. Y.C. Tai, Y. Wang, J.M.N.T. Gray, K. Hutter: Methods of similitude in granular avalanche flows. In: K. Hutter, Y. Wang, H. Beer (eds): *Advances in Cold-Region Thermal Engineering and Sciences.* (Springer, Berlin Heidelberg New York 1999) pp 415–428
412. Y.C. Tai: *Dynamics of Granular Avalanches and Their Simulations with Shock-Capturing and Front-Tracking Numerical Schemes.* PhD Dissertation, Darmstadt University of Technology, Darmstadt, Germany (2000)

413. Y.C. Tai, K. Hutter, J.M.N.T. Gray: Steady motion of a finite granular mass in a rotating drum. *Chin. J. Mech.* **16**(2) 67–72 (2000)
414. Y.C. Tai, J.M.N.T. Gray, K. Hutter: Dense granular avalanches: mathematical description and experimental validation. In: N.J. Balmforth, A. Provenzale (eds): *Geomorphological Fluid Mechanics.* (Springer, Berlin Heidelberg New York 2001) pp 339–366
415. Y.C. Tai, S. Noelle, J.M.N.T. Gray, K. Hutter: Shock-capturing and front-tracking methods for granular avalanches. *J. Comput. Phys.* **175**, 269–301 (2002)
416. T. Takahashi: *Debris flow.* (IAHR-AIRH Monograph Series A), (Balkema, Rotterdam 1991)
417. J. Tejchman, W. Wu: Experimental and numerical study of sand-steal interfaces. *Int. J. Num. Anal. Meth. Geomech.* **19**, 513–536 (1995)
418. T.W. Tesche: A three dimensional dynamic model of turbulent avalanche flow. In: *Proc. Int. Snow Science Workshop* (Lake Tahoe, CA 1986) pp 1–27
419. The Ministry for the Environment, Iceland: *Reglugerð nr. 505/2000 um hættumat vegna ofanflóða, flokkun og nýtingu hættusvæða og gerð bráðabirgðahættumats* [Regulation on hazard zoning due to snow- and landslides classification and utilisation of hazard zones and preparation of provisional hazard zoning]. [Available in an English translation] (2000)
420. P.D. Thomas, C.K. Lombard: Geometric conservation law and its applications to flow computations on moving grids. *AIAA J.* **17**, 1030–1037 (1979)
421. K.M. Theuerdank: *(Kaiser Maximilian's Theuerdank): Facsimile edition of the original edition of 1517.* (Verlag Müller and Schindler, Plochingen Stuttgart 1968)
422. P.A. Thompson, G.S. Grest: Granular flow: Friction and the dilatancy transition. *Phys. Rev. Lett.* **67**, 1751–1754 (1991)
423. M. Tischer, M.I. Bursik, E.B. Pitman: Kinematics of sand avalanches using particle image Velocimetry. *J. Sediment. Res.* **71**(3), 355–364 (2001)
424. E.F. Toro: *Riemann solvers and numerical methods for fluid dynamics.* 2nd edition. (Springer, Berlin Heidelberg New York, 1999)
425. E.F. Toro: *Shock-Capturing Methods for Free-Surface Shallow Flows.* (Springer, Wiley, 2001)
426. G. Tóth, D. Odstrčil: Comparison of some flux corrected transport and total variation diminishing numerical schemes for hydrodynamic and magnetohydrodynamic problems. *J. Comput. Phys.* **128**(1), 82–100 (1996)
427. G.K. Tustinskii: *Laviny. Vozniknovenie I zashchita ot nikh* [Avalanches. Appearance and protection]. (Geografgiz, Moscow 1949)
428. N. Vandewalle: Phase segregation and avalanches in multispecies sandpiles. *Physica A* **272**, 450–458 (1999)
429. J.P. Vila: *Sur la théorie et l'approximation numérique des peoblèmes hyperboliques non-linéaries, application aux équations de Saint-Venant et à la modélisation des avalanches denses.* Thèse de Doctorat, Paris VI (1986)
430. A. Voellmy: Über die Zerstörungskraft von Lawinen. *Schweizerische Bauzeitung* **73**, 159–162, 212–217, 246–249, 280–285 (1955)
431. P. Vollmöller: A shock-capturing wave-propagation method for dry and saturated granular flows. *J. Comput. Phys.* **199**, 150–174 (2004)
432. N.A. Volodicheva, E.M. Mironova, A.D. Oleinikov, M.E. Eglit: The use of mathematical modelling to determine the boundaries of propagation of

avalanches. *Materialy Glyatsiologicheskikh Issledovaniy* [Data of Glaciological Studies] **56**, 78–81 [In Russian with English summary] (1986)
433. B. Voight (Ed.): *Rockslides and Avalanches, Vols. I and II.* (Elsevier, New York 1978)
434. K.F. Voitkovskii: *Lavinovedenie.* [Avalanches study] (Moscow, Moscow State University, 1989)
435. Th. von Kármán: Über laminare und turbulente Reibung. *ZAMM* **1**, 233–252 (1921)
436. L. Vulliet, K. Hutter: Viscous-type sliding laws for landslides. *Can. Geotech. J.* **25**, 467–477 (1988)
437. O.R. Walton, R.L. Braun: Simulation of rotary-drum and repose tests for frictional spheres and rigid sphere clusters. In: *Joint DOE/NSF Workshop on Flow of Particulates and Fluids.* (September 29–October 1, Ithaca, NY) (1993)
438. Z. Wang, H.T. Shen: Lagrangian simulation of one-dimensional dam-break flow. *J. Hydr. Engin.* **125**(11), 1217–1220 (1999)
439. Y. Wang, K. Hutter: Comparisons of numerical methods with respect to convectively-dominated problems. *Int. J. Numer. Meth. Fluids* **37**, 721–745 (2001)
440. Y. Wang, K. Hutter, S.P. Pudasaini: The Savage–Hutter Theory: a system of partial differential equations for avalanche flows of snow, debris and mud. *ZAMM* **84**(8), 507–527 (2004)
441. J. Werther: Measurement techniques in fluidized beds. *Powder Technology* **102**, 15–36 (1999)
442. J. Westerweel, D. Dabiri, M. Gharib: The effect of a discrete window offset on the accuracy of cross-correlation analysis of digital PIV recordings. *Exp. Fluids* **23**, 20–28 (1997)
443. K.X. Whipple: Open-channel flow of Bingham fluids: Applications in debris-flow research. *J. Geol.* **105**, 243–262 (1997)
444. M. Wieland: *Experimentelle und theoretische Studie einer in eine Ebene sich ausbreitenden Runsenlawine oder eines Bergsturzes.* Diploma Thesis, Darmstadt University of Technology, Darmstadt, Germany (1995)
445. M. Wieland, J.M.N.T. Gray, K. Hutter: Channelized free surface flow of cohessionless granular avalanches in a chute with shallow lateral curvature. *J. Fluid Mech.* **392**, 73–100 (1999)
446. H.C. Yee: Construction of explicit and implicit symmetric TVD schemes and their applications. *J. Comput. Phys.* **68**, 151–179 (1987)
447. L. Zabielski, A.J. Mestel: Steady flow in a helically symmetric pipe. *J. Fluid Mech.* **370**, 297–320 (1998)
448. L. Zabielski, A.J. Mestel: Unsteady blood flow in a helically symmetric pipe. *J. Fluid Mech.* **370**, 321–345 (1998)
449. T. Zwinger: *Dynamics of Dry Snow Avalanches on Natural Terrains.* PhD Dissertation, Vienna University of Technology, Austria (2000)
450. T. Zwinger, A. Kluwick, P. Sampl: Avalanche flow of dry snow over natural terrain. Part II: numerical simulation. In: K. Hutter, N. Kirchner (eds): *Dynamic Response of Granular and Porous Materials under Large and Catastrophic Deformations.* (Springer, Berlin Heidelberg New York 2003)
451. http://www.rcsd.k12.ms.us/∼web08/bhs_main/teachers/WEB_JHOLLIS/avalanches2.htm

452. http://www.natives.co.uk/news/2001/1101/25ava.htm
453. http://www.coe.montana.edu/ce/research/Dent/instrumentation.htm
454. http://www.pbs.org/newshour/bb/weather/jan-june99/snow_2-25.html
455. http://www.unisdr.org/unisdr/forum/avawmo.htm
456. http://www1.brunel.ac.uk/depts/geo/iainsub/Disasters/aval.html
457. http://www.crealp.ch/en/contenu/crealp_gondo_photos.asp
458. http://www.avalanche.org/∼moonstone/ISSW%2098/harald.htm
459. http://www.janod.biz/services/snowavalanche.htm
460. http://cnh.caminos.upm.es/index.php
461. http://www.solarviews.com/eng/mars.htm
462. http://www.earthsci.unimelb.edu.au/mars/Avalanche.html
463. http://www.ei-montagne.fr/index-gb.htm
464. http://www.avalanche.org/∼issw/96/art55.html
465. http://www.nepalnews.com/
466. http://www.issw.noaa.gov/avalanche_dynamics.htm
467. http://www.gmfg.buffalo.edu/pubs.php
468. http://www.tsi.com/
469. http://www.emergency.com/turkydis.htm
470. http://www.rcsd.k12.ms.us/∼web08/bhs_main/teachers/WEB_JHOLLIS/avalanches2.htm

Name Index

Index